Universität Stuttgart

Quantum Monte Carlo Studies of Strongly Correlated Systems for Quantum Simulators

Von der Fakultät Mathematik und Physik der Universität Stuttgart zur Erlangung der Würde eines Doktors der Naturwissenschaften (Dr. rer. nat.) genehmigte Abhandlung.

Vorgelegt von

Stephan Humeniuk

aus Freiburg i. Br.

Hauptberichter:	Prof. Dr. Hans Peter Büchler	-	Universität Stuttgart
Mitberichterin:	Prof. Dr. Maria Daghofer	-	Universität Stuttgart
Mitberichter:	Prof. Dr. Stefan Weßel	-	RWTH Aachen

Tag der mündlichen Prüfung: 21. Juni 2018

Institut für Theoretische Physik III
Universität Stuttgart
2018

Kurzzusammenfassung

Viele stark korrelierte Quantensysteme entziehen sich einer exakten numerischen Computersimulation aufgrund der exponentiell anwachsenden Größe des Hilbertraums verbunden mit dem Versagen effizienter numerischer Verfahren in wichtigen Parameterbereichen. Dies erschwert das theoretische Verständis ungelöster Fragestellungen der Festkörperphysik; Beispiele sind die Hochtemperatursupraleitung und der frustrierte Magnetismus. Eine Lösung des Problems versprechen sogenannte Quanten-Simulatoren, experimentelle (synthetische) Quanten-Systeme, die hochreine Modelle der Festkörperphysik mit genau kontrollierbaren Parametern realisieren können, wobei die Komplexität schrittweise erhöht werden kann. Diese Dissertation beschäftigt sich mit numerischen Simulationen, die durch Quanten-Simulatoren motiviert sind.

Mithilfe großangelegter Quanten-Monte-Carlo-Simulationen sowie Molekularfeldtheorie wird das Grundzustands-Phasendiagramm kalter Ionen in einer Penningfalle bestimmt, die als Quantensimulator ein langreichweitiges Ising-Modell im transversen Feld und auf dem Dreiecksgitter realisieren. Weiterhin untersuchen wir die thermischen und Quanten-Phasenübergänge eindimensionaler Ising-Ketten im transversen Feld, welche einen Kosterlitz-Thouless-Übergang und Universalitätsklassen mit kontinuierlich variierenden kritischen Exponenten aufweisen.

Der zweite Teil dieser Dissertation behandelt das Fermi-Hubbard-Modell, das gerade im mehreren Experimenten weltweit mit ultrakalten Atomen in optischen Gittern sowohl für repulsive als auch attraktive Wechselwirkungen realisiert wurde. Ein Quantengas-Mikroskop erlaubt es in diesen Experimenten, die Verteilungsfunktion der Teilchenanzahl mit Einzel-Atom-Auflösung in projektiven Messungen zu bestimmen. In dieser Arbeit wurde eine Methode entwickelt, um solche "full counting statistics" für quadratische kollektive Operatoren wie zum Beispiel die Teilchenanzahl oder Magnetisierung auf einem Subsystem mittels Determinanten-Quanten-Monte-Carlo zu berechnen. Eine Analyse der "full counting statistics" liefert Aufschluss über die Größe der Cooper-Paare oder nicht langreichweitig phasenkohärenter gebundener Zustände im attraktive Hubbard-Modell. Die ausgezeichnete Übereinstimmung der numerisch berechneten Wahrscheinlichkeitsverteilung der Néel-Magnetisierung mit Ergebnissen eines Experiments unter einem Quantengas-Mikroskop zeigt, dass gegenwärtige Experimente in der Lage sind, zwischen dem Hubbard-Modell und seinem Grenzfall für starke Wechselwirkungen, dem Heisenberg-Modell, zu unterscheiden.

Ein ausführlicher Methodenteil gibt eine Übersicht über die "Stochastic Series Expansion" Quanten-Monte-Carlo-Methode für Ising-Modelle im transversen Feld, die für beliebige Wechselwirkungen kein Vorzeichenproblem aufweist, wobei die effiziente Simulation langreichweitiger Wechselwirkungen im Mittelpunkt steht. Die Determinanten-Quanten-Monte-Carlo-Methode wird ebenfalls eingeführt.

Abstract

Many strongly correlated quantum systems are difficult to study numerically because of the exponential growth of the Hilbert space combined with the failure of numerical methods in important parameter regimes. This includes the long-standing problems of high-temperature superconductivity and frustrated magnetism. A promising solution to this dilemma are *quantum simulators*, well-controlled (synthetic) quantum systems, emulating model Hamiltonians not only of condensed matter systems, where parameters can be tuned at will and model complexity can be added step by step. This dissertation presents numerical simulation studies that are motivated by quantum simulators.

Using large-scale quantum Monte Carlo computer simulations and mean-field theory the semiquantitative ground state phase diagram of a Penning ion trap quantum simulator, realizing a two-dimensional model of quantum magnetism with long-range interactions, is obtained. We study also thermal and quantum phase transitions in one-dimensional transverse-field Ising models with long-range interactions, which exhibit a Kosterlitz-Thouless transition and universality classes with continuously varying critical exponents.

The second part of this thesis is concerned with the Fermi-Hubbard model, which has been realized recently with ultracold atoms in optical lattices, both for repulsive and attractive interactions. Equipped with a quantum gas microscope, which allows single-site single-atom detection, these experimental setups can collect histograms of the particle number from repeated projective measurements. This dissertation presents a method to compute such *full counting statistics* for quadratic operators such as particle number or magnetization in the framework of determinantal quantum Monte Carlo. From an analysis of the full counting statistics of the particle number for different subsystem sizes the size of preformed pairs or Cooper pairs in the attractive Hubbard model is inferred. Furthermore, excellent agreement of the numerically computed probability distribution of the staggered magnetization with a recent quantum gas experiment demonstrates that current experiments are capable of resolving the differences between the Hubbard model and its limiting Heisenberg model.

An extensive method section reviews the stochastic series expansion quantum Monte Carlo method for Ising models in a transverse field, which is free of the sign problem for arbitrary interactions, with special emphasis on the efficient simulation of long-range interactions. Also a self-contained introduction to the determinantal quantum Monte Carlo method is provided.

Contents

Appendices   259

A   Hubbard-Stratonovich transformation   259

B   The Trotter-Suzuki mapping for quantum Ising models   263

C   Full counting statistics for a BCS mean-field state   267

D   Wick's theorem and determinant formula   269

E   List of symmetry-related classes of states for a single plaquette   273

List of Figures

Chapter 1

Introduction

Many phenomena of condensed matter physics are described by an effective single-particle picture. This is the basic assumption underlying simple band structure calculations. A very successful theory of the normal state of metals, Landau's famous Fermi liquid theory [1, Chapt. 1], describes the electrons interacting through the Coulomb repulsion in terms of non-interacting quasiparticles which are "dressed" by the interactions and have the same quantum numbers as free electrons. Even in the case of magnetically ordered states, which arise from very strong electron-electron repulsion, often the low-temperature and low-energy properties are governed by small fluctuations around the ordered state; if these bosonic quasiparticle excitations, which are called spin waves or magnons, are weakly interacting, again a single-particle description is appropriate [2, Chapt. 6]. However, if the interactions between quasiparticles are very strong, the energy spectrum of the many-particle system can no longer be expressed by filling up single-particle energy eigenstates and one has to solve the problem in the many-body basis. These are *strongly correlated systems*, where, through interactions between the quasiparticles, the bands themselves depend on the filling. This terminology emphasizes the role which the instantaneous correlations between particles (rather than the mere strength of interactions) play in rendering a description in terms of non-interacting entities, which interact with the "mean-field" caused by the other particles, invalid.

An exact diagonalization of the full many-body Hamiltonian is often impossible for systems that are large enough to capture the relevant physics due to the exponential increase of the Hilbert space with system size. Nonetheless, powerful numerical methods [3] exist to overcome this "exponential wall". The quantum Monte Carlo technique can, when it is applicable, sample the relevant contributions to exponentially large sums in polynomial time. Although Hilbert space is a very large space in principle, the quantum states in the relevant portions can sometimes be parametrized by a polynomial number of coefficients. To be more explicit, the ground states of all local gapped Hamiltonians are characterized by an area of the entanglement entropy [4], which means that at least in one spatial dimension they can be described accurately by a matrix product state [3]

with a number of variational parameters which is not exponential. However, in some of the most interesting cases the quantum Monte Carlo method fails due to the infamous sign problem, while generalizations of matrix product states in dimension larger than one become inefficient due to an exponential growth of entanglement with system size. Strongly correlated problems for which numerical simulations are extremely challenging include the question of high-temperature superconductivity in cuprate compounds [5], where both the charge and spin degrees of interacting fermions play a role, and the controversial search for exotic quantum states in frustrated spin systems, so-called quantum spin liquids [6, 7], which are characterized by long-range entanglement.

As a general solution of the quantum many-body problem the idea of a *quantum simulator* has been put forward by Feynman [8, 9], i.e. using a well-controlled quantum system, where the parameters can be tuned at will, to emulate another quantum system, adding complexity step by step. A number of promising platforms for quantum simulation have been developed in the last decades. With regard to addressing many-body problems, two of the most advanced ones are ultracold atoms in optical lattices [10] and ion traps [11].

An optical lattice is a crystal of light that stores neutral atoms in an array of optical dipole traps. The trapping mechanism is the interaction of an oscillating light field, provided by a laser beam, with the induced dipole moment of the atom. If the frequency of the laser light is off-resonant with respect to the selected electronic transition, resonant absorption and the subsequent spontaneous emission processes are suppressed and the trapping potential is purely conservative. By superimposing laser beams to a standing wave, periodic optical potentials can be created. In this way an enlarged replica of a solid-state system is created, where the ultracold fermionic atoms (e.g. ^{6}Li or ^{40}K) can tunnel from site to site. Since they are much heavier than electrons, the time scales of motion are slowed down by orders of magnitude compared to solid state systems.

Optical lattice systems are very clean and highly tunable. The absence of phonons and other decay channels allows to observe theoretically proposed phenomena such as repulsively bound pairs [12] that cannot persist in solid state systems. Interactions can be tuned by varying the lattice depth and by changing the *s*-wave scattering length through a magnetic Feshbach resonance [10], which allows to realize both repulsive and attractive interactions in the strongly correlated regime. A particulary spectacular development of the rapidly evolving field of ultracold atoms is the single-site single-atom detection under a quantum gas microscope [13, 14]. Several recent experiments have realized both the repulsive [15–20] and the attractive [21, 22] two-dimensional (2D) Fermi-Hubbard model in such a setup at temperature scales that are already relevant for comparison with solid state materials.

Energies and temperatures have to be measured in units of the Fermi energy. The temperatures achieved to date for two-component ultracold fermionic quantum gases are in the nano-Kelvin regime. Measured in units of the Fermi energy of the dilute gas of fermionic atoms, which is a few tens of nK, this corresponds to a temperature of

a few hundred Kelvin in an equivalent solid state system. As ultracold atoms form well-isolated systems, the entropy per particle, rather than the temperature is the relevant physical quantity [10]. One of the main challenges for observing strongly correlated phases is the preparation of low-entropy states in the optical lattice. Even exact thermometry itself is a difficult problem in an isolated lattice system and often relies on comparison with numerical simulations [17, 20].

One of the most ambitious goals for studying the 2D Hubbard model with cold atoms is to learn something about the phase diagram of the cuprates, a strongly correlated system whose physics appears particularly rich and complicated. Fig. 1.1 shows a detailed schematic phase diagram of hole-doped cuprates [5]. An antiferromagnetic region around half filling quickly gives way to d-wave superconductivity upon doping. The most puzzling regions, which are believed to hold the key to the understanding of the phase diagram, are the *pseudogap* regime below a crossover temperature T^*, which shows tendencies to multiple competing orders, and the "strange" or "bad" metal phase, which is characterized by the absence of well-defined quasi-particles and exhibits a resistivity that is linear in temperature rather than quadratic, as for usual Fermi liquids. Furthermore, there are, most likely, multiple quantum critical points at zero temperature, which are masked by the superconducting region, but which are often regarded as an organizing principle of the entire phase diagram.

One does not expect all these phases to appear in the 2D Hubbard model, which is generally believed to describe certain aspects of the cuprate phenomenology, while the degree, to which it is a realistic model, is debated [23]. The problem comes from the fact that its phase diagram away from zero doping is not understood despite decades of research, which is related to the challenges for numerical methods in this regime. Recent cold atoms experiments have reached low enough temperature scales for observing antiferromagnetic correlations [17, 20] and may already be relevant e.g. for investigating anomalous properties related to the "strange metal" phase. At the same time these temperatures are still high enough so that numerically exact quantum Monte Carlo simulation can be performed in spite of a sign problem. The fact that the connection between very clean cold-atom experiments and realistic unsolved problems of condensed matter physics is not obvious illustrates the importance of numerically exact studies of model Hamiltonians both for benchmarking such quantum simulators and for identifying relevant phenomena. An important aspect is that the *attractive* Hubbard model, which has recently been realized under a quantum gas microscope [21, 22], can be simulated without a sign problem with unbiased quantum Monte Carlo simulations in its entire parameter regime [24–26]. This provides an opportunity for developing benchmarks and analysis techniques. In chapter 9 of this thesis a method is presented for measuring the size of Cooper pairs (or preformed pairs) [27] based on measurements with single-site and single-atom resolution.

The other topic of strongly correlated systems that is actively pursued with various quantum simulator platforms is frustrated magnetism [28, 29], where competing interactions lead to a huge ground state degeneracy that can give rise to emergent
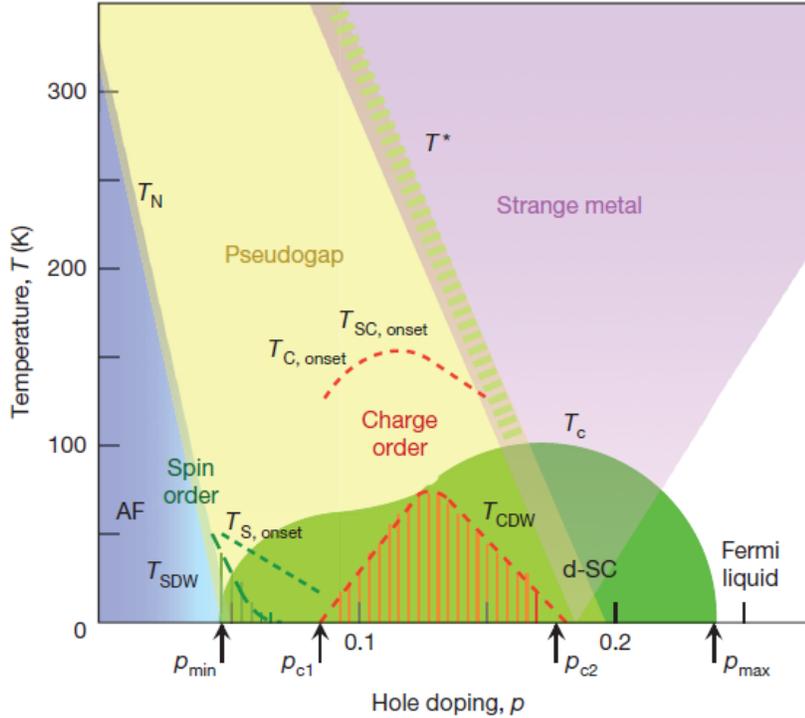
Fig. 1.1: Phase diagram of hole-doped cuprates as a function of doping and temperature. Reprinted with permission from Macmillan Publishers Ltd: *Nature*. B. Keimer et al., Nature **518**, 179 (2015) [5], © 2015.

phenomena governed by degrees of freedom that are quite distinct from those of the underlying spin system [28–30]. The simplest model of a frustrated quantum system is a frustrated Ising model augmented by quantum fluctuations due to a transverse field. These models have been studied entensively on different lattice geometries [31, 32]. A general picture is that quantum fluctuations tend to select an ordered state from the hugely degenerate ground state manifold of the classical frustrated model in a process called "order by disorder" [30–35].

Several synthetic transverse-field Ising systems are being developed as quantum simulators, notably trapped laser-cooled ions [11, 36, 37] and Rydberg atoms in optical dipoles traps [38, 39]. In both cases the interactions are naturally long-ranged, decaying like a power-law $J_{ij} = 1/|\mathbf{r}_i - \mathbf{r}_j|^\alpha$. In ultracold ions which are cooled down in their motion to a Coulomb crystal, electronic two-level system of the ions, serving as a spin-$\frac{1}{2}$ degree of freedom, are coupled through the normal modes of the ion crystal [36, 37]. This gives rise to long-range spin-spin interactions, which can be tuned to be ferromagnetic or antiferromagnetic [40–42]. Chapter 6 of this thesis presents quantum Monte Carlo simulations for long-range transverse-field Ising antiferromagnets on the triangular lattice, a system that has recently been realized in the Penning ion trap

quantum simulator of Ref. [41].

1.1   Overview

In Chapter 2 we review some general aspects of the Monte Carlo method and then introduce in Chapters 3 and 4 in detail the two quantum Monte Carlo (QMC) techniques we have used in this thesis, the Stochastic Series Expansion (SSE) QMC [43, Chapt. 5] for the simulation of spin systems and the determinantal QMC method for finite temperature simulation of itinerant fermion systems, which is based on the Blankenbecler-Scalapino-Sugar (BSS) algorithm [44]. The presentation of the SSE method includes a section on the computation of imaginary time correlation functions [45, 46]. Chapter 5 discusses the finite-size scaling method at second-order phase transitions for extracting critical exponents from numerical data on finite systems.

Motivated by the recent experiments with a Penning ion trap quantum simulator [41], we present in Chapt. 6 numerically exact SSE QMC simulations of long-range transverse-field (i.e. quantum) Ising models on a triangular lattice for different decay powers α of the interactions. The phase boundary for the ferromagnet is obtained as a function of α using finite-size scaling for the data analysis [47]. In the case of antiferromagnetic interactions, the mechanism "order by disorder", occuring in the nearest neighbour antiferromagnet on the triangular lattice, is found to persist for long-range interactions. A combination of mean-field theory and Lanczos exact diagonalization for small systems allows us to extend the Monte Carlo results to a semiquantitative phase diagram as a function of α and transverse field Γ. Furthermore, magnetization curves for the ferromagnet for experimentally relevant system sizes and with open boundary conditions are presented to facilitate direct comparison with possible future Penning ion trap experiments.

In Chapt. 7 we study the thermal and quantum phase transitions of one-dimensional (1D) ferromagnetic long-range Ising models in a transverse field Γ. For interactions decaying with distance r as $1/r^2$, there are topological defects (kinks and antikinks of the spin configuration), which interact with a potential that depends logarithmically on their distance, so that the thermal phase transition is of the Kosterlitz-Thouless (KT) type. It is characterized by an exponential divergence of the correlation length. Through a data collapse according to an appropriate finite-size scaling ansatz we demonstrate that, even in the presence of a transverse field, the thermal phase transition remains a Kosterlitz-Thouless transition. The transverse field reduces the critical temperature $T_{\mathrm{KT}}(\Gamma)$ and introduces a new length scale, the smeared width of a kink. Furthermore, the quantum ($T = 0$) phase transitions of long-range Ising chains are studied in detail. We determine the line of critical field $\Gamma_c(\alpha)$ as a function of the power law exponent α of the interactions and compare the critical exponents with values derived from dimensional analysis. The decay of the spin-spin correlation function in imaginary time gives evidence for the anisotropy of these quantum critical points. This means

that, unlike in the short-range quantum Ising model, critical correlation functions in the space and imaginary time direction decay with different power laws.

Chapter 8 introduces the symmetries and the phase diagram of the attractive Fermi-Hubbard model as well as other aspects which are relevant for the subsequent chapters.

Chapters 9, 10 and 11 are devoted to the Fermi-Hubbard model and its realization with ultracold atoms in optical lattices, specifically in experimental setups that are equipped with a quantum gas microscope. In chapter 9, we present a method for computing the full probability distribution function of quadratic observables such as particle number or magnetization for the Fermi-Hubbard model [27] within the framework of determinantal quantum Monte Carlo. In cold atoms experiments with single site resolution, such a full counting statistics (FCS) can be obtained from repeated projective measurements. We demonstrate, that the full counting statistics can provide important information on the size of "preformed pairs", which appear in the normal state of the attractive Hubbard model for large interactions and can be regarded as the precursors of Cooper pairs before long-range phase coherence and superconductivity sets in at lower temperature. We compute the full counting statistics of the staggered magnetization in the repulsive Hubbard model at half filling (i.e. at average particle number per site $\langle n_i \rangle = 1$). From the excellent agreement with the recent experimental results of Mazurenko *et al.* [20] we conclude that current experiments are capable of probing the difference between the Hubbard model and the limiting Heisenberg model since they can resolve the dominant charge fluctuations which are responsible for the kinetic exchange mechanism of antiferromagnetism.

In ultracold atomic systems, time-of-flight absorption imaging reveals the momentum distribution function $\langle n_{\mathbf{k},\sigma} \rangle$ for the spin species $\sigma = \uparrow, \downarrow$ prior to release of the trapping potential. Information on momentum-momentum correlation functions $\langle n_{\mathbf{k},\uparrow} n_{\mathbf{k}',\downarrow} \rangle$ is contained in the *noise correlations* of those images [48]. Peaks in $\langle n_{\mathbf{k},\uparrow} n_{-\mathbf{k},\downarrow} \rangle$ for momenta $\mathbf{k}$ on the Fermi surface are a signature of "preformed pairs" or Cooper pairs formed from particles of opposite spin and opposite momenta. At half filling, the Hubbard model possesses an enlarged symmetry [49], which implies that in addition to superconducting fluctuations there are charge fluctuations of equal magnitude. We show in chapter 10 that both types of fluctuations are visible in the noise correlations as characteristic peaks. By considering an integrated noise correlation signal, we observe pairs at finite center of mass momentum. Finally, we attempt to link the divergence of the integrated noise signal to the divergence of the *s*-wave superconducting pairing structure factor, which may lead towards experimental finite-size scaling at the Kosterlitz-Thouless phase transition to the superconducting state.

While current quantum gas microscopes can measure the probabilities of Fock space configurations, i.e. the diagonal elements of the (reduced) density matrix describing a thermal state, this does not amount to full quantum state tomography (QST), since the off-diagonal matrix elements are still missing. We conclude in chapter 11 with a determinantal QMC calculation of all elements of the reduced density matrix on

a square plaquette embedded in a much larger system. This is done by exploiting the point group symmetry and particle number conservation which gives the reduced density matrix block diagonal structure and allows to attach symmetry labels to the eigenvalues.

Chapter 2

The Monte Carlo method

This chapter introduces the quantum Monte Carlo (QMC) method, which is a powerful technique for numerically exact simulations of strongly correlated quantum systems. In this thesis, we have employed it in two flavours: the Stochastic Series Expansion (SSE) method [43] for spin systems and the determinantal QMC (DQMC) method for interacting fermions in its finite temperature version, which is known as the Blankenbecler-Scalapino-Sugar (BSS) algorithm [44]. To set the stage for the exposition of the different QMC methods, we first review general aspects of the Monte Carlo technique.

2.1   The classical Monte Carlo method

The Monte Carlo method is a very general method for calculating high-dimensional integrals and has a vast scope of applications in many different fields of physics. One fundamental application is the calculation of the expectation value of an observable O in a many-body systems in statistical physics

$$\langle O \rangle_P = \int_\Omega d^d \vec{x}\, O(\vec{x}) P(\vec{x}), \tag{2.1}$$

where $\vec{x}$ is a vector in the d-dimensional integration space Ω and $P(\vec{x})$ is a probability distribution satisfying

$$P(\vec{x}) \geq 0 \quad \forall \vec{x} \in \Omega \quad \text{and} \quad \int_\Omega d^d x P(\vec{x}) = 1. \tag{2.2}$$

For a problem of classical statistical mechanics $P(\vec{x})$ is the Boltzmann distribution $P(\vec{x}) = \frac{1}{Z} e^{-\beta \mathcal{H}(\vec{x})}$ and a configuration is specified by $\vec{x} = (\{\mathbf{r}_j\}, \{\mathbf{p}_j\}) \in \mathbb{R}^{6N}$, i.e. the set of space and momentum coordinates of all particles in the $6N$-dimensional phase space.

The essence of the problem is that for conventional integration methods based on a quadrature formula the number of grid points that are required for a certain

accuracy scales very unfavourably with the number of dimensions [50, Chapt. 8]. The error for integration with quadrature formulae in d dimensions scales like $\mathcal{O}(M^{-a/d})$ with the number of sampling points M where a is an integer that depends on the chosen quadrature method [1]. For large d the convergence is very slow. This scaling is connected to the mathematical fact that the volume of a high-dimensional sphere is almost entirely concentrated around the surface of the sphere, which is where the quadrature formula introduces the discretization error.

The basic idea of the Monte Carlo technique is to sample the integrand stochastically. Suppose we have M independent and identically distributed random variables $\vec{x}_i \in \Omega$ drawn from the distribution $P(\vec{x}_i)$. Then $\langle O \rangle_P$ can be approximated by the mean

$$I \equiv \frac{1}{M} \sum_{\substack{i=1 \\ \vec{x}_i \in P(\vec{x}_i)}}^{M} O(\vec{x}_i) \tag{2.3}$$

The notation $\vec{x}_i \in P(\vec{x}_i)$ means that the point $\vec{x}_i$ is sampled according to the probability distribution $P(\vec{x}_i)$.

According to the Central Limit Theorem (for a proof see [50, Chapt. 8]), in the large M limit the probability $\mathcal{P}(I)$ of obtaining a given I is a Gaussian distribution

$$\mathcal{P}(I) = \frac{1}{\sqrt{2\pi}\sigma} \exp\left[-\frac{(I - \langle O \rangle_P)^2}{2\sigma^2}\right] \tag{2.4}$$

with

$$\sigma^2 = \frac{1}{M} \left[\langle O^2 \rangle_P - \langle O \rangle_P^2\right]. \tag{2.5}$$

The standard deviation σ is the error associated with I. Thus, independent of the dimension d of the integration space Ω, the approximation I tends to the exact result $\langle O \rangle_P$ as $\frac{1}{\sqrt{M}}$. This means that in order to increase the accuracy by a factor of two we need to increase the number of samples M by a factor of four.

2.1.1 Markov chain importance sampling

We have not yet specified how to sample points $\vec{x}$ according to the distribution $P(\vec{x})$. In the general case where they are drawn from some distribution $\rho(\vec{x})$ this can be corrected for by computing

$$\langle O \rangle_P = \lim_{M \to \infty} \frac{\sum_{i=1}^{M} \langle O \rangle_{x_i} P(\vec{x}_i) \rho(\vec{x}_i)^{-1}}{\sum_{i=1}^{M} P(\vec{x}_i) \rho(\vec{x}_i)^{-1}}. \tag{2.6}$$

---

[1] For example, the convergence of the error for the trapezoidal rule is $M^{-2/d}$, for Simpson's rule $M^{-4/d}$ and for m-point Gaussian quadrature it is $M^{-(2m-1)/d}$ [51].

If the points $\vec{x}$ are picked "randomly", i.e. from a uniform distribution $\rho = \frac{1}{|\Omega|}$, which is called *simple sampling*, most of them will come to lie in regions of configuration space Ω where the integrand $\langle O \rangle_{x_i} P(\vec{x}_i)$ is vanishing. The optimal choice of ρ is proportional to the true probability density $P(\vec{x})$ such that each sample is picked as often as corresponds to its statistical weight $P(\vec{x})$. Then the expectation value Eq. (2.6) reduces to the sample mean of Eq. (2.3)

$$\bar{O} \approx \frac{1}{M} \sum_{i=1}^{M} O(\vec{x}_i) \overset{M \to \infty}{\longrightarrow} \langle O \rangle_P. \tag{2.7}$$

This choice is known as *importance sampling* and can be achieved with the help of Markov chains [52, 53]. As shown in the previous section $\bar{O}$ is asymptotically normally distributed with a standard deviation scaling like $1/\sqrt{(M)}$ with the number M of statistically independent samples. The price to pay for importance sampling is that the samples generated with a Markov chain are no longer perfectly independent, but correlated on a characteristic "time" scale of Monte Carlo steps.

Our goal is to generate a set of points $\vec{x}$ that are distributed according to $P(\vec{x})$. For this we introduce a Monte Carlo "time" t and a time-dependent probability distribution $P_t(\vec{x}_t)$ which evolves in time according to a Markov process: A Markov chain of variables $\{\vec{x}_1, \vec{x}_2, \ldots, \vec{x}_t, \vec{x}_{t+1}\}$ is generated following a rule which specifies the probability $P_{t+1}(\vec{x}_{t+1})$ of the $(t+1)^{\text{th}}$ element $\vec{x}_{t+1}$ only on the basis of the tth element $\vec{x}_t$, which means that the stochastic process has no memory. The Markov process is defined through a transition matrix $T(\vec{x}_t \to \vec{x}_{t+1}) \equiv T_{\vec{x}_t, \vec{x}_{t+1}}$ which encodes the probability of reaching configuration $\vec{x}_{t+1}$ from configuration $\vec{x}_t$ as the matrix element $T_{\vec{x}_t, \vec{x}_{t+1}}$. The time evolution of the probability distribution in one time step is given as

$$P_{t+1}(\vec{x}_{t+1}) = \sum_{\vec{x}} T(\vec{x}_t \to \vec{x}_{t+1}) P_t(\vec{x}_t), \tag{2.8}$$

where $T(\vec{x}_t \to \vec{x}_{t+1})$ has to satisfy the following properties[2]

$$\sum_{\vec{x}_{t+1}} T(\vec{x}_t \to \vec{x}_{t+1}) = 1 \quad \text{and} \quad T(\vec{x}_t \to \vec{x}_{t+1}) \geq 0. \tag{2.9}$$

Furthermore, we wish that the desired distribution $P(\vec{x})$ be a stationary solution of the Markov chain:

$$\sum_{\vec{x}_t} T(\vec{x}_t \to \vec{x}_{t+1}) P(\vec{x}_t) = P(\vec{x}_{t+1}), \tag{2.10}$$

---

[2] The normalization condition and the non-negative entries are the defining properties of a *stochastic matrix*. Its largest eigenvalue is 1 and the corresponding right eigenvector is the invariant distribution. The remaining eigenvalues obey $-1 < \lambda_i < 1, i = 2, \ldots, N$. The second largest eigenvalue of the transition matrix λ_2 is related to the correlation time [54].

which means that, once the target distribution $P(\vec{x}_t)$ has been reached, the further Markov dynamics does not change it. Starting from an arbitrary initial configuration $\vec{x}_{t=0}$, the distribution of the generated configurations $\{\vec{x}_t\}$ is guaranteed to converge against the target distribution if the following two important conditions are met:

1. **Ergodicity**: Each configuration $\vec{x}$ can be reached from any other configuration $\vec{y}$ with non-vanishing probability in a finite number of steps: $\left(T^k\right)_{\vec{x},\vec{y}} > 0$ for some $k < \infty$.

2. **Detailed balance:** The transition probabilities are related to the target distribution in the following way:

$$\frac{T(\vec{x}_t \to \vec{x}_{t+1})}{T(\vec{x}_{t+1} \to \vec{x}_t)} = \frac{P(\vec{x}_{t+1})}{P(\vec{x}_t)}. \tag{2.11}$$

With this choice, stationarity is automatically satisfied

$$\sum_{\vec{x}_t} T(\vec{x}_t \to \vec{x}_{t+1})P(\vec{x}_t) = P(\vec{x}_{t+1})\sum_{\vec{x}_t} T(\vec{x}_{t+1} \to \vec{x}_t) = P(\vec{x}_{t+1}), \tag{2.12}$$

where in the last step the conservation of probability Eq. (2.9) was used. One should note that *detailed balance*, which is also known as micro-reversibility[3], is a sufficient, but not a necessary condition for the weaker condition of stationarity or *balance* Eq.(2.10). While detailed balance is easier to check, it has been recently shown [55] that algorithms that generally satisfy balance without imposing the detailed balance condition can be more versatile and efficient.

Having established the properties of the transition matrix, we need to construct it for a given physical system based on the desired stationary probability distribution. The transition probability is written as

$$T(\vec{x}_t \to \vec{x}_{t+1}) = g(\vec{x}_t \to \vec{x}_{t+1})A(\vec{x}_t \to \vec{x}_{t+1}), \tag{2.13}$$

where $g(\vec{x}_t \to \vec{x}_{t+1})$ is the probability to propose a certain move, which depends on the chosen Monte Carlo algorithm, and $A(\vec{x}_t \to \vec{x}_{t+1})$ is the probability to accept it, which can be adjusted so as to satisfy the detailed balance condition.

Setting the acceptance probability $A(\vec{x}_t \to \vec{x}_{t+1}) \equiv \mathcal{F}(R)$ to some function $\mathcal{F}$ of the ratio

$$R = \frac{g(\vec{x}_{t+1} \to \vec{x}_t)P(\vec{x}_{t+1})}{g(\vec{x}_t \to \vec{x}_{t+1})P(\vec{x}_t)}, \tag{2.14}$$

the detailed balance condition reads

$$\frac{\mathcal{F}(R)}{\mathcal{F}(1/R)} = R. \tag{2.15}$$

---

[3] While most physical systems at equilibrium do obey micro-reversibility, the Monte Carlo dynamics does not need in any way be connected to the actual equilibrium dynamics.

There are several choices to satisfy this equation, the most common ones are the Metropolis algorithm [56, 57]

$$A(\vec{x}_t \to \vec{x}_{t+1}) = \mathcal{F}(R) = \min(1, R) = \min\left(1, \frac{P(\vec{x}_{t+1})}{P(\vec{x}_t)}\right) \tag{2.16}$$

or the heat bath algorithm

$$A(\vec{x}_t \to \vec{x}_{t+1}) = \mathcal{F}(R) = \frac{R}{1+R} = \frac{\frac{P(\vec{x}_{t+1})}{P(\vec{x}_t)}}{1 + \frac{P(\vec{x}_{t+1})}{P(\vec{x}_t)}}, \tag{2.17}$$

where we have chosen the proposal probabilities symmetrically

$$\frac{g(\vec{x}_t \to \vec{x}_{t+1})}{g(\vec{x}_{t+1} \to \vec{x}_t)} = 1. \tag{2.18}$$

The transition probability depends on the target distribution $P(\vec{x})$ only through ratios of the form $\frac{P(\vec{x}_{t+1})}{P(\vec{x}_t)}$ at the sample points $\vec{x}_t$ and $\vec{x}_{t+1}$ such that the normalization constant need not be known. Other optimized choices of transition probabilities obeying detailed balance are also possible [58]. As a rule of thumb the acceptance ratio should be close to one-half.

2.1.2 Monte Carlo error and autocorrelation times

In principle the statistical error attached to the Monte Carlo (MC) estimate $\langle O \rangle_{\mathrm{MC}}$ can be calculated by performing many stochastic walks in configuration space along each of which one calculates $\langle O \rangle_{\mathrm{MC}} = \frac{1}{M} \sum_{i=1}^{M} A_i$. From the distribution of values $\langle O \rangle$ the statistical error Δ_O can be inferred. In practice a single Monte Carlo run is sufficient to estimate the error. Introducing the variance over the entire random walk, $\sigma_O^2 = \langle (O - \langle O \rangle_{MC})^2 \rangle_{MC}$, the error would read $\Delta_O = \sqrt{\sigma_O^2/M}$ if subsequent measurements were completely uncorrelated so that the Central Limit Theorem applies. Instead a realistic stochastic process has correlations on a typical time scale (=number of MC steps) τ_O, which is called the *autocorrelation time*. This reduces the effective number of uncorrelated steps from M to $M/(2\tau_O)$ since, roughly speaking, each measurement is correlated with the τ_O previous and the τ_O following measurement steps. Knowing the autocorrelation time, the error is then given by

$$\Delta_O = \sqrt{(2\tau_O)\frac{\sigma_O^2}{M}}. \tag{2.19}$$

The integrated autocorrelation time τ_O^{int} is the characteristic time scale on which the autocorrelation function decays. It depends on the observable O and is defined as

$$C_{OO}(j) = \frac{1}{(M-j)\sigma_O^2} \sum_{i=1}^{M-j} (O_i - \langle O \rangle_{MC})(O_{i+j} - \langle O \rangle_{MC}). \tag{2.20}$$

A small autocorrelation time means that the system has a short memory about its previous states. We estimate the autocorrelation time by means of the *binning* or *blocking method* [59]. In this scheme the MC time series is devided into n_b blocks each comprising $N_b = M/n_b$ subsequent measurements. It requires only storage of the last part of the time series, which - whenever a block is full - is averaged over to give the *block variables* $\bar{O}_k$:

$$\bar{O}_k = \frac{1}{N_b} \sum_{i=(k-1)*N_b+1}^{k*N_b} O_i. \tag{2.21}$$

Provided that $N_b \gg \tau_O$, the block variables are completely uncorrelated. Each block, on the other hand, is composed of $N_b/(2\tau_O)$ sub-bins of correlated measurement. If the measurements in a block were completely uncorrelated, then according to the Central Limit Theorem the variance of the block variables $\sigma_{\bar{O}}^2$ and the variance of the stochastic process σ_O^2 would be related through $\sigma_{\bar{O}}^2 = \sigma_O^2/N_b$. This generalizes to $\sigma_{\bar{O}}^2 = \sigma_O^2/[N_b/(2\tau_O)]$ for the case of correlated sub-bins. Solving for the autocorrelation time gives

$$\tau_O = \frac{N_b}{2} \frac{\sigma_{\bar{O}}^2}{\sigma_O^2}. \tag{2.22}$$

In an actual simulation it has to be verified that the bin size is really much bigger than the autocorrelation time for the result to be reliable.

Close to a phase transition the autocorrelation times diverge, which is known as *critical slowing down* [59, Chapt. 5]. To deal with this issue, *non-local* update schemes have been devised that flip entire clusters of spins [60, 61]. To quantify the ability of an algorithm to overcome critical slowing down one can measure the scaling $\tau_O(L) \sim L^z$ of the autocorrelation time at the critical point as a function of linear system size L. The dynamical critical exponent z is a property of the algorithm[4]. For the single spin-flip Metropolis algorithm at criticality $z \approx 2.17$ [54], whereas cluster algorithms can achieve $z < 1$.[5]

In large-scale Monte Carlo simulations it is often necessary to parallelize the Monte Carlo run over several hundred processors (CPUs). In this case each processor starts an independent Markov chain with a different random seed. After a thermalization stage,

---

[4] This needs to be distinguished from the dynamical critical exponent z of a quantum system, which is a property of the system at criticality [62].

[5] To make cluster algorithms, which may update only a part of the lattice per Monte Carlo step, comparable to a sweep of the lattice with L^d sites with single spin-flip updates requires a useful definition of "work" per unit of Monte Carlo time. If $\langle N_c \rangle$ is the average number of sites updated per Monte Carlo step with a cluster update, then the correlation time in Monte Carlo steps per site is

$$\tau_{\text{step}} \sim L^z \frac{\langle N_c \rangle}{L^d}. \tag{2.23}$$

the averages $\bar{A}_k$ from different Markov chains are combined to $\langle \bar{A} \rangle = \frac{1}{N_{\text{CPUs}}} \sum_{k=1}^{N_{\text{CPUs}}} \bar{A}_k$ and, as said above, since the Markov chain on each processor can be regarded as an independent simulation, the error of the average is given by the spread over different independent simulations

$$\Delta_A = \sqrt{\frac{1}{N_{\text{CPUs}}} \sum_{k=1}^{N_{\text{CPUs}}} \left(\bar{A}_k - \langle \bar{A} \rangle \right)^2}. \tag{2.24}$$

As long as the number of samples per processor (i.e. per bin) is much larger than the autocorrelation time, a (correct) error estimate according to Eq. (2.24) should not depend on the number of processors N_{CPUs} over which the total Markov chain was parallelized. A detailed discussion of the convergence of the error estimate with bin size is given in [63].

2.2 Overview of quantum Monte Carlo methods

In recent years there has been tremendous progress in the application of numerical methods to strongly correlated quantum systems. For one-dimensional systems, the density matrix renormalization group (DMRG) [64] has emerged as the method of choice and generalizations to higher dimensions have been proposed in the form of tensor network states, although they are less effective due to the perimeter law scaling of the entanglement entropy [65], which entails an exponential cost of the algorithm in two dimensions. A particularly successful ansatz of this type in more than one dimension is the projected entangled pair state (PEPS) method [66, 67].

For two and three dimensions the quantum Monte Carlo method remains the most powerful technique for unfrustrated bosonic or spin systems and fermionic systems [68] in the absence of a sign problem due to its polynomial scaling with system size. Various different QMC techniques have been developed to study quantum many-body systems. Path integral (or world-line) QMC method were among the earliest QMC methods to be developed [69–71]. Their modern variants work in continuous imaginary time [72, 73] without the Trotter discretization error. Extended with a cluster or loop algorithm [74, 75] and applied to non-frustrated spin systems, path integral methods have proven very successful.

However, with regard to fermionic systems, world-line methods inevitably suffer from a sign problem in more than one spatial dimension due to fermionic exchange processes.

The standard algorithm for fermionic lattice systems at finite temperature is the determinantal QMC (DQMC) or auxiliary field QMC method, which in its finite-temperature version is known as the Blankenbecler-Scalapino-Sugar (BSS) algorithm [44]. Published as early as 1981, the BSS algorithm, which consists in decoupling the fermionic interactions at the expense of introducing a bosonic auxiliary field to be sampled by Monte Carlo, has been applied to numerous problems of itinerant fermions

in condensed matter physics. Conceptually closely related is the ground state projector DQMC [76, 77], where the ground state is projected out from a trial wave function by applying to it a large power of the Hamiltonian.

Some methods, especially for the simulation of fermionic system, are approximate in that they need to introduce some systematic error in order to deal with the so-called *sign problem* such as the Constrained Path MC [78] or the Fixed Node MC [79]. These methods are variational as they rely on some trial wave function to guide the random walk in configurations space.

More recent developments in the field of QMC method development include the Full Configuration Interaction (FCI) MC in Slater determinant space [80] with applications to problems of quantum chemistry and the Diagrammatic MC method, which stochastically samples Feynman diagrams to high order and has stood the test of mutual benchmarking against a Fermi gas quantum simulator [81]. Drawing inspiration from quantum information theory, the role of entanglement in condensed matter systems has recently become accessible via Monte Carlo simulations [82–85]. Finally, techniques of machine learning have been employed in the self-learning MC method [86] to propose suitable update moves or to try and circumvent [87] the notorious sign problem, which will be discussed in Sect. 4.6.

In the next chapters we will describe in detail the two algorithms that were used in this thesis: first, the Stochastic Series Expansion (SSE) method for the transverse field Ising model with particular emphasis on including long-range interactions and, second, the determinantal QMC (DQMC) method in its finite temperature version for simulating the Fermi-Hubbard model.

Chapter 3

Stochastic Series Expansion quantum Monte Carlo

In this and the following chapter we describe in detail two quantum Monte Carlo (QMC) methods which allow an unbiased, numerically exact simulation of equilibrium properties. In the absence of a sign problem, the computational effort scales polynomially in the volume of the system so that large system sizes can be reached, which is important for studying critical behaviour at phase transitions. In general, simulating interacting fermions hopping on a lattice directly, which is discussed in the next chapter, is computationally much more expensive than simulating the low energy effective spin model that often arises in some limit. This chapter presents a very efficient QMC method for spin systems, the Stochastic Series Expansion QMC method (hereafter referred to as SSE), which is generally applicable to non-frustrated spin or boson models in arbitrary dimensions (and also to the Hubbard model in one dimension [88]). Like path integral quantum Monte Carlo [69] it is a finite temperature method. Very comprehensive references are [89] and [43].

3.1 SSE representation of the partition function

The Stochastic Series Expansion (SSE) QMC method [88–92] is based on a high-temperature series expansion of the partition function of a lattice spin system with Hamiltonian $\mathcal{H}$ in powers of $(-\beta\mathcal{H})$,

$$Z = \text{Tr}(e^{-\beta\mathcal{H}}) = \sum_{n=0}^{\infty} \frac{(-\beta)^n}{n!}\text{Tr}(\mathcal{H}^n),\tag{3.1}$$

with inverse temperature $\beta = 1/(k_B T)$. The Hamiltonian $\mathcal{H}$ is decomposed into bond operators

$$\mathcal{H} = -\sum_{a,b} H_{a,b},\tag{3.2}$$

17

where $b = (i, j)$ labels the bond connecting sites i and j and a labels the type of operator. Note the minus sign in the definition of the bond operators. A bond operator could be for instance an Ising interaction, $H_{D,b(i,j)} = S_i^z S_j^z$, or spin-flip term, $H_{oD,b(i,j)} = S_i^+ S_j^- + S_i^- S_j^+$, acting between sites i and j. $H_{D,b(i,j)}$ is diagonal (D) in the S^z-basis, while $H_{oD,b(i,j)}$ is off-diagonal (oD).

Having decomposed the Hamiltonian into bond operators, we can write the powers of the Hamiltonian under the trace in Eq. (3.1) as

$$\mathcal{H}^n = \left(-\sum_{a,b} H_{a,b} \right)^n = \sum_{\{S_n\}} (-1)^n \prod_{i=1}^n H_{a_i,b_i}, \tag{3.3}$$

where $\{S_n\}$ are all the sequences (i.e. products) of single-bond operators that arise from multiplying out the sum in Eq. (3.3): $S_n = \{[a_1, b_1], [a_2, b_2], ..., [a_n, b_n]\}$ with a_i a label denoting different types of diagonal (D) or off-diagonal (oD) operators. Writing out the trace operation in Eq. (3.1) in the *computational basis* $|\alpha\rangle = |S_1^z, S_2^z, \dots S_N^z\rangle$ of tensor product states of eigenstates of S_i^z, one obtains for the partition sum the expression

$$Z = \sum_n^\infty \frac{(-\beta)^n}{n!} \sum_{\{S_n\}} \sum_{\{|\alpha\rangle\}} \langle\alpha|(-1)^n \prod_{i=1}^n H_{a_i,b_i}|\alpha\rangle, \tag{3.4}$$

where the two sums run over all operator sequences $\{S_n\}$ and all basis states $\{|\alpha\rangle\}$. Note here that the artificially introduced minus sign in the decomposition of $\mathcal{H}$ into bond operators cancels the minus sign in front of β.

In general, the bond operators must be chosen such that $H_{a,b(i,j)}$ acting on any basis state $|\alpha\rangle$ produces some multiple of another basis state $|\beta\rangle$

$$H_{a,b(i,j)}|\alpha\rangle \propto |\beta\rangle \tag{3.5}$$

and not a superposition of states. A note on terminology: In the expression $|\alpha_1\rangle = H_{a_1,b_1}|\alpha\rangle$ we say that H_{a_1,b_1} *propagates* the initial state $|\alpha\rangle$ to the state $|\alpha_1\rangle$. The extra dimension, in which the sequence of operators $H_{a_3,b_3} H_{a_2,b_2} H_{a_1,b_1} \cdots$ extends, is called the *propagation direction* or *imaginary time*, in analogy to the path integral formulation of statistical mechanics [50] to which the SSE scheme is closely related. It is useful to the define the normalized propagated states $|\alpha(p)\rangle$ that are obtained after applying the first p bond operators in the operator sequence

$$|\alpha(p)\rangle \propto \prod_{i=1}^p H_{a(i),b(i)}|\alpha(0)\rangle. \tag{3.6}$$

Now, if the traces in Eq. (3.4) could be evaluated analytically, the partition function could be rewritten as a sum over computable weights,

$$Z = \sum_{n=0}^\infty \sum_{\{S_n\}} W(S_n), \tag{3.7}$$

where $W(S_n)$ is the relative probability of creating a sequence S_n and the estimation of expectation value occurs by sampling all those sequences. This is the Monte Carlo scheme proposed by Handscomb [93] already in the year 1962, which, however, is only applicable to the Heisenberg ferromagnet [93, 94] and a small number of other systems. In most cases the traces in Eq. (3.4) cannot be evaluated analytically. Therefore one needs to sample additionally over a basis of states $\{|\alpha\rangle\}$, which brings us to the generalization of Handscomb's method, the more widely applicable Stochastic Series Expansion (SSE) formulation [88, 90]. With this generalization of sampling over basis states the method closely resembles the path integral approach in continuous imaginary time to which it can be related in a mathematically rigorous way [45, 91] (see Sect. 3.4.2).

In conclusion, the SSE representation of the partition function is

$$Z = \sum_{n=0}^{\infty} \sum_{\{|\alpha\rangle\}} \sum_{\{S_n\}} w(\alpha, S_n) \tag{3.8}$$
$$\equiv \sum_{\{\mathcal{C}\}} w(\mathcal{C}),$$

where the weight of a configuration

$$w(\alpha, S_n) = \frac{\beta^n}{n!} \prod_{p=1}^{n} \langle \alpha(p)|H_{l_p}|\alpha(p-1)\rangle \tag{3.9}$$

is the product of the matrix elements of all bond operators in the operator string S_n. The effective configuration space $\{\mathcal{C}\}$ to be sampled in a Monte Carlo simulation is the tensor product between the space of operator strings, $\{S_n\}$, and the set of initial spins states $\{|\alpha\rangle\} \equiv \{|\alpha(0)\rangle\} = \{|S_1^z(0), S_2^z(0), \ldots, S_N^z(0)\rangle\}$ at propagation step $p = 0$, i.e. $\{C\} = \{S_n\} \otimes \{|\alpha\rangle\}$. A fundamental property of the above scheme is that, starting from an initial state $|\alpha\rangle$, an operator sequence S_n defines uniquely a sequence of configurations $|\alpha_1\rangle, |\alpha_2\rangle, \ldots$ all belonging to the computational basis, and such that $|\alpha_1\rangle = H_{a_1,b_1}|\alpha\rangle, |\alpha_2\rangle = H_{a_2,b_2}|\alpha_1\rangle, \ldots$ Therefore the propagated spin states need not be stored as this information is redundant. Furthermore, the weights $w(\alpha, S_n) = \ldots \langle \alpha_2|H_{a_2,b_2}|\alpha_1\rangle\langle \alpha_1|H_{a_1,b_1}|\alpha\rangle$ can be computed efficiently as products of matrix elements of bond operators involving only two spins.[1]

3.1.1   Expressions for equal-time SSE estimators

The expectation value of a generic operator $\hat{A}$ in SSE is given by

$$\langle\hat{A}\rangle = \frac{1}{Z} \sum_{\alpha} \sum_{n=0}^{\infty} \sum_{S_n} \frac{(-\beta)^n}{n!} \langle\alpha|\hat{A}\prod_{i=1}^{n} H_{l_i}|\alpha\rangle, \tag{3.10}$$

---

[1]If the decomposition of the Hamiltonian is done according to plaquettes rather than bonds, we have to deal with matrix elements of plaquette operators.

where $l_i = (a_i, b_i)$ is a multi-index denoting the type and the bond on which the operator at propagation step i sits. It can be shown [88] that the expectation value for a single-bond Hamiltonian operator H_k takes a particularly simple and intuitive form; it is related to the average number $\langle N_k \rangle$ of occurrences of this single-bond operator in the operator string:

$$\langle \hat{H}_k \rangle = -\frac{1}{\beta} \langle N_k \rangle. \tag{3.11}$$

In particular, the total energy, i.e. the sum of all single-bond operators, is related to the average number of (diagonal or off-diagonal) operators in the string:

$$\langle E \rangle = -\frac{1}{\beta} \langle n \rangle. \tag{3.12}$$

The heat capacity is obtained by taking the derivative of the above expression with respect to temperature:

$$C_V = -\beta^2 \frac{\partial}{\partial \beta} \langle E \rangle = \langle n^2 \rangle - \langle n \rangle^2 - \langle n \rangle. \tag{3.13}$$

On the other hand the fluctuation dissipation theorem tells us that the fluctuations of the energy are related to the specific heat via

$$\mathrm{Var}(E) = -\frac{\partial \langle E \rangle}{\partial \beta} \tag{3.14}$$

$$= \langle E^2 \rangle - \langle E \rangle^2 = k_B T^2 C_V \tag{3.15}$$

As can be seen from Eqs. (3.12) and (3.13) this relation does not hold for the corresponding SSE estimators (there is an additional $\langle n \rangle$). Generally speaking, the fluctuations of a quantity are not the same as the fluctuations of its SSE estimator.

Eq. (3.12) shows the significance of the average expansion order $\langle n \rangle$. According to $\langle n \rangle = N |\langle e \rangle| \beta$ with $\langle e \rangle$ being the average energy per site and N the number of sites, the expansion order diverges in the thermodynamic limit $N \to \infty$, and as the temperature approaches zero, $\beta \to \infty$. As expected the area of the simulation cell increases for both limits and the time required to update it will scale $\sim \beta N^2$ (more precisely $\sim \beta N^\alpha$ with $1 < \alpha < 2$) with system size and temperature, which provides an estimate of the efficiency of the algorithm.

3.1.2 Fixed length scheme

Any computer simulation has finite memory, so one has to truncate the series expansion to some upper power $n_{\max} \equiv \mathcal{L} \sim N\beta$. The choice of $\mathcal{L}$ is made in such a way that the algorithm is still exact without any approximation. This can be motivated from the
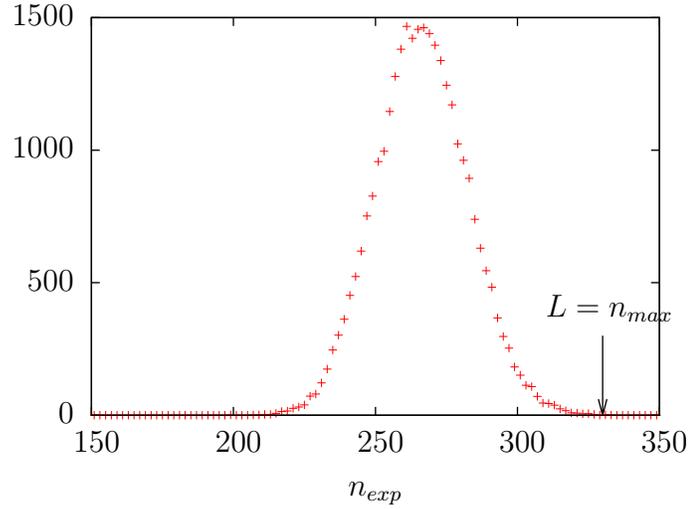
Fig. 3.1: Histogram of the expansion orders n for a one-dimensional XX model $[J = 1, \Delta = 0$ in Eq. (3.18)] with 20 sites at temperature $T/J{=}0.05$. With the chosen cut-off $\mathcal{L}$, which is determined during thermalization, the fixed length scheme does not lead to any approximation.

expression for the specific heat C_V in Eq. (3.13). As $T \to 0$, C_V should vanish. Then from Eq. (3.13) we have $\langle n^2 \rangle - \langle n \rangle^2 = \langle n \rangle$, i.e. the variance of n is $\langle n \rangle$ so that the distribution vanishes exponentially beyond some expansion order $n \sim N\beta$. Thus the error of the truncation (i.e. the probability of having a configuration that requires an expansion order $n > n_{\max}$) vanishes exponentially in $n_{\max}$ (see Fig. 3.1).

To get a *fixed length scheme* with operator strings of the same size $\mathcal{L}$ each we insert $\mathcal{L} - n$ identities $\mathbb{1}$ at arbitrary locations into an operator string of length n so that it is stretched to length $\mathcal{L}$. The location of the $\mathcal{L} - n$ identity operators in an n-long operator string is completely random. Therefore we have enlarged the configuration space. We must compensate for this and ask how many equivalent operator strings $S_\mathcal{L}$ of $n(S_\mathcal{L})$ non-trivial operators ($a = \mathrm{D}, \mathrm{oD}$) and $\mathcal{L} - n(S_\mathcal{L})$ identity operators $a = \mathbb{1}$ we can build by moving the identities around. This results in $\frac{\mathcal{L}!}{n(S_\mathcal{L})!(\mathcal{L}-n(S_\mathcal{L}))!}$ equivalent configurations. The numerator gives all possible permutations of $\mathcal{L}$ operators which have to be divided by a factor $n(S_\mathcal{L})!$ to account for the fact that permuting non-trivial operators is not allowed and by $(\mathcal{L} - n(S_\mathcal{L}))!$ because permuting only identities does not give anything new. We divide by this number to restore the original size of the configurations space and arrive at

$$Z = \sum_{\{S_\mathcal{L}\}} \sum_{|\alpha\rangle} \frac{\beta^{n(S_\mathcal{L})}}{n(S_\mathcal{L})!} \frac{n(S_\mathcal{L})!(\mathcal{L} - n(S_\mathcal{L}))!}{\mathcal{L}!} \langle\alpha| \prod_{i=1}^{\mathcal{L}} H_{a_i,b_i} |\alpha\rangle \qquad (3.16)$$

$$= \sum_{\{S_\mathcal{L}\}} \sum_{|\alpha\rangle} \frac{\beta^{n(S_\mathcal{L})}}{\mathcal{L}!} (\mathcal{L} - n(S_\mathcal{L}))! \langle\alpha| \prod_{i=1}^{\mathcal{L}} H_{a_i,b_i} |\alpha\rangle \qquad (3.17)$$

where the sum over $\{S_{\mathcal{L}}\}$ runs over all possible operator strings with repetitions, that is including equivalent operator strings that have the same sequence of non-trivial operators. The cut-off $\mathcal{L}$ that is appropriate for a given temperature and system size is adapted during the thermalization phase of the simulation till it is large enough.

3.1.3   Monte Carlo update procedure

In order to sample the partition function Eq. (3.4) with a Monte Carlo scheme we need to make changes both to the operator sequence $S_{\mathcal{L}}$ and the stored initial state $|\alpha\rangle \equiv |\alpha(0)\rangle$. The changes are not independent since a modification of the operator sequence affects the propagated states and ultimately the initial state. Each update needs to respect certain configuration constraints for the resulting new configuration to have non-zero weight. The fact that the partition sum Eq. (3.4) is a trace imposes periodic boundary conditions in propagation direction and thus the constraint $|\alpha(0)\rangle = |\alpha(\mathcal{L})\rangle$. There may be additional constraints that are related to symmetries of the Hamiltonian. Consider for example the spin-$\frac{1}{2}$ XXZ model

$$\mathcal{H}_{\text{XXZ}} = J \sum_{\langle ij \rangle} \left\{ \frac{1}{2}(S_i^+ S_j^- + S_j^+ S_i^-) + \Delta S_i^z S_j^z \right\}, \tag{3.18}$$

an anisotropic generalization of the Heisenberg model $\mathcal{H}_{\text{XXX}} = J \sum_{\langle i,j \rangle} \mathbf{S}_i \cdot \mathbf{S}_j$, to which it reduces for $\Delta = 1$. Here, $S_i^+ = S_i^x + iS_i^y$ and $S_i^- = S_i^x - iS_i^y$ are the raising and lowering operators for spin-$\frac{1}{2}$. The Hamiltonian $\mathcal{H}_{\text{XXZ}}$ commutes with the z-component of the total magnetization $M_z = \sum_i S_i^z$

$$[H_{\text{XXZ}}, M_z] = 0, \tag{3.19}$$

since each bond operator in Eq. (3.18) conserves the magnetization per bond. Therefore, the size of the phase space of the (D+1)-dimensional lattice which is generated by propagating initial states $|\alpha\rangle$ under the action of the operator sequence $S_{\mathcal{L}}$ is not 2^N as for the classical (D+1)-dimensional Ising model with N sites, but reduced, since the total magnetization must be preserved. Monte Carlo updates must take such constraints of the configuration space into account. In the SSE framework, the updating of a configuration $\mathcal{C} = (\alpha, S_{\mathcal{L}})$ is achieved by two subsequent procedures:

- **Diagonal update:** At every propagation step p^2, a diagonal operator is either inserted into the operator string $S_{\mathcal{L}}$ in lieu of an identity operator or removed in exchange for an identity [See Fig. 3.2]. The diagonal update changes the number of non-trivial operators, i.e. the expansion order n, and thus by Eq. (3.12) the energy of an SSE configuration. The initial state $|\alpha(0)\rangle$ is not altered.

---

[2]Note that there is at most one operator per propagation step.
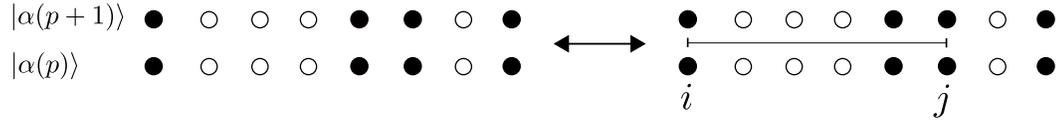
Fig. 3.2: Diagonal update: The empty and closed circles denote, respectively, spin up and spin down in the computational basis. A diagonal bond operator $H_{D,b=(i,j)}$ acting between sites i and j of bond $b=(i,j)$ is either inserted $[0,0]_p \to [\mathrm{D}; b=(i,j)]_p$ or removed $[\mathrm{D}; b=(i,j)]_p \to [0,0]_p$ at propagation step p. This changes the number of non-trivial operators in the operator sequence, i.e. the expansion order $n \to n \pm 1$.

- **Off-diagonal update:** Operator types are exchanged without changing the expansion order n. The diagonal operators, which have been inserted in the diagonal update, are converted into off-diagonal operators by a loop or cluster update, which may also modify the initial state $|\alpha(0)\rangle$ and thus the magnetization in the SSE configuration.

A large part of this thesis is concerned with the transverse-field Ising (TFI) model

$$\mathcal{H}_{\mathrm{TFI}} = \sum_{i<j} J_{ij} S_i^z S_j^z - \Gamma \sum_i S_i^x, \tag{3.20}$$

with spin-$\frac{1}{2}$ operators satisfying $[S_j^a, S_j^b] = i\epsilon_{abc} S_j^c$ with $a, b, c \in \{x, y, z\}$ and arbitrary (i.e. long-range or frustrated) interactions J_{ij} between site i and j.

The following sections introduce SSE Monte Carlo schemes [89, 95] that are suitable for the TFI model. We discuss the diagonal update, with a particular emphasis on the efficient treatment of long-range interactions [Sect. 3.3.1], and several types of off-diagonal updates: First, we introduce the operator-loop update, which is particularly appealing since it requires only small modifications to a well-known algorithm for the XXZ-model [89] if the local basis is rotated into the eigenbasis of the transverse field. Then, in Sect. 3.3, we present a specialized algorithm for the TFI model [95], which allows also to simulate frustrated Ising interactions without a sign problem. The corresponding off-diagonal updates are the single-site cluster update discussed in Sect. 3.3.2 and the multibranch cluster update, which is explained in Sect. 3.3.2. Finally, we discuss in Sect. 3.3.2 an extension of the multibranch update, the Wolff quantum cluster algorithm, which, although it turns out to be inefficient, adds to the understanding of what the crucial ingredients of the multibranch cluster algorithm are.

3.2 Operator loop update for TFI model in the field eigenbasis

The Hamiltonian of the TFI model Eq. (3.20) in the S^z-basis does not contain off-diagonal bond operators which are crucial for designing an operator-loop update (see

Fig. 3.4 for a first impression of the opreator loop update). This is related to the fact that the TFI model does not preserve the z-magnetization. The transverse field term is off-diagonal, but it acts only on a single site. The presence of off-diagonal bond operators can be achieved by a local basis rotation by $\frac{\pi}{2}$ about the y-axis realized by the unitary operator $U = e^{i\frac{\pi}{2}S^y}$:

$$S^x \to US^xU^\dagger = S^z, \quad S^y \to S^y, \quad S^z \to -S^x, \tag{3.21}$$

which leads to the transformed Hamiltonian

$$\mathcal{H}'_{\text{TFI}} = U\mathcal{H}_{\text{TFI}}U^\dagger = \sum_{ij} J_{ij}(-1)^2 S^x_i S^x_j - \Gamma \sum_i S^z_i \tag{3.22}$$

with the off-diagonal bond operators

$$J_{ij}S^x_{i(b)}S^x_{j(b)} = \frac{J_{ij}}{4}\left(S^+_{i(b)}S^+_{j(b)} + S^-_{i(b)}S^-_{j(b)} + S^+_{i(b)}S^-_{j(b)} + S^-_{i(b)}S^+_{j(b)}\right) \tag{3.23}$$
$$\equiv -H_{\text{oD,b}} \equiv \sum_{a\in[2,3,4,5]}(-H_{a,b}).$$

As in Eq. (3.3), a minus sign is introduced in the definition of the bond operators. Different types of off-bond operators are labelled by $a \in [2,3,4,5]$. Their four non-zero matrix elements,

$$\langle S^z_i S^z_j | H_{\text{a,b}} | \tilde{S}^z_i \tilde{S}^z_j \rangle = -\frac{J_{i(b)j(b)}}{4} \quad \text{for } S^z_i = -\tilde{S}^z_i \text{ and } S^z_j = -\tilde{S}^z_j, \tag{3.24}$$

are all of the same magnitude. The matrix elements are represented by so-called *vertices*

$$\langle \uparrow_i \uparrow_j | S^+_{i(b)} S^+_{j(b)} | \downarrow_i \downarrow_j \rangle = \begin{matrix} \bullet \qquad \bullet \\ \rule{2cm}{0.4pt} \\ \circ \qquad \circ \end{matrix}, \qquad \langle \downarrow_i \downarrow_j | S^-_{i(b)} S^-_{j(b)} | \uparrow_i \uparrow_j \rangle = \begin{matrix} \circ \qquad \circ \\ \rule{2cm}{0.4pt} \\ \bullet \qquad \bullet \end{matrix},$$

$$\langle \uparrow_i \downarrow_j | S^+_{i(b)} S^-_{j(b)} | \downarrow_i \uparrow_j \rangle = \begin{matrix} \bullet \qquad \circ \\ \rule{2cm}{0.4pt} \\ \circ \qquad \bullet \end{matrix}, \qquad \langle \downarrow_i \uparrow_j | S^-_{i(b)} S^+_{j(b)} | \uparrow_i \downarrow_j \rangle = \begin{matrix} \circ \qquad \bullet \\ \rule{2cm}{0.4pt} \\ \bullet \qquad \circ \end{matrix},$$

with the horizontal bar denoting any of the pairwise spin-flip operators in Eq. (3.23) and filled and open circles corresponding to spin up ($S^z = +1$) and spin down ($S^z = -1$), respectively. The off-diagonal matrix elements are positive only for FM interactions, $J_{ij} < 0$, while for AFM interactions, $J_{ij} > 0$, a sign problem arises on frustrated lattices (see Sect. 3.2.2 below for an explanation), which cannot be remedied by simply adding a constant due to the off-diagonal nature of the operators.

The only diagonal part, labelled by $a = 1$, comes from the field term in Eq. (3.22). It is written as a bond operator connecting nearest neighbour sites

$$\Gamma \sum_i S^z_i \quad \to \quad \frac{\Gamma}{z} \sum_b \left(S^z_{i(b)} + S^z_{j(b)}\right) + \frac{N_b\Gamma}{z} \equiv -H_{\text{D,b}} \equiv -H_{1,b}, \tag{3.25}$$

where z is the coordination number of the lattice coming from the conversion of the sum over N_s sites to a sum over N_b bonds. The additional constant $N_b\Gamma/z$ guarantees that all matrix elements of the field term are positive definite. For a generalization to long-range interactions J_{ij}, it is advantageous to distribute the field term $\sum_i S_i^z$ over bonds of arbitrary range as follows (again with a constant added to ensure positivity of the matrix elements)

$$\Gamma \sum_i S_i^z \quad \rightarrow \quad \frac{\Gamma N_s}{2\sum_b J_{i(b),j(b)}} \sum_b J_{i(b),j(b)} \left(S_{i(b)}^z + S_{j(b)}^z + 1 \right). \tag{3.26}$$

This is important since for the diagonal update and the off-diagonal loop update to work well hand in hand it is mandatory that for every off-diagonal bond operator there is a corresponding diagonal bond operator of the same range so that the two can be converted into each other in the off-diagonal update. With the choice of constants as in Eq. (3.25) there is only one non-zero diagonal matrix element

$$\langle \uparrow_i\uparrow_j \,|\, (-H_{\mathrm{D,b}}) \,|\, \uparrow_i\uparrow_j \rangle = \frac{2\Gamma N_s J_{i(b),j(b)}}{2\sum_b J_{i(b),j(b)}} \quad \xrightarrow[\text{interactions}]{\text{n.n.}} \quad \frac{2\Gamma}{z}. \tag{3.27}$$

This expression can be verified for the simple case of nearest neighbour (n.n.) interactions by recalling that there the relation between the number of bonds N_b and the number of sites is $N_b = \frac{z}{2}N_s$ so that with $J_{i(b),j(b)} \equiv J$ we have $\sum_b J_{i(b),j(b)} = J\frac{z}{2}N_s$. qw For the discussion of the loop update it is necessary to introduce the notion of *vertices*. The matrix elements of the transverse-field Ising model formulated in the eigenbasis of the field are represented by the diagonal and off-diagonal vertices shown in Fig. 3.3(a-b). The circles are the spin states before and after the operator, indicated by the horzontal bar, acts. These spins are called *legs*. Note that here filled circles denote "spin-up" in the field basis (i.e. $|\rightarrow\rangle$ in the original S^z-basis) and open circles denote "spin-down" ($|\leftarrow\rangle$ in the original S^z-basis). The left and right end of the horizontal bar is located, respectively, at site i and j of the bond $b = (i,j)$. A graphical representation of the sequence of vertices as they appear in an SSE configuration ($S_{\mathcal{L}}$, $|\alpha\rangle$) is shown in Fig. 3.4. As a first impression, an *operator loop* is drawn in red. It is a worm-like object that travels on the *linked list* of vertex legs and flips the spins which it encounters, thereby converting one type of vertex into another. For details on the implementation of a linked vertex list[3] we refer to Refs. [43, 89]. The requirement that the loop needs to close to obtain a new valid SSE configuration ensures that $|\alpha(0)\rangle = |\alpha(\mathcal{L})\rangle$ is maintained. In Fig. 3.3(c) the transition processes are depicted in

---

[3] For implementing a loop update we need another data structure, in which the connectivity of vertex legs along the propagation direction is stored. In the pictorial representation of Fig. 3.4 constant spin states in propagation direction have been replaced by vertical lines. The vertex legs at the endpoints, which we call e.g. *leg*1 and *leg*2, are associated with another through a doubly-linked (i.e. bi-directional) list, where $link[leg1] = leg2$ implies $link[leg2] = leg1$. This allows to follow loop segments quickly from one vertex to the next.
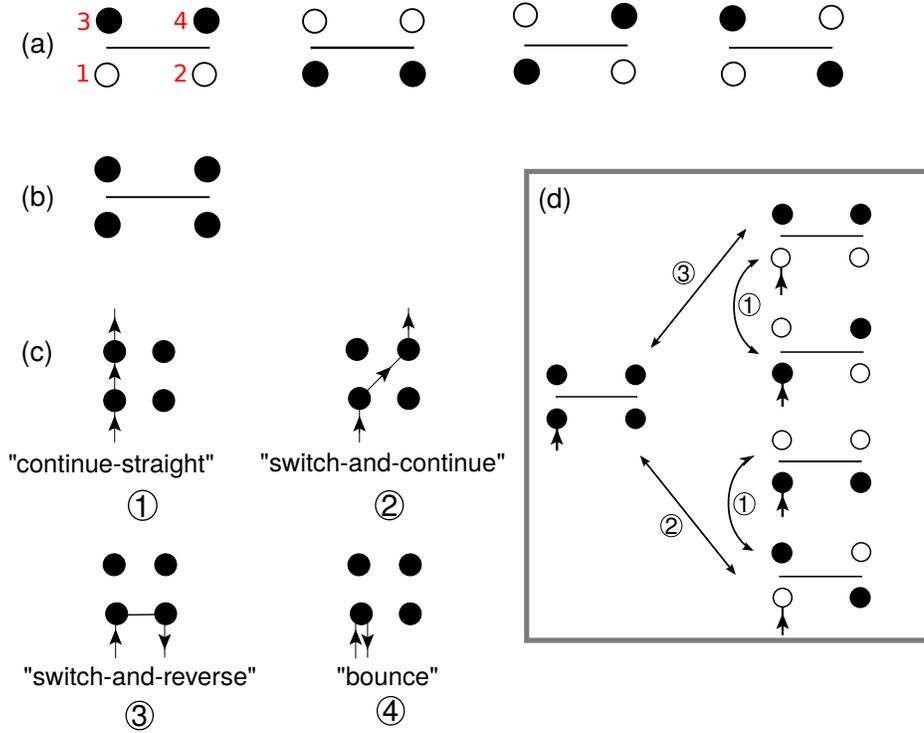
Fig. 3.3: Allowed vertices for the transverse-field Ising model written in the eigenbasis of the field. Filled circles denote spin up, open circles spin down. (a) All off-diagonal vertices, which have the same weight. In one of the vertices the labelling of the four legs is indicated. For more details about the notation see the main text. (b) With the choice of constants as in Eq. (3.25), there is only a single diagonal vertex corresponding to a non-zero matrix element. (c) Possible "scattering processes" of the loop head at a vertex. (d) As the worm traverses a vertex, it flips the spins on its path thereby converting one vertex into another. The transitions shown in (d) are labelled by the "scattering processes" ①, ②, and ③. A "bounce" process flips the spin on the entrance leg twice and leaves the vertex unchanged. The entrance leg is assumed to be the lower left leg.

which a loop enters a vertex at a particular leg, which is called the *entrance leg*, and leaves it at one of four possible *exit legs*, flipping the spins on its way. In this way the processes "continue-straight" (1), "switch-and-continue" (2) and "switch-and-reverse" (3) allow to convert vertices into each other [Fig. 3.3(d)]. The "bounce" process (4) flips the spin on the entrance leg twice so that the vertex remains unchanged and the loop reverses its path. The subject of the next section is how a loop update with correct probabilities for the transition processes can be designed for the TFI model in complete analogy to the standard loop update for the XXZ-model described in [89].

3.2.1   Diagonal update for short-range interactions

In the diagonal update substitutions of identity operators $[0,0]_p$ for diagonal bond operators $[1,b]_p$ and vice versa are attempted for all propagation steps $p = 1, \ldots, \mathcal{L}$. The Metropolis acceptance probabilities for inserting or removing a diagonal bond operator are [89]:

$$P([0,0]_p \to [1,b]_p) = \min\left(1, \frac{N_b\beta\langle\alpha(p)|H_{1,b}|\alpha(p)\rangle}{\mathcal{L} - n}\right), \tag{3.28a}$$

$$P([1,b]_p \to [0,0]_p) = \min\left(1, \frac{\mathcal{L} - n + 1}{N_b\beta\langle\alpha(p)|H_{1,b}|\alpha(p)\rangle}\right). \tag{3.28b}$$

The factor N_b is due to the fact that there are N_b random positions where the bond can be inserted, while there is only one way to remove a particular bond. When traversing the operator sequence, the state $|\alpha\rangle$ is propagated whenever a spin-flip operator is encountered so that the instantaneous state $|\alpha(p)\rangle$ is always available for calculating the probabilities (3.28a) and (3.28b).

3.2.2   Off-diagonal update: Operator loop

For a first impression of how the operator loop update for the TFI model in the field eigenbasis works consider the example of a loop construction depicted in Fig. 3.4. Filled circles in Fig. 3.4(a-c) denote "spin-up", the spin state aligned along the field, i.e. $|\to\rangle$, open circles are "spin-down", i.e. $|\leftarrow\rangle$.

In Fig. 3.4(a) an operator loop drawn in red is initiated on the third spin at propagation step $p = 0$. After entering a vertex on one spin, which is called the *entrace leg*, the loop head selects probabilistically one of four possible *exit legs* and progresses, flipping the spins on its way. Thereby it also changes the vertex type. When the loop head returns to the start leg, the loop closes [Fig. 3.4(c)]. The loop update ensures that only allowed vertices are generated and that the are respected by the new configuration. In going from the SSE configuration in Fig. 3.4(a) to that in Fig. 3.4(c) the operator loop has changed the global magnetization. In Fig. 3.4(b) an intermediate step of the loop construction is shown for clarity, because two vertices are traversed by the loop
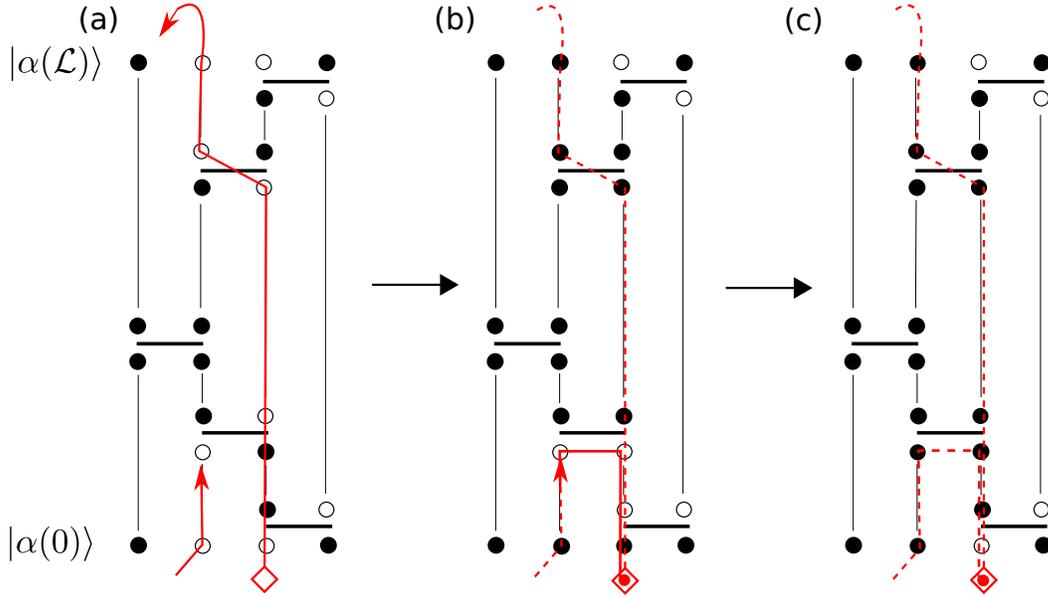
Fig. 3.4: Operator-loop update for the TFI model in the field eigenbasis, i.e. the computational basis consisting of the eigenstates of S^x. Vertical lines between vertex legs indicate that the spin state does not change in between. They represent the bidirectional *linked list* [89] of vertex legs, which allows to travel from one vertex leg directly to the connecting one. (a) Beginning with the first entrance leg (marked by a red diamond), the loop head travels on the linked list, flipping spins on its way and thereby converting different vertex types into each other. The loop construction terminates when the loop head reaches again the start leg (c). The intermediate configuration in (b) is not a valid SSE configuration.

twice and thus have an intermediate spin configuration which differs from the final one. The intermediate configuration in Fig. 3.4(b) is not a valid SSE configuration since the periodic boundary conditions in imaginary time have not yet been re-established.

Operator loops [89, 92] are capable of achieving global updates based on purely local decisions at each vertex. In the following we derive how the "scattering probabilities" af the worm head at each vertex type have to be chosen so as to satisfy global detailed balance. The detailed balance requirement

$$P(C \to C')W(C) = P(C' \to C)W(C') \tag{3.29}$$

involves the configurations $C = (\alpha, S_{\mathcal{L}})$ and $C' = (\alpha', S'_{\mathcal{L}})$ before and after the action of the operator loop as well as the global weight of an SSE configuration, $W(C) = W(\alpha, S_n) = \frac{\beta^n}{n!} \prod_{p=1}^{n} \langle \alpha(p)|H_{l_p}|\alpha(p-1)\rangle$ (an similarly for C'), which is the product over all vertices in the operator string. The probability that the construction

of an operator loop transforms configuration C into C' is [89]

$$P(C \to C') = \sum_{\{\infty\}} P(C, e_0)P(v, e_0 \to v_1, e_1)$$
$$\times P(v_1, e_1 \to v_2, e_2) \times \ldots \times P(v_{n-1}, e_{n-1} \to C', e_0), \tag{3.30}$$

where $P(C, e_0)$ is the probability for choosing the vertex leg e_0 as the initial starting point and $P(v, e_0 \to v_1, e_1)$ is the "scattering probability" of the loop head, i.e. the probability, given vertex v and entrance leg e_0, to leave the vertex on the exit leg e_1 thereby transforming it into vertex v_1. The sum is over all possible closed loops that lead from configuration C to configuration C'. For the reverse processes one can write

$$P(C' \to C) = \sum_{\{\infty\}} P(C', e_0)P(v, e_0 \to v_{n-1}, e_{n-1})$$
$$\times P(v_{n-1}, e_{n-1} \to v_{n-2}, e_{n-2}) \times \ldots \times P(v_1, e_1 \to C, e_0), \tag{3.31}$$

where the sum is over the same closed loops as in the previous equation. By inserting these expressions into the detailed balance equation (3.29), one sees that detailed balance can be satisfied locally

$$W(v_i)P(v_i, e_i \to v_{i+1}, e_{i+1}) = W(v_{i+1})P(v_{i+1}, e_{i+1} \to v_i, e_i) \tag{3.32}$$

by considering the update of each vertex v_i separately, since in the product of vertex weights $W(\alpha, S_n) = \frac{\beta^n}{n!} \prod_{p=1}^n \langle \alpha(p)|H_{l_p}|\alpha(p-1)\rangle$ all other factors, corresponding to unaffected vertices, cancel.

With the notation $W(v)P(v, e \to v', x) \equiv \mathcal{V}(v, e, x)$ for the weight[4] for assigning to vertex v a loop segment entering the vertex at the entrance leg $e = l_1$ and leaving it at the exit leg $x = l_2$, the condition for local detailed balance reads

$$\mathcal{V}(v, l_1, l_2) = \mathcal{V}(v', l_2, l_1). \tag{3.33}$$

Furthermore, conservation of probability demands

$$\sum_x \mathcal{V}(v, e, x) = \sum_x W(v)P(v, e \to v', x)$$
$$= W(v) \underbrace{\sum_x P(v, e \to v', x)}_{=1} = W(v), \tag{3.34}$$

which imposes additional relations among the $\mathcal{V}(v, l_1, l_2)$.

---

[4] Unlike the vertex weight $W(v)$ or the global weight of an SSE configuration, which is the product of all vertex weights in the operator string, the weight $\mathcal{V}(v, e, x)$ belongs to configurations in an extended space of invalid SSE configurations that do not contribute to the partition sum (see Ref. [89] for details).

Fig. 3.5 shows different combinations of $(v, l_1, l_2) \equiv$ (vertex, entrance leg, exit leg). In total there are 52 such combinations that lead, after flipping the spins on the entrance and exit leg, again to one of the five vertices corresponding to non-zero matrix elements. The combinations of vertices and loop segments assigned to them form an extended configuration space (see Ref. [89]). The letters on top of the configurations in Fig. 3.5 are the weights $\mathcal{V}(v, l_1, l_2)$. Fig. 3.5 lists only two subsets of all extended configurations. The left and right subset each have the important property that they are closed under the operation of flipping spins on the entrance and exit leg and inverting the direction of the loop [89]. The other configurations are related to these sets by exchanging the left and right site of a bond and by imaginary time inversion, which amounts to switching pairs of spins below and above the horizontal bar representing the bond operator. Therefore, the detailed balance condition Eq. (3.33) and the conservation of probability Eq. (3.34) can be satisfied for each set separately and we can use the same solutions for sets that are related by symmetry.

In Fig. 3.5 equal weights $\mathcal{V}(v, l_1, l_2) \in [a, b, c, b_1, b_2, b_3]$ are assigned to configurations (v, l_1, l_2) and (v', l_2, l_1) which are related by flipping the spins under the loop segments and inverting its arrow (i.e. by exchanging the entrance and exit legs l_1 and l_2). With this choice, the detailed balance condition Eq. (3.33) is already fulfilled.

Note that the actual transition probability $P(v, e \rightarrow v', x)$ for selecting an exit leg based on the current vertex and an entrance leg is

$$P(v, e \rightarrow v', x) = \frac{\mathcal{V}(v, e, x)}{W(v)}, \tag{3.35}$$

i.e. we need to divide the weight in the extended configuration space by the weight of the "bare" vertex weight. For programming the loop update only $P(v, e \rightarrow v', x)$ is needed.

Next the conservation of probability needs to be satisfied, which can be achieved by considering each row of vertices in Fig. 3.5 separately. According to Eq. (3.34) the sum of weights $\mathcal{V}(v, e, x)$ for all configuration that can be reached by entering the same vertex on the same entrance leg and leaving it on all possible exit legs has to be equal to the vertex weight $W(v)$. Applying this requirement to the left-hand side of Fig. 3.5 one obtains from the three rows the linear system of equations

$$\begin{aligned} W_1 &\equiv W \left(\begin{smallmatrix} \bullet & \!\!\!\!-\!\!\!\!- & \bullet \\ \circ & & \circ \end{smallmatrix} \right) = a + b + b_1, \\ W_2 &\equiv W \left(\begin{smallmatrix} \circ & \!\!\!\!-\!\!\!\!- & \bullet \\ \bullet & & \circ \end{smallmatrix} \right) = c + b + b_2, \\ W_3 &\equiv W \left(\begin{smallmatrix} \bullet & \!\!\!\!-\!\!\!\!- & \bullet \\ \bullet & & \bullet \end{smallmatrix} \right) = a + c + b_3. \end{aligned} \tag{3.36}$$

The right-hand side of Fig. 3.5 gives an independent set of equations

$$\begin{aligned} W_1 &\equiv W \left(\begin{smallmatrix} \bullet & \!\!\!\!-\!\!\!\!- & \bullet \\ \circ & & \circ \end{smallmatrix} \right) = b' + b'_1, \\ W_2 &\equiv W \left(\begin{smallmatrix} \circ & \!\!\!\!-\!\!\!\!- & \bullet \\ \bullet & & \circ \end{smallmatrix} \right) = b' + b'_2. \end{aligned} \tag{3.37}$$
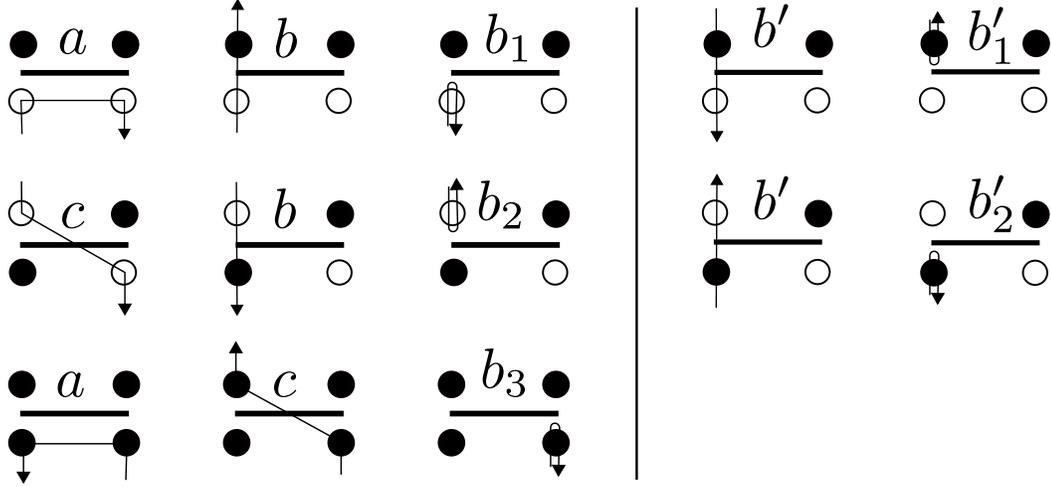
Fig. 3.5: Assignment of weights $\mathcal{V}(v, e, x)$ in the extended configuration space of vertices and directed-loop segments. In total there are 52 possible combinations of (vertex, entrance leg, exit leg) which, after flipping the spins on the entrance and exit leg of the loop segment, lead to a new allowed vertex. Only one fourth of all these configurations is listed here, the others being related by symmetry.

The sets of Eqs. (3.36) and (3.37) are the *directed-loop equations* [89]. With 3 (respectively, 2) equations for 6 (respectively, 4) unknowns they are underdetermined and there are in principle inifinitely many solutions. A heuristic rule of thumb for the design of an efficient algorithm is that the probability of bounce processes, b_i, should be minimized [89] so as to avoid backtracking of the loop. Setting $b_1' = b_2' = 0$ in Eq. (3.37), two types of bounce processes are completely eliminated and the only remaining process for the given vertex and entrance leg depicted on the right in Fig. 3.5 becomes deterministic[5]. To find solutions that minimize the bounce weights b_i, we rearrange Eqs. (3.36) so that all bounce weights are on the right-hand side

$$
\begin{aligned}
a &= \frac{\Gamma}{z} + \frac{-b_1 + b_2 - b_3}{2}, \\
b &= \frac{J}{4} - \frac{\Gamma}{z} + \frac{-b_1 - b_2 + b_3}{2}, \\
c &= \frac{\Gamma}{z} + \frac{b_1 - b_2 - b_3}{2}.
\end{aligned}
\tag{3.38}
$$

We have $\Gamma, J > 0$. The requirement that the weights in the extended configuration space of vertices and loop segments be positive, $a, b, c > 0$, imposes a constraint on the bounce weights, i.e. we can set them all to zero only as long as $\frac{\Gamma}{z} < \frac{J}{4}$, since otherwise $b < 0$. For larger transverse field Γ, at least the bounce weight b_3 must

---

[5] Recalling that the transition probability Eq. (3.35) is given by the weight in the extended configuration space divided by the bare vertex weight gives $\frac{b_{1/2}'}{W_{1/2}} = \frac{W_{1/2}}{W_{1/2}} = 1$.

be non-zero. Fig. 3.6 shows the resulting algorithmic phase diagram with the region I, where all bounce weights can be eliminated, and the region II, where at least one bounce weight is non-zero[6]. One can easily show that $b_3/W_3 \to 1$ as $\Gamma/J \to \infty$. Then
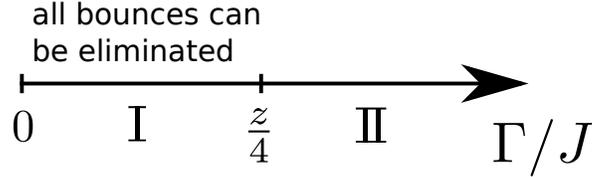
Fig. 3.6: Algorithmic phase diagram for the operator-loop update of the TFI model in the field eigenbasis. If the transverse field is smaller than $\frac{zJ}{4}$, with z the coordination number of the lattice, then all bounce weights in the detailed balance equations can be set to zero (region I). Otherwise at least one bounce weight is non-zero (region II).

every loop starting on a leg of the transverse-field vertex bounces off and closes immediately onto itself without any changes to the configuration so that the update becomes less efficient. Furthermore, the vertex is the only diagonal vertex of the transverse-field Ising model in the eigenbasis of the field so that after the first diagonal update only this vertex type is contained in the operator string. Due to the frequent bounces, in the limit $\Gamma/J \to \infty$ virtually no off-diagonal update is carried out any more and the algorithm reduces to the diagonal update, which consists of inserting and removing transverse-field vertices.

The number of loops per Monte Carlo step is determined during the thermalization phase such that for example each vertex will be visited on average twice per Monte Carlo step. After the thermalization phase, the number of loops per Monte Carlo step must be kept fixed. In summary, one Monte Carlo step consists of the diagonal update, followed by the construction of the linked vertex list and the off-diagonal update with the construction of a fixed number of operator loops.

Sign problem on non-bipartite lattices

The problem with this approach is that there is a "sign problem" on frustrated lattices such as the triangular lattice, which makes Monte Carlo simulations impossible (The sign problem is discussed in detail in Sect. 4.6.). On a non-bipartite[7], i.e. frustrated

---

[6] For longer-range interactions there are detailed balance equations like (3.38) for every class of bonds $b = (i, j)$ of certain range and interaction strength $J_{i(b), j(b)}$ and the transition probabilities in the loop update are different for each bond type. There are separate algorithmic phase diagrams, with the coordination number z in Fig. 3.6 replaced by $\frac{2\sum_b J_{i(b), j(b)}}{N_s J_{i(b), j(b)}}$, which is the coordination number *per bond type*, counting how many bonds of a certain range emanate from a lattice site.

[7] The definition of a *bipartite lattice* is that all sites can be divided into two sublattices A and B such that spins on sublattice A only interact with spins on sublattice B. Examples for bipartite lattices are the hypercubic lattices, the honeycomb lattice or the Lieb lattice; non-bipartite lattices are the triangular, kagomé and the 2D and 3D pyrochlore lattices.

lattice periodic boundary conditions in propagation direction, $|\alpha(p=0)\rangle = |\alpha(p=\mathcal{L})\rangle$, can be satisfied for an odd number of off-diagonal bond operators in the operator string (see Fig. 3.7). In this case the weight of the SSE configuration, being the product of the weights of all bond operators, is negative and we encounter a sign problem [43, Sect.5.2]. On a bipartite lattice, on the other hand, there is no sign problem even if some of the off-diagonal matrix elements are negative. This is because an even number of off-diagonal operators is required for a valid configuration so as to satisfy the periodicity $|\alpha(p=0)\rangle = |\alpha(p=\mathcal{L})\rangle$ in propagation direction [8]. The absence of a sign problem for bipartite lattices can also be demonstrated in an alternative way by means of a canonical transformation, which rotates all spins on the A-sublattice by an angle π around the z-axis:

$$S_j^x \to -S_j^x, \quad S_j^y \to -S_j^y, \quad S_j^z \to S_j^z \quad \text{for } j \in A. \tag{3.39}$$

The spectrum of the Hamiltonian is not affected since the new operators again obey the canonical commutation relations, but the sign of the interaction term relative to

---

[8]For a bipartite lattice with periodic boundary conditions this is only true if the number of sites N_γ in any direction γ is even. Strictly speaking, a bipartite lattice with an odd number of sites in any direction ceases to be bipartite once periodic boundary conditions are imposed.
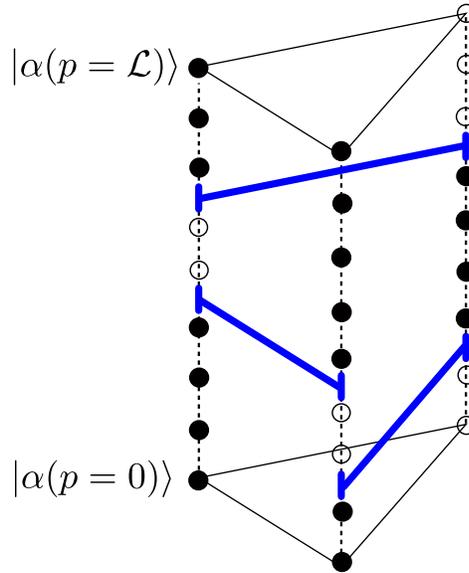
Fig. 3.7: On non-bipartite lattices the presence of off-diagonal bond operators with negative matrix elements leads to a sign problem. The figure shows an SSE configuration for a single triangular plaquette. Initial and final states $|\alpha(p=0)\rangle$ and $|\alpha(p=\mathcal{L})\rangle$ are the same, as required by the trace structure of the partition sum, since each site is acted on an even number of times by an off-diagonal operator (drawn as blue bars). The weight of this SSE configuration is negative due to an odd number of off-diagonal bond operators with negative matrix elements.

the field term in Eq. (3.22) has changed so that all matrix elements are positive. For a frustrated system, no unitary transformation can be found that makes all negative matrix elements positive.

We have not adopted the above approach of simulating the TFI model in the eigenbasis of the field due to this sign problem on frustrated lattices. In the next section a special algorithm for the TFI model with arbitrary, frustrated and long-range interactions based on Ref. [95] will be described. This algorithm was used in Chapts. 6 and 7 of this thesis.

3.3   SSE method for TFI model with arbitrary (frustrated and long-range) interactions

In Ref. [95] Sandvik proposed a SSE QMC method that can deal with transverse field Ising models with arbitrary, long-range or frustrated, interactions. The Hamiltonian Eq. (3.20) of the transverse-field Ising model is decomposed as

$$\mathcal{H}_{\text{TFI}} = -\sum_{i=1}^{N} \sum_{j=0}^{N} H_{i,j} \tag{3.40}$$

into the following bond or single-site operators

$$H_{0,0} = \mathbb{1} \qquad\qquad [0,0], \tag{3.41}$$

$$H_{i,0} = \Gamma\hat{\sigma}_i^x = \Gamma\left(\hat{\sigma}_i^+ + \hat{\sigma}_i^-\right)[i,0], \quad i > 0, \tag{3.42}$$

$$H_{i,i} = \Gamma\mathbb{1} \qquad\qquad [i,i], \quad i > 0, \tag{3.43}$$

$$H_{i,j} = |J_{ij}| - J_{ij}\hat{\sigma}_i^z\hat{\sigma}_j^z \qquad [i,j], \quad i \neq j; i,j > 0, \tag{3.44}$$

where $\hat{\sigma}_i$ are the Pauli spin matrices with eigenvalues $\sigma_i^z = \pm 1$. The right column in Eq. (3.41) illustrates how the bond operators are represented in computer memory by a pair of integers $i \in \{1, 2, \ldots, N\}$ and $j \in \{0, 1, 2, \ldots, N\}$. In this formulation, the interactions J_{ij} can in principle have any range and any sign.

With the constants $|J_{ij}|$ added to the Ising bond operators $H_{i,j}$ ($i \neq j$) the matrix elements $w_{ij} = \langle\sigma_i^z(p+1)\sigma_j^z(p+1)|H_{i,j}|\sigma_i^z(p)\sigma_j^z(p)\rangle$ are either $2|J_{ij}|$ or 0 and thus positive and usable as relative probabilities in an importance sampling scheme. Furthermore, the special choice of constant for each bond imposes a constraint: Ising operators $[i,j]_p$ at propagation step p may act only on states with $\sigma_i^z(p) = \sigma_j^z(p)$ (FM spin configuration) if $J_{ij} < 0$, or $\sigma_i^z(p) = -\sigma_j^z(p)$ (AFM spin configuration) if $J_{ij} > 0$ since otherwise the weight of the configuration is zero due to the zero matrix element w_{ij}. This is a *completely local* constraint acting in the SSE propagation direction, regardless of the range of interactions.

The artificially introduced constant operators $H_{i,0} = \Gamma\mathbb{1}$ will be used for easily inserting spin-flip operators in the off-diagonal update (see Sect. 3.3.2 below). With

constant operators $\Gamma \mathbb{1}$ and spin-flip operators $\Gamma \sigma^x$ having the same matrix element Γ, exchanging one for the other does not change the weight of an SSE configuration.

3.3.1   Diagonal update with long-range interactions

As will be discussed below, in the case of long-range interactions, the SSE formulation with constants added to the diagonal operators in such a way that the spin-spin term either gives zero or a constant when acting on any basis state [see Eq. (3.41) and also Eq. (3.25) for the case of the loop update] avoids the interaction summation [95] that is typically necessary in worldline Monte Carlo methods, and the scaling of the number of operations with system size is reduced from $\mathcal{O}(N^2)$ to $\mathcal{O}(N \ln N)$ [95, 96], which can be further reduced down to $\mathcal{O}(N)$ [97]. This approach was used e.g. for the long-range XXZ model in [98, 99].

To appreciate how this SSE formulation gives an advantage for long-range interacting systems, we have to take a few steps back and review some related algorithms. First consider a naive single spin-flip Metropolis update of an Ising system with long-range interactions. Since each spin interacts with all other spins, it takes $\mathcal{O}(N)$ operations to evaluate the energy difference and acceptance probability for a single spin-flip and $\mathcal{O}(N^2)$ operations for an entire sweep of the lattice. The same $\mathcal{O}(N^2)$ scaling applies to the conventional Swendsen-Wand cluster algorithm [60] which proceeds as follows: Inspect each bond $b = (i, j)$ sequentially; depending on whether the spins at i and j are in an allowed configuration (i.e. the energetically favourable configuration $S_i^z = S_j^z$ for FM interactions) or not, a bond variable σ_l is *activated* ($\sigma_l = 1$) or *deactivated* ($\sigma_l = 0$) with probability [60]

$$P_{ij} = \delta_{S_i^z, S_j^z}[1 - e^{-2\beta J_{ij}}]. \tag{3.45}$$

Connected activated bonds form a cluster. After all clusters have been constructed, each cluster is flipped with probability $1/2$ which leads to a new configuration.[9] Since for long-range interactions each of $N_b = N(N-1)/2$ bonds has to be visited, the method scales like $\mathcal{O}(N_b) = \mathcal{O}(N^2)$.

Luijten and Blöte [96] made the crucial observation that, even in a long-range interacting system, only $\mathcal{O}(N)$ from the $\mathcal{O}(N^2)$ bonds contribute to the cluster construction. In fact, the average number of candidate bonds in the Swendsen-Wang algorithm is approximately [97]

$$\sum_{l=1}^{N_b} p_l = \frac{1}{2} \sum_{i=1}^{N} \sum_{j \neq i} (1 - e^{-2\beta J_{ij}}) \sim \frac{1}{2} \sum_{i=1}^{N} \int_1^L dr \, r^{d-1} \left(1 - e^{-2\beta J(r)}\right)$$

$$\sim \beta N \int_1^L dr \, r^{d-1} J(r). \tag{3.46}$$

---

[9]It can be shown [60] that this cluster algorithm satisfies detailed balance and ergodicity and greatly reduces critical slowing down at a phase transition.

Assuming that the interaction integral converges, the number of candidate bonds at fixed temperature thus scales like N instead of N^2. The number of bonds that are actually inspected per Monte Carlo sweep can then be drastically reduced from $\mathcal{O}(N^2)$ to $\mathcal{O}(N)$ by separating the activation probability into two parts [96, 97]:

$$
\begin{aligned}
P_l &= p_l \, \delta_{\sigma_l,1}, \\
p_l &= 1 - \exp(-2\beta J_{ij}).
\end{aligned}
\tag{3.47}
$$

By sampling bonds $l \in \{1, 2, \ldots, N_b\}$ from the discrete probability distribution p_l and activating them with probability $\delta_{\sigma_l,1}$, the probability P_l is eventually realized. It its this efficient two-step process of first selecting candidate bonds to be activated (or inserted in the SSE framework) according to probability tables that are *independent* of the spin state and then activating them depending on the spin state afterwards, which is at the heart of the $\mathcal{O}(N)$ Monte Calo methods for long-range interacting spin systems [95–97].

Now we return to discussing how this strategy is realized in the diagonal update of the SSE framework [95]. Traversing the operator sequence $S_{\mathcal{L}}$, at each propagation step p diagonal operators, constants $H_{i,i}$ or Ising operators $H_{i,j}$ $(i \neq j)$, are exchanged for identity operators: $[0,0]_p \leftrightarrow [i,j]_p$. The removal of a diagonal operator, $[i,j]_p \to [0,0]_p$ is always possible without any constraint. The insertion of an Ising operator $H_{i,j}(i \neq j)$ between sites i and j, however, may be forbidded due to an incompatible spin configuration. Initially the indices i and j are left undetermined and it is assumed that any $[i,j]$ would be allowed. The corresponding Metropolis acceptance probabilities are obtained from relating the weight of a configuration before and after the insertion or removal.

$$
P(\mathbb{1} \to [i,j]_p) = \min\left(1, \frac{\sum w_{\text{new}}}{w_{\text{old}}}\right) = \min\left(1, \frac{\beta(N\Gamma + 2\sum_{i\neq j}|J_{ij}|)}{L-n}\right)
\tag{3.48a}
$$

$$
P([i,j]_p \to \mathbb{1}) = \min\left(1, \frac{w_{\text{new}}}{\sum w_{\text{old}}}\right) = \min\left(1, \frac{L-n+1}{\beta(N\Gamma + 2\sum_{i\neq j}|J_{ij}|)}\right)
\tag{3.48b}
$$

Here, the change in the expansion order $n \to n \pm 1$ contributes a prefactor $\beta^{\pm} \frac{[L-(n\pm1)]!}{(L-n)!}$ which multiplies the ratio between the matrix element 1 of the identity operator $[0,0]$ and the sum $N\Gamma + 2\sum_{i\neq j}|J_{ij}|$ of the non-zero matrix elements of all $[i,j]$ operators. Note that these probabilities are independent of the propagated state $|\alpha(p)\rangle$. [10]

---

[10]If the Ising operator $H_{i,j}$, $i \neq j$, had two different non-zero matrix elements $\langle\alpha(p+1)|H_{i,j}|\alpha(p)\rangle$ depending on whether the bond (i,j) is in the FM state $\sigma_i^z(p) = \sigma_j^z(p)$ or in the AFM state $\sigma_i^z(p) = -\sigma_j^z(p)$, then the cumulative probability tables would depend explicitly on the instantaneous state $|\alpha(p)\rangle$ at propagation step p. When traversing all propagation steps p in the diagonal update, the probability tables would then need to be recomputed each time the state $|\alpha(p)\rangle$ has changed due to a spin flip operator. This would clearly thwart the efficiency of the algorithm and explains the special choice of constants $|J_{ij}|$ added in Eq. (3.41) which guarantee that the probabilities for inserting a diagonal operator are independent of the spin state.

Once it has been decided that an operator should be inserted, the indices i and j need to be determined according to the weight, i.e. the matrix element

$$M_{ij} = \begin{cases} 2|J_{ij}| & \text{for } i \neq j \\ \Gamma & \text{for } i = j \end{cases} \tag{3.49}$$

of the corresponding bond operator. Under the assumption that any $[i, j]$ is allowed in the update $[0, 0]_p \to [i, j]_p$, the relative probability for the first index i is

$$P^{(1)}(i) = \sum_j M_{ij}, \tag{3.50}$$

which involves the sum over all possible choices for the second index j. The relative probability for selecting the second index j of the operator $[i, j]$, given that the first index i was chosen, is

$$P^{(2)}(j|i) = M_{ij}. \tag{3.51}$$

In the case of translational invariance, the first index i can be selected at random and the selection process simplifies to:

1. Select a site i with probability $1/N$.

2. Select another site j with relative probability $P^{(2)}(j|i)$.

Having determined an index pair $[i, j]$ according to the probability distributions (3.50) and (3.51), it is checked whether the insertion of the operator $[i, j]$ is allowed at propagation step p, i.e. whether the FM ($J_{ij} > 0$) or AFM ($J_{ij} < 0$) nature of the Ising operator $H_{i,j}$ is compatible with the instantaneous spin configuration $|\alpha(p)\rangle$. If it is forbidden due to a vanishing matrix element in Eq. (3.41), the selection process is repeated until an allowed operator is found. There is no risk of the search never ending as a constant operator $H_{i,i}, i \neq 0$, can always be inserted (for $\Gamma \neq 0$). Typically an operator compatible with the spin configuration is quickly found since the interactions favour the allowed spin configuration [95].

Binary search of cumulative probability tables

Picking the bond indices i and j of an operator that is to be inserted in the diagonal update according to the relative probabilities $P^{(1)}(i)$ and $P^{(2)}(j|i)$ requires the efficient sampling of these discrete probability distributions.

One method consists in constructing cumulative probability tables

$$P^{(1)}_{\text{cumul}}(k) = \frac{\sum_{i=1}^{k} P^{(1)}(i)}{\sum_{i=1}^{N} P^{(1)}(i)}, \quad \text{for} \quad k = 1, \dots, N \tag{3.52}$$

and

$$P^{(2)}_{\text{cumul}}(k|i) = \frac{\sum_{j=1}^{k} P^{(2)}(j|i)}{\sum_{j=1}^{N} P^{(2)}(j|i)}, \quad \text{for} \quad k = 1, \ldots, N. \tag{3.53}$$

For selecting the first index i of an operator $[i, j]$ to be inserted, a random number $\eta \in [0, 1]$ is generated. Then the table $P^{(1)}_{\text{cumul}}(k)$ is searched for the smallest index k such that $\eta \leq P^{(1)}_{\text{cumul}}(k)$ (see Fig. 3.8(a)) and we set $i = k$. The second index j is determined in the same way, using this time the cumulatice probability table $P^{(2)}_{\text{cumul}}(k|i)$. The
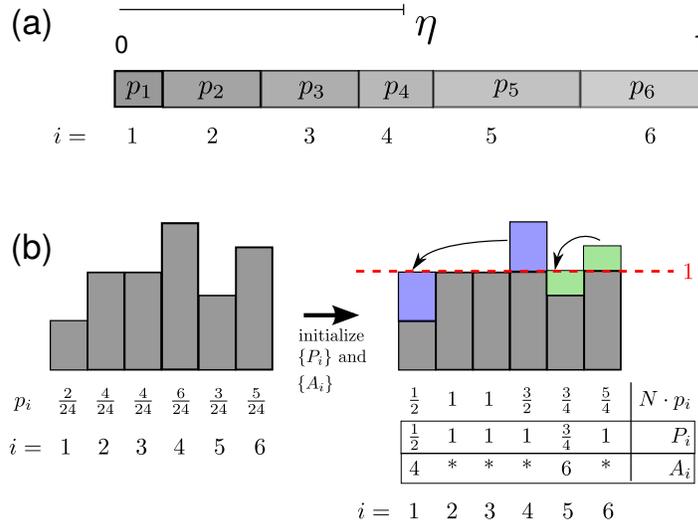
Fig. 3.8: (a) Cumulative probability table. The length of the sum of the first k segments corresponds to $P_{\text{cumul}}(k) = \sum_{i=1}^{k} p_i$. A uniformly distributed random variable $\eta \in [0, 1)$ satisfies $P_{\text{cumul}}(k-1) \leq \eta < P_{\text{cumul}}(k)$ with probability p_k. Thus, the discrete probability distribution p_i can be sampled by drawing a uniform random number η and locating its position with respect to the segments of the cumulative probability table. This is achieved with a binary search in $\mathcal{O}(\ln N)$ operations. (b) Simple example illustrating the idea behind Walker's method of alias for sampling a discrete probability distribution with $\mathcal{O}(1)$ operations.

probability tables are pre-generated before the simulation since the probabilities for inserting an operator are independent of the spin configuration. (Sect. 3.3.2 discusses a modified algorithm where the cumulative probability tables need to be recomputed after each change to the spin configuration.)

For systems without translational invariance, i.e. systems with random interactions or open boundary conditions [as in Sect. 6], all pregenerated probability tables for choosing the second index j have in total N^2 elements. In translationally invariant systems the first index can be chosen with uniform probability $1/N$ and there is only one table $P^{(2)}_{\text{cumul}}$ of size N. The search of a cumulative probability table with N entries can be achieved with a binary search in $\mathcal{O}(\ln N)$ operations.

Walker's method of alias

An even faster method for sampling a discrete probability distribution is Walker's method of alias [97, 100, 101]. It allows to generate integer random numbers $X \in \{1, \ldots, N\}$ from a probability distribution $p_i = P(X = i)$ in constant, $\mathcal{O}(1)$, time. Initially, a table of modified probabilities $\tilde{P}_i$ and an alias table A_i need to be set up, based on the probability distribution p_i.

The method relies on the observation [100] that a biased dice with N faces [Fig. 3.8(b) left] can be simulated by an unbiased dice in combination with a biased coin [Fig. 3.8(b) right]. Fig. 3.8(b) illustrates the idea of redistributing the probability weight of the distribution p_i in such a way over N slots of equal magnitude (the "faces of the dice") that there are only two options per slot, which are then picked at random by throwing a biased coin. The procedure for sampling an integral random number from the distribution p_i is:

1. Generate a uniform integral random number K with $1 \leq K \leq N$.

2. Generate a random real number $\eta \in [0, 1)$ from a uniform distribution.

3. If $\eta < P_K$, then $X = K$, otherwise return the alias number for the slot K, i.e. $X = A_K$.

An explanation of how to set up the tables of modified probabilities $\tilde{P}_i$ and alias numbers A_i efficiently can be found in [97].

3.3.2   Off-diagonal update

Within the setting of Eqs. (3.40) and (3.41), there are several possibile ways of performing the off-diagonal update, where constant operators, $H_{i,i} \equiv [i, i]$, and spin-flip operators, $H_{i,0} \equiv [i, 0]$, are exchanged. In this process the expansion order n stays the same, but the initial state $|\alpha(0)\rangle$ may be updated so that the magnetization of SSE configuration changes while the energy $E = -\langle n \rangle / \beta$ remains constant.

The most straightforward way of exchanging constants and spin-flip operators is the local update (Sect. 3.3.2), where a cluster is confined to individual sites and extends only in imaginary time [95]. Close to the quantum critical point this method suffers from long autocorrelation times, though.

In the quantum cluster update (Sect. 3.3.2), the constructed clusters are irregularly shaped both in space an imaginary time. Rather than loops, as in Sect. 3.2, they are multibranch stuctures. The autocorrelation times at criticality are reduced, but for small transverse field Γ the clusters tend to span the entire lattice rendering the Monte Carlo update inefficient. In Sect. 3.3.2 we report an attempt at designing a *probability changing cluster algorithm*, which we dub the *quantum* Wolff algorithm (in analogy to the Wolff algorithm [61] for classical spin systems). There, a tunable parameter controls the growth of the clusters in real space so that the probability of adding a branch to a cluster can be maintained below the percolation threshold.

Local off-diagonal update

In the local off-diagonal update [95], successive pairs of spin flip operators that sit on the same site are exchanged for pairs of constant operators and vice versa:

$$[i, i]_{p1} [i, i]_{p2} \quad \longleftrightarrow \quad [i, 0]_{p1} [i, 0]_{p2}, \quad i \neq 0. \tag{3.54}$$

This flips all spins between propagation step p_1 and p_2 where the operators are located. The pairwise exchange ensures that the spin configuration preserves the periodic boundary conditions in imaginary time, $|\alpha(p = 0)\rangle = |\alpha(p = \mathcal{L})\rangle$. Otherwise the resulting SSE configuration would have zero weight. Furthermore, the update Eq.(3.54) only leads to a new configuration with non-zero weight if there is no Ising operator $[i, j]_p$ or $[j, i]_p$ at propagation step $p_1 < p < p_2$ since flipping only the spins on the two legs at site i would convert a previously satisfied bond into an unsatisfied one, which has vanishing weight according to Eq. (3.41).

Unlike the diagonal update, the off-diagonal update can change the global magnetization of the system. The operator substrings $\{S_L^{(i)}\}$ are periodic in imaginary time: When exchanging according to Eq. (3.54) a pair of non-constrained operators that are connected through the boundary in imaginary time, the initial spin configuration $|\alpha(p = 0)\rangle = |S_1^z(0), \dots, \S_N^z(0)\rangle$ needs to be updated, i.e. $S_i^z(p = 0) \to -S_i^z(p = 0)$, at the respective site i. The local off-diagonal update is illustrated in Fig. 3.9.

To carry out the local off-diagonal update, taking into account the Ising constraints, the operator string S_L is first partitioned into subsequences $\{S_L^{(i)}\}_{i=1}^N$ for each site i, in which a constraint on site i, which is imposed by Ising operators $[i, j]_p$ or $[j, i]_p$ sitting at propagation step p, is recorded as a special flag ("Ising delimiter") in the subsequence. Successive "Ising delimiters" that are not separated by constants or spin flip operators can be collapsed into a single flag indicating the presence of one or more such operators. Each subsequence is updated by selecting at random two non-constrained neighbouring operators and performing the substitution Eq. (3.54) if the two operators are of the same type. If they are of different type, they can be permuted. For each subsequence $S_L^{(i)}$, this procedure is performed a number of times that is proportional to the length of the subsequence.

The final step of the local off-diagonal update consists in the reconstruction of the full operator string S_L from the updated subsequences $S_L^{(i)}$ at each site.

Spins that do note have any operator acting on them anywhere in the operator string can be flipped with probability $1/2$. This occurs only at high temperature, where the operator string is short, and is in general not sufficient to ensure ergodicity.

Multibranch quantum-cluster update

Cluster algorithms [60, 61, 74] are known to lead to a Monte Carlo dynamics with much shorter autocorrelation times than single-site updates. This is particularly important at a phase transition, where critical slowing down occurs. The superiority of
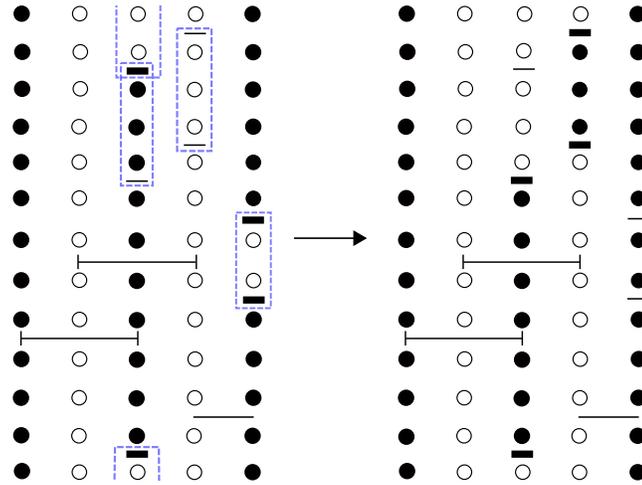
Fig. 3.9: Illustration of the local off-diagonal update. On each site, adjacent constants or spin-flip operators, which are not constrained by a Ising vertex sitting in between, are collected pairwise (indicated by blue dashed lines). The spins in between the pairs of two-leg vertices form single-site clusters, which can wrap around the boundaries in imaginary time. With probability one-half it is decided to flip each of the clusters, which is done at the level of the operator string by exchanging spin flip operators for constant operators and vice versa: $H_{i,0} \leftrightarrow H_{i,i}$ (■ $\longleftrightarrow$ —). This type of pairwise update guarantees that periodic boundary conditions in imaginary time are preserved. If a cluster wraps around imaginary time, the initial spin configuration $|\alpha(0)\rangle$ is updated, too.

cluster updates is due to a mathematically rigorous observation, the Fortuin-Kasteleyn transformation, which maps a ferromagnetic Potts model[11] to a corresponding bond percolation problem (see [102] for a review). Importantly, simulations of percolation models generate independent configurations in every sweep so that the autocorrelation time is exactly zero.

The guiding principle for the construction of multibranch clusters, which are irregulary shaped in space and imaginary time, is that after flipping all spins that are part of the cluster the new configuration should have non-zero weight. Fig. 3.10 gives a first impression of the cluster shapes. With the vertex weights according to Eq. (3.41) a new configuration with non-zero weight can only be reached if all spins connected to an Ising vertex are flipped simultaneously. This causes clusters to branch out spatially and in imaginary time. A cluster branch stops if it hits a spin flip or constant operator. The resulting cluster construction rules are illustrated in Fig. 3.11(a-c): A dashed

---

[11]The s-state Potts model, a generalization of the Ising model, is defined as

$$\mathcal{H} = K \sum_{\langle i,j \rangle} (\delta_{S_i, S_j} - 1),$$

where the spin S_i on lattice size i can take on the values $1, 2, \ldots, s$. The Ising model is a two-state ($s = 2$) Potts model.
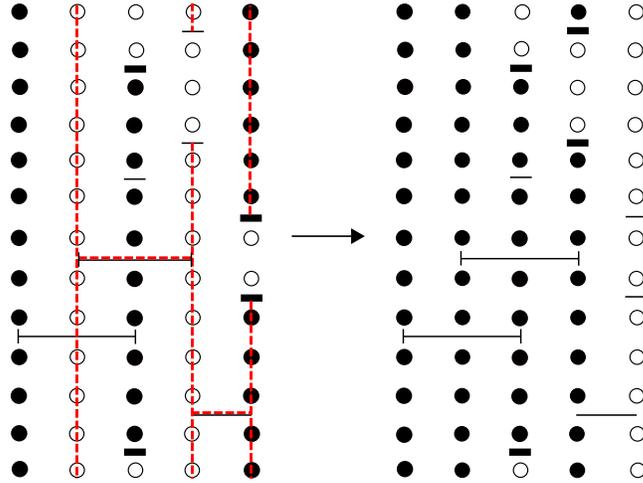
Fig. 3.10: Illustration of the multibranch off-diagonal update for a five-site chain. The right-hand side shows the SSE configuration after flipping the red cluster on the left. The simulation cell can be decomposed deterministally into disjoint Swendsen-Wang clusters. Since the configurations before and after flipping a cluster have the same weight, each cluster can be flipped with probability one-half. The cluster construction rules ensure that periodic boundary conditions in imaginary time are maintained.

arrow points at the entrance leg where an incoming cluster branch enters a vertex; all spins are flipped according to the rules in Fig. 3.11(a-c); outgoing arrows in Fig. 3.11 denote new cluster branches.

Essential for the cluster construction is the doubly linked vertex list [43, 89], which connects legs of vertices accross imaginary time. We refer to Ref. [89] for a pseudocode implementation and to Sect. 3.3.3 for an illustrative example how vertex legs are numbered in a practical implementation.

The construction of one cluster proceeds in the following steps. To start a cluster, one of the legs of the n non-trivial vertices in the operator string S_L is picked at random as an entrance leg and the corresponding spin is flipped. The type of vertex to which the leg is connected is enquired. If it is an Ising vertex, the cluster branches out at all legs (see Fig. 3.11 (a)), which means that all its legs except for the current entrance leg are put onto a stack to be processed later one by one as new entrance legs. If the entrance leg is connected to a constant or spin-flip operator (see Fig. 3.11 (b)), only the entrance spin is flipped and the vertex type changes from $H_{0,0}$ to $H_{i,i}$, and vice versa. No legs are put on the stack and this branch of the cluster terminates. The cluster is completed when all legs on the stack have been processed. Details for an efficient implementation of the multibranch cluster update are given below in Sect. 3.3.3.

Without a longitudinal field (coupling to S_i^z) a cluster can always be flipped because the weight of the configuration is not changed: the matrix element of the Ising bond operators depends only on the relative orientation of the spins and is not affected when both spins are flipped simultaneously while the matrix elements of the constant and

spin-flip operators are both equal to Γ so that exchanging them does not modify the weight.

Note that, unlike in the loop update of Sect. 3.2, here the cluster construction is completely deterministic once the operator string is given. Therefore, it is most convenient to construct all clusters, flipping each one with heat-bath probability $1/2$ as in the classical Swendsen-Wang algorithm [60]. In fact, it can be shown [95] that in the classical limit $\Gamma = 0$, where imaginary time collapses to a single time slice, the clusters that are built according to the procedure outlined above are identical to those of the classical Swendsen-Wang construction. Whether to flip a cluster or not can be decided randomly before the cluster construction. But even if is not to be flipped, the cluster needs to be constructed fully so that all visited legs can be marked and are not used again as entrance legs for a new cluster. We record the distribution of cluster sizes, where the size is defined as the number of legs $n_{\text{legs}} = n_{2-\text{leg}} + n_{4-\text{leg}}$ that belong to a cluster.

The quantum cluster updates the initial spin configuration $|\alpha(0)\rangle$ whenever a cluster branch winds around the boundary in imaginary time. To detect a winding branch, the direction of the cluster growth along the linked vertex list is recorded as "up" or "down". A winding branch corresponds to an increase (decrease) of the leg numbers when going "down" ("up").

We define one Monte Carlo step (MCS) as a full sweep of diagonal updates, followed by the construction of the linked vertex list and a Swendsen-Wang type quantum-cluster update in which all clusters are constructed and flipped with heat-bath probability $1/2$. Free spins that do not belong to any cluster can be flipped with probability $1/2$.

Comparison between local off-diagonal and multibranch cluster update

To validate our implementation of the local off-diagonal and the multibranch cluster update, we present in Fig. 3.12 high-precision results for a small chain of $L = 16$ sites and compare with Lanczos exact diagonalization at zero temperature. The interactions are long-range, decaying like an inverse square power law, $1/|i - j|^\alpha$ with $\alpha = 2$, and with periodic boundary conditions (PBC) according to Ref. [97] (see Sect. 7.1 for details). For the local off-diagonal update, the test simulation lasted for 10^6 MCS preceded by a thermalization phase of 10^4 MCS. In the case of the multibranch cluster update, the test run consisted of 10^4 thermalization steps followed by 10^5 MCS. The bin size for computing autocorrelation times ranges between 2000 and 4000 MCS (in the critical region).

The main panel of Fig. 3.12 shows that for low temperature and small values of Γ/J the local off-diagonal update, which was demonstrated to be very efficient at high temperature [95], is not entirely satisfactory: For some initial conditions (i.e. random seed values) a sudden deterioration of ergodicity is observed, where the timeseries of observables, rather than fluctuate around the mean value, suddenly goes on a long excursion before coming back to the vicinity of the correct mean value. Another related
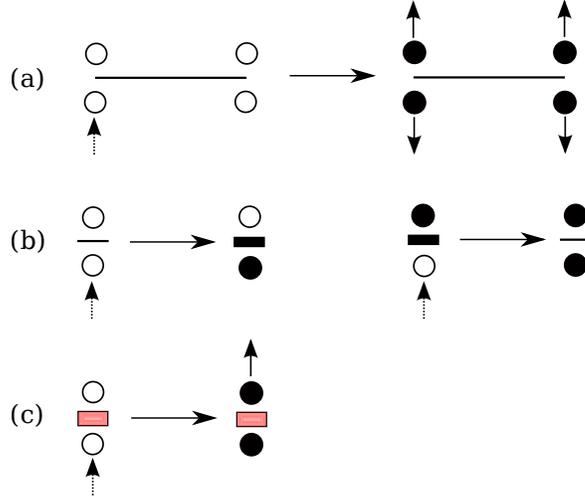
Fig. 3.11: Cluster construction rules for the multibranch cluster update of Ref. [95]. (a) Branching out along a ferromagnetic Ising vertex. (b) The cluster branch stops when a constant is converted into a spin-flip operator (left) or vice versa (right). (c) Longitudinal field (Zeeman) vertices do not affect the process of constructing a cluster, only the probability with which it can be flipped.
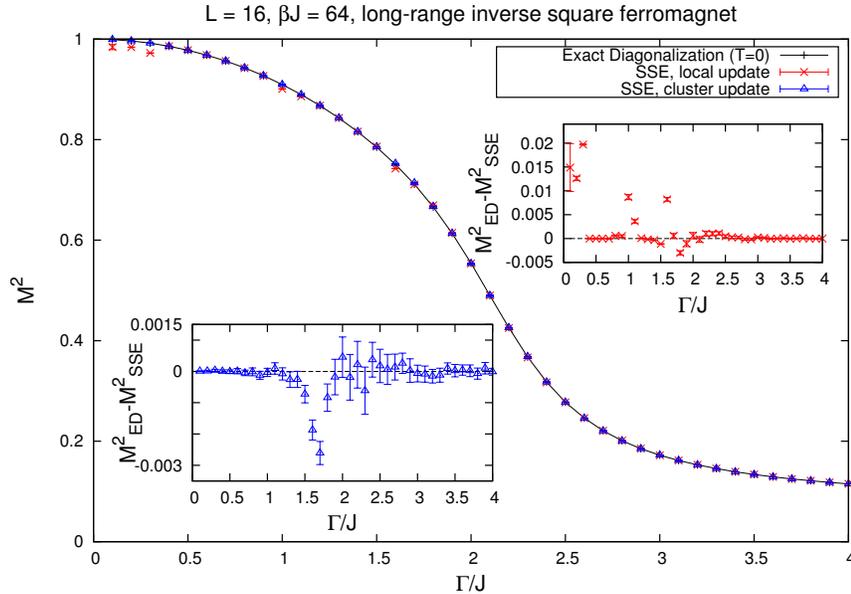
Fig. 3.12: Benchmarking of the local off-diagonal update and the multibranch cluster update for the long-range transverse-field Ising chain with interactions decaying as $J_{ij} = J/|i - j|^2$ (PBC include all periodic images of the simulation cell). Exact diagonalization calculations are performed at zero temperature. The insets zoom in on the statistical fluctuations of the Monte Carlo data. The small systematic deviation in the critical region around $\Gamma/J \approx 1.5$ (see left inset) is due to the finite temperature ($\beta J = 64$) of the QMC simulations.
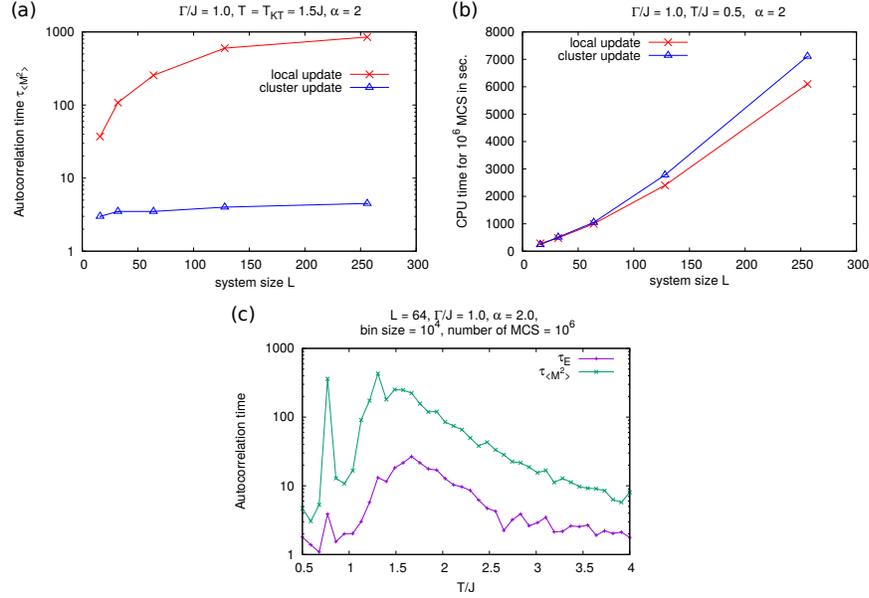
Fig. 3.13: Comparison between local off-diagonal update and multibranch cluster update with regard to their autocorrelation times (a) and CPU times (b) as a function of linear system size L. For the cluster update the autocorrelation time of the magnetization M^2 near the critical temperature $T \approx T_{KT}$ is two orders of magnitude smaller than for the local update, at comparable computational cost (b). With a local off-diagonal update the autocorrelation times for energy E and magnetization M^2 diverge in the critical region near the finite-temperature phase transition at $T \approx T_{KT}$ (c).

phenomenon is that the timeseries converges to the wrong value and jumps to the correct one only after an exceedingly long time. The outliers in the main panel and the right inset of Fig. 3.12 are related to such issues with ergodicity. The quantum cluster update, on the other hand, reliably converges to the exact result for all values of Γ. The small systematic deviation from the result of exact diagonalization in the left inset can be attributed to the finite temperature ($\beta J = 64$) at which the QMC simulations are preformed.

In the critical region around a phase transition, the autocorrelation times, e.q. for $(\langle \sum_i S_i^z \rangle)^2$, are two orders of magnitude shorter for the cluster update that for the local update [Fig. 3.13(c)], at comparable computational cost [Fig. 3.13(b)].

Digression: Quantum Wolff algorithm

For small transverse fields, there are only few transverse field or constant operators in the operator string that stop the cluster from growing in imaginary time. As a consequence the deterministically built cluster percolates in imaginary time, i.e. it spans almost the entire simulation cell. This is particularly severe for long-range

interactions where the cluster can branch out in large steps in the spatial direction[12]. When the cluster percolates, the off-diagonal update becomes inefficient since almost all spins in the simulation cell are flipped simultaneously back and forth. This leads to a serious deterioration of ergodicity. A possible remedy is to let the cluster grow *non-deterministically* by introducing a parameter that allows to control the growth of the cluster in the spatial direction. The cluster construction then resembles the classical Wolff algorithm [61]. When a constant $C_{\text{Wolff}} > 0$ is added to the Ising bond operators

$$H_{ij} = -J_{ij}S_i^z S_j^z + |J_{ij}| + C_{\text{Wolff}}, \tag{3.55}$$

their matrix elements become

$$\begin{aligned}
w_{ij} &= \langle S_i^z, S_j^z | H_{ij} | S_i'^z, S_j'^z \rangle \\
&= \begin{cases} 2|J_{ij}| + C_{\text{Wolff}} & \text{FM (AFM) operator on FM (AFM) spin configuration ,} \\ C_{\text{Wolff}} & \text{otherwise,} \end{cases}
\end{aligned}$$

$$\tag{3.56}$$

and there is a non-zero probability to place an Ising exchange operator on an unsatisfied spin configuration, i.e. a FM operator on an AFM spin configuration or vice versa. Of course, subsequently one needs to subtract a constant $N_b C_{\text{Wolff}}$ from the energy estimator, with N_b the number of Ising exchange bonds in the Hamiltonian.

Like in the classical Wolff algorithm [61], the construction of the cluster becomes non-deterministic and additional processes in the cluster construction are possible when the constraint that FM (AFM) bonds have non-zero weight only on FM (AFM) spin configurations, which is imposed by the choice of constants in Eq. (3.41), is relaxed to Eq. (3.55). Then unsatisfied bonds (i.e. FM bonds on AFM spin configurations and vice versa) have weight C_{Wolff} and the following cluster construction processes, illustrated in Fig. 3.14, are allowed (i.e. they do not lead to vanishing weight of the resulting configuration):

- ① Branch out along a satisfied bond.

- ② Do not branch out along a satisfied bond, thereby making it unsatisfied, which is indicated by two slanted dashes (⟍) in Fig. 3.14.

- ③ Do not branch out along an unsatisfied bond, thereby restoring it (⊘).

- ④ Branch out along an unsatisfied bond such that the bond remains unsatisfied.

- ⑤ Another branch of the same cluster visits the cut bond on the other legs of the vertex, thereby undoing the cut and making the bond satisfied or unsatisfied again (⊗) depending on the previous state.

---

[12] The dynamics of the movement of a single branch head is that of random Lévy flights [103].
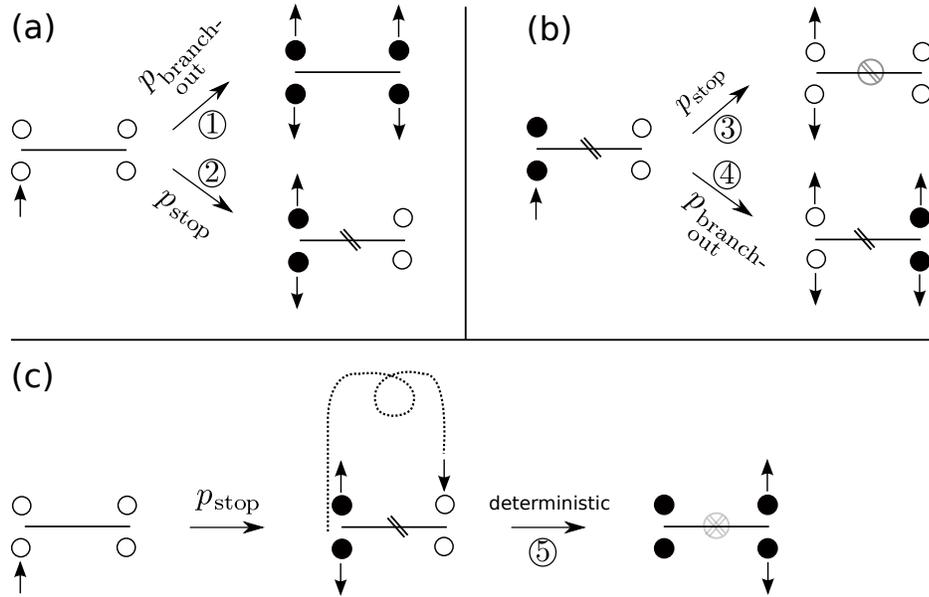
Fig. 3.14: Cluster construction rules for the non-deterministic quantum Wolff algorithm. See the main text for an explanation of the processes ① to ⑤. $p_{\text{stop}}(w_{ij}) = 1 - p_{\text{branch-out}}(w_{ij})$ is the probability for not branching out along a particular Ising bond operator H_{ij} (with weight w_{ij}). $p_{\text{stop}}(w_{ij})$ must be determined from considerations of detailed balance.

Now the cluster construction is non-deterministic and it needs to be decided either, with probability $p_{\text{branch-out}}(w_{ij})$, to follow all four legs of an Ising vertex (processes ① and ④) or, with probability $p_{\text{stop}}(w_{ij})$, not to branch out along the Ising vertex and to follow instead only the exit leg which is on the same site as the entrance leg (processes ② and ③). We mark all legs that have been visited while growing the cluster so that branches that retrace the path of another branch are excluded. Process ⑤, therefore, is deterministic as branching out along an Ising operator that was visited before by the same cluster cannot occur.

Next, $p_{\text{stop}}(w_{ij}) = 1 - p_{\text{branch-out}}(w_{ij})$ needs to be determined such that detailed balance is satisfied. For this, recall that the transition probability $T(\mu \to \nu)$ for going from a global configuration μ to another global configuration ν by flipping an entire cluster of spins can be decomposed into the probability for algorithmically generating the cluster move, $g(\mu \to \nu)$, and the acceptance probability, $A(\mu \to \nu)$. The cluster is built according to local decisions in each of the branching processes depicted in Fig. 3.14 and $g(\mu \to \nu)$ should, therefore, be a product of the branching probabilities $p_{\text{branch-out}}(w_{ij})$ or $p_{\text{stop}}(w_{ij}) = 1 - p_{\text{branch-out}}(w_{ij})$, which, in turn, should depend in some functional form on the weight w_{ij} of the Ising operator H_{ij} where the branching process occurs. The question is how $p_{\text{stop}}(w_{ij})$ needs to be chosen such that detailed balance is obeyed with respect to the weights $W_\mu = \prod_{p=1}^{\mathcal{L}} w_{ij}(p)$ and $W_\nu = \prod_{p=1}^{\mathcal{L}} w'_{ij}(p)$ of the global configuration before and after the cluster move, respectively.

In the conventional cluster update [95], which assigns zero weight to unsatisfied bonds, (and in the absence of a longitudinal field) the weight of a cluster is the same before and after flipping it and each constructed cluster can be flipped with probability $1/2$. In contrast, when a quantum Wolff cluster is flipped, the weight may change if unsatisfied bonds are created (or removed). Satisfied or unsatisfied bonds in the bulk of the cluster, i.e. bonds along which the cluster has branched out, do not play a role for the transition probabilities as their weight remains the same when the cluster is flipped. Bonds that were cut (restored) by one branch of the cluster and uncut (cut again) by another branch of the same cluster (process ⑤) do not contribute to the transition probabilities either, since their weight has not changed when the total cluster is completed. In summary, only the boundary (or cut) bonds are relevant to the transition probabilities, which are the bonds with one leg belonging to the cluster and the other leg not so that their weight changes in the following way when the cluster is flipped:

$$
\begin{array}{llll}
\text{sat. bond } (i,j): & w_{ij} = 2|J_{ij}| + C_{\text{Wolff}} & \rightarrow & \text{unsat. bond}: w'_{ij} = C_{\text{Wolff}} \\
\text{unsat. bond } (i,j): & w_{ij} = C_{\text{Wolff}} & \rightarrow & \text{sat. bond}: w'_{ij} = 2|J_{ij}| + C_{\text{Wolff}}
\end{array}
\tag{3.57}
$$

Considering only the m boundary bonds that are being cut, the total ratio of weights after and before flipping the cluster is

$$
\frac{W_\nu}{W_\mu} = \frac{W_{\text{new}}}{W_{\text{old}}} = \prod_{\substack{(i,j) \\ \text{boundary} \\ \text{bonds}}} \frac{w'_{ij}}{w_{ij}}.
\tag{3.58}
$$

Inserting Eq. (3.58) into the detailed balance equation

$$
\frac{W_\nu}{W_\mu} = \frac{g(\mu \rightarrow \nu)}{g(\nu \rightarrow \mu)} \cdot \frac{A(\mu \rightarrow \nu)}{A(\nu \rightarrow \mu)},
\tag{3.59}
$$

and noting that $g(\mu \rightarrow \nu)$ is the probability for not branching out along any of the m cut boundary bonds, we obtain a condition on $p_{\text{stop}}(i,j) \equiv p_{\text{stop}}(w_{ij})$:

$$
\prod_{\substack{(i,j) \\ \text{boundary} \\ \text{bonds}}} \frac{w'_{ij}}{w_{ij}} = \frac{p_{\text{stop}}(i_1,j_1)p_{\text{stop}}(i_2,j_2)\cdots p_{\text{stop}}(i_m,j_m)}{p'_{\text{stop}}(i_1,j_1)p'_{\text{stop}}(i_2,j_2)\cdots p'_{\text{stop}}(i_m,j_m)} \frac{A(\mu \rightarrow \nu)}{A(\nu \rightarrow \mu)}.
\tag{3.60}
$$

Choosing $p_{\text{stop}}(i,j) = \frac{1}{w_{ij}}$, detailed balance can be fulfilled with an acceptance ratio $A(\mu \rightarrow \nu)/A(\nu \rightarrow \mu)$ equal to unity, just like in the classical Wolff algorithm [61]. With the weights Eq. (3.56) the probabilities for constructing the Wolff cluster are

$$
\begin{aligned}
p_{\text{branch-out}}(i,j) &= 1 - p_{\text{stop}}(i,j) \\
&= \begin{cases} 1 - \frac{1}{2|J_{ij}|+C_{\text{Wolff}}} & \text{for satisfied bonds,} \\ 1 - \frac{1}{C_{\text{Wolff}}} & \text{for unsatisfied bonds.} \end{cases}
\end{aligned}
\tag{3.61}
$$
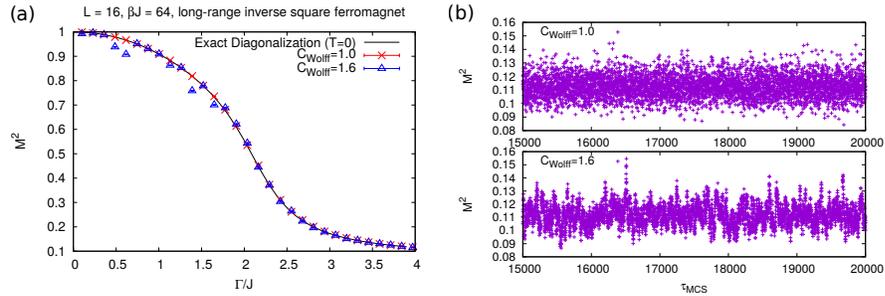
Fig. 3.15: Benchmark of the Wolff single cluster algorithm for $C_{\text{Wolff}} = 1.0$ and $C_{\text{Wolff}} = 1.6$ (a). With increasing C_{Wolff} the autocorrelation times grow as can be seen from the comparison of timeseries in (b). The simulations consist of 10^3 thermalization steps and $2 \cdot 10^4$ measurement steps. The outliers in (a) for $C_{\text{Wolff}} = 1.6$ appear to be not thermalized.

This shows that the quantum Wolff cluster tends to branch out preferentially along "strong" bonds which have a large weight w_{ij}. The requirement $0 \leq p_{\text{branch-out}} \leq 1$ imposes $C_{\text{Wolff}} \geq 1$, which is guaranteed by writing $C_{\text{Wolff}} = 1 + \varepsilon_{\text{Wolff}}$ with $\varepsilon_{\text{Wolff}} > 0$. With the choice $C_{\text{Wolff}} = 1.0$, branching out along unsatisfied Ising vertices is excluded, but branching out along satisfied bonds is possible.

However, there is a serious downside to the quantum Wolff algorithm, which appears in the diagonal update. The efficient two-step process of the conventional quantum cluster update [95] in which positions for an Ising bond operator are selected independently of the spin configuration and then rejected if a FM bond comes to lie on an AFM spin configuration (or vice versa) is no longer possible; the insertion probabilities depend on the spin configuration at every propagation step. Therefore, during the diagonal update the cumulative probability tables have to be recomputed after each propagation step in which a spin flip operator changes the instantaneous spin configuration, which poses a serious bottleneck. As in the parameter regime where the quantum Wolff algorithm is advantageous, namely for small transverse field Γ, spin flip operators in the operator string are rare, one may hope that recomputing the probability tables is still feasible.

One Monte Carlo step consists of a diagonal update, the construction of the linked list and the construction of a fixed number of Wolff clusters that is chosen during the thermalization phase such that a large fraction of the simulation cell is covered. Fig. 3.15 shows a rough comparison of results obtained with the Wolff algorithm ($C_{\text{Wolff}} = 1.0$ and 1.6) for a short Monte Carlo run of 10^3 steps with exact diagonalization for the same parameters as in Fig. 3.12. The overall agreement indicates that the Markov chain generated with the modified cluster growth probabilities Eq. (3.61) samples the correct stationary probability distribution, but both the inefficiency of the diagonal update and the extremely slow and poor exploration of phase space especially for small Γ render this approach inferior to the original multibranch cluster update [95] described in Sect. 3.3. The properties of the algorithm deteriorate with increasing value of the

parameter C_{Wolff}. Thermalization is very slow for $C_{\text{Wolff}} = 1.6$ ($t_{\text{therm}} > 5000$ MCS are needed for thermalization for small Γ versus $t_{\text{therm}} < 100$ MCS for $C_{\text{Wolff}} = 1.0$). Likewise the autocorrelation times become increasingly long for $C_{\text{Wolff}} > 1.0$.

Worst of all, the quantum Wolff algorithm does not seem to solve the problem of cluster percolation for small Γ. Conversely, the failure of the quantum Wolff algorithm highlights the importance of the special choice of weights Eq. (3.41) in the conventional cluster update for the transverse field Ising model.

Digression: Cluster update with longitudinal field

In principle, a longitudinal (or Zeeman) field term of the form $h^z \sum_i S_i^z$ can be easily included into the algorithm by introducing a diagonal operator, labelled by the site index $i \geq 1$,

$$H_{i,-i} = |h^z| - h^z S_i^z + C_{\|}, \tag{3.62}$$

which corresponds to two two-leg vertices with weights

$$\langle S_i^z(p+1)|H_{i,-i}|S_i^z(p)\rangle = \begin{cases} C_{\|}, & \text{if } S_i^z(p) = +\text{sign}[h^z] \\ 2|h^z| + C_{\|}, & \text{if } S_i^z(p) = -\text{sign}[h^z]. \end{cases} \tag{3.63}$$

The parameter $C_{\|} \geq 0$ must be suitably chosen. As far as the diagonal update is concerned, the Zeeman vertices are treated in the same way as other two-leg vertices. Modifications arise in the off-diagonal update: The Zeeman vertices (see Fig. 3.11(c)) do not affect the cluster construction, but they impede the flipping of a Swendsen-Wang cluster in the quantum cluster update. When $C_{\|} = 0$, the constraint is sharp, i.e. flipping a cluster which has at least one Zeeman vertex attached to one of its branches results in a configuration with zero weight. For $C_{\|} > 0$, there is a finite Metropolis probability to flip a cluster

$$P_{\text{flip}} = \min\left(1, \frac{W_{\text{new}}}{W_{\text{old}}}\right), \tag{3.64}$$

$$\frac{W_{\text{new}}}{W_{\text{old}}} = \prod_{p \in \text{cluster}} \frac{\langle \bar{S}_{i(p+1)}^z(p+1)|H_{i,-i}|\bar{S}_{i(p)}^z(p)\rangle}{\langle S_{i(p+1)}^z(p+1)|H_{i,-i}|S_{i(p)}^z(p)\rangle} = \left(\frac{C_{\|}}{2|h^z| + C_{\|}+}\right)^{N_+ - N_-}. \tag{3.65}$$

The notation "$p \in \text{cluster}$" means that the Zeeman vertex at propagation step p forms part of the cluster that is to be flipped; $\bar{S}_i^z \equiv -S_i^z$ is the opposite spin state of S_i^z; and $N_{\pm}$ is the number of Zeeman vertices in the Swendsen-Wang cluster with spin states along (+) and opposite to (-) the longitudinal field. For large longitudinal fields, the update may become inefficient due to frequent rejections of cluster moves if the ratio $W_{\text{new}}/W_{\text{old}}$ becomes too small.

Also, in the presence of a longitudinal field, it is no longer possible to decide whether a cluster should be flipped before it has been constructed. If a cluster move is

rejected, all changes to the initial spin configuration and operator list have to be undone. Therefore, a Wolff-type cluster update, where only a single cluster is constructed per Monte Carlo step, is more appropriate in this case. If a cluster move is rejected, all changes that were effectuated during the cluster construction can be undone by immediately starting a new diagonal update [89].

Digression: Plaquette-based quantum-cluster update

The SSE scheme of Eq. (3.41), where the Hamiltonian is decomposed into Ising bond operators is not optimal for simulating frustrated systems with elementary triangular plaquettes. This can be understood by looking at the highly degenerate ground state manifold of the classical triangular Ising AFM, i.e. Eq. (3.20) with $\Gamma = 0$ [104]. The defining property of a ground state is that it contains only minimally frustrated triangular plaquettes Δ, which can be expressed as the constraint $\sum_{i \in \Delta} S_i^z = \pm 1$ for all plaquettes Δ. As illustrated in Fig. 3.16, flipping spins bond-wise creates maximally frustrated plaquettes, characterized by $\sum_{i \in \Delta} S_i^z = \pm 3$, so that the Monte Carlo random walker jumps between the ground state manifold and excited states rather than moving from one minimally frustrated configuration to the next.
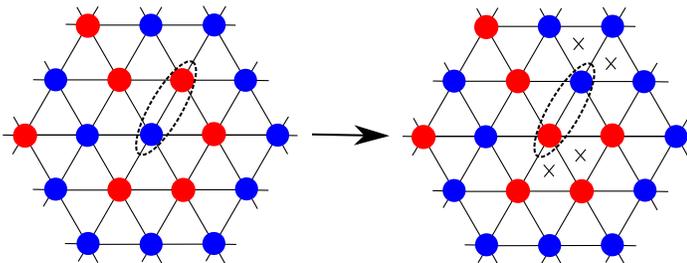
Fig. 3.16: The highly degenerate ground state manifold of the classical triangular Ising AFM [104] contains only minimally frustrated triangular plaquettes (left). ↑-spins (↓-spins) are red (blue). A Monte-Carlo update algorithm which flips spins bond-wise (dashed ellipse) generates maximally frustrated triangular plaquettes (indicated by the crosses) thereby bringing the configuration far away from the ground state manifold.

As shown in Ref. [105] a plaquette-based quantum cluster update leads to a significantly faster decay of autocorrelation functions for the triangular antiferromagnet than the conventional, bond-based quantum-cluster update and to a broader distribution of cluster sizes. The algorithm[13] of Ref. [105] is generally applicable to antiferromagnetic TFI models on lattices that can be decomposed into elementary triangular plaquettes

---

[13]The author has implemented the plaquette-based cluster update according to Ref. [105]. However, since Ref. [105] appeared only after the completion of the study on the triangular lattice presented in Sect. 6, all simulations were performed with the algorithm of Sect. 3.3.2, which is not optimal for frustrated lattices.

(e.g. triangular and kagomé lattice). The main idea consists in replacing the nearest-neighbour bond operators by a plaquette operator

$$H_{-i,-i} = \frac{3}{2}J_1 - \frac{J_1}{2}\left(S^z_{A(i)}S^z_{B(i)} + S^z_{B(i)}S^z_{C(i)} + S^z_{A(i)}S^z_{C(i)}\right). \tag{3.66}$$

In order to stick with the labelling of operators in the operator sequence by at most two indices, we label the plaquette operator of the i-th triangular plaquette by a negative index. The constants are chosen such that maximally frustrated plaquette configurations have zero weight, $\langle\uparrow\uparrow\uparrow\,|H_{-i,-i}|\,\uparrow\uparrow\uparrow\rangle = \langle\downarrow\downarrow\downarrow\,|H_{-i,-i}|\,\downarrow\downarrow\downarrow\rangle = 0$, and minimally frustrated plaquette configurations have weight $2J_1$. The factor of $1/2$ in front of the second term compensates for the double-counting of sites when summing over all plaquettes due to the fact that each link is shared by two plaquettes. Since nearest-neighbour interactions are already accounted for by the plaquette operators, the bond operators $H_{i,j}$ in Eq. (3.41) include only Ising interactions beyond nearest neighbours.

The Metropolis probabilities for inserting or removing a diagonal operator in the diagonal update are:

$$\begin{aligned}P(\mathbb{1} \to \text{diag. operator}) &= \min\left(1, \frac{\beta(N_{\text{sites}}\Gamma + \sum_{i,j}2|J_{ij}| + 2J_1 N_\Delta)}{\mathcal{L} - n}\right), \\ P(\text{diag. operator} \to \mathbb{1}) &= \min\left(1, \frac{\mathcal{L} - n + 1}{\beta(N_{\text{sites}}\Gamma + \sum_{i,j}2|J_{ij}| + 2J_1 N_\Delta)}\right).\end{aligned} \tag{3.67}$$

As before, the insertion of operators proceeds in a two-step process, where it is first assumed that any operator can always be inserted, and once a particular operator has been selected it may be rejected based on the spin configuration. Once the decision is made to replace an identity with a diagonal operator, a class of diagonal operators is selected from which an operator should be picked. With $\Sigma = N_{\text{sites}}\Gamma + \sum_{i,j}2|J_{ij}| + 2J_1 N_\Delta$ the sum of all diagonal matrix elements, the probability to choose the class of constant operators is $N_{\text{sites}}\Gamma/\Sigma$, for the class of Ising bonds it is $\sum_{ij}2|J_{ij}|/\Sigma$ and for the plaquette operators $2N_\Delta J_1/\Sigma$. Within the respective classes, plaquettes are inserted with uniform probability $1/N_\Delta$, constants with uniform probability $1/N_{\text{sites}}$, and (long-range) bond operators are inserted according to the cumulative probability tables described in Sect. 3.3.1.

If a particular Ising bond operator $H_{i,j}$ $(i \neq j; i, j > 0)$ or plaquette operator $H_{-i,-i}$ is selected, but not allowed since on the given spin configuration its insertion would result in a zero matrix element according to Eqs. (3.41) or (3.66), then no update is made at that propagation step and the sweep through the operator string continues.

The quantum cluster update remains deterministic and the only modification is an additional cluster construction rule [105] that applies when the entrance leg is connected to a triangular plaquette vertex. A useful prescription for updating a plaquette Ising vertex should transform a minimally frustrated triangular plaquette into another

minimally frustrated one since otherwise the weight of the resulting configuration would be zero. Furthermore, ergodicity and detailed balance must be satisfied. These requirements lead to the cluster construction rules depicted in Fig. 3.17.

In order to specify rules that guarantee that the cluster stays in the subspace of minimally frustrated vertex configurations whenever a cluster branch reaches a triangular Ising exchange vertex, it is necessary to introduce the notion of *privileged sites* [105]. The two legs of a triangular vertex that sit on a privileged site are called *privileged legs*, the remaining four legs are *ordinary legs*. In each of the elementary triangular plaquettes of the lattice one site is singled out as a privileged site. There is considerable freedom in the choice of privileged sites, each corresponding to a different cluster construction protocol. A natural choice is based on the tripartite decomposition of the triangular lattice into A, B, and C sublattices and a protocol in which all privileged sites are A-sites is defined as an *A-update* [105], which is illustrated in Fig. 3.17.

First note that each minimally frustrated Ising exchange vertex corresponds to a triangular plaquette in which two sites take part in the *majority* spin configuration and one site hosts a *minority* spin. The cluster construction rules now depend on whether the privileged site (in Fig. 3.17 this is the A-site) is in the majority or minority spin configuration. This distinction ensures that no maximally frustrated triangular plaquettes (with zero weight) are generated. If the privileged site is a majority site and the entrance leg is a privileged leg (upper left corner of Fig. 3.17), then the other privileged leg on the same site is put onto the stack and both privileged legs are flipped. If the entrance leg is an ordinary leg, then all other ordinary legs are put onto the stack and flipped (lower left corner of Fig. 3.17). If, on the other hand, the privileged site is a minority site (right column of Fig. 3.17), then the nature of the entrance leg is irrelevant and all legs of the Ising exchange vertex (except for the entrance leg) are put onto the stack and flipped.

The cluster construction procedure just described has a number of features that are crucial to ensure detailed balance. First, in each process the privileged leg retains its property of being a majority or minority leg. Second, if an entrance leg is an ordinary (privileged) leg, the exit legs are also ordinary (privileged) legs, while for the processes in the right column there is no distinction between privileged or ordinary entrance legs. These two symmetry properties of the cluster construction rules guarantee that, with an exit leg chosen as an entrance leg of a reverse process, a symmetric scenario for the transition processes and their reverse processes arises. Together with the fact that all plaquette configurations have the same weight, this makes detailed balance possible. Note that the construction of individual clusters is fully determined by the given operator string. In this case, the processes that are related through the detailed balance condition are the full construction of a cluster, which is then flipped, and the reverse process of constructing the same cluster on the reversed spin configuration and
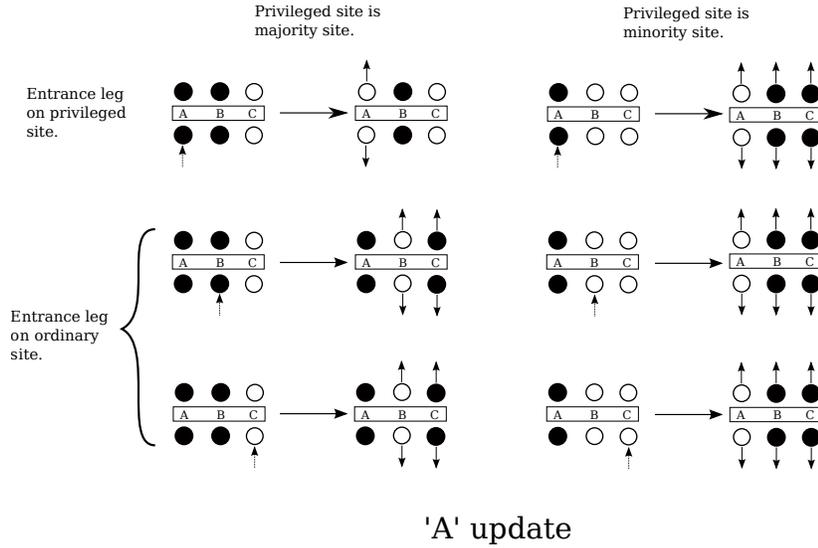
'A' update

Fig. 3.17: Cluster construction rules for the plaquette-based quantum cluster update of Ref. [105]. In an *A-update*, the sites on the *A*-sublattice have been singled out as "privileged" sites.

flipping it[14].

3.3.3 Implementation details

Given an efficient implementation of the quantum-cluster update, the CPU time per Monte Carlo sweep is dominated in most parameter regimes by the computational cost of the diagonal update. For very large fields ($\Gamma > 10$) the CPU time spent on the cluster update becomes comparable to the diagonal update. This is due to the large number of relatively small clusters that are bounded in imaginary time by constant or spin-flip operators, which abound for large transverse fields.

"Ghost legs"

In modern computer architectures memory access is very slow compared to the high number of operations that the processor can carry out during the time that is required to fetch a piece of memory. Therefore it is advantageous to avoid storing information in arrays whenever it can be computed with few operations on the fly. In the cluster construction algorithm a mapping is needed that relates each leg to the vertex to which it is connected and to the site on which it sits. Vertex types (together with the sites on which the operator acts) are stored in the operator string `opstring(p)` (i.e. $S_{\mathcal{L}}$) and accessed through the propagation index p. Thus, a mapping leg number

---

[14] In contrast, the construction of an operator loop in the loop update (Sect. 3.2) is non-deterministic and detailed balance is ensured locally at every vertex.

$\rightarrow$ propagation index is required. In principle, this mapping needs to be stored in a data structure that is constructed while building the linked list. However, if all vertices have the same number of legs, such a data structure can be avoided. In the operator loop update for the XXZ model or the transverse-field Ising model in the field eigenbasis (see Sect. 3.2) all vertices have 4 legs (see Fig. 3.3) and therefore the non-trivial propagation step $\tilde{p} \in [1, 2, \ldots, n_{\exp}]$ at which a non-trivial operator sits is given by $\tilde{p} = (leg - 1)/4 + 1$. In the multibranch cluster algorithm described in Sect. 3.3.2 the problem arises that non-trivial operators have a different number of legs: constants and spin-flip operators have 2 legs, bond operators have 4 legs and plaquette operators have 6 legs. With the introduction of "ghost legs", the leg counter is incremented by 6 even if a 2-leg or 4-leg vertex is encountered (see Fig.3.18). Then the propagation step $\tilde{p}$ in the list of non-trivial operators can be again directly inferred from the leg number as $\tilde{p} = (leg - 1)/6 + 1$.

Before the cluster update the non-trivial operators (i.e. excluding fill-in identities) are extracted from the operator string and the non-trivial propagation steps $\tilde{p}$ are recorded so that the full operator string including identities can be reconstructed easily after the off-diagonal update. Note that the off-diagonal update changes neither the expansion order nor the location of non-trivial operators in propagation time.
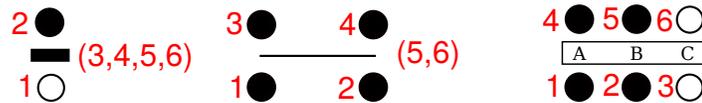
Fig. 3.18: Numbering of legs around 2-leg, 4-leg and 6-leg vertices. For 2-leg and 4-leg vertices, so-called "ghost legs" (in brackets) are included so that the increment of the leg counter per non-trivial operator is constant. Without 6-leg plaquette vertices, "ghost legs" need to be introduced only for 2-leg vertices.

The stack of unprocessed legs

The central structure of the multibranch cluster algorithm is the *stack*, a data structure holding a list of vertex legs which works according to the "last-in-first-out" principle. How the stack is used during the cluster update is best described by means of an example SSE configuration. A number of points, some of which will be illustrated by the example SSE configuration in Fig. 3.19, should be noted:

- The entrance leg of a vertex is never put onto the stack except for the very first entrance leg with which the cluster was started (the "start leg", leg 1 in the example). This ensures that the cluster grows in all directions.

- When the cluster winds around imaginary time ("winding macrospin"), the initial spin configuration is updated.
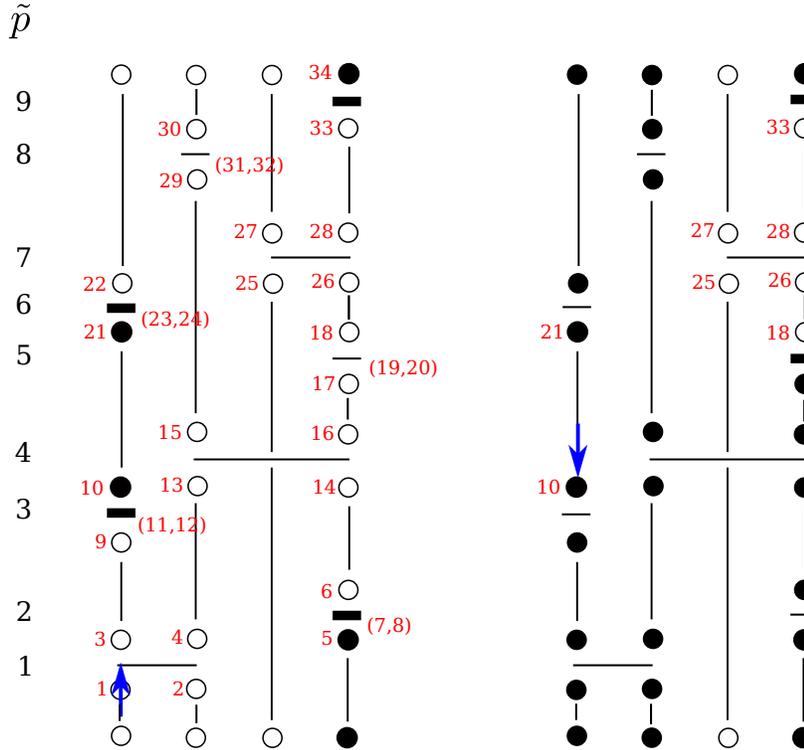
Fig. 3.19: Illustration of the constructing a single cluster during the off-diagonal update. Constant spin states between operators have been replaced by lines. In the graphical representation the lines correspond to the doubly-linked list of vertex legs. Leg labels include "ghost legs" (in brackets), i.e. leg numbers that are skipped by the leg counter. The initial configuration on the left is transformed into the final configuration on the right by growing a cluster with the leg with number 1 (indicated by the blue arrow) as a start leg and by flipping all spins that belong to the cluster. The initial and final configuration have the same weight.

- If on one site there sits a single constant and no other 2-leg operator throughout imaginary time, it is necessarily touched by the cluster twice from two directions, with one branch wrapping around imaginary time. The exchange const $\leftrightarrow$ spin-flip operator is done twice in the sequence const $\rightarrow$ spin-flip operator $\rightarrow$ const, so that a constant operator remains on an inverted spin configuration.

- If a cluster branch reaches a leg that belongs to an already visited vertex (this situation is not shown in Fig. 3.19), the branch stops and no legs are put onto the stack. To take care of this scenario legs are marked as "visited" when they are put onto the stack; when they are popped from the stack, they are marked as "done" so that they cannot be used again as start legs for a new cluster.

In the following we list the successive stack configurations of unprocessed legs as the cluster branches move from one vertex to the next for the example configuration shown in Fig. 3.19. The stack is denoted as a list of legs [leg1 leg2 ... legn],

where it is understood that the rightmost leg was put on the stack last and will be retrieved from the stack first. Each line below gives the current stack of unprocessed legs. The rightmost leg `legn` is popped from the stack; the linked vertex list returns the leg `leg' = link[legn]` to which `legn` is connected; depending on the vertex to which `leg'` belongs an action is taken: in the case of a 2-leg vertex the cluster branch stops; in the case of an Ising vertex the other three legs are pushed onto the stack. This leads to a new stack configuration which is given in the subsequent line, etc. When the stack is empty, one Swendsen-Wang cluster is completed.

`[]` empty stack, start leg `1` → Ising vertex: put legs on the stack
`[1 3 2 4]` → `13 = link[4]` → Ising vertex: put legs on the stack
`[1 3 2 15 14 16]` → `17 = link[16]` → 2-leg vertex: cluster branch stops
`[1 3 2 15 14]` → `6 = link[14]` → 2-leg vertex: cluster branch stops
`[1 3 2 15]` → `29 = link[15]` → 2-leg vertex: cluster branch stops
`[1 3 2]` → `30 = link[2]` → 2-leg vertex: cluster branch stops; winding
macrospin
`[1 3]` → `9 = link[3]` 2-leg vertex: cluster branch stops
`[1]` → `22 = link[1]` 2-leg vertex: cluster branch stops
`[ ]` empty stack, cluster completed

We start the next Swendsen-Wang cluster using the unprocessed leg with the lowest leg number as a start leg. In the example of Fig. 3.19 this is leg number 10. It is part of the smallest possible cluster consisting only of 2 legs. The next cluster construction starts from leg 18, and so forth. By processing start legs in sequential order (rather than randomly) we need to loop over the total number of legs only once and it is ensured that every leg is visited by a cluster. Furthermore, both the last-in-first-out principle of the stack and the fact that we grow successive clusters from start legs that are close to each other maintains a certain data locality. Having the array elements that need to be accessed at contiguous memory locations helps to reduce the number of cache misses.

3.4   Time-displaced correlation functions

Correlation functions in imaginary time contain important information about the spectral properties and excitations of a quantum system. Linear response functions such as the magnetic susceptibility of an observable $\hat{A}$ with respect to a perturbation $H \to H - h_B \hat{B}$ are given in terms of a Kubo integral over imaginary time [43]

$$
\begin{aligned}
\chi_{AB} &= \left. \frac{\partial \langle \hat{A} \rangle_{h_B}}{\partial h_B} \right|_{h_B=0} \\
&= \int_0^\beta d\tau \langle \hat{A}(\tau)\hat{B}(0)\rangle - \beta \langle \hat{A}\rangle\langle \hat{B}\rangle.
\end{aligned}
\tag{3.68}
$$

The integral in Eq. (3.68) corresponds to the zero-frequency component of the Fourier transform of the imaginary-time correlation function for the operators $\hat{A}$ and $\hat{B}$

$$C_{AB}(\tau) \equiv \langle \hat{A}(\tau)\hat{B}(0) \rangle = \langle e^{\tau\hat{H}}\hat{A}e^{-\tau\hat{H}}\hat{B} \rangle, \tag{3.69}$$

where $\hat{A}(\tau)$ is an operator in the Heisenberg picture.

With regard to correlations in imaginary time the difficulty with the SSE representation is that the method is not formulated directly in continuous imaginary time. Rather an SSE operator string is parametrized by a discrete propagation step. The following Sect. 3.4.1 clarifies the probabilistic relation between discrete SSE propagation steps and imaginary time [106], while Sect. 3.4.2 reviews an efficient strategy for computing imaginary-time correlations in the SSE framework by "embedding" the SSE configuration into continuous imaginary time [45, 91].

3.4.1 Transforming SSE propagation steps to imaginary time

An estimator for the time-displaced correlation function

$$C_{AB}(\tau) \equiv \langle \hat{A}(\tau)\hat{B}(0) \rangle = \langle e^{\tau\hat{H}}\hat{A}e^{-\tau\hat{H}}\hat{B} \rangle \tag{3.70}$$

is obtained by Taylor expanding the exponentials and decomposing H into bond operators [88]:

$$\langle \hat{A}(\tau)\hat{B}(0) \rangle = \frac{1}{Z}\sum_{\alpha}\sum_{n=0}^{\infty}\sum_{m=0}^{n}\sum_{\{S_n\}}\frac{(-\tau)^n(\tau-\beta)^{n-m}}{(n-m)!\,m!}$$
$$\langle \alpha \mid \prod_{i=m+1}^{n}\hat{H}_{[b(i),t(i)]}\hat{A}\prod_{j=1}^{m}\hat{H}_{[b(j),t(j)]}\hat{B} \mid \alpha \rangle. \tag{3.71}$$

We first consider two operators $\hat{A}$ and $\hat{B}$ that are diagonal in the basis $\{| \alpha \rangle\}$, for example $\hat{A}(\tau) = S_i^z(\tau)$ and $\hat{B}(0) = S_j^z(0)$ in the computational S^z-basis. Then the operators $\hat{A}$ and $\hat{B}$ can be replaced by their eigenvalues for the respective propagated states, i.e. $\hat{B}|\alpha(0)\rangle = B[\alpha(0)]|\alpha(0)\rangle$ and $\hat{A}|\alpha(m)\rangle = A[\alpha(m)]|\alpha(m)\rangle$, and we can pull them out of the matrix element. The matrix element of the remaining operator string can be identifed with the statistical weight of an SSE configuration via

$$W(\alpha, S_n) = \frac{(-\beta)^n}{n!}\langle \alpha \mid \prod_{i=1}^{n}H_{[b(i),t(i)]} \mid \alpha \rangle. \tag{3.72}$$

Using the cyclic property of the trace which allows to average observables over all propagation steps, we finally obtain

$$\langle \hat{A}(\tau)\hat{B}(0)\rangle = \frac{1}{Z}\sum_{\alpha,\{S_n\}}W(\alpha,S_n)\frac{1}{n}\sum_{p=0}^{n-1}\sum_{m=0}^{n-1}\frac{\tau^m(\beta-\tau)^{n-m}}{\beta^n}\frac{n!}{(n-m)!\,m!}A[\alpha(p)]B[\alpha(p+m)] \tag{3.73}$$

$$= \left\langle \frac{1}{n}\sum_{p=0}^{n-1}\sum_{m=0}^{n-1}\frac{\tau^m(\beta-\tau)^{n-m}}{\beta^n}\frac{n!}{(n-m)!\,m!}A[\alpha(p)]B[\alpha(p+m)]\right\rangle_{W(\alpha,S_n)}. \tag{3.74}$$

The last expression can be written more compactly as [106]

$$\langle \hat{A}(\tau)\hat{B}(0)\rangle = \left\langle \sum_{m=0}^{n-1}\mathcal{B}(\tau,n;m)\bar{C}_{AB}(m)\right\rangle_{W(\alpha,S_n)}, \tag{3.75}$$

where $\bar{C}_{AB}(m)$ is an averaged correlator between states separated by m propagation steps

$$\bar{C}_{AB}(m) = \frac{1}{n}\sum_{p=0}^{n-1}A[\alpha(p)]B[\alpha(p+m)], \tag{3.76}$$

and $\mathcal{B}(\tau,n;\Delta p)$ is the binomial distribution

$$\mathcal{B}(\tau,n;\Delta p) = \left(\frac{\tau}{\beta}\right)^{\Delta p}\left(1-\frac{\tau}{\beta}\right)^{n-\Delta p}. \tag{3.77}$$

An imaginary time distance τ therefore corresponds to a binomial distribution of propagation distances Δp [88]. For large values of β, the binomial distribution $\mathcal{B}(\tau,n;\Delta p)$ is sharply peaked close to its mean value $\langle \Delta p\rangle = \frac{n\tau}{\beta}$ with standard deviation $\sigma_{\Delta p} = \sqrt{n\frac{\tau}{\beta}\left(1-\frac{\tau}{\beta}\right)}$ and is non-zero only for a few propagation steps Δp around $\langle \Delta p\rangle$. In the fixed length scheme (see Sect. 3.1.2), where one one chooses a fixed length $\mathcal{L}$ of the operator string S_n after thermalization and fills it up with $\mathcal{L}-n$ identities, the identity operators are uniformly distributed in the operator string so that they do not affect the mapping between propagation distances and imaginary time. Here, it is important that, with $\mathcal{L}$ fixed, the function $\mathcal{B}(\tau,n=\mathcal{L};\Delta p)$ needs to be computed only once after the thermalization phase for the desired values of τ and the propagation distances Δp that are relevant for a given τ. The transformation Eq. (3.75) from SSE propagation steps to imaginary time is performed after each Monte Carlo step [106].

For off-diagonal operators $\hat{A}$ and $\hat{B}$ the simplest case is that they are Hamiltonian terms (such as S_i^x in the transverse-field Ising model) so that they directly appear as operators $\hat{A} = \hat{H}_{[b(k_1),t(k_1)]}$ and $\hat{B} = \hat{H}_{[b(k_2),t(k_2)]}$ in the bond decomposition of the

Hamiltonian and then in the SSE operator sequence $S_{\mathcal{L}}$. It follows from Eq. (3.71) that their time-displaced correlation function is

$$\langle \hat{H}_{k_2}(\tau)\hat{H}_{k_1}(0)\rangle = \left\langle \sum_{m=0}^{n-2} \frac{\tau^m(\beta-\tau)^{n-m-2}}{\beta^n} \frac{(n-1)!}{(n-m-2)!\,m!} N(k_1,k_2;m) \right\rangle_W \quad (3.78)$$

where $N(k_1,k_2;m)$ counts the number of times the indices k_1 and k_2 appear in the sequence S_n in the given order and separated by m positions. A disadvantage of the estimators in Eq. (3.75) and Eq. (3.78) is that one needs to traverse the operator sequence twice.

3.4.2 Embedding of SSE configurations in continuous imaginary time

A more efficient method for computing imaginary time correlation functions, put forward in [45, 46], is based on the fact that each SSE configuration can be embedded in a continuous-time worldline formulation [91]. With the Hamiltonian $H = H_0 + V$ split into e.g. a diagonal part H_0 and an off-diagonal part V, which is formally considered as the perturbation although it does not need to be small, the imaginary-time perturbation expansion [107, Chapt. 3] of Z reads[15]

$$Z = \text{Tr}\left[e^{-\beta H}\right] = \text{Tr}\left[e^{-\beta H_0}T_\tau\left\{e^{-\int_0^\beta d\tau V_I(\tau)}\right\}\right], \quad (3.79)$$

where $V_I(\tau) = e^{\tau H_0}Ve^{-\tau H_0}$ is the operator in the interaction representation. The symbol T_τ, the "time ordering operator", means that all operators have to be arranged from left to right in order of decreasing τ. Expanding the time-ordered exponential yields

$$Z = \sum_{n=0}^{\infty} \int_0^\beta d\tau_n \int_0^{\tau_n} d\tau_{n-1} \cdots \int_0^{\tau_2} d\tau_1 \text{Tr}\left[e^{-\beta H_0}\left(-V_I(\tau_n)\right)\left(-V_I(\tau_{n-1})\right)\cdots\left(-V_I(\tau_1)\right)\right]. \quad (3.80)$$

We decompose the perturbation V into M_V off-diagonal bond operators, $V = \sum_{b=1}^{M_V} V_b$ [For the case of the transverse-field Ising model the decomposition would be according to sites $V = \sum_j V_j = \sum_j \Gamma\left(S_j^+ + S_j^-\right)$]. Like in the SSE scheme, each bond operator V_b is required to satisfy the "non-branching" property [91],

$$V_b|\alpha\rangle = v_b(\alpha,\beta)|\beta\rangle, \quad (3.81)$$

meaning that both $|\alpha\rangle$ and $|\beta\rangle$ are states in the computational basis and no superpositions are generated. The multiplication of sums of bond operators in Eq. (3.80)

---

[15] Unlike the Trotter decomposition this way of factorizing two non-commuting operators in an exponential does not introduce any error.

gives rise to a sum over index sequences. To distinguish such an index sequence, which contains only off-diagonal bond operators, from the SSE operator sequence S_n, containing both diagonal and off-diagonal bond operators, it is denoted by

$$T_n = [b_1, b_2, \ldots, b_n] \quad \text{with} \quad b_p \in [1, \ldots, M_V]. \tag{3.82}$$

Inserting complete sets of eigenstates $\{|\alpha\rangle\}$ of H_0, with $H_0|\alpha\rangle = E_\alpha|\alpha\rangle$, we arrive at the final result for the perturbation expansion of the partition sum [73, 91]

$$Z = \sum_{n=0}^\infty \sum_\alpha \sum_{\{T_n\}} \int_0^\beta d\tau_n \int_0^{\tau_n} d\tau_{n-1} \cdots \int_0^{\tau_2} d\tau_1 w\left(\alpha, T_n, \{\tau_i\}_{i=1}^n\right). \tag{3.83}$$

The weight of a configuration in the perturbation expansion is

$$w\left(\alpha, T_n, \{\tau_i\}_{i=1}^n\right) = e^{-\beta E_0} \prod_{p=1}^n e^{-\tau_p(E_p - E_{p-1})} (-1)^n \langle\alpha| \prod_{p=1}^n \left(V_{b(p)}\right) |\alpha\rangle, \tag{3.84}$$

where $E_p = \langle\alpha(p)|H_0|\alpha(p)\rangle$ is the eigenvalue of H_0 at the instantaneous state $|\alpha(p)\rangle$. This expression is the basis for continuous-time QMC [73]. where the operators $V_b(p)$, whose matrix elements $\langle\alpha(p+1)|V_b(p)|\alpha(p)\rangle$ are called *vertices* like in the SSE framework, sit at continuous imaginary time locations $\tau_i \in [0, \beta]$.

For a given perturbation expansion operator sequence T_n, the time integral over the locations of the vertices can be related to a sum of equivalent SSE weights [91]

$$\sum_{n'=n}^\infty \sum_{[S_{n'}]=T_n} w(\alpha, S_{n'}) = \int_0^\beta d\tau_n \int_0^{\tau_n} d\tau_{n-1} \cdots \int_0^{\tau_2} d\tau_1 w\left(\alpha, T_n, \{\tau_i\}_{i=1}^n\right). \tag{3.85}$$

Here, the operator sequence $S_{n'}$ has been augmented with all possible diagonal operator insertions. The notation $[S_{n'}] = T_n$ means that the sequence $S_{n'}$ is identical to T_n if all insertions of H_0 are removed. Eq. (3.85) shows the close relationship between the configuration space of continuous time QMC and the SSE method, which is the basis for the "embedding" of SSE configurations into continuous imaginary time.

Now consider the extreme case when all terms, diagonal and off-diagonal, are included into $V = H$. Then the operator strings in the SSE representation and in the perturbation expansion coincide, $[S_n] = S_n = T_n$, and Eq. (3.85) reduces to

$$w(\alpha, S_n) = \int_0^\beta d\tau_n \int_0^{\tau_n} d\tau_{n-1} \cdots \int_0^{\tau_2} d\tau_1 w\left(\alpha, T_n, \{\tau_i\}_{i=1}^n\right). \tag{3.86}$$

With $H_0 \equiv 0$, $V(\tau)$ does not depend on τ and the weight on the right-hand side of Eq. (3.86) is actually independent of the precise locations of the operators in imaginary time as the prefactor depending on $\{\tau_i\}_{i=1}^n$ in Eq. (3.84) is unity. Carrying out the time integrals leads to the identity

$$\int_0^\beta d\tau_n \int_0^{\tau_n} d\tau_{n-1} \cdots \int_0^{\tau_2} d\tau_1 = \frac{\beta^n}{n!}, \tag{3.87}$$

which can be proven by induction over n. Due to Eq. (3.87) one may write the SSE representation of the partition sum in the form of a perturbation expansion

$$Z = \sum_\alpha \sum_{n=0}^\infty \sum_{S_n} w(\alpha, S_n) \underbrace{\int_0^\beta d\tau_n \int_0^{\tau_n} d\tau_{n-1} \cdots \int_0^{\tau_2} d\tau_1 \, p\left(\{\tau_i\}_{i=1}^n \big| n, \beta\right)}_{=1}, \qquad (3.88)$$

provided that one chooses $p\left(\{\tau_i\}_{i=1}^n \big| n, \beta\right) = \frac{n!}{\beta^n}$, which is to be interpreted as the probability distribution for $\{\tau_i\}_{i=1}^n$, given n, β. Eq. (3.88) represents the embedding of the SSE configurations into continuous imaginary time. By performing a standard SSE Monte Carlo simulation and drawing in each Monte Carlo step imaginary time locations for the operators according to the distribution $p\left(\{\tau_i\}_{i=1}^n \big| n, \beta\right) = \frac{n!}{\beta^n}$, the resulting Monte Carlo ensemble is identical to that of the perturbation expansion in continuous imaginary time [45, 46].

One can sample times $\{\tau_i\}_{i=1}^n$ according to $p\left(\{\tau_i\}_{i=1}^n \big| n, \beta\right)$ by the simple prescription of generating n random numbers from a uniform distribution over $[0, \beta]$ and sorting them in ascending order $\tau_1 < \tau_2 < \ldots < \tau_n$. That this procedure indeed generated times $\{\tau_i\}_{i=1}^n$ distributed according to the probability density $\frac{n!}{\beta^n}$ can be seen as follows:

- The probability density for a single number in $[0, \beta]$ is $\frac{1}{\beta}$.

- For n independent numbers it is $\frac{1}{\beta^n}$.

- Taking into account the different permutations of numbers that lead to the same ordered sequence $\tau_1 < \tau_2 < \ldots < \tau_n$ gives a factor of $n!$.

This leads us to a recipe for computing imaginary time correlation functions: One performs a usual SSE Monte Carlo simulation and in each Monte Carlo measurement step does the following

1. Draw n random numbers $\{\tau_p\}_{p=1}^n$ uniformly distributed in the interval $[0, \beta]$.

2. Order the numbers in ascending sequence and assign them to the n non-trivial operators: $A_p \to A_{\tau_p}$, $B_p \to B_{\tau_p}$.

3. Measure correlations between A_τ and B_0 either on a regular imaginary time grid with $N_\tau = \beta/(\delta\tau)$ "slots" for each $\tau = l\delta\tau$ with $l = 1, \ldots, N_\tau$ or by computing Fourier components.

Since the imaginary times τ are drawn from a uniform distribution over the interval $[0, \beta]$, they do not lie on a regular imaginary-time grid and introducing such a discretization would reduce the temporal resolution of the operator locations in imaginary time. Rather it is preferable to perform a Fourier transformation to Matsubara frequencies [108, Chapt.2] $\omega_m = \frac{2\pi m}{\beta}$, $m \in \mathbb{N}$, and average the Fourier components during the Monte Carlo run. This allows to make use of the full information that is contained in

the simulation cell. First consider the case where A and B are diagonal operators in the computational basis, for example $A = B = S_i^z$. Then

$$C_{AB}(i\omega_m) = \int_0^\beta d\tau e^{-i\omega_m\tau} C_{AB}(\tau) \tag{3.89}$$

$$= \int_0^\beta d\tau e^{-i\omega_m\tau} \langle A(\tau)B(0)\rangle \tag{3.90}$$

$$= \int_0^\beta d\tau e^{-i\omega_m(\tau-\tau')} \underbrace{\langle A(\tau)B(\tau')\rangle}_{\langle A(\tau-\tau')B(0)\rangle} \tag{3.91}$$

$$= \frac{1}{\beta} \int_0^\beta d\tau \int_0^\beta d\tau' e^{-i\omega_m(\tau-\tau')} \langle A_\tau B_{\tau'}\rangle. \tag{3.92}$$

In the last step we have used the fact that A and B are diagonal operators and can be replaced by their eigenvalues A_τ and $B_{\tau'}$ at the respective imaginary times τ and τ'. We have also used the periodic property of the trace which allows to introduce and additional average over imaginary time.

As A_τ is constant on the interval $[\tau_p, \tau_{p+1}]$ between two successive SSE propagation steps, we set $A_\tau = A_p$ and $B_\tau = B_p$ for $\tau \in [\tau_p, \tau_{p+1}]$ and integerate piecewise using

$$\int_{\tau_p}^{\tau_{p+1}} e^{\mp i\omega_m\tau} d\tau = \frac{1}{\mp i\omega_m}\left[e^{\mp i\omega_m\tau_{p+1}} - e^{\mp i\omega_m\tau_p}\right], \tag{3.93}$$

which yields for $m \geq 1$ the final result:

$$C_{AB}(i\omega_m) = \frac{1}{\omega_m^2\beta}\left\langle\left(\sum_{p=0}^n A_p[e^{-i\omega_m\tau_{p+1}} - e^{-i\omega_m\tau_p}]\right)\left(\sum_{p=0}^n B_p[e^{i\omega_m\tau_{p+1}} - e^{i\omega_m\tau_p}]\right)\right\rangle. \tag{3.94}$$

The case $m = 0$ is special:

$$C_{AB}(i\omega_m = 0) = \frac{1}{\beta}\left\langle\left(\sum_{p=0}^n A_p(\tau_{p+1} - \tau_p)\right)\left(\sum_{p=0}^n B_p(\tau_{p+1} - \tau_p)\right)\right\rangle. \tag{3.95}$$

Here, $\tau_0 \equiv 0$ and $\tau_{n+1} \equiv \beta$, which are the first and last supporting points of the Riemann sums Eqs. (3.94) and (3.95). The expressions Eqs. (3.94) and (3.95) can be efficiently evaluated, since the SSE operator string needs to be traversed only once to compute the two separate sums.

For an efficient implementation it should first be noted that in an SSE configuration there is only one operator per non-trivial propagation step. Therefore the distance between kinks in the imaginary-time spin configuration at a given site, which are created by the action of spin-flip operators sitting on that site, is on average at least as long as the number of lattice sites N_s, measured in non-trivial SSE propagation
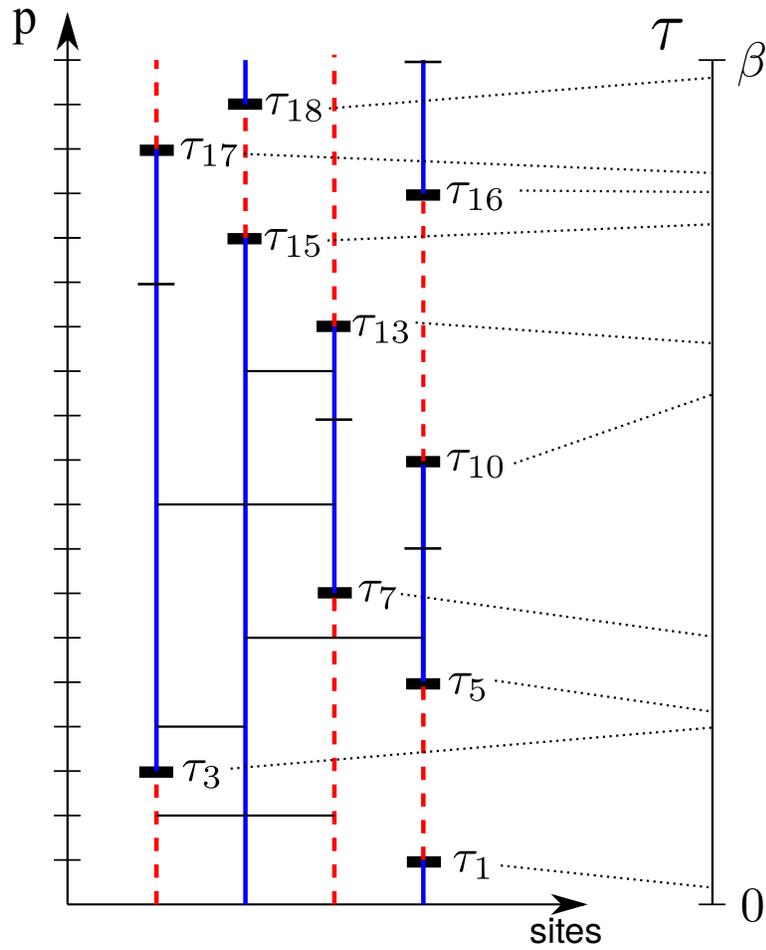
Fig. 3.20: Illustration of the embedding of an SSE configuration into continuous imaginary time. The times $\{\tau_p\}_{p=1}^n$ are drawn randomly from a uniform distribution over $[0, \beta]$, ordered in ascending sequence and assigned to the non-trivial operators in the SSE operator string. For computing the spin-spin correlation function $C_{zz}(\tau)$, only times assigned to spin-flip operators need to be considered since the spin states (continuous lines for ↑ and dashed lines for ↓) are constant in between.

steps. Thus, the spin state $S_{i,\tau}^z$ is not only constant on $[\tau_p, \tau_{p+1}]$ but on the entire interval $[\tau_{\tilde{p}^{(i)}}, \tau_{\tilde{p}^{(i)}+1}]$ where the index $\tilde{p}^{(i)}$ runs only over propagation steps with a spin-flip operator (or, more generally, an off-diagonal operator) touching site i. This is illustrated in Fig. 3.20.

We focus in the following on the spin-spin correlation function

$$C_{zz}(\tau) = \frac{1}{N_{\rm s}} \sum_{i=1}^{N_{\rm s}} \langle S_i^z(\tau) S_i^z(0) \rangle. \tag{3.96}$$

To calculate intermediate quantity $C_{S_i^z S_i^z}(i\omega_m)$ at $N_{\rm Matsubara}$ Matsubara frequencies for all N_s lattice sites requires $\mathcal{O}(N_{\rm Matsubara} N_s \frac{n_{\rm spin-flip}}{N_s})$ operations and with the scaling of the number of spin-flip operators in the simulation cell $n_{\rm spin-flip} \sim \beta N_s$ the complexity of calculating the imaginary time spin-spin correlation function $C_{zz}(\tau)$ in Eq. (3.96) becomes $\mathcal{O}(N_{\rm Matsubara} \beta N_s) = \mathcal{O}(\beta N_s)$.

In order to compute $C_{zz}(\tau)$ as a function of imaginary time τ we need to Fourier transform back from $C_{zz}(i\omega_m)$, which is done after the Monte Carlo simulation. Accurate Monte Carlo data can only be obtained for a finite number of Matsubara frequencies ω_m. In the inverse Fourier transformation the correlation function $C_{zz}(i\omega_m)$ is supplemented with its analytically known high-frequency behaviour using the fact that for "normal" spin systems it decays asymptotically like $\frac{1}{\omega_m^2}$. Similarly to Ref. [109], we fit the high-frequency tail of $C_{AB}(i\omega_m)$ for $1000 < m < 1400$ to $f(x) = \frac{a}{x^2} + \frac{b}{x^4}$ and extrapolate to $m \to \infty$ so that essentially all Matsubara frequencies ω_m enter the inverse Fourier transformation although they have been computed, with adaptive stepsize[16], only at around 200 values of m.

Error bars on $C_{zz}(\tau)$ are obtained by repeating the inverse Fourier transformation multiple times each time adding Gaussian noise of the order of the error bars to the Fourier components $C_{zz}(i\omega_n)$. The spread of the results quantifies the error on $C_{zz}(\tau)$. Note that this simple approach for estimating the error is not entirely correct since the values of $C_{zz}(i\omega_n)$ at different Matsubara frequencies ω_n, being obtained simultaneously from the same SSE configurations, are correlated among each other, and the *jackknife* technique [110] may be more appropriate for a reliable error estimation.

3.5 Summary

In the SSE framework of QMC, the TFI model can be simulated with two different approaches: (i) By adding suitable constants to the TFI model in the S^z-basis an

---

[16]We compute $C_{zz}(i\omega_m)$ for all Matsubara indices m up to $m = 150$, then increment m in steps of $\Delta m = 10$ up to $m = 400$ and then in steps of $\Delta m = 40$ up to $m = 1400$. The values of $C_{zz}(i\omega_m)$ at missing m are interpolated with a cubic spline. An appropriate scheme of including all Matsubara frequencies depends on the system parameters and requires some fine-tuning. A useful criterion for a good choice of stepsizes Δm is the fulfilment of the normalization condition $C_{AB}(\tau = 0) = \sum_{m=0}^{\infty} C_{zz}(i\omega_m) = 1$.

algorithm without sign problem for arbitrary interactions of any sign [95] is possible [Sect. 3.3]. This algorithm proves very effective for long-range ferromagnetic systems, particulary at large transverse fields, where the quantum phase transition occurs (see Chapts. 6 and 7). (ii) By rotating the quantization axis into the direction of the transverse field, so that the computational basis becomes the tensor product of S^x-eigenstates, the TFI model can be simulated with a loop update [Sect. 3.2]. This has the advantage, that the well-documented operator loop algorithm for the XXZ model [89] can be straightforwardly extended to the TFI model, merely by changing the vertex weights and the "scattering probabilities" of the loop head, $P(v, e_0 \to v_1, e_1)$, leaving the remainder of the code untouched. However, in this approach, antiferromagnetic interactions on a non-bipartite lattice such as the triangular one lead to a sign problem.

The absence of a sign problem is only a necessary but not a sufficient condition for an efficient simulation of frustrated systems. It turns out that even with the approach (i) it is not always possible to sample the manifold of low-energy states without getting stuck in metastable regions of configuration space. As will be shown in Sect. 6.4.3, on a frustrated lattice this is particular severe for small transverse fields Γ, where the multibranch clusters tend to percolate in imaginary time so that one large cluster spanning almost the entire system is flipped back and forth, which ultimately ruins ergodicity. In a (failed) attempt to solve this issue, we have designed a non-deterministic Wolff cluster algorithm [Sect. 3.3.2], which allows to control the growth of the cluster in the spatial direction by a tunable parameter C_{Wolff}. While it correctly samples the partition sum, the autocorrelation times are large and the fact that the probabilities for inserting operators in the diagonal update depend now on the spin configurations necessitates recomputing probability tables at each step. The algorithm is not useful, however it highlights the specific ingredients which make approach (i) effective for long-range ferromagnetic interactions.

A promising algorithm for TFI models on frustrated lattices that are composed of triangular units is provided by the plaquette-based cluster update [Sect. 3.3.2] of Ref. [105], which ensures that the random walk in configuration space explores predominantly minimally frustrated configurations.

Chapter 4

Determinantal quantum Monte Carlo

This chapter is intended to give a self-contained introduction to the auxiliary field or determinantal QMC (hereafter referred to as DQMC) method.[1] Its finite-temperature version, the Blankenbecler-Scalapino-Sugar (BSS) algorithm [44], is the standard method for the unbiased simulating of lattice fermion models where both spin and charge degrees of freedom are involved. Compared to the scaling $\sim \beta N^x$, with $1 < x < 2$, of the computational effort for the previously described Stochastic Series Expansion QMC method for spin systems, which can often be regarded as effective low-energy description of some Hubbard-type models, the determinantal QMC method, which simulates the fermions directly, is much more expensive, with its computational effort scaling like βN^3. A pedagogical introduction to the DQMC technique with additional details can be found in Refs. [77, 111, 112].

4.1   Formulation of the partition sum

The purpose of the determinantal quantum Monte Carlo method is to sample the partition function

$$Z = \text{Tr}\left[e^{-\beta H}\right] \tag{4.1}$$

for a lattice Hamiltonian H in the grand-canonical ensemble and to compute finite-temperature expectation values of observables

$$\langle O \rangle = \frac{\text{Tr}\left[Oe^{-\beta H}\right]}{Z} \tag{4.2}$$

---

[1]The core of the determinantal QMC code that was used in this thesis was written by Dr. Su in the research group of Prof. Dr. Lin at the Chinese University of Hongkong.

on the sampled configurations. We illustrate the method for the Fermi-Hubbard model

$$H = -t \sum_{\langle i,j \rangle, \sigma} \left(c_{i,\sigma}^\dagger c_{j,\sigma} + H.c. \right) + U \sum_i n_{i,\uparrow} n_{i,\downarrow} + \mu \sum_i n_i$$
$$= H_t + H_U + H_\mu, \tag{4.3}$$

focusing especially on attractive on-site interactions, $U < 0$. As usual, $c_{i,\sigma}^\dagger (c_{i,\sigma})$ are creation and annihilation operators for fermions with spin σ at site i ($i = 1, \ldots, N$ with N the number of lattice sites). The hopping parameter is t and μ is the chemical potential fixing the average particle number.

In the auxiliary field QMC methods the single-body Hamiltonian $H_0 = H_t + H_\mu$ is separated from the two-body interaction term H_U with the help of a Trotter-Suzuki decomposition [113, 114] after splitting "imaginary time" β into infinitesimal propagation steps $\beta = m\Delta\tau$

$$Z = \text{Tr} \left[e^{-\beta H} \right] \approx \text{Tr} \left[\left(e^{-\Delta\tau H_t} e^{-\Delta\tau(H_U + H_\mu)} \right)^m \right] + \mathcal{O}(\Delta\tau^2 tU). \tag{4.4}$$

Since $[H_t, H_U] \neq 0$, splitting these terms in the exponential introduces a systematic Trotter error of order $\mathcal{O}(\Delta\tau^2 tU)$ for finite time step $\Delta\tau$.[2]

Once the interaction terms have been separated, at each propagation step we use the Hubbard-Stratonovich (HS) transformation [115, 116] in its discrete version due to Hirsch [117] for $U < 0$

$$e^{-\Delta\tau U \sum_i n_{i,\uparrow} n_{i,\downarrow}} = \frac{1}{2^N} e^{-\frac{\Delta\tau}{2} U \sum_i (n_{i,\uparrow} + n_{i,\downarrow} - 1)} \sum_{\{s_i = \pm 1\}} e^{\alpha \sum_i s_i (n_{i,\uparrow} + n_{i,\downarrow} - 1)} \tag{4.5}$$

on each time slice and for each interaction term. This reduces quartic (two-body) operators, containing four fermion creation or annihilation operators, to quadratic (single-body) ones, at the expense of introducing an imaginary-time dependent auxiliary field $s_i(\tau = l\Delta\tau)$, which can take the values ± 1 independently for each index i of the decoupled interaction term (for each site $i = 1, \ldots, N$). The parameter α is determined through $\cosh\alpha = e^{\Delta\tau|U|/2}$, which will be derived in Appendix A, where the HS transformation is discussed in more detail.

Substituting expression (4.5) back into the approximated form of the partition sum Eq. (4.4) gives for $U < 0$ [112]

$$Z_{TS} = \sum_{\{\mathbf{s}\}} \text{Tr} \left\{ \prod_{\sigma = \uparrow, \downarrow} \prod_{l=1}^m \exp \left[(\alpha s_i(l) - \Delta\tau(\mu - \frac{|U|}{2}))(n_{i,\sigma} - \frac{1}{2}) \right] e^{-\Delta\tau H_{t,\sigma}} \right\}, \tag{4.6}$$

---

[2] Considering that the Trotter approximation

$$e^{-\Delta\tau(H_1 + H_1)} = e^{-\Delta\tau H_1} e^{-\Delta\tau H_2} - \frac{\Delta\tau^2}{2} [H_1, H_2] + \mathcal{O}(\Delta\tau^3)$$

occurs m times in the product (4.4), the systematic error is a priori $\mathcal{O}(m\Delta\tau^2) = \mathcal{O}(\beta\Delta\tau) = \mathcal{O}(\Delta\tau)$. However, it can be shown that the error proportional to $\Delta\tau$ vanishes in the partition sum and in expectation values for an observable $O = O^\dagger$ as long as O and H_1, H_2 are simultaneously real representable in a given basis [77, 114]. Hence the global error is of order $\Delta\tau^2$.

where we have dropped a global irrelevant prefactor and it is understood that $Z_{TS} \to Z$ for $\Delta\tau \to 0$. Note also that the factor independent of the HS fields $\{\mathbf{s}\}$ in Eq. (4.5) has been absorbed in Eq. (4.6) by the chemical potential. The partition sum can be written more compactly as

$$Z_{TS} = \sum_{\{\mathbf{s}\}} \text{Tr} \left\{ \prod_{\sigma=\uparrow,\downarrow} \prod_{l=1}^{m} e^{-\Delta\tau \mathbf{c}^\dagger V^\sigma(l)\mathbf{c}} e^{-\Delta\tau \mathbf{c}^\dagger K \mathbf{c}} \right\} \cdot e^{-\alpha \sum_{i,l} s_i(l)} \tag{4.7}$$

$$= \sum_{\{\mathbf{s}\}} \text{Tr} \left\{ \prod_{\sigma=\uparrow,\downarrow} \hat{U}_m^\sigma \hat{U}_{m-1}^\sigma \cdots \hat{U}_1^\sigma \right\} \cdot e^{-\alpha \sum_{i,l} s_i(l)} \tag{4.8}$$

with the operators

$$\hat{U}_l^\sigma = e^{-\Delta\tau \mathbf{c}^\dagger V^\sigma(l)\mathbf{c}} e^{-\Delta\tau \mathbf{c}^\dagger K \mathbf{c}}, \tag{4.9}$$

where we have used the abbreviation $\mathbf{c}^\dagger K \mathbf{c} \equiv \sum_{ij} c_i^\dagger K_{ij} c_j$ and $\mathbf{c}^\dagger V^\sigma(l) \mathbf{c} \equiv \sum_{ij} c_i^\dagger V_{ij}^\sigma(l) c_i$. The matrix kernels of these single-particle operators are the *hopping matrix*

$$K_{ij} \equiv \begin{cases} -t & \text{for } i, j \text{ nearest neighbours,} \\ 0 & \text{otherwise,} \end{cases} \tag{4.10}$$

and the *potential matrix*

$$-\Delta\tau V_{ij}^\sigma(l) \equiv \delta_{ij}[\alpha b_\sigma s_i(l) - \Delta\tau(\mu - |U|/2)], \tag{4.11}$$

which through the auxiliary fields depends on the time slice l. A subtlety of the HS transformation for the $U < 0$ Hubbard model is the additional factor $e^{-\alpha \sum_{i,l} s_i(l)}$ in Eq. (4.7), which is independent of the fermionic degrees of freedom. We omit it in the following to keep the exposition sufficiently general. The only place where it needs to be considered is in the Monte Carlo update [see Sect. 4.3.1]. Except for this factor, Eqs. (4.7) to (4.11) apply to both the attractive ($U < 0$) and the repulsive ($U > 0$) Hubbard model provided that one defines for $U < 0$

$$b_\sigma \equiv 1 \quad \text{for } \sigma =\uparrow,\downarrow \tag{4.12}$$

and for $U > 0$

$$b_\sigma = \begin{cases} +1 & \text{for } \sigma =\uparrow \\ -1 & \text{for } \sigma =\downarrow. \end{cases} \tag{4.13}$$

More details are provided in Appendix A.

After the HS transformation the partition sum Eq. (4.7) contains only exponentials of bilinear fermionic operators. The fermions can be integrated out using the well-known determinant formula for the grand canonical fermionic trace [112]. With the definition of

$$B_l^\sigma \equiv e^{-\Delta\tau V^\sigma(l)} e^{-\Delta\tau K} \tag{4.14}$$

as the matrix representation of the operator $\hat{U}_l^\sigma$ we obtain

$$Z_{TS} = \sum_{\{\mathbf{s}\}} \prod_{\sigma=\uparrow,\downarrow} \det\left(\mathbb{1} + B_m^\sigma B_{m-1}^\sigma \cdots B_1^\sigma\right) \tag{4.15}$$

$$\equiv \sum_{\{\mathbf{s}\}} \det M_{\{\mathbf{s}\}}^\uparrow \det M_{\{\mathbf{s}\}}^\downarrow = \sum_{\{\mathbf{s}\}} w_{\{\mathbf{s}\}}. \tag{4.16}$$

This completes the mapping of the partition sum of a quantum model Eq. (4.4) to a functional integral over classical weights, each given by a determinant of an $N \times N$ matrix. Note that $\hat{U}_l^\sigma$ is a second quantized operator of size $2^N \times 2^N$, while B_l^σ is its matrix representation of size $N \times N$, representing a single-particle propagator in an imaginary time dependent external potential $\{\mathbf{s}\}$. The sum over the huge number of 2^{Nm} configurations of HS degrees of freedom $\{\mathbf{s}\}$ in Eq. (4.16) is carried out with the Monte Carlo method.

We notice from Eq. (4.12) that in the case of the attractive Hubbard model the determinants for spin up and spin down are exactly identical $\det(M_{\{\mathbf{s}\}}^\uparrow) = \det(M_{\{\mathbf{s}\}}^\downarrow)$ so that only one of the two needs to be computed in the numerical simulation. Furthermore, this implies that the weight $w_{\{\mathbf{s}\}} = \left|\det M_{\{\mathbf{s}\}}^\uparrow\right|^2 \geq 0$, and being always positive it can be used for importance sampling in a Monte Carlo simulation. This is no longer true for the repulsive Hubbard model where another HS transformation must be chosen [see Appendix A] in which the HS field $s_i(l)$ couples with different sign to $n_{i,\uparrow}$ and $n_{i,\downarrow}$ and which is the origin for the factor $b_\sigma = \pm 1$ in Eq. (4.11). In either case the weight factorizes into parts for each spin species, $w_{\{\mathbf{s}\}} = w_{\{\mathbf{s}\}}^\uparrow w_{\{\mathbf{s}\}}^\downarrow$.

Unlike in world-line methods such as path integral QMC or the Stochastic Series Expansion (SSE) QMC, where the Monte Carlo sum extends over intermediate states of a *physical* computational basis (e.g. the Fock basis or the S^z basis), individual Monte Carlo configurations of auxiliary field methods allow no direct physical interpretation and are rather arbitrary since their configurations depend on the particular choice of HS transformation.

4.2 Fermionic observables and Wick's theorem

Before integrating out the fermions, the estimator for a generic fermionic observable in one auxiliary field configuration $\{\mathbf{s}\}$ reads

$$\langle \mathcal{O} \rangle_{\{\mathbf{s}\}}(\tau) = \frac{\text{Tr}\left[U_m \cdots U_{l+1} \mathcal{O} U_l \cdots U_1\right]}{\text{Tr}\left[U_m \cdots U_1\right]}, \tag{4.17}$$

Since we have seen in Eq. (4.16) that the weight in one HS configuration factorizes between spin species, expectation values for one HS configuration can be computed separately for operators of different spin. Averaging over all HS samples introduces correlations between them.

In the following derivations, the spin index σ is omitted where all operators belong to only one spin species. First, we consider an observable which is a bilinear form of fermionic creation and annihilation operators and can be written as $\mathcal{O} = \mathbf{c}^\dagger A \mathbf{c}$ where A is some Hermitian $N \times N$ matrix. Introducing the source term $e^{\eta\mathcal{O}}$, Eq. (4.17) can be expressed as

$$\langle\mathcal{O}\rangle_{\{\mathbf{s}\}}(\tau) = \left.\frac{\partial \ln \mathrm{Tr}\left[U_m \cdots U_{l+1} e^{\eta\mathcal{O}} U_l \cdots U_1\right]}{\partial \eta}\right|_{\eta=0} \tag{4.18}$$

$$= \left.\frac{\partial \ln \det\left[\mathbb{1} + B_m \cdots B_{l+1} e^{\eta A} B_l \cdots B_1\right]}{\partial \eta}\right|_{\eta=0}, \tag{4.19}$$

where in going from the first to the second equation we have carried out the grand canonical fermionic trace. Using the identity $\ln \det X = \mathrm{Tr}\ln X$, which holds for any non-singular matrix X and is easily proven at the level of eigenvalues, we can pull out the trace operation

$$\langle\mathcal{O}\rangle_{\{\mathbf{s}\}}(\tau) = \mathrm{Tr}\left.\frac{\partial \ln\left[\mathbb{1} + B_m \cdots B_{l+1} e^{\eta A} B_l \cdots B_1\right]}{\partial \eta}\right|_{\eta=0} \tag{4.20}$$

$$= \mathrm{Tr}\left[\left(\mathbb{1} + B_m \cdots B_{l+1} e^{\eta A} B_l \cdots B_1\right)^{-1} B_m \cdots B_{l+1} A e^{\eta A} B_l \cdots B_1\right]\Bigg|_{\eta=0} \tag{4.21}$$

$$= \mathrm{Tr}\left[B_l \cdots B_1 \left(\mathbb{1} + B_m \cdots B_{l+1} B_l \cdots B_1\right)^{-1} B_m \cdots B_{l+1} A\right]. \tag{4.22}$$

Due to the matrix identity $X(\mathbb{1} + YX)^{-1}Y = \mathbb{1} - (\mathbb{1} + XY)^{-1}$ the last equation can be recast as

$$\langle\mathcal{O}\rangle_{\{\mathbf{s}\}}(\tau) = \mathrm{Tr}\left[\left(\mathbb{1} - \left(\mathbb{1} + \overbrace{B_l \cdots B_1}^{X}\overbrace{B_m \cdots B_{l+1}}^{Y}\right)^{-1}\right)A\right] \tag{4.23}$$

$$= \mathrm{Tr}\left[\left(\mathbb{1} - G_{\{\mathbf{s}\}}(\tau)\right)A\right], \tag{4.24}$$

where we have introduced the equal-time Green's function

$$G_{\{\mathbf{s}\}}(\tau = l\Delta\tau) \equiv \left[\mathbb{1} + B_l \cdots B_1 B_m \cdots B_{l+1}\right]^{-1} \tag{4.25}$$

at time slice l. Let us evaluate the expectation value of the observable $\mathcal{O} = c_b^\dagger c_a$ with the matrix A given by $A_{ij} = \delta_{i,b}\delta_{j,a}$ (only the element $A_{ba} = 1$ is different from zero):

$$\langle c_b^\dagger c_a\rangle_{\{\mathbf{s}\}} = \mathrm{Tr}\left[(\mathbb{1} - G_{\{\mathbf{s}\}}(\tau))\delta_{i,b}\delta_{j,a}\right] \tag{4.26}$$

$$= \delta_{b,a} - \left[G_{\{\mathbf{s}\}}(\tau)\right]_{a,b} \tag{4.27}$$

Thus, we have $\langle c_a c_b^\dagger \rangle_{\{\mathbf{s}\}} = \left[G_{\{\mathbf{s}\}}(\tau) \right]_{a,b}$, which shows that $G_{\{\mathbf{s}\}}(\tau)$ defined in Eq. (4.25) is indeed the single-particle Green's function. The fermion matrix $M^\sigma \equiv \mathbb{1} + \prod_{l=1}^m B_l^\sigma$ appearing in the configurational weight Eq. (4.16) is the inverse of the Green's function.

We have seen that the weight of an auxiliary field configuration is given by the inverse of the determinant of the Green's function. For a given HS field, the Green's function Eq. (4.25) depends on the time slice l. Nonetheless due to the determinant property $\det(AB) = \det(A)\det(B)$ its determinant satisfies

$$\det(G^{-1}(l)) = \det\left(\mathbb{1} + B_l B_{l-1} \cdots B_1 B_m \cdots B_{l+1}\right) \tag{4.28}$$

$$= \det\left(B_l^{-1}\left[\mathbb{1} + B_l B_{l-1} \cdots B_1 B_m \cdots B_{l+1}\right] B_l\right) \tag{4.29}$$

$$= \det\left(\mathbb{1} + B_{l-1} \cdots B_1 B_m \cdots B_{l+1} B_l\right) \tag{4.30}$$

$$= \det(G^{-1}(l-1)) \tag{4.31}$$

so that it is independent of the time slice l. For computing the weight of a HS configuration the Green's function at any time slice can be used.

4.2.1 Free fermion decomposition

In the DQMC algorithm the problem of interacting fermions is reduced to a sum over single-particle problems ("free fermions") in an external potential of auxiliary fields. Therefore, for a fixed configuration of HS fields $\{\mathbf{s}\}$, Wick's theorem [118] applies, allowing to reduce any multi-point correlation function into sums of products of single-particle Green's functions [77]. A frequently used relation is [112]

$$\langle c_{i_2}^\dagger c_{j_2} c_{i_1}^\dagger c_{j_1} \rangle_{\{\mathbf{s}\}} = \langle c_{i_2}^\dagger c_{j_2} \rangle_{\{\mathbf{s}\}} \langle c_{i_1}^\dagger c_{j_1} \rangle_{\{\mathbf{s}\}} + \langle c_{i_2}^\dagger c_{j_1} \rangle_{\{\mathbf{s}\}} \langle c_{j_2} c_{i_1}^\dagger \rangle_{\{\mathbf{s}\}}. \tag{4.32}$$

For higher-order products of fermionic operators Wick's theorem can be expressed compactly through the determinant formula

$$\left\langle \left(c_{i_1} c_{j_1}^\dagger\right) \left(c_{i_2} c_{j_2}^\dagger\right) \cdots \left(c_{i_n} c_{j_n}^\dagger\right) \right\rangle_{\{\mathbf{s}\}} = \det\left(\left[G_{\{\mathbf{s}\}}(\tau = 0)\right]_{i_\alpha, j_\beta}\right), \tag{4.33}$$

where

$$\left[G_{\{\mathbf{s}\}}(\tau)\right]_{i_\alpha, j_\beta} = \langle c_{i_\alpha}(\tau) c_{j_\beta}^\dagger(0) \rangle_{\{\mathbf{s}\}} \tag{4.34}$$

are the matrix elements of the single-particle Green's function of the respective free fermion system, and $\alpha, \beta = 1, \ldots, n$. Eq. (D.1) is proven by induction [see Appendix D].

Thus, knowledge of the equal-time Green's function suffices to evaluate any equal-time observable. The fact that any observable that can be computed for a free fermion system is also accessible in DQMC simulations by virtue of Wick's theorem has been referred to as the "free fermion decomposition" [119].

4.2.2 Imaginary time displaced correlation functions

For completeness, we consider also time-displaced correlation functions for observables $\mathcal{O}_1$ and $\mathcal{O}_2$ at times $\tau_1 = l_1\Delta\tau$ and $\tau_2 = l_2\Delta\tau$, with $\tau_1 \geq \tau_2$:

$$\langle\mathcal{O}_1(\tau_1)\mathcal{O}_1(\tau_2)\rangle_{\{\mathbf{s}\}} = \frac{\text{Tr}\left[U_m \cdots U_{l_1+1}\mathcal{O}_1 U_{l_1} \cdots U_{l_2+1}\mathcal{O}_2 U_{l_2} \cdots U_1\right]}{\text{Tr}\left[U_m \cdots U_1\right]}. \tag{4.35}$$

Let us start with the single-particle time-displaced Green's function, which is defined as

$$\left(G_{\{\mathbf{s}\}}(\tau_1, \tau_2)\right)_{\alpha,\beta} = \begin{cases} \langle c_\alpha(\tau_1)c_\beta^\dagger(\tau_2)\rangle_{\{\mathbf{s}\}}, & \text{if } \tau_1 \geq \tau_2 \\ -\langle c_\beta^\dagger(\tau_2)c_\alpha(\tau_1)\rangle_{\{\mathbf{s}\}}, & \text{if } \tau_2 > \tau_1. \end{cases} \tag{4.36}$$

Here, α and β are composite indices, $\alpha = (\mathbf{i}, \sigma)$, combining the site index $\mathbf{i}$ and the spin state σ. Following [120] we write for $\tau_1 \geq \tau_2$

$$\left(G_{\{\mathbf{s}\}}(\tau_1, \tau_2)\right)_{\alpha,\beta} = \frac{\text{Tr}\left[U_m \cdots U_{l_2+1}\left(U_{l_1} \cdots U_{l_2+1}\right)^{-1} c_\alpha U_{l_1} \cdots U_{l_2+1}c_\beta^\dagger U_{l_2} \cdots U_1\right]}{\text{Tr}[U_m \cdots U_1]} \tag{4.37}$$

In this expression terms of the form $U_l^{-1}c_\alpha U_l$ appear. Recalling that U_l is an exponential of bilinear operators (see Eq. (4.7)), we see that what we need to compute is $e^{\tau\mathbf{c}^\dagger A\mathbf{c}}c_\alpha e^{-\tau\mathbf{c}^\dagger A\mathbf{c}}$ for some matrix A. We will show in the following that this amounts to some form of basis rotation in the space of single-particle operators [112, 120]. We differentiate the term with respect to τ to obtain a differential equation in τ:

$$\frac{d}{d\tau}\left[e^{\tau\mathbf{c}^\dagger A\mathbf{c}}\mathbf{c}e^{-\tau\mathbf{c}^\dagger A\mathbf{c}}\right]_\alpha = \mathbf{c}^\dagger A\mathbf{c}e^{\tau\mathbf{c}^\dagger A\mathbf{c}}c_\alpha e^{-\tau\mathbf{c}^\dagger A\mathbf{c}} - e^{\tau\mathbf{c}^\dagger A\mathbf{c}}c_\alpha\mathbf{c}^\dagger A\mathbf{c}e^{-\tau\mathbf{c}^\dagger A\mathbf{c}} \tag{4.38}$$

$$= e^{\tau\mathbf{c}^\dagger A\mathbf{c}}\left[\mathbf{c}^\dagger A\mathbf{c}\, c_\alpha - c_\alpha\mathbf{c}^\dagger A\mathbf{c}\right]e^{-\tau\mathbf{c}^\dagger} \tag{4.39}$$

$$= e^{\tau\mathbf{c}^\dagger A\mathbf{c}}\underbrace{\sum_{\gamma,\delta}A_{\gamma,\delta}\left[c_\gamma^\dagger c_\delta, c_\alpha\right]}_{=-\sum_\delta A_{\alpha,\delta}c_\delta}e^{-\tau\mathbf{c}^\dagger A\mathbf{c}} \tag{4.40}$$

$$= -\left[A \cdot \left(e^{\tau\mathbf{c}^\dagger A\mathbf{c}}\,\mathbf{c}\,e^{-\tau\mathbf{c}^\dagger A\mathbf{c}}\right)\right]_\alpha \tag{4.41}$$

In going from the third to the fourth equation we have used the fermionic commutation relations $[c_\alpha, c_\beta] = 2c_\alpha c_\beta$ and $[c_\alpha^\dagger, c_\beta] = 2c_\alpha^\dagger c_\beta - \delta_{\alpha,\beta}$. Eq. (4.41) is the differential equation of the exponential function and we conclude that

$$e^{\tau\mathbf{c}^\dagger A\mathbf{c}}c_\alpha e^{-\tau\mathbf{c}^\dagger A\mathbf{c}} = \left[e^{-\tau A} \cdot \mathbf{c}\right]_\alpha, \tag{4.42}$$

where the dot denotes matrix-vector multiplication. Using relation (4.42) repeatedly in Eq. (4.37) results in [77]

$$
\left[G_{\{\mathbf{s}\}}(\tau_1, \tau_2)\right]_{\alpha,\beta} = \frac{\operatorname{Tr}\left[U_m \cdots U_{l_2+1}\left(B_{l_1} \cdots B_{l_2+1} \cdot \mathbf{c}\right)_\alpha c_\beta^\dagger U_{l_2} \cdots U_1\right]}{\operatorname{Tr}\left[U_m \cdots U_1\right]} \tag{4.43}
$$

$$
= \sum_\gamma \left(B_{l_1} \cdots B_{l_2+1}\right)_{\alpha,\gamma} \frac{\operatorname{Tr}\left[U_m \cdots U_{l_2+1} c_\gamma c_\beta^\dagger U_{l_2} \cdots U_1\right]}{\operatorname{Tr}\left[U_m \cdots U_1\right]} \tag{4.44}
$$

$$
= \sum_\gamma \left(B_{l_1} \cdots B_{l_2+1}\right)_{\alpha,\gamma} \langle c_\gamma c_\beta^\dagger \rangle_{\{\mathbf{s}\}}(\tau_2) \tag{4.45}
$$

$$
= \left[B_{l_1} \cdots B_{l_2+1} \cdot G_{\{\mathbf{s}\}}(\tau_2, \tau_2)\right]_{\alpha,\beta}. \tag{4.46}
$$

Thus, the imaginary time displace Green's function is related to the equal time Green's function through multiplication with the string of matrices B_l between time slice l_2 and l_1 (including the latter).

In a similar calculation for $\tau_2 > \tau_1$ the positions of the operators $c_\beta^\dagger$ and c_α are exchanged and we need the relation

$$
e^{\tau \mathbf{c}^\dagger A \mathbf{c}} c_\beta^\dagger e^{-\tau \mathbf{c}^\dagger A \mathbf{c}} = \left[\mathbf{c}^\dagger \cdot e^{\tau A}\right]_\beta, \tag{4.47}
$$

which finally yields

$$
\left[G_{\{\mathbf{s}\}}(\tau_1, \tau_2)\right]_{\alpha,\beta} = -\langle c_\beta^\dagger(\tau_2) c_\alpha(\tau_1) \rangle_{\{\mathbf{s}\}} \tag{4.48}
$$

$$
= -\left[(\mathbb{1} - G_{\{\mathbf{s}\}}(\tau_1, \tau_1)) \cdot B_{l_1+1}^{-1} \cdots B_{l_2}^{-1}\right]_{\alpha,\beta}. \tag{4.49}
$$

The fact that time-displaced Green's functions can be reduced to equal-time Green's functions implies the validity of Wick's theorem for n-point correlation functions at different imaginary times [77].

4.3   Monte Carlo update

The equal-time Green's function in Eq. (4.25) is the central object of the DQMC algorithm, playing an essential role at two stages. The first is the measurement of fermionic observables since for fixed auxiliary field configuration all expectation values can be expressed as sums of products of single-particle Green's functions thanks to Wick's theorem.

The second role appears in the importance sampling of the bosonic auxiliary field configurations, where the diagonal elements of the Green's function determine the acceptance ratio of a single spin flip update.

4.3.1 Local updates

Because the Monte Carlo weight in DQMC is given as a determinant of the inverse of the Green's function, which is a highly non-local function of its entries, flipping a single spin affects the subsequent update of any other spin in the space-time lattice. Therefore, a structured update procedure is necessary for an efficient algorithm. This is also the reason why effective cluster updates, which are routinely employed in world-line Monte Carlo methods [74, 89] and rely on the property that global updates can be achieved based on local decisions (see Sect. 3.2), have not yet been found for updating the space-time lattice of auxiliary fields.

Computation of determinant ratio

The basic update mechanism is the single-spin flip Metropolis algorithm where an update $s_i(l) \rightarrow s_i'(l) = -s_i(l)$ is proposed sequentially at each lattice site i and time slice l. Based on the ratio

$$r = \frac{w(\{\mathbf{s}'\})}{w(\{\mathbf{s}\})} = \frac{\det G^{\uparrow}(\{\mathbf{s}\}) \det G^{\downarrow}(\{\mathbf{s}\})}{\det G^{\uparrow}(\{\mathbf{s}'\}) \det G^{\downarrow}(\{\mathbf{s}'\})} = R_{\uparrow} R_{\downarrow}, \tag{4.50}$$

the move is accepted with heat bath probability $p = r/(1+r)$.

For the attractive ($U < 0$) Hubbard model, the special factor $e^{-\alpha \sum_{i,l} s_i(l)}$ coming from the HS transformation in the partition sum in Eq. (4.3.1) needs to be taken into account since it is affected by the update $s_i(l) \rightarrow s_i'(l) = -s_i(l)$. In this case, a spin flip is accepted based on the ratio

$$r_{U<0} = \frac{w(\{\mathbf{s}'\})}{w(\{\mathbf{s}\})} \frac{e^{-\alpha \sum_{j \neq i, k \neq l} s_k(j) + \alpha s_i(l)}}{e^{-\alpha \sum_{j \neq i, k \neq l} s_k(j) - \alpha s_i(l)}}$$
$$= r \cdot e^{2\alpha s_i(l)}. \tag{4.51}$$

For importance sampling only relative Monte Carlo weights are required, which is why it suffices to consider the additional factor $e^{-\alpha \sum_{i,l} s_i(l)}$ only at this stage.

Evaluation of the determinants in $w(\{\mathbf{s}'\})$ and $w(\{\mathbf{s}\})$ in Eq. (4.50) is very expensive, scaling like $\mathcal{O}(N^3)$ with the number of lattice sites. However, if only one entry (or a few) in $\{\mathbf{s}\}$ is changed to obtain $\{\mathbf{s}'\}$, the determinant ratio R_{σ} ($\sigma = \uparrow, \downarrow$) is easily calculated since it can be expressed in terms of Green's functions. The determinant ratio for a single spin is

$$R_{\sigma} = \frac{\det\left(\mathbb{1}_N + B_m^{\sigma} B_{m-1}^{\sigma} \cdots (B_l^{\sigma})' \cdots B_1^{\sigma}\right)}{\det\left(\mathbb{1}_N + B_m^{\sigma} B_{m-1}^{\sigma} \cdots B_l^{\sigma} \cdots B_1^{\sigma}\right)} \tag{4.52}$$

$$= \frac{\det\left(\mathbb{1}_N + \Delta_l^{\sigma}(i) B_l^{\sigma} B_{l-1}^{\sigma} \cdots B_1^{\sigma} B_m^{\sigma} \cdots B_{l-1}\right)}{\det\left(\mathbb{1}_N + B_l^{\sigma} B_{l-1}^{\sigma} \cdots B_1^{\sigma} B_m^{\sigma} \cdots B_{l+1}^{\sigma}\right)}, \tag{4.53}$$

where we have used the cyclic property of the matrix string under the determinant and expressed the change $B_l^\sigma \to (B_l^\sigma)'$ due to an update at site i on time slice l by multiplication with a correction matrix[3]

$$\Delta_l^\sigma(i) \equiv (B_l^\sigma)'\,(B_l^\sigma)^{-1} = e^{-\Delta\tau V_l^\sigma(\{\mathbf{s}'\})} e^{+\Delta\tau V_l^\sigma(\{\mathbf{s}\})}, \tag{4.54}$$

which has the sparse structure

$$[\Delta_l^\sigma(i)]_{jk} = \begin{cases} 0 & j \neq k, \\ 1 & j = k \neq i, \\ e^{\alpha b_\sigma[s_i'(l)-s_i(l)]} = e^{-2\alpha b_\sigma s_i(l)} & j = k = i. \end{cases} \tag{4.55}$$

Identifying in Eq. (4.53) the Green's function $G^\sigma(l)$ [Eq. (4.25)] at time slice l, the ratio is then

$$R_\sigma = \det\left(\left[\mathbb{1}_N + \Delta_l^\sigma(i)\left([G^\sigma(l)]^{-1} - \mathbb{1}_N\right)\right] G^\sigma(l)\right)$$
$$= \det\left(G^\sigma(l) + \Delta_l^\sigma(i)\,(\mathbb{1} - G^\sigma(l))\right). \tag{4.56}$$

Noting that the matrix defined as

$$\Gamma_l^\sigma(i) \equiv \Delta_l^\sigma(i) - \mathbb{1} \tag{4.57}$$

has only one non-zero element, namely the i-th position on the diagonal, which is $\gamma_l^\sigma(i) = e^{-2\alpha b_\sigma s_i(l)} - 1$, it is advantageous to rewrite Eq. (4.56) in terms of $\Gamma_l^\sigma(i)$ to make use of its sparseness

$$R_\sigma = \det\left(\mathbb{1} + (\Delta_l^\sigma(i) - \mathbb{1})\,(\mathbb{1} - G^\sigma(l))\right). \tag{4.58}$$

Explicitly, the matrix under the determinant reads

$$\left[\mathbb{1} + \underbrace{(\Delta_l^\sigma(i) - \mathbb{1})}_{\Gamma_l^\sigma(i)}\,(\mathbb{1} - G^\sigma(l))\right]^T = \begin{pmatrix} 1 & & & a_{1i}\gamma_l^\sigma(i) & & \\ & \ddots & & a_{2i}\gamma_l^\sigma(i) & & \\ & & 1 & a_{3i}\gamma_l^\sigma(i) & & \\ & & & a_{4i}\gamma_l^\sigma(i) & & \\ & & & \vdots & \ddots & \\ & & & a_{N_s i}\gamma_l^\sigma(i) & & 1 \end{pmatrix} \tag{4.59}$$

---

[3] With this notation it is important that we have defined $B_l \equiv e^{-\Delta\tau V_l(\{\mathbf{s}\})} e^{-\Delta\tau K}$ with the potential matrix on the left of the kinetic matrix. With the opposite choice the correction matrix

$$\Delta_l^\sigma(i) = (B_l^\sigma)'\,B_l^{-1} = e^{-\Delta\tau K^\sigma} e^{-\Delta\tau V_l^\sigma(\{\mathbf{s}'\})} e^{+\Delta\tau V_l^\sigma(\{\mathbf{s}\})} e^{\Delta\tau K^\sigma}$$
$$= e^{-\Delta\tau V_l^\sigma(\{\mathbf{s}\})} e^{-\Delta\tau V_l^\sigma(\{\mathbf{s}\})} + \mathcal{O}(\Delta\tau^2)$$

would only be approximate, with an error $\mathcal{O}(\Delta\tau^2)$ per low-rank update.

with the abbreviation $a_{ij} = \delta_{ij} - G_{ij}(l)$. (In Eq. (4.59) the transpose has been written merely for typographical reasons.) By developing the determinant of this matrix with respect to the i-th column it can be shown that it reduces to the product of the diagonal elements, yielding [112]

$$R_\sigma = 1 + (1 - [G^\sigma(l)]_{ii})\,\gamma_l^\sigma(i). \tag{4.60}$$

All one needs to know to compute the ratio of determinants Eq. (4.50) after a single spin flip update at point (i, l) of the space-time grid is one diagonal element of the old Green's function $G^\sigma(l)$. However, the spin flip affects the entire Green's function; in particular, the diagonal elements of the new Green's function, which are required to compute the acceptance ratio R for the next step, depend on the off-diagonal elements of the old Green's function so that the full Green's function at time slice l needs to be updated to continue with the importance sampling.

Updating the Green's function

Updating the Green's function after a single spin flip can be achieved with a *low-rank update* [44, 77] that makes use of the sparseness of the correction matrix $\Delta_l^\sigma(i)$ and can be carried out in $\mathcal{O}(N^2)$ operations. The new Green's function is (dropping the spin index σ as well as the dependence on auxiliary fields $\{\mathbf{s}\}$)

$$G_l' \equiv [\mathbb{1} + B_l' B_{l-1} \cdots B_1 B_m \cdots B_{l+1}]^{-1} \tag{4.61}$$

$$= \left[\mathbb{1} + B_l' B_l^{-1}\left(G_l^{-1} - \mathbb{1}\right)\right]^{-1} \tag{4.62}$$

$$= \left[\mathbb{1} + \Delta_l(i)\left(G_l^{-1} - \mathbb{1}\right)\right]^{-1}. \tag{4.63}$$

Rewriting this again in terms of the matrix $\Gamma_l(i) = \Delta_l(i) - \mathbb{1}$ gives

$$G_l' = \left[\mathbb{1} + (\Gamma_l(i) + \mathbb{1})\left(G_l^{-1} - \mathbb{1}\right)\right]^{-1}$$

$$= \left[\left(\mathbb{1} + \Gamma_l(i) - \Gamma_l(i)G_l\right)G_l^{-1}\right]^{-1}$$

$$= G_l\left[\mathbb{1} + \Gamma_l(i)(\mathbb{1} - G_l)\right]^{-1}. \tag{4.64}$$

The calculation of the inverse in Eq. (4.64) is done by assuming

$$[\mathbb{1} + \Gamma_l(i)(\mathbb{1} - G_l)]^{-1} = \mathbb{1} + x\Gamma_l(i)(\mathbb{1} - G_l) \tag{4.65}$$

with x a scalar to be determined. This ansatz is possible due to the sparseness of $L = \Gamma_l(i)(\mathbb{1} - G_l)$, which contains only one non-zero row[4] so that $L^2 \sim L$. Therefore

$$\frac{1}{\mathbb{1} + L} = \mathbb{1} + xL. \tag{4.66}$$

---

[4]In more general cases, where the matrix $\Gamma_l(i)$ contains several non-zero elements, the matrix inverse in Eq. (4.64) can be expressed through the Sherman-Morrison-Woodbury formula [121, Sect. 2.1.3].

x is obtained from the condition that the product of both matrices in Eq. (4.65) is unity

$$\mathbb{1} = [\mathbb{1} + x(\mathbb{1} - G_l)\Gamma_l(i)]\,[\mathbb{1} + (\mathbb{1} - G_l)\Gamma_l(i)]$$
$$\Rightarrow (\mathbb{1} - G_l)\Gamma_l(i) = -x\left(1 + (1 - [G_l]_{ii})\gamma_l^\sigma(i)\right)(\mathbb{1} - G_l)\Gamma_l(i),$$

so that

$$x = -\frac{1}{1 + (1 - [G_l]_{ii})\gamma_l^\sigma(i)} = -\frac{1}{R^\sigma}, \qquad (4.67)$$

and we obtain the updated Green's function for spin σ after a single spin-flip update at site i and time slice l as

$$[G_l^{\sigma\prime}]_{jk} = [G_l^\sigma]_{jk} - \frac{\left(\delta_{ik} - [G_l^\sigma]_{ik}\right)\gamma_l^\sigma(i)\,[G_l^\sigma]_{ji}}{1 + \left(1 - [G_l^\sigma]_{ii}\right)\gamma_l^\sigma(i)}. \qquad (4.68)$$

In this expression, no sum over repeated indices is implied. $\mathcal{O}(N^2)$ operations are necessary for updating all N^2 elements of the Green's function[5], which must be contrasted with a naive inversion and dense matrix multiplication of Eq. (4.64), which would require $\mathcal{O}(N^3)$ operations.

Wrapping the Green's function

We attempt single spin flips for every lattice site of a time slice in sequential order and update the Green's function according to Eq. (4.68) if a spin flip is accepted. In order to compute the acceptance ratio Eq. (4.60), the Green's function for the current time slice l needs to be known. When moving to the next time slice $l + 1$, the Green's function $G(l+1)$ is required in order to proceed with the updating. Given then Green's function $G(l)$ at time slice l, this can be easily accomplished by virtue of the following identity:

$$
\begin{aligned}
G(l+1) &\equiv [\mathbb{1} + B_{l+1}\cdots B_1 B_m \cdots B_{l+2}]^{-1} \\
&= \left[B_{l+1}\left(\underbrace{B_{l+1}^{-1}B_{l+1}}_{\mathbb{1}} + B_l\cdots B_1 B_m \cdots B_{l+1}\right)B_{l+1}^{-1}\right]^{-1} \\
&= B_{l+1}G(l)B_{l+1}^{-1}
\end{aligned}
\qquad (4.69)
$$

---

[5] Actually, only partial knowledge of the new Green's function which arises from updating a single HS variable is needed for computing the ratio r and updating the next HS field. This is the basis for more efficient "delayed" [122] and "submatrix" updates [123], which delay the calculation of unneeded matrix elements to make better use of the hierarchical memory structure of modern CPUs by replacing a rank-1 update by a rank-k ($k > 1$) update, which results in more floating point operations per memory access.
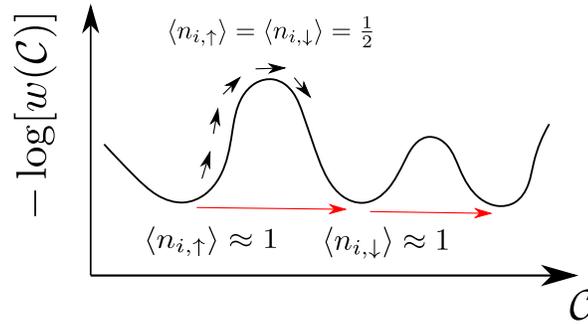
Fig. 4.1: In the repulsive Hubbard model, for $U/t \gg 1$ and $\beta t \gg 1$, the subspace of configurations $\mathcal{C}$ with singly-occupied sites, characterized by $\langle n_{i,\uparrow} \rangle \approx 1$ or $\langle n_{i,\downarrow} \rangle \approx 1$, is divided by high potential barriers of configurations with doubly occupied or empty sites, which are difficult to cross by successive single flips of Hubbard-Stratonovich fields. Global moves (drawn as red arrows) tunnel between configurations of maximal weight by reversing an entire imaginary time column of Hubbard-Stratonovich fields.

Analogously, one obtains

$$G(l-1) = B_l^{-1} G(l) B_l. \tag{4.70}$$

The procedure of propagating the Green's function from time slice l to time slice $l+1$ with the help of Eq. (4.69) or to time slice $l-1$ with Eq. (4.70) is commonly referred to as "wrapping up" or "wrapping down", respectively. When a checkerboard decomposition is used, the B_l matrices are sparse and it takes $\mathcal{O}(N^2)$ operations to bring the Green's function to the next or previous time slice. However, due to the large condition number of the B_l matrices only a limited number of "wrapping operations" can be carried out before numerical precision is lost and the Green's function needs to be recomputed from scratch.

4.3.2 Global spin-flip updates

This section discusses a well-known ergodicity problem [124] that the determinantal QMC algorithm suffers from in the regime of large Hubbard interaction and low temperatures. The loss of ergodicity manifests itself in an apparent breaking of spin-inversion symmetry $\langle n_\uparrow \rangle \neq \langle n_\downarrow \rangle$ where the values of $\langle n_\sigma \rangle$ stick to "canonical" values, namely integer multiples of $\frac{1}{N_{\text{sites}}}$, with seemingly vanishing error bars. Sometimes also the average density $\langle n_\uparrow + n_\downarrow \rangle$ is computed incorrectly.

To highlight the source of the problem, we consider the strong-coupling limit $U/t \gg 1$ where the kinetic term can be neglected with respect to the on-site interactions so that the model reduces to one of decoupled sites with Hamiltonian

$$H_i = U n_{i,\uparrow} n_{i,\downarrow} - \mu(n_{i,\uparrow} + n_{i,\downarrow}). \tag{4.71}$$

Using the HS transformation for $U < 0$ Eq. (A.10b) and (A.11), the strong-coupling form of the partition sum for the attractive Hubbard model is

$$
\begin{aligned}
Z &= \sum_{\{n_\sigma=0,1\}} \prod_{l=1}^{m} \left(e^{-\Delta\tau U n_\uparrow n_\downarrow} e^{\Delta\tau\mu(n_\uparrow+n_\downarrow)} \right) \\
&= \frac{1}{2^m} \sum_{\{n_\sigma=0,1\}} \prod_{l=1}^{m} \left(e^{-\frac{\Delta\tau}{2} U(n_\uparrow+n_\downarrow-1)} \sum_{s(l)=\pm 1} e^{\alpha s(l)(n_\uparrow+n_\downarrow-1)} e^{\Delta\tau\mu(n_\uparrow+n_\downarrow)} \right) \\
&= \frac{1}{2^m} \sum_{\{n_\sigma=0,1\}} \sum_{\{s(l)=\pm 1\}_{l=1}^{m}} e^{\frac{\Delta\tau U}{2}} e^{-\beta\left(\frac{U}{2}-\mu\right)(n_\uparrow+n_\downarrow)} e^{\alpha\sum_l s(l)(n_\uparrow+n_\downarrow-1)} \\
&= \frac{1}{2^m} e^{\frac{\Delta\tau U}{2}} \sum_{\{s(l)=\pm 1\}_{l=1}^{m}} \left(\underbrace{e^{-\alpha\sum_l s(l)}}_{n_\uparrow=n_\downarrow=0} + 2\underbrace{e^{-\beta\left(\frac{U}{2}-\mu\right)}}_{n_\sigma=0, n_{\bar\sigma}=1} + \underbrace{e^{-2\beta\left(\frac{U}{2}-\mu\right)} e^{\alpha\sum_l s(l)}}_{n_\uparrow=n_\downarrow=1} \right)
\end{aligned}
$$

(4.72)

For half filling at $\mu = \frac{U}{2}$ the partition function in the strong coupling limit thus becomes

$$
Z = \frac{1}{2^m} e^{\frac{\Delta\tau U}{2}} \sum_{\{s(l)=\pm 1\}_{l=1}^{m}} \left[2 + 2\cosh\left(\alpha \sum_{l=1}^{m} s(l) \right) \right].
$$

(4.73)

It follows that the weight of a configuration is maximal if $|\sum_l s(l)|$ takes on its maximum value, i.e. when at the given site all Hubbard-Stratonovich spins in imaginary time point up or down. At large β and half filling, a Hubbard-Stratonovich field configuration with all $s(l)$ aligned corresponds to a doubly occupied site, $n_\uparrow n_\downarrow \approx 1$, or an empty site, $n_\uparrow n_\downarrow \approx 0$, respectively. A potential barrier arises for $\sum_l s(l) = 0$.

Using the Hubbard-Stratonovich decoupling in the spin channel (see Appendix A), the strong-coupling partition sum in the case of repulsive interactions is [124]

$$
\begin{aligned}
Z &= \sum_{\{n_\sigma=0,1\}} \frac{1}{2^m} \prod_{l=1}^{m} e^{\Delta\tau\left(\mu-\frac{U}{2}\right)(n_\uparrow+n_\downarrow)} \sum_{s(l)=\pm 1} e^{-\alpha s(l)(n_\uparrow-n_\downarrow)} \\
&= \frac{1}{2^m} e^{\beta(\mu-\frac{U}{2})} \sum_{\{s(l)=\pm 1\}_{l=1}^{m}} \left[2\cosh\left(\beta\left(\mu-\frac{U}{2}\right) \right) + 2\cosh\left(\alpha\sum_{l=1}^{m} s(l) \right) \right].
\end{aligned}
$$

(4.74)

(4.75)

Again the weight of a configuration is maximal if all Hubbard-Stratonovich spins are aligned in imaginary time, except that this time the maximal contribution comes from fermionic configurations where the site is singly occupied with $n_\uparrow = 0, n_\downarrow = 1$ or $n_\uparrow = 1, n_\downarrow = 0$. The intermediate potential barrier of $\sum_l s(l) = 0$ corresponds to $n_\uparrow = n_\downarrow = \frac{1}{2}$.

Therefore, a suitable global move that tunnels between configurations of maximal weight consists in flipping a line of Hubbard-Stratonovich spins at a given lattice site

at all imaginary time slices [124]: $s_i(l) \to -s_i(l)$ for $l = 1, \ldots, m$. Since it effectively takes n_σ to $n_{-\sigma}$, this move can be interpreted as reversing a spin in the Heisenberg model, which is the strong-coupling limit of the Hubbard model. The same global moves can be used for the repulsive and the attractive Hubbard model as long as the doping away from half filling is low enough so that a Heisenberg-like description is appropriate. The general idea is sketched for the repulsive Hubbard model in Fig. 4.1.

After each global move the Green's function needs to be recomputed from scratch in order to evaluate the acceptance ratio Eq. (4.50). The complexity of calculating the acceptance ratio after a global move is $\mathcal{O}(\beta N^2 + N^3)$. The term $\mathcal{O}(\beta N^2)$ originates from the evaluation of the product of B-matrices in Eq. (4.25) of length $\sim \beta$ where each B-matrix is the product of $\mathcal{O}(N)$ sparse matrices (e.g. Eq. (4.82)) with the complexity of sparse matrix multiplication here being $\mathcal{O}(N)$, while the computational cost $\mathcal{O}(N^3)$ comes from evaluating the determinant

$$\det(G^{-1}_{\{\mathbf{s}\}}(\tau = l\Delta\tau)) = \det\left(\mathbb{1} + B_l \cdots B_1 B_m \cdots B_{l+1}\right), \tag{4.76}$$

which enters the acceptance ratio Eq. (4.50). In practice, here the logarithm of the determinant should be computed in order to avoid numerical overflow.

If the global move is rejected, the changes to the auxiliary field configuration at the selected site have to be undone. Thus, global moves are very expensive and we perform a global update on only $\mathcal{O}(1)$ randomly chosen lattice sites after each full sweep of the lattice, in parameter regimes where ergodicity is at risk (typically at $\beta t > 4$ for $U/t > 12$).

In a recently introduced so-called self-learning Monte Carlo method [125] an algorithm is designed to learn the relevant low-energy dynamics automatically in order to generate cumulative moves with high acceptance ratio, which constitutes an important generalization of the simple heuristics based on strong-coupling theory. More importantly, such global updates reduce the autocorrelation times by orders of magnitude [86, 125].

4.4 Efficient and stable linear algebra

The checkerboard decomposition allows to replace dense matrix multiplications by sparse products.

4.4.1 Checkerboard decomposition

The hopping matrix $\mathbf{K}$ can be exponentiated easily with a unitary transformation such that $\mathbf{UKU} = \mathbf{D}$ where $\mathbf{D}$ is diagonal, hence

$$e^{\Delta\tau\mathbf{K}} = \mathbf{U}e^{\Delta\tau\mathbf{D}}\mathbf{U}^\dagger. \tag{4.77}$$

Since the hopping matrix is independent of the Hubbard-Stratonovich fields, the transformation matrix $\mathbf{U}$ needs to be computed only once. However, whereas the matrix $\mathbf{K}$ is sparse, its matrix exponential $\exp(\Delta\tau K)$ (and also the transformation matrix U) is a dense matrix and multiplying it with another dense matrix has a computational cost of $\mathcal{O}(N_s^3)$.

In order to transfer the sparseness of the hopping matrix $\mathbf{K}$ to its matrix exponential, Loh and Gubernatis [111, 126] use the following approximation

$$e^{\Delta\tau\mathbf{K}} = e^{\Delta\tau\sum_{\langle i,j\rangle}\mathbf{K}^{(ij)}} \approx \prod_{\langle i,j\rangle} e^{\Delta\tau\mathbf{K}^{(ij)}}. \tag{4.78}$$

In this expression we have omitted the error of the approximation since its precise form depends on how the kinetic term is written as a sum of local terms. Consider the hopping matrix between two nearest-neighbour sites i and j

$$\mathbf{K}^{(i,j)} = \begin{bmatrix} 0 & \cdots & 0 & \cdots & 0 & \cdots & 0 \\ \vdots & & \vdots & & \vdots & & \vdots \\ 0 & \cdots & 0 & \cdots & t_{ij} & \cdots & 0 \\ \vdots & & \vdots & & \vdots & & \vdots \\ 0 & \cdots & t_{ij} & \cdots & 0 & \cdots & 0 \\ \vdots & & \vdots & & \vdots & & \vdots \\ 0 & \cdots & 0 & \cdots & 0 & \cdots & 0 \end{bmatrix} \begin{matrix} \\ \\ \leftarrow i \\ \\ \leftarrow j \\ \\ \\ \end{matrix} . \tag{4.79}$$

The matrix exponential of $\mathbf{K}^{(i,j)}$

$$e^{\pm\Delta\tau\mathbf{K}^{(i,j)}} = \pm\mathbf{K}^{(i,j)}\sinh(\Delta\tau t_{ij}) + \mathbb{1}\cosh(\Delta\tau t_{ij}) \tag{4.80}$$

is again a sparse matrix with only four entries so that the multiplication with the matrix of Eq. (4.78) is realized as a product of N_b sparse matrix multiplications where N_b is the number of hopping terms $c_i^\dagger c_j + c_j^\dagger c_i$ in the Hamiltonian, which is typically proportional to the number of sites (for a square lattice with nearest neighbour hopping $N_b = 2N_s$). The computational cost of multiplying the hopping matrix to a dense matrix is thus reduced to $\mathcal{O}(N_b N_s) = \mathcal{O}(N_s^2)$. The systematic error of the decomposition depends on how often the exponentials of non-commuting matrices have to be factorized. One possible way to minimize this error is to group the bond hopping matrices into four sets such that all matrices in each set commute among each other [126]. In this so-called checkerboard decomposition the kinetic term reads

$$K = K_{x,\text{even}} + K_{x,\text{odd}} + K_{y,\text{even}} + K_{y,\text{odd}}, \tag{4.81}$$
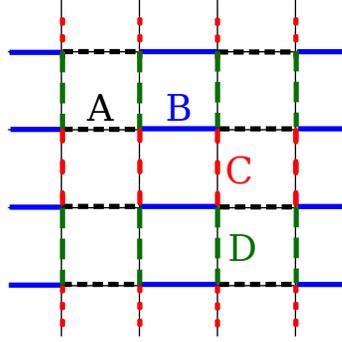
Fig. 4.2: Checkerboard decomposition of the hopping terms on the square lattice into "even" and "odd" bonds in vertical and horizontal direction.

where $K_{x,\text{even}}$ is the sum of hopping processes between sites (i_x, i_y) and $(i_x + 1, i_y)$ for even i_x and $K_{x,\text{odd}}$ for odd i_x. Similarly, $K_{y,\text{even}}$ and $K_{y,\text{odd}}$ account, respectively, for hopping processes between sites (i_x, i_y) and $(i_x, i_y + 1)$ for i_y even or odd (see Fig. 4.2(a)). Thus, for a square lattice (see Fig. 4.2) we end up with a multiplication by four sparse matrices

$$
\begin{aligned}
e^{-\Delta\tau K} M &= e^{-\Delta\tau K_{x,\text{even}}} e^{-\Delta\tau K_{x,\text{odd}}} e^{-\Delta\tau K_{y,\text{even}}} e^{-\Delta\tau K_{y,\text{odd}}} M + \mathcal{O}\left(\Delta\tau^2\right) \\
&= \prod_{b=1}^{N/4} e^{-\Delta\tau K_{x,\text{even}}^{(b)}} \prod_{b=1}^{N/4} e^{-\Delta\tau K_{x,\text{odd}}^{(b)}} \prod_{b=1}^{N/4} e^{-\Delta\tau K_{y,\text{even}}^{(b)}} \prod_{b=1}^{N/4} e^{-\Delta\tau K_{y,\text{odd}}^{(b)}} M + \mathcal{O}\left(\Delta\tau^2\right),
\end{aligned}
\tag{4.82}
$$

where the index b runs over the individual hopping processes in each of the four set of Eq. (4.81). The order in which the factors in each product in the second line of Eq. (4.82) are mutliplied together does not matter since they commute. The checkerboard breakup in this form does not introduce any additional errors to the simulations since the systematic error coming from the Trotter-Suzuki decomposition in the general DQMC setup is already $\mathcal{O}(\Delta\tau^2)$. Note that if the Trotter-Suzuki approximation in Eq. (4.78) is carried out in arbitrary order without the appropriate grouping of factors an error $\mathcal{O}(N_s \Delta\tau^2)$ is incurred, which scales with the system size. Another advantage of the checkerboard decomposition is that the inverse is easily expressed just by changing the sign in the exponent.

The potential matrices containing the auxiliary field variables are diagonal and can be multiplied to a dense matrix on $\mathcal{O}(N^2)$ operations.

4.4.2   Numerical stabilization

Whereas the low-rank update of the Green's function after each spin-flip can be accomplished exactly, the multiplications with the B_l matrices in the wrapping operations introduce rounding errors, which accumulate. Therefore the Green's function needs to

be recomputed periodically from scratch according to Eq. (4.25)

$$G_{\{\mathbf{s}\}}(\tau = l\Delta\tau) = [\mathbb{1} + B_l \cdots B_1 B_m \cdots B_{l+1}]^{-1}, \tag{4.83}$$

to avoid detrimental loss of numerical precision. To evaluate this expression a long chain of B_l matrices must be multiplied together. It is well-known that the multiplication of long chains of matrices becomes numerically unstable, especially if they are badly conditioned. The condition number of a matrix A is defined as the ratio $\kappa(A) = ||A^{-1}|| \cdot ||A||$ where $|| \cdot ||$ is a matrix norm, and choosing the Euclidean matrix norm $|| \cdot ||_2$ the condition number is given as the ratio $\kappa(A) = \sigma_{\max}(A)/\sigma_{\min}(A)$ of the largest and smallest singular values of A [121, Sect. 2.7.2]. It is an upper bound to the amplification of errors in matrix multiplication and quantifies the loss of precision when a matrix is inverted: $\delta D = \log_{10}\kappa(A)$ is the number of significant digits that are lost after matrix inversion [127, Chapt. 11] .

To see the origin of the ill-conditioned nature of the fermion matrix consider a free fermion system $\mathcal{H} = -\sum_{i,j} c_i^\dagger c_j$ at half filling ($\mu = 0$) with eigenvalues $\varepsilon_{\mathbf{k}} = -2t(\cos k_x + \cos k_y)$, lying in the range $-4t \leq \varepsilon_{\mathbf{k}} \leq 4t$. The corresponding fermion matrix is $G^{-1} = \mathbb{1} + e^{-K}$, which has a condition number $\kappa = e^{4\beta t}$ that diverges exponentially for large β so that already for moderate values of βt the amplification of numerical errors is dramatic. The physical picture is that for a fermionic system the largest contributions to the partition sum $\text{Tr}(e^{-\beta(\mathcal{H}-\mu N)})$ at low temperatures come from the bottom of the Fermi sea. Due to the Pauli principle, however, the relevant dynamics is governed by states of relatively high energy close to the Fermi level which are exponentially suppressed due to their small Boltzmann weights. Sufficient care has to be taken to preserve these small energy scales in the computation of the string of B_l matrices and the matrix inversion when evaluating the Green's function Eq. (4.83) [111].

4.4.3   Matrix decomposition techniques

To achieve stable matrix multiplication of long chains of possibly ill-conditioned matrices various matrix decomposition techniques have been devised. The matrices are represented in the form UDV, where U and V have a better condition number. In the case of the singular-value decomposition (SVD), U and V are unitary (orthogonal) and the diagonal matrix D contains the singular values of the matrix [121, Sect. 2.5.3]. An alternative *stratification technique*[6] for separating the numerical scales that are contained implicitly in a matrix is the modified Gram-Schmidt (MGS) factorization [77, 111, 128], where U is orthogonal, D is diagonal and V is upper triangular with unit diagonal entries.

---

[6]Stratification means that the elements in the matrix are organized according to scale. For example, in a column stratified matrix elements in the same column have similar numerical scales.

To get an impression of the problem at hand, consider the UDV decomposition of a matrix, which contains large diverging numerical scales:

$$UDV = \underbrace{\begin{pmatrix} X & X & X & X \\ X & X & X & X \\ X & X & X & X \\ X & X & X & X \end{pmatrix}}_{\text{unit scales}} \cdot \underbrace{\begin{pmatrix} \mathbf{X} & & & \\ & \mathbf{X} & & \\ & & X & \\ & & & \text{\scriptsize x} \end{pmatrix}}_{\text{diverging scales separated}} \cdot \underbrace{\begin{pmatrix} X & X & X & X \\ X & X & X & X \\ X & X & X & X \\ X & X & X & X \end{pmatrix}}_{\text{unit scales}}. \tag{4.84}$$

When the matrices in Eq. (4.84) are multiplied out, different numerical scales get mixed and the resulting matrix

$$UDV = \begin{pmatrix} \mathbf{X} & \mathbf{X} & \mathbf{X} & \mathbf{X} \\ \mathbf{X} & \mathbf{X} & \mathbf{X} & \mathbf{X} \\ \mathbf{X} & \mathbf{X} & \mathbf{X} & \mathbf{X} \\ \mathbf{X} & \mathbf{X} & \mathbf{X} & \mathbf{X} \end{pmatrix}$$

appears like an outer product of the first column of U with the first row of V. Small scales are present only implicitly, as small differences of large matrix elements, an inevitably get lost since the floating point precision on any computer is finite. Therefore, it is important to keep the different numerical scales explicitly separate to prevent large scales from "drowning" smaller ones.

Our task in the following is to compute the chain of B_l matrices in Eq. (4.83) in a numerically stable way by carefully separating scales throughout the computation. Suppose that r of the B_l matrices can be multiplied together without loss of numerical precision. This means that for imaginary time $\tau_0 = r\Delta\tau$ all energy scales in the single-particle propagator $B_r B_{r-1} \cdots B_1$ must be representable in finite floating point precision [53, 111]. Thus, τ_0 is set on the one hand by the bandwidth of the Hubbard model and on the other hand by the "double precision" floating point accuracy of 10^{-16}. The partial product is stabilized with a matrix factorization (either SVD or MGS): $B_r B_{r-1} \cdots B_1 = UDV$. Then another batch of r matrices B_l is multiplied onto this

product:

$$(B_{2r}B_{2r-1}\ldots B_{r+1})UDV = ((B_{2r}B_{2r-1}\ldots B_{r+1})UD)\,V \tag{4.85}$$

$$= \left((B_{2r}B_{2r-1}\ldots B_{r+1})U \begin{pmatrix} \mathbf{X} & & & \\ & \mathbf{X} & & \\ & & \mathrm{X} & \\ & & & \mathrm{x} \end{pmatrix} \right) V \tag{4.86}$$

$$= \underbrace{\begin{pmatrix} \mathbf{X} & \mathbf{X} & \mathrm{X} & \mathrm{x} \\ \mathbf{X} & \mathbf{X} & \mathrm{X} & \mathrm{x} \\ \mathbf{X} & \mathbf{X} & \mathrm{X} & \mathrm{x} \\ \mathbf{X} & \mathbf{X} & \mathrm{X} & \mathrm{x} \end{pmatrix}}_{M} V \tag{4.87}$$

$$= (U'D'V')V = U'D'(V'V) \tag{4.88}$$

In the matrix $M = (B_{2r}B_{2r-1}\ldots B_{r+1})UD$, different numerical scales are still separated according to columns. If M were multiplied directly onto V, small scales would get lost. With a matrix factorization $(B_{2r}B_{2r-1}\ldots B_{r+1})UD = U'D'V'$, which can be carried out in a numerically stable manner for a column stratified matrix, the divergent scales are first collected again into a diagonal matrix D'. This procedure is repeated until the entire string of matrices B_l in the single-particle Green's function Eq. (4.25) is computed

$$B_l B_{l-1} \cdots B_1 B_m B_{m-1} \cdots B_{l+1} = U_n D_n (V_n \cdots V_1), \tag{4.89}$$

where $nr = m$. For this to work it is required that a large number of matrices V can be multiplied together stably, which is the case for SVD, where V is unitary, and also turns out to be the case for MGS, where V is upper triangular with unit diagonal. Intermediate partial products can be stored for later reuse to avoid unnecessary computations; details are discussed in Refs. [77, 111].

Finally, we need to obtain the Green's function from the decomposed product by matrix inversion

$$G = (\mathbb{1} + UDV)^{-1} = V^{-1}(\underbrace{U^{-1}V^{-1} + D}_{\to\text{factorize}})^{-1}U^{-1} \tag{4.90}$$

$$= V^{-1}\,(U'D'V')^{-1}\,U^{-1} = (V'V)^{-1}(D')^{-1}(UU')^{-1} \tag{4.91}$$

Mixing of scales occurs only before the last matrix factorization when the diagonal matrix D, containing the divergent scales, is combined with the unit elements of

$U^{-1}V^{-1}$, which cut off the smallest scales. While this addition introduces numerical errors and $(\mathbb{1} + UDV)^{-1}$ multiplied by the original matrix $\mathbb{1} + UDV$ may not reproduce the identity matrix, the operation is numerically stable in an *operational sense* meaning that it does not introduce significant errors into the computation of the relevant elements of the Green's function [111]. If the singular value decomposition is used, then the matrices U and V are unitary with inverse $U^{-1} = U^{\dagger}$ and $V^{-1} = V^{\dagger}$ and the only inversion that needs to be performed is that of a diagonal matrix.

4.5   Summary: One Monte Carlo step (MCS)

One Monte-Carlo sweep of the space-time lattice consists in updating sequentially the auxiliary fields $\{\mathbf{s}\}$ at all sites and time slices. After each accepted spin-flip $s_i(l) \to -s_i(l)$ of the auxiliary field the Green's function is upgraded according to the low-rank update Eq. (4.68). When one time-slice l has been fully processed, we proceed to the next one by "wrapping" the Green's function according to Eq. (4.69) so that the equal-time Green's function for time slice $l + 1$ is available for computing the acceptance ratio Eq. (4.60) and for performing the low-rank update of the Green's function. After a number of $r \approx 10$ "wrapping" operations rounding errors have accumulated so that the Green's function needs to be re-computed from scratch. This is achieved by decomposing the string of ill-conditioned B_l matrices in Eq. (4.25) into partial products which are stabilized via singular-value decomposition.[7]

In all computations in this thesis we have used a Trotter discretization of $\Delta\tau t = 0.125$, which together with a stabilization at every 10th time slice is a generally accepted value [53, 112] for the Hubbard model.

After each sweep equal-time observables are measured using Wick's theorem. When computationally expensive observables O, such as the momentum-momentum correlation function (see Chapt. 10), are computed, the measurement of observables is performed only every $\tau_{\text{meas}} \approx 4 - 8$ Monte Carlo steps since successive samples are correlated on the time scale of the autocorrelation time τ_{AC}^O and more measurements do not necessarily yield additional statistics.

4.6   The sign problem

The notorious sign problem [129] is the biggest challenge for simulating fermionic systems with quantum Monte Carlo. This is one of the main motivations for developing

---

[7] To avoid recomputing partial products of the stabilized product of B_l matrices it is advantageous to store their UDV decompositions [77, 111] for later use. To make optimal use of the stack of partial products a sweep upwards from time slice $\tau = \Delta\tau$ to $\tau = m\Delta\tau = \beta$ needs to be followed by a sweep downwards [77, 111] from $\tau = m\Delta\tau$ to $\tau = \Delta\tau$. In the code used by the author this feature is not implemented, therefore the sweeps of the space-time lattice are simply from bottom ($\tau = \Delta\tau$) to top ($\tau = \beta$).

cold atom systems as quantum simulators for fermionic systems in parameter regimes where numerical methods fail.

4.6.1   Exponentially bad signal-to-noise ratio

The essence of the problem is that the sign or the phase of the fermion determinant can lead to dramatic cancellations [130, 131] which make the statistical error scale exponentially with inverse temperature and system size. The issue is that one tries to measure a small number, the Monte Carlo expectation value, as the difference of two huge numbers of opposite sign, which leads to a poor signal-to-noise ratio.

The following exposition is based on Refs. [130, 131]. Let $\mathcal{C}$ stand for a configuration of the effective classical system to which the quantum system has been mapped for the purpose of Monte Carlo simulations, i.e. for SSE (see Sect. 3.1) $\mathcal{C} = (\alpha, S_L)$ is a pair of initial state α and operator string S_L and in the case of DQMC a configuration $\mathcal{C} = \{s_{i,l}\}$ is a set of auxiliary fields at all sites $i = 1, \ldots, N$ and time slices $l = 1, \ldots, m$. When the weight can become negative[8] for some configurations, we write

$$w(\mathcal{C}) = \text{sign}(w(\mathcal{C}))|w(\mathcal{C})| \equiv \text{sign}(\mathcal{C})|w(\mathcal{C})|.$$

The Monte Carlo average of an observable O then takes the form

$$\langle \hat{O} \rangle = \frac{1}{Z} \sum_{\mathcal{C}} O(\mathcal{C}) w(\mathcal{C})$$
$$= \frac{\sum_{\mathcal{C}} O(\mathcal{C}) \text{sign}(\mathcal{C})|w(\mathcal{C})|}{\sum_{\mathcal{C}} \text{sign}(\mathcal{C})|w(\mathcal{C})|}. \tag{4.92}$$

A positive definite probability distribution, which is required for importance sampling, can be obtained with a *re-weighting technique* where the sign from the Monte Carlo weight is shifted onto the observable

$$\langle \hat{O} \rangle = \frac{\sum_{\mathcal{C}} \text{sign}(\mathcal{C}) O(\mathcal{C})|w(\mathcal{C})| / \sum_{\mathcal{C}} |w(\mathcal{C})|}{\sum_{\mathcal{C}} \text{sign}(\mathcal{C})|w(\mathcal{C})| / \sum_{\mathcal{C}} |w(\mathcal{C})|} = \frac{\langle \text{sign}(\mathcal{C}) O(\mathcal{C}) \rangle_{|w|}}{\langle \text{sign}(\mathcal{C}) \rangle_{|w|}}. \tag{4.93}$$

Here $\langle \cdot \rangle_{|w|}$ has been introduced as the average $\frac{\sum_{\mathcal{C}} (\cdot)|w(\mathcal{C})|}{\sum_{\mathcal{C}} |w(\mathcal{C})|}$ with respect to the effective bosonic system with weights $|w(\mathcal{C})|$. Now both the numerator and the denominator in Eq. (4.93) can in principle be sampled in a Monte Carlo simulation where the bosonic weights $|w(\mathcal{C})|$ are used for importance sampling. However, this is only possible if the average sign is close to ± 1 since otherwise strong cancellations occur in the averages $\langle \text{sign}(\mathcal{C}) O(\mathcal{C}) \rangle_{|w|}$ and $\langle \text{sign}(\mathcal{C}) \rangle_{|w|}$ and we are taking the ratio of two very noisy

---

[8]In the general case, e.g. for certain Hubbard-Stratonovich transformations in DQMC, the weight is a complex number $w(\mathcal{C}) = e^{i\phi}|w(\mathcal{C})|$ and we encounter a "phase problem".

quantities. The average sign turns out to be the ratio of the partition sums for the fermionic system and its bosonic counterpart that is used for sampling [131]

$$\langle \text{sign}(\mathcal{C}) \rangle_{|w|} = \frac{\sum_{\mathcal{C}} w(\mathcal{C})}{\sum_{\mathcal{C}} |w(\mathcal{C})|} = \frac{Z_w}{Z_{|w|}} \tag{4.94}$$

$$= \frac{e^{-\beta V f_w}}{e^{-\beta V f_{|w|}}} = \exp[-\beta V (f_w - f_{|w|})], \tag{4.95}$$

where $V = L^d$ is the volume of the simulated system and f_w and $f_{|w|}$ are the free energy densities of the systems with weight $w(\mathcal{C})$ and $|w(\mathcal{C})|$, respectively.
Now we have that

$$Z_w \leq Z_{|w|} \tag{4.96}$$

because $\sum_{\mathcal{C}} w(\mathcal{C}) \leq \sum_{\mathcal{C}} |w(\mathcal{C})|$, and since $f = -\frac{1}{\beta V} \ln Z$,

$$f_w \geq f_{|w|}, \qquad \Delta f = f_w - f_{|w|} \geq 0 \tag{4.97}$$

so that $\langle \text{sign}(\mathcal{C}) \rangle_{|w|} = \exp(-\beta V \Delta f)$ is an **exponentially decreasing** quantity when $\beta, V \to \infty$. The relative statistical error of the sign is [130, 131]

$$\frac{\Delta \text{sign}}{\langle \text{sign} \rangle} = \frac{\sqrt{\langle \text{sign}^2 \rangle - \langle \text{sign} \rangle^2}}{\sqrt{N} \langle \text{sign} \rangle} \tag{4.98}$$

$$= \frac{\sqrt{1 - \exp(-2\beta V \Delta f)}}{\sqrt{N} \exp(-\beta V \Delta f)} \approx \frac{e^{\beta V \Delta f}}{\sqrt{N}}, \tag{4.99}$$

where we have inserted the Monte Carlo scaling of the error $\sim \frac{1}{\sqrt{N}}$ and used $\text{sign}^2 = 1$. Thus, in order to obtain an accurate estimate of the sign one needs to generate $N \sim e^{2\beta V \Delta f}$ Monte Carlo configurations which is forbidding for large inverse temperatures β and large system volumes V. The detrimental signal-to-noise ratio of the average sign propagates to all other expectation values through Eq. (4.93) due to a large statistical uncertainty $\sim \left[\langle \text{sign} \rangle_{|w|} \right]^{-2}$. This destroys the very favourable polynomial scaling of the Monte Carlo method with system size and inverse temperature and converts it into an exponentially hard problem.

4.6.2 Absence of the sign problem

In few cases, special symmetries of the Hamiltonian guarantee that the fermion determinant is always positive.

Attractive and repulsive Hubbard model

As shown in Sect. 4.1, for the attractive Hubbard model the HS transformation Eq. (A.10b) results in a Monte Carlo weight for each HS configuration which is the product of two identical determinants

$$Z_{TS}^{U<0} = \sum_{\{\mathbf{s}\}} \det M_{\{\mathbf{s}\}}^{\uparrow} \det M_{\{\mathbf{s}\}}^{\downarrow} = \sum_{\{\mathbf{s}\}} \left| \det M_{\{\mathbf{s}\}}^{\uparrow} \right|^2 \geq 0. \tag{4.100}$$

Therefore the attractive Hubbard model is free of the sign problem for any filling.

On a bipartite lattice, such as the square or honeycomb lattice, and at half filling the repulsive ($U > 0$) Hubbard model has no sign problem [120], since in this case it is identical to the attractive Hubbard model: The spin-down particle-hole transformation Eq. (4.102) below converts one model into the other by changing the sign of the interactions while leaving the hopping term invariant. To emphasize that the absence of a sign problem is a property of the single-particle Hamiltonian after HS transformation we repeat this proof starting from the discrete HS decoupling for $U > 0$, Eq. (A.10a). In this case, the HS field $s_i(l)$ couples to the spin degree of freedom $n_{i,\uparrow} - n_{i,\downarrow}$ and the partition function reads

$$Z_{TS}^{U>0} = \sum_{\{\mathbf{s}\}} \mathrm{Tr} \left\{ \prod_{l=1}^{m} e^{\sum_i \left[\alpha s_i(l) - \Delta\tau(\mu - \frac{U}{2}) \right] n_{i,\uparrow}} e^{-\Delta\tau H_{t,\uparrow}} \prod_{l=1}^{m} e^{\sum_i \left[-\alpha s_i(l) - \Delta\tau(\mu - \frac{U}{2}) \right] n_{i,\downarrow}} e^{-\Delta\tau H_{t,\downarrow}} \right\}. \tag{4.101}$$

Performing a canonical transformation, which affects only spin down, the so-called Shiba transformation

$$\begin{aligned} d_{i,\downarrow} &= (-1)^{\mathbf{i}} c_{i,\downarrow}^{\dagger} \\ c_{i,\downarrow}^{\dagger} c_{i,\sigma} &= 1 - d_{i,\downarrow}^{\dagger} d_{i,\sigma}, \end{aligned} \tag{4.102}$$

leaves the kinetic term $H_{t,\downarrow}$ invariant if the lattice is bipartite [see Sect. 8.2.3]. Furthermore, at half filling, $\mu = \frac{U}{2}$, and we can rewrite the fermionic determinants in Eq. (4.101) as

$$\begin{aligned} \det \left(M_{\{\mathbf{s}\}}^{\downarrow} \right) &= \mathrm{Tr}_c \left\{ \prod_{l=1}^{m} e^{-\sum_i \alpha s_i(l) c_{i,\downarrow}^{\dagger} c_{i,\downarrow}} e^{-\Delta\tau H_{t,\downarrow}} \right\} \\ &= \mathrm{Tr}_d \left\{ \prod_{l=1}^{m} e^{-\sum_i \alpha s_i(l) \left(1 - d_{i,\downarrow}^{\dagger} d_{i,\downarrow} \right)} e^{-\Delta\tau H_{t,\downarrow}} \right\} \\ &= e^{-\alpha \sum_{i,l} s_i(l)} \mathrm{Tr}_d \left\{ \prod_{l=1}^{m} e^{\sum_i \alpha s_i(l) d_{i,\downarrow}^{\dagger} d_{i,\downarrow}} e^{-\Delta\tau H_{t,\downarrow}} \right\} \\ &= \underbrace{e^{-\alpha \sum_{i,l} s_i(l)}}_{>0} \det \left(M_{\{\mathbf{s}\}}^{\uparrow} \right). \end{aligned} \tag{4.103}$$

Thus, for the $U > 0$ Hubbard model, at half filling and on a bipartite lattice the determinants for spin up and down differ only by the factor $e^{\alpha \sum_{i,l} s_i(l)} > 0$ and therefore always have the same sign such that their product is positive definite. Away from half filling or on a frustrated lattice there is no simple relation between the two determinants and their product can become negative.

Generalized time reversal symmetry

The proof of the absence of a sign problem for the attractive Hubbard model relied on the property that the fermion determinant factorizes into two real parts with the same sign and therefore is positive definite. In fact, this is a special case of a more general criterion relating the absence of a sign problem to the question of time reversal symmetry of the single-particle Hamiltonian after HS decoupling [132]. The criterion is expressed by the following theorem:

Theorem 4.6.1. *If an antiunitary[9] operator T exists with the property $T^2 = -\mathbb{1}$ that leaves the kinetic term K and the potential term V of the single-particle Hamiltonian after Hubbard-Stratonovich transformation invariant, i.e.*

$$TKT^{-1} = K \quad and \quad TVT^{-1} = V, \quad with \quad T^2 = -\mathbb{1}, \tag{4.104}$$

hen the eigenvalues λ_i of the fermionic matrix

$$M = \mathbb{1} + \prod_{l=1}^{m} B_l = \mathbb{1} + \prod_{l=1}^{m} e^{-\Delta\tau V(\{\mathbf{s}_l\})} e^{-\Delta\tau K} \tag{4.105}$$

always come in complex conjugate pairs, i.e. if λ_i is an eigenvalues, then λ_i^* is also an eigenvalue. If they are real, they are two-fold degenerate. As a consequence, the fermion determinant, which can be expressed as the product of eigenvalues, is positive definite

$$\det\left(\mathbb{1} + \prod_{l=1}^{m} B_l\right) = \prod_i |\lambda_i|^2 > 0. \tag{4.106}$$

This theorem is a generalization of Kramers' theorem [133, Chapt. XV,§21] in quantum mechanics stating that the (real) eigenenergies of a time-reversal invariant system with half-integer total spin are at least two-fold degenerate.

Proof: We see directly from (4.104) that $TMT^{-1} = M$. Let v be an eigenvalue of M with eigenvalue λ, i.e. $Mv = \lambda v$. Using the antiunitarity of T it follows that

$$MTv = TM\underbrace{T^{-1}T}_{\mathbb{1}}v = T\lambda v = \lambda^*(Tv). \tag{4.107}$$

---

[9]An antiunitary operator U acting on Hilbert space $U : \mathscr{H} \to \mathscr{H}$ is an antilinear operator, satisfying $U(a|x\rangle + b|y\rangle) = a^*U|x\rangle + b^*U|y\rangle$ for all $|x\rangle, |y\rangle \in \mathscr{H}$, with the property that it preserves the scalar product up to complex conjugation: $\langle Ux, Uy \rangle = \langle x, y \rangle^*$.

Therefore Tv is also an eigenvector of M with eigenvalue λ^*. In order to ensure that λ and λ^* belong indeed to linearly independent eigenvectors, we need to invoke the property $T^2 = -\mathbb{1}$ together with the antiunitarity of T:

$$\langle v, Tv \rangle = \langle Tv, \underbrace{T^2}_{-\mathbb{1}} v \rangle^* = -\langle Tv, v \rangle^* = -\langle v, Tv \rangle, \tag{4.108}$$

which shows that the eigenvectors v and Tv are orthogonal and completes the proof.

Note that due to the imaginary time dependent auxiliary fields the fermion matrix M in determinantal QMC is in general non-Hermitian, which happens as soon as two of the B_l matrices do not commute

$$M = \mathbb{1} + B_1 B_2 \Rightarrow M^\dagger = \mathbb{1} + B_2^\dagger B_1^\dagger = \mathbb{1} + B_2 B_1 \neq M, \tag{4.109}$$

and therefore M may not be diagonalizable, i.e. there is no basis of linearly independent eigenvectors of M which spans the Hilbert space. Ref. [132] provides a proof of the above theorem also for this case.

To illustrate the application of this theorem we consider how it captures the case of the attractive Hubbard model, while it fails for the repulsive Hubbard model away from half filling. The time-reversal operator for a spin-$\frac{1}{2}$ particle [133, Chapt. XV.§18] is given as the antiunitary operator

$$\Theta = -i\sigma_y \mathcal{K} = \begin{pmatrix} 0 & -1 \\ 1 & 0 \end{pmatrix} \mathcal{K}, \tag{4.110}$$

where $\mathcal{K}$ denotes complex conjugation. It has the additional property $\Theta^2 = -\mathbb{1}$. Acting on a fermionic operator it has the effect of flipping the spin and giving a minus sign to the down spin. Then, the kinetic term and the charge density are invariant under the time reversal transformation

$$\Theta \left(c_{i,\uparrow}^\dagger c_{j,\uparrow} + c_{i,\downarrow}^\dagger c_{j,\downarrow} + h.c \right) \Theta^{-1} = c_{i,\downarrow}^\dagger c_{j,\downarrow} + (-1)^2 c_{i,\uparrow}^\dagger c_{j,\uparrow} + h.c. \tag{4.111}$$

$$\Theta \left(n_{i,\uparrow} + n_{i,\downarrow} \right) \Theta^{-1} = n_{i,\downarrow} + (-1)^2 n_{i,\uparrow}. \tag{4.112}$$

On the other hand, the magnetization degree of freedom changes sign

$$\Theta S^z \Theta^{-1} = \Theta \frac{1}{2}(n_\uparrow - n_\downarrow)\Theta^{-1} = -S^z, \tag{4.113}$$

so that a HS transformation that couples the auxiliary field to the magnetization density cannot be time reversal invariant.

Using for the $U > 0$ Hubbard model the HS transformation in Eq. (A.10b) that couples the auxiliary field to the charge density $n_{i,\uparrow} + n_{i,\downarrow}$ instead does not solve the problem either, since then the coupling constant $\tilde{\alpha} = \cosh^{-1}\left(e^{-\Delta\tau U}\right) = i\alpha$ acquires an imaginary factor i, which again spoils time-reversal symmetry

$$\Theta \left[i\alpha s_i(l)(n_{i,\uparrow} + n_{i,\downarrow}) \right] \Theta^{-1} = -i\alpha s_i(l)(n_{i,\uparrow} + n_{i,\downarrow}). \tag{4.114}$$

Thus, the repulsive Hubbard model does not satisfy the criteria of the above theorem with neither of the two HS transformations in Eqs. (A.10a),(A.10b), while the attractive Hubbard model satisfies it for both types of HS transformation.

Other sign-problem-free models

Recently, more general sign-problem-free formulations have been discovered. A HS decoupling of the interactions in the hopping channel of Majorana fermions [134] has allowed the simulation of some interacting spinless (spin-polarized) fermion models and models with $SU(N)$ symmetry with N odd, while the concepts of the split orthogonal group [135] and Majorana positivity [136, 137] have provided a new unified mathematical understanding of sufficient conditions for the positive definiteness of the fermion determinant. For completeness we mention also the meron cluster [130] and fermion bag [138, 139] methods which are based, respectively, on the path integral QMC and continuous-time QMC frameworks and which solve the sign problem by identifying and excluding those fermionic world line configurations whose weights cancel exactly and which therefore only contribute to the noise.

A few concluding remarks concerning the significance of the sign problem are in order:

1. The sign problem is not an intrinsic property of a physical system since it is basis dependent. We have seen in Sect. 3.3 and 3.2 that the formulation of the transverse field Ising model in the S^z-basis is free of a sign problem even on frustrated lattices whereas in the S^x-basis (eigenbasis of the transverse field) a sign problem appears. More generally, if all eigenvalues and eigenvectors of a many-body Hamiltonian are known, the sign problem can be avoided by writing the partition sum in the energy eigenbasis. However, this corresponds already to a full solution of the problem.

2. By reducing the problem of classical spin glass models [140] to the problem of a quantum system with a sign problem, Troyer and Wiese proved that the sign problem is in the complexity class of nondeterministic polynomial (NP) hard problems [131]. This means that unless the generally accepted conjecture $NP \neq P$ is disproven, a generic polynomial (P) solution of the sign problem cannot be found. On the other hand, this does not exclude the discovery of sign-problem-free formulations for specific models [141].

3. The sign problem manifests itself as an exponential deterioration of the signal-to-noise ratio and can in principle be beaten by "exponential" computational resources. Therefore, one can find parameter regimes of particle densities, interaction strength and lattice geometry [142] where, although a sign problem exists, simulations are still feasible for high temperature and moderate lattice sizes. Sect. 11 presents simulations of the repulsive Hubbard model away from half filling at an inverse temperature $\beta t = 4$, where the average sign $\langle \mathrm{sign}(w_{\{\mathbf{s}\}}) \rangle_{|w|} \approx 1$.

4. In the determinantal QMC framework, where the fermionic degrees of freedom are integrated out, the sign problem is less severe than in the path integral approach with the fermionic anticommutation relations being already accounted for by the

fermion determinant. The slightly milder sign problem is connected both to the "thinning out" of degrees of freedom [143] due to a HS transformation in which the local Hilbert space of four fermionic states (empty, singly occupied with spin up and down, and doubly occupied) is replace by two states of the auxiliary Ising variables and to the fact that determinants constitute a re-summation over fermion world-lines of different sign.

5. Even in the presence of a sign problem the Markov chain of configurations that is generated samples the correct stationary probability distribution. It is only when measuring expectation values that the poor signal-to-noise ratio makes it impossible to obtain meaningful results. Attempts to "see through the noise" with the help of neural networks have been made [144].

Chapter 5

Finite-size scaling at second-order phase transitions

One of the main applications of Monte Carlo simulations is the study of phase transitions and the associated critical behaviour. This is due to the favourable polynomial scaling of the Monte Carlo method with system size, allowing to simulate relatively large systems. Finite-size scaling is a standard technique of Monte-Carlo data analysis [59], which is why we discuss it in this methods chapter.

Close to a continuous (second-order) phase transition, induced either by temperature (thermal phase transition) or by a control parameter Γ of the Hamiltonian (e.g. a transverse field), quantifying the competition between two non-commuting terms (quantum-phase transition at $T = 0$), the correlation length ξ diverges as

$$\xi \propto |\tau|^{-\nu}, \tag{5.1}$$

where $\tau = |T - T_c|/T_c$ (or $|\Gamma - \Gamma_c|/\Gamma_c$) is the reduced distance from the critical point T_c (Γ_c) and ν is a critical exponent. ξ is the typical length scale of the order parameter fluctuations, which are either thermal or of quantum mechanical origin and destroy long-range order. At the critical point the system becomes scale invariant and correlation functions and thermodynamic quantities obey power law scaling with a set of critical exponents which are precisely determined by the universality class of the respective phase transition [145]. The existence of common universality classes for microscopically very different systems, depending only on few properties of a physical system such as the dimensionality of space, the symmetry of the order parameter or the range of interactions, is a fundamental result of the renormalization group theory [145]. We first discuss finite-size scaling for thermal phase transitions and then briefly turn to the generalization for quantum phase transitions. The presentation largely follows Sandvik's lecture notes [43]. For an introduction to quantum phase transitions the reader is referred to Ref. [62].

5.1 Finite-size scaling hypothesis

The critical exponents of the order parameter $\langle m \rangle$ and the susceptibility χ for the response to a field term $h \sum_i S_i^z$ are defined as

$$\langle m \rangle \sim |\tau|^\beta \tag{5.2}$$

and

$$\chi = \left. \frac{\partial \langle m \rangle}{\partial h} \right|_{h \to 0} \sim |\tau|^{-\gamma}. \tag{5.3}$$

In the following we treat both cases simultaneously by introducing a general thermodynamic quantity

$$Q \sim |\tau|^{-\kappa}, \tag{5.4}$$

which is either divergent (e.g. $\kappa = \gamma$ for the susceptibility) or singular but non-divergent (e.g. $\kappa = \beta$ for the order parameter) at the critical point.

Numerical simulations are done for systems of finite size L so that divergences appear necessarily rounded. The basic idea underlying finite-size scaling theory [146] is that, as long as $\xi \ll L$, the finite system size should not affect the behaviour of the system, which can be considered as infinite. However, if $\xi \gg L$, then L, not ξ, is the most relevant length scale. The finite system size L caps the divergence of ξ and limits how close the system can come to criticality. Using Eq. (5.1) the distance from the critical point can be expressed in terms of the correlation length (of the infinite system),

$$|\tau| \sim \xi^{-1/\nu}, \tag{5.5}$$

so that we can write

$$Q \sim \xi^{\kappa/\nu}. \tag{5.6}$$

The maximum value that Q can attain on a finite system is obtained by setting $\xi = L$:

$$Q_{\max}(L) \sim L^{\kappa/\nu}. \tag{5.7}$$

Similarly, inserting $\xi = L$ into Eq. (5.5) gives the finite-size shift of the reduced temperature, where divergent quantities reach their maximum, compared to the true critical point of the infinite system

$$|\tau_{\max}(L)| \sim L^{-1/\nu}. \tag{5.8}$$

This shift is present in any temperature-dependent feature that develops singular behaviour as $T \to T_c$ and its location $T^*(L)$ can be used as a size-dependent critical temperature.

Eqs. (5.7) and (5.8) can be combined into a finite-size scaling ansatz that any singular quantity Q (with its respective critical exponent κ) should obey in the scaling limit, i.e. sufficiently close to the critical point:

$$Q(\tau, L) = L^{\kappa/\nu} \Psi(\tau L^{1/\nu}). \tag{5.9}$$

Here, $\Psi(x)$ is the *scaling function*, which is also universal (although depending on the boundary conditions [147]). $Q(\tau, L)$ does not depend on τ and L independently, but only through the product $\tau L^{1/\nu} = (\xi/L)^{-1/\nu}$. This expresses the hypothesis that, when the correlation length diverges at a second-order phase transition, microscopic details become irrelevant and any singular quantity scales as a power law of the system size multiplied by a non-singular function which only depends on the ratio ξ/L. In the thermodynamic limit $L \to \infty$, we should recover the scaling $Q(\tau, L \to \infty) \sim |\tau|^{-\kappa}$, which implies that the scaling function should symptotically decay as $\Psi(x) \sim x^{-\kappa} \sim \tau^{-\kappa} L^{-\kappa/\nu}$ for $L \to \infty$ so that the L-dependent prefactor in Eq. (5.9) is cancelled.

5.2 Data collapse

The scaling ansatz Eq. (5.9) provides a practical way for extracting critical exponents from simulation data for finite system sizes. Defining rescaled x- and y-variables as

$$x_L = \tau L^{1/\nu} \quad \text{and} \quad y_L = Q(\tau, L) L^{-\kappa/\nu} \tag{5.10}$$

and plotting y_L versus x_L for all values of L, the points from different data sets should come to lie onto a single curve, namely the scaling function $\Psi(x)$, if the scaling hypothesis underlying Eq. (5.9) holds and the critical exponents κ and ν as well as the critical temperature T_c in $\tau = |T - T_c|/T_c$ are chosen correctly. This is referred to as a *data collapse*.

Close to a quantum phase transition [62] there are two relevant variables, the control parameter Γ driving the phase transition as well as temperature T, and we obtain a two-parameter scaling form

$$Q(\Gamma, T) = L^{\kappa/\nu} \Psi(|\Gamma - \Gamma_c| L^{1/\nu}, T L^z) \tag{5.11}$$

where z is the dynamical critical exponent [62]. To work directly with a two-parameter scaling function is usually difficult. If the temperature is rescaled with the system size according to $T = L^{-z}$, then the aspect ratio of the spatial extent of the system and the length of imaginary time $\beta = 1/T$ (measured in units of the correlation lengths ξ and ξ_τ) remains constant. The second variable in Eq. (5.11) drops out and we are left with a single-parameter scaling form

$$Q(\Gamma, T) = L^{\kappa/\nu} \Psi(|\Gamma - \Gamma_c| L^{1/\nu}, 1), \tag{5.12}$$

for which a data collapse is feasible.

Let us briefly discuss how a data collapse can be performed in practice. To obtain the critical exponents (and the critical temperature if it is not known from another data analysis), one can iterate over all possible values on a fine grid, each time fitting a single high-order polynomial through all data points (x_L, y_L). Taking the values which result in the best fit, the stability of the fit with respect to small modifications of the fixed parameters (e.g. previously known critical exponents or the known critical temperature) is investigated.

To emphasize the region of x-values where the fit should be particulary good a weight function, $\alpha(x_i) = \exp\left[-x_i^2/(2\sigma^2)\right]$, is introduced, The width σ of this window around $x = 0$ corresponds to the critical region, where the scaling ansatz for thermodynamic quantities is valid, and needs to be adjusted to obtain a good fit. To include the weight function, the standard linear regression of the fitting procedure needs to be slightly modified. Let

$$f(x_i) = \sum_{n=0}^{n_{\max}} \beta_n x_i^n = \vec{g}^T(x_i) \cdot \vec{\beta} \quad \text{with} \quad g_n(x_i) = x_i^n \tag{5.13}$$

be the fit polynomial, e.g. of order $n_{\max} = 8$, which should approximate the scaling function and

$$\mathcal{L}[\vec{\beta}] = \frac{1}{2} \sum_{i=1}^{N_{\substack{\text{data} \\ \text{points}}}} \alpha(x_i) \left| y_i - \vec{g}^T(x_i) \cdot \vec{\beta} \right|^2 \tag{5.14}$$

the least-squares cost function including the weight function $\alpha(x_i)$. $N_{\substack{\text{data} \\ \text{points}}}$ is the number of value pairs (x_L, y_L). From the minimization of $\mathcal{L}$ with respect to $\vec{\beta}$ the optimal coefficients of the fit polynomial take the usual form

$$\vec{\beta}^* = \left(\tilde{X}^T \tilde{X}\right)^{-1} \tilde{X}^T \vec{\tilde{y}}, \tag{5.15}$$

with the modified matrix $\left[\tilde{X}\right]_{i,n} = \sqrt{\alpha(x_i)} x_i^n$ and the vector $\tilde{y}_i = \sqrt{\alpha(x_i)} y_i$, for $n = 0, \ldots, n_{\max}$ and $i = 1, \ldots, N_{\substack{\text{data} \\ \text{points}}}$.

5.3   Binder cumulant

The previous discussion shows that it is desirable to be able to estimate the critical temperature independent of the critical exponent estimates so as to have one fit parameter less. This is possible with the help of the Binder cumulant [148, 149].

For a one-component order parameter m the Binder cumulant is defined as

$$U_L = \frac{3}{2} \left(1 - \frac{\langle m^4 \rangle_L}{3 \langle m^2 \rangle_L^2} \right) \tag{5.16}$$

in terms of the moments $\langle m^s \rangle_L = \int m^s P_L(m) dm$ of the order parameter distribution [148, 149]

$$P_L(m) \sim e^{-\mathcal{F}_L[m]}, \tag{5.17}$$

where $\mathcal{F}_L[m]$ is the Landau free energy functional, which can be expanded in a power series of m. The Binder cumulant characterizes how close the distribution $P_L(m)$ is to a Gaussian. In the disordered phase, for $T > T_c$ (or $\Gamma > \Gamma_c$, if Γ is a disordering field), and as long as $L \gg \xi$, the probability distribution of the order parameter m is Gaussian around $m = 0$. This follows from the Central Limit Theorem since regions much farther apart than ξ in a large system are uncorrelated. Then Wick's theorem for Gaussian integrals implies that $\langle m^4 \rangle = 3\langle m^2 \rangle^2$ so that $U_L \to 0$. In the opposite limit of an ordered state, fluctuations in m disappear so that $\langle m^4 \rangle = \langle m^2 \rangle \langle m^2 \rangle$ and $U_L \to 1$. Precisely at the critical point, the Central Limit Theorem does not necessarily hold anymore as the correlation length diverges and different blocks of spins become long-range correlated. $P_L(m)$ may be distinctly non-Gaussian and U_L approaches a non-trivial "fixed-point value" U_L^*, which is characteristic of the universality class [150]. At the critical point, the power laws according to Eq. (5.7), $\langle m^2 \rangle \sim L^{-2\beta/\nu}$ and $\langle m^4 \rangle \sim L^{-4\beta/\nu}$, cancel in Eq. (6.24) so that the finite-size correction is much smaller than the typical finite-size shift $L^{-1/\nu}$ [Eq. (5.8)] of other singular quantities that may be used to locate the critical temperature. Therefore, at the critical temperature T_c, Binder cumulants for different system sizes intersect at a common point U_L^* (with a small finite-size drift for the crossing points of successive system sizes). An analysis of the crossing points of the Binder cumulant thus gives already the critical point T_c without requiring knowledge of the critical exponents.

Let us finally note that we can also make a scaling ansatz for the full probability distribution of the order parameter [147, 148]:

$$P_L(m, T) = L^{\beta/\nu} \tilde{P}(\xi/L, mL^{\beta/\nu}). \tag{5.18}$$

$P_L(m)$ depends on the three variables m, L and $\xi(T)$ only in the combination $r = \xi/L$ and $\tilde{m} = mL^{\beta/\nu}$. From Eq. (5.18), which holds in the limit $L \to \infty$ and $\xi \to \infty$, with ξ/L finite, the standard finite-size scaling relations of Sect. 5.1 can be derived. The scaling function $\tilde{P}(r, \tilde{m})$ is universal (although depending on the chosen boundary conditions [149]).

Chapter 6

Long-range transverse Ising model on the triangular lattice

6.1 Introduction

Britton *et al.* [41] describe a Penning trap quantum simulator which is expected to simulate a transverse field Ising model with Hamiltonian

$$\hat{\mathcal{H}} = \sum_{i<j} J_{ij} \hat{S}_i^z \hat{S}_j^z - \Gamma \sum_i \hat{S}_i^x \qquad (6.1)$$

with tunable long-range interactions $J_{ij} = J|\mathbf{r}_i - \mathbf{r}_j|^{-\alpha}$, where $\alpha \equiv \sigma + d$ is the interaction exponent (in spatial dimension $d = 2$). Since we have taken great care to mimic in our simulations the experimental conditions as closely as possible, we first summarize the experimental setup [41], which is depicted in Fig. 6.1.

   When a collection of ions is laser-cooled in a Penning trap, below a certain temperature the ions undergo a structural phase transition from a plasma to a Wigner crystal that is stabilized by their mutual Coulomb repulsion. For a strong trapping potential in z-direction the system becomes two-dimensional (2D) and the corresponding Wigner crystal is a triangular lattice. The number of trapped ions in a Penning trap ranges from a few to a few millions; in Ref. [41] the creation of a triangular Wigner crystal with ≈ 300 $^9\mathrm{Be}^+$ ions was reported. There, the valence electron of each ion serves as a qubit, which is represented by the spin-$\frac{1}{2}$ operators $(\hat{S}_i^x, \hat{S}_i^y, \hat{S}_i^z)$ in Eq. (6.1). It can be driven by applying microwave radiation, which corresponds to an effective magnetic field that can be tuned to have both transverse and longitudinal components. The use of a spin-dependent optical dipole force allows to engineer a long-range Ising-type spin-spin interaction $J_{i,j} \propto |r_i - r_j|^{-\alpha}$ between the internal two-level systems of the ions [37], where the exponent α can be continuously varied between 0 (infinite range) and 3 (dipolar decay) by adjusting a laser detuning parameter. The mechanism by which this interaction arises is naturally long-range and antiferromagnetic (AFM) if the direction of the spin-dependent optical dipole-force is perpendicular to the 2D Coulomb

crystal so that ions with opposite spin move away from each other in the z-direction thereby minimizing their Coulomb repulsion. Ferromagnetic (FM) interactions can be generated by additionally adjusting a detuning from the eigenfrequencies of normal modes of the Coulomb crystal. The goal of this chapter is to map out the ground state phase diagram of this effective spin model as a function of α and Γ for both ferromagnetic and antiferromagnetic interactions, which may help to benchmark such a potential quantum simulator.

On a bipartite lattice, long-range AFM interactions induce only weak frustration. The triangular lattice, on the other hand, is already frustrated, giving rise, in the case of the short-range Ising AFM, to a disordered classical ground state manifold with the long-range interactions leading - in principle - to additional frustration. The minimum energy configurations of the classical model (6.1) with $\Gamma = 0$ on the triangular lattice may depend sensitively on α and computing them may amount to a difficult optimization problem. To the best of our knowledge the classical phase diagram of (6.1) as a function of decay exponent α is not known. It will be shown in the following that including quantum fluctuations through a transverse field, however, stabilizes
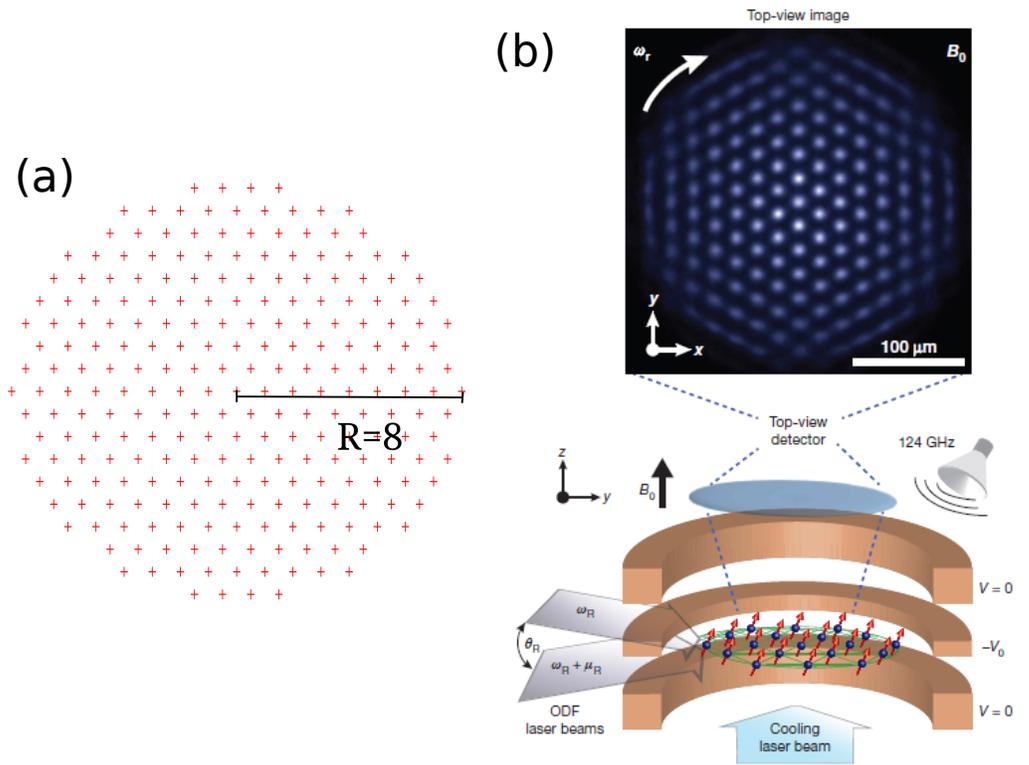
Fig. 6.1: (a) For radius $R \le 6$ the shape of the simulation cell is that of a hexagon centered at a lattice site; for $R \ge 7$ it has a circular shape similar to the experimental setup of the Penning trap quantum simulator of Ref. [41] (b). Reprinted with permission from Macmillan Publishers Ltd: *Nature*. Britton *et al.*, Nature **484**, 489 (2012), © 2012.
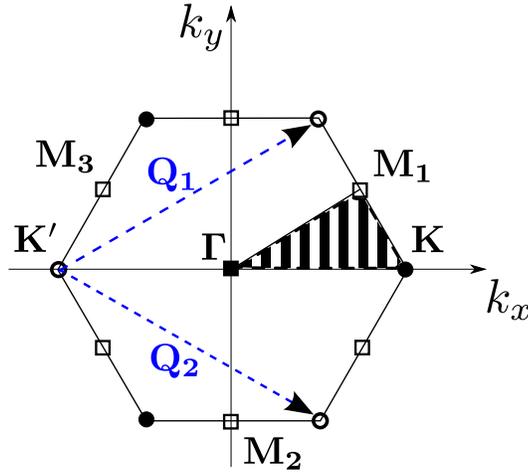
Fig. 6.2: First Brillouin zone (BZ) of the triangular lattice. The corners of the hexagonal BZ are at wave vectors $\mathbf{K} = (\frac{4\pi}{3}, 0)$ and $\mathbf{K'} = (-\frac{4\pi}{3}, 0)$; the other letters label points of high symmetry. The reciprocal lattice vectors of the triangular lattice, which connect equivalent points in the BZ, are $\mathbf{Q}_{1,2} = (2\pi, \pm\frac{2\pi}{\sqrt{3}})$ and $\mathbf{Q}_1 - \mathbf{Q}_2 = (0, \frac{4\pi}{\sqrt{3}})$. The shaded region indicates the *irreducible* BZ, to which all wave vectors inside the BZ can be mapped by symmetry operations of the point group of the triangular lattice.

a phase that extends over a range of decay exponents α, thus merging potentially different classical ground states.

The structure of this chapter is as follows: Sect. 6.2 introduces the concept of "order by disorder" and the Landau-Ginzburg-Wilson Hamiltonian describing the field theory at the critical point of the triangular transverse field Ising AFM. Sect. 6.3 gives a mean-field analysis of both the ferromagnetic and antiferromagnetic problem with long-range interactions. In Sect. 6.4 we briefly discuss simulation details and challenges that a long-range frustrated system has posed for the QMC algorithm we have used (see Sect. 3.3). QMC results on the long-range transverse field Ising ferromagnet and antiferromagnet are presented in Sect. 6.5 and a summary of the main results and open questions is given in Sect. 6.6

6.2 "Order by disorder"

The phase diagram of the classical triangular Ising antiferromagnet, which is obtained by setting $\Gamma = 0$ in equation (6.1), is well-known from the work of Wannier [104] and Stephenson [151]: It is disordered at all temperatures with a macroscopic ground state degeneracy [104] and critical spin-spin correlations at $T = 0$ where $\langle S_0^z S_r^z \rangle$ decreases asymtotically as $r^{-1/2}$ [151]. The ground state degeneracy can be explained by looking at the Fourier transformation, $\tilde{J}(\mathbf{q})$, of the Ising interactions on the triangular lattice

and taking into account the nature of the Ising spins. While

$$\tilde{J}(\mathbf{q}) = J \left[\cos q_x + 2 \cos \left(\frac{q_x}{2} \right) \cos \left(\frac{\sqrt{3}q_y}{2} \right) \right] \tag{6.2}$$

has minima of $-3J/2$ at the corners of the hexagonal Brillouin zone (see Fig. 6.2), at $\mathbf{Q}_\pm = (\pm\frac{4\pi}{3}, 0)$ and equivalent points, such ordering vectors are not compatible with the hard-spin constraint of classical Ising spins [152]. The lowest possible energy per frustrated triangle can be realized in a multitude of ways so that a macroscopic ground state degeneracy arises. The ground state manifold comprises any state without three parallel spins in the same triangle [104]. The situation changes for stacked triangular antiferromagnets [153]. If several triangular layers are stacked ferromagnetically on top of each other, chains of spins in the stacking direction can be combined to form an averaged macrospin. Then, for finite temperature, the spins, which are coupled ferromagnetically within a chain, fluctuate and the averaging removes the hard-spin constraint so that the 2D system of chains can settle into the minima at ordering vectors $\mathbf{Q}_\pm$ and a three-sublattice ordered ("clock ordered") state emerges. This is the classical, i.e. finite-temperature induced version of the phenomenon "order by disorder".

The transverse field quantum Ising model can be mapped by the Trotter-Suzuki formalism [154] to a ferromagnetically stacked classical Ising model so that the statements made above for stacked triangular magnets carry over to the 2D transverse field Ising model on the triangular lattice [30, 155]. Explicitly, in the path integral formalism, the quantum Ising model of Eq. (6.1) on a D-dimensional lattice is mapped to an effective classical Hamiltonian acting on a (D+1)-dimensional lattice

$$H_{\text{class.}}(\{S_{i,k}\}) = \sum_{i,j=1}^{N} \sum_{k=1}^{M} \left[-K_{ij}S_{i,k}S_{j,k} - \delta_{ij}K_M S_{i,k}S_{i,k+1} \right], \tag{6.3}$$

which again is an Ising model, this time with classical spin variables $S_{i,k} = \pm 1$ and with rescaled spatial couplings $K_{ij} = \frac{J_{ij}}{M}$ and *ferromagnetic* couplings $K_M = \frac{1}{2\beta} \ln \coth \left(\frac{\beta\Gamma}{M} \right)$ in the additional "Trotter" dimension. The equivalence holds strictly in the limit where the number of layers M in the additional dimension is infinite. This quantum-to-classical mapping, which is derived in Appendix B, explains why one can relate the physics of the quantum Ising model to a classical Ising model consisting of ferromagnetically stacked layers.

The mechanism that is responsible for the appearance of three-sublattice order in a transverse field is the quantum version of "order by disorder": Quantum fluctuations induced by the transverse field stabilize those states from the classical ground state manifold which can lower their energy the most by resonance processes. Thus, the exponential degeneracy of the ground state manifold is lifted and - since the favoured states tend to be regularly structured spin configurations - an ordered state emerges. This concept is illustrated in Fig. 6.3 for the triangular lattice. The degenerate
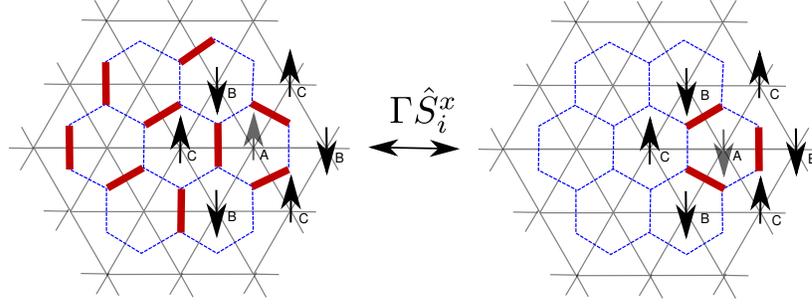
Fig. 6.3: Resonance processes on the triangular lattice. Quantum fluctuations induced by a transverse field favour a regularly structured spin configuration (see main text for details).

ground states of the classical triangular lattice Ising AFM are equivalent to dimer coverings on the dual honeycomb lattice [31, 156], with exactly one dimer (red bar) emanating from each dual lattice site. The dimers cross the frustrated bonds of the original triangular lattice. In the spin configuration shown in Fig. 6.3, the spin on sublattice A can fluctuate freely in a transverse field ΓS_i^x, since this costs zero net interaction energy. In the language of dimers, this corresponds to a resonance move on a hexagon. The partially disordered AFM state (see below) with sublattice magnetizations $(m_A, m_B, m_C) = (1, -1, 0)$ maximizes the number of possible resonance moves and thus gains most energy from quantum fluctuations introduced by the action of a transverse field.

Which resonance processes are possible within the ground state manifold (and to which order in Γ) is determined by the lattice structure and the interactions [31, 32]. For instance, if one always needs to flip two spins in order to get back to the ground state manifold, the action of the transverse field to lowest order is equivalent to $\hat{S}_i^+ \hat{S}_j^- + \hat{S}_i^- \hat{S}_j^+ \sim \hat{S}_i^x \hat{S}_j^x + \hat{S}_i^y \hat{S}_j^y$.

6.2.1 Landau-Ginzburg-Wilson theory and XY order parameter

The ordering vectors $\mathbf{Q}_\pm = (\pm 4\pi/3, 0)$ of the critical modes, i.e. the wave vectors that minimize the Fourier transform $\tilde{J}(\mathbf{q})$ of the interactions, correspond to inequivalent points in the Brillouin zone. This means that $\mathbf{Q}_+$ and $\mathbf{Q}_-$ are not related by a reciprocal lattice vector (see Fig. 6.2); however, they can be transformed into each other by symmetry elements of the point group of the triangular lattice. The existence of two degenerate modes implies a two-component order parameter

$$\vec{\eta} = \begin{pmatrix} \psi_+(\mathbf{q}) \\ \psi_-(\mathbf{q}) \end{pmatrix}, \tag{6.4}$$

with the components being the average spin configuration im momentum space at the critical and nearby modes, $\psi_\pm(\mathbf{q}) \equiv \langle \tilde{s} \rangle (\mathbf{Q}_\pm \pm \mathbf{q})$, where $|\mathbf{q}| \ll 1$ gives the distance[1] from the minima $\mathbf{Q}_\pm$ at the corners of the hexagonal Brillouin zone. Close to a second-order phase transition the order parameter $\vec{\eta}$ is small and an effective (long-wavelength) Landau-Ginzburg-Wilson Hamiltonian can be written down as a polynomial expansion (see [157, Chapt. 17]) of the components of $\vec{\eta}$ as [152, 153]

$$
\begin{aligned}
\mathcal{H}_{\text{LGW}} = \frac{1}{2} \sum_{|\mathbf{q}| \ll 1} & \left(r + \mathbf{q}^2 \right) \psi_+(\mathbf{q})\psi_-(\mathbf{q}) \\
&+ u_4 \sum_{\substack{\mathbf{q}_1, \mathbf{q}_2, \\ \mathbf{q}_3, \mathbf{q}_4}} \psi_+(\mathbf{q}_1)\psi_-(\mathbf{q}_2)\psi_+(\mathbf{q}_3)\psi_-(\mathbf{q}_4)\delta_{\mathbf{q}_1+\mathbf{q}_2+\mathbf{q}_3+\mathbf{q}_4,n\mathbf{Q}_1+m\mathbf{Q}_2} \\
&+ u_6 \sum_6 (\psi_+\psi_-)^3 + v_6 \sum_6 \left(\psi_+^6 + \psi_-^6 \right) + \dots
\end{aligned}
\tag{6.5}
$$

The sums $\sum_p$ are over p quasi-momentum arguments which add to zero up to an integer multiple of reciprocal lattice vectors $n\mathbf{Q}_1 + m\mathbf{Q}_2$, with $n, m \in \mathbb{Z}$ and $\mathbf{Q}_{1,2} = (2\pi, \pm\frac{2\pi}{\sqrt{3}})$ (see Fig. 6.2). For clarity, in the second line the sum $\sum_4$ over 4 quasi-momentum arguments has been written out explicitly. The expression for H_{LGW} is purely based on symmetry considerations and contains all possible invariants under the point group symmetry of the triangular lattice.

In the following we try to give a detailed justification for the form of H_{LGW} in Eq. (6.5). Since ψ_+ and ψ_- can be transformed into each other through symmetry operations of the point group, they must appear symmetrically in H_{LGW} so that the latter is invariant under echanging ψ_+ and ψ_-. A natural question is then why for example the terms $\sum_\mathbf{q} (\psi_+(\mathbf{q})\psi_+(-\mathbf{q}) + \psi_-(\mathbf{q})\psi_-(-\mathbf{q}))$ or $\sum_4 \left(\psi_+^4 + \psi_-^4 \right)$ are forbidden by symmetry. This has to do with quasi-momentum conservation on the triangular lattice. Recalling the definition $\psi_+(\mathbf{q}) \equiv \langle \tilde{s} \rangle (\mathbf{Q}_+ + \mathbf{q})$ in terms of the Fourier transform of the average spin configuration $\langle \tilde{s} \rangle$ and writing explicitly

$$
\sum_4 \psi_+^4 = \sum_{\substack{\mathbf{q}_1, \mathbf{q}_2 \\ \mathbf{q}_3, \mathbf{q}_4}} \tilde{s}(\mathbf{Q}_+ + \mathbf{q}_1)\tilde{s}(\mathbf{Q}_+ + \mathbf{q}_2)\tilde{s}(\mathbf{Q}_+ + \mathbf{q}_3)\tilde{s}(\mathbf{Q}_+ + \mathbf{q}_4) \, \delta_{4\mathbf{Q}_+ + \sum_{i=1}^4 \mathbf{q}_i, n\mathbf{Q}_1+m\mathbf{Q}_2}, \tag{6.6}
$$

one sees that quasi-momentum conservation would require that $4\mathbf{Q}_+ = (\frac{16\pi}{3}, 0)$ be an integer combination of the reciprocal lattice vectors $\mathbf{Q}_1$ and $\mathbf{Q}_2$. Since this is not the case, the term $\sum_4 \psi_+^4$ must vanish. On the other hand, the term $\sum_6 \psi_+^6$ is allowed since $6\mathbf{Q}_+ = (8\pi, 0)$ is an integer multiple of the combination $\mathbf{Q}_1 + \mathbf{Q}_2 = (4\pi, 0)$ of reciprocal lattice vectors. Similarly, $\sum_\mathbf{q} \psi_+(\mathbf{q})\psi_+(-\mathbf{q})$ is forbidden since $2\mathbf{Q}_+ = (\frac{8\pi}{3}, 0)$ is not an integer combination of $\mathbf{Q}_1$ and $\mathbf{Q}_2$, whereas $\sum_\mathbf{q} \psi_+(\mathbf{q})\psi_-(\mathbf{q})$ is allowed because of

---

[1] For the following discussion, $\mathbf{q}$ can just as well be set to zero for simplicity. Then the sums over momenta in H_{LGW} in Eq. (6.5) disappear and we are left with a simple polynomial of two parameters ψ_+ and ψ_-, which are the amplitudes of the ordered spin configurations corresponding to wave vectors $\mathbf{Q}_+$ or $\mathbf{Q}_-$, respectively.

$\mathbf{Q}_+ + \mathbf{Q}_- = \mathbf{0}$. Note that in this argument we have left aside the quasi-momenta $\mathbf{q}_i$, which are by definition centred around the critical modes $\mathbf{Q}_\pm$ and which are too small to provide the momentum transfer that is missing in the case of quasi-momentum non-conservation. Of course, the allowed values of the $\mathbf{q}_i$ in the sums in Eq. (6.5) are also restricted by quasi-momentum conservation.

Another important issue is the relation of the coefficients r, u_4, u_6 and v_6 in the effective long-wavelength Hamiltonian H_{LGW} to the parameters of the microscopic Hamiltonian. Although it will turn out that a direct connection is not straightforward, it is worthwhile to discuss how such a relation can be established in principle. For a classical Ising model $\mathcal{H} = 1/\beta \left(\sum_{ij} S_i^z K_{ij} S_j^z + \sum_i H_i S_i^z \right)$, with $K_{ij} = \beta J_{ij}$ and $H_i = \beta h_i$, the Gaussian integral identity [158, 159] (which is also known as Hubbard-Stratonovich transformation) can be used to transform the partition sum into a functional integral over a continous field variable $\phi_i \in [-\infty, \infty]$:

$$
\begin{aligned}
Z &= \sum_{\{S_i^z = \pm 1\}} \exp \left\{ \frac{1}{2} \sum_{i,j} S_i^z K_{ij} S_j^z + \sum_i H_i S_i^z \right\} \\
&= \frac{1}{(2\pi)^{N/2}} \frac{1}{\sqrt{\det K}} \sum_{\{S_i^z = \pm 1\}} \int_{-\infty}^{\infty} \underbrace{\prod_{i=1}^{N} d\phi_i}_{\mathcal{D}\phi} \exp \left\{ -\frac{1}{2} \sum_{i,j} \phi_i \left(K^{-1} \right)_{ij} \phi_j + \sum_i (\phi_i + H_i) S_i^z \right\}
\end{aligned}
$$

(6.7)

This yields a problem of independent spins $S_i^z \in [-1, 1]$ coupled to the space-dependent field ϕ_i, and the sum over the spins can be performed exactly

$$
\prod_{i=1}^{N} \sum_{S_i^z} e^{S_i^z(\phi_i + H_i)} = 2^N \exp \left(\sum_{i=1}^{N} \ln \cosh(\phi_i + H_i) \right).
$$

(6.8)

After another linear transformation $\psi_i = \sum_j K_{ij}^{-1} \phi_j$, which leads to $\sum_{i,j} \phi_i \left(K^{-1} \right)_{ij} \phi_j = \sum_{i,j} \psi_i K_{ij} \psi_j$, the functional integral formulation of the partition sum finally reads, with all multiplicative constants absorbed into a constant C:

$$
\begin{aligned}
\mathcal{Z}[\{H_i\}] &= C \int \mathcal{D}\psi \exp \left\{ -\frac{1}{2} \sum_{i,j} \psi_i K_{ij} \psi_j + \sum_i \ln \cosh \left(\sum_j K_{ij} \psi_j + H_i \right) \right\} \\
&\sim \int \mathcal{D}\psi \, e^{-\beta H_{\text{LGW}}}.
\end{aligned}
$$

(6.9)

By expanding

$$
\ln \cosh x = x^2/2 - x^4/12 + x^6/45 - 17x^8/2520 + \cdots
$$

(6.10)

and Fourier transforming a Landau-Ginzburg-Wilson Hamiltonian of the form Eq. (6.5) is obtained. The sum $\sum_i$ over real space sites in Eq. (6.9) imposes quasi-momentum

conservation. The continuous field ψ_i is the *local order parameter*. Close to the phase transition the order parameter essentially extends over a linear dimension equal to the correlation length ξ, which diverges at the phase transition. When $\xi/a \gg 1$, with a the lattice spacing, the continuum limit is appropriate. Considering only long wavelength fluctuations of the order parameter, we can restrict the momentum sums to $|\mathbf{q}| \ll 1$ (see Eq. (6.5)) and develop $\tilde{J}(\mathbf{q})$ up to quadratic order around the minima at $\mathbf{Q}_\pm$. In our case $|\mathbf{q}| \ll 1$ means that deviations from the ordering pattern associated with wave vector $\mathbf{Q}_+$ (not the ordering pattern itself) vary slowly in space.

The coefficient r of the quadratic term in Eq. (6.5) is the reduced control parameter [158, 159] $r \sim \frac{g-g_c}{g_c}$. It drives the phase transition occuring at $r = 0$ with g standing for either temperature T (for the ferromagnetically stacked classical model) or transverse field Γ (for the quantum model). Not all coefficients of H_{LGW} can be straightforwardly derived from Eq. (6.9) and Eq. (6.10). For example, the term $\sim (\psi_+^6 + \psi_-^6)$ appears again at higher orders, e.g. as $\psi_+ \psi_- (\psi_+^6 + \psi_-^6)$ at order eight, and due to the alternating sign of the series (6.10) one cannot determine the sign of the coefficient v_6 close to the phase transition reliably from the microscopic Hamiltonian in this way [30]. In fact, the coefficients of the Landau-Ginzburg-Wilson Hamiltonian drift as a function of control parameter [30] and the only reliable way to obtain them is directly from Monte Carlo simulations [30, 160].

Having explained and justified the form of $\mathcal{H}_{\mathrm{LGW}}$ for the transverse field Ising AFM, we can use it to make predictions about the possible ordering patterns that are induced by quantum fluctuations. For this it is convenient to change the parametrization of the two-component order parameter $\vec{\eta} = (\psi_+(\mathbf{q}), \psi_-(\mathbf{q}))$ and write it as a complex number. The fact that the average spin configuration $\langle s \rangle (\mathbf{r}_i)$ is real implies $\langle \tilde{s} \rangle (-\mathbf{k}) = (\langle \tilde{s} \rangle (\mathbf{k}))^*$ and motivates to write $\psi_\pm(\mathbf{q}) = m(\mathbf{q}) e^{\pm i\phi}$ so that $\psi_+(\mathbf{q}) = (\psi_-(\mathbf{q}))^*$. With this parametrization[2] of the two-component order parameter as a pair (m, ϕ) the Landau-Ginzburg-Wilson Hamiltonian reads

$$
\begin{aligned}
\mathcal{H}_{\mathrm{LGW}} = {} & \frac{1}{2} \sum_{|\mathbf{q}| \ll 1} \left(r + \mathbf{q}^2 \right) m(\mathbf{q})^2 \\
& + u_4 \sum_{\substack{\mathbf{q}_1, \mathbf{q}_2, \\ \mathbf{q}_3, \mathbf{q}_4}} m(\mathbf{q}_1) m(\mathbf{q}_2) m(\mathbf{q}_3) m(\mathbf{q}_4) \delta_{\mathbf{q}_1+\mathbf{q}_2+\mathbf{q}_3+\mathbf{q}_4, n\mathbf{Q}_1+m\mathbf{Q}_2} \\
& + u_6 \sum_6 m^6 + v_6 \sum_6 m^6 \cos(6\phi).
\end{aligned}
\tag{6.11}
$$

Up to fourth order in m the effective Hamiltonian (6.11) has an *emergent XY symmetry*, which means that there is no dependence on the order parameter component ϕ. The XY symmetry is brought about by the frustration on the triangular lattice, where, as discussed above, the anisotropic term $\sum_4 \left(\psi_+^4 + \psi_-^4 \right)$ must vanish by momentum conservation. At sixth order in m a sixfold *clock anisotropy* term $m^6 \cos(6\phi)$ appears

---

[2] Note that here m is not the S^z-magnetitzation; it is the amplitude of the average spin configuration associated with the ordering vector $\mathbf{Q}_+$.

which, depending on the sign of v_6, gives an energetic preference to the six values $\phi = \frac{(2n+1)\pi}{6}$, with $n = 0, 1, \ldots, 5$.

The microscopic pattern of the long-range ordered phases is obtained by Fourier transforming the thermal average of the critical modes

$$
\begin{aligned}
\langle s \rangle(\mathbf{r}_i) &= \int_{1^{\text{st}}\text{BZ}} d^2 k e^{i\mathbf{k}\cdot\mathbf{r}_i} \langle \tilde{s} \rangle(\mathbf{k}) \\
&\sim \int_{\mathbf{k} \text{ around } \mathbf{Q}_+} d^2 k \, e^{i\mathbf{k}\cdot\mathbf{r}_i} \langle \tilde{s} \rangle(\mathbf{k}) + \int_{\mathbf{k} \text{ around } \mathbf{Q}_-} d^2 k \, e^{i\mathbf{k}\cdot\mathbf{r}_i} \langle \tilde{s} \rangle(\mathbf{k}) \\
&\sim e^{i\mathbf{Q}_+\cdot\mathbf{r}_i} \underbrace{\langle \tilde{s} \rangle(\mathbf{Q}_+)}_{m\,e^{i\phi}} + e^{i\mathbf{Q}_-\cdot\mathbf{r}_i} \underbrace{\langle \tilde{s} \rangle(\mathbf{Q}_-)}_{m\,e^{-i\phi}}
\end{aligned}
\tag{6.12}
$$

With $\mathbf{Q}_+ = -\mathbf{Q}_-$ spin configuration of the long-range ordered state becomes

$$
\langle s \rangle(\mathbf{r}_i) \sim M \cos(\mathbf{Q}_+ \cdot \mathbf{r}_i + \Phi),
\tag{6.13}
$$

where $M = m$ and $\Phi = \phi$ are the values which minimize H_{LGW}. The scenario of XY symmetry (in the case of a vanishing coefficient v_6) means that all spin configurations that can be obtained from Eq. (6.13) by varying Φ are energetically degenerate.

Depending on the sign of the coefficient v_6, the clock anisotropy term selects between two different three-sublattice ordered states [153] according to Eq. (6.13), namely, denoting the sublattice magnetizations as $(\langle s \rangle(r_A), \langle s \rangle(r_B), \langle s \rangle(r_C))$, a ferrimagnetic state $(M, -\frac{M}{2}, -\frac{M}{2})$ for $\phi = 0$ and a partially disordered antiferromagnetic state $(\frac{\sqrt{3}M}{2}, -\frac{\sqrt{3}M}{2}, 0)$ for $\phi = \pi/6$. Both states are six-fold degenerate, which can be seen by relabelling the sublattices and by making use of spin-inversion symmetry. Monte Carlo simulations [153, 161] showed that at intermediate temperatures the stacked triangular antiferromagnet orders according to $(1, -1, 0)$ and at low temperatures approximately according to $(1, -\frac{1}{2}, -\frac{1}{2})$ with possibly unsaturated magnetization. However, the nature of the low-temperature phase has been the subject of controversy [162–165].

The fact that the frustration on the triangular lattice generates an XY order parameter has several consequences: With the clock term in (6.11) being dangerously irrelevant, the transition from the paramagnetic to the clock ordered phase is believed to be in the 3D XY universality class [30, 153]. The location of this quantum critical point was determined to be at $\Gamma_c/J = 1.65 \pm 0.05$ [30]. The Kosterlitz-Thouless transition [166] from a clock-ordered phase with sublattice magnetization $(1, -1, 0)$ to a paramagnetic phase via an extended critical phase, which occurs as a consequence of a finite-temperature induced dimensional crossover in the (D+1)-dimensional quantum system, was also investigated in Ref. [30]. The possibility of a Kosterlitz-Thouless transition at finite temperature in the long-range system is beyond the scope of this work.

In Chapt. 7 a Kosterlitz-Thouless transition in a one-dimensional spin model is investigated in detail and we introduce the relevant theory there. Here, we confine ourselves to asking the curious question: Which configurations of Ising spins on the
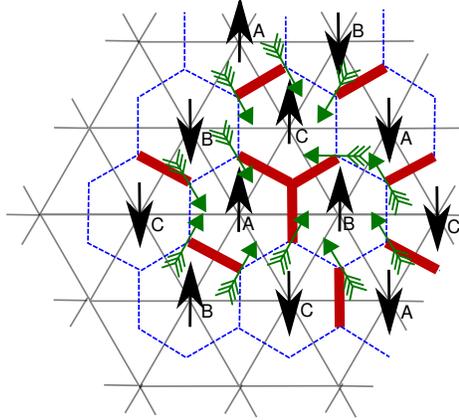
Fig. 6.4: A maximally frustrated plaquette, with three parallel spins (three dimers touching each other on the dual lattice), corresponds to an isolated topological defect of the local order parameter field $\psi(\mathbf{r}) = S_A^z(\mathbf{r}) + S_B^z(\mathbf{r})e^{2\pi i/3} + S_C^z(\mathbf{r})e^{4\pi i/3}$. Note that a triangular plaquette with three parallel spins has $|\psi| = 0$ as it should be for a vortex core. (Figure adapted from [155].)

triangular lattice are related to the vortices and antivortices giving rise to a Kosterlitz-Thouless transition ? Consider the local complex XY vector which can be expressed in terms of the spin configuration on each triangle centered at $\mathbf{r}$ as

$$\psi(\mathbf{r}) = S_A^z(\mathbf{r}) + S_B^z(\mathbf{r})e^{2\pi i/3} + S_C^z(\mathbf{r})e^{4\pi i/3}, \tag{6.14}$$

where the indices A, B and C refer to the three sublattices of the triangular lattice. Drawing $\psi(\mathbf{r})$ as compass needles into the exemplary spin configuration in Fig. 6.4 we see that maximally frustrated plaquettes (three dimers touching at a lattice site) correspond to topological excitations of the field $\psi(\mathbf{r})$ living on the sites of the dual honeycomb lattice. Three parallel spins on a triangle correspond, respectively, to a vortex with positive (for ↑-spins) or negative (for ↓-spins) vorticity.

6.3   Mean field theory

It is well-known that for the infinitely coordinated Ising model, that is with weak constant interactions $J_{ij} = \frac{J}{N}$, where N is the number of sites, the saddle point approximation, which maps the system to a mean-field problem, becomes exact. It is intuitively clear that for long-range systems mean-field theory provides a good description. However, this is only true for FM interactions since long-range AFM interactions lead to additional frustration. We start from the Hamiltonian

$$\hat{\mathcal{H}} = \frac{1}{2}\sum_{i,j} J_{ij}\hat{S}_i^z\hat{S}_j^z - \Gamma\sum_i \hat{S}_i^x - h_\parallel\sum_i \hat{S}_i^z \tag{6.15}$$

where for the sake of completeness we have added a longitudinal field $h_\parallel$. Writing the spin operator in terms of small fluctuations around an average value, $\hat{S}_i^z = \langle S_i^z \rangle + \delta \hat{S}_i^z \equiv m + \delta \hat{S}_i^z$, and neglecting second-order fluctuations, a mean-field Hamiltonian can be obtained

$$\hat{\mathcal{H}}_{MF} = \frac{1}{2} N \tilde{J}(0) m^2 - (\tilde{J}(0)m + h_\parallel) \sum_i \hat{S}_i^z - \Gamma \sum_i \hat{S}_i^x, \tag{6.16}$$

where $\tilde{J}(\mathbf{q}) = \sum_{\mathbf{R}} J(\mathbf{R}) \exp(-i\mathbf{q} \cdot \mathbf{R})$ is the Fourier transform of the interactions. Thus, dropping an overall constant, the thermodynamics reduces to that of paramagnetic spins in a longitudinal and transverse field. The single-spin Hamiltonian can easily be diagonalized with eigenenergies $E_\pm = \pm \sqrt{(\tilde{J}(0)m + h_\parallel)^2 + \Gamma^2}$ and eigenvectors

$$|\phi_+\rangle = \begin{pmatrix} \cos \frac{\theta}{2} \\ \sin \frac{\theta}{2} \end{pmatrix}, \quad |\phi_-\rangle = \begin{pmatrix} -\sin \frac{\theta}{2} \\ \cos \frac{\theta}{2} \end{pmatrix}$$

with

$$\tan \theta = \frac{\Gamma}{\tilde{J}(0)m + h_\parallel},$$

so that the self-consistency condition for the thermal average (with $\beta = 1/k_B T$) is given by

$$m = \langle \hat{S}^z \rangle = \frac{\langle \phi_- | \hat{S}^z | \phi_- \rangle e^{-\beta E_-} + \langle \phi_+ | \hat{S}^z | \phi_+ \rangle e^{-\beta E_+}}{e^{-\beta E_-} + e^{-\beta E_+}}$$

$$= \frac{\tilde{J}(0)m + h_\parallel}{\sqrt{\Gamma^2 + (\tilde{J}(0)m + h_\parallel)^2}} \tanh \left(\beta \sqrt{\Gamma^2 + (\tilde{J}(0)m + h_\parallel)^2} \right) \tag{6.17}$$

In the limit $\Gamma \to 0$ this reduces to the well-known mean-field equation for an Ising ferromagnet in a longitudinal field. In the following we consider $h_\parallel = 0$ so that the only contribution to the longitudinal field is the mean field coming from the interaction with other spins. Taking the limit $m \to 0$ gives the phase boundary $\frac{\Gamma}{\tilde{J}(0)} = \tanh(\beta_c \Gamma)$ with a zero-temperature critical point at $\Gamma_c = \tilde{J}(0)$ and a critical point a zero field at $k_B T_c = \tilde{J}(0)$. At $T = 0$ the order parameter increases as $m = \pm \sqrt{1 - \frac{\Gamma}{\tilde{J}(0)}}$, as is typical of mean-field solutions. Thus, in this admittedly very simple model the extent of the ordered phase scales with the interaction sum $\tilde{J}(0)$, which - as will be shown below - provides already qualitatively correct predictions of the phase boundary for both ferromagnetic and antiferromagnetic long-range interactions. For a mean-field treatment of the antiferromagnet we assume that the magnetic unit cell consists of three sites. Then, the self-consistency equation for each of the sublattices A,B and C reads

$$m_A \equiv \langle S_l^z \rangle = \frac{H_l^z(m_A, m_B, m_C, h_\parallel)}{\sqrt{\Gamma^2 + (H_l^z)^2}} \tanh \left(\beta \sqrt{\Gamma^2 + (H_l^z)^2} \right) \tag{6.18}$$

with the longitudinal mean field $H_l^z = \tilde{J}_{AA}(0)m_A + \tilde{J}_{AB}(0)(m_B + m_C)$ acting at sites $l \in A$. The equations for m_A and m_B are obtained by cyclic permutation of the indices A, B, C. The interaction sum $\tilde{J}_{AA}(0) = \sum_{i \in A} \frac{J}{r_i^\alpha}$ gives the interaction of a spin in sublattice A with all other spins in the same sublattice. $\tilde{J}_{AB}(0) = \tilde{J}_{AC}(0) = \sum_{i \in B} \frac{J}{r_i^\alpha}$ is the interaction of a spin in sublattice A with all spins in either of the other two sublattices B or C, and $\tilde{J}(0) = \tilde{J}_{AA}(0) + \tilde{J}_{AB}(0) + \tilde{J}_{AC}(0)$. With the reasonable assumption that the total magnetization has to be zero, $m_A + m_B + m_C = 0$, the mean field simplifies to $H_l^z = m_A(\tilde{J}_{AA}(0) - \tilde{J}_{AB}(0))$. Thus, the mean-field phase boundary of the antiferromagnet is the same as that of the ferromagnet, except that it is scaled by the interaction sum $\tilde{J}_{AA}(0) - \tilde{J}_{AB}(0)$. The lattice sums are absolutely summable for $\alpha > 2$ (FM interactions) and $\alpha > 0$ (AFM interactions) and we compute them as a function of α analytically in the thermodynamic limit[3] ,and numerically for a large triangular lattice with hexagonal boundaries. Figs. 6.5 and 6.6 show the resulting mean-field phase boundaries as a function of the decay exponent α:

$$\Gamma_c^{\text{MF}}(0; \alpha) = \begin{cases} \tilde{J}(0; \alpha) \\ \tilde{J}_{\text{AA}}(0; \alpha) - \tilde{J}_{\text{AB}}(0; \alpha), \end{cases} \tag{6.19}$$

where the first line applies to FM and the second line to AFM interactions. To illustrate the issue of convergence with system size, the lattice sum $\Gamma_c^{\text{MF}}(0; \alpha) = \tilde{J}(0; \alpha)$ was computed for a system of lattice points with hexagonal shape, the size of which is parametrized by its radius R (see Appendix). For $\alpha < 2$, the lattice sum diverges as the system size tends to infinity; for $\alpha = 2$ it diverges logarithmically with the linear extent R of the system. This can be seen from Fig.6.5, where the dotted lines correspond to systems with radius $R = 10, 100, 1000$, and 2000 (in units of the lattice constant). The curve of the phase boundary in the thermodynamic limit (red line) is the exact result $\tilde{J}(0; \alpha) = 6\,\zeta(\frac{\alpha}{2})L_{-3}(\frac{\alpha}{2})$.

If the Ising interactions do not decay with distance, i.e. $\alpha = 0$ and $J_{ij} = J$ for all (i, j), the Hamiltonian can be rewritten in terms of a single macroscopic spin operator

---

[3] $\tilde{J}_{AA}(0; \alpha) - \tilde{J}_{AB}(0; \alpha) \equiv H_2(\alpha)$ is equivalent to the hexagonal lattice sum, i.e. the interaction sum of an antiferromagnetic configuration on the (bipartite) hexagonal lattice which in turn corresponds to a sublattice magnetization $(1, -1, 0)$ on the triangular lattice. A useful parametrization for the hexagonal lattice sum is [167]

$$H_2(2s = \alpha) = \frac{4}{3} \sum_{m,n=-\infty}^{\infty} \frac{\sin(n+1)\theta \sin(m+1)\theta - \sin n\theta \sin(m-1)\theta}{\left[(n + \frac{1}{2}m)^2 + 3(\frac{1}{2}m)^2\right]^s}.$$

with $\theta = 2\pi/3$. An analytical formula is given in [167] as $H_2(\alpha) = 3(3^{1-\frac{\alpha}{2}} - 1)\zeta(\frac{\alpha}{2})L_{-3}(\frac{\alpha}{2})$ in terms of the Riemann ζ-function $\zeta(s) = \sum_{n=1}^{\infty} \frac{1}{n^s}$ and a Dirichlet L-series $L_{-3}(s) = 1 - 2^{-s} + 4^{-s} - 5^{-s} + 7^{-s} - 8^{-s} \cdots$. The exact result for the triangular lattice sum is [167]

$$\tilde{J}(0; 2s = \alpha) = \sum_{m,n=-\infty}^{\infty} \frac{1}{[n^2 + nm + m^2]^s} = 6\,\zeta(\frac{\alpha}{2})L_{-3}(\frac{\alpha}{2}).$$
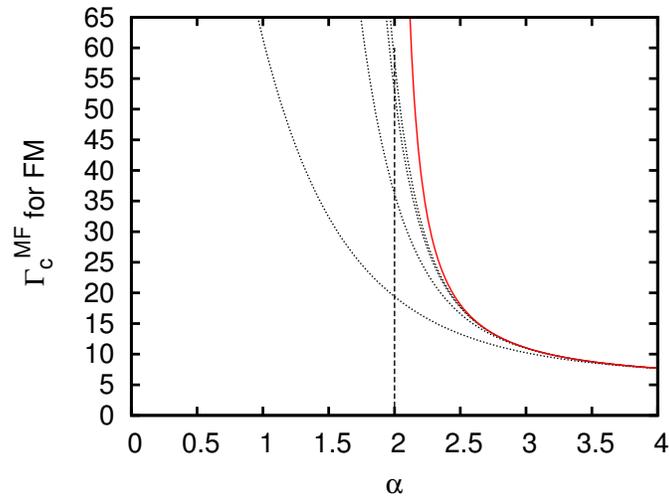
Fig. 6.5: Mean-field phase boundary (red line) of the ferromagnetic Ising model on the triangular lattice and in a transverse field as given by Eq.(6.19). The dotted lines are for successively larger hexagonally shaped systems of radius $R = 10, 100, 1000$, and 2000.
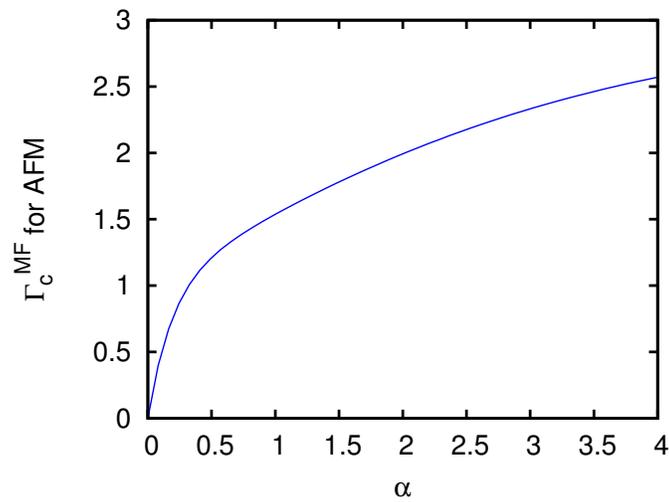
Fig. 6.6: Mean-field phase boundary of the antiferromagnetic Ising model on the triangular lattice and in a transverse field as given by Eq.(6.19).

$\hat{S}_{\text{tot}}^{z(x)} = \sum_{i=1}^{N} \hat{S}_i^{z(x)}$:

$$\mathcal{H} = \frac{J}{2} \left(\sum_{i=1}^{N} \hat{S}_i^z \right) \left(\sum_{j=1}^{N} \hat{S}_j^z \right) - \Gamma \left(\sum_{i=1}^{N} \hat{S}_i^x \right)$$

$$= \frac{J}{2} (\hat{S}_{\text{tot}}^z)^2 - \Gamma \hat{S}_{\text{tot}}^x. \tag{6.20}$$

where we have omitted an additive constant. This is an anisotropic variant of the Lipkin-Meshkov-Glick model [168]. For this infinitely coordinated Ising model the lattice structure becomes irrelevant. The AFM model ($J > 0$) for $\Gamma = 0$ has a degeneracy which is exponential in ($N/2$): Any configuration with $S_{\text{tot}}^z = 0$ is a ground state. The transition into the paramagnetic state should occur immediately at $\Gamma_c = 0^+$ since for $S_{\text{tot}}^z = 0$ there is no opposing Ising interaction.

As for nearest neighbour interactions, the Fourier transformation of $J_{ij} = J/|\mathbf{r}_i - \mathbf{r}_j|^\alpha$ displays minima at the corners of the hexagonal Brillouin zone. However, they become increasingly shallow as α decreases and vanish around $\alpha_c \approx 1$. This means that for $\alpha < \alpha_c$ the lattice structure cannot dictate the ordered state to be selected by the quantum fluctuations.

6.4   Details of the QMC simulations

We have used the Stochastic Series Expansion (SSE) QMC method that was proposed by A. Sandvik in Ref. [95] and which we have described at length in Sect. 3.3. It can deal with transverse field Ising models with arbitrary, long-range or frustrated, interactions. In the case of long-range interactions, it avoids the interaction summation that is typically necessary, and the scaling of the CPU time with system size is reduced from N^2 to $N \ln(N)$. The main trick (see Sect. 3.3) consists in adding constants $|J_{ij}|$ to the Ising bond operators

$$H_{i,j} = |J_{ij}| - J_{ij} S_i^z S_j^z, \quad i \neq j \tag{6.21}$$

in such a way that only satisfied bonds (i.e. FM bonds, $J_{ij} < 0$, on FM spin configurations, $S_i^z = S_j^z$, or AFM bonds on AFM spin configurations) have non-zero weight. This constraint, which is active in the propagation direction of the SSE algorithm, obviates techniques such as Ewald summation of the interactions in real space that are typically used for long-range interacting systems. Furthermore it is evident from (6.21) that even a frustrated transverse field Ising model has no sign problem in the S^z basis since any negative matrix elements can be shifted by a constant. As the Monte Carlo update depends crucially on the presence of single-spin flip (transverse field) terms in the Hamiltonian, ergodicity may be lost for small transverse fields. By the same token, we find that, for AFM interactions, the algorithm does not perform well at finite temperatures as soon as the thermal fluctuations become comparable to the

quantum fluctuations, $k_B T \sim \Gamma$. On the other hand, this update mechanism proves extremely efficient in the case of large transverse fields. For all simulations we have used the multibranch cluster update [95] described in detail in Sect. 3.3.2.

6.4.1 Finite-size gap

Deep in the paramagnetic regime $\Gamma/J \to \infty$ the lowest energy excitations of the transverse field Ising model are spin waves (here, small deviations from the alignment along the field), and for long-range interactions decaying with exponent α their dispersion relation reads

$$\omega(q) = \sqrt{\Delta^2 + aq^{\alpha-d} + bq^2} \quad \text{for} \quad q \to 0. \tag{6.22}$$

Δ is the gap, which vanishes at the QCP, and a and b are constants that can be obtained explicitly by diagonalizing a spin-wave approximation to the Hamiltonian in the eigenbasis of the transverse field [Eq. (3.22)]. Given that long-range interactions lead to mean-field like behaviour the description in terms of spin-wave excitations is rather accurate. Assuming that close to the QCP the excitations with lowest energy are still spin waves, we can use their dispersion relation to estimate the finite-size gap, which suppresses thermal excitations and allows to simulate effectively "T=0" on a finite system at criticality. By developing Eq. (6.22) for $q \to 0$ and inserting the smallest possible wavenumber $q_{\min} = \frac{2\pi}{L}$ it can be seen that the finite-size gap scales with system size L as

$$\Delta_{\text{fs}} \sim \left(\frac{2\pi}{L}\right)^{(\alpha-d)/2} \sim L^{-\sigma/2} \quad \text{for} \quad \sigma = \alpha - d < 2. \tag{6.23}$$

An important caveat is that we have not determined the prefactor in Eq. (6.23), which may be small, requiring correspondingly lower temperatures for accessing ground state properties.

6.4.2 Simulation parameters

The simulation cell with open boundaries is hexagonal and parametrized by its "radius" R so that the total number of spins is $N(R) = 1 + 3R(R+1)$. To be closer to the experimental situation in a cylindrically symmetric trapping potential [Fig. 6.1(b)], for $R \geq 7$ additional spins were included which extend the hexagon to an approximately circular shape [Fig. 6.1(a)] so that in those cases the number of spins is larger than given by this formula. Due to the six-fold symmetry the total number of spins is always $N = 6n + 1$ where n is an integer. The largest systems studied consisted of 613 spins for FM interactions and 301 spins for AFM interactions, respectively.

The simulations were performed at $T = 1/(2R)^{z_{\text{SR}}}$, where $2R$ is the diameter of the simulation cell and $z_{\text{SR}} = 1$ is the dynamical critical exponent of the short-range Ising
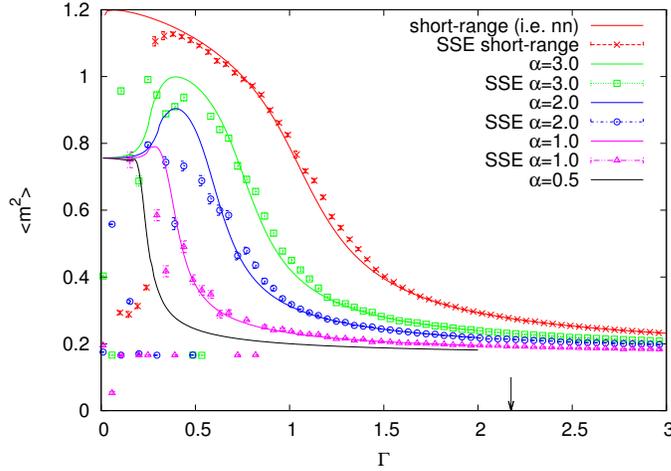
Fig. 6.7: Comparison between Lanczos exact diagonalization and SSE QMC for a hexagonal system of 19 spins ($R = 2$) with AFM interactions. Shown are the fluctuations of the modulus of the complex XY order parameter $\langle m^2 \rangle$. In the region of interest around $\Gamma \approx 1$ the results from both algorithms agree nicely. For some values of Γ the mean fluctuation of the magnetization could not be determined due to technical issues. Those points lie around $\langle m^2 \rangle = 0.2$ and are meaningless. For comparison, the critical value in the AFM mean field theory for $\alpha = 2.5$ is indicated by an arrow at $\Gamma_c^{\mathrm{MF}}(\alpha = 2.5) = 2.1758$.

model [62]. Given that according to Eq. (6.23) the finite-size gap scales as $(2R)^{-1/2}$ (for $\alpha = 3$), rescaling the temperature as $T = (2R)^{-1}$ is a conservative approach ensuring that the thermal energy $k_B T$ is smaller than the finite-size gap. On the other hand, to obtain suitable data sets for finite-size scaling [see Sect. 5] at a quantum-critical point the temperature should actually be rescaled with the correct dynamical exponent of the long-range system, i.e. as $T = (2R)^{-z_{\mathrm{LR}}}$ with $z_{\mathrm{LR}} = \frac{\sigma}{2}$ (see Ref. [169] and Sect. 7). This is a deficiency of our data sets. We still attempt a data collapse based on the assumption that the system is at "$T = 0$" due to the large finite-size gap so that the second variable TL^z in the scaling function Eq. (6.25) drops out.

While for FM interactions around $50-100$ thermalization steps and 10^4 measurement steps were sufficient to study the critical behaviour, in the long-range, frustrated AFM case $\approx 10^4$ thermalization steps and up to $4 \cdot 10^6$ measurement steps were required due to long thermalization and autocorrelation times.

6.4.3 Code verification

The Monte Carlo code was successfully checked against Lanczos exact diagonalization (ED) on a hexagonal system of radius $R = 2$ with $N = 19$ spins. Note that the next larger sytem size R=3, N=37 with *open boundary conditions* was not amenable to exact diagonalization since momentum is not a good quantum number. The agreement between QMC and ED for ferromagnetic interactions is excellent. For antiferromagnetic

interactions, on the other hand, the error bars are only meaningful in the paramagnetic phase. In Fig. 6.7 the square of the clock order parameter (6.26), that is its fluctuations, versus the transverse field Γ is shown for different decay powers α. There is good agreement between QMC and ED in the paramagnetic phase whereas in the ordered phase the curves do not agree within error bars. This is due to the fact that in the ordered phase the fluctuations are non-Gaussian, exhibiting asymmetric tails as can be seen from the histogram of the squared clock order parameter, which is discussed in Sect. 6.5.3. Furthermore for small transverse fields ergodicity may be lost when the quantum clusters used in the Monte Carlo update percolate in imaginary time (see Ref. [95] for a discussion of this issue). As a consequence, the error bars in our simulations of the antiferromagnet are only reliable for the paramagnetic phase and for the onset of order, but not within the ordered phase. For determining the critical field only the former parameter regions are needed so that the phase boundary can still be obtained quantitatively. As an illustration of the quantitative inaccuracy of mean field theory, an arrow has been added in Fig. 6.7 indicating the critical value in mean field theory for $\alpha = 2.5$, which lies at $\Gamma_c^{\mathrm{MF}}(\alpha = 2.5) = 2.1758$.

6.5   QMC results

6.5.1   Long-range ferromagnet on the triangular lattice

The value of the critical field can be estimated with various methods.

Fig. 6.8 gives already a first impression of how the order parameter fluctuations $\langle m^2 \rangle$ behave around the quantum critical point for the long-range ferromagnet with decay exponent $\alpha = 3$. In the disordered phase they are increasingly suppressed for growing system size. By eye inspection one would place the critical point around $\Gamma \approx 9$; however, a pronounced finite-size shift of the magnetization curves is apparent.

We determine the critical field by locating the crossing points of the Binder cumulant [150] for consecutive system sizes and extrapolating to the thermodynamic limit. For a scalar order parameter the appropriate Binder cumulant is

$$U_L = \frac{3}{2}\left(1 - \frac{\langle m^4 \rangle}{3\langle m^2 \rangle^2}\right), \tag{6.24}$$

where $\langle m^i \rangle$ is the i-th moment of the z-component of the magnetization. As already discussed in Sect. 5, it has scaling dimension zero since at the critical point the power laws in the linear system size R for $\langle m^4 \rangle$ and $\langle m^2 \rangle$ cancel out. In the limit $R \to \infty$ the Binder cumulant has the following properties: $U_R \to 1$ in the ordered phase, $U_R \to 0$ in the disordered phase and at the critical point $U_R \to U^\star$, i.e. the Binder cumulants for different system sizes intersect at a common point $U^\star$, which is also universal. Often there are subleading finite-size corrections so that the crossing points for pairs of system sizes drift providing a size-dependent critical point which typically converges
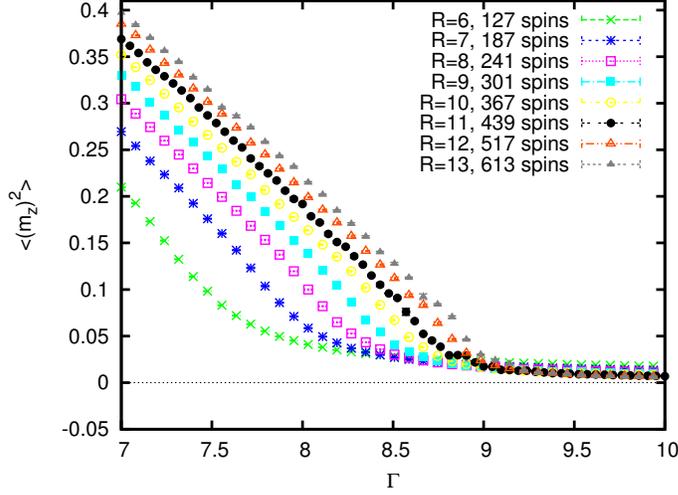
Fig. 6.8: Squared magnetization per site for $\alpha = 3.0$. For a mean-field transition, $\beta = 0.5$ and $\langle m_z^2 \rangle$ should vanish linearly in the vicinity of the critical field.

much faster than the usual finite-size shift $\propto R^{-1/\nu}$ of other quantities with singular behaviour at the critical point [43].

Fig. 6.9 shows the Binder cumulant U_R for system sizes ranging from $N = 241$ to $N = 613$. The two limiting regions of an ordered state with $U_R \to 1$ and a disordered state for $U_R \to 0$ are clearly visible. The Binder cumulants for different system sizes cross in a region where U_R is small so that the distribution function of the order parameter $P_R(m)$ is expected to be almost Gaussian, pointing towards a phase transition of mean-field type.

The fact that the crossing points for successive system sizes occur at small values of U_R renders this otherwise very accurate method of determining the critical field problematic. (An error propagation shows that small $\langle m^2 \rangle$ lets the error on the Binder cumulant increase drastically.) Fig. 6.10 shows the extrapolation of the crossing points of the Binder cumulant vs. $1/N$ which leads to an estimate for the critical field of $\Gamma_c \approx 10.0$. Smaller system sizes are more affected by boundary effects due to the open boundary conditions and therefore they were excluded from the fit. The fact that a fit including only the smaller system sizes would underestimate the critical transverse field is consistent, as a larger boundary to bulk ratio reduces the restoring Ising interaction energy relative to the energy of the spins aligned with the transverse field, the latter being independent of the boundary to bulk ratio.

The critical behaviour of long-range ferromagnetic quantum Ising and rotor models has been studied by Dutta and Bhattacharjee [169] using field theory and renormalization group equations. They find that in two dimensions the critical exponents attain values of the short-range system for $\alpha \geq 4$. For $\alpha_u \leq \alpha < 4$ the critical exponents depend continuously on α and reach mean-field values for $\alpha < \alpha_u$ where $\alpha_u = 10/3$
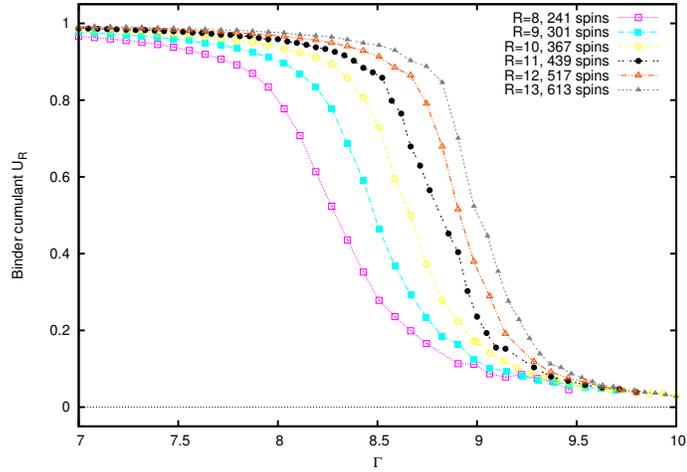
Fig. 6.9: Binder cumulants for $\alpha = 3.0$.
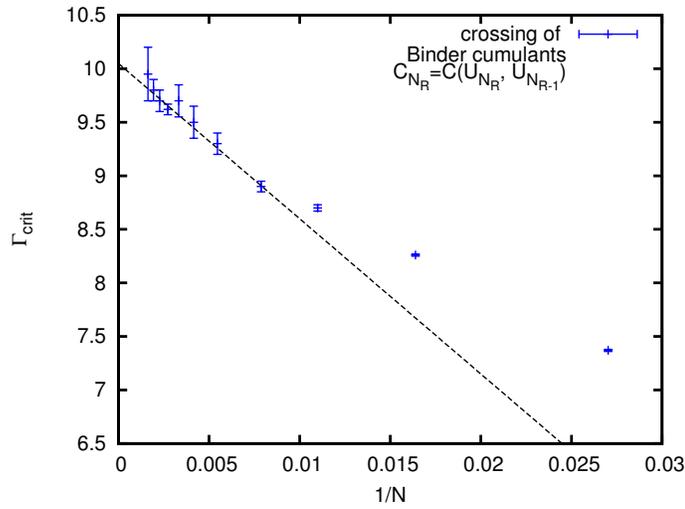
Fig. 6.10: Extrapolation of the crossing points of the Binder cumulant for $\alpha = 3.0$. N_R is the number of lattice sites for a system with radius R; $C_{N_R} = C(U_{N_R}, U_{N_{R-1}})$ denotes the value of the Binder cumulant U_{N_R} for system size N_R at the crossing point with the Binder cumulant for the sucessively smaller system size N_{R-1}. The range of system sizes is $R = 3, 4, \ldots, 13$.
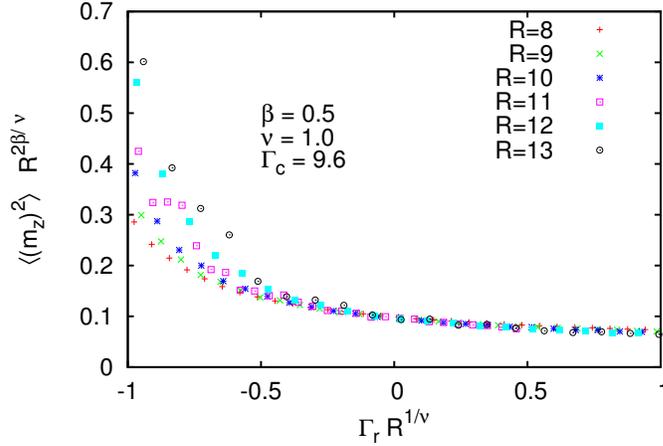
Fig. 6.11: Data collapse for $\alpha = 3.0$ with mean-field critical exponents $\beta = 1/2$, $\nu = \frac{1}{\sigma} = 1$. The linear extent of the system is measured in terms of the radius R of the simulation cell. $\Gamma_r = (\Gamma - \Gamma_c)/\Gamma_c$ denotes the reduced field. The best data collapse is achieved for $\Gamma_c \approx (9.6 \pm 0.1)J$.

is the upper critical range in two dimensions. We verify this prediction of mean-field critical exponents for $\alpha = 3$ using finite-size scaling. According to the finite-size scaling hypothesis [145], close to the critical point the order parameter squared scales with the linear system size R and the reduced control parameter $\Gamma_r = \frac{\Gamma - \Gamma_c}{\Gamma_c}$ as

$$\langle m^2 \rangle (\Gamma_r, T, R) = R^{-2\beta/\nu} \Psi(\Gamma_r R^{1/\nu}, T L^z), \tag{6.25}$$

where β is the exponent for the order parameter, $\langle m^2 \rangle \propto |\Gamma_r|^{2\beta}$, $\nu = \frac{1}{\sigma}$ is the critical exponent for the correlation length, $\xi \propto |\Gamma_r|^{-\nu}$, and $z = \frac{\sigma}{2}$ is the dynamic critical exponent for long-range interactions that decay with exponent $\alpha = \sigma + d$. If the temperature is rescaled with system size according to $T = 1/(2R)^z$, the second argument of the scaling function Ψ becomes a constant for all data sets, and then the scaling function depends only on a single parameter. Then, when plotting $y_R = \langle m^2 \rangle (\Gamma_r, R) R^{2\beta/\nu}$ against $x_R = \Gamma_r R^{1/\nu}$, data sets for different linear system size should collapse onto the scaling function $\Psi(x)$ if the critical exponents β and ν are chosen appropriately.

It is a well-established fact that the 2D transverse field Ising model on any integer-dimensional regular lattice has a dynamical critical exponent of $z = 1$ [62]. It is argued in Ref. [169] that the dynamical exponent for the long-range transverse field Ising model depends continuously on the decay exponent α, reaching $z = 1$ only for $\alpha = 4$ (or for $\sigma = 2$ in the notation, where $\alpha = d + \sigma$ and the spatial dimensionality is $d = 2$). For $\alpha < 4$, Ref. [169] predicts $z < 1$, which reflects the expectation that the correlation length in imaginary time grows slower than that in the spatial direction as

a consequence of the long-range interactions.[4]

On the other hand, in [170] it was found by extensive QMC simulations that the infinitely coordinated Ising model in a transverse field has $z = 1$. Here, we did not attempt to determine z numerically, but naively assumed $z = 1$ for rescaling the temperature with system size. This should not affect the validity of the finite size scaling as long as the temperature is always below the respective finite-size gap such that the system is effectively at $T = 0$. Then, the second variable TL^z in the scaling function drops out.

Fig. 6.11 shows that for $\alpha = 3$ a satisfactory data collapse can be achieved with mean-field critical exponents $\beta = \frac{1}{2}$ and $\nu = \frac{1}{\sigma}$ [169]. The best data collapse is obtained for $\Gamma_c = (9.6 \pm 0.1)J$. A critical field of $\Gamma_c = (10.0 \pm 0.4)J$ is thus consistent with the two estimates based on the extrapolation of the crossing points of the Binder cumulant and the data collapse. This value is, as expected, smaller but very close to the value $\Gamma_c^{\mathrm{MF}}(\alpha = 3.0) = 10.95$ of mean field theory, which is not obvious since the critical field is not a universal quantity. Since for increasingly long-range interactions mean field theory should become a better approximation, with the true phase boundary never exceeding that given by mean field theory, this fact implies that for $\alpha < 3$ the mean-field phase boundary gradually becomes the *true* phase boundary.

The quantum critical behaviour of the dipolar ($\alpha = 3$) Ising ferromagnet differs in a subtle way from the behaviour at the finite-temperature phase transition in zero field: While in $d = 2$ the exponent $\alpha = 3$ places the classical system in its thermal phase transition on the boundary between long-range (i.e. α-dependent) and mean-field critical exponents, leading to logarithmic corrections for the divergence of the correlation length and susceptibility at the critical point [146], the increased dimensionality $d_{\mathrm{eff}} = d + z$ of the quantum critical point results in mean-field critical behaviour *without any corrections*. Therefore one can expect that for the dipolar Ising FM an experiment in the thermodynamic limit could show that the finite-temperature phase transition has logarithmic corrections to its critical behaviour whereas the zero-temperature phase transition does not. However, it is extremely difficult to observe the presence or absence of logarithmic corrections in numerical studies on finite-size systems. A similar dimensional cross-over of the values of critical exponents has been experimentally observed in the 3d nearest neighbour Ising model which exhibits mean-field critical exponents at its quantum critical point in a transverse field [171]. Of course, this is a much more pronounced effect than the absence or presence of logarithmic corrections in the dipolar ferromagnet.

Fig. 6.12 shows magnetization curves for $\alpha = 2.5, 2.0$ and 1.5. In view of possible experiments on finite-size systems it needs to be pointed out that the approach of the critical field to the value of mean field theory in the thermodynamic limit is very slow for $\alpha < 3$. For $\alpha \leq 2$ the interaction energy $\tilde{J}(0)$ is superextensive in the system size

---

[4] In Sect. 7.3.1 we provide a derivation of $\nu = \frac{1}{\sigma}$ and $z = \frac{\sigma}{2}$ [169] for long-range quantum Ising models and discuss the anisotropic scaling of the real-space correlation length ξ and the correlation length in imaginary time, $\xi_\tau \sim \xi^z$, when $z < 1$.
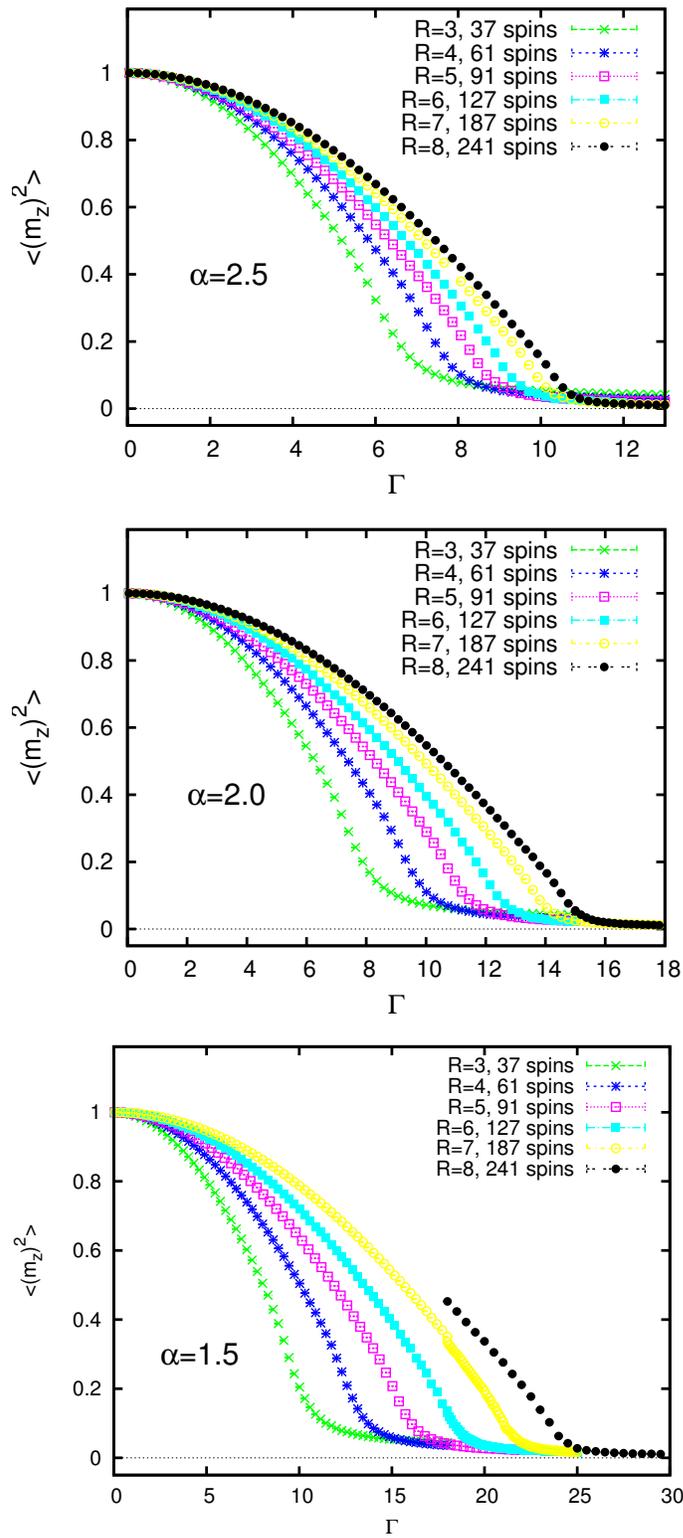
Fig. 6.12: Squared magnetization per site for $\alpha = 2.5, 2.0$, and 1.5. The error bars are smaller than the symbol size.

and the mean-field critical field diverges in the thermodynamic limit. This is typically remedied by introducing a regularizing factor $1/N$ into the model, which corresponds to rescaling the energy and time scales and gives a well-defined thermodynamic limit. Since the experimental system under consideration is always finite with a few hundreds to thousand spins, the question of stability in the thermodynamic limit is not important.

6.5.2   Long-range antiferromagnet on the triangular lattice

Clock order parameter: The complex XY order parameter following from the Landau-Ginzburg-Wilson analysis of Sect. 6.2.1 can be constructed and measured in the Monte Carlo simulations as (see [30] and references therein):

$$me^{i\theta} \equiv (m_A + m_B e^{i(4\pi/3)} + m_C e^{i(-4\pi/3)})/\mathcal{C}, \tag{6.26}$$

where $m_j, j = A, B, C$ are the magnetizations of the three sublattices.[5] The normalization is $\mathcal{C} = \sqrt{3}$ for $(1, -1, 0)$ order and $\mathcal{C} = 3/2$ for $(1, -\frac{1}{2}, -\frac{1}{2})$ order.

Binder cumulant: The correct Binder cumulant for an n-component order parameter (n=2 in our case) is [43]

$$U = \frac{n+2}{2} \left(1 - \frac{n}{n+2} \frac{\langle m^4 \rangle}{\langle m^2 \rangle^2} \right). \tag{6.27}$$

Whether the Binder cumulant has to be extrapolated against $1/N$ or $1/N^x$ where x is another power greater than 1 depends on the subleading finite-size corrections of the Binder cumulant [150]. The values for Γ_c in the thermodynamic limit vary strongly with the chosen extrapolation scheme, but here we attempt to determine Γ_c for large, but finite system sizes.

Structure factor: The structure factor defined as

$$S(\mathbf{q}) = \langle S_{\mathbf{q}}^z S_{-\mathbf{q}}^z \rangle = \frac{1}{N} \sum_{ij} \langle S_i^z S_j^z \rangle \, e^{i\mathbf{q} \cdot (\mathbf{r}_i - \mathbf{r}_j)}$$

diverges $\sim N$ if there is order with wave vector $\mathbf{q} = \mathbf{Q}$. Fig. 6.13 shows the structure factor for $R = 8$, $N = 241$ spins at transverse fields Γ below [(a),$\Gamma = 0.8$] and above [(b-c), $\Gamma = 1.2$ and 1.4] the phase transition to a clock ordered phase. The Bragg peaks at ordering vectors $\mathbf{Q}_\pm = (\pm 4\pi/3, 0)$ and vectors related by reciprocal lattice vectors, i.e. at the corners of the hexagonal Brillouin zone, clearly indicate clock order without any trace of competing orderings.

In Fig. 6.14 the structure factor at $\mathbf{Q}_+$ is presented for $\alpha = 3.0$ and for different system sizes. The dome-like structure indicates a clock-ordered phase roughly between $\Gamma \approx 0.2$ and $\Gamma \approx 1.0$. As opposed to the nearest-neighbour AFM, where clock order

---

[5] This definition differs from Eq. (6.14) only by a local gauge transformation re-defining the reference point from which angles are measured on each sublattice.

appears for infinitesimally small $\Gamma = O^+$, in the long-range case there is a threshold in Γ for the onset of clock order. It was not possible to perform a scaling analysis of the height of the structure factor due to metastable states that appear for larger systems: Already for systems with radius $R = 7, 8, 9$ the structure factor fails to increase further. Both the ferrimagnetic $(1, -\frac{1}{2}, -\frac{1}{2})$ and the partially antiferromagnetic $(1, -1, 0)$ states have the same ordering vectors being distinguished only by the value of Φ in Eq. (6.13).

In the thermodynamic limit long-range order of ferrimagnetic of partially disordered antiferromagnetic type is signaled by a divergence of the same Bragg peaks at $\mathbf{Q}_+$ and $\mathbf{Q}_-$ Thus the two types of states cannot be distinguished at the level of the structure factor, and one needs to look at the sublattice magnetization. Since there is no spontaneous symmetry breaking in a finite system, we consider the squares of the sublattice magnetizations. They are shown in Fig. 6.15 for $\alpha = 3.0$. The values $\langle (m_A)^2 \rangle$, $\langle (m_B)^2 \rangle$, $\langle (m_C)^2 \rangle$ for R=4, N=61 spins in Fig. 6.15(middle panel) appear to be consistent with the ferrimagnetic state $(M, -\frac{M}{2}, -\frac{M}{2})$ where M is below the saturation value of 1. The sublattice magnetizations compensate each other so that there is no net magnetic moment. This justifies the assumption $m_A + m_B + m_C = 0$ in the mean-field analysis of section 6.3. For N=37 spins (Fig. 6.15, upper panel) or N=61 spins (Fig. 6.15, lower panel), one sublattice must have one spin more than the other two, which explains the small deviation of $\langle (m_z)^2 \rangle$ from zero. In a larger system with N=187 spins (Fig. 6.15, lower panel) where metastabilities are more pronounced (see Fig. 6.19 in the Appendix) such that an interpretation is difficult, the ordered phase has sublattice magnetizations $(m_B + m_C, -m_B, -m_C)$ which would reduce to the ferrimagnetic state if $m_B \approx m_C = \frac{M}{2}$. For a small system of $N = 37$ spins (Fig. 6.15, upper panel) the structure of the sublattice magnetizations is quite different with two sublattices having a larger modulus of the magnetization than the third sublattice, $|m_A|, |m_B| > |m_C|$. Apparently, resonance processes due to the transverse field which stabilize the clock ordered phase [32] and its characteristic sublattice magnetization cannot fully develop on this small system as they are strongly influenced by the open boundary conditions.

Due to the open boundary conditions and the failure of our QMC algorithm in the ordered phase the sublattice magnetizations in Fig. 6.15 do not allow any conclusive statement about the type of clock order.

It has been argued in Ref. [162] for the closely related stacked triangular short-range AFM that Landau-Ginzburg-Wilson theory is unreliable for the low-temperature behaviour and that the low-temperature phase should not be in the ferrimagnetic state $(1, -\frac{1}{2}, -\frac{1}{2})$. Based on entropy considerations, in [162] a three sublattice structure was conjectured in which the spin chains in the stacking direction are fully ordered and where most configurations are such that the chains on two sublattices align antiparallel while the third one is randomly oriented. This phase has been referred to as the 3D analog of the 2D Wannier phase [104, 163] and its character was subsequently supported by Monte Carlo simulations [163, 164]. More recent Monte Carlo simulations [165] also favour this scenario with sublattice magnetizations $(m_A, m_B, m_C) = (M, -M, 0)$ whose
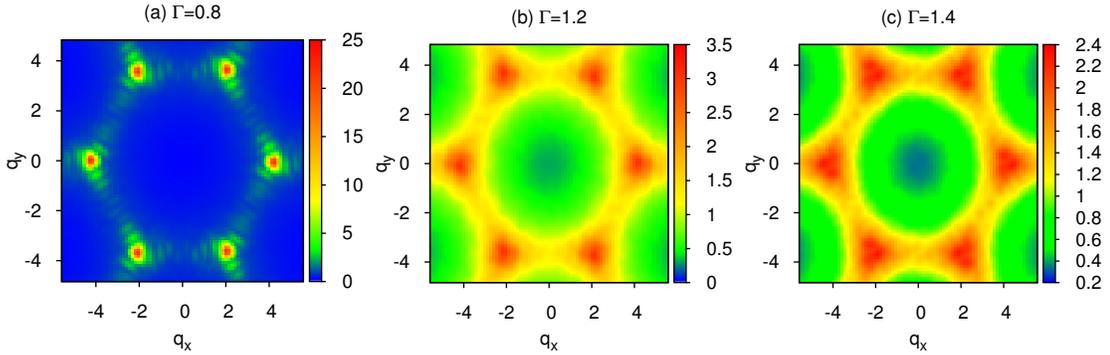
Fig. 6.13: Structure factor for $R = 8, N = 241$ spins and $\alpha = 3.0$ for different values of the transverse field Γ below ($\Gamma/J = 0.8$) and above ($\Gamma/J = 1.2, 1.4$) the phase transition, i.e. in the clock ordered and the fully x-polarized phase, respectively.
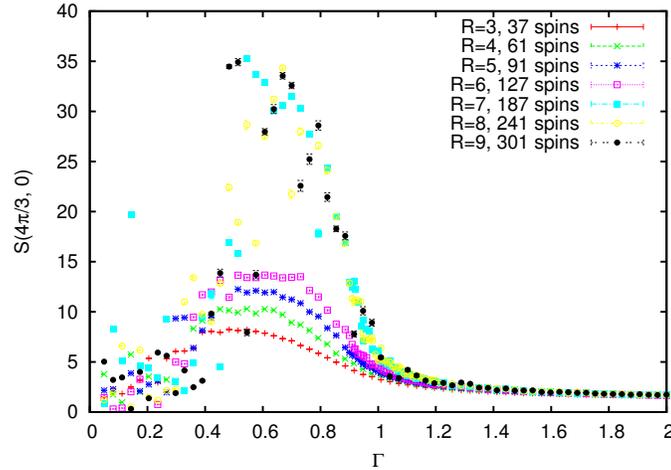
Fig. 6.14: Structure factor $S(\mathbf{Q})$ at $\mathbf{Q}_+ = (4\pi/3, 0)$ for $\alpha = 3$.

magnitude M is unsaturated, $M < 1$, and decays as a power law with system size such that in the thermodynamic limit all sublattice magnetizations vanish and the low-temperature phase of the stacked triangular AFM shows no long-range order. In view of this controversy in a closely related system and because a reliable scaling analysis of the structure factor *within* the order phase was not possible in our simulations due to metastable states, a conclusive statement about true long-range order in the thermodynamic limit cannot be made.

A very recent $2D$ inifinite-DMRG study including long-range interactions [172] considered an infinite triangular strip with a width of six sites and periodic boundary conditions and detected three-sublattice (clock) order of the type $(1, -1, 0)$ (in our notation), which agrees with the clock order found for the short-range model [30].

Location of the quantum critical point: Fig. 6.16 shows the rescaled structure factor $S(\mathbf{Q})/N$, where N is the number of spins, at the ordering vector $\mathbf{Q}_+ = (4\pi/3, 0)$
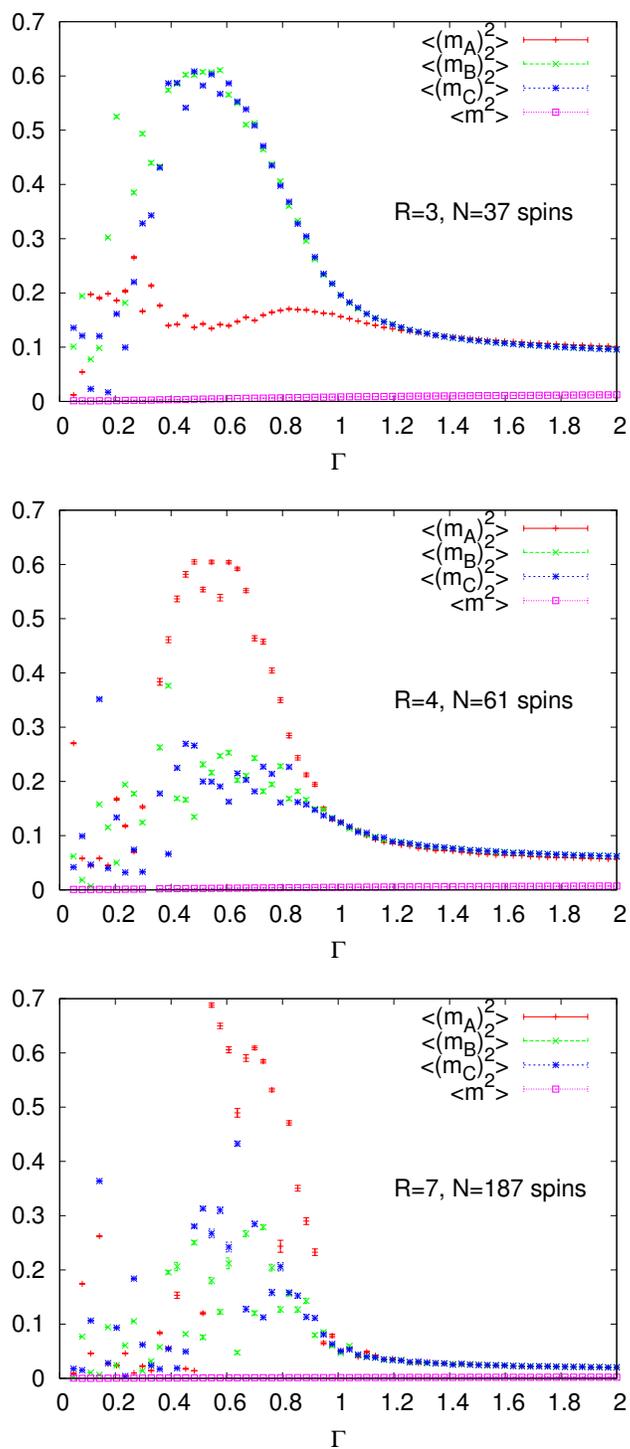
Fig. 6.15: Squared sublattice magnetizations for decay exponent $\alpha = 3.0$ for R=3, N=37 spins (upper panel); R=4, N=61 spins (middle panel); and R=7, N=183 spins (lower panel).
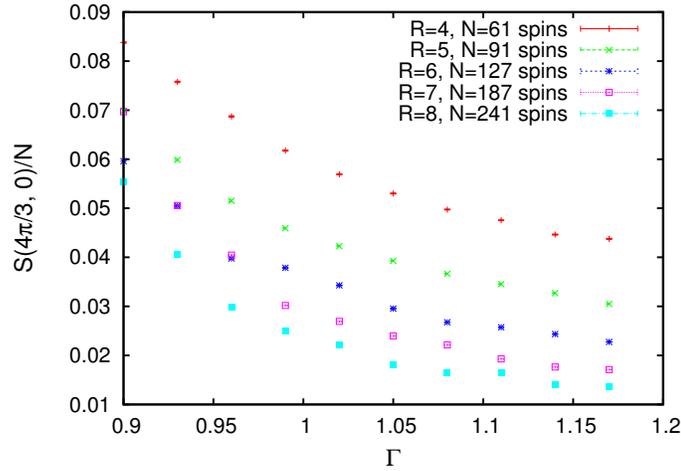
Fig. 6.16: Rescaled structure factor $S(\mathbf{Q})/N$ at $\mathbf{Q}_+ = (4\pi/3, 0)$ around the critical field $\Gamma_c = 1.05$ for $\alpha = 3$.

around the critical field. In order to determine the quantum critical point in the thermodynamic limit we extrapolate the rescaled structure factor $S(\mathbf{Q}_+)/N$ versus inverse system size $1/N$. The extrapolation is done with a third-order polynomial fit in $1/N$ as shown in the inset of Fig. 6.17. The value in the thermodynamic limit $1/N \to 0$ has an error attached to it which is determined by repeating the fitting procedure 10^5 times, each time adding Gaussian noise to the data points with a spread of the size of the error bars. Then the distribution of extrapolated values gives a mean value and quantifies its error. In this way we obtain the thermodynamic limit of $S(\mathbf{Q}_+)/N$ in the main panel of Fig. 6.17. From the field-dependence of the structure factor $S(\mathbf{Q}_+)/N$ at $\mathbf{Q}_+ = (4\pi/3, 0)$, extrapolated to the thermodynamic limit, we can make an estimate of the critical field $\Gamma_c = 1.00 \pm 0.05$ at which the structure factor vanishes. Clearly, there is some arbitrariness in the choice of extrapolation scheme regarding the degree of the extrapolation polynomial and the included system sizes. From the crossing points of the Binder cumulant (see Fig.6.18) a critical field of $\Gamma = 1.05 \pm 0.05$ can be deduced.

6.5.3 Histograms for energy and XY order parameter

Metastable states: As already pointed out in Sect. 6.4.3, the error bars in the clock ordered phase are not reliable. The reason is that the histograms of the modulus squared $|m|^2$ of the complex XY order parameter are not Gaussian, but exhibit long tails, or even show no well-defined shape at all due to metastabilities. This is illustrated by the histograms in Fig. 6.19 where the distribution of $|m|^2$ and the distribution of the energy per spin are contrasted. For the chosen parameters ($\alpha = 3.0, \Gamma = 0.7$) the system is deep in the clock ordered phase. The histograms in Figs. 6.19(a),(c), and (e) are examples of distributions with asymmetric tails. Fig. 6.19(i) shows a distribution
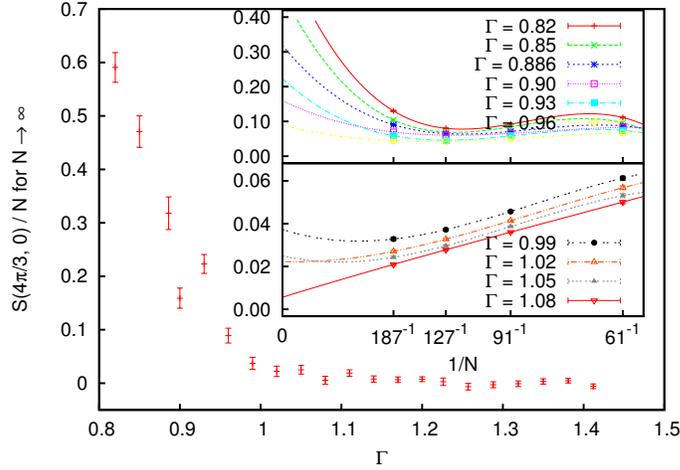
Fig. 6.17: Extrapolation analysis for decay exponent $\alpha = 3$. The main panel shows the structure factor $S(\mathbf{Q})/N$ at $\mathbf{Q}_+ = (4\pi/3, 0)$, extrapolated to the thermodynamic limit. The extrapolation vs. $1/N$ with a third-order polynomial is shown in the inset for different transverse fields Γ.
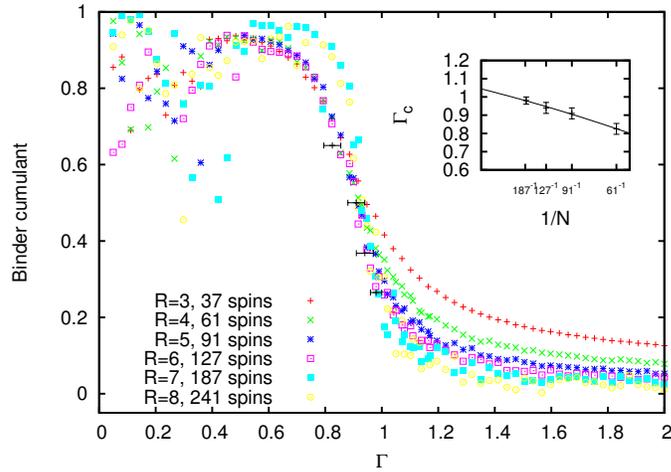
Fig. 6.18: Binder cumulants U_{N_R} for different system sizes; $\alpha = 3.0$. Inset: Extrapolation of their crossing points $C_{N_R} = C(U_{N_R}, U_{N_{R-1}})$, which are indicated with horizontal error bars in the main graph, versus inverse system size.

in the presence of strong metastabilities, which can no longer be described by a mean value and a standard deviation.

As a rule, in the ordered phase, for $\xi \ll L$, the order parameter distribution $P_L(m)$ [see Sect. 5] should be Gaussian, a result which can be understood based on the Central Limit Theorem: The value of the order parameter is a sum over contributions from uncorrelated blocks of spins. The asymmetric tails in the distribution of $|m|^2$ im Fig. 6.19 are due to a large density of metastable states, where the Monte Carlo algorithm gets stuck, resulting in large autocorrelations times and ultimately wrong averages. This is a consequence of the bond-based cluster update we have used (described in Sect. 3.3), which cannot explore efficiently the low-energy manifold of minimally frustrated triangular plaquettes and also leads to an unfovourable distribution of cluster sizes (few very large cluster and many tiny ones [105]). A promising improvement of the algorithm is the plaquette-based update (see Sect. 3.3.2) proposed in Ref. [105].

On the other hand, the histograms of the energy per spin in Fig. 6.19 are always Gaussian and their width shrinks with increasing system size, an effect called "self-averaging" [173] which is to be expected according to the Central Limit Theorem. This provides evidence for closely spaced metastable states. Their density of states increases with system size rendering the simulation of the ground state for large systems very difficult.

Universality class of the quantum critical point: The short-range model has a quantum critical point which is believed to be in the 3D *XY* universality class [30, 153, 160]. The *XY* order parameter is the result of the interplay between frustration on the triangular lattice and quantum fluctuations. So the effective model at the quantum critical point is that of a *ferromagnetic XY* model that undergoes a clock-order symmetry breaking transition where the anisotropy does not affect the critical behaviour [153]. For the long-range ferromagnetic quantum *XY* model one expects mean-field critical exponents for $\alpha < \alpha_u = 10/3$ [169]. Whereas the correlation length exponent for the usual Ising mean-field universality class is $\nu = \frac{1}{2}$ [174, Chapt. 4], here we need to take the mean-field exponent of the long-range model, which for $\alpha = \sigma + d = 3$ is $\nu = \frac{1}{\sigma} = 1$ (see Ref. [169] and also Sect. 7.3.1). A comparison of the data collapse with one or the other set of exponents for the long-range AFM with $\alpha = 3$ is shown in Fig. 6.20. With mean-field exponents, $\nu = 1$ and $\beta = \frac{1}{2}$, the best achievable data collapse, shown in the upper panel ofFig. 6.20, is obtained for $\Gamma_c = 1.15 \pm 0.05$. The best data collapse with 3D *XY* exponents, $\nu = 0.669$ and $\beta = 0.346$, is shown in the lower panel. Slightly different transverse fields lead to a similar unsatisfactory data collapse in that case.

Semiquantitative phase diagram: The intuition from mean field theory and the results of this section can be combined into a semiquantitative phase diagram (Fig. 6.21). There we denote by dots the known results for the nearest neighbour model ($\alpha \to \infty$), the results of the present simulation ($\alpha = 3$), and the infinite-range model ($\alpha = 0$). The clock symmetry broken phase that extends for the short-range model between $\Gamma = 0^+$ and $\Gamma_c(\alpha = \infty) = 1.65 \pm 0.5$ [30] persists for long-range interactions,

(a) R=3, $|m|^2$ **(b)** R=3, energy

(c) R=4, $|m|^2$ **(d)** R=4, energy

(e) R=5, $|m|^2$ **(f)** R=5, energy

(g) R=6, $|m|^2$ **(h)** R=6, energy

(i) R=7, $|m|^2$ **(j)** R=7, energy
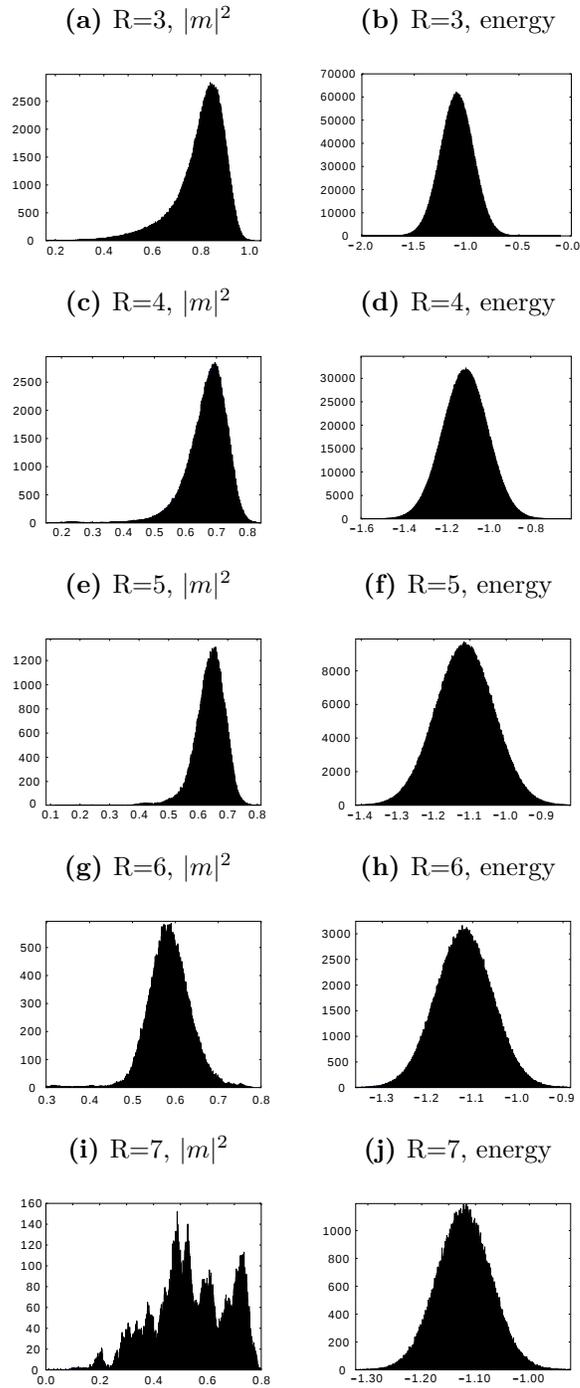
Fig. 6.19: Histograms for the average energy $e = E/N$ per spin and the modulus squared $|m|^2$ of the complex XY order parameter for $(\alpha = 3, \Gamma = 0.7)$ and different radii R of the simulation cell. The different

with a critical field that decreases with decreasing α as the additional frustration due to long-range AFM interactions destabilizes order. For $\alpha = 3$ the critical point is located at $\Gamma_c(\alpha = 3) = 1.05 \pm 0.05$, most likely with mean-field critical exponents. For $\alpha = 2$ we find that the critical point is around $\Gamma_c(\alpha = 2) \approx 0.8$. Whether the ordered phase for $\alpha < 2$ is still clock-ordered is not clear. At any rate, for $\alpha \leq \alpha_c$ with $\alpha_c \approx 1$ the Fourier transformation of the interactions becomes flat so that there is no longer a preferred state dictated by the lattice structure that quantum fluctuations can select. The infinitely coordinated classical Ising AFM at $(\alpha = 0, \Gamma = 0)$ has an exponential ground state degeneracy: All states with $S_{\text{tot}}^z = \sum_i S_i^z = 0$ are ground states. Upon introducing a transverse field, the model at $\alpha = 0$ turns into an anisotropic variant of the Lipkin-Meshkov-Glick model [168] (see Eq. (6.20)). From exact diagonalization for 19 spins (see Fig. 6.22) and from the behaviour of the structure factor at small fields in Fig. 6.13 one can conclude that for long-range interactions there is a threshold for quantum fluctuations to establish order. The continuous line in Fig. 6.21 corresponds to this expectation of a classically dominated region, where the possible phases of the classical model ($\Gamma = 0$) extend to finite values of the transverse field Γ. However, with all caveats pointed out so far, it should be stressed that this phase diagram remains a semiquantitative one.

6.6 Conclusion

The ground state phase diagrams of ferromagnetic and antiferromangetic long-range transverse field Ising models on the triangular lattice have been examined. The critical transverse field strength Γ_c at which the transition from the fully x-polarized phase to the clock-ordered phase occurs was determined by two independent procedures: by data collapse and by extrapolation of the crossing points of the Binder cumulants. The results of both methods agree within the error bars. For the ferromagnet with
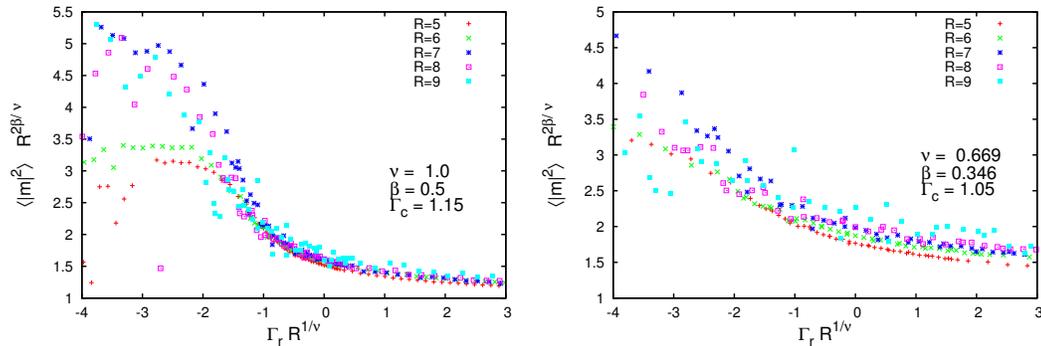
Fig. 6.20: Data collapse for $\alpha = 3$ with mean-field exponents ($\beta = \frac{1}{2}$ and $\nu = \frac{1}{\sigma} = 1$) and $\Gamma_c = 1.15$ (left panel) and data collapse with 3D XY exponents and $\Gamma_c = 1.05$ (right panel). $\Gamma_r \equiv (\Gamma - \Gamma_c)/\Gamma_c$ is the reduced field.
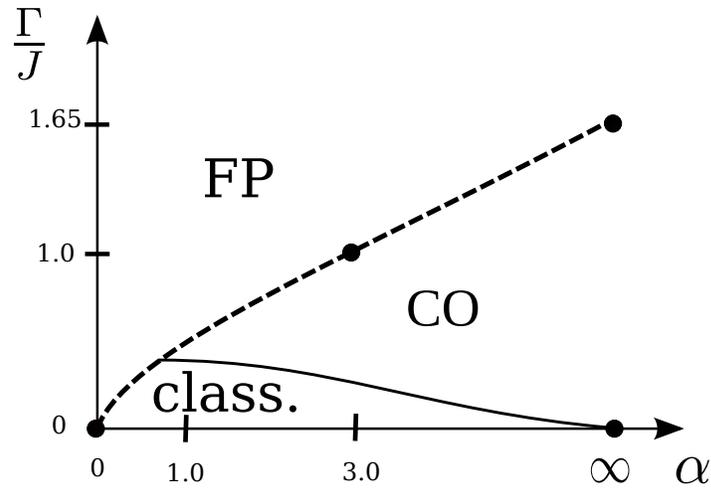
Fig. 6.21: Semiquantitative phase diagram for the long-range transverse field Ising AFM on the triangular lattice. **FP:** fully x-polarized phase, **CO:** clock-ordered phase, **class.:** region dominated by classical ground states.
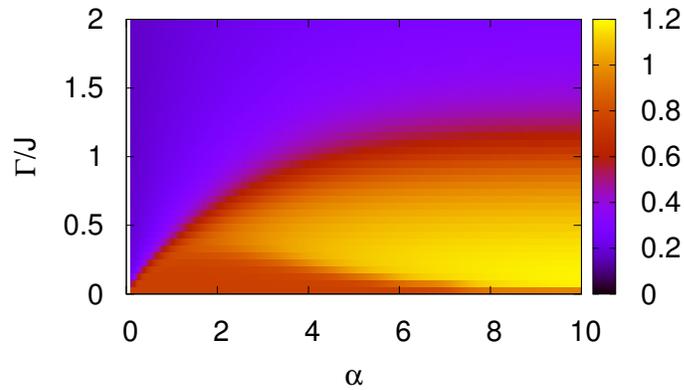
Fig. 6.22: Modulus m of the complex XY order parameter $me^{i\theta} \equiv (m_A + m_B e^{i4\pi/3} + m_C e^{-i4\pi/3})/\mathcal{C}$ with $\mathcal{C} = 3/2$ computed with Lanczos exact diagonalization for a hexagon of 19 spins.

dipolar decay exponent, $\alpha = 3$, the critical field is located at $\Gamma_c = (9.6 \pm 0.1)J$ (from data collapse) or $\Gamma_c = (10.0 \pm 0.4)J$ (from extrapolation), which is only slightly below the value from mean field theory. This is remarkable as the critical field is not a universal quantity. For the antiferromagnet, there is strong indication for a quantum phase transition from the fully x-polarized phase to a clock ordered phase at $\Gamma_c = (1.15 \pm 0.05)J$ (from data collapse) or $\Gamma_c = (1.05 \pm 0.05)J$ (from extrapolation).

It remains an open problem to investigate the transition to the clock-ordered phase from the side of small Γ. The simulation results indicate that the classical ground states at zero field extend to finite field, before they finally yield to the strength of quantum fluctuations, which results in the clock-ordered phase. The QMC algorithm suffers from loss of ergodicity in this region of small transverse field, which hampered a quantitative study. It might be possible to overcome this problem by parallel tempering [175] in Γ which lets simulations at small Γ, which tend to get stuck in some region of phase space, profit from the increased ability to explore phase space that simulations at larger Γ possess. In the mean time, a recent 2D DMRG study [172] of the long-range triangular quantum Ising AFM has found in the region of small Γ and α a columnar AFM ordered phase.

Another open issue is the finite-temperature phase diagram of the long-range AFM, in particular whether there is a Kosterlitz-Thouless phase transition as in the short-range AFM [30].

With regards to future Penning ion trap experiments it should be pointed out that the large density of metastable states in the clock ordered phase may pose even larger experimental challenges for thermalizing to the ground state than in the numerical simulations due to the limited time over which the coherence of the synthetic quantum system can be maintained. So far the Penning trap experiments by Britton *et al.* [41] and Bohnet *et al.* [176] investigated the non-equilibrium spin precession dynamics for power-law interactions with $0 \lesssim \alpha \lesssim 1.4$, which could be well described my mean-field theory. Based on our findings and Ref. [172], in this range of α one does not expect clock order in the ground state.

Chapter 7

Critical properties of long-range ferromagnetic quantum Ising chains

In this chapter, we discuss the finite temperature and quantum critical properties of ferromagnetic long-range transverse-field Ising (LRTFI) models with interactions that decay as a power law with exponent α. The Hamiltonian is

$$H = -\sum_{i<j=1}^{L} J_{ij} S_i^z S_j^z - \Gamma \sum_{i=1}^{L} S_i^x \quad \text{with} \quad J_{ij} = \frac{J}{|i-j|^\alpha}, \tag{7.1}$$

where (S_i^x, S_i^y, S_i^z) are spin-$\frac{1}{2}$ operators satisfying $[S_i^x, S_i^y] = iS_i^z$. The long-range interactions J_{ij} are ferromagnetic and Γ is the strength of the transverse field. Since the transverse field term does not commute with the Ising interactions, quantum fluctuations drive a quantum phase transition at zero temperature from a ferromagnetic long-range ordered state at small Γ to a paramagnetic state at large Γ.

For $\alpha \leq 2$, the LRTFI model also has a finite temperature phase transition from a paramagnet to a ferromagnet, while for $\alpha > 2$ there is no long-range order at any finite temperature. The boundary case $\alpha = 2$ exhibits a finite-temperature Kosterlitz-Thouless transition [177–179] due to the presence of topological defects with a mutual interaction that depends logarithmically on their distance. This one-dimensional (1D) Ising chain with interactions decaying as $1/r^2$ deserves special attention from a historic point of view [180], being the first physical system for which a Kosterlitz-Thouless (KT) transition was described quantitatively and to which an early version of the renormalization group (RG) was applied [177, 181]. Thus the model is a milestone in the development of two very important concepts of condensed matter physics. The exponential divergence of the correlation length, which is a characteristic feature of the Kosterlitz-Thouless transition, is very challenging for numerical simulations on finite systems. The 1D setting has allowed to study system sizes that span six orders of magnitude [179], which has facilitated precise verification of RG predictions and scaling laws. The quantum $1/r^2$ ferromagnet, i.e. Eq. (7.1) with $\Gamma \neq 0$, was partially studied in Ref. [95] and for the case of $\Gamma = 1$ in Ref. [97].

The LRTFI model can be simulated at zero temperature in trapped ion chains with an exponent α that is tunable [40, 42]. However, the experimentally realizable system sizes are small. Structural phase transitions to a zig-zag arrangement [182], limitations on the lifetime of the ion crystal, which scales inversely with the number of ions [183], and the required fine control over increasingly closely spaced transverse phonon modes that mediate the effective spin-spin interactions [40] have limited the number of ions that can be confined in a linear radio-frequency Paul trap to $N \lesssim 100$ [183]. Most simulations of magnetic models in linear ion traps have involved only $N \lesssim 10$ qubits [11, 42]. Knap *et al.* [184] proposed to use Ramsey interferometry combined with the spatial addressability in cold atoms and ion trap experiments to measure real-space and time-resolved correlation functions and computed critical exponents for spatial correlations on system sizes up to $L = 20$. An issue is to which degree critical properties are visible on such small systems [185].

This chapter is organized as follows: Sect. 7.1 discusses how to implement periodic boundary conditions for long-range systems and some related finite-size effects. In Sect. 7.2, we map out the full phase diagram of the $1/r^2$ ferromagnet in the $T - \Gamma$ plane and provide evidence that, in the presence of a transverse field Γ, the finite-temperature transition remains of the Kosterlitz-Thouless type. Sect. 7.3 is concerned with the verification of mean-field and renormalization group predictions of critical exponents for the quantum phase transitions of the LRTFI model as a function of interaction exponent α.

7.1 Boundary conditions and finite-size effects

For systems with long-range interactions the implementation of boundary conditions requires special care. Fukui and Todo [97] use the following periodic boundary conditions (PBC) for the inverse square ($1/r^2$) ferromagnetic chain

$$J_{ij} = J \sum_{n=-\infty}^{\infty} \frac{1}{(i-j-nL)^2} = J \frac{\pi^2}{L^2 \sin^2 \frac{\pi(i-j)}{L}} \equiv \frac{J}{\zeta^2(|i-j|)}, \tag{7.2}$$

which minimize finite-size effets by replacing the "bare" interactions $J_{ij} = 1/(i-j)^2$ with the sum over all periodic images of the simulation cell. For decay exponent $\alpha = 2$ the summation over periodic images can be performed analytically, which leads to the definition of the *conformal length*

$$\zeta(r) \equiv \frac{L}{\pi} \sin \left(\frac{\pi r}{L} \right). \tag{7.3}$$

As can be verified by elementary trigonometry it is the length of the secant subtending an arclength r on a circle of circumference L (inset in Fig. 7.1(a)). Visualizing a system of length L with periodic boundary conditions as a circle, the mapping $r \to \zeta(r)$ has the effect of folding points with the same shortest distance from the origin $r = 0$ onto
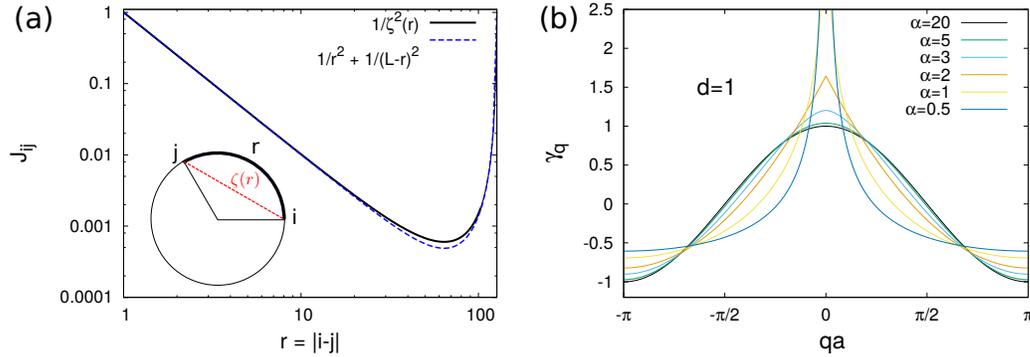
Fig. 7.1: (a) Comparison between the interactions J_{ij} with PBC according to Eq. (7.2) (continuous line) and Eq. (7.5) (dashed line); $\alpha = 2$, $L = 128$. The inset illustrates the meaning of the conformal length (or *cord* length) $\zeta(r)$ (b) Fourier transform γ_q of the long-range interactions $1/|r_i - r_j|^\alpha$ in one dimension. Three regimes can be distinguished: For $\alpha \leq 1$, the function γ_q diverges as $qa \to 0$; for $1 < \alpha \leq 2$ a cusp appears at $qa = 0$; the limit $\alpha \to \infty$ corresponds to short-range interactions.

each other. For other values of α we could not find an analytical expression, which is why we have computed the sum

$$J_{ij}^{(\alpha)} = \sum_{n=-I}^{I} (i - j - nL)^{-\alpha} \tag{7.4}$$

numerically, choosing I large enough for convergence.

In Ref. [95] the $1/r^2$ ferromagnet in a transverse field was studied with another choice of PBC,

$$J_{ij} = J \left(\frac{1}{|i - j|^2} + \frac{1}{(L - |i - j|)^2)} \right), \tag{7.5}$$

and concomitantly crossings in the average squared magnetization $\langle (m_z)^2 \rangle$ were observed as as a function of system length L [95], which contradicts the finite-size scaling that is expected from the model without transverse field [95, 179]. The hypothesis suggested in [97] that the crossings are due to a relaxation problem in the Monte Carlo calculation of Ref. [95], where only a single spin-flip update algorithm was used, can be ruled out since we obtain the same crossings (Fig. 7.2) with a multi-branch cluster update as long as we use the PBC of Eq. (7.5) rather than those of Eq. (7.2). As can be seen from Fig. 7.2(a-d) the crossings become more pronounced as Γ increases. With larger transverse field, the kinks, which are responsible for the Kosterlitz-Thouless transition, are smeared out in space making finite-size effects more relevant. If PBC according to Eq. (7.2) are used, the crossings disappear.

Including all periodic images of the system into the interactions as in Eq. (7.4) effectively lowers the strength of the transverse field relative to the interaction term
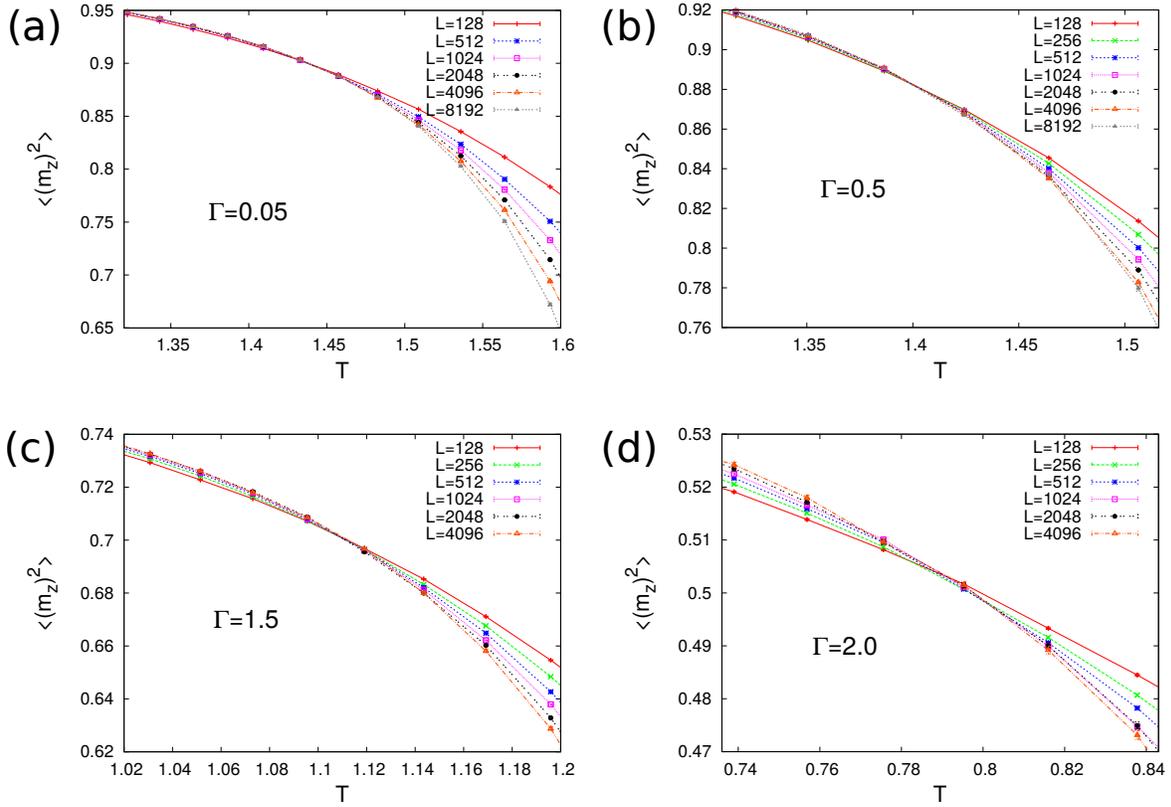
Fig. 7.2: Crossings in $\langle (m_z)^2 \rangle$ as a function of system size L at the Kosterlitz-Thouless transition for $\Gamma = 0.05$ (a), $\Gamma = 0.5$ (b), $\Gamma = 1.5$ (c) and $\Gamma = 2.0$ (d). Periodic boundary conditions (PBC) according to Eq. (7.5) were used. For larger transverse field the crossings become more pronounced due to stronger finite-size effects. With the PBC of Eq. (7.2) finite-size effects can essentially be eliminated and the crossings disappear.

(see Fig. 7.1(a)). For a fast decay of interactions, i.e. for $\alpha > 3$, the interactions $J_{ij}^{(\alpha)}$ with PBC according to Eq. (7.4) are indistinguishable from those in Eq. (7.5).

7.2 Line of Berezinskii-Kosterlitz-Thouless transitions

It is well-known that the one-dimensional classical Ising model with short-range interactions has no long-range order at any finite temperature [186, Chapt.16],[187]. The reason is that there are two competing tendencies, the tendency towards alignment to minimize the interaction energy and the tendency to randomization of the spin configuration to maximize entropy. In one dimension the tendency towards alignment alway loses in the minimization of the free energy $F = E - TS$, because there are not enough neighbours. The balance between energy and entropy can be shifted in favour
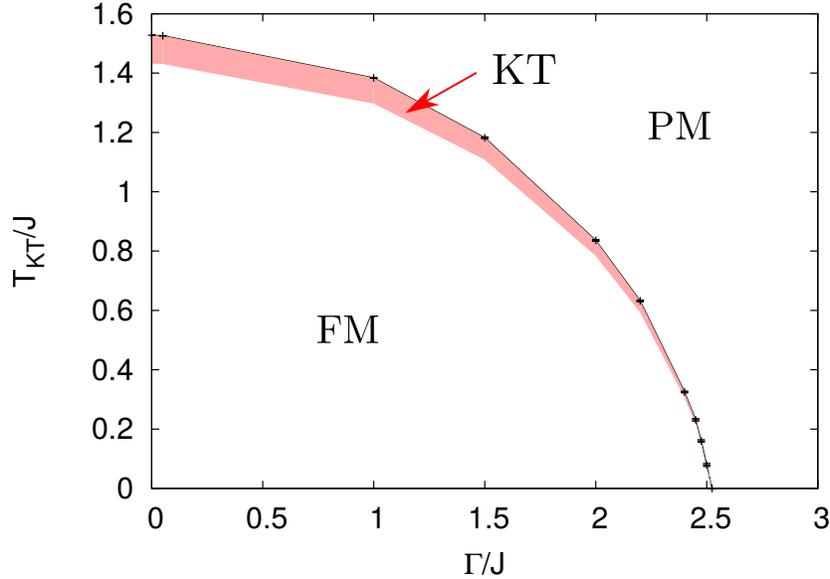
Fig. 7.3: Phase boundary of the inverse-square ferromagnet in a transverse field. The red area of width [169, 178] $\frac{15}{16}T_{KT} < T < T_{KT}$ indicates the Kosterlitz-Thouless phase (KT) with infinite susceptibility and algebraically decaying spin-spin correlation function [178]; Below the red area, there is long-range ferromagnetic order (FM), above the red area the chain is in a paramagnetic state (PM). The quantum critical point at $\Gamma/J = 2.5240(4)$ [97] is that of an order-disorder transition. The points of the phase boundary are obtained from a data collapse according to the Kosterlitz-Thouless scaling relations (see Fig. 7.8).

of alignment by long-range interactions [188].

7.2.1   Universal jump of the magnetization

As proven by Dyson [188], for long-range interactions decaying more slowly than $1/r^\alpha$ with $\alpha \leq 2$, there is true long-range order at finite temperature. The boundary case $\alpha = 2$ is special in that the magnetization cannot go continuously to zero at the critical temperature, as was shown by Thouless [189] based on an argument that balances energy and entropy of domain walls. With long-range interactions, a finite magnetization density $\langle m^2 \rangle = \langle (\frac{1}{N}\sum_i \hat{S}_i^z)^2 \rangle$ provides an energy barrier against the entropy-driven proliferation of domain walls. If the transition temperature is finite, the average magnetization at the transition point has to be finite, too, to keep check of the entropic generation of domain walls which would destroy long-range order immediately if the magnetization dropped below a threshold value [189]. It turns out that at the critical temperature T_{KT} the ratio

$$\frac{\langle m^2 \rangle (T_{KT})}{T_{KT}} = \frac{1}{2} \tag{7.6}$$

is universal (in the analogous KT transition of the 2D XY model the universal jump [190] is in the spin stiffness ρ_s), i.e. it does not depend on microscopic details of the model. In our present case the universality of the magnetization jump is seen from the fact that Eq. (7.6) holds for any value of the transverse field Γ, which indeed does not affect the universality class as argued in Ref. [169].

7.2.2   Renormalization group (RG) equations

The Hamiltonian of the one-dimensional *classical* inverse-square ferromagnet in a longitudinal field reads

$$\beta H = -K \sum_{i<j} \frac{S_i^z \, S_j^z}{|i-j|^2} - h \sum_i S_i^z, \tag{7.7}$$

where the temperature has been absorbed into the coupling constants $K \equiv \beta J \equiv \frac{J}{k_B T}$ and $h \equiv \beta \tilde{h} \equiv \frac{\tilde{h}}{k_B T}$. Ultimately, we are interested in the finite-temperature phase transition of the *quantum* inverse-square ferromagnet, i.e. model Eq. (7.7) with an additional transverse-field term $-\Gamma \sum_i S_i^x$. The phase diagram in the $T-\Gamma$ plane, which is the main result of this chapter, is shown in Fig. 7.3. Since it has been argued that a transverse-field term does not change the universality class of the finite-temperature phase transition [62, 169], we first review the renormalization group equations of the classical model Eq. (7.7) before discussing the role of a transverse-field term.

The thermodynamics of Eq. (7.7) can be rephrased as a problem of kinks (spin flips or domain walls) since all possible spin configurations can be specified by the locations of a sequence of domain walls (see Fig. 7.4(a)). The kinks inveract via a logarithmic potential [181, 191] so that, subtracting the ground state energy, we can write the leading terms in the Hamiltonian as [178, 181, 191]

$$\beta H = -K \sum_{j\neq k} (-1)^{j-k} \ln \left| \frac{r_i - r_j}{a} \right| + N\beta\mu, \tag{7.8}$$

where r_i and r_j are the positions of the sequentially labelled kinks and $\mu = E_{\text{kink}}$ is the chemical potential associated with the local energy needed for the creation of a kink in the absence of a field h.

In Eq. (7.8), the original system Eq. (7.7), in which the kinks are located in between lattice sites, has beeen replaced by a continuous model, where kinks are free to move on a line, but have a repulsive core of size a. The cutoff a is the equivalent of a lattice spacing. The interaction potential between kinks, which can be obtained by computing the interaction energy according to Eq. (7.7) for a kink-antikink profile as in Fig. 7.4(a), has been replaced by its asymptotic form $-\ln(r/a)$ for all $r > a$ [192]. Generally, the energy of a topological defect [174], such as a kink (domain wall) in one dimension, consists of two parts: (i) the core energy E_{kink} of the kink and (ii) the elastic energy E_{el} of the medium around and between kinks. The core energy is
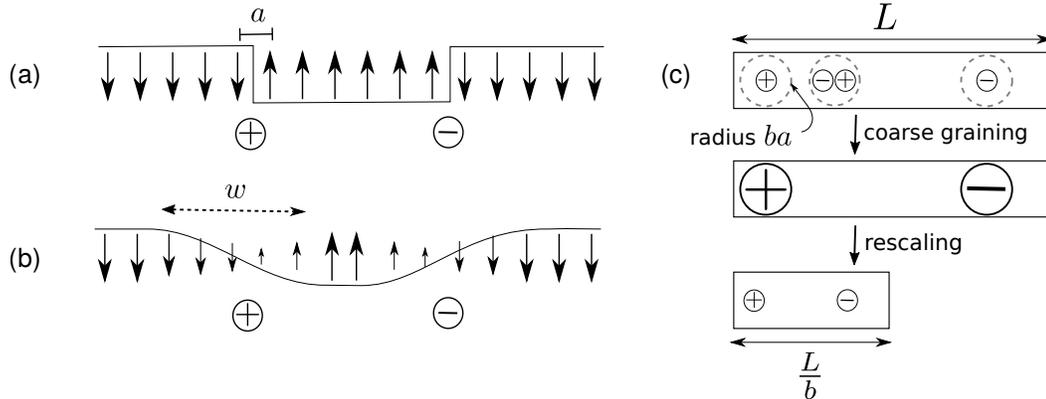
Fig. 7.4: Domain walls in the classical Ising model (a) and in the transverse-field Ising model (b) with $\Gamma \neq 0$, where domain walls are smeared out on a length scale w. For $1/r^2$ long-range ferromagnetic spin-spin interactions, kinks $\oplus$ and antikinks $\ominus$ can be regarded as positive and negative electric charges that interact via an electrostatic potential that depends logarithmically on their distance. (c) Steps in the Kosterlitz-Thouless renormalization.

associated with the destruction of the local order parameter at the domain wall and needs to be computed from a microscopic model, which may not even be known or involve complicated calculations. It determines the *kink fugacity* $y = e^{-E_{\text{kink}}/(k_B T)}$, i.e. the probability to form a single kink in the system. In the following it is assumed that y is a small parameter, which means that kinks occur rarely.

By integrating out short-scale degress of freedom a renormalization group (RG) flow for the parameters K and y can be established [181, 191]. The steps of coarse graining and rescaling that constitute the renormalization group transformation are illustrated in Fig. 7.4(c). A kink-antikink pair ($\oplus$ - $\ominus$) is analogous to an electric dipole and $K^{-1} = \left(\frac{J}{k_B T}\right)^{-1}$ is analogous to the dielectric constant of a polarizable medium [145, Chapt. 6.4],[193]. Then, a tightly-bound kink-antikink pair in between distant kinks (see Fig. 7.4(c)) has the effect of screening their logarithmic interactions. Furthermore, under the coarse graining transformation the kink core size increases and the elastic energy in the interval $a < r < ba \equiv (1 + dl)a$ needs to be included into the renormalized core energy, which modifies the kink fugacity $y = e^{-E_{\text{kink}}/(k_B T)}$. Finally, the rescaling of lengths $L \to \frac{L}{b}$ lets the density of kinks per unit length appear larger. This also contributes to modifying the kink fugacity.

Detailed calculations [181, 191] in which the lattice spacing is rescaled[1] as $a \to ba \equiv (1 + dl)a$ and blocks of length between a and $(1 + dl)a$ are averaged out (see Fig. 7.4(c)) show that the system parameters have to be adjusted as follows to keep

---

[1] In the derivation of the RG equations (7.10a),(7.10b),(7.9c) the lattice spacing is successively rescaled according to $a \to ba$ with $b = 1 + dl$, where dl is the infinitesimal appearing in the RG equations. After n coarse graining steps the cumulative rescaling factor is $b(l) = \prod_{i=1}^{n}(1 + dl) \approx \prod_{i=1}^{n} e^{dl} = e^{ndl} = e^{l}$.

the partition function of the coarse grained system identical to that of the original system [178, 181, 191]:

$$\frac{dK}{dl} = -4y^2, \tag{7.9a}$$

$$\frac{dy}{dl} = y\left(1 - K\right), \tag{7.9b}$$

$$\frac{dh}{dl} = h(1 - 2y^2). \tag{7.9c}$$

Eq. (7.9a) describes the screening of the interactions due to the elimination of kink-antikink pairs at small scales; Eq. (7.9b) captures the inclusion of elastic energy into the renormalized core energy and the change of the density of kinks under rescaling; Eq. (7.9c) is easily understood in the limit $y = 0$: The longitudinal field h must be rescaled proportional to the size of the block of spins which has been averaged out. Kink-antikink pairs, which occur with Boltzmann weight $y^2 = e^{-2E_{\text{kink}}/(k_BT)}$, renormalize the average magnetization and this is accounted for by renormalizing the coupling constant h accordingly. Introducing the variable $x \equiv 1 - K \equiv 1 - \frac{J}{k_BT}$, Eqs. (7.10a) and (7.10b) can be brought to the concise form

$$\frac{dx}{dl} = 4y^2, \tag{7.10a}$$

$$\frac{dy}{dl} = yx. \tag{7.10b}$$

The RG equations (7.10a) and (7.10b) are identical to those derived by Kosterlitz [177] for classical two-dimensional systems with two-component continuous order parameter such as the XY spin model. The common thread is the presence of topological defects that interact with each other with a potential that depends logarithmically on the distance. Historically, the Kosterlitz RG equations were first obtained by Anderson and Yuval [194] in the context of the Kondo problem, the path integral formulation of which maps to a one-dimensional ferromagnet with $1/r^2$ interactions.

The variables $x(l)$ and $y(l)$ in the Kosterlitz equations (7.10) are renormalized system parameters after a number of coarse graining operations up to the length scale $L = L_0e^l$, where l can be thought of as related to the number of coarse graining steps and L_0 is a length scale of the order of the lattice spacing. By integrating the RG equations (7.10a),(7.10b) the critical behaviour of the correlation length, specific heat and susceptibility as a function of temperature can be obtained.

By taking the ratio of both sides of (7.10a) and (7.10b) the scale variable l can be eliminated, and integrating the resulting differential equation $\frac{dy}{dx} = \frac{x}{4y}$, the trajectories $x(l), y(l)$ turn out to be a family of hyperbolae

$$\Delta(T) = x^2(l) - 4y^2(l), \tag{7.11}$$

parametrized by the constant $\Delta(T)$, which is independent of the scale variable l. For $x = 0$, $\Delta(T) < 0$ parametrizes the distance of a trajectory from the x-axis and for $y = 0$ the distance from the y-axis. The RG flow Eq. (7.11) is depicted in Fig. 7.5. As will be
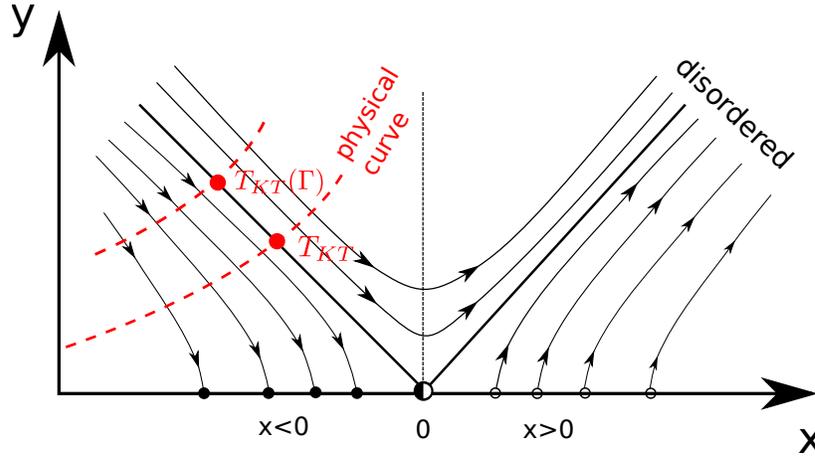
Fig. 7.5: Renormalization group flow for the Kosterlitz equations. The variable $x = 1 - \frac{J}{k_B T}$ is the temperature field and $y = e^{-E_{\text{kink}}/(k_B T)}$ is the *kink fugacity* (or chemical potential field). For the inverse square ferromagnet with finite transverse field Γ the physical curve is shifted towards higher kink fugacity (lower kink core energy E_{kink}) compared to the model without transverse field.

shown below, x increases with l independently of its sign so that the arrows of "time" (or rather evolution under an increasing number of coarse graining steps) in the RG flow are to the right. The characteristic feature of the Kosterlitz-Thouless RG flow is a line of attractive fixed points for $x < 0$ and unstable fixed points for $x \geq 0$. This means that y is renormalized to zero under the RG flow if $x \leq 0$ and if y is below the separatrix $y = -\frac{1}{2}x$. On the other hand, if y is above the separatrix, then y grows beyond bounds. We can interpret the different behaviours of the kink fugacity y under successive coarse graining steps in the following way [177]: The energy of a isolated kink diverges logarithmically with the system size. Therefore, below the critical temperature (i.e. below the separatrix for $x < 0$), isolated kinks are energetically unfavourable and kinks and antikinks come in small pairs so that under coarse graining transformations they are gradually scaled out of the system until on large length scales a homogeneous state without domain walls but with renormalized magnetization is reached. Above the transition temperature (i.e. above the separatrix for $x < 0$) the entropy term in the free energy dominates and the ordered state is destroyed by the unbinding of kink-antikink pairs, which generates entropy.

The "bare" parameters x and y before any renormalization steps, i.e. at length scale l_0, lie on the *physical curve* (dashed red line in Fig. 7.5)

$$\left(x_{[J, E_{\text{kink}}]}(T), y_{[J, E_{\text{kink}}]}(T) \right) = \left(1 - \frac{J}{k_B T}, e^{-E_{\text{kink}}/(k_B T)} \right). \tag{7.12}$$

It is a function of temperature and its location in the RG flow diagram Fig. 7.5 depends parametrically on the system parameters, i.e. on J and E_{kink}. Its crossing point with the separatrix $y = -\frac{1}{2}x$ marks the transition temperature T_{KT}, the red dot in Fig. 7.5. Now, a transverse-field term $-\Gamma \sum_i S_i^x$ can be incorporated into the RG treatment of the Kosterlitz-Thouless transition by considering its effect on the physical curve. A transverse field affects the energy $E_{\text{kink}} = E_{\text{kink}}(\Gamma)$ for the local formation of a domain wall, which in the presence of a transverse field appears smeared out (Fig. 7.4(b)). Thus, a transverse-field term shifts the location of the physical curve Eq. (7.12) through its effect on $E_{\text{kink}}(\Gamma)$ (see upper red dashed line in Fig. 7.5), but it does not change the fix point structure of the RG flow so that the phase transition remains of the Kosterlitz-Thouless type as was argued in Ref. [169]. This is discussed in detail in Sect. 7.2.6 below.

7.2.3   Exponentially diverging correlation length

We can use the RG equations (7.10a) and (7.10b) to compute the correlation length as $T \to T_{KT}^+$. To do this we follow a particular renormalization group trajectory slightly above the transition temperature T_{KT}, where we have from Eq. (7.11) and Eq. (7.10a) that

$$x^2 - 4y^2 = -Ct \ \to \ \frac{dx}{dl} = 4y^2 = x^2 + Ct \tag{7.13}$$

with $C > 0$ and the reduced temperature $t = \frac{T - T_{KT}}{T_{KT}}$. The precise value of C depends on the linearization of the physical curve around $t = 0$. Eq. (7.13) has the solution [195, Chapt. 7.6],[177]

$$l = l_0 + \frac{1}{\sqrt{Ct}} \arctan\left(\frac{x}{\sqrt{Ct}}\right), \tag{7.14}$$

which shows that x increases with l independently of its sign so that the RG flow in Fig. 7.5 is to the right.

   Under the renormalization group mapping, length scales are reduced and the correlation length ξ' measured in rescaled length units is related to the correlation length ξ in original units via $\xi' = \xi/b$. We suppose that we have followed the trajectory given by Eq. (7.13) up to some maximum possible number of coarse graining steps $l \to l_{\text{max}} = l_0 + \frac{1}{\sqrt{Ct}}\frac{\pi}{2}$, where the length scale $b(l) = e^l$ has reached the system size and where the correlation length in rescaled units is some finite quantity ξ_0. In original length units the correlation length is then [177]

$$\xi_{T \to T_{KT}^+} \approx \xi_0 e^{l_{\text{max}}} \approx \exp\left(+\frac{\text{const}}{\sqrt{(T - T_{KT})/T_{KT}}}\right). \tag{7.15}$$

Thus, the correlation length, and also the suscpetibility, diverge *exponentially* as the transition temperature is approached from above. This extremely fast divergence must

be contrasted with the power law behaviour $\xi \sim t^{-\nu}$ with correlation length exponent ν of conventional second-order phase transitions. For simulations on finite systems, this implies very slow convergence of the system size dependent critical temperature $T^*(L)$ with linear system size L to the value in the thermodynamic limit

$$T^*(L) - T_{KT} \sim \frac{1}{\log^2(L)}, \tag{7.16}$$

which can be seen from Eq. (7.15) by replacing ξ with the maximally attainable length L of the finite system. In ordinary finite-size scaling there is a more benign power law shift $(T^*(L) - T_c) \sim L^{1/\nu}$.

The singular part of the specific heat, being related to the free energy density $f \sim \xi_+^{-1}$ of unbound kinks, vanishes as [174, Chapt.9]

$$C_V^{\mathrm{sing}}(T) \sim \xi_+^{-1} \sim \exp\left(-\frac{\mathrm{const}}{\sqrt{(T - T_{KT})/T_{KT}}}\right) \tag{7.17}$$

and is unobservable if there is another non-universal contribution to the specific heat. Note that the singularities in Eqs. (7.15) and (7.17) are *essential singularities.*

Fig. 7.6 shows the specific heat $C_V = \frac{1}{k_B T^2}(\langle E^2 \rangle - \langle E \rangle^2)$, computed with QMC as the fluctuations of the energy, for different system sizes and transverse fields. Similarly to the Kosterlitz-Thouless transition in the 2D XY model [174, Chapt. 9], the peak in the specific heat occurs at a higher temperature than T_{KT}, where the magnetization jump is observed, and saturates with increasing system size [178]. $T_{KT}(\Gamma)$ is indicated in Fig. 7.6 by vertical lines. The singularity of Eq. (7.17) at the transition temperature is essentially unobservable. The non-universal peak in the specific heat above T_{KT} is the result of entropy generation due to the gradual unbinding of kink-antikink pairs, in accordance with the thermodynamic relation $C_V = T (\partial S/\partial T)_V$. The fact that the peak becomes smaller and much broader for increasing transverse field is a strong sign that the kinks are spatially smeared out so that their unbinding does not create much entropy. The large kink size makes the system more susceptible to finite-size effects, as evidenced by the more pronounced crossings of $\langle (m_z)^2 \rangle$ as a function of L in Fig. 7.2 for larger Γ.

As expected the specific heat shows large statistical noise at low temperatures since it is computed as the difference of two large macroscopic quantities.

In the ordered phase the susceptibility is computed with QMC according to

$$\chi^{(\mathrm{qm.})} = L \int_0^\beta \langle m^z(\tau) m^z(0) \rangle d\tau - L\beta \langle |m^z| \rangle^2 \tag{7.18}$$

where $m^z = \frac{1}{L} \sum_{i=1}^L S_i^z$ is the average magnetization and $m^z(\tau) = e^{\tau H} m^z e^{-\tau H}$. Since in the transverse field Ising model $[H, m^z] \neq 0$, this quantity is not identical to

$$\chi^{(\mathrm{class.})} = \beta L(\langle m^2 \rangle - \langle |m| \rangle^2), \tag{7.19}$$
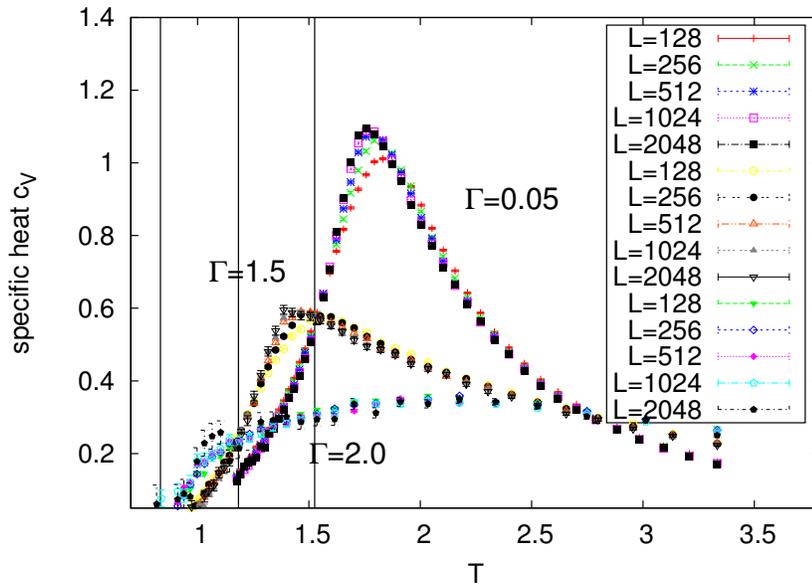
Fig. 7.6: Specific heat in the $1/r^2$ ferromagnetic chain in a transverse field. Vertical lines show the Kosterlitz-Thouless transition temperatures $T_{KT}(\Gamma)$ for the three indicated transverse fields $\Gamma = 0.05, 1.5,$ and 2.0. The non-universal bump in the specific heat occurs above the transition temperature and is due to the entropy that is generated when kink-antikink pairs unbind. The essential singularity of Eq. (7.17) at the transition temperature is not discernible.
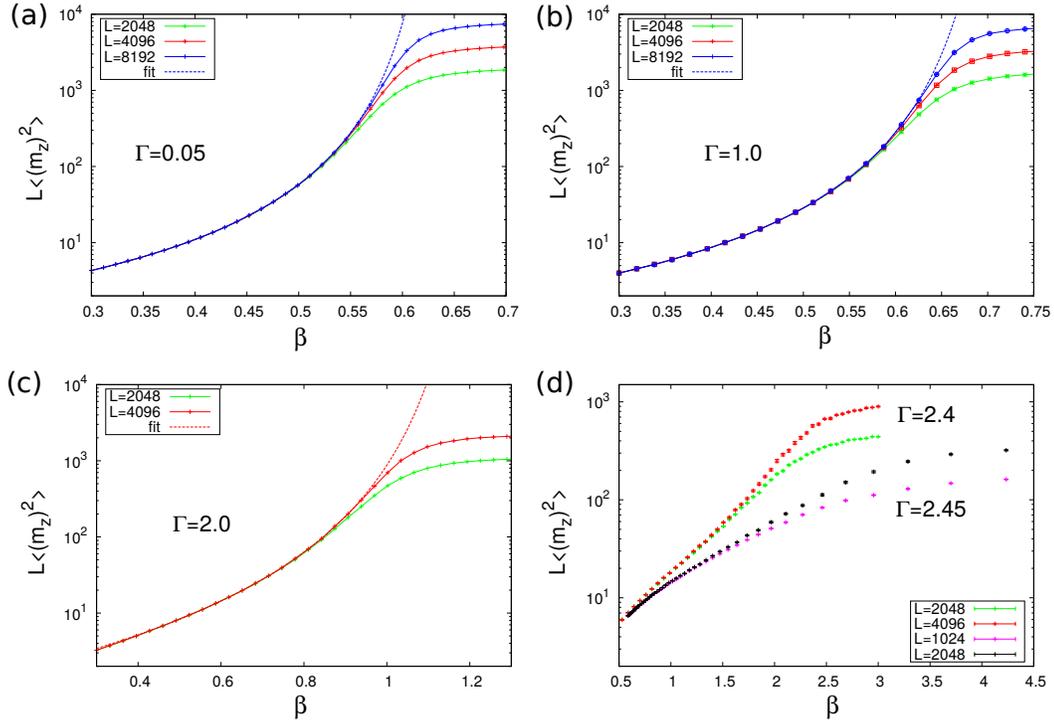
Fig. 7.7: Susceptibility calculated according to Eq. (7.19) for different values of the transverse field. Dashed lines are fits to the exponential divergence of Eq. (7.15).

which is only valid for the classical Ising model with $[H, m^z] = 0$. However, close to a thermal phase transition the difference $\chi^{(\text{qm.})} - \chi^{(\text{class.})} > 0$ is a non-diverging quantity. For the purpose of capturing the exponentially diverging correlation length we computed the susceptibility according to Eq. (7.19), which is less computationally demanding than the Kubo integral over imaginary time in Eq. (7.18). Fig. 7.7 illustrates the exponential divergence of the suscpetibility with inverse temperature. Curves are shown, for system sizes up to $L = 8192$ sites, for five different transverse field values Γ together with fits to the exponential divergence $\chi \sim \exp\left[B(\beta - \beta_c)^{\tilde{\nu}}\right]$ according to Eq. (7.15). For $\Gamma = 2.0$, the fit range was $\beta \in [0.3, 0.8]$ and the exponent $\tilde{\nu} = \frac{1}{2}$ was fixed during the fit which resulted in $\beta_c = 1.2 \pm 0.1$. The fit is rather insensitive to the choice of $\tilde{\nu}$. For $\Gamma = 2.4, 2.45$ the exponential divergence is no longer clearly visible. This suggests that at least up to $\Gamma = 2.0$ the Kosterlitz-Thouless scaling relations which lead to Eq. (7.15) hold.

7.2.4   Finite-size scaling form

The shift of the transition temperature with system size in Eq. (7.16) motivates the following finite-size scaling form [196, 197] of the universal jump relation Eq. (7.6):

$$\frac{\langle m^2 \rangle (L)}{T_{KT}(L)} = \frac{1}{2} \left(1 + \frac{A}{\log^2(L/L_0)} \right). \tag{7.20}$$

Here, L_0 is some characteristic length of the order of the lattice spacing [197].

Standard finite-size scaling, which rests on the algebraic divergence of the correlation length, cannot be used in the case of a Kosterlitz-Thouless transition, where the correlation length diverges exponentially. Instead an alternative scaling form has been suggested based on the renormalization group equations [97, 177, 196, 197]:

$$\frac{2\langle m^2 \rangle}{T} - 1 = l^{-1} \Psi(t l^2), \tag{7.21}$$

where $\Psi(x)$ is a scaling function, $t = T/T_{KT} - 1$ is the reduced temperature and $l = \log(L/L_0)$. We use both Eq. (7.20) and a data collapse analysis based on Eq. (7.21) to estimate the Kosterlitz-Thouless transition temperature $T_{KT}(\Gamma)$ for different transverse field values Γ with high accuracy. The results are presented in Fig. 7.3.

Fig. 7.8(a) shows the approach of the magnetization curve $\langle m^2 \rangle(\beta)$ with system size to the universal jump, $\langle m^2 \rangle = \frac{1}{2} T_{KT}(\Gamma)$ in the thermodynamic limit. The value of the transverse field is $\Gamma = 1.0$. For comparison, the diamond indicates the critical temperature $T_{KT} = 1.3840(7)$ obtained from a data collapse (see 7.8(b)) according to Eq. (7.21). The inset in Fig. 7.8(a) shows the size-dependent critical temperature $T_{KT}(L)$, determined from the universal jump relation Eq. (7.6) as the point where $\langle m^2 \rangle(L)/T_{KT}(L) = \frac{1}{2}$. A fit to $T_{KT}(L) = T_{KT}(\infty) + \frac{a}{\log^2(L)}$ (see also [198] for finite-size scaling of KT transition for 2d XY model) verifies that there are logarithmic scaling corrections. $T_{KT}(\infty)$ obtained from this fit is drawn as a dotted line, while the dashed line indicates the more reliable value for T_{KT} resulting from the data collapse (Fig. 7.8(b)). The extrapolation to the thermodynamic limit is inaccurate due to the slow, logarithmic convergence with L.

Fig. 7.8(b-d) shows a data collapse according to the scaling relation Eq. (7.21) for $\Gamma = 1.0, 1.5$, and 2.0. When $(2\langle m^2 \rangle/T - 1) \log(L/L_0)$ is plotted against $(T/T_{KT} - 1) \log^2(L/L_0)$, data points for different temperatures T and system sizes L should collapse onto a single scaling curve $\Psi(x)$, provided that the critical temperature T_{KT} is chosen correctly. The data collapse is realized with a least-squares fit to a polynomical of order eight with T_{KT} and L_0 as fitting parameters. In order to enforce that the fit is particularly good close to the critical point, a Gaussian weight function is included in the sum of residuals. The critical temperature $T_{KT} = 1.3840(7)$ thus obtained for $\Gamma = 1$ is in excellent agreement with the only published value at non-zero Γ, $T_{KT}(\Gamma = 1) = 1.38460(25)$ from Ref. [97], which was obtained with the same type of data collapse but including much larger system sizes up to $L = 2^{20} = 1048576$.
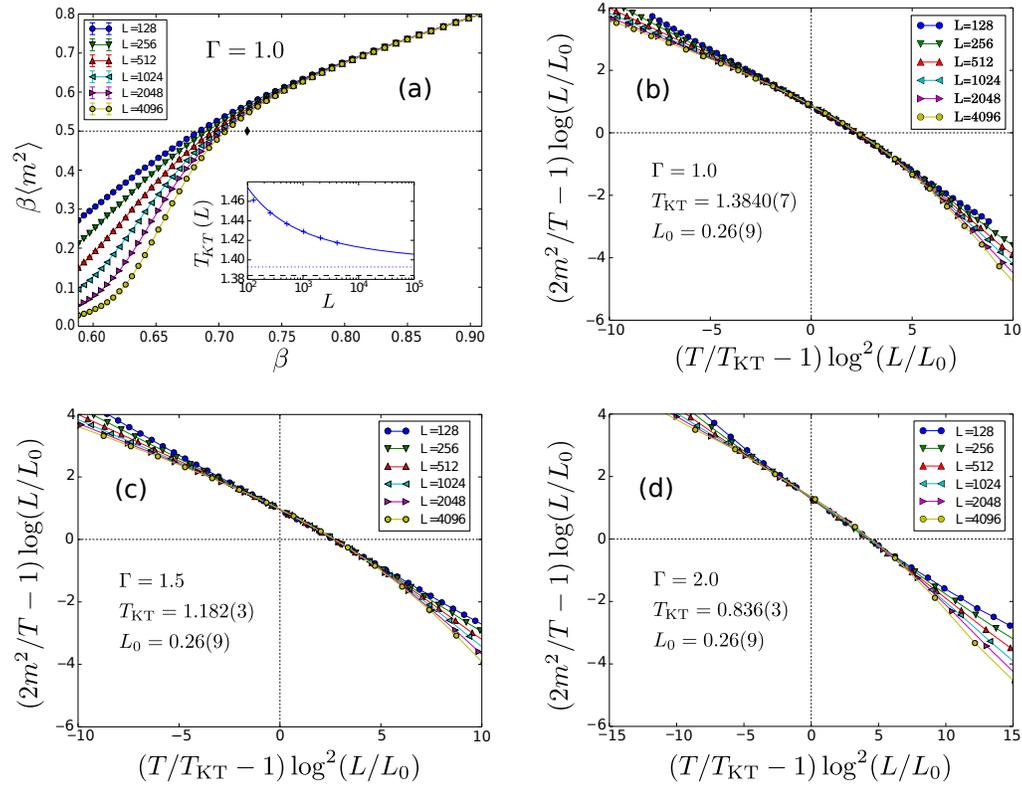
Fig. 7.8: Estimation of the Kosterlitz-Thouless transition temperature from an extrapolation of the universal jump relation Eq. (7.20) (a) and from a data collapse according to Eq. (7.21) (b-d). The inset in (a) shows a fit of the system-size dependent critical temperature $T_{KT}(L)$ to $T_{KT}(L) = T_{KT}(\infty) + \frac{a}{\log^2(L)}$ for $\Gamma = 1.0$. (b-d) Scaling plot of the magnetization density for $\Gamma = 1.0$ (b), $\Gamma = 1.5$ (c), and $\Gamma = 2.0$ (d).

The similarity of the scaling function $\Psi(x)$ for different transverse field values Γ in Fig. 7.8(b-d) suggests that $\Psi(x)$ is universal.

7.2.5　RG prediction for the spin-spin correlation function

The behaviour of the spin-spin correlation function below and close to the critical temperature follows from the RG equation (7.9c) for the longitudinal magnetic field. First we recall how the spin-spin correlation function in d spatial dimensions transforms under a renormalization group transformation [159]: The connected correlation function

$$X(\mathbf{r}_i - \mathbf{r}_j) = \langle S^z(\mathbf{r}_i) S^z(\mathbf{r}_j) \rangle^c \equiv \langle S^z(\mathbf{r}_i) S^z(\mathbf{r}_j) \rangle - \langle S^z(\mathbf{r}_i) \rangle \langle S^z(\mathbf{r}_j) \rangle \tag{7.22}$$

is computed from the partition function with an additional source term $h(\mathbf{r}_i) \equiv \frac{\tilde{h}(\mathbf{r}_i)}{k_B T}$ as

$$X(\mathbf{r}_i - \mathbf{r}_j) = \left. \frac{\partial^2 \ln Z}{\partial h(\mathbf{r}_i) \partial h(\mathbf{r}_j)} \right|_{h(\mathbf{r})=0} . \tag{7.23}$$

The source term before and after the RG transformation reads

$$-\sum_{\mathbf{r}_i} h(\mathbf{r}_i) S(\mathbf{r}_i) \rightarrow -\sum_{\mathbf{R}_i} h'(\mathbf{R}_i) S'(\mathbf{R}_i), \tag{7.24}$$

where $\mathbf{R}_i$ is the center of the coarse graining cell and $S'(\mathbf{R}_i)$ is the new block spin variable. $h'(\mathbf{R}_i) = \lambda_h h_i$ with λ_h the so-called magnetic eigenvalue of the RG transformation. For the present KT transition one can see from Eq. (7.9c) that the scale-dependent magnetic eigenvalue is $\lambda_h(l) = 1 - 2y^2(l)$.

Using the defining property of a valid coarse graining transformation, namely that it preserves the partition function, $Z[H'] = Z[H]$, we obtain the correlation function after coarse graining

$$\frac{\partial^2 \ln Z[H']}{\partial h'(\mathbf{R}_i) \partial h'(\mathbf{R}_j)} = \frac{\partial^2 \ln Z[H]}{\partial h'(\mathbf{R}_i) \partial h'(\mathbf{R}_j)} \tag{7.25}$$

$$= \left\langle \left(S^{(1)}_{\mathbf{R}_i} + S^{(2)}_{\mathbf{R}_i} + \cdots + S^{(b^d)}_{\mathbf{R}_i} \right) \left(S^{(1)}_{\mathbf{R}_j} + S^{(2)}_{\mathbf{R}_j} + \cdots + S^{(b^d)}_{\mathbf{R}_j} \right) \right\rangle^c \tag{7.26}$$

$$\sim \frac{(b^d)^2}{\lambda_h^2} \langle S(\mathbf{r}_i) S(\mathbf{r}_j) \rangle^c_H \tag{7.27}$$

In the last step it was assumed that $h(\mathbf{r}_i)$ varies over distances much larger than ba so that it can be treated as uniform on the level of a coarse grained block. Hence, the recursion relation of the spin-spin correlation function in one RG step reads [159]

$$X\left(\frac{|\mathbf{r}_i - \mathbf{r}_j|}{b} \right)_{H'} = \frac{b^{2d}}{\lambda_h^2} X\left(|\mathbf{r}_i - \mathbf{r}_j| \right)_H , \tag{7.28}$$

which relates the spin-spin correlation function of the physical system described by Hamiltonian H to that described by H' after one coarse graining transformation. To see the effect of l successive coarse graining transformations we have to integrate Eq. (7.9c) to obtain the magnetic eigenvalue of the combined transformations,

$$\frac{dh}{dl} = \lambda_h(l)\, h \quad \rightarrow \quad h(l) = e^{\int_0^l \lambda_h(l')dl'} h(0), \tag{7.29}$$

and use $b(l) = e^l$, which yields [178]

$$\langle S^z(r)S^z(0)\rangle_H = e^{-2l} e^{2\int_0^l \lambda_h(l')dl'} \langle S^z(r/e^l)S^z(0)\rangle_{H'}. \tag{7.30}$$

Integrating up to the point where $r/e^l = 1$, replacing $S^z(1)S^z(0) \approx \langle m \rangle^2$ and using Eqs. (7.10b) and (7.11) on the critical trajectory $\Delta = 0$, one finally obtains the spin-spin correlation function at the critical point [178]

$$C(r) = \langle S^z(r)S^z(0)\rangle - \langle S^z(r)\rangle\langle S^z(0)\rangle = \langle m \rangle^2 \left(e^{1/\ln(r)} - 1 \right) \tag{7.31}$$

$$= \langle m \rangle^2 \left(1 + \frac{1}{\ln(r)} + \frac{1}{2\ln^2(r)} + \ldots - 1 \right) \xrightarrow[r \to \infty]{} \langle m \rangle^2 \frac{1}{\ln(r)}. \tag{7.32}$$

Thus, asymptotically the spin-spin correlation function at T_{KT} decays like $1/\ln(r/a_0)$ with distance r [178], which was verified in a large-scale Monte Carlo study [179] for the classical (i.e. $\Gamma = 0$) system for up to 10^6 lattice sites. This behaviour is different from the XY model, where the universal decay exponent at the critical temperature is $\eta = \frac{1}{4}$, and is related to the fact that the $1/r^2$-ferromagnet has true long-range order at finite temperature.

The spatial decay of the spin-spin correlation function $C(r) = \langle S^z(r)S^z(0)\rangle$ is shown in Fig. 7.9 at $\Gamma = 0.5$ for a range of temperatures above, at, and below T_{KT}. The critical correlation function is fit to Eq. (7.31). According to a theorem of Ref. [199] the spin-spin correlations cannot decay faster than the long-range forces themselves in the ferromagnetic Ising model and thus are bounded from below by $1/r^\alpha$. This lower bound is indicated in Fig. 7.9 by a dashed line.

7.2.6   Influence of the transverse field on the KT transition

It is well established that the thermal phase transition of a quantum system is unaffected by quantum fluctuations [62, Chapt.1] as soon as the diverging correlation length exceeds the length of the *finite* Trotter dimension of the effective classical system to which the finite-temperature system is mapped; hence this length scale drops out. Applied to the present model, it follows that the KT transition at finite Γ should be described by the same RG equations as the transition at $\Gamma = 0$, with a reduced temperature $T(\Gamma)$ [169]. As the phase boundary $T_{KT}(\Gamma)$ approaches the quantum critical point, the universal jump in the magnetization decreases and vanishes at $\Gamma_c/J \approx 2.52$. The entire
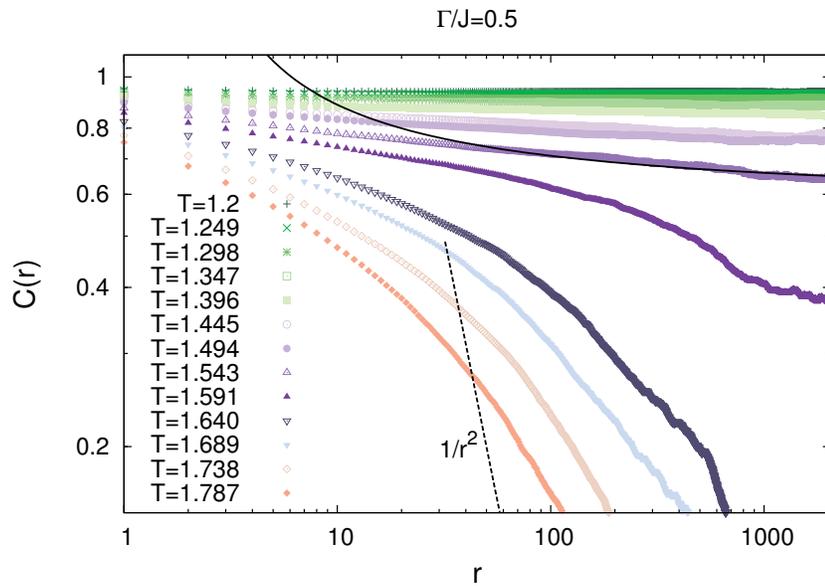
Fig. 7.9: Spatial decay of the spin-spin correlation function $C(r)$ for temperatures above and below the KT transition temperature for $\Gamma/J = 0.5$. The system size is $L = 4096$. The dashed line is the lower bound on the decay of the spin-spin correlations for inverse square long-range interactions. The continuous black line is a fit of the critical correlation function to the asymptotic RG expression Eq. (7.31).

phase boundary as well as the disappearance of the KT transition at Γ_c is in agreement with the universal jump relation Eq. (7.6). However, close to the quantum critical point the thermal KT phase transition is only observable once the correlation length in imaginary time $\xi_\tau \sim \xi^z$ exceeds the Trotter dimension, and due to the space-time anisotropy of the quantum critical point (see also Sect. 7.3.3 below) with $z = \frac{1}{2}$ [169], this happens only for exceedingly large system sizes. Outside a narrow window around the transition temperature, the thermal transition is masked by quantum effects. In the presence of a transverse field Γ a new length scale appears, namely the width of a kink $w(\Gamma)$ (see Fig. 7.4), which increases for larger transverse field. To recover a sharp kink, several coarse graining steps have to be performed. A transverse field may change the RG equations for the kink fugacity. i.e. it lowers the microscopic energy cost of inserting a kink. However, it will not affect the fixed point structure of the RG flow and the kink fugacity remains an irrelevant variable. Only the location of the physical curve of initial conditions where the RG dynamics starts is shifted upwards to $(x_{m^2(\Gamma),E_{\mathrm{kink}}(\Gamma)}(T), y_{m^2(\Gamma),E_{\mathrm{kink}}(\Gamma)}(T))$ (see Fig. 7.5), and more coarse graining steps are needed to reach scale invariance for $\Gamma \neq 0$ than for $\Gamma = 0$. In combination with the slow divergence of the correlation length in imaginary time $\xi_\tau \sim \xi^{\frac{1}{2}}$ in the vicinity of the anisotropic quantum critical point and the logarithmic corrections to scaling of Eq. (7.16), this makes the thermal KT transition essentially unobservable for $\Gamma/J > 2.2$ with the system sizes studied here. Still, the preceding discussion suggests that the transition remains of the Kosterlitz-Thouless type for all values of Γ, as was conjectured in Ref. [169] and demonstrated numerically for $\Gamma/J \leq 1$ in Ref. [97].

7.3   Line of ferromagnetic quantum critical points

In this section, the quantum critical properties of the ferromagnetic LRTFI chain Eq. (7.1) are investigated as a function of decay exponent α. Apart from the fact that this model can be realized experimentally in trapped chains of ions [36, 37, 200], there is theoretical interest coming from the possibility to interpolate between discrete dimensions by tuning continously the decay exponent α of the interactions and thus change the universality class of the phase transition. Universality classes depend on spatial dimension, symmetry of the order parameter, number of components of the order parameter and the range of interactions. It is no coincidence that long-range interactions were studied very early in the development of renormalization group theory [146]. As will be argued in detail below, for $\alpha < 5/3$ mean-field theory becomes exact and for $\alpha > \frac{7}{4} + 1 = \frac{11}{4}$ the critical exponents are those of the short-range 2D classical Ising model. In between, the critical exponents depend continuously on α. For $\alpha < 1$ the system is not themodynamically stable with an interaction energy that is superextensive in the system size and diverges in the thermodynamic limit.

Fig. 7.10(a) shows the quantum critical point separating the ferromagnetic from the paramagnetic phase as a function of decays exponent α. The critical field $\Gamma_c(\alpha)$ is

obtained with SSE QMC from an extrapolation of the crossing points of the Binder cumulant $U_L = \frac{\langle m^4 \rangle_L}{\langle m^2 \rangle_L^2}$, which is presented in Fig. 7.10(b). For comparison, the critical fields $\Gamma_c(\alpha)$ computed with different methods in Refs. [184] and [201] are also included in Fig. 7.10(a).
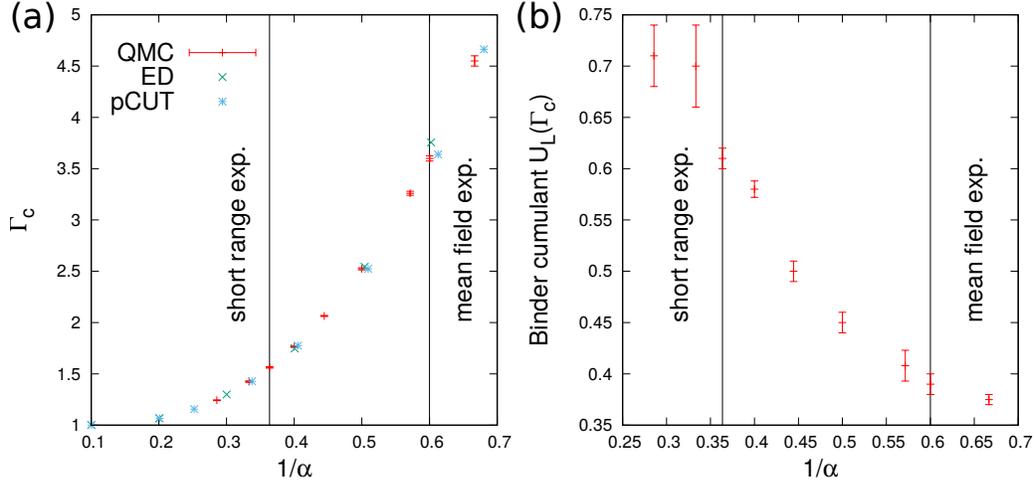
Fig. 7.10: (a) Critical transverse field Γ_c for the zero-temperature transition from a ferromagnet to a paramagnet as function of interaction exponent α. For $\alpha \geq \frac{7}{4} + 1 = \frac{11}{4}$ the critical exponents are in the short-range universality class, while for $\alpha < 5/3$ mean-field theory becomes exact. For comparison the critical fields found with exact diagonalization (ED) [184] and with the method of perturbative continuous unitary transformations (pCUT) [201] are also shown. (b) Binder cumulant $U_L = \frac{\langle m^4 \rangle_L}{\langle m^2 \rangle_L^2}$ at the quantum critical point.

7.3.1   Dimensional analysis and mean-field critical exponents

In the following, we derive the critical exponents for long-range quantum Ising models in the mean-field regime. We consider the ϕ^4 field theory in $d+1$ dimensions with long-range interactions in real space. The Euclidean action in real space x and imaginary time τ takes the form $S = S_{SR} + S_{LR}$ with the short-range and long-range parts

$$S_{SR} = \int d\tau \int d^d x \left[A \left(\partial_\tau \phi(\tau, \mathbf{x}) \right)^2 + |\nabla \phi(\tau, \mathbf{x})|^2 + r \phi^2(\tau, \mathbf{x}) \right] + u \int d\tau \int d^d x \, \phi^4(\tau, \mathbf{x}),$$

(7.33)

$$S_{LR} = B_\sigma \int d\tau \int d^d x \int d^d y \, \frac{\phi(\tau, \mathbf{x}) \phi(\tau, \mathbf{y})}{|\mathbf{x} - \mathbf{y}|^{d+\sigma}}.$$

(7.34)

Here, $\phi(\mathbf{x}, \tau)$ is the order parameter field, a coarse-grained field related to $\langle S_i^z \rangle$ in the original lattice model. The continuum model is a valid description close to the critical

point where the correlation length diverges and the system becomes invariant under a scaling transformation of the coordinates [62, Chapt. 4]

$$\mathbf{x} \to \mathbf{x}' = \frac{\mathbf{x}}{b}, \quad \tau \to \tau' = \frac{\tau}{b^z} \tag{7.35}$$

with the rescaling factor $b > 1$, when the fields and coefficients in the action are rescaled accordingly

$$\phi \to \phi' \stackrel{\text{def}}{=} b^{\dim[\phi]}\phi. \tag{7.36}$$

Space and time are rescaled differently, which is accounted for by the dynamical critical exponent z. Eq. (7.36) defines [2] the scaling dimension $\dim[\phi]$ of the field ϕ. Following closely the exposition of Ref. [202], we demand that the action in Eq. (7.34) be dimensionless. From this requirement one obtains a simultaneous set of equalities relating the so-called *engineering dimensions*

$$\dim[A] = -z + d - 2\dim[\phi], \tag{7.37a}$$
$$\dim[r] = z + d - 2\dim[\phi], \tag{7.37b}$$
$$\dim[B_\sigma] = z - \sigma + d - 2\dim[\phi], \tag{7.37c}$$
$$\dim[u] = z + d - 4\dim[\phi]. \tag{7.37d}$$

Terms higher than quadratic in ϕ are irrelevant in the RG sense (meaning that their coefficient has negative canonical scaling dimension), when they appear in conjunction with the long-range interactions $1/|\mathbf{x} - \mathbf{y}|^{1+\sigma}$, and they have already been omitted in the action [202].

The critical point is characterized by scale invariance. For the moment we neglect the interaction term with coefficient u, which is equivalent to considering the Gaussian or *mean-field* regime. In the action Eq. (7.34), $r \sim \frac{|\Gamma - \Gamma^*|}{\Gamma^*}$ parametrizes the distance of the control parameter from the mean-field critical point Γ^* and therefore the mass term $r \int d\tau \int d^d x \phi^2(x, \tau)$ vanishes by construction at the critical point. It remains to demand that the other quadratic terms in ϕ be scale invariant, which corresponds to $\dim[A] = \dim[B_\sigma] = 0$ and yields two equations for the two unknowns z and $\dim[\phi]$:

$$-z + d - 2\dim[\phi] = 0 \tag{7.38}$$
$$z - \sigma + d - 2\dim[\phi] = 0, \tag{7.39}$$

valid at the mean-field level. The combination of both equations gives the solution [169]

$$z^{(\text{MF})} = \frac{\sigma}{2}. \tag{7.40}$$

---

[2]Alternatively, one can think of the coarse graining procedure as taking the continuum limit in which the lattice spacing a goes to zero. In this case the scaling dimension $[\phi]$ is defined as $\phi \stackrel{\text{def}}{\sim} a^{-\dim[\phi]}$. If $\dim[\phi] < 0$, then ϕ becomes irrelevant in the continuum limit $a \to 0$.

In general, the scaling dimension is not identical to the engineering dimension from dimensional analysis. The difference is quantified by the *anomalous dimension* [3] η, which is defined through

$$\dim[\phi] \stackrel{\text{def}}{=} \frac{1}{2}(d - 1 + \eta). \tag{7.42}$$

With the definition Eq. (7.42), η appears in the exponent for the asymptotic decay of the order parameter correlation function, $C(r) = \langle \phi(r)\phi(0) \rangle \sim 1/r^{d-1+\eta}$, and in one dimension $C(r) \sim 1/r^\eta$. It is the correction that the scaling dimension of the order parameter field receives when interactions are turned on. Inserting Eq. (7.42) into Eq. (7.39) and using Eq. (7.40) gives

$$\eta^{(\text{MF})} = 1 - \frac{\sigma}{2}. \tag{7.43}$$

For the short-range 2D Ising model $\eta_{SR} = \frac{1}{4}$.

The correlation length exponent ν for long-range interactions can be derived from the Gaussian propagator in the same way as for short-range systems in Ornstein-Zernike theory [174, Chapt. 4.3]. From now on we use the notation $\alpha = d + \sigma$ for the decay exponent, which has the advantage that many results can be stated without referring to the spatial dimension d. It can be established quite generally that the long-wavelength behaviour $\mathbf{q} \to 0$ of the Fourier transform $\mathcal{FT}[\cdot]$ of the interaction matrix $\gamma_{\mathbf{q}} = \sum_{\mathbf{x} \neq 0} \frac{e^{i\mathbf{q} \cdot \mathbf{x}}}{|\mathbf{x}|^{d+\sigma}}$ around its minimum for long-range interactions takes the form (see for example [203] for an explicit derivation for different dimensions d)

$$\gamma_0 - \mathcal{FT}\left[\frac{1}{|\mathbf{x}|^{d+\sigma}}\right] = \begin{cases} \gamma_0 - \gamma_{\mathbf{q}} \sim |\mathbf{q}|^\sigma + \mathcal{O}(q^2) & -d < \sigma < 2 \\ \gamma_0 - \gamma_{\mathbf{q}} \sim q^2 & \sigma > 2. \end{cases} \tag{7.44}$$

Details of the specific lattice structure are encoded in the prefactors, which are of no importance as far as the critical properties close to the phase transition are concerned. The Fourier transformation of the interactions $\gamma_{\mathbf{q}}$ has a cusp at $\mathbf{q} = 0$ for $0 < \sigma < 1$ and diverges in the limit $\mathbf{q} \to 0$ as $|\mathbf{q}|^{-\sigma}$ for $\sigma < 0$, as can be seen from Fig. 7.1(b) where $\gamma_{\mathbf{q}}$ is shown for a one-dimensional system.

In the spirit of describing the long-wavelength physics close to the phase transition where the continuum description is appropriate and details of the lattice become unimportant, we keep only the powers of $\mathbf{q}$ that are dominant in the limit $\mathbf{q} \to 0$, which is why, in the field theory of the critical point, we must neglect the gradient

---

[3] For the Gaussian model in $d + 1$ dimensions

$$S_0 = \frac{1}{2} \int d^{d+1}x \, [\nabla \phi(\mathbf{x})]^2, \tag{7.41}$$

the canonical scaling dimension of the field ϕ, obtained from simple dimensional analysis, is $\dim[\phi] = \frac{1}{2}(d - 1)$.

term $\mathcal{FT}\left[(\nabla\phi(\mathbf{x},\tau))^2\right] = q^2|\phi(\mathbf{q},\tau)|^2$ compared to long-range interactions $\sim |q|^\sigma$ for $\sigma < 2 - \eta_{\text{SR}}$ [204]. On the other hand, for $\sigma > 2 - \eta_{\text{SR}}$ the gradient term is dominant and we recover the field-theory of the short-range model. For $\sigma > 2 - \eta_{\text{SR}}$, the Gaussian action in Fourier space reads

$$S_0 = \int d\omega \int d^d\mathbf{q}(A\omega^2 + r + B_\sigma|q|^\sigma)|\phi(\omega,q)|^2. \tag{7.45}$$

The form of the term $A\omega^2$ comes from the quantum-to-classical mapping of the quantum Ising model to a $d + 1$-dimensional effective system. As can be demonstrated in the path integral formalism (see Appendix B), the resulting interactions in imaginary time are always short-ranged so that the long-wavelength limit of their Fourier transform is proportional to ω^2.

From this Gaussian action we can derive the correlation function in Fourier space by the same reasoning that lead to the Ornstein-Zernike correlation function starting from the Ginzburg-Landau free energy [174, Chapt. 4.3]. The Fourier transform of the correlation function reads

$$\tilde{C}(\omega,\mathbf{q}) = \frac{1}{A\omega^2 + r + B_\sigma|q|^\sigma}. \tag{7.46}$$

Following [202], we integrate first over imaginary time frequencies, which does not pose any risk of divergence and is equivalent to considering the equal-time correlation function $\tilde{C}(\mathbf{q},\tau = 0)$. Using the identity $\int_{-\infty}^\infty \frac{d\omega}{2\pi}\frac{1}{A\omega^2+B} = \frac{1}{2\sqrt{AB}}$ one obtains

$$\tilde{C}(\tau = 0,\mathbf{q}) = \int_{-\infty}^\infty d\omega\tilde{C}(q,\omega) = \frac{1}{2\sqrt{A}\sqrt{r + B_\sigma|q|^\sigma}}, \tag{7.47}$$

and the Fourier transform with respect to $\mathbf{q}$ yields the correlation function in real space

$$C(\tau = 0,|\mathbf{x}|) = \int \frac{d^d\mathbf{q}}{(2\pi)^d}\frac{e^{i\mathbf{q}\cdot\mathbf{x}}}{2\sqrt{A}\sqrt{r + B_\sigma|q|^\sigma}} \tag{7.48}$$

$$= \frac{1}{|\mathbf{x}|^{d-\frac{\sigma}{2}}}Y_\sigma\left(\frac{|\mathbf{x}|}{\xi}\right), \tag{7.49}$$

where

$$Y_\sigma\left(\frac{|\mathbf{x}|}{\xi}\right) = \int y^{d-1}dy \int \frac{d\Omega_d}{(2\pi)^d}\frac{e^{iy\cos\vartheta}}{2\sqrt{A}\sqrt{\left(\frac{|\mathbf{x}|}{\xi}\right)^\sigma + y^\sigma}} \tag{7.50}$$

with $d\Omega_d$ the differential of the angular variables in d-dimensional spherical coordinates. As a consistency check we may convince ourselves that the correct scaling behaviour $C(|\mathbf{x}|) \sim 1/|\mathbf{x}|^{d-\frac{\sigma}{2}}$ emerges, which follows directly from the general definition

$$C(|\mathbf{x}|) \sim 1/|\mathbf{x}|^{d-1+\eta} \tag{7.51}$$

with the substitution of the expression $\eta^{(MF)} = 1 - \frac{\sigma}{2}$, as obtained earlier in Eq. (7.43) based purely on dimensional analysis. Furthermore, in going from Eq. (7.48) to Eq. (7.49) we have identified the correlation length as

$$\xi = \left(\frac{r}{B_\sigma} \right)^{1/\sigma} \sim r^{-1/\sigma} = \frac{1}{(|\Gamma - \Gamma_c|/\Gamma_c)^{1/\sigma}}, \tag{7.52}$$

which yields the correlation length exponent [169]

$$\nu^{(MF)} = \frac{1}{\sigma}. \tag{7.53}$$

Again, this is a mean-field exponent since the starting point was the Gaussian action Eq. (7.45).

When $\xi \to \infty$, which happens exactly at the critical point in the thermodynamic limit, the correlation length decays with the power law $C(|\mathbf{x}|) \sim |\mathbf{x}|^{-(d-\frac{\sigma}{2})}$. If, on the other hand, ξ is finite, then, on length scales $|\mathbf{x}| > \xi$, the correlation function obeys an exponential decay governed by the correlation length ξ and the precise functional form of $Y_\sigma(|\mathbf{x}|/\xi)$, i.e. the correlation length becomes "visible" on length scales $|\mathbf{x}| > \xi$.

The correlation length exponent ν is important for assessing the influence of finite-size effects. Corrections to scaling in standard finite-size scaling [43] are proportional to $L^{-1/\nu}$. With $\nu^{(MF)} = \frac{1}{\sigma}$ this results in scaling corrections proportional to $L^{-\sigma}$ that vanish more and more slowly as σ decreases. For comparison, in the short-range transverse-field Ising model, which is in the same universality class as the 2D classical Ising model, $\nu = 1$. One can thus conclude that, even if the problem of periodic boundary conditions in the presence of long-range interactions has been solved by an interaction sum over periodic images as in Eq. (7.4), long-range systems are particularly affected by finite-size effects due to the stronger divergence of the correlation length $\xi \sim (|\Gamma - \Gamma_c|/\Gamma_c)^{-1/\sigma}$ for $\sigma < 1$ compared to the short-range system.

The critical exponents obtained above are mean-field exponents; they are valid above the upper critical dimension, which is defined as the spatial dimension $d = d_u$ above which the local interaction term u becomes irrelevant. Setting its scaling dimension dim$[u]$ to zero [202] and using the definition of the anomalous dimension η and Eqs. (7.43) and (7.40) results in [169]

$$d_u = \frac{3\sigma}{2}. \tag{7.54}$$

Conversely, Eq. (7.54) allows to define an *upper critical range* of interaction for a given spatial dimension. For $d = 1$, the upper critical range is $\sigma_u = \frac{2}{3}$, which means that, for interactions decaying with exponent $\alpha = 1 + \sigma$, mean-field critical exponents apply if $\sigma < \sigma_u$. Similarly, one can define a *lower critical range* σ_l such that for $\sigma > \sigma_l$ the critical behaviour is described by the exponents of the short-range (i.e. nearest

neighbour) model. In one dimension, the lower critical dimension for classical spin models was found to be [204]:

$$\sigma_l(d=1) = 2 - \eta_{SR}, \tag{7.55}$$

where η_{SR} is the anomalous dimension of the corresponding short-range system.

The boundary value $\sigma = 2 - \eta_{SR}$ can be justified heuristically as follows [145, Chapt. 4.3],[202]: Treat S_{LR} as a perturbation on top of the short-range ϕ^4 field theory. By perturbation we mean that the scaling dimension of the order parameter field ϕ and the dynamical critical exponent z are assumed to be those of the short-range model: $\dim[\phi] = \frac{1}{2}(d-1+\eta_{SR})$ and $z = z_{SR} = 1$. Then, by dimensional analysis (or employing directly Eq. (7.37c)) we obtain $\dim[B_\sigma] = 2 - \eta_{SR} - \sigma$. Thus, as long as $\sigma > 2 - \eta_{SR}$, the canonical scaling dimension $\dim[B_\sigma] < 0$ and the long-range term scales to zero under coarse graining transformations.

7.3.2 Critical spin-spin correlation function

Fig. 7.11 presents the decay of the spin-spin correlation function for four different interaction exponents σ at criticality, as well as slightly above and below. By plotting the spin-spin correlation function $C(r) = \frac{1}{L}\sum_{i=1}^{L}\langle S_{i+r}^z S_i^z \rangle$ against the cord length $\zeta(r)$ of Eq. (7.3) the effects of periodic boundary conditions can be largely eliminated and all points come to lie on a straight line for a power law decay when plotted in double logarithmic scale. From a fit to $C(\zeta(r)) \sim \zeta(r)^{-\eta}$ (cf. Eq. (7.51)) the anomalous dimension η is extracted, which is shown in Fig. 7.12 as a function of σ in comparison with the mean-field prediction

$$\eta = \begin{cases} \max\left(1 - \frac{\sigma}{2}, \eta_{\mathrm{SR}} = \frac{1}{4}\right) & \text{1D quantum Ising} \\ \max\left(2 - \sigma, \eta_{\mathrm{SR}} = \frac{1}{4}\right) & \text{2D class. Ising.} \end{cases} \tag{7.56}$$

We show in Eq. (7.56) also the prediction for the 2D classical long-range Ising model [146, 204] to illustrate the point that there the mean-field exponent $\eta_{\mathrm{cl}}^{(MF)} = 2 - \sigma$ can be connected smoothly to the short-range exponent at the lower critical range $\sigma_l = 2 - \eta_{\mathrm{SR}} = \frac{7}{4}$ [204], whereas for the 1D quantum Ising model there is a jump discontinuity between the short-range and the mean-field exponent $\eta_{\mathrm{qm}}^{(\mathrm{MF})} = 1 - \frac{\sigma}{2}$ at $\sigma_l = 2 - \eta_{\mathrm{SR}}$. This discontinuity for the quantum Ising model was found to persists in a renormalization group calculation up to two-loop order [202]. However, judging from the continuous and monotonic σ-dependence in Fig. 7.12, it appears unlikely that the jump discontinuity in η at $\sigma_l = \frac{7}{4}$ really exists.

Another question concerning the long-range 2D classical models is whether the exponent η follows strictly Eq. (7.56), as proposed in Ref. [204] and corroborated by numerical simulations in Ref. [205], or whether there is a smooth crossover in between regions of intermediate- and short-range interactions as suggested in [206, 207]. The smooth crossover observed in the simulations of Ref. [206] is according to the analysis
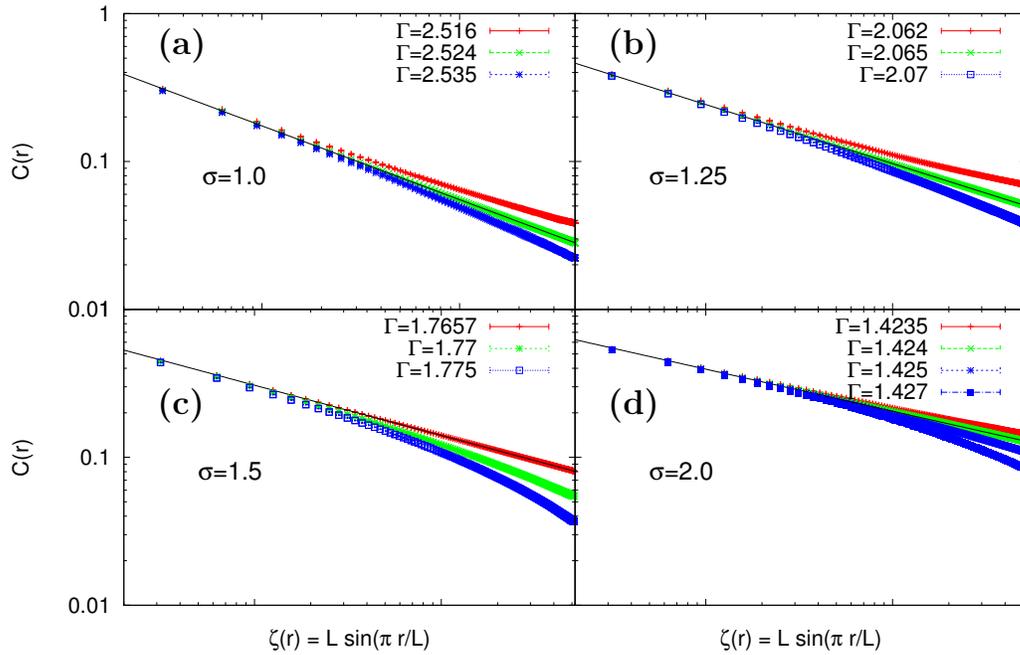
Fig. 7.11: Algebraic decay of the critical spin-spin correlation function $C(r)$. For each decay exponent $\alpha = 1 + \sigma$, the correlation function is shown at as well as slightly above and below criticality (except for $\sigma = 1.5$ (c) where $C(r)$ below criticality is missing). System size $L = 512$ and inverse temperature $\beta = 100$.
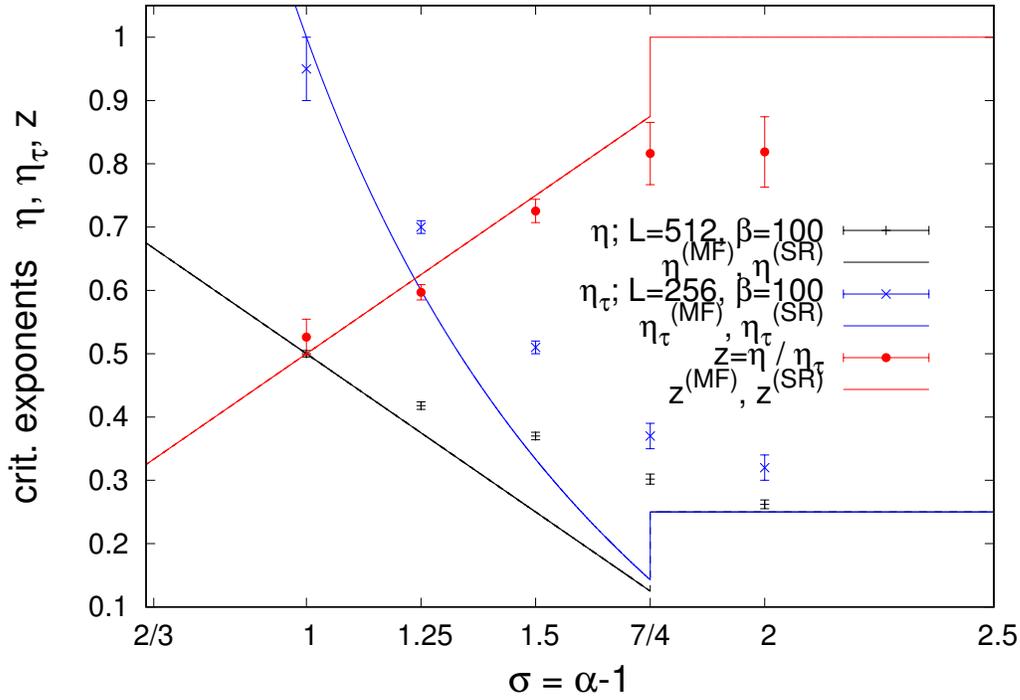
Fig. 7.12: Anomalous dimension η, decay exponent of the spin correlations in imaginary time, η_τ, and dynamical critical exponent, $z = \eta/\eta_\tau$, as a function of $\sigma = \alpha - 1$. The continuous lines are the mean-field critical exponents $\eta^{(\mathrm{MF})}, \eta_\tau^{(MF)}$, and $z^{(MF)}$, connected to the critical exponents for short-range systems $\eta^{(\mathrm{SR})} = \eta_\tau^{(\mathrm{SR})} = \frac{1}{4}$ and $z^{(\mathrm{SR})} = 1$ at the lower critical range $\sigma_l = 2 - \eta_{\mathrm{SR}} = \frac{7}{4}$. The resulting discontinuity at $\sigma = \frac{7}{4}$ is not reflected in the numerical data, which rather seem to follow a smooth crossover from short-range to mean-field critical exponents, which are strictly valid below the upper critical range, i.e. for $\sigma < \sigma_u = \frac{2}{3}$.

of Ref. [208] just an artifact of pronounced logarithmic corrections to scaling. In view of this controversy over the crossover between intermediate- and short-range interactions in the *classical* long-range Ising models, similar cautious considerations apply to the long-range 1D *quantum* Ising models studied here. It is plausible that corrections to scaling [208] or the presence of a subdominant power law [209] affect the estimate of the correlation-function exponent η and have to be taken into account. A new renormalization group scheme for the crossover between the regions of intermediate- and short-range interactions has recently been proposed [210].

7.3.3   Anisotropic quantum critical point (QCP)

The spectral information of a quantum system is captured by the imaginary-time correlation function

$$C(\tau) = \langle \hat{O}(\tau)\hat{O}^\dagger \rangle = \frac{1}{Z}\text{Tr}\left[e^{\tau H}\hat{O}e^{-\tau H}\hat{O}^\dagger e^{-\beta H}\right] \tag{7.57}$$

$$= \frac{1}{Z}\sum_{n,n'} c_{n,n'} e^{-\tau(E_n - E_{n'})} e^{-\beta E_{n'}} \tag{7.58}$$

$$\rightarrow \sum_{n\geq 1} c_n e^{-\tau(E_n - E_0)} \quad \text{for } \beta \rightarrow \infty. \tag{7.59}$$

Here, $\{|n\rangle\}$ is the complete set of energy eigenstates with eigenvalues $\{E_n\}$ and the matrix elements of the operator $\hat{O}$ are $c_{n,n'} = |\langle n'|\hat{O}|n\rangle|^2$. In the following we concentrate on the spin-spin correlation function $C_{zz}(\tau) = \frac{1}{N_s}\sum_{i=1} N_s \langle S_i^z(\tau)S_i^z(0)\rangle$, which was defined already in Eq. (3.96). At a quantum critical point the gap between the ground state and the first excited state vanishes in the thermodynamic limit and the exponential decay of the imaginary time correlations in Eq. (7.59) goes over into an algebraic decay. In the case of the short-range transverse field Ising model, which has a dynamical critical exponent of $z = 1$, the QCP is isotropic in real space an imaginary time, i.e. the correlations decay in both directions with the same power $\eta = \eta_\tau = \frac{1}{4}$ and can be written as [62, Chapt. 10.4]

$$C(r,\tau) \sim \frac{1}{(r^2 + (c\tau)^2)^{1/8}}, \tag{7.60}$$

where c has the dimension of a velocity. For long-range interacting systems, on the other hand, the correlation length im imaginary time grows more slowly than in real space, the two being related by the dynamical critical exponent $\xi_\tau \sim \xi^z$ where $z^{(\text{MF})} = \sigma/2$ in mean-field theory [Eq. (7.40)].

Fig. 7.13(a) shows the decay of $C_{zz}(\tau)$ at the quantum critical point for different interaction exponents α. The inset shows the same data in double-logarithmic scale. In Fig. 7.13(b) we present the Fourier transform $C_{zz}(i\omega_m)$ of $C_{zz}(\tau)$ as a function of Matsubara indices m, which is the quantity that is computed with Monte Carlo (see Sect. 3.4.2). The generaic behaviour $C_{zz}(i\omega_m) \sim 1/\omega_m^2$ for large ω_m is clearly visible.

There are two points that deserve attention. First, the correlations in imaginary time decay faster as the range of the interactions in real space increases. The ratio of the power law exponents for the decay of the critical spin-spin correlations in real space and in imaginary time defines the dynamical critical exponent as $z = \frac{\eta}{\eta_\tau}$. Combining the data of Fig. 7.11 and Fig. 7.13(a) into this formula, z is plotted as a function of $\sigma = \alpha - 1$ in Fig. 7.12. There is good agreement with the mean-field prediction $z^{(\text{MF})} = \sigma/2$ of Eq. (7.40) except for $\alpha = 3$.

Second, as can be seen from the inset of Fig. 7.13 the algebraic decay of $C_{zz}(\tau)$ crosses over into exponential decay on a timescale that depends on α, with smaller α corresponding to a faster exponential decay. In Fig. 7.14 we investigate this crossover phenomenon in detail for the case $\alpha = 2.0$. The arrow in Fig. 7.14 approximately marks the time scale on which the finite correlation length in imaginary time becomes apparent so that the algebraic decay turns into an exponential decay. A fit to

$$C_{zz}(\tau) \sim \tau^{-\eta_\tau} \exp\left[-\left(\frac{\tau}{\xi_\tau}\right)^{d(\alpha)}\right] \tag{7.61}$$

for system size $L = 256$ (continuous black line in Fig. 7.14) is able to capture the crossover from algebraic to exponential decay with $\eta_\tau = 0.95(5)$ and $d(\alpha = 2) \gtrsim 2$, suggesting that $C_{zz}(\tau)$ decays exponentially with a correlation area or volume $v = \xi_\tau^{d(\alpha)}$ rather than a length scale. The crossover of the imaginary time correlation function from algebraic to exponential decay gives evidence for the strong anisotropy of the QCP at $\alpha = 2.0$ where $\xi_\tau \sim \xi^{\frac{1}{2}}$. The time scale on which the crossover occurs increases with increasing lattice size (Fig. 7.14). This supports the intuitive picture that the saturation of the real-space correlation length on the finite system limits the divergence of the correlation length in imaginary time (see inset in Fig. 7.14). Thus, we have encountered the interesting situation where a finite system appears to be critical and scale invariant in real space, once the correlation length reaches the lattice size, but the actual finiteness of the correlation length is still visible in the decay of the imaginary time correlations and dictates the time scale where a crossover from algebraic to exponential decay occurs.

Another method for estimating the dynamical critical exponent z is based on a data collapse for the Binder cumulant $U = \frac{\langle m^2 \rangle^2}{\langle m^4 \rangle}$. The Binder cumulant has scaling dimension zero and its finite-size scaling form reads

$$U(T, \Gamma, L) = \tilde{U}((\Gamma - \Gamma_c)L^{1/\nu}, TL^z). \tag{7.62}$$

When the Binder cumulant U for different system sizes L is plotted at the critical point $\Gamma = \Gamma_c$ against TL^z, all points collapse onto a scaling function $\tilde{U}$ provided that z is chosen correctly. Although it was not possible to determine the dynamical critical exponent z directly from a data collapse, Fig. 7.15 shows that with the choice of the mean-field prediction $z^{(\text{MF})} = \frac{\sigma}{2} = \frac{\alpha-1}{2}$ of Eq. (7.40) an acceptable data collapse can be achieved for $\alpha = 2.0$, 2.5, and 2.75 [Fig. 7.15(a-c)].
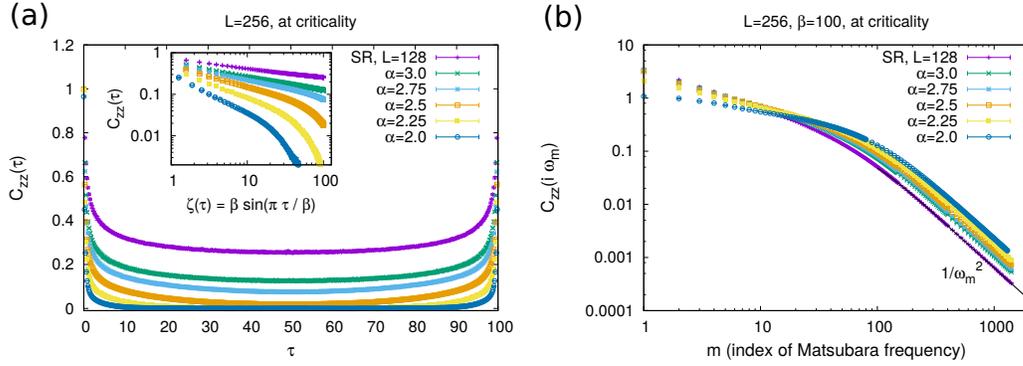
Fig. 7.13: (a) Decay of the critical spin-spin correlation function in imaginary time $C_{zz}(\tau)$. Inverse temperature $\beta = 100$. The inset shows a double-logarithmic plot versus the cord length $\zeta(\tau)$, illustrating the change of power-law exponent η_τ with α. (b) Fourier transform $C_{zz}(i\omega_m)$ of $C_{zz}(\tau)$ as a function of Matsubara indices m (where $\omega_m = \frac{2\pi m}{\beta}$). The dashed line shows the generic asymptotic decay $\sim 1/m^2$ for large Matsubara indices.
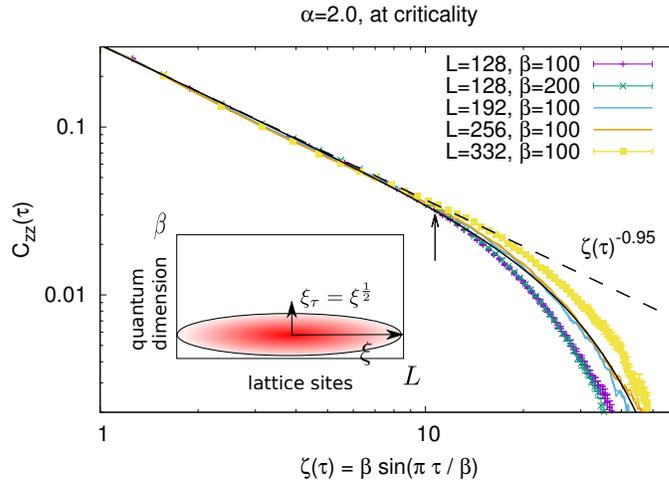
Fig. 7.14: Imaginary time spin-spin correlation function at the QCP for the inverse-square ferromagnet ($\alpha = 2.0$). Error bars for $L = 192$ and $L = 256$ have been omitted for better visibility. The inset shows the $d+1$ dimensional effective classical system to which the LRTFI model has been mapped in the path integral formalism. The QCP is highly anisotropic with the correlation length in imaginary time growing like $\xi_\tau \sim \xi^{\frac{1}{2}}$.
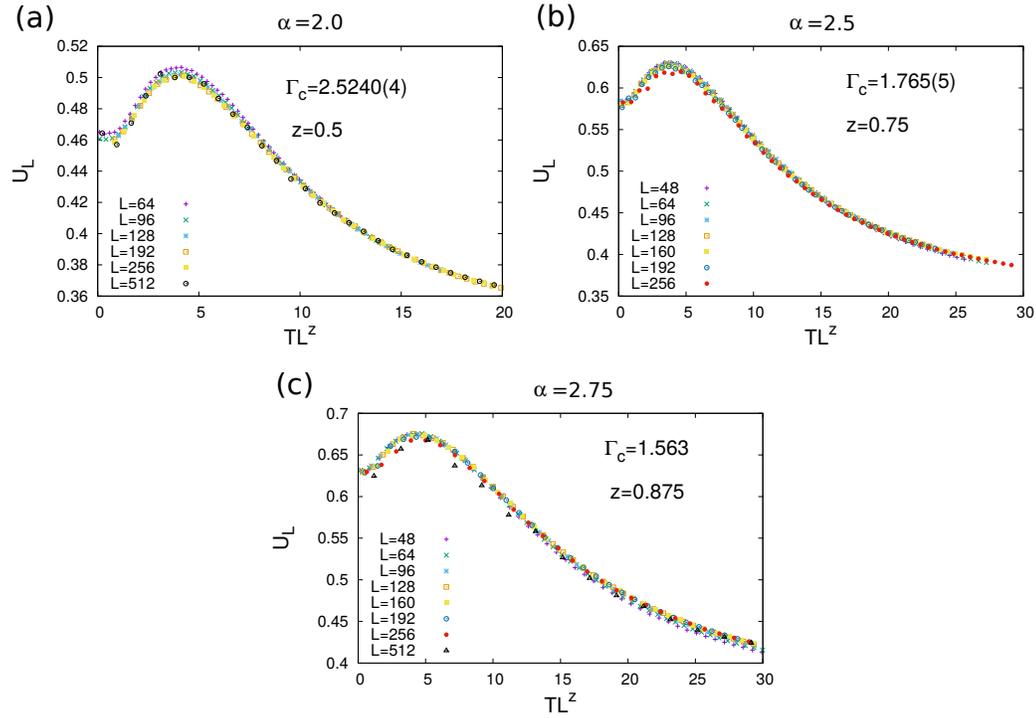
Fig. 7.15: Data collapse of the Binder cumulant $U_L = \frac{\langle m^2 \rangle^2}{\langle m^4 \rangle}$ atop the quantum critical point for $\alpha = 2.0$(a), $\alpha = 2.5$(b), and $\alpha = 2.75$(c) with dynamical critical exponent $z^{(\mathrm{MF})} = \frac{\sigma}{2} = \frac{\alpha-1}{2}$.

A model that is closely related to the $1/r^2$ ferromagnetic transverse-field Ising model is the dissipative short-range transverse-field Ising model. Introducing dissipation by coupling the spins to a thermal bosonic bath and integrating out the bosons leads to long-range interactions in imaginary time τ that decay like $1/\zeta(\tau)^2$ where $\zeta(\tau)$ is the conformal length [211]. The critical properties in such a case are similar, with space and imaginary time coordinates interchanged, which leads to a dynamical critical exponent of $z = 2$.

Chapter 8

Introduction to the Hubbard model

The Hubbard model [212–214] provides a simplified theoretical framework for the description of strongly correlated electron systems. The term "strongly correlated" refers to the situation where the independent electron description of band theory fails and the electronic bands themselves depend on the electron filling. In solid state physics it was introduced by John Hubbard for describing d-electrons in transition metals [213, 215] and independently by Kanamori as a model of itinerant ferromagnetism [214]. Since then it has become a paradigmatic model for the description of the Mott metal-insulator transition [212, 216, 217], where a material that should be a metal due to band structure considerations becomes an insulator as a consequence of strong electron interactions. The discovery of high-temperature superconductivity in cuprate compounds [218] and later in iron based layered superconductors [219] has further spurred the interest in the 2D Hubbard model since it is believed to exhibit some of the basic phenomena that are observed in these unconventional superconductors [220]. In theoretical chemistry the Hubbard model is known as the Pariser-Parr-Pople model [216, Chapt. 2.4] and has been used even earlier for modeling unsaturated hydrocarbons.

To write down the Hubbard model in second quantized form, we set out with the general Hamiltonian for fermionic particles in an external potential $V(\mathbf{r})$ that interact pairwise through the potential $U(\mathbf{r} - \mathbf{r}')$:

$$
\begin{aligned}
\mathcal{H} = &\sum_{\sigma=\uparrow,\downarrow} \int d\mathbf{r}\, \hat{\Psi}_\sigma^\dagger(\mathbf{r}) \left[-\frac{\hbar^2}{2m}\nabla^2 + V(\mathbf{r}) \right] \hat{\Psi}_\sigma(\mathbf{r}) \\
&+ \frac{1}{2}\sum_{\sigma,\sigma'=\uparrow,\downarrow} \int d\mathbf{r}\, d\mathbf{r}'\, \hat{\Psi}_\sigma^\dagger(\mathbf{r})\hat{\Psi}_{\sigma'}^\dagger(\mathbf{r}')U(\mathbf{r} - \mathbf{r}')\hat{\Psi}_{\sigma'}(\mathbf{r}')\hat{\Psi}_\sigma(\mathbf{r})
\end{aligned}
\tag{8.1}
$$

Here, $V(\mathbf{r})$ is the potential of the ionic cores of the crystal and $U(\mathbf{r} - \mathbf{r}')$ is the Coulomb repulsion between electrons. The field operators $\hat{\Psi}_\sigma(\mathbf{r})$ obey fermionic anti-commutation relations

$$
\left\{ \hat{\Psi}_\sigma(\mathbf{r}), \hat{\Psi}_{\sigma'}^\dagger(\mathbf{r}') \right\} = \delta_{\sigma,\sigma'}\delta(\mathbf{r} - \mathbf{r}').
\tag{8.2}
$$

They are expanded as

$$\hat{\Psi}_\sigma(\mathbf{r}) = \sum_{i,\alpha} w_{i,\sigma}^{(\alpha)}(\mathbf{r})\, \hat{c}_{i,\sigma} \tag{8.3}$$

in terms of the single-particle basis of localized Wannier functions $w_{i,\sigma}^{(\alpha)}(\mathbf{r}) \equiv w_\sigma^{(\alpha)}(\mathbf{r}-\mathbf{r}_i)$, which are orthogonal on different sites i and between different bands α. Inserting Eq. (8.3) into Eq. (8.1) and using the orthogonality relations of Wannier functions, a second quantized Hamiltonian is obtained.

The Hubbard model involves a number of strong approximations: Only a single effective band[1] is considered, which is based on the assumption that just one band (or a small number of bands) crosses the Fermi level. Furthermore, from the Coulomb interactions, only the on-site repulsion

$$U = \int d^d\mathbf{r}\, d^d\mathbf{r}'\, |w_{i\sigma}(\mathbf{r})|^2 \frac{e^2}{|\mathbf{r}-\mathbf{r}'|} |w_{i-\sigma}(\mathbf{r}')|^2 \tag{8.4}$$

is retained, which neglects off-site density-density interactions, ferromagnetic direct exchange and Coulomb assisted hopping terms [2, Chapt. 5.3]. One sees from Eq. (8.4) that $U > 0$. Attractive interactions with $U < 0$ in Eq. (8.6) have also been considered in condensed matter systems [24], but in this case the Hubbard model is an effective model similar to the reduced BCS Hamiltonian [221] and describes a net electron-electron attraction mediated e.g. by a local phonon mode [117]. The overlap of two neighbouring atomic Wannier functions leads to a hopping matrix element

$$t_{ij} = -\int d^d\mathbf{r}\, w_{i\sigma}^*(\mathbf{r}) \left[-\frac{\hbar^2}{2m}\nabla^2 \right] w_{j\sigma}(\mathbf{r}) \tag{8.5}$$

between nearest neighbour sites $\langle i,j \rangle$. With these approximations we obtain the Hubbard Hamiltonian in second quantized form as

$$\begin{aligned}
\mathcal{H} &= \mathcal{H}_t + \mathcal{H}_U - \mu\hat{N} \\
&= -\sum_{\langle i,j\rangle,\sigma=\uparrow,\downarrow} t_{ij} \left(\hat{c}_{i,\sigma}^\dagger \hat{c}_{j,\sigma} + \text{h.c.} \right) + U\sum_i n_{i,\uparrow}\hat{n}_{i,\downarrow} - \sum_{i,\sigma=\uparrow,\downarrow} \mu_\sigma \hat{n}_{i,\sigma},
\end{aligned} \tag{8.6}$$

where the creation (annihilation) operators $\hat{c}_{i,\sigma}^\dagger$ $(\hat{c}_{i,\sigma})$ of a single-band fermion at site i with spin σ obey canonical commutation relations $\{\hat{c}_{i,\sigma}^\dagger, \hat{c}_{j,\sigma'}\} = \delta_{i,j}\delta_{\sigma,\sigma'}$, and $\hat{n}_{i,\sigma} = \hat{c}_{i,\sigma}^\dagger \hat{c}_{i,\sigma}$ is the number operator. The chemical potential $\mu \equiv \mu_\uparrow = \mu_\downarrow$ fixes the band filling $\langle n \rangle = (\langle \hat{N}_\uparrow \rangle + \langle \hat{N}_\downarrow \rangle)/N_s \in [0,2]$, where N_s is the number of lattice sites and $\hat{N}_\sigma = \sum_i \hat{n}_{i,\sigma}$ counts the total number of particles with spin σ. Due to the Pauli principle there are at most two particles of opposite spin per lattice site. The special

---

[1] For non-Bravais lattices, which have several bands, what is meant by this approximation is rather that we consider only a single orbital, i.e. a single Wannier function per lattice site.

point of half filling with an average particle number $\langle \hat{n}_i \rangle = \langle \hat{n}_{i,\uparrow} + \hat{n}_{i,\downarrow} \rangle = 1$ corresponds to $\mu_\uparrow = \mu_\downarrow = \frac{U}{2}$ for any temperature.[2]

The Hubbard Hamiltonian describes the interplay of delocalization, due to the kinetic term $\mathcal{H}_t$, and interactions $\mathcal{H}_U$, which tend to localize particles. By Fourier transforming to creation operators for single-particle eigenstates, i.e. eigenstates of $\mathcal{H}_t$,

$$\hat{c}_{\mathbf{k},\sigma} = \frac{1}{\sqrt{N_s}} \sum_{\mathbf{i}} e^{i\mathbf{k}\cdot\mathbf{r}_i} \hat{c}_{\mathbf{i},\sigma}, \quad \text{with} \quad k_{x,y} = \frac{2\pi}{N_{x,y}} n_{x,y}, \frac{-N_{x,y}}{2} \leq n_{x,y} < \frac{N_{x,y}}{2}, \quad (8.7)$$

we obtain the Hubbard Hamiltonian in momentum space

$$\mathcal{H} = \sum_{\mathbf{k},\sigma=\uparrow,\downarrow} (\varepsilon_{\mathbf{k}} - \mu)\hat{c}^\dagger_{\mathbf{k},\sigma}\hat{c}_{\mathbf{k},\sigma} + \frac{U}{N_s} \sum_{\mathbf{k},\mathbf{k}',\mathbf{q}} \hat{c}^\dagger_{\mathbf{k}+\mathbf{q}/2,\uparrow}\hat{c}^\dagger_{-\mathbf{k}+\mathbf{q}/2,\downarrow}\hat{c}_{\mathbf{k}'+\mathbf{q}/2,\uparrow}\hat{c}_{-\mathbf{k}'+\mathbf{q}/2,\downarrow}, \quad (8.8)$$

where $\varepsilon_{\mathbf{k}} = -2t(\cos(k_x a) + \cos(k_y a))$ is the single-particle band structure of a square lattice with lattice spacing a. The ground state of the non-interacting case ($U = 0$), the so-called *band limit*, is simply the Fermi sea of single-particle states, $|FS\rangle = \prod_{\mathbf{k},\sigma} c^\dagger_{\mathbf{k},\sigma}|0\rangle$, filled up to the Fermi energy. The opposite szenario $t/U = 0$ is the *atomic limit*. Here, the ground state manifold is hugely degenerate, consisting of all configurations with only singly-occupied lattice sites.

Over the last decade it has become possible to simulate the Fermi-Hubbard model with ultracold atoms in optical lattices [222]. Unlike in complicated solid state materials, here, the Hubbard model comes much closer to a true *ab initio* Hamiltonian and both the repulsive [20] and the attractive [22] Hubbard model can be realized microscopically. The two electronic spin states are emulated as two distinct hyperfine states of a fermionic atom species such as ^{6}Li or ^{40}K [10]. For ultracold quantum gases the low collision energies are not sufficient to overcome the centrifugal barrier for non-vanishing relative angular momentum. Therefore only *s*-wave scattering is relevant for the description and the scattering potential $U(\mathbf{r} - \mathbf{r})$ can be replaced by an effective pseudo-potential [10]

$$U(\mathbf{r} - \mathbf{r}') = \frac{4\pi\hbar^2 a_s}{2m_r}\delta(\mathbf{r} - \mathbf{r}'), \quad (8.9)$$

which is parametrized by the *s*-wave scattering length a_s in three dimensions. Here, m_r is the reduced mass in the two-particle scattering problem.

For weak interactions and deep optical lattices, the on-site interaction U is approximately [223]

$$U = \frac{4\pi\hbar^2 a_s}{2m_r} \int d^d\mathbf{r}|w(\mathbf{r})|^4, \quad (8.10)$$

---

[2] If the interaction term is written in the particle-hole symmetric form $H_U = U\sum_i(n_{i,\uparrow} - \frac{1}{2})(n_{i,\downarrow} - \frac{1}{2})$, half filling occurs at $\mu = 0$ for any temperature or interaction strength U.
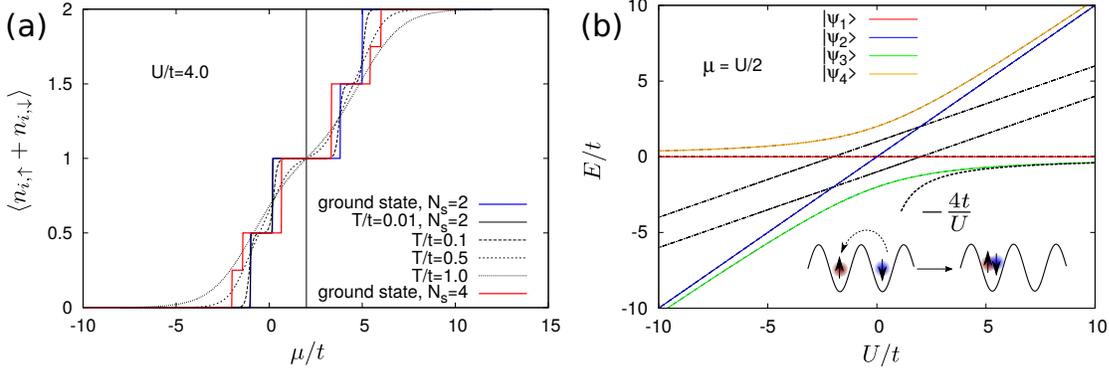
Fig. 8.1: (a) Equation of state $\langle n \rangle(\mu)$ of the two-site and four-site Fermi-Hubbard model for $U/t = 4$. The plateau at half filling $\langle n \rangle = 1$ evolves in the thermodynamic limit and for larger Hubbard-U into the Mott phase, characterized by zero compressibility $\kappa = \frac{\partial \langle n \rangle}{\partial \mu} = 0$. (b) Spectrum of the two-site Hubbard model. The labelled states are in the particle number sector $N_\uparrow = N_\downarrow = 1$.

where $w(\mathbf{r})$ is the Wannier function of the lowest band. Both attractive and repulsive tunable interactions can be realized by controlling the sign and magnitude of the atomic scattering length a_s with the help of a magnetic-field Feshbach resonance [10]. Only for deep optical lattices, where the system can be safely restricted to the lowest band, the δ-function potential Eq. (8.9) in combination with the projection onto the lowest band, Eq. (8.10), give a good approximation for U. For shallower lattices or strong inter-atomic interactions, where the s-wave scattering length a_s exceeds the lattice spacing, higher bands need to be included in the derivation of effective Hubbard parameters [224].

8.1   Two-site Hubbard model

Some of the essential features of the Hubbard model can already be illustrated by a two-site system [225] since it contains the most relevant energy scales: the on-site interaction U and the spin-exchange coupling $J = \frac{4t^2}{U}$. The eigenstates in the particle number sector of one $\uparrow$- and one $\downarrow$-particle are

$$|\psi_1\rangle = \frac{1}{\sqrt{2}} \left(|\uparrow, \downarrow\rangle + |\downarrow, \uparrow\rangle \right), \tag{8.11a}$$

$$|\psi_2\rangle = \frac{1}{\sqrt{2}} \left(|\uparrow\downarrow, 0\rangle - |0, \uparrow\downarrow\rangle \right), \tag{8.11b}$$

$$|\psi_3\rangle \sim 2t \left(|\uparrow\downarrow, 0\rangle + |0, \uparrow\downarrow\rangle \right) + E_4 \left(|\uparrow, \downarrow\rangle - |\downarrow, \uparrow\rangle \right), \tag{8.11c}$$

$$|\psi_4\rangle \sim 2t\left(|\uparrow\downarrow, 0\rangle + |0, \uparrow\downarrow\rangle\right) + E_3(|\uparrow, \downarrow\rangle - |\downarrow, \uparrow\rangle), \tag{8.11d}$$

with energies $E_1 = 0$, $E_2 = U$, $E_{3/4} = \frac{1}{2}\left(U \mp \sqrt{16t^2 + U^2}\right)$. Importantly, the ground state is not the localized triplet state $|\psi_1\rangle$, but rather the singlet state $|\psi_3\rangle$, which has a small admixture of a doublon-hole pair. It turns out that fluctuations in the double occupancy allow to lower the kinetic energy, and expanding E_3 for $U/t \gg 1$, we obtain the energy difference $E_3 - E_1 \approx -\frac{4t^2}{U}$ and $|\psi_3\rangle \approx \frac{1}{\sqrt{2}}(|\uparrow, \downarrow\rangle - |\downarrow, \uparrow\rangle) + \mathcal{O}(t/U)$, which shows that the amplitude of the doublon-hole pair is small although it is decisive in favouring an antiferromagnetic spin configuration. This is the *kinetic exchange* mechanism of antiferromagnetism [2, Chapt.5]: If neighbouring spins are antiparallel, a virtual hopping process can create a doublon-hole pair which costs energy U; in second order perturbation theory, the ground state energy is lowered by $-t^2/U$, which outweighs the energy cost of the on-site interaction. There are four such pathways that lead from an initial antiferromagnetic arrangement through a doublon-hole configuration back to an antiferromagnetic arrangement, giving a total energy reduction of $-\frac{4t^2}{U}$. The state $|\psi_1\rangle$ has zero kinetic energy due to the fermionic anticommutation relations and $|\psi_2\rangle$ is the simplest example of a so-called η-pair, which will be discussed below. $|\psi_1\rangle$ is a spin triplet state, while the states $|\psi_2\rangle$, $|\psi_3\rangle$ and $|\psi_4\rangle$ are spin singlets. Their respective eigenenergies foreshadow that the Hubbard model in the thermodynamic limit has a charge gap, the Mott gap $\Delta \approx U$, while the spin sector is gapless. The width of the plateau at $\langle n \rangle = 1$ in the equation of state $\langle n \rangle(\mu)$ shown in Fig. 8.1(a), which is characterized by zero compressibility $\kappa = \frac{\partial \langle n \rangle}{\partial \mu} = 0$, is the precursor of the Mott gap that develops in the thermodynamic limit due to large repulsion between opposite spins.

The two-site Hubbard model has been realized experimentally by preparing two ultracold fermionic atoms in an isolated double-well potential [226]. Furthermore, the equation of state of the two-dimension repulsive Hubbard model was recently measured through high-resolution imaging of ultracold fermionic atoms in an optical lattice at high temperatures [227].

8.2   Symmetries

Except in one dimension, where a Bethe ansatz [228] can be used, there is no exact solution of the Hubbard model. Rigorously proven facts that constrain the phase diagram of the Hubbard model in higher dimensions derive from its symmetries [Chapt. 2][216].

8.2.1 Particle-hole symmetry

At half filling and on a bipartite lattice, i.e. a lattice that can be divided into two sublattices $\mathcal{A}$ and $\mathcal{B}$ such that the hopping integral $t_{\mathbf{ij}}$ vanishes if the sites $\mathbf{i}$ and $\mathbf{j}$ both belong to the same sublattice, the Hubbard model is symmetric under the particle-hole transformation

$$c_{\mathbf{i},\sigma} \to (-1)^{\mathbf{i}} c_{\mathbf{i},\sigma}^{\dagger} \quad \text{with} \quad (-1)^{\mathbf{i}} = \begin{cases} +1 \text{ for } \mathbf{i} \in A \\ -1 \text{ for } \mathbf{i} \in B. \end{cases} \tag{8.12}$$

The ground state and all excited states are invariant under this canonical transformation, which has consequences for the correlation functions [229]. For example the one-body density matrix $\rho_\sigma(\mathbf{i},\mathbf{j}) = \langle c_{\mathbf{i},\sigma}^{\dagger} c_{\mathbf{j},\sigma} \rangle$ vanishes in a translationally invariant system whenever two sites $\mathbf{i} \neq \mathbf{j}$ belong to the same sublattice, since then $\langle c_{\mathbf{i},\sigma} c_{\mathbf{j},\sigma}^{\dagger} \rangle = \langle c_{\mathbf{i},\sigma}^{\dagger} c_{\mathbf{j},\sigma} \rangle \left[(-1)^{\mathbf{i}} \right]^2 = -\langle c_{\mathbf{j},\sigma} c_{\mathbf{i},\sigma}^{\dagger} \rangle$; in particular, $\rho_\sigma(\mathbf{i},\mathbf{i}) = \frac{1}{2}$, so that half filling is imposed locally for every site $\mathbf{i}$. For the momentum distribution function $n_\sigma(\mathbf{k}) = \langle c_{\mathbf{k},\sigma}^{\dagger} c_{\mathbf{k},\sigma} \rangle$ this implies

$$n(\mathbf{Q} - \mathbf{k}) = 1 - n(\mathbf{k}) \tag{8.13}$$

with the nesting vector $\mathbf{Q} \equiv (\pi/a, \pi/a)$ of the square lattice. As a consequence, on the loci in momentum state where the nesting condition $\mathbf{k} = \mathrm{mod}(\mathbf{Q} - \mathbf{k}, \mathbf{G})$, with $\mathbf{G}$ a reciprocal lattice vector, is satisfied the momentum distribution function alway has the value $\frac{1}{2}$. This happens on the non-interacting Fermi surface at half filling, which is depicted in Fig. 8.3.

8.2.2 Spin and pseudospin symmetry, η-pairing

The Hubbard Hamiltonian Eq. (8.6) is invariant under global spin rotations which are generated by the $SU(2)$ algebra

$$\begin{aligned} \hat{S}_+ &= \frac{1}{2} \sum_{\mathbf{i}} c_{\mathbf{i},\uparrow}^{\dagger} c_{\mathbf{i},\downarrow}, \\ \hat{S}_- &= \hat{S}_+^{\dagger}, \\ \hat{S}^z &= \frac{1}{2} \sum_{\mathbf{i}} \left(n_{\mathbf{i},\uparrow} - n_{\mathbf{i},\downarrow} \right) \end{aligned} \tag{8.14}$$

where $\hat{S}_{\pm} = \hat{S}^x \pm i\hat{S}^y$ and the global spin operators are defined as $S^\alpha = \sum_i S_i^\alpha$ based on the local spin operators

$$\mathbf{S}_i = (S_i^x, S_i^y, S_i^z) = \sum_{\alpha,\beta} c_{i,\alpha}^{\dagger} \vec{\sigma}_{\alpha,\beta} c_{i,\beta}, \tag{8.15}$$

with $\vec{\sigma} = (\sigma_x, \sigma_y, \sigma_z)$ the Pauli matrices.

On a bipartite lattice the Hubbard model has an additional global charge $SU(2)$ pseudospin symmetry [49], which is generated by

$$\hat{\eta}_+ = \sum_{\mathbf{i}\in\mathcal{A}} c_{\mathbf{i},\uparrow}^\dagger c_{\mathbf{i},\downarrow}^\dagger - \sum_{\mathbf{i}\in\mathcal{B}} c_{\mathbf{i},\uparrow}^\dagger c_{\mathbf{i},\downarrow}^\dagger = \sum_{\mathbf{i}} (-1)^{\mathbf{i}} c_{\mathbf{i},\uparrow}^\dagger c_{\mathbf{i},\downarrow}^\dagger$$

$$\hat{\eta}_- = \hat{\eta}_+^\dagger \tag{8.16}$$

$$\hat{\eta}_0 = \frac{1}{2} \sum_{\mathbf{i}} \left(n_{\mathbf{i},\uparrow} + n_{\mathbf{i},\downarrow} - 1 \right).$$

The generators obey the commutation relations $[\hat{\eta}_0, \hat{\eta}_\pm] = \pm\hat{\eta}_\pm$, $[\hat{\eta}_+, \hat{\eta}_-] = 2\hat{\eta}_0$ and therefore form an $SU(2)$ algebra. $\hat{\eta}_z$ measures the deviation from half filling. $\hat{\eta}_+$ and $\hat{\eta}_-$ are ladder operators of the Hubbard Hamiltonian in the sense that

$$[H, \eta_\pm] = \pm(U - 2\mu))\eta_\pm, \quad [H, \eta_0] = 0. \tag{8.17}$$

Exactly at half filling, $\mu = \frac{U}{2}$ and the Hamiltonian $\mathcal{H}$ commutes with all generators of the pseudospin symmetry Eq. (8.16) just like it commutes with the spin generators of Eq. (8.14), so that the system is invariant under global rotations of the pseudospin. In momentum space the "η-operator" for a d-dimensional hypercubic lattice reads

$$\eta_+ = \sum_{\mathbf{k}} c_{\vec{\pi}-\mathbf{k},\downarrow}^\dagger c_{\mathbf{k},\uparrow}^\dagger \quad \text{with} \quad \vec{\pi} = (\underbrace{\pi, \pi, \ldots, \pi}_{d\text{ times}}). \tag{8.18}$$

When acting on an eigenstate of the Hamiltonian, it generates a new eigenstate with one more spin-up and one more spin-down particle and an increase of the total momentum by $\vec{\pi}$. These so-called "η-pairing states", which were discovered by C.N. Yang [230], form a class of exact excited states of the Hubbard model. In particular,

$$\psi_N = \mathcal{N}(\eta_+)^N |\text{vac}\rangle \tag{8.19}$$

is an eigenstate with N η-pairs and total momentum $N\vec{\pi}$. The essential condition for the existence of η-pairing is that the single-particle dispersion relation satisfies [230]

$$\epsilon(\mathbf{k}) + \epsilon(\vec{\pi} - \mathbf{k}) = \text{const.}, \tag{8.20}$$

which is the case for hypercubic lattices. Thus, η-pairs are peculiar to lattice models and absent in continuum models.

The generators of the first $SU(2)$ symmetry (8.14) and the second set of generators (8.16) commute with one another so that the Hubbard model has an enlarged $SO(4) = SU(2) \times SU(2)/\mathbb{Z}_2$ symmetry at half filling, as discussed by Yang and Zhang [49].

8.2.3   Relation between attractive and repulsive Hubbard model

On a bipartite lattice, a spin-down particle-hole transformation, the so-called Shiba transformation [231, 232]

$$c_{\mathbf{i},\downarrow}^\dagger \to (-1)^{\mathbf{i}} c_{\mathbf{i},\downarrow}$$

$$c_{\mathbf{i},\uparrow} \to c_{\mathbf{i},\uparrow}. \tag{8.21}$$

maps the attractive $(-|U|)$ to the repulsive $(+|U|)$ Hubbard model and vice versa. It leaves the kinetic part of the Hubbard Hamiltonian invariant

$$- t \sum_{\langle \mathbf{i},\mathbf{j} \rangle} \sum_{\sigma=\uparrow,\downarrow} \left(c_{\mathbf{i},\sigma}^{\dagger} c_{\mathbf{j},\sigma} + c_{\mathbf{j},\sigma}^{\dagger} c_{\mathbf{i},\sigma} \right) \tag{8.22}$$

$$\rightarrow - t \sum_{\langle \mathbf{i},\mathbf{j} \rangle} \left(\underbrace{(-1)^{\mathbf{i}+\mathbf{j}} c_{\mathbf{i},\downarrow} c_{\mathbf{j},\downarrow}^{\dagger}}_{(-1)^{\mathbf{i}+\mathbf{j}}(-1)c_{\mathbf{j},\downarrow}^{\dagger} c_{\mathbf{i},\uparrow}} + \underbrace{(-1)^{\mathbf{i}+\mathbf{j}} c_{\mathbf{j},\downarrow} c_{\mathbf{i},\downarrow}^{\dagger}}_{(-1)^{\mathbf{i}+\mathbf{j}}(-1)c_{\mathbf{i},\downarrow}^{\dagger} c_{\mathbf{j},\downarrow}} + c_{\mathbf{i},\uparrow}^{\dagger} c_{\mathbf{j},\uparrow} + c_{\mathbf{j},\uparrow}^{\dagger} c_{\mathbf{i},\uparrow} \right) \tag{8.23}$$

$$= -t \sum_{\langle \mathbf{i},\mathbf{j} \rangle} \left(c_{\mathbf{i},\sigma}^{\dagger} c_{\mathbf{j},\sigma} + c_{\mathbf{j},\sigma}^{\dagger} c_{\mathbf{i},\sigma} \right), \tag{8.24}$$

where due to the bipartiteness of the hopping terms $(-1)^{\mathbf{i}+\mathbf{j}} = -1$, which cancels the sign coming from the commutation of fermionic operators. At the same time, the transformation changes the sign of the Hubbard interaction

$$U \left(n_{i,\uparrow} - \frac{1}{2} \right) \left(n_{i,\downarrow} - \frac{1}{2} \right) \rightarrow -U \left(n_{i,\uparrow} - \frac{1}{2} \right) \left(n_{i,\downarrow} - \frac{1}{2} \right) \tag{8.25}$$

and converts the chemical potential term into an external Zeeman field

$$-\mu \sum_{\mathbf{i}} (n_{\mathbf{i},\uparrow} + n_{\mathbf{i},\downarrow}) \rightarrow -\mu \sum_{\mathbf{i}} (n_{\mathbf{i},\uparrow} - n_{\mathbf{i},\downarrow}) - \mu \underbrace{\sum_{\mathbf{i}} 1}_{N_s}. \tag{8.26}$$

By this transformation, a repulsive Hubbard model with spin-imbalance is equivalent to an attractive Hubbard model doped away from half filling. Exactly at half filling and in the spin-balanced case ($\mu_{\uparrow} = \mu_{\downarrow}$), the repulsive and the attractive Hubbard model on a bipartite lattice are identical, provided that observables are transformed according to Eq. (8.21). Related observables in the attractive and repulsive Hubbard model are listed in Tab. 8.1. (See Ref. [233] for a complete table of mappings between observables in the positive- and negative-U Hubbard model.) The generators of the spin $SU(2)$ symmetry Eqs. (8.14) and the pseudospin $SU(2)$ symmetry Eqs. (8.16) are also mapped onto each other by the transformation Eq. (8.21).

Even though the attractive and repulsive Hubbard model can be related by a spin-down particle-hole transformation and thus are mathematically equivalent, their physical realization is different and it has been argued that the attractive Hubbard model offers experimental advantages for the observation of its phases in ultracold atom experiments [234], spin imbalance being easier to control than doping, at least in harmonically trapped clouds.

The relation between the doped attractive Hubbard model and the equivalent spin-imbalanced repulsive one has been explored in the two complementary cold atoms experiments of, respectively, Refs. [22] and [21], where canted antiferromagnetic correlations were observed.

attractive $(-|U|)$	repulsive $(+|U|)$
Potential energy	Potential energy
$-U\left(n_{i,\uparrow}-\frac{1}{2}\right)\left(n_{i,\downarrow}-\frac{1}{2}\right)$	$+U\left(n_{i,\uparrow}-\frac{1}{2}\right)\left(n_{i,\downarrow}-\frac{1}{2}\right)$
Zeeman field	Chemical potential
$h\sum_i(n_{i,\uparrow}-n_{i,\downarrow})$	$h\sum_i(n_{i,\uparrow}+n_{i,\downarrow})-hN_s$
CDW	AFM (zz spin components)
$S_{\mathrm{CDW}}=\sum_{ij}(-1)^{\mathbf{i}+\mathbf{j}}n_i n_j$	$S^{zz}_{\mathrm{AFM}}=\sum_{ij}(-1)^{\mathbf{i}+\mathbf{j}}m_i m_j+\sum_{ij}(-1)^{\mathbf{i}+\mathbf{j}}\left(m_i+m_j+3\right)$
s-wave SC	AFM (xy spin components)
$P_s=\sum_{ij}c^{\dagger}_{i,\uparrow}c^{\dagger}_{i,\downarrow}c_{j,\downarrow}c_{j,\uparrow}$	$S^{+-}_{\mathrm{AFM}}=\sum_{ij}(-1)^{\mathbf{i}+\mathbf{j}}c^{\dagger}_{i,\uparrow}c_{i,\downarrow}c^{\dagger}_{j,\downarrow}c_{j,\uparrow}$
Particle number	Magnetization
$\sum_i(n_{i,\uparrow}+n_{i,\downarrow})$	$\sum_i(n_{i,\uparrow}-n_{i,\downarrow})+N_s$
Staggered magnetization	Staggered particle number
$\sum_i(-1)^{\mathbf{i}}(n_{i,\uparrow}-n_{i,\downarrow})$	$\sum_i(-1)^{\mathbf{i}}(n_{i,\uparrow}+n_{i,\downarrow})-\sum_i(-1)^{\mathbf{i}}$

Table 8.1: Observables in the attractive and repulsive Hubbard model, which are related by the spin-down particle-hole transformation $c_{i,\downarrow}\to(-1)^{\mathbf{i}}c^{\dagger}_{i,\downarrow}$. The operator $m_i\equiv n_{i,\uparrow}-n_{i,\downarrow}$ is the local magnetization and N_s is the total number of lattice sites.

8.3 Phase diagram of the 2D attractive Hubbard model

The simplified microsopic model, which is believed to capture essential aspects of the cuprate high-T_c superconductors, is the *repulsive* Hubbard model [235]. Nonetheless, there are several analogies to the physics of high-T_c superconductors which make also the *attractive* Hubbard model an interesting theoretical laboratory, although there is no direct microscopic connection.

1. It is believed that the key to understanding the intricate phase diagram of high-T_c superconductors [5] and to achieving superconductivity at room temperature lies in the enigmatic *pseudogap phase* where, below a characteristic temperature T^*, a partial gap in spectroscopic data appears [5]. The attractive Hubbard model features a similar (but well-understood) "pseudogap" in the single-particle spectral function, which is associated with "preformed Cooper pairs". Here, the
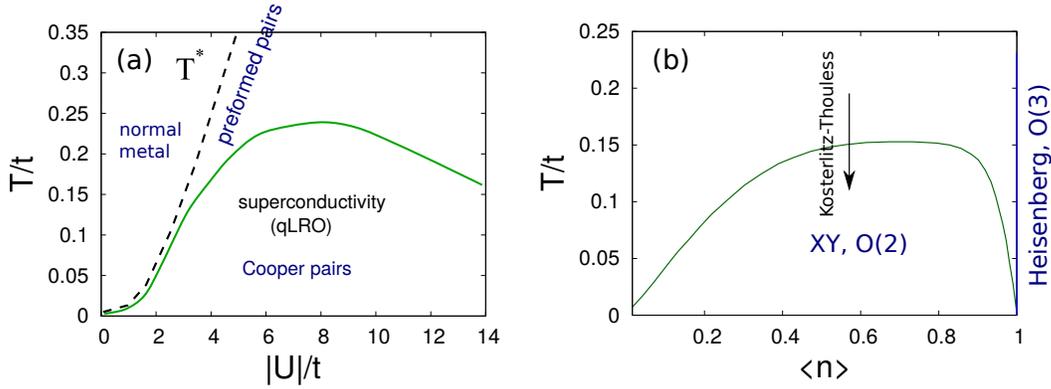
Fig. 8.2: Schematic phase diagram of the attractive Hubbard model in $d = 2$ dimensions. The temperature T_{KT} (green line) of the Kosterlitz-Thouless transition to a quasi-longe-range ordered (qLRO) superconducting state is shown in (a) as a function of attractive interactions $|U|/t$ at filling $\langle n \rangle = 0.7$ and in (b) as a function of filling $\langle n \rangle$. Data curves are reproduced from Refs. [25, 26].

    gap is due to the binding energy that needs to be provided to break a preformed pair (or preformed magnetic moment, in the language of the repulsive Hubbard model).

2. Conventional BCS type superconductors are characterized by large overlapping Cooper pairs [221] which extend over several hundred lattice spacings. A striking characteristic of high-T_c superconductors, on the other hand, is their short coherence length which can be interpreted as a pair size [236]. In the attractive Hubbard model the pair size is tunable as a function of $|U|$, with the extreme case of on-site singlet pairs for large $|U|$.

3. Superconductivity in cuprates is driven by a gain in kinetic energy [237] rather than potential energy as in conventional BCS type superconductors [221]. The same is true for the $U < 0$ Hubbard model in the regime $|U| > W$ where W is the bandwidth.

    The phase diagram of the 2D attractive Hubbard model [24–26] is summarized schematically in Fig. 8.2.

    We first discuss the case of half filling $\langle n \rangle = 1$. Here, the Hubbard model has a three-component $O(3)$ order parameter, namely the Néel ordering vector of the antiferromagnetic Heisenberg model which can point in any direction on a sphere, and the Mermin-Wagner theorem [238], which states that there is no spontaneous symmetry breaking of a continuous order parameter at finite temperature in $d \leq 2$ spatial dimensions, precludes true long-range order at any finite temperature. At zero temperature there is long-range antiferromagnetic order due to the *nesting* property of the Fermi surface at half filling, where large parallel sections of the Fermi surface are

connected by the same momentum vector $\mathbf{Q} = [(\pi/a, \pi/a) \quad \text{or} \quad (-\pi/a, \pi/a)]$, which is called the nesting vector (see Fig. 8.3). Furthermore, on the square lattice, the density of states $\rho(\varepsilon)$ of the tight binding band structure $\varepsilon(\mathbf{k})$ diverges logarithmically (see Fig. 8.3) at the center of the band [2, Chapt. 4],[239]

$$\rho(\varepsilon) = \sum_{\mathbf{k}} \delta[\varepsilon - \varepsilon(\mathbf{k})] \sim \frac{1}{2\pi^2 t} \ln \frac{t}{|\varepsilon|}. \tag{8.27}$$

This divergence is due to a saddle point van Hove singularity at $\varepsilon = 0$. Thus, a half-filled Fermi system on the square lattice is very susceptible to interactions, which predominantly scatter particles with a momentum transfer $\mathbf{Q} = (\pi/a, \pi/a)$. As a result, the ground state of the half-filled repulsive Hubbard model on the square lattice exhibits antiferromagnetic long-range order for any $U > 0$ [120].

By virtue of the Shiba transformation, the existence of antiferromagnetic long-range order in the ground state of the *repulsive* Hubbard model implies (cf. Tab. 8.1) the existence of simultaneous long-range superconducting (SC) and chequerboard charge-density wave (CDW) order in the ground state of the *attractive* Hubbard model [24]. This coexistence of diagonal (CDW) and off-diagonal (SC) long-range order is a form of "supersolidity", albeit a trivial one since it is not stabilized by interactions and, viewed in the language of the repulsive Hubbard model, has its origin in the fact that the three-component Néel vector can spontaneously point in any direction, its xy-components being associated with SC and its zz-component corresponding to CDW in the attractive Hubbard model.

Next, we consider the phase diagram away from half filling, i.e. in the regime of finite doping. As can be shown by a particle-hole transformation, the phase diagram
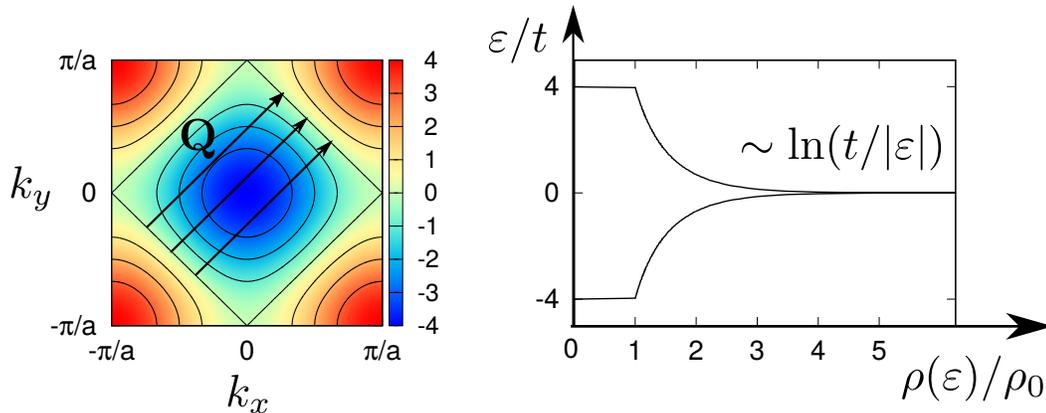
Fig. 8.3: Left: First Brillouin zone of the square lattice with the non-interacting band structure $\varepsilon_{\mathbf{k}}$, shown as a contour plot. At half filling the Fermi surface has the shape of a rotated square with parallel sections connected by the nesting vector $\mathbf{Q} = (\pi/a, \pi/a)$. **Right:** Density of states with logarithmic van Hove singularity $\rho(\varepsilon) \sim \rho_0 \ln(t/|\varepsilon|)$ at half filling. The band width is $W = 8t$.

is symmetric about half filling $\langle n \rangle = 1$ so that the phase boundary at filling $\langle n \rangle$ is identical to that at $2 - \langle n \rangle$. Therefore, in Fig. 8.2(b) only the phase boundary for $\langle n \rangle \leq 1$ is shown.

Although the Mermin-Wagner theorem forbids a second-order phase transition, for the special case of an $O(2)$ (or XY) order parameter with $n = 2$ components in $d = 2$ dimensions, such as the superconducting order parameter in the attractive Hubbard model *away from half-filling*, there is a different type of phase transition, the Kosterlitz-Thouless (KT) transition [166], which is of topological nature. Topologically stable defects (vortices) lead to a finite transition temperature to a quasi-long-range ordered state which is characterized by a power-law decay of the superconducting pairing correlations [24, 25]. Only in the ground state the model possesses true long-range superconducting order.

As a function of attraction U, the Hubbard model realizes the so-called *BCS-to-BEC crossover* where pairs formed from opposite spin species evolve from large overlapping Cooper pairs (BCS-limit) to small on-site singlet pairs, which, as composite bosons, undergo Bose Einstein condensation (BEC-limit). Remarkably, as first pointed out by Leggett [240] and Nozières and Schmitt-Rink [241], no phase transition occurs in between so that both extremes can be described by the same variational state that depends parametrically on U. For small attraction, the transition temperature T_{KT} increases exponentially and proportional to the gap parameter Δ_{MF}, as expected from BCS mean-field theory, which for the square lattice at half filling gives $T_c \sim t e^{-2\pi\sqrt{t/U}}$ [120].

Once the attraction $|U|$ is larger than the bandwidth W, which for the non-interacting 2D model is equal to $8t$, the transition temperature decreases again as $\sim \frac{t^2}{|U|}$ (see Fig. 8.2(a)). This is an effect of the lattice, which inhibits the flow of pairs. For a pair to hop from one site to the next it must first separate, which costs an energy $|U|$, and the resulting pair-hopping amplitude in second-order perturbation theory is $-\frac{2t^2}{|U|}$. For $|U| < W$ (BCS regime, conventional SC), the driving force behind superconductivity is the gain of potential energy, which outweighs the accompanying increase of kinetic energy due to the broadening of the Fermi surface when the superconducting state is formed [242], whereas for $|U| > W$ (BEC regime, short coherence-length SC) the condensation of pairs is driven by the gain of kinetic energy [243], as in the Bose-Einstein condensation of free bosons.

While in conventional BCS superconductors [221] the formation of Cooper pairs and of a superconducting state with long-range phase coherence occurs at the same temperature, in the attractive Hubbard model there is a second clearly separated temperature scale $T^* \sim |U|$ which marks the onset of pair formation [232], yet without the long-range phase coherence, which sets in at a lower temmperature. T^* is indicated in Fig. 8.2(a) with a dashed line.

As already mentioned, at half filling, there is no exception from the Mermin-Wagner theorem and the transition temperature is suppressed to zero. At small but finite

temperature T, the model at half filling shows a cross-over as T is lowered, which, in the limit of large $|U|/t$, manifests itself in a correlation length ξ that grows exponentially with inverse temperature as the ground state is approached, i.e. $\xi(T) \sim \exp(2\pi\rho_s/T)$, where ρ_s is the spin stiffness in the ground state of the $2D$ Heisenberg model [244]. Near half filling $\langle n \rangle \rightarrow 1$ the transition temperature decreases sharply (see Fig. 8.2(b)) as [24] $T_{\mathrm{KT}} = -2\pi J/\ln(1 - \langle n \rangle)$ with J the Heisenberg coupling [3].

8.4 Effective spin-only models: canonical transformation method

For $t/U = 0$ the spectrum of the Hubbard model consists of macroscopically degenerate subspaces, characterized by the number of doubly occupied sites. Any state without double occupancy is a ground state. For N electrons on N_s lattice sites, $N < N_s$, there are $\binom{N_s}{N} 2^N$ such spin-only ground states.

If a small hopping $t/U \ll 1$ is switched on, the degeneracy is lifted and the lower and upper Hubbard bands acquire a dispersion. We wish to describe the low energy dynamics induced by the perturbation H_t by an effective spin Hamiltonian that acts in the spin-only subspace of Hilbert space.

We use the *canonical perturbation method* [246],[2, Chapt. 5] since it connects neatly observables in the effective spin model to the observables of the original Hubbard model. The idea is to construct a basis transformation that eliminates order by order in t/U terms in the Hamiltonian which couple the low-energy subspace of at most singly occupied sites (in other words: the *lower Hubbard band* or spin-only subspace) to excited states with doubly occupied sites. Terms connecting the high- and low-energy subspace are replaced by interactions inside the modified low-energy subspace.

A basis transformation induced by the unitary operator e^{iS} can be expanded with

---

[3]This formula follows from a mapping of the slightly doped negative-U Hubbard model to a positive-U Hubbard model in a small Zeeman field in z-direction, which in the large-U limit can be mapped to an antiferromagnetic Heisenberg model in a field. The interactions being antiferromagnetic, a uniform field in z-direction makes it favourable for the spins to lie in the xy-plane so that they can gain field energy by tilting out of the plane without losing too much exchange energy. This reduces the symmetry of the order parameter from $O(3)$ to $O(2)$. In a small field $h/J \rightarrow 0$ the vortex core size in the Heisenberg model is very large [245], diverging like $\sim J/h \gg 1$, and by equating it with the correlation length of the Heisenberg model the formula $T_{\mathrm{KT}} = -2\pi J/\ln(1 - \langle n \rangle)$ is obtained [24]. We mention these details here especially because in Sect. 7.2 of this thesis another instance of a KT transition is presented where also an increasing vortex core size suppresses the KT transition temperature.

the help of the Baker-Campbell-Hausdorff formula

$$H_{\text{eff}} = e^{iS} H e^{-iS} = H + [iS, H] + \frac{1}{2!}[iS, [iS, H]] \tag{8.28}$$

$$+ \frac{1}{3!}[iS, [iS, [iS, H]]] \ldots . \tag{8.29}$$

We partition the hopping Hamiltonian H_t into hopping events summarized as H_t^+ (H_t^-) that increase (decrease) the number of doubly occupied sites by one and those hopping events summarized as H_t^0 that do not change the number of doubly occupied sites:

$$H_t = H_t^+ + H_t^- + H_t^0. \tag{8.30}$$

For the moment it is sufficient to note that H_t^+, H_t^- and H_t^0 are eigenoperators of the interaction part H_U with commutation relations

$$[H_t^+, H_U] = -U H_t^+, \quad [H_t^-, H_U] = U H_t^-. \tag{8.31}$$

Inserting the decomposition of the hopping Hamiltonian Eq. (8.30) in Eq. (8.29) leads to

$$\begin{aligned} H_{\text{eff}} = & H_U + H_t^+ + H_t^- + H_t^0 + [iS, H_U] \\ & + [iS, H_t^+ + H_t^-] + [iS, H_t^0] + [iS, [iS, H_U]] \\ & + [iS, [iS, H_t^+ + H_t^-]] + [iS, [iS, H_t^0]] + \ldots . \end{aligned} \tag{8.32}$$

The goal is to choose the generator S in such a way as to eliminate the terms H_t^+ and H_t^- that mix subbands with different numbers of doubly occupied sites. H_U being of order U, one needs to choose $S \sim \mathcal{O}(t/U)$ and so that $[iS, H_U]$ can cancel $H_t^+ + H_t^-$, which leads to

$$iS = -\frac{1}{U}\left(H_t^+ - H_t^-\right), \tag{8.33}$$

from which the effective Hamiltonian is obtained as

$$H_{\text{eff}} = H_t^0 + H_U + \frac{1}{U}\left[H_t^+, H_t^-\right] + \mathcal{O}(t^3/U^2). \tag{8.34}$$

The canonical transformation also generates new terms that mix different subbands, but they are of order t^3/U^2. Specifying now explicitly the projected hopping operators

$$H_t^+ = -t \sum_{\langle \mathbf{i,j} \rangle} \sum_\sigma \left[\hat{n}_{i,-\sigma} c_{\mathbf{i},\sigma}^\dagger c_{\mathbf{j},\sigma}(1 - \hat{n}_{\mathbf{j},-\sigma}) + \hat{n}_{\mathbf{j},-\sigma} c_{\mathbf{j},\sigma}^\dagger c_{\mathbf{i},\sigma}(1 - \hat{n}_{\mathbf{i},-\sigma}) \right], \tag{8.35a}$$

$$H_t^- = -t \sum_{\langle \mathbf{i,j} \rangle} \sum_\sigma \left[(1 - \hat{n}_{\mathbf{i},-\sigma}) c_{\mathbf{i},\sigma}^\dagger c_{\mathbf{j},\sigma} \hat{n}_{\mathbf{j},-\sigma} + (1 - \hat{n}_{\mathbf{j},-\sigma}) c_{\mathbf{j},\sigma}^\dagger c_{\mathbf{i},\sigma} \hat{n}_{\mathbf{i},-\sigma} \right], \tag{8.35b}$$

$$H_t^0 = -t \sum_{\langle \mathbf{i},\mathbf{j} \rangle} \sum_{\sigma} \left[(1 - \hat{n}_{\mathbf{i},-\sigma}) c_{\mathbf{i},\sigma}^\dagger c_{\mathbf{j},\sigma} (1 - \hat{n}_{\mathbf{j},-\sigma}) + \hat{n}_{\mathbf{i},-\sigma} c_{\mathbf{i},\sigma}^\dagger c_{\mathbf{j},\sigma} \hat{n}_{\mathbf{j},-\sigma} + \text{H.c.} \right], \quad (8.35c)$$

and inserting them into Eq. (8.34), one obtains to order t^2/U the so-called t-J model

$$H_{\text{eff}} = + \frac{4t^2}{U} \sum_{\langle \mathbf{i},\mathbf{j} \rangle} \left[\mathbf{S_i} \cdot \mathbf{S_j} - \frac{\hat{n}_{\mathbf{i}} \hat{n}_{\mathbf{j}}}{4} \right] - t \sum_{\langle \mathbf{i},\mathbf{j} \rangle} \sum_{\sigma} \left[\tilde{c}_{\mathbf{i},\sigma}^\dagger \tilde{c}_{\mathbf{j},\sigma} + H.c. \right] \tag{8.36}$$

$$+ \text{ three-site hopping} \tag{8.37}$$

with the projected fermion operators $\tilde{c}_{\mathbf{i},\sigma} = c_{\mathbf{i},\sigma}(1 - \hat{n}_{\mathbf{i},-\sigma})$. From the evaluation of the commutator $\frac{1}{U}\left[H_t^+, H_t^- \right]$ in Eq. (8.34) also special three-site hopping processes appear

$$H_{3\text{-site}}^{(A)} = -\frac{t^2}{U} \sum_{\langle \mathbf{ijk} \rangle} \sum_{\sigma} \left(\tilde{c}_{\mathbf{i},\sigma}^\dagger \hat{n}_{\mathbf{j},-\sigma} \tilde{c}_{\mathbf{k},\sigma} + H.c. \right), \tag{8.38}$$

$$H_{3\text{-site}}^{(B)} = +\frac{t^2}{U} \sum_{\langle \mathbf{ijk} \rangle} \sum_{\sigma} \left(\tilde{c}_{\mathbf{i},-\sigma}^\dagger \tilde{c}_{\mathbf{j},-\sigma}^\dagger \tilde{c}_{\mathbf{j},\sigma} \tilde{c}_{\mathbf{k},\sigma} + H.c. \right), \tag{8.39}$$

with $\langle \mathbf{ijk} \rangle$ denoting a collinear (or non-collinear) triple of sites such that $\mathbf{j}$ is a nearest neighbour of both $\mathbf{i}$ and $\mathbf{k}$. Three-site hopping processes of the type $H_{3\text{-site}}^{(A)}$ are important since they make it possible for a hole to move on one sublattice of a bipartite lattice without disturbing the antiferromagnetic spin configuration, as ordinary first-order hopping would do. $H_{3\text{-site}}^{(B)}$ describes next-nearest neighbour spin-flip hopping. Exactly at half filling all charge degrees of freedom are suppressed and the effective Hamiltonian reduces to the spin-$\frac{1}{2}$ antiferromagnetic Heisenberg model

$$H_{\text{eff}} = J \sum_{\langle i,j \rangle} \mathbf{S}_i \cdot \mathbf{S}_j \quad \text{with} \quad J = \frac{4t^2}{U}. \tag{8.40}$$

The low-energy subspace in which the t-J model acts is characterized by $\tilde{n}_{i,\uparrow} \tilde{n}_{i,\downarrow} |\tilde{\Psi}\rangle = 0$. However, the dressed electron operators $\tilde{c}_{i,\sigma} = e^{iS} c_{i,\sigma} e^{-iS}$ [246] after the canonical transformation act here on a transformed state $|\tilde{\Psi}\rangle = e^{iS}|\Psi\rangle$, whereas the lower Hubbard band expressed in terms of the original fermions $c_{i,\sigma}$ may well contain double occupancies. In fact, the doublon density is related to the nearest neighbour spin-spin correlations in the Heisenberg model according to [2, Chapt. 5]:

$$n_d = \langle \Psi | \hat{n}_{\mathbf{i},\uparrow} \hat{n}_{\mathbf{i},\downarrow} | \Psi \rangle = 2z \frac{t^2}{U^2} \langle \tilde{\Psi} | \left(\frac{1}{4} - \mathbf{S}_1 \cdot \mathbf{S}_2 \right) | \tilde{\Psi} \rangle \tag{8.41}$$

with z the nearest neighbour coordination number. An important aspect is that observables in the effective spin model need to be transformed according to the unitary transformation e^{iS} if comparison with the original Hubbard model is to be made [247].

8.4.1   Relevance of ring exchange for the Hubbard model at intermediate coupling

For intermediate Hubbard-U one needs to carry out the canonical transformation method to higher orders in t/U, which results in cyclic ring-exchange and longer-range pairwise spin-spin interactions [248, 249]. At half filling the resulting effective spin Hamiltonian reads

$$
\begin{aligned}
H_{\text{eff}} =& J_1 \sum_{\langle i,j \rangle} \mathbf{S}_i \cdot \mathbf{S}_j + J_2 \sum_{\langle i,j_2 \rangle} \mathbf{S}_i \cdot \mathbf{S}_{j_2} + J_3 \sum_{\langle i,j_3 \rangle} \mathbf{S}_i \cdot \mathbf{S}_{j_3} \\
&+ J_c \sum_{\langle i,j,k,l \rangle} [(\mathbf{S}_i \cdot \mathbf{S}_j)(\mathbf{S}_k \cdot \mathbf{S}_l) + (\mathbf{S}_i \cdot \mathbf{S}_l)(\mathbf{S}_j \cdot \mathbf{S}_k) \\
&- (\mathbf{S}_i \cdot \mathbf{S}_k)(\mathbf{S}_j \cdot \mathbf{S}_l)] + \mathcal{O}\left(t(t/U)^4\right)
\end{aligned}
\tag{8.42}
$$

with the coupling constants [247]

$$
J_1 = 4t^2/U - 24t^4/U^3, \quad J_2 = J_3 = 4t^4/U^3, \quad J_c = 80t^4/U^3.
\tag{8.43}
$$

$\langle i,j_2 \rangle$ and $\langle i,j_3 \rangle$ denotes the next-nearest (i.e. across the diagonal) and next-to-next nearest neighbours of site i and $\langle i,j,k,l \rangle$ are the four sites that form an elementary square plaquette labelled in a clockwise sequence.

As a consistency check, we can convince ourselves that at half filling the Hubbard model is symmetric under $t \leftrightarrow -t$, therefore only even powers in t/U can contribute in the effective Hamiltonian Eq. (8.42); furthermore, the basic building blocks $(\mathbf{S}_i \cdot \mathbf{S}_j)$ conform with the spin-rotational symmetry of the original Hubbard model.

At intermediate $U/t = 5 - 9$ terms of order t^4/U^3 are not small and need to be included to describe the Hubbard model in a spin-only low-energy subspace [247]. The exchange matrix elements in Eq. (8.43) are plotted as a function of t/U in Fig. 8.4. Considering that there are 8 next-nearest neighbour couplings J_2, J_3, but only 4 couplings J_1 per site, and that J_2, J_3 are also AFM and thus competing with and weakening J_1 ($J_1 - J_2$ model), one can argue that none of the couplings in Eq. (8.42) are negligible. The additional terms tend to frustrate the antiferromagnetic order of the 2D plain Heisenberg model [Eq. (8.40)].

8.5   Two-body bound states on the lattice

This section deals with the special case of the Hubbard model with only two particles interacting through an on-site potential of strength U, which can bind them into a pair. Remarkably, in a lattice model both attractively and repulsively bound pairs are possible [12].

The existence of a bound state is independent of the presence of a lattice potential since at the onset of binding the pair size is very large, extending over many lattice

sites, and only the dimensionality of space and the form of the dispersion relation $\sim k^2$ at small momenta is relevant [250, Sec. § 45]. In one dimension, an attractive potential always has a bound state and the binding energy $E_b < 0$ at the onset of binding is a small quantity that depends algebraically (quadratically) on the interaction strength. In two dimensions, the binding energy is exponentially small in the strength of the attractive interaction and exhibits an essential singularity. Explicitly, for a shallow potential well $-V(|\mathbf{r}|)$ of range a the binding energy is [250, Sec. § 45]:

$$E_b = -\frac{\hbar^2}{2ma^2} \exp\left[-\frac{\hbar^2}{m} \left| \int_0^\infty V(r) r\, dr \right|^{-1} \right], \tag{8.44}$$

where m is the mass of the "relative particle" (or, equivalently, the reduced mass of the two partners of the bound pair). On the other hand, in three dimensions even a purely attractive two-body potential has a threshold for binding. This means that in three dimensions a weak potential can be considered merely a perturbation to free motion, whereas in one or two dimensions this is never possible.

There are important consequences for Cooper pairing in different spatial dimensions. The Cooper pairing mechanism [251, 252] describes how pairwise scattering of fermions with opposite momenta and opposite spin states on the Fermi surface leads to a volume-independent energy gap, which is the microscopic origin of superconductivity. To trigger this instability an infinitesimally small attractive interaction is sufficient due to the large density of states at the surface of the Fermi sea. Thus, the Pauli exclusion principle and the Fermi sea are crucial in creating a large degeneracy of single-particle electron levels, and Cooper pairing emerges as a cooperative phenomenon when, in
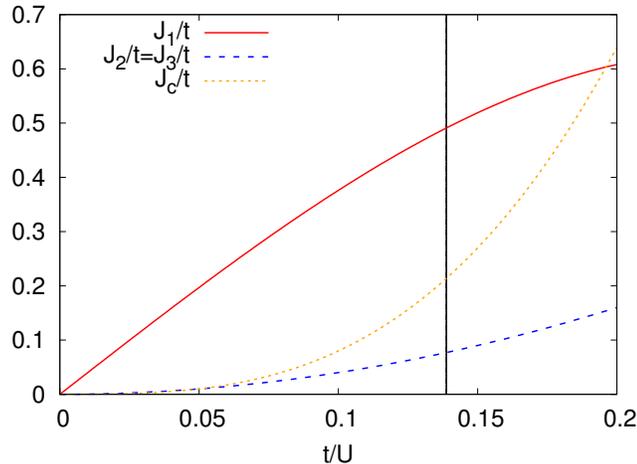

Fig. 8.4: Exchange matrix elements of the ring-exchange Hamiltonian Eq. (8.42) in units of the small parameter t/U. The vertical line marks the Hubbard interaction $U/t = 7.2$ that was realized in the Harvard experiment [20], which will be referred to in Chapt. 9.

the conventional three-dimensional case, the attractive interaction is still too weak that a two-body bound state could arise *in vacuum*, i.e. in the absence of a Fermi sea. In contrast, in two dimensions the existence of a two-body bound state for a given interaction potential is a necessary and sufficient condition [253] for a many-body pairing instability and there is no clear-cut distinction between the two-body and the many-body binding effect.

8.5.1   Two-body bound state wave function

Our goal in the following is to quantify the size of a two-body bound state in a way that is experimentally measurable. After deriving expressions for the bound state wave function, the delocalization probability will be introduced as a measure of the pair size.

The Hamiltonian on a d-dimensional hypercubic lattice is assumed as

$$\mathcal{H} = -\sum_{m>0} t_m \left(\Delta_{\mathbf{r}_1}^{(m)} + \Delta_{\mathbf{r}_2}^{(m)} + 4d \right) + U(\mathbf{r}_1, \mathbf{r}_2) \tag{8.45}$$

with the m-th lattice Laplacian

$$\Delta_{\mathbf{r}}^{(m)} f(\mathbf{r}) = \sum_{i=1}^{d} \Delta_i f(\mathbf{r}) = \sum_{i=1}^{d} \left[f(\mathbf{r} + ma\hat{e}_i) + f(\mathbf{r} - ma\hat{e}_i) - 2f(\mathbf{r}) \right] \tag{8.46}$$

and $U(\mathbf{r}_1, \mathbf{r}_2) = -U\delta_{\mathbf{r}_1, \mathbf{r}_2}$ an attractive onsite potential between the two particles of opposite spin. We restrict ourselves in the following to $m = 1$, which corresponds to a single-particle band structure with a perfect cosine dispersion resulting from nearest neighbour hopping only. For realistic optical lattice potentials higher values of m need to be included.

Since the two particles, labelled by position $\mathbf{r}_1$ and $\mathbf{r_2}$, have different spin, they are distinguishable and their fermionic nature does not matter. We introduce the center of mass coordinate $\mathbf{R} = \frac{\mathbf{r}_1 + \mathbf{r}_2}{2}$ and the relative coordinate $\mathbf{r} = \mathbf{r}_1 - \mathbf{r}_2$ and make the separation ansatz $\Psi(\mathbf{r}_1, \mathbf{r}_2) = e^{i\mathbf{K}\mathbf{R}}\psi_{\mathbf{K}}(\mathbf{r})$, where $\mathbf{K}$ is the quasimomentum for the center of mass motion and $\psi_{\mathbf{K}}(\mathbf{r})$ is the internal pair wave function. Then, for each value of $\mathbf{K}$, a one-body Schrödinger equation for the relative motion is obtained [12]

$$\underbrace{\left[-2t \sum_{i=1}^{d} \cos\left(\frac{K_i a}{2} \right) (\Delta_i + 2) + U\delta_{\mathbf{r},\mathbf{0}} \right]}_{\mathcal{H}_{\mathbf{K}}} \psi_{\mathbf{K}}(\mathbf{r}) = E\psi_{\mathbf{K}}(\mathbf{r}). \tag{8.47}$$

In two dimensions, we have to resort to a numerical solution of Eq. (8.47) on a finite lattice. With the abbreviation $t_{K_{x,y}} = t\cos K_{x,y}a/2$, the matrix notation of the Hamiltonian in two dimensions reads

$$(\mathcal{H}_{\mathbf{K}})_{\mathbf{0},\mathbf{0}} = U$$
$$(\mathcal{H}_{\mathbf{K}})_{\mathbf{r},\mathbf{r}\pm\hat{e}_x} = -2t_{K_x} \tag{8.48}$$
$$(\mathcal{H}_{\mathbf{K}})_{\mathbf{r},\mathbf{r}\pm\hat{e}_y} = -2t_{K_y},$$
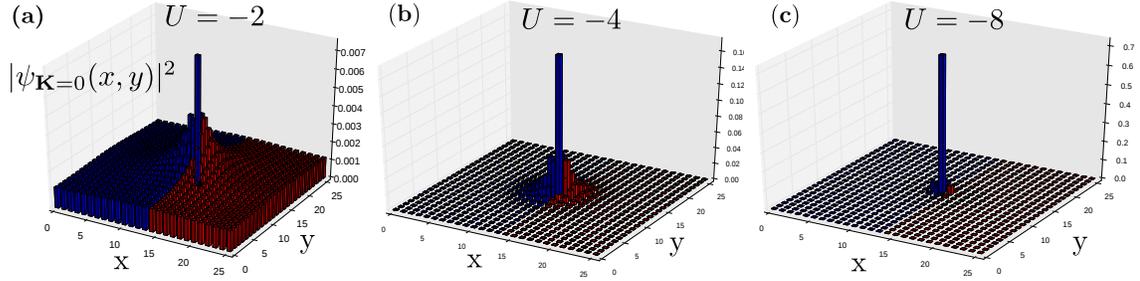
Fig. 8.5: Modulus squared $|\psi_{\mathbf{K}=0}(x,y)|^2$ of the wave function of the two-body bound state in vacuum for an on-site attraction of $U/t = -2$ (a), $U/t = -4$ (b), and $U/t = -8$ (c) on the square lattice. The red bars denote the weight of the two-body wave function in the right half-space. The center of mass of the wave function is located on a lattice site to the left of the boundary between the left and right half-spaces.

with all other elements equal to zero. $\hat{e}_{x,y}$ are unit vectors in x- and y-direction, respectively. The lowest energy eigenstate of $\mathcal{H}_{\mathbf{K}}$ is the two-body bound state; it is displayed for $\mathbf{K} = 0$ in Fig. 8.5 for three different attractive interactions.

Note that in one dimension both the spectrum and the bound and scattering states for a δ-function potential can be obtained analytically with the Green's function method [12, 254]. Up to normalization the bound state wave function for center of mass momentum $K \equiv K_x$ is given by [12]

$$\psi_K^{(bs)}(x) \sim G_K^0(E_{\mathrm{bs}}, x) = \frac{1}{2\pi} \int_{-\pi}^{\pi} \frac{e^{ikx}}{E_{\mathrm{bs}} + 4t_K \cos(ka)} dk, \tag{8.49}$$

where $G_K^0(E, x)$ denotes the Green's function (i.e. operator inverse) of the non-interacting Schrödinger equation $\mathcal{H}_K(U = 0)\,\psi_K(x) = E\psi_K(x)$. The integral in Eq.(8.49) can be solved with the help of contour integration, where it is assumed that $|E_{\mathrm{bs}}| > 4t_K$ such that the integrand never becomes singular. The condition $UG_K^0(E = E_{\mathrm{bs}}, x = 0) = 1$ determines the bound state energy [12]

$$E_{\mathrm{bs}}(K) = \pm 2t \sqrt{4\left(\cos\left(\frac{Ka}{2}\right)\right)^2 + \left(\frac{U}{2t}\right)^2} \tag{8.50}$$

where the minus (plus) sign stands for an attractively (repulsively[4]) bound pair. Inserting Eq. (8.50) into (8.49) and assuming that the pair has zero center of mass momentum, $K = 0$, yields an exponentially decaying bound state wave function

$$\psi_{K=0}^{(bs)}(x) = \frac{1}{\sqrt{\mathcal{N}(|U|/t)}} \left[\frac{1}{4}\left(\sqrt{16 + (|U|/t)^2} - |U|/t\right)\right]^x \tag{8.51}$$

---

[4] A repulsively bound pair is a stable composite object that cannot decay since the energy that needs to be released exceeds the maximum allowed kinetic energy for two atoms in a periodic potential, which is twice the bandwidth of the Bloch band. Repulsively bound pairs can exist in an optical lattice due to the absence of decay channels such as interactions with phonons [12].

with $\mathcal{N}(|U|/t)$ a normalization constant ensuring that $\sum_{z=-\infty}^{\infty} |\psi_{K=0}^{(bs)}(x)|^2 = 1$.

8.5.2 Delocalization probability

Having obtained the bound state wave function in one and two dimensions, we need to quantify its spread. As a measure of the pair size we introduce the delocalization probability in $d = 1$ and $d = 2$ dimensions

$$P_{\text{deloc}}^{(d=1)} = \sum_{x=1}^{\infty} |\psi_{K=0}^{(bs)}(x)|^2 \quad \text{and} \quad P_{\text{deloc}}^{(d=2)} = \sum_{x=1}^{\infty} \sum_{y=-\infty}^{\infty} |\psi_{K=0}^{(bs)}(x,y)|^2, \tag{8.52}$$

which is the probability that a pair centered at $x = 0$ spreads into the right half-space $x \geq 1$. While the mean square radius

$$\langle r^2 \rangle_{\psi^{(bs)}} = \frac{\int d^d\mathbf{r}\, r^2\, |\psi^{(bs)}(r)|^2}{\int d^d\mathbf{r}\, |\psi^{(bs)}(r)|^2} \tag{8.53}$$

is a more conventional measure of the spread of a d-dimensional wave function, the delocalization probability across a straight boundary (a line in d=2, see Fig.8.5) turns out to be a more practical quantity for our purposes. In fact, we will show that the delocalization probability can be measured with the help of a quantum gas microscope in Sect.9.4.2, giving experimental access to the size of preformed pairs or Cooper pairs.

$P_{\text{deloc}}^{(d=1)}$ is shown in Fig. 8.6(a) for the 1D bound state wave function of Eq. (8.51). In order to obtain the behaviour of $P_{\text{deloc}}^{(d=1)}$ for large $|U|/t$ it is easiest to re-derive the bound state wave function in perturbation theory. On a one-dimensional lattice, the internal wave function of a two-body bound state centered at lattice site i can be written as [255]

$$|\psi_i^{(bs)}\rangle = c_{i,0}|d_i\rangle + \sum_r \left[c_{i,r}|s_i\rangle|s_{i+r}\rangle + c_{i,-r}|s_i\rangle|s_{i-r}\rangle \right], \tag{8.54}$$

with $|d_i\rangle$ and $|s_i\rangle$ denoting a doubly or singly occupied site i, respectively, and r the distance from site i. To zeroth order in the hopping amplitude t/U, the pair is perfectly localized at site i with amplitudes $c_{i,0} = 1$ and $c_{i,\pm r} = 0$ for all $r \neq 0$. Tunneling processes to neighbouring sites lead to a spreading of the wave function, which in first

order in t/U is accounted for by the correction [5]

$$|\psi_i^{(1)}\rangle = \sum_r \left(2\frac{\langle s_i|\langle s_{i+r}|H_t|\psi_i^{(0)}\rangle}{-U}|s_i\rangle|s_{i+r}\rangle + 2\frac{\langle s_i|\langle s_{i-r}|H_t|\psi_i^{(0)}\rangle}{-U}|s_i\rangle|s_{i-r}\rangle \right) \quad (8.55)$$

$$= 2\left(-\frac{t}{U}\right)[|s_i\rangle|s_{i+1}\rangle + |s_s\rangle|s_{i-1}\rangle]. \quad (8.56)$$

Similarly, the r-th order correction is [255]:

$$c_{i,\pm r} \approx 2\left(\frac{-t}{U}\right)^r c_{i,0}. \quad (8.57)$$

Then, the probability that the pair has delocalized into the right half-space amounts again to a geometric series:

$$P_{\text{deloc}}^{(d=1)} = \sum_{r\geq 1} |c_{i,r}|^2 = \sum_{r\geq 1} 4\left(-\frac{t}{U}\right)^{2r}|c_{i,0}|^2 \quad (8.58)$$

$$= |c_{i,0}|^2 \frac{4t^2}{U^2 - t^2}. \quad (8.59)$$

From the normalization of the wave function $|c_{i,0}|^2\left(1 + \sum_{r\geq 1} 4\left(\frac{t}{U}\right)^{2r}\right) = 1$ it follows that $|c_{i,0}|^2 = (U^2 - t^2)/(U^2 + 3t^2)$ and we arrive at

$$P_{\text{deloc}}^{(d=1)} = \frac{4}{(U/t)^2 + 3} \xrightarrow{U/t\to\infty} \sim \left(\frac{t}{U}\right)^2, \quad (8.60)$$

which is shown in Fig. 8.6 (a) next to the analytical result based on Eq. (8.51).

On a two-dimensional lattice, keeping track of all hopping paths into the right half-space is too cumbersome, which is why we do not give a perturbative answer in this case. The numerical solution of the Schrödinger equation displayed in Fig. 8.6 (b) shows that also in two dimensions the delocalization probability of a single pair across a boundary scales like $(t/U)^2$ for large interactions. The delocalization probability is indicated by red bars in the plots of the wave functions in Fig. 8.5.

For $\mathbf{K}^\star = (\frac{\pi}{a}, \frac{\pi}{a})$, we have $t_{K_x} = t_{K_y} = 0$ and the Hamiltonian in Eq. (8.48) takes a special form with all elements equal to zero except for $(H_{\mathbf{K}^\star})_{\mathbf{r}=0,\mathbf{r}=0} = U$. The

---

[5] The factor of two in Eqs. (8.56,8.57) comes from the fact that a pair consists of two distinguishable spin states in terms of which the wave function reads:

$$|\psi_i^{(bs)}\rangle = c_{i,0}|d_i\rangle + \sum_r \left[c_{i,r}\sum_{\sigma=\uparrow,\downarrow}|\sigma_i\rangle|\bar{\sigma}_{i+r}\rangle + c_{i,-r}\sum_{\sigma=\uparrow,\downarrow}|\sigma_i\rangle|\bar{\sigma}_{i-r}\rangle \right]$$

with $\bar{\sigma}_i = -\sigma_i$. Thus, each coefficient $c_{i,r}$ for $r \neq 0$ in Eq. (8.54) is actually associated with two configurations that are related by exchange of the two spin states.
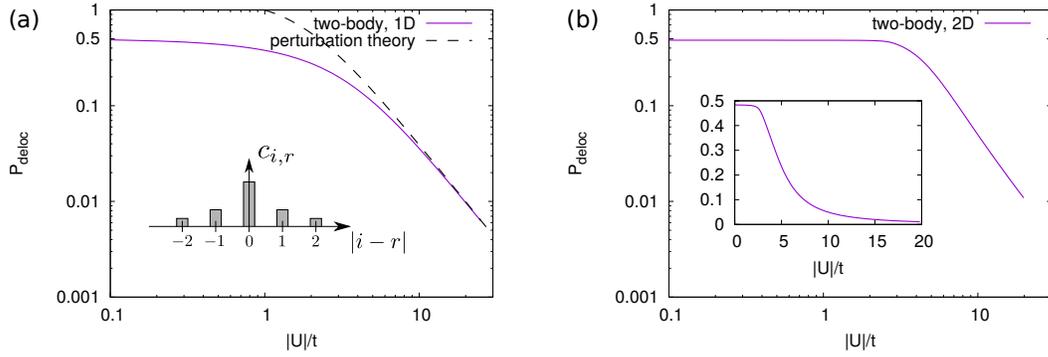
Fig. 8.6: Probability P_{deloc} to find one atom of the bound pair in the right half-space when the pair is centered on the left of the boundary between the half-spaces, in one (a) and two dimensions (b). The continuous line in (a) is based on the analytical formula Eq. (8.51), the dashed line is the perturbative result Eq. (8.60). The small deviation of $P_{\mathrm{deloc}}(U \to 0)$ from 0.5 in the inset of subfigure (b) is due to the finite lattice size of $L \times L$ with $L = 60$ for which the 2D Schrödinger equation was solved numerically.

Hamiltonian has a bound state with energy U, with a tightly localized internal wave function: $\psi_{\mathbf{K}^\star}(\mathbf{r} = \mathbf{0}) = 1$, $\psi_{\mathbf{K}^\star}(\mathbf{r} \neq \mathbf{0}) = 0$. This is a so-called η-pair, which was already mentioned in Sect. 8.2.2. Its total wave function $\Psi_\eta = e^{i\mathbf{K}^\star \mathbf{R}} \psi_{\mathbf{K}^\star}(\mathbf{r})$ is that of a doubly occupied site that is coherently displaced across the lattice with an alternating (i.e. staggered) phase factor $e^{i\mathbf{K}^\star \mathbf{R}} = \pm 1$, which leads to perfect destructive interference of all hopping processes of the pair. As a consequence the η-pair is an exact eigenstate of the kinetic part H_t of the Hamiltonian with zero eigenvalue (and as an onsite pair it is also obviously an eigenstate of the interaction part H_U.).

Chapter 9

Full counting statistics in the Hubbard model

A basic question posed in quantum mechanics is: Given an observable $\hat{O}$ with eigenvalues $\{\lambda_i\}$, what is the probability to obtain a certain eigenvalue λ_i when measuring $\hat{O}$ in the state $|\psi\rangle$? The answer is given by *Born's rule* as $P(\lambda_i) = |\langle\lambda_i|\psi\rangle|^2$, where $|\lambda_i\rangle$ is the (non-degenerate) eigenvector of $\hat{O}$ satisfying $\hat{O}|\lambda_i\rangle = \lambda_i|\lambda_i\rangle$. Answering this question for collective operators in many-body systems, such as e.g. the total particle number $\hat{N} = \sum_{i\in A}(\hat{n}_{i,\uparrow} + \hat{n}_{i,\downarrow})$ on a subsystem A in the Fermi-Hubbard model, as shown in Fig. 9.1, leads to the subject of *full counting statistics* For a thermal state, described
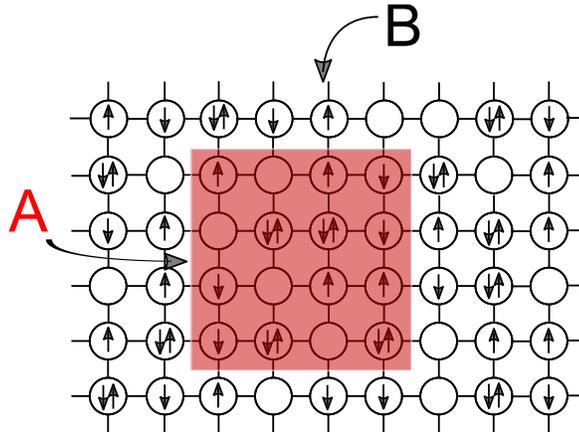
Fig. 9.1: Setup of a square subsystem A of dimension $L_A \times L_A$ with N_s sites embedded in a larger $L \times L$ square lattice with periodic boundary conditions. We are interested in the probability $P(N_A)$ to obtain a certain eigenvalue N_A of the particle number operator $\hat{N} = \sum_{i\in A}(\hat{n}_{i,\uparrow} + \hat{n}_{i,\downarrow})$ in a projective measurement.

on subsystem A through the reduced density matrix $\rho_A = \mathrm{Tr}_B(\rho)$, Born's rule reads

$$P(N_A) = \mathrm{Tr}(\rho_A \hat{\Pi}_{N_A}) \tag{9.1}$$

with the projector $\hat{\Pi}_{N_A} = \sum_\gamma |N_A, \gamma\rangle\langle N_A, \gamma|$. Here, γ denotes quantum numbers labeling the states in the block of fixed particle number N_A. Inserting the Fourier representation of the delta function

$$\hat{\Pi}_{N_A} = \delta(N_A - \hat{N}) = \int_0^{2\pi} \frac{d\phi}{2\pi} e^{-i\phi N_A} e^{i\phi \hat{N}} \tag{9.2}$$

into Born's rule Eq. (9.1) gives

$$P(N_A) = \int_0^{2\pi} \frac{d\phi}{2\pi} e^{-i\phi N_A} \chi(\phi) \tag{9.3}$$

$$= \frac{1}{N_s} \sum_{m=0}^{N_s} e^{-i\phi_m N_A} \chi(\phi_m), \tag{9.4}$$

where we have defined the *generating function* $\chi(\phi) \equiv \mathrm{Tr}(\rho_A e^{i\phi \hat{N}})$ for the operator $\hat{N}$. The variable ϕ is called the *counting field*. Since the operator $\hat{N}$, counting the number of particles on subsystem A, has only $N_s + 1$ discrete eigenvalues $N_A = 0, 1, \ldots, N_s$, the distribution $P(N_A)$ in Eq. (9.3) reduces to a Fourier series with discrete components $\chi(\phi_m)$ at $\phi_m = \frac{2\pi m}{N_s}$, where $m = 0, 1, \ldots, N_s$. With these preliminaries out of the way we can turn our attention to synthetic quantum systems with single-site single-particle resolution, where the issue of full counting statistics naturally appears.

9.1   Introduction

Full counting statistics has emerged as a very powerful tool to characterize and obtain information about a quantum mechanical system by gaining knowledge on the full probability distribution function of an observable rather than just its expectation value. These concepts have been pioneered by Lesovik and Levitov [256] for transport measurements in nano-structures [257]; a remarkable application being the demonstration of the fractional charge of quasiparticles in a fractional quantum Hall fluid [258, 259]. The concept of full counting statistics turns out to be very powerful in the context of cold atomic gases, where the observable of interest is the number of particles on a set of lattice sites, which is accessible with site-resolved quantum gas microscopes [13, 14]. Especially, it has been applied to characterize quantum states of cold atomic gases in equilibrium [260–263] as well as non-equilibrium states [176, 264–266]. In Ref. [266] full counting statistics of the phase contrast of interfering Bose-Einstein condensates was used to characterize a non-equilibrium state.

Several cold atoms setups for fermionic atoms are currently equipped with a quantum gas microscope [15–20, 22] and have achieved single-site and single-atom detection, which is required for the measurement of probability distributions in Fock space by accumulating histograms of particle configurations over independent measurement realizations [20]. Notably, both the repulsive [16–20] and the attractive [22] Hubbard

model have been realized in cold atoms experiments at temperature scales that may be already relevant in the context of normal-state properties of high-T_c cuprates. While for bosonic systems, the full counting statistics is accessible within path integral quantum Monte Carlo simulations, in the fermionic situation the notorious sign problem renders such path integral approaches inefficient. In turn, for auxiliary field QMC methods such as determinantal quantum Monte Carlo (DQMC) [77], suitable to study such fermionic systems in certain parameter regimes, there is no direct correspondence between the computational configuration space of auxiliary fields and states in Fock space.

In this chapter, we demonstrate a method to compute the full counting statistics (FCS) within the framework of determinantal quantum Monte Carlo simulations and provide first comparisons with experiments for fermionic cold atomic gases. The main observation for this ability is the fact that DQMC simulations decomposes the interacting fermionic system into an incoherent sum over density matrices for free fermions in an external potential [119]. For such free fermions, the spectrum of the reduced density matrix required for the determination of the full counting statistics is related to the eigenvalues of a one-particle correlation function [267, 268]. Furthermore, the generating function for the FCS of the particle number, magnetization, and the staggered magnetization is still quadratic in the fermionic field operators. This allows us to calculate the relevant trace over the exponentially large Hilbert space of fermionic Fock states in all particle number sectors as the determinant of a single-particle operator.

9.2 FCS of particle number and magnetization

In this section we give a detailed description of the numerical methods for the determination of the FCS. The quantity of interest is the probability $P(N_A^\uparrow, N_A^\downarrow)$ that there are $N_A^\uparrow$ fermions with spin up and $N_A^\downarrow$ fermions with spin down on a subsystem A with $N_s = L_A \times L_A$ sites, see Fig. 9.1. The observable of interest is therefore given by the spin density operator $\hat{N}_A^\sigma = \sum_{i \in A} \hat{c}_{i,\sigma}^\dagger \hat{c}_{i,\sigma}$ with $\sigma \in \{\uparrow, \downarrow\}$ and eigenvalues $N_A^\sigma = 0, \ldots, N_s$. Its distribution function is most conveniently derived by the generating function

$$\chi(\phi^\uparrow, \phi^\downarrow) = \langle e^{i\phi^\uparrow \hat{N}_A^\uparrow + i\phi^\downarrow \hat{N}_A^\downarrow} \rangle = \text{Tr}\left(\rho_A \, e^{i \sum_\sigma \phi^\sigma \hat{N}_A^\sigma}\right). \tag{9.5}$$

Here, $\rho_A = \text{Tr}_{B=\bar{A}}(\rho)$ denotes the reduced density matrix with $B = \bar{A}$ the complement of subsystem A. Then, the joint probability $P(N_A^\uparrow, N_A^\downarrow)$ is determined as the coefficient of the Fourier series of the generating function

$$P(N_A^\uparrow, N_A^\downarrow) = \sum_{n,m=0}^{N_s} \frac{e^{-i\phi_n^\uparrow N_A^\uparrow - i\phi_m^\downarrow N_A^\downarrow}}{(N_s + 1)^2} \chi(\phi_n^\uparrow, \phi_m^\downarrow) \tag{9.6}$$

with $\phi_n^\sigma = \frac{2\pi n}{N_s + 1}$. Note that the maximal number of fermions with a given spin in the subsystem A is limited by N_s, and therefore, there are only $N_s + 1$ coefficients in

the Fourier series. In general, one is mostly interested in the probability distributions $P_N(N_A)$ for the total particle number $N_A = N_A^\uparrow + N_A^\downarrow$ and $P_M(M_A)$ for the magnetization $M_A = N_A^\uparrow - N_A^\downarrow$ on subsystem A. These quantities derive directly from the joint probability distribution via

$$P_N(N_A) = \sum_{N_A^\downarrow=0}^{N_s} P(N_A - N_A^\downarrow, N_A^\downarrow) \tag{9.7}$$

with $N_A = 0, \ldots, 2N_s$. An analogous expression follows for $P_M(M_A) = \sum_{N_A^\downarrow=0}^{N_s} P(M_A + N_A^\downarrow, N_A^\downarrow)$ with $M_A = -N_s, \ldots, N_s$.

In the following, we demonstrate that we can efficiently determine the generating function χ within DQMC. The standard procedure of DQMC (see Chapt. 4) discretizes the inverse temperature β and then decouples the interactions with a Hubbard-Stratonovich (HS) transformation at the expense of introducing an auxiliary field at every site and time slice. Then, the partition function can be written as a sum over free fermion systems coupled to an (imaginary) time-dependent Ising field. The expectation value of an observable $\hat{O}$ is

$$\langle \hat{O} \rangle = \mathrm{Tr}\left(\hat{O} e^{-\beta \hat{H}}\right) / \mathrm{Tr}\left(e^{-\beta \hat{H}}\right) = \frac{1}{Z} \sum_{\{\mathbf{s}\}} w_{\{\mathbf{s}\}} O_{\{\mathbf{s}\}}, \tag{9.8}$$

where $Z = \sum_{\{\mathbf{s}\}} w_{\{\mathbf{s}\}}$ is the partition sum and $w_{\{\mathbf{s}\}}$ is the weight of one auxiliary field configuration $\{\mathbf{s}\}$. The latter takes the form [77]

$$w_{\{\mathbf{s}\}} = \det\left(G_{\{\mathbf{s}\}}^\uparrow\right)^{-1} \left(G_{\{\mathbf{s}\}}^\downarrow\right)^{-1}, \tag{9.9}$$

where $G_{\{\mathbf{s}\}}^\sigma = \langle \hat{c}_{i,\sigma} \hat{c}_{j,\sigma}^\dagger \rangle_{\{\mathbf{s}\}}$ denotes the single-particle Green's function for spin species σ. Such a decomposition naturally carries over to more complex quantities such as the generating function [119]

$$\chi(\phi^\uparrow, \phi^\downarrow) = \sum_{\{\mathbf{s}\}} w_{\{\mathbf{s}\}} \chi_{\{\mathbf{s}\}}^\uparrow\left(\phi^\uparrow\right) \chi_{\{\mathbf{s}\}}^\downarrow\left(\phi^\downarrow\right) \tag{9.10}$$

with $\chi_{\{\mathbf{s}\}}^\sigma(\phi^\sigma) = \mathrm{Tr}\left(\rho_{\{\mathbf{s}\},A}^\sigma e^{i\phi^\sigma \hat{N}_A^\sigma}\right)$ and $\rho_{\{\mathbf{s}\},A}^\sigma$ the reduced density matrix for the free fermions with auxiliary field configuration $\{\mathbf{s}\}$ and spin σ. It is important to stress that within a Hubbard-Stratonovich configuration the reduced density matrix factorices into a spin up and spin down part. Each can be written in the form of a "Boltzmann weight" as [267–269]

$$\rho_{\{\mathbf{s}\},A}^\sigma = \mathcal{K}_{\{\mathbf{s}\},A}^\sigma \, e^{-H_A^\sigma} \tag{9.11}$$

with the *entanglement Hamiltonian* for spin species σ

$$H_A^\sigma = -\sum_{i,j\in A} \hat{c}_{i,\sigma}^\dagger \log\left(\left[\mathcal{G}_{\{\mathbf{s}\},A}^\sigma\right]^{-1} - \mathbb{1}\right)_{ij} \hat{c}_{j,\sigma} \tag{9.12}$$

and normalization $\mathcal{K}^\sigma_{\{\mathbf{s}\},A} = \det\left(\mathbb{1} - \mathcal{G}^\sigma_{\{\mathbf{s}\},A}\right)$. Here, $\left[\mathcal{G}^\sigma_{\{\mathbf{s}\},A}\right]_{ij} = \langle \hat{c}^\dagger_{i,\sigma}\hat{c}_{j,\sigma}\rangle_{\{\mathbf{s}\};i,j\in A}$ is the one-body density matrix (OBDM) for a given HS field configuration $\{\mathbf{s}\}$ and with sites i and j restricted to subsystem A [269]. Therefore, the generating function for a fixed auxiliary field configuration $\{\mathbf{s}\}$ reduces to

$$\chi^\sigma_{\{\mathbf{s}\}}(\phi) = \prod_{\alpha=1}^{N_s}(1 - \lambda^\sigma_\alpha)\prod_{\alpha=1}^{N_s}\left(1 + e^{-\epsilon^\sigma_\alpha + i\phi}\right),\tag{9.13}$$

where $\{\epsilon^\sigma_\alpha\}$ are the eigenvalues of the entanglement Hamiltonian H^σ_A and $\{\lambda^\sigma_\alpha\}$ those of the OBDM. In deriving the above expression, we have used the crucial fact that the particle number operator $\hat{N}^\sigma_A = \sum_{i\in A}\hat{c}^\dagger_{i,\sigma}\hat{c}_{i,\sigma}$ is also a quadratic operator, and commutes with the entanglement Hamiltonian H^σ_A, i.e., they have a common eigenbasis. Within this basis the grand canonical trace can be performed analytically.

Finally, the eigenvalues $\{\epsilon^\sigma_\alpha\}$ and $\{\lambda^\sigma_\alpha\}$ are related through $\epsilon^\sigma_\alpha = \log(\frac{1}{\lambda^\sigma_\alpha} - 1)$ [268], and we obtain the important result

$$\chi^\sigma_{\{\mathbf{s}\}}(\phi) = \prod_{\alpha=1}^{N_s}(1 + (e^{i\phi} - 1)\lambda^\sigma_\alpha),\tag{9.14}$$

which allows for the efficient determination of the generating function χ by quantum Monte Carlo sampling of the auxiliary field configurations. If the transformations Eqs. (9.6) and (9.7) are performed in every Monte-Carlo measurement step, error bars for $P_N(N_A)$ and $P_M(M_A)$ can be obtained in the standard way.

The idea of how to use the free fermion decomposition of determinantal QMC for computing probability distributions of collective quadratic observables is sketched in Fig. 9.2. Each HS sample $\{\mathbf{s}\}$ corresponds to a free fermion system, for which the probability distribution $P(N^\sigma_A)_{\{\mathbf{s}\}}$ for $\sigma = \uparrow, \downarrow$, can be computed from the generating function $\chi^\sigma_{\{\mathbf{s}\}}(\phi)$. The two spin species in one HS sample $\{\mathbf{s}\}$ are statistically independent so that the distribution of the total particle number $N_A = N^\uparrow_A + N^\downarrow_A$ is a sum over joint probability distributions, which are simply products $P(N^\uparrow_A)_{\{\mathbf{s}\}} \cdot P(N^\downarrow_A = N_A - N^\uparrow_A))_{\{\mathbf{s}\}}$. Averaging over all HS samples introduces correlations between the spin species.

Note that the equal-time OBDM $\mathcal{G}^\sigma_{\{\mathbf{s}\},A}(\tau)$ depends explicitly on imaginary time τ, which is suppressed in our notation. Due to the cyclic property of the trace in Eq. (9.8) all imaginary time slices are equivalent and it is possible to average over them to acquire additional statistics.

9.2.1   Benchmarking

In order to verify the correctness of our numerical implementation we compare our DQMC method with Stochastic Series Expansion [92] (SSE) QMC for a Fermi-Hubbard chain [88], where the FCS can be obtained straightforwardly by accumulating histograms over Monte Carlo measurement steps. Open boundary conditions are necessary to
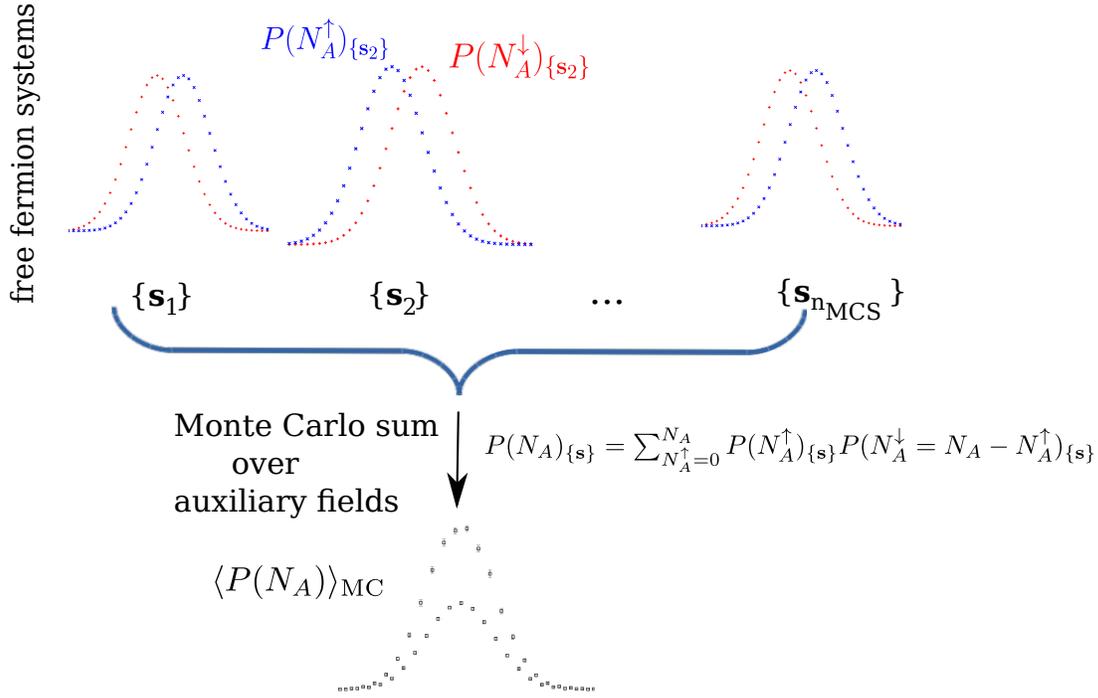
Fig. 9.2: Computation of the probability distribution $P(N_A)$ of the subsystem particle number $N_A = N_A^\uparrow + N_A^\downarrow$ with determinantal QMC. Each HS sample $\{\mathbf{s}\}$ represents a free fermion system in the external potential of auxiliary fields $\{\mathbf{s}\}$. See the main text for details.

ensure that the SSE QMC has no sign problem.[1] The agreement between the two methods is excellent (see Fig. 9.3).

9.3 FCS of the staggered particle number

To compute the full counting statistics (FCS) of the staggered particle number $N_A^{st} = \sum_{i \in A} (-1)^{\mathbf{i}} (\hat{n}_{i,\uparrow} + \hat{n}_{i,\downarrow})$ a modification of the method described in the previous section is necessary. The generating function of $P(N_A^{st})$ in one Hubbard-Stratonovich sample is

$$\chi_{\{\mathbf{s}\}}^{st}(\phi) = \mathrm{Tr}_\uparrow \left(e^{-H_A^\uparrow} e^{i\phi \sum_{\mathrm{B} \in A} (-1)^{\mathbf{i}} \hat{n}_{i,\uparrow}} \right) \quad \mathrm{Tr}_\downarrow \left(e^{-H_A^\downarrow} e^{i\phi \sum_{i \in A} (-1)^{\mathbf{i}} \hat{n}_{i,\downarrow}} \right). \tag{9.15}$$

Unlike the particle number $\hat{N}_A^\sigma = \sum_{i \in A} \hat{c}_{i,\sigma}^\dagger \hat{c}_{i,\sigma}$, the operator $i\phi \sum_{i \in A} (-1)^{\mathbf{i}} \hat{c}_{i,\sigma}^\dagger \hat{c}_{i,\sigma}$ does not commute with the single-particle entanglement Hamiltonian H_A^σ due to the staggering factor $(-1)^{\mathbf{i}}$. Therefore, there is no common eigenbasis in which one can simply add the eigenvalues of the two operators as was done in the last step leading to Eq. 9.12 of the main text. Instead, it is necessary to compute the single-particle matrix

---

[1] The SSE QMC benchmark results have been provided by Stefan Weßel.
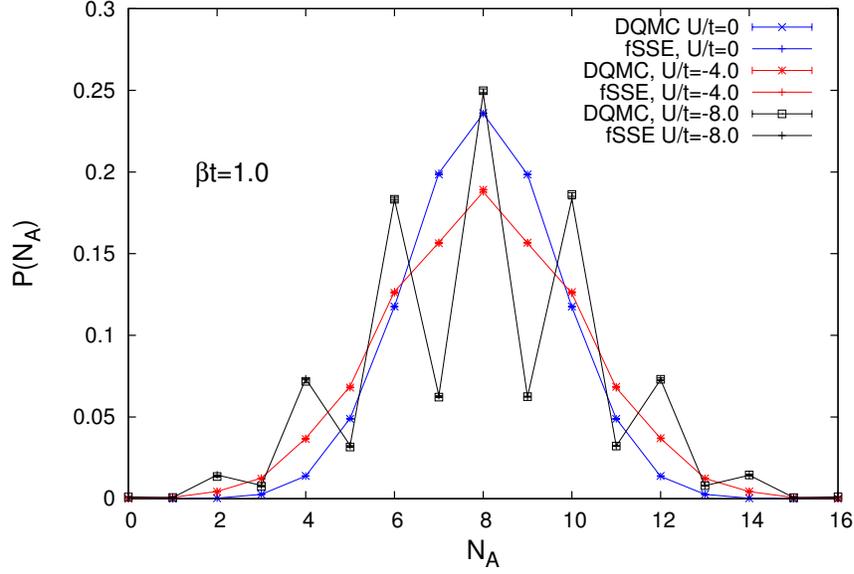
Fig. 9.3: Comparison of our DQMC method with Stochastic Series Expansion (SSE) QMC for a Fermi-Hubbard chain (fSSE) of $L = 16$ sites with open boundary conditions at inverse temperature $\beta t = 1.0$; shown is the particle number distribution $P(N_A)$; the subsystem size is $L_A = 8$.

representation of H_A^σ explicitly in the site basis[2], add the non-commuting operators

$$\left[\tilde{H}_A^\sigma\right]_{i,j} = [H_A^\sigma]_{i,j} + i\phi(-1)^{\mathbf{i}}\delta_{i,j} \tag{9.16}$$

and diagonalize the resulting modified entanglement Hamiltonian $\tilde{H}_A^\sigma$, which gives the eigenvalues $\tilde{\epsilon}^\sigma(\phi)$. The peculiarity of DQMC that the equal-time OBDM $\mathcal{G}_{\{\mathbf{s}\},A}^\sigma$ is non-Hermitian [119] and does not necessarily have a spectral decomposition leads to the complication that the single-particle matrix representation of the entanglement Hamiltonian H_A^σ in Eq. 9.12,

$$\left[H_{\{\mathbf{s}\},A}^\sigma\right]_{i,j} = -\left[\log\left(\left[\mathcal{G}_{\{\mathbf{s}\},A}\right]^{-1} - \mathbb{1}\right)\right]_{i,j} \tag{9.17}$$

---

[2] The entanglement Hamilonian for the interacting system is given through the definition

$$\rho_A = \sum_{\{\mathbf{s}\}} \rho_{\{\mathbf{s}\},A}^\uparrow \rho_{\{\mathbf{s}\},A}^\downarrow = \sum_{\{\mathbf{s}\}} \mathcal{K}_{\{\mathbf{s}\},A}^\uparrow \mathcal{K}_{\{\mathbf{s}\},A}^\downarrow e^{-H_{\{\mathbf{s}\},A}^\downarrow} e^{-H_{\{\mathbf{s}\},A}^\uparrow}$$

$$\equiv \mathcal{K}_A e^{-H_A},$$

where we have introduced explicitly the dependence of the non-interacting entanglement Hamiltonian on the auxiliary fields $\{\mathbf{s}\}$. This expression suggests that there is no straighforward connection between the single-particle matrix representation of the non-interacting entanglement Hamiltonian and the interacting many-body entanglement Hamiltonian H_A. A discussion how to compute H_A with determinantal QMC can be found in [270].

has to be computed explicitly through the power series of the matrix logarithm [271]. This needs to be done only once per Hubbard-Stratonovich sample as H_A^σ can be reused in (9.16) for different values of ϕ.

The grand-canonical trace (9.15) over fermionic degrees of freedom results in a single-particle determinant which is expressed in terms of the eigenvalues $\tilde{\epsilon}^\sigma(\phi)$ as

$$\chi_{\{\mathbf{s}\}}^{st}(\phi) = \prod_{\sigma=\uparrow,\downarrow} \left[\prod_{\alpha=1}^{N_s} (1 - \lambda_\alpha^\sigma) \left(1 + e^{-\tilde{\epsilon}_\alpha^\sigma(\phi)} \right) \right]. \tag{9.18}$$

Issues of numerical stability

The computation of the determinant Eq. (9.18) may be severely affected by numerical inaccuracies. For low temperatures the occupation numbers λ_α^σ in the free fermion system tend to 0 or 1 and, consequently, the OBDM $\mathcal{G}_{\{\mathbf{s}\},A}^\sigma$ is a nearly singular matrix. The evaluation of Eq. (9.17) in finite-precision arithmetic is beset with numerical instabilities and, even if a high-quality implementation of the matrix logarithm [271] is used, not all eigenvalues ϵ_α^σ of the entanglement Hamiltonian H_A^σ can be obtained with sufficient accuracy across the entire spectrum. Consider small (negative) "entanglement energy" ϵ_α^σ for which according to the Fermi-Dirac statistics $\lambda_\alpha^\sigma = \frac{1}{1+e^{\epsilon_\alpha^\sigma}} \approx 1$. The evaluation of $\epsilon_\alpha^\sigma = \log\left(\frac{1}{\lambda_\alpha^\sigma} - 1\right) \approx \log(1-1)$, or equivalently the evaluation of Eq. (9.17), is very inaccurate for the small (negative) real part of the entanglement spectrum since $\log(x)$ varies greatly for $x \to 0^+$. In view of round-off and cancellation errors it is therefore crucial to compute Eq. (9.12) with the mathematically equivalent formula

$$[H_A^\sigma]_{i,j} = - \left[\log\left(\mathcal{G}_{\{\mathbf{s}\},A}^\sigma (\mathbb{1} - \mathcal{G}_{\{\mathbf{s}\},A}^\sigma)^{-1} \right) \right]_{i,j}. \tag{9.19}$$

This expression shifts the accuracy to small (negative) ϵ_α^σ (large $\lambda_\alpha^\sigma \approx 1$) since $\log(x)$ is not much affected by errors in its *large* argument $x = \frac{\lambda_\alpha^\sigma}{1-\lambda_\alpha^\sigma}$. For the computation of Eq. (9.18) errors in the large (positive) part of the entanglement spectrum ϵ_α^σ are not problematic because large $\tilde{\epsilon}_\alpha^\sigma(\phi)$ are irrelevant in the factor $(1 - \lambda_\alpha^\sigma)\left(1 + e^{-\tilde{\epsilon}_\alpha^\sigma(\phi)}\right)$. Here it is assumed that the spectrum $\tilde{\epsilon}_\alpha^\sigma(\phi)$ of the modified entanglement Hamiltonian (9.16) is qualitatively similar to that of the entanglement Hamiltonian (9.17) in the sense that the accuracy of the relevant small $\tilde{\epsilon}_\alpha^\sigma(\phi)$ is not affected by the inaccuracy of large ϵ_α^σ.

Fig. 9.4 illustrates how, due to issues of finite numerical precision, neither Eq. (9.17) nor Eq. (9.19) can ensure perfect accuracy[3] over the entire spectrum once the $N_s \times N_s$ matrix $G_{\{\mathbf{s}\},A}^\sigma$ exceeds a certain size. The spectra shown in Fig. 9.4 are for a subsystem A of size $N_s = 80$ at $\beta t = 4$ and $U/t = -8$. The green crosses in Fig. 9.4(a-d) refer to the real (a-b) or imaginary (c-d) part of the entanglement spectrum $\varepsilon_n^\sigma =$

---

[3] To ensure a high-quality implementation of the matrix logarithm, here MATLAB's `logm()` function [271] has been used to evaluate Eqs. (9.17) and (9.19).

(a) Real part of entanglement spectrum ε_n^σ from diagonalizing H_A^σ, computed with Eq. (9.19).
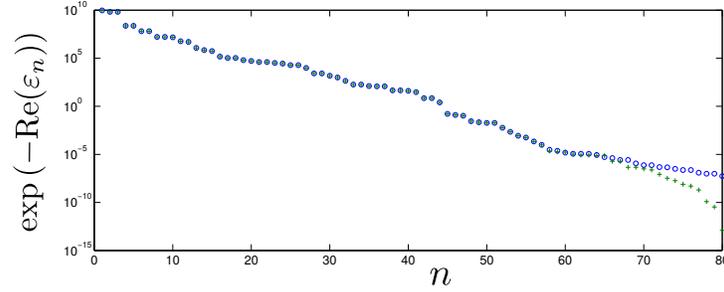
(b) Real part of entanglement spectrum ε_n^σ from diagonalizing H_A^σ, computed with Eq. (9.17).
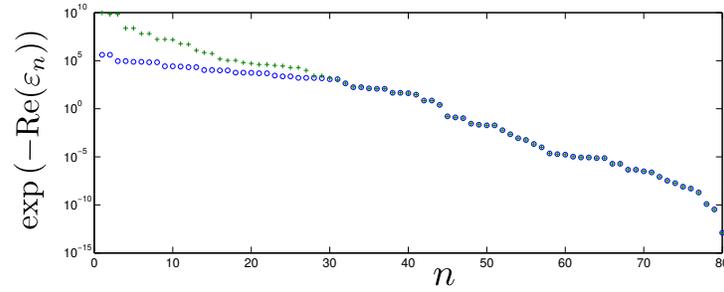
(c) Imaginary part of ε_n^σ computed according to Eq. (9.19).
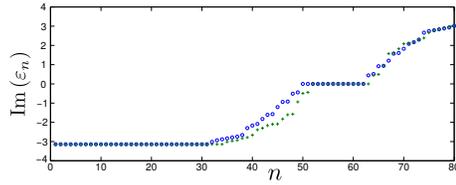
(d) Imaginary part of ε_n^σ computed according to Eq. (9.17).
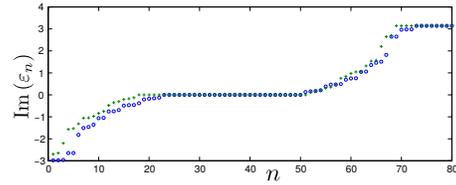
Fig. 9.4: Eigenvalue spectrum ε_n of the reduced density matrix $\rho_{\{s\},A}$ in one HS sample. Comparison of the spectrum computed from the entanglement Hamiltonian according to Eq. (9.19) (a,c) and according to Eq. (9.17) (b,d). Subfigures (a,b) show the real part of ε_n; (c,d) show the imaginary part. The parameters are: subsystem size $N_s = 80$, $\beta t = 4$, $U/t = -8$; the system size is $L = 20$.

$-\log\left(\frac{1}{\lambda_n^\sigma}-1\right)$ computed directly from the eigenvalues of the equal-time OBDM $\mathcal{G}_{\{\mathbf{s}\},A}^\sigma$. They serve as a benchmark to assess the accuracy with which formula Eq. (9.19) and the mathematically equivalent formula Eq. (9.17) for the single-particle entanglement Hamiltonian reproduce different parts of the spectrum. In these cases the entanglement Hamiltonian is computed either according to formula Eq. (9.19) [see Fig. 9.4(a,c)] or Eq. (9.17) [see Fig. 9.4(b,d)] and then diagonalized, resulting in the spectrum shown as open blue circles. Note that for obtaining merely the entanglement spectrum ε_n^σ the procedure of computing first the entanglement Hamiltonian is unnecessary, but it provides a way to compare the numerical accuracy of Eq. (9.19) and Eq. (9.17). The appropriate choice is of course Eq. (9.19) since it is accurate for small "entanglement energies" [see Fig. 9.4(a)], while Eq. (9.19) shifts the accuracy to large "entanglement energies" [see Fig. 9.4(b)] and gives inaccurate results for the most important eigenvalues of the reduced density matrix.

9.4   Results

In the following, we demonstrate our approach for the determination of the full counting statistics in the two-dimensional Fermi-Hubbard model [232] on a square lattice. The model can be efficiently simulated with DQMC for the attractive case $U < 0$ at arbitrary fillings, and for repulsive interactions at half-filling. Especially, at half filling and on bipartite lattices, we recall that a spin-down particle-hole transformation $\hat{c}_{\mathbf{r},\downarrow} \to (-1)^{r_x+r_y}\hat{c}_{\mathbf{r},\downarrow}^\dagger$ maps the attractive Hubbard model into the repulsive one. We have preformed all simulations for the attractive Hubbard model. For discussing the repulsive model at half filling we transform the observables according to the table given in Sect. 8.2.3. For example

$$N_A^{(st,U<0)} \to M_A^{(st,U>0)} = \sum_{i\in A}(-1)^{\mathbf{i}}(\hat{n}_{i,\uparrow}-\hat{n}_{i,\downarrow}) + \sum_{i\in A}(-1)^{\mathbf{i}}, \tag{9.20}$$

i.e. the staggered particle number in the attractive Hubbard model corresponds to the staggered magnetization plus a constant in the half-filled repulsive Hubbard model.

9.4.1   BCS-to-BEC crossover

We start with the presentation of the results for the *attractive Hubbard* model. The full counting statistics $P_N(N_A)$ for the particle number N_A on the sublattice A is derived within the setup illustrated in Fig. 9.1. The finite-temperature phase diagram [25, 26] of the attractive Hubbard model features, away from half filling, a Berezinskii-Kosterlitz-Thouless (BKT) transition at temperature T_{BKT} to a quasi long-range *s*-wave superconducting state. At half-filling, there is a degeneracy of s-wave superconductivity and charge density wave order, and the $SU(2)$ symmetry of the order parameter suppresses the transition temperature to zero according to the Mermin-Wagner theorm.

In both cases, there is a second clearly separated temperature scale $T^\star \sim |U|$ which marks the onset of pair formation without long-range phase coherence.
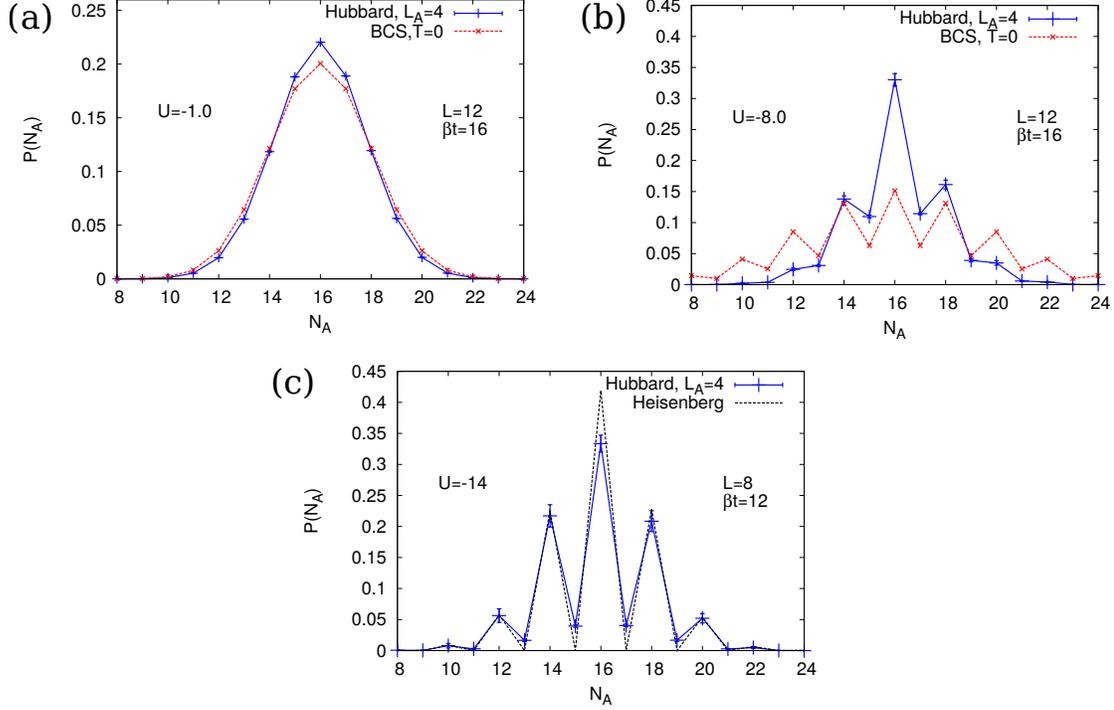
Fig. 9.5: Particle number distribution $P_N(N_A)$ along the BCS-to-BEC crossover at half filling for $U/t = -1, -8, -14$ (a-c). For comparison, the distribution for a BCS mean-field ansatz at $T = 0$ is shown in red (a,b), as well as the Heisenberg model for strong interactions (c). The Heisenberg model refers here to the strong-coupling limit of the *attractive* Hubbard model.

In Fig. 9.5(a-c), we present the behaviour of the full counting statistics in the crossover from the BCS-type superfluid of large overlapping Cooper pairs for weak interactions to a Bose Einstein condensate (BEC) of hardcore bosonic on-site pairs [241, 272, 273] for strong interactions. The temperature is chosen well below the characteristic temperature $T^\star$ for pair formation. A crucial aspect about the BEC-BCS crossover is that, as the attractive interaction is varied, no phase transition occurs, which is why it is termed a "crossover". In fact, for the continuum model, it was shown by Nozières and Schmitt-Rink [241] that the BCS ground state wave function

$$|\mathrm{BCS}\rangle = \prod_{\mathbf{k}} \left(u_{\mathbf{k}}(\mu, \Delta) + v_{\mathbf{k}}(\mu, \Delta) \hat{c}^{\dagger}_{\mathbf{k},\uparrow} \hat{c}^{\dagger}_{-\mathbf{k},\downarrow} \right) |0\rangle, \tag{9.21}$$

describes exactly both the extreme BCS and the BEC limit. Here, $u_{\mathbf{k}}$ and $v_{\mathbf{k}}$ are the usual Bogoliubov amplitudes and $\mu(n, U)$ and $\Delta(n, U)$ are self-consistent solutions of the gap and number equation [273], which depend on the density n and attractive

interaction U. The FCS for a BCS state, which is the ground state of a quadratic Hamiltonian, is derived in Appendix C.

It is instructive to compare the FCS for the BCS state of the lattice model with the numerically exact DQMC results at intermediate interactions and for low temperatures. With increasing $|U|$ the local number fluctuations of the BCS state Eq. (C.3) acquire a large unphysical extensive contribution (see Fig. 9.5(b) and Fig. 9.6), which obeys the Poisson distribution with $\langle (\langle N_A \rangle - N_A)^2 \rangle \sim \langle N_A \rangle$. Indeed, for the continuum model in the BEC limit one expects a Poissonian number statistics of pairs of atoms [262]. However, the wave function (C.3), when applied to a lattice model, fails to account for the nearest-neighbour repulsion [232] of tightly bound pairs in the limit of strong correlations $|U| \gg t$, where interactions between Bogoliubov quasiparticles need to be included [274]. As already mentioned, this is different from the equivalent model in the continuum where (C.3) becomes the exact ground state wavefunction both in the extreme BCS and BEC limit [241, 272, 273] and reproduces the correct particle number variance and higher cumulants [262].

In the limit of strong attraction [see Fig. 9.5(c)] the Heisenberg limit of strongly localized hard-core bosonic pairs with nearest neighbour repulsion is reached [232]. The resulting checkerboard charge density wave (CDW) ordered state is the equivalent of the Néel ordered state in the *repulsive* Hubbard model.

9.4.2 Pair size
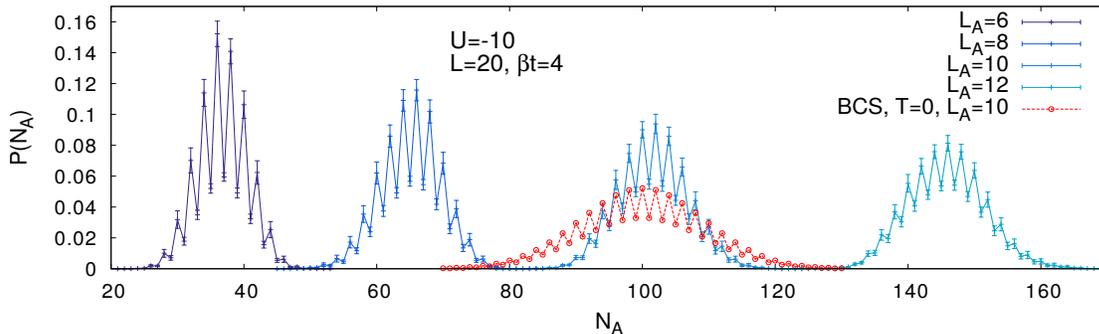
Fig. 9.6: Broadening of the distribution function $P(N_A)$ and smearing of the even-odd oscillations for increasing subsystem size L_A. The red dotted curve is for a BCS mean-field state at $T = 0$.

We observe a strong even-odd effect for increasing interactions. This phenomenon can be well understood through the size of the pairing wave function: in the extreme limit of very strong interactions, all fermions are paired up with a pair wave function localized on a single lattice site. Then, we expect a vanishing probability to find an odd number of fermions on subsystem A. An odd number of fermions can only appear due to unpaired fermions or a pairing function spreading over several lattice sites. The
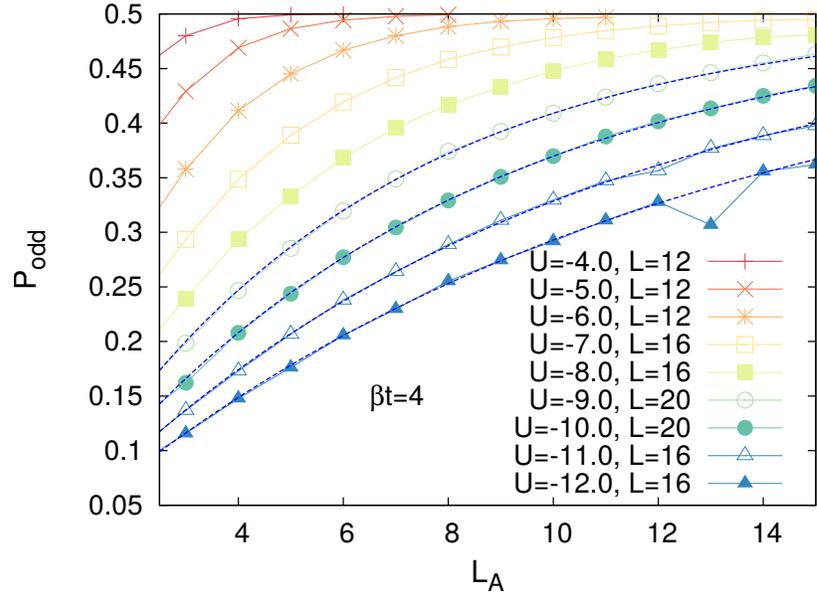
Fig. 9.7: Scaling of the even-odd splitting P_{odd} with linear subsystem size L_A. Blue dashed curves represent the fit function Eq. (9.22).

latter provides only a contribution for pairs along the boundary of subsystem A. In order to quantify this effect, we introduce $P_{\mathrm{odd}} = \sum_{N_A \in \mathrm{odd}} P(N_A)$ as a measure of the even-odd splitting. With increasing subsystem size L_A the even-odd oscillations are gradually smeared out [Fig. 9.6] and P_{odd} approaches $\frac{1}{2}$ for large L_A. We expect a scaling behavior

$$P_{\mathrm{odd}}(L_A) = \frac{1}{2} - \frac{1}{2}(1 - 2p_{\mathrm{deloc}})^{4L_A \cdot \langle n \rangle} \tag{9.22}$$

as a function of subsystem size L_A and atomic density $\langle n \rangle$; $4L_A \cdot \langle n \rangle$ estimates the number of pairs along the boundary. This ansatz is motivated by the idea of independent pairs randomly distributed in the sample.

Heuristic derivation of the scaling behaviour of $P_{\mathbf{odd}}(L_A)$

The ultimate justification for Eq. (9.22) is that it works extremely well as a fitting function over a large range of Hubbard interactions and densities. We can only provide a heuristic derivation of Eq. (9.22) that allows to identify p_{deloc} as a measure of the extent of the pair wave function. Assuming that pairs are randomly distributed in the sample, at filling $\langle n \rangle$ the average number of pairs along the boundary of a square of linear dimension L_A is $4\langle n \rangle L_A$. Pairs in the bulk do not contribute to P_{odd}. Each of the pairs along the boundary can delocalize across the boundary with a probability p_{deloc}. In the case of non-interating pairs, each of which is described by a pair wave function $\psi(x, y)$, we have that $p_{\mathrm{deloc}} = \sum_{x>0} |\psi(x, y)|^2$ where $r = (x, y)$ is the relative

coordinate between the two particles and p_{deloc} is the probability to find one partner of the pair in the right half-space while the other is in the left half-space. Under the assumption that pairs delocalize independently across the boundary, the probability that in total k pairs delocalize is given by the binomial distribution $\mathcal{B}_{4\langle n \rangle L_A, p_{\mathrm{deloc}}}(k)$ with $4\langle n \rangle L_A$ denoting the length of the Bernoulli sequence of delocalization events with probability p_{deloc} each. Then, the probability that an odd number of pairs delocalizes is

$$\sum_{k \in \mathrm{odd}} \mathcal{B}_{4\langle n \rangle \cdot L_A, p_{\mathrm{deloc}}}(k) = \frac{1}{2} - \frac{1}{2}(1 - 2p_{\mathrm{deloc}})^{4\langle n \rangle \cdot L_A}, \tag{9.23}$$

which is equal to $P_{\mathrm{odd}} = \sum_{N_A \in \mathrm{odd}} P(N_A)$ as long as unpaired fermions are suppressed at sufficiently low temperature. For a BCS mean-field state at $T = 0$ the fits to Eq. (9.22) are so perfect over a wide range of interactions and fillings that one may conjecture the fitting function (9.22) to be an analytically obtainable result for the BCS state, where, indeed, Cooper pairs are independent.

Pair size versus density and interaction strength

Then, for a pair centered next to the boundary, p_{deloc} denotes the weight of the pair wave function to be on the other side of the boundary. The inset in Fig. 9.9(a) shows the modulus squared of the pair wave function $\psi(x, y)$, with relative coordinate $\mathbf{r} = (x, y)$, computed for a single pair on a square lattice with onsite interation $U/t = -4$. The red bars indicate the probability $\sum_{x>0} |\psi(x, y)|^2$ for a pair to delocalize into the right half-space $x > 0$ when its center of mass is located next to the bounday in the left half-space. Therefore, we can interpret p_{deloc} as a measure for the size of the wave function. Indeed, we find a perfect fitting of P_{odd} to (9.22) for a large parameter regime, see dashed lines in Fig. 9.7, which allows us to extract the value p_{deloc} for
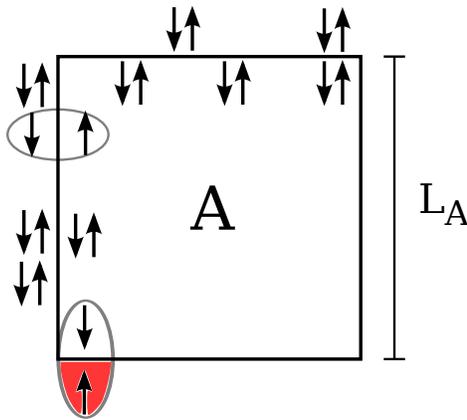
Fig. 9.8: Pairs around a square subregion A. The probability density of a pair wave function $\sum_{(x,y)\in B} |\psi(x,y)|^2$ outside subregion A is drawn schematically in red.
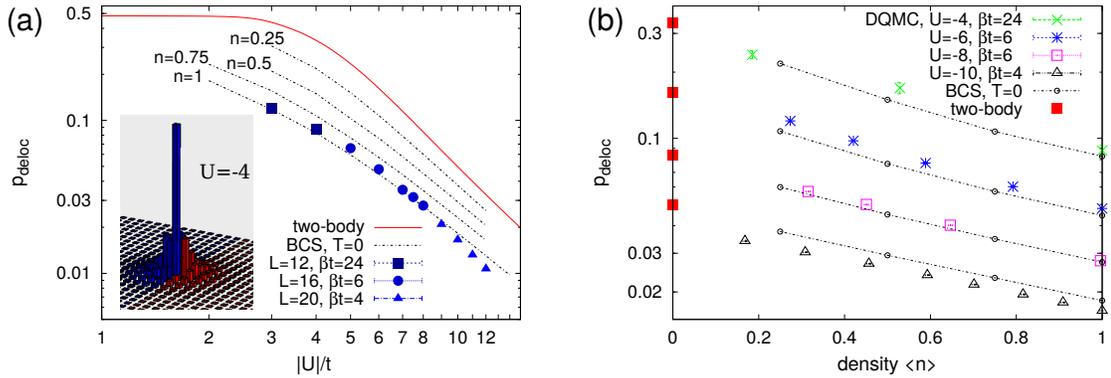
Fig. 9.9: Pair size p_{deloc} as a function of attractive interaction $-|U|/t$ (a) and filling $\langle n \rangle$ (b) in comparison with the predictions by mean-field theory in the BEC-BCS crossover. For clarity, data points in (b) for $\langle n \rangle \neq 1$ are not reproduced again in (a). The inset in (a) shows the two-body bound state in vacuum at $U/t = -4$ (see main text); the corresponding p_{deloc} is indicated by the solid red line in (a) and the red squares in (b). In the limit $\langle n \rangle \to 0$, the pair size as computed with DQMC approaches p_{deloc} for the two-body bound state in vacuum at the same interaction U.

different interactions and densities. The resulting p_{deloc} for the Hubbard model are shown in Fig. 9.9(a) at density $\langle n \rangle = 1$ and as a function of $|U|$; note that sufficiently low temperatures are required to suppress thermal pair breaking. In 2D the binding energy of a bound state is exponentially small in the attractive interaction [253, 275]. Therefore for $U/t = -3$, $L = 12$, a temperature as low as $\beta t = 24$ was necessary to achieve a fit to Eq. (9.22), whereas for large $|U|$, e.g. $U/t = -9$, "low enough" temperature is $\beta t = 4$. For large attraction $|U|$, p_{deloc} decreases approximately like $(t/U)^2$, as to be expected from perturbation theory. In Fig. 9.9(b) the behavior of p_{deloc} is shown for decreasing densities. The minimum of the the measure of the pairs size p_{deloc} at half filling, $\langle n \rangle = 1$, is a lattice effect (see [253] for the 2d continuum model), due to the logarithmically diverging van Hove singularity in the tight-binding density of states on the square lattice, which enhances pairing at half filling. As Fig. 9.9(b) demonstrates, BCS theory at T=0 gives a reasonably accurate estimate of the pair size even for intermediate values of U and densities $\langle n \rangle$.

From this quantitative analysis of the even-odd splitting we conclude that the FCS can serve as a powerful tool to observe the formation of pairing in a superconducting state and provides useful information about the size of the pairing wave function. We expect that this analysis carries over to systems where DQMC simulations are hard, such as the repulsive Hubbard model away from half-filling, and can serve as a powerful experimental detection tool.

9.4.3 Comparison with a quantum gas microscope experiment

Finally, we study the FCS for the staggered magnetization in the *repulsive Hubbard* model at half-filling. Recently, this model was extensively studied experimentally using cold atoms in optical lattices by Mazurenko *et al.* [20] at interactions $U/t = 7.2$ with a circular central region of homogeneous density involving approximately 80 sites surrounded by a dilute particle bath. For optimal comparison with the experiment, we determine the FCS of the staggered magnetization inside the same circular geometry as in the experiment, which is embedded in a large system of size $L \times L$ with $L = 20$ and periodic boundary conditions (see Fig. 9.10). In contrast to the experiment [Fig. 9.10(a)], where the particle reservoir around the sample area has a lower density, in the numerical simulations the reservoir is at the same chemical potential as the sample region [Fig. 9.10(b)].

In each experimental realization, a rapid ramp-up of the optical lattice suppresses the tunneling between sites and freezes out the atomic positions thus realizing a projective measurement in Fock space. Then the occupations on each lattice site are detected through gentle fluorescence imaging with simultaneous Raman sideband cooling [16]. This detection has some important limitations, which will be discussed below. Given this single-site resolution in the experiment, histograms of the staggered magnetization $M^{st} = \sum_i (-1)^{\mathbf{i}} (n_{i,\uparrow} - n_{i,\downarrow})$ inside the circular region were accumulated over more than 250 experimental realizations [20]. In Fig. 9.11, we show the original data points of Ref. [20] as the red histograms. As can be seen from Fig. 9.11, we find excellent agreement without any adjustable fit parameter. The width of the distribution of the staggered magnetization, $P(M_A^{st})$, shrinks with increasing temperature due to the
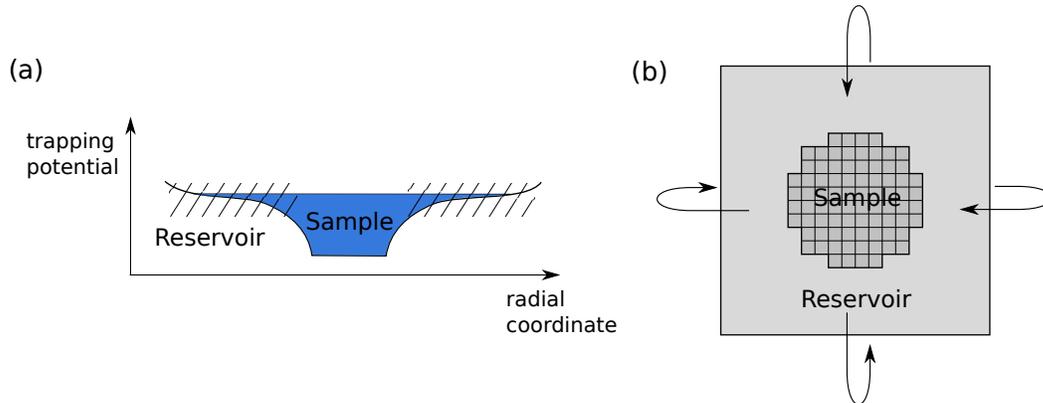
Fig. 9.10: (a) Optical box trap in the experiment of Mazurenko *et al.* [20], with a central homogeneous sample area of $N_s \approx 80$ sites surrounded by a large *dilute* particle reservoir. (b) Numerical simulation cell with the same shape of the sample area (where particles are counted) as in the experiment. It is embedded in a *homogeneous* $L \times L$ system of linear size $L = 20$ with periodic boundary conditions. For the simulation of the Heisenberg model the linear size is $L = 32$. (Figure (a) adapted from Mazurenko *et al.* [20].)
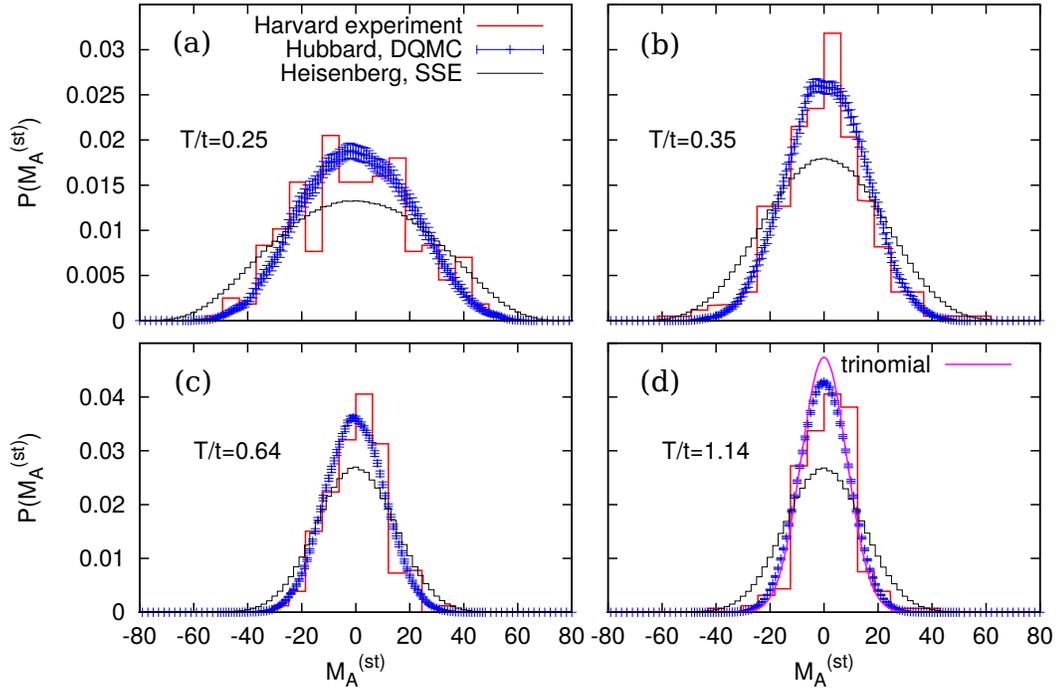
Fig. 9.11: FCS of the staggered magnetization on a disc-shaped subsystem of $N_s = 80$ sites for repulsive Hubbard interaction $U/t = 7.2$ at half filling and for the same temperatures (a)-(d) as in Ref. [20]. Red histograms are reproduced from Ref. [20] (with permission of the authors), blue error bars are our DQMC simulations. Binned FCS of the Heisenberg model at an equivalent temperature are shown in black. The magenta line in (d) is a simple model of independent sites (see Sect. 9.4.3).

disappearance of antiferromagnetic correlations. Furthermore, we find strong deviation from the predictions of the staggered magnetization from the $S = 1/2$ antiferromagnetic Heisenberg model. The latter takes the form $\mathcal{H}_{SO} = J \sum_{\langle i,j \rangle} \hat{\mathbf{S}}_i \cdot \hat{\mathbf{S}}_j$ with super-exchange coupling $J = 4t^2/U$, and follows as limiting theory of the Hubbard model for large interactions $U \gg t$; the corresponding temperature is given by $T/J = (T/t)U/(4t)$. The Heisenberg model is simulated with SSE QMC at the corresponding temperatures with the same circular geometry of $N_s = 80$ sites which is embedded in a larger system of linear dimension $L = 32$. For all temperatures, the half width of the distribution of the staggered magnetization for the Hubbard model is systematically smaller than that of the Heisenberg model. We expect charge fluctuations, namely doubly occupied sites and holes which reduce the staggered magnetization and which already play an important role at the given interaction strength $U/t = 7.2$, to be the cause of this difference: it is well established, that the next order correction to the Heisenberg model in t/U leads to second and third neighbour exchange as well as four-spin ring exchange interactions of order t^4/U^3 [248, 249]. Furthermore, the operator measuring the staggered magnetiztion is reduced by a renormalization factor $\left(1 - 8\frac{t^2}{U^2}\right)$ due to doublon-hole pairs [247]. We therefore conclude that at intermediate interaction strength $U/t = 7.2$ the differences between the Hubbard model and the Heisenberg model already play a significant role. The perfect agreement of the experimental data with our DQMC analysis demonstrates that the experiments are indeed capable of probing these corrections to the Heisenberg model. Furthermore it provides an independent and very accurate confirmation of the experimental temperatures, which were inferred in the experiment from comparing the value of the nearest-neighbour spin correlator [20] to DQMC predictions for the Hubbard model. Also, the large dilute particle reservoir can be regarded as equivalent to the homogeneous reservoir with periodic boundary conditions used in the numerical simulations.

Single-site single-atom resolution and parity projection

An important caveat for the comparison of our theoretical predictions with the experimental results is that most current setups have a limitation that has been referred to as *parity projection*. Due to light-assisted collisions during the imaging processes [13] pairs of atoms on the same site are ejected from the trap. Therefore doublons and holes (which have even particle number parity) cannot be distinguished in the final images. Furthermore, only one spin species could be measured at a time in the experiment of Ref. [20]. To measure one spin species selectively atoms of the opposite spin were ejected from the trap by a spin-removal pulse [16]. In this step doubly occupied sites are lost due to light-assisted collisions so that they do not contribute to the final image.[4]

---

[4] These limitations are experimental details rather than fundamental issues. They can be overcome by separating the two spin species spectrally in a magnetic field as in Ref. [227]. Full spin and atom-number resolved readout has been demonstrated in a bilayer optical lattice in Ref. [276].

As a consequence not all microscopic particle configurations and not all eigenvalues of observables derived from them can be counted correctly. This is illustrated in Figs. 9.12(a-d) for four representative configurations by means of comparing the true and measured magnetization $M_z = \sum_{\mathbf{i}}(n_{\mathbf{i},\uparrow} - n_{\mathbf{i},\downarrow})$ and staggered magnetization $M_z = \sum_{\mathbf{i}}(-1)^{\mathbf{i}}(n_{\mathbf{i},\uparrow} - n_{\mathbf{i},\downarrow})$. The measurement protocol consists in assuming that after a $\downarrow$-spin removal pulse all holes in the resulting image of $\uparrow$-spins are due to the presence of $\downarrow$-spins before the removal pulse. This is only a reasonable assumption at half filling and for large enough U/t such that doublons and the concomitant holes are

(a)　no holes or doublons　　　　　　　　　**(c)　doublon-hole pair on neigbouring sites**

	M_z	$M_z^{(st)}$
staggering factor $(-1)^{\mathbf{i}}$　　+　　−　　+ ↑ ↓ ↑ →	+1	+3
↓-spin removal　　　　　　　✓	✓	
↑ ○ ↑ →	+1	+3
experimentally measured　+1　-1　+1		

	M_z	$M_z^{(st)}$
+　　−　　+ ↑ ⇅ ○ →	+1	+1
✗	✓	
↑ ○ ○ →	-1	+1
+1　-1　-1		

(b)　isolated hole/doublon in an AFM configuration
h/d in ↑-position (↓-position)

(d)　doublon and hole on the same sublattice

	M_z	$M_z^{(st)}$
+　　−　　+ ↑ ↓ ○ →	0 (0)	+2 (-2)
✗	✗	
↑ ○ ○ →	-1	+1
+1　-1　-1	(-1)	(-3)

	M_z	$M_z^{(st)}$
+　　−　　+ ⇅ ↑ ○ →	+1	-1
✗	✗	
○ ↑ ○ →	-1	-3
-1　+1　-1		
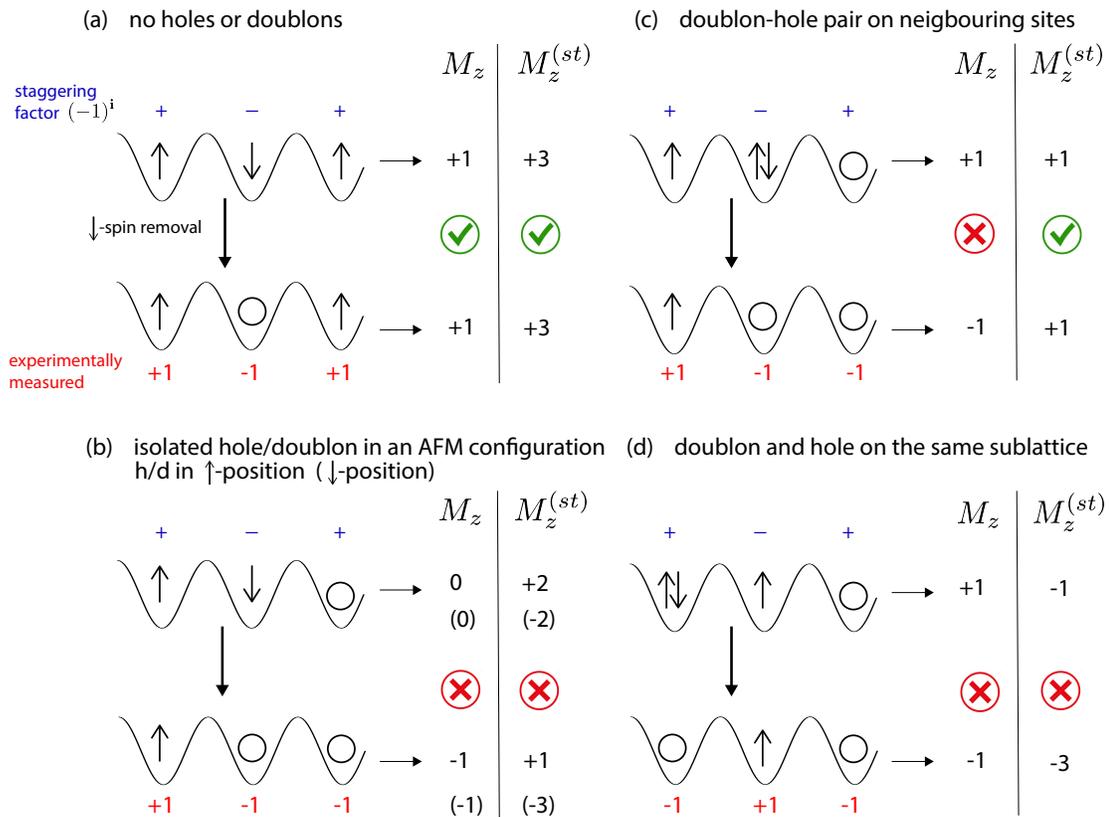
Fig. 9.12: Measurement protocol for reconstructing occupation number configurations in the quantum gas microscope experiment of Ref. [20]. Holes in the measured configuration after a $\downarrow$-spin removal pulse are assumed to be due to $\downarrow$-spins in the original configuration and are added as (-1) to the magnetization. Thus spin-only configurations (a) are reconstructed correctly. To reconstruct the staggered magnetization $M_z^{(st)} = \sum_i(n_{i,\uparrow} - n_{i,\downarrow})$ the staggering factor (blue plus or minus) is multiplied onto the reconstructed magnetization. As a consequence neighbouring doublon-hole pairs (c) contribute correctly to the staggered magnetization since two wrong values in the reconstructed magnetization are canceled by the staggering factor. Isolated holes or doublons (d) or doublon-holes pairs separated by a lattice site (d) are counted incorrectly.

largely suppressed. Fig. 9.12 shows three neighbouring sites of the square lattice, which can be thought to be collinear or non-collinear (i.e. sharing the same plaquette). Fig. 9.12(a) shows that spin-only configurations, which are in the state space of the Heisenberg model, are detected correctly. As can be seen from Fig. 9.12(c), because of the staggering factor, doublon-hole pairs on neighbouring sites are still counted correctly to the staggered magnetization while giving a wrong contribution to the magnetization. These configurations are the dominant charge fluctuations in the ground state wave function, with amplitude $\sim t/U$, and responsible for the kinetic AFM spin exchange. For configurations with isolated doublons and holes [Fig. 9.12(b)] or doublon-hole pairs that are separated by one site [Fig. 9.12(d)], neither the magnetization nor the staggered magnetization can be reconstructed with the given measurement protocol. However, in second order perturbation theory their amplitude is suppressed by a factor of t^2/U^2. In conclusion, doublon-hole pairs on neighbouring sites, which are the dominant charge fluctuations, are counted correctly to the staggered magnetization as a consequence of the staggering factor. Therefore, the experiments are currently exactly performing the measurement to observe the leading deviations between Heisenberg and Hubbard model. However, the observation of further corrections for lower interactions will require the precise experimental detection of the staggered magnetization.

Note that the present discussion pertains only to the full counting statistics of observables. Expectation values such as correlation functions can be obtained in spite of parity projection by combining averages of suitable correlators [17, 20].

Trinomial distribution at high temperatures

A simple model that is capable of describing the distribution of the staggered magnetization M_A^{st} in the limit of high temperatures (see Fig. 9.11(d)) regards the staggered magnetization at each lattice site as an independent random variable m_i^{st} which can take on the values $0, +1, -1$ with the probabilities

$$
\begin{aligned}
p_1 &\equiv p(m_i^{st} = +1) = p(\uparrow, +) + p(\downarrow, -) \\
p_2 &\equiv p(m_i^{st} = -1) = p(\uparrow, -) + p(\downarrow, +) \\
p_3 &\equiv p(m_i^{st} = 0) = p(d) + p(h) = 1 - p_1 - p_2,
\end{aligned}
\tag{9.24}
$$

with $p(\sigma, f)$ denoting the probability of the elementary event that a spin $\sigma \in (\uparrow, \downarrow)$ is placed on a lattice site with staggering factor $(-1)^{\mathbf{i}} \equiv f \in (+, -)$ and d and h signifying the placement of a doublon and hole, respectively. In the presence of particle-hole symmetry and equal chemical potentials for spin up and down, $p(d) = p(h)$ and $p(\uparrow, f) = p(\downarrow, -f)$, such that the probabilities of all three elementary events are described by the single parameter p_d, which we set to the average double occupancy $p_d \leftarrow \langle d \rangle = \frac{1}{N} \sum_i \langle \hat{n}_{i\uparrow} \hat{n}_{i\downarrow} \rangle$ as computed with Monte Carlo. The total staggered magnetization on a subsystem with N_s sites is given by a sum over a trinomial distribution

$$
P(M_A^{st} = k - l) = \sum_{k=0}^{N_s} \sum_{l=0}^{N_s - k} \delta_{M_A^{st}, k-l} P_3(X = k, Y = l)
\tag{9.25}
$$

where

$$P_3(X = k, Y = l) = \frac{N_s!}{k!\, l!\, (N_s - k - l)!}\, p_1{}^k p_2{}^l (1 - p_1 - p_2)^{N_s - k - l}. \tag{9.26}$$

For the distribution function in Fig. 9.11(d), the value $\langle d \rangle = 0.066(1)$ as extracted from the Monte Carlo simulations at temperature $T/t = 1.14$ was used. Thus, at this temperature the correlation length hardly exceeds one lattice site, which is in agreement with the conclusions of Ref. [20].

9.4.4 FCS of the magnetization
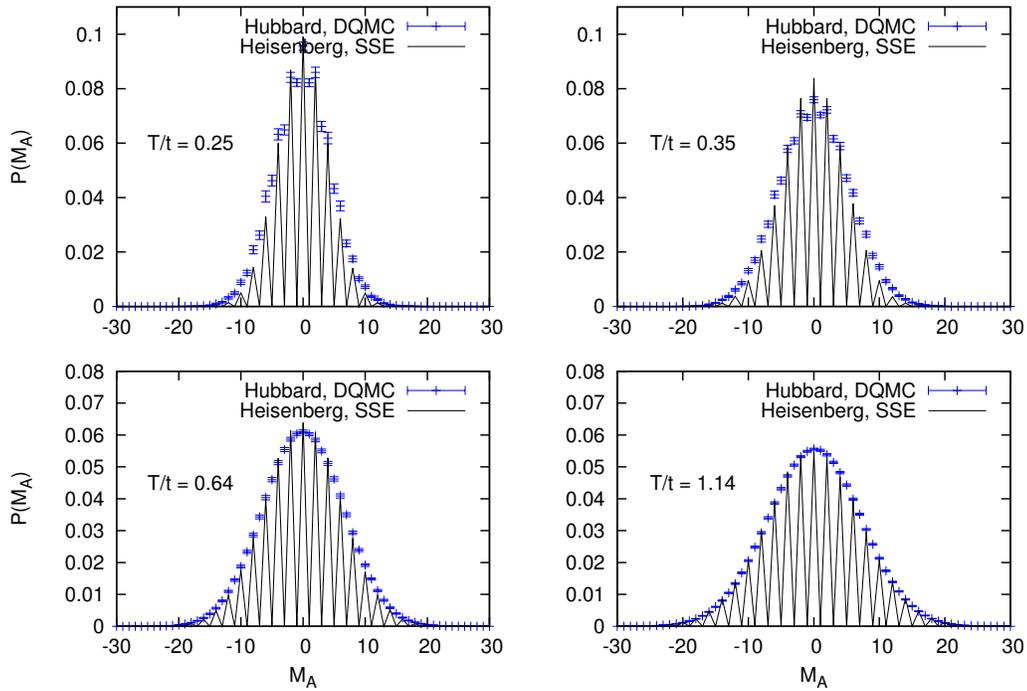
Fig. 9.13: FCS of the magnetization $\hat{M}_A = \sum_{i \in A}(\hat{n}_{i,\uparrow} - \hat{n}_{i,\downarrow})$ in the repulsive Hubbard model at half filling for a disc-shaped subsystem A of $N_s = 80$ sites. The parameters are the same as in Fig. 9.11.

In Fig. 9.13 we show the FCS of the magnetization $\hat{M}_A = \sum_{i \in A}(\hat{n}_{i,\uparrow} - \hat{n}_{i,\downarrow})$ for the *repulsive* Hubbard model, which, by virtue of a spin-down particle-hole transformation, corresponds to the particle number $\hat{N}_A = \sum_{i \in A}(\hat{n}_{i,\uparrow} + \hat{n}_{i,\downarrow})$ in the attractive Hubbard model. The origin of the even-odd splitting in language of the repulsive Hubbard model is the formation of local moments, which, when expressed in terms of the transformed observables for the attractive Hubbard model, corresponds to the formation of on-site

pairs. The FCS of the magnetization shown in Fig. 9.13 agrees much better between Hubbard and Heisenberg model than that of the staggered magnetization. This can be traced back to the fact that the total magnetization $\hat{M}^{\text{tot}} = \sum_i (\hat{n}_{i\uparrow} - \hat{n}_{i\downarrow})$ commutes with the Hubbard Hamiltonian $\mathcal{H}$ and the magnetization on a subsystem A commutes up to an operator $\hat{O}_{\partial A}$ that has support only on the boundary of A, $[\mathcal{H}, \hat{M}_A] = \hat{O}_{\partial A}$, which comes from the change of magnetization due to particles hopping into and out of the subsystem. A possible renormalization factor of the magnetization that derives from the canonical transformation of the Hubbard model into a spin-only Hamiltonian [247] should then be at most a boundary effect. For temperatures $T/t = 0.25$ and $T/t = 0.35$ a tiny even-odd modulation is visible in the FCS of the magnetization. This is the precursor of the full suppression of odd magnetizations in the FCS of the Heisenberg model. Unlike in Fig. 9.11, in Fig. 9.13 odd magnetizations have not been binned together with the nearest even magnetization to give a smooth histogram. Instead, the probability distribution $P(M_A)$ for the Heisenberg model has been divided by the bin width, i.e. by two, to aid the visual comparison with the probability distribution for the Hubbard model which has twice as many possible values for M_A on the abscissa.

In Fig. 9.14 the distribution $P(M_A)$ of the magnetization in the repulsive Hubbard model at half filling is shown for small subsystems of size 3×3 and 4×4. The interaction strength ranges from $U = 4$ to $U = 14$ and the inverse temperature from $\beta t = 0.5$ to $\beta t = 2$. Already at these high temperatures an even-odd splitting is visible for large enough Hubbard repulsion U.

9.4.5 Staggered magnetization at low temperatures

Fig. 9.15 shows the distribution $P(M_A^{st})$ of the staggered magnetization $\hat{M}_A^{st} = \sum_{i \in A} (-1)^{\mathbf{i}} (\hat{n}_{i,\uparrow} - \hat{n}_{i,\downarrow})$ in the half-filled repulsive Hubbard model at $U/t = 7.2$ for small subsystems A. In the left column of Fig. 9.15, the FCS is shown for the highest and lowest temperatures realized in the experiment of Ref. [20]. For the highest temperature $T/t = 1.14$, we find good agreement with a simple model based on the trinomial distribution (magenta line) which treats each lattice site as independent (see previous section) and is parametrized solely by the average double occupancy $p_d = \frac{1}{N} \sum_{\mathbf{r}} \langle \hat{n}_{\mathbf{r},\uparrow} \hat{n}_{\mathbf{r},\downarrow} \rangle = 0.066(1)$ as computed with Monte Carlo for the given temperature. Interestingly, the even-odd splitting in $P(M_A^{st})$ is smeared out much more quickly with increasing subsystem size than in the case of $P(M_A)$. The origin of the even-odd asymmetry is in both cases the formation of local moments; however, contrary to M_A (N_A for $\mathcal{H}_{U<0}$ and half filling), which can only change by $\Delta M_A = \pm 1$ when a particle crosses the boundary of subsystem A, M_A^{st} (N_A^{st} for $\mathcal{H}_{U<0}$ and half filling) is additionally affected by hopping processes in the bulk of A, which change the staggered magnetization by $\Delta M_A^{st} = \pm 2$. At this level of analysis and at half filling, the even-odd splitting in $P(M_A^{st})$ provides no additional information beyond the parameter p_{deloc} extracted earlier from the even-odd splitting in $P(M_A)$ (or rather $P(N_A)$ for $H_{U<0}$).

The right column of Fig. 9.15 shows the distribution $P(M_A^{st})$ at low temperature

$T/t = 0.0625$. On the 2×2 subsystem it is rather similar to its high-temperature counterpart at $T/t = 0.25$. For the larger subsystems of 3×3 and 4×4 sites, however, the distribution at low temperature is considerably wider than at $T/t = 0.25$. Furthermore, it is non-Gaussian, and for the 4×4 subsystem there seems to be a sharp drop of $P(M_A^{st})$ at a maximum value of the staggered magnetization M_A^{st}. The underlying physical picture is that of a local Néel ordering vector that can point in any direction in spin space [20]. The distribution of $P(M_A^{st})$ results then from averaging the z-component of this local ordering vector over all orientations on the sphere (as well as from averaging over the distribution of lengths of the ordering vector). With the assumption that the length $\langle |\vec{S}| \rangle$ of the local order parameter does not fluctuate one obtains the distribution

$$P(M_A^{(st)}) = \frac{2}{\pi \langle |\vec{S}| \rangle} \sqrt{1 - \left(\frac{M_A^{(st)}}{\langle |\vec{S}| \rangle} \right)^2}, \qquad M_A^{(st)} \leq \langle |\vec{S}| \rangle, \tag{9.27}$$

for its z-component, which already captures qualitatively the distribution for the 4×4 system at low temperature shown in Fig. 9.15. Deviations from Eq. (9.27), for instance for $M_A^{(s)} > \langle |\vec{S}| \rangle$, can be attributed to fluctuations of the length of the local order parameter vector. For large subsystem sizes the distribution becomes flat. In contrast, for the Ising model, which in the ordered phase breaks a discrete symmetry, one expects, on a finite system, a bimodal order parameter distribution with peaks at $\pm M_A$.

9.5 Conclusion and outlook

In this chapter, a method has been presented to compute full quantum mechanical probability distributions of quadratic operators in interacting fermion systems which can be simulated with DQMC. For the attractive Hubbard model the dependence of an even-odd splitting in the particle number distribution function allows one to infer the size of a preformed pair or Cooper pair from *in situ* images. Furthermore, we apply the method to the repulsive Hubbard model, which has recently been studied experimentally [20]. The excellent agreement with the experimental FCS of the staggered magnetization demonstrates that the experiments are capable of observing corrections to the Heisenberg model for the intermediate interaction strength $U/t = 7.2$. Additionally, the comparison of the FCS gives an independent and sensitive validation of the temperatures, which in the experiment of Ref. [20] were inferred by comparing the value of the nearest-neighbour spin correlator to DQMC predictions.

The methodology described in this chapter can be extended in several directions. By introducing additional counting fields in the generating function joint probability distributions can be computed, e.g. between the outcomes of different observables or observables on different subsystems. Starting from the single-particle Green's function in momentum space, all details of the method carry over to the computation of the

eigenvalue distribution of observables in momentum space, which are accessible in cold atoms experiments in time-of-flight (projective) measurements [48]. The FCS in time-of-flight images of one-dimensional Bose gases has been investigated in Ref. [277], where universal regimes of particle number distributions were observed. A similar, interesting question concerns the universality of order parameter distribution functions [278] at a quantum critical point. A suitable quantum critical point that can be approached with DQMC would be the transition from a semi-metal to an antiferromagnetic Mott insulator on the honeycomb lattice at half filling [279, 280].

The problem of parity projection leading to the loss of particles on doubly occupied sites [17, 20], has been overcome in the experiment of Ref. [22] with a special detection scheme that allows to image doublons. Furthermore, the relevance of doublon-hole correlations away from half filling for the putative anomalous transport properties of the Hubbard model in the "strange metal phase" [5] at high temperatures has been emphasized [17]. This provides a strong motivation for developing a numerical scheme for DQMC that can also access the FCS of the number of doublons, holes or singly occupied sites

$$\hat{n}_i^{(d)} = \hat{n}_{i,\uparrow}\hat{n}_{i,\downarrow}, \tag{9.28a}$$

$$\hat{n}_i^{(h)} = (1 - \hat{n}_{i,\uparrow})(1 - \hat{n}_{i,\downarrow}), \tag{9.28b}$$

$$\hat{n}_i^{(soc)} = \hat{n}_{i,\uparrow}(1 - \hat{n}_{i,\downarrow}) + \hat{n}_{i,\downarrow}(1 - \hat{n}_{i,\uparrow}), \tag{9.28c}$$

which are, unfortunately, quartic in fermionic creation and annihilation operators. The DQMC scheme presented in Sect. 9.2 for quadratic operators such as particle number or magnetization is therefore not directly applicable. Let $\hat{N}_A^{(q)} = \sum_{i \in A} \hat{n}_i^{(q)}$ be the number operator for entities composed of four fermion operators, with $q \in \{d, h, soc\}$. Preliminary studies suggest that the quartic terms in the generating function

$$\chi_A^{(q)} = \frac{\text{Tr}\left(e^{i\phi \hat{N}_A^{(q)}} e^{-\beta(\hat{H}_t + \hat{H}_U - \mu\hat{N})}\right)}{\text{Tr}\left(e^{-\beta(\hat{H}_t + \hat{H}_U - \mu\hat{N})}\right)} \tag{9.29}$$

can be decoupled with the same Hubbard-Stratonovich transformation that is applied to the interaction terms $\hat{H}_U$ in the partition sum after Trotter-Suzuki decomposition.
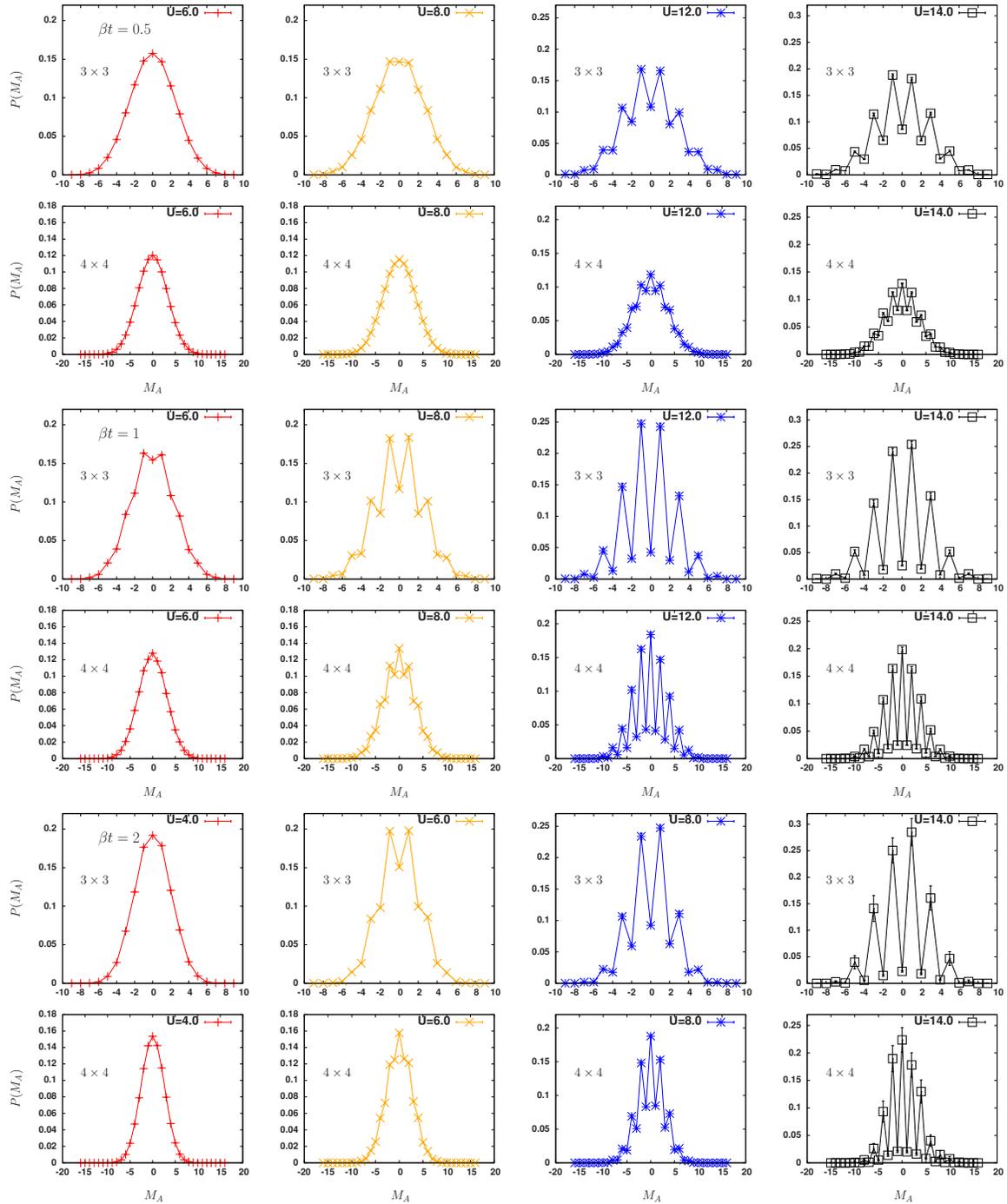
Fig. 9.14: FCS of the magnetization $\hat{M}_A = \sum_{i \in A}(\hat{n}_{i,\uparrow} - \hat{n}_{i,\downarrow})$ in the repulsive Hubbard model at half filling for $N_s = 3 \times 3$ and $N_s = 4 \times 4$ subsystems. The total system size is 16×16 lattice sites with periodic boundary conditions. The inverse temperature is $\beta t = 0.5$ (upper two rows), $\beta t = 1$ (middle two rows), and $\beta t = 2$ (lowest two rows).
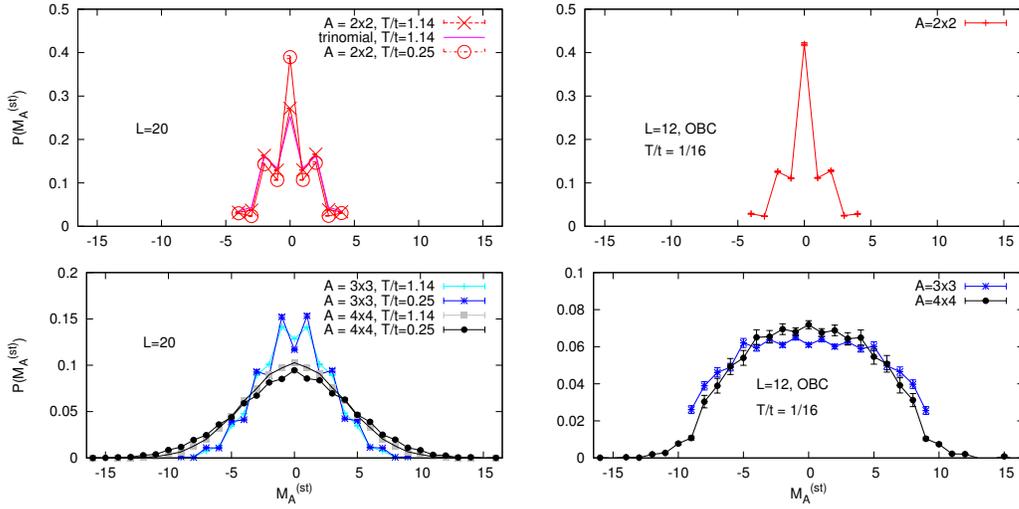
Fig. 9.15: FCS of the staggered magnetization $\hat{M}_A^{st} = \sum_{i \in A} (-1)^{\mathbf{i}} (\hat{n}_{\mathbf{i},\uparrow} - \hat{n}_{\mathbf{i},\downarrow})$ in the repulsive Hubbard model at half filling on small subsystems of $N_s = 2 \times 2, 3 \times 3$, and 4×4 sites at $U/t = 7.2$. **Left column:** FCS for the highest and lowest temperature of Ref. [20]. Total linear system size $L = 20$ with periodic boundary conditions. The magenta line is calculated from a trinomial distribution according to Eq. (9.25). The only parameter entering this calculation is the double occupancy $p_d = 0.0661$ (see Sect. 9.4.3), which was extracted from the Monte Carlo simulations at temperature $T/t = 1.14$. **Right column:** FCS for a low temperature $T/t = 1/16 = 0.0625$. The linear system size is $L = 12$ with open boundary conditions (OBC). The probe area A is located at the center of the $L \times L$ square with OBC.

Chapter 10

Noise correlations

In this chapter, numerical results for momentum-momentum correlation functions from DQMC calculations of the Hubbard model at half filling are presented. In time-of-flight measurements in cold atoms experiments, these correlations appear in the fluctuations of the recorded signal, i.e. as correlations in the atom shot noise in absorption images [48]. Ultimately, such experimentally measured *noise correlations* contain the probabilistic element due to wave function collapse im momentum space.

10.1 Significance of the one- and two-body momentum distribution

The one-body and two-body momentum distributions $\langle \hat{n}_{\mathbf{k}} \rangle$ and $\langle \hat{n}_{\mathbf{k}} \hat{n}_{\mathbf{k}'} \rangle$ are fundamental conceptual quantities of many-body theory. At zero temperature, the discontinuity of the momentum distribution at the Fermi surface $\Delta n_{k_F} = \lim_{k \to k_F^-} \langle \hat{n}_{\mathbf{k}} \rangle - \lim_{k \to k_F^+} \langle \hat{n}_{\mathbf{k}} \rangle$ is exactly equal to the electronic quasiparticle weight [281, 282]. In fact, a non-zero quasiparticle weight is equivalent to the validity of Landau's Fermi liquid theory, which is based on the presence of long-lived quasiparticles in the vicinity of a well-defined Fermi surface. A discontinuity in $\langle \hat{n}_{\mathbf{k}} \rangle$ coincides with a finite direct current (DC) conductivity (Drude weight) [283] and thus it provides a (formal) criterion to distinguish between metals and insulators: In the transition from a metal to an insulator at zero temperature the discontinuity at the Fermi level vanishes and the momentum distribution function $\langle n_{\mathbf{k}} \rangle$ becomes a smooth function of the single-particle energies $\epsilon_{\mathbf{k}}$. Thus, the discontinuity of the momentum distribution is the hallmark of a Fermi liquid (at least at zero temperature).

In a fermionic superfluid the momentum distribution is a smooth function [284] that resembles the Fermi function of a normal Fermi gas at finite temperature [285, Chapt. 2.5]. For strong attractive interactions it represents the pair wave function in momentum space [284]; however, without being sensitive to the phase coherence between the pairs. Therefore the momentum density is not a good indicator of superfluidity.

Long-range superconducting order appears instead in a second-order order correlation function: A sharp peak in the momentum-momentum correlation function $\langle \hat{n}_{\mathbf{k}} \hat{n}_{\mathbf{k}'} \rangle$ can be shown to imply a non-zero superfluid weight [283, 286] and the presence of the Meissner effect, which is the signature of superconductivity. This is quite analogous to the sharp peak in $\langle n_{\mathbf{k}} \rangle$ at zero momentum signaling the transition to a Bose-Einstein condensate and the macroscopic occupation of a single-particle state, except that for a fermionic superfluid a two-particle pairing state becomes macroscopically occupied.

10.2 Time-of-flight measurements

In experiments with ultracold quantum gases, the momentum distribution and momentum correlations have played an important role from the very beginning [48], since they can be obtained directly from time-of-flight measurements. Starting with the milestone experiment of the observation of the superfluid to Mott insulator transition for ultracold bosonic atoms [287] through the vanishing of the coherence peak in the momentum distribution, correlations between momentum states were observed for a bosonic Mott-insulating state [288, 289] and a (band-insulating) Fermi gas [290] in the noise correlations in time-of-flight images. Momentum correlations of dissociating bound atom pairs which have initially zero center of mass (COM) momentum, and whose components therefore fly into opposite directions, were also probed experimentally [291].

Noise correlations have revealed the breaking of translational symmetry due to (diagonal) density order [292, 293], for example in a honeycomb Hubbard model where density wave order was enforced by a staggered potential [294]. To date noise correlations that are indicative of superconducting correlations, as proposed in [295], have not been experimentally observed yet since the required temperatures for fermionic off-diagonal long-range order are much lower than for density order.

If the confining potential is released, the atomic cloud expands, with atoms in higher momentum states moving faster. For long times of flight t, their position $\mathbf{r}(t)$ in the expanding cloud is mapped to the in-trap momentum $\mathbf{k}$ through the ballistic expansion formula $\mathbf{k}(\mathbf{r}) = m\mathbf{r}(t)/\hbar t$ [10]:

$$\langle \hat{n}(\mathbf{r}) \rangle_{\text{TOF}} = \langle \hat{c}^{\dagger}_{\text{TOF}}(\mathbf{r}) \hat{c}_{\text{TOF}}(\mathbf{r}) \rangle_{\text{TOF}}$$
$$= \left(\frac{m}{\hbar t} \right)^{d} |\tilde{w}(\mathbf{k})|^2 \langle \hat{c}^{\dagger}(\mathbf{k}) \hat{c}(\mathbf{k}) \rangle_{\text{trap}} \sim \langle \hat{n}(\mathbf{k}) \rangle_{\text{trap}}. \tag{10.1}$$

Here, $(m/\hbar t)^d$ is a factor coming from the transformation of the volume element $d^d x$ to $d^d k$ and $\tilde{w}(\mathbf{k})$ is the Fourier transform of the Wannier function in the lattice. It is assumed that during the expansion no interactions are present that could modify the momentum distribution. For interpreting these measurements it is crucial to note that, in each experimental image, a single realization of the density is observed, not an average. The momentum distribution in Eq. (10.1) is the result of an average

over many time-of-flight images, which is indicated by the angular brackets $\langle \cdot \rangle_{\text{TOF}}$. This means that density-density correlations obtained from a correlation analysis over different (single-shot) time of flight absorption images contain information about the momentum-momentum correlations of the initial quantum state in the trap [10, 295]

$$\langle \hat{n}(\mathbf{r})\hat{n}(\mathbf{r}') \rangle_{\text{TOF}} \sim \langle \hat{c}^\dagger(\mathbf{k})\hat{c}(\mathbf{k})\hat{c}^\dagger(\mathbf{k}')\hat{c}(\mathbf{k}') \rangle_{\text{trap}}$$
$$= \langle \hat{n}(\mathbf{k}) \rangle_{\text{trap}}\delta_{\mathbf{k},\mathbf{k}'} + \langle \hat{c}^\dagger(\mathbf{k})\hat{c}^\dagger(\mathbf{k}')\hat{c}(\mathbf{k}')\hat{c}(\mathbf{k}) \rangle_{\text{trap}}. \tag{10.2}$$

Here, a momentum-dependent factor $|\tilde{w}(\mathbf{k})|^2|\tilde{w}(\mathbf{k}')|^2$ was omitted [1]. We define the noise correlations as the connected correlation function

$$\mathcal{C}_{\sigma\sigma'}(\mathbf{k},\mathbf{k}') = \langle \hat{n}_{\mathbf{k},\sigma}\hat{n}_{\mathbf{k}',\sigma'} \rangle - \langle \hat{n}_{\mathbf{k},\sigma} \rangle\langle \hat{n}_{\mathbf{k}',\sigma'} \rangle. \tag{10.3}$$

Momenta $\mathbf{k}$ are defined up to reciprocal lattice vectors. The measurement of $\mathcal{C}_{\uparrow\downarrow}(\mathbf{k},\mathbf{k}')$ requires that in the absorption images both spin states can be addressed independently and quasi-instantaneously, which was demonstrated in Ref. [291]. As a consequence of the Pauli principle $\hat{n}_{\mathbf{k},\sigma}^2 = \hat{n}_{\mathbf{k},\sigma}$ and the noise correlation function of the same species $\mathcal{C}_{\uparrow\uparrow}(\mathbf{k},\mathbf{k}' = \mathbf{k}) = \langle \hat{n}_{\mathbf{k},\uparrow}\hat{n}_{\mathbf{k},\uparrow} \rangle - \langle \hat{n}_{\mathbf{k},\uparrow} \rangle\langle \hat{n}_{\mathbf{k},\uparrow} \rangle$ reduces simply to the binomial variance $\langle \hat{n}_{\mathbf{k},\uparrow} \rangle(1 - \langle \hat{n}_{\mathbf{k},\uparrow} \rangle)$ of the probability $0 < \langle \hat{n}_{\mathbf{k},\uparrow} \rangle < 1$ for mode $(\mathbf{k},\uparrow)$ to be occupied or not. $\mathcal{C}_{\uparrow\uparrow}$ is non-zero whenever the momentum distribution deviates from the Fermi step function, be it due to finite temperature or interactions. For the special case of an ideal Fermi gas, $\mathcal{C}_{\uparrow\downarrow}$ vanishes due to the factorization of the correlator in Eq. (10.3).

10.3   Noise correlations in mean-field theory

For a BCS mean-field state at zero temperature [285]

$$|\text{BCS}\rangle = \prod_{\mathbf{k}} \left(u_{\mathbf{k}} + v_{\mathbf{k}}c^\dagger_{\mathbf{k},\uparrow}c^\dagger_{-\mathbf{k},\downarrow} \right) |\text{vac}\rangle, \tag{10.4}$$

the noise correlation function for opposite spins evaluates to [295]

$$\mathcal{C}^{\text{BCS}}_{\uparrow\downarrow}(\mathbf{k},\mathbf{k}') = \delta_{\mathbf{k},-\mathbf{k}'}u_{\mathbf{k}}^2 v_{\mathbf{k}}^2 = \delta_{\mathbf{k},-\mathbf{k}'}\frac{|\Delta_{\mathbf{k}}|^2}{4E_{\mathbf{k}}^2}, \tag{10.5}$$

and the one for the same spin species becomes

$$\mathcal{C}^{\text{BCS}}_{\uparrow\uparrow} = \delta_{\mathbf{k},\mathbf{k}'}\frac{|\Delta_{\mathbf{k}}|^2}{4E_{\mathbf{k}}^2}, \tag{10.6}$$

---

[1]For a deep optical lattice, the Wannier function in the lowest band is a Guassian and consequently its Fourier transform is also a Gaussian. On a finite system the experimental noise correlation signal exhibits interference fringes that develop into sharp Bragg peaks in the thermodynamic limit. In our notation these effects are left aside.

with $E_{\mathbf{k}} = +\sqrt{(\epsilon_{\mathbf{k}} - \mu)^2 + \Delta_{\mathbf{k}}^2}$ the dispersion relation of Bogoliubov quasiparticles. The gap parameter $\Delta_{\mathbf{k}}$ and the chemical potential μ are self-consistent simultaneous solutions of the gap equation (C.4) and the number equation (C.5). Already the fact that the product of coherence factors $u_{\mathbf{k}} v_{\mathbf{k}}$ appears in Eq. (10.5), suggests a connection with pairing correlations since $\langle c_{\mathbf{k},\uparrow} c_{-\mathbf{k},\downarrow} \rangle \sim u_{\mathbf{k}} v_{\mathbf{k}}$. The δ-function in Eq. (10.5) can be understood as follows: In the BCS state, for every atom in state $\mathbf{k} \uparrow$ there is with certainty another atom in state $-\mathbf{k} \downarrow$.

Furthermore Eq. (10.5) shows that the symmetry of the pair wave function is also reflected in the noise correlations [295]. If e.g. the gap parameter has d-wave symmetry, $\Delta_{\mathbf{k}} = \Delta_0(\cos(k_x) - \cos(k_y))$, then $\mathcal{C}_{\uparrow\downarrow}(\mathbf{k}, \mathbf{k}' = -\mathbf{k})$ plotted as a function of $\mathbf{k}$ exhibits nodes along the lines $k_x = \pm k_y$ where the gap $\Delta_{\mathbf{k}}$ vanishes [234]. The noise correlations are maximal in the region in momentum space where the dispersion $E_{\mathbf{k}}$ takes on its smallest value, that is on the non-interacting Fermi surface.

A peculiarity of the Hubbard model at half filling is that in the ground state charge density wave (CDW) order is degenerate with s-wave superconductivity [24]. This coexistence of diagonal (CDW) and off-diagonal (superconductivity) long-range order is some form of "supersolidity". Broken translational invariance due to formation of a CDW is also reflected in the noise correlations [296]. A mean-field ansatz for a CDW state on the square lattice is given by [2]

$$|\text{CDW}\rangle = \prod_{|\mathbf{k}| < k_F} \prod_{\sigma} \left[u_{\mathbf{k}} c_{\mathbf{k},\sigma}^{\dagger} + v_{\mathbf{k}} c_{\mathbf{k}+\mathbf{Q},\sigma}^{\dagger} \right] |\text{vac}\rangle. \tag{10.7}$$

By inserting, for every $\mathbf{k}$-factor, an identity $\mathbb{1} = c_{\mathbf{k},\sigma}^{\dagger} c_{\mathbf{k},\sigma} + c_{\mathbf{k}} c_{\mathbf{k},\sigma}^{\dagger}$ in front of the vacuum for c-operators, we obtain an expression of the CDW state in terms of particle-hole excitations on top of a filled Fermi sea (FS) [297, 298]:

$$|\text{CDW}\rangle = \prod_{|\mathbf{k}| < k_F} \prod_{\sigma} \left[u_{\mathbf{k}} + v_{\mathbf{k},\sigma} c_{\mathbf{k}+\mathbf{Q},\sigma}^{\dagger} c_{\mathbf{k},\sigma} \right] \underbrace{\prod_{|\mathbf{k}| < k_F, \sigma} c_{\mathbf{k},\sigma}^{\dagger} |\text{vac}\rangle}_{|\text{FS}\rangle}. \tag{10.8}$$

The structure of Eq. (10.8) is analogous to the BCS state and indeed it can be obtained from Eq. (10.4) by a spin-down particle-hole transformation (see Eq. (10.23) below) in which also the vacuum state is transformed accordingly [234]. When there is a hole with spin σ at $\mathbf{k}$ in the state $|\text{CDW}\rangle$, then there is definitely a particle with the same spin at $\mathbf{k} + \mathbf{Q}$, and one expects anticorrelations between $n_{\mathbf{k},\sigma}$ and $n_{\mathbf{k}+\mathbf{Q},\sigma}$. As a consequence $\mathcal{C}_{\uparrow\uparrow}(\mathbf{k}, \mathbf{k}' = \mathbf{k} + \mathbf{Q})$ exhibits a negative dip on the Fermi surface.

The momentum scattering processes on the Fermi surface associated with the BCS, the CDW and the η-paired state, which has center of mass momentum (COM) $\mathbf{Q} = (\pi, \pi)^2$, are depicted in Fig. 10.1(a-c).

---

[2] It shall be understood that momenta are always in units of inverse lattice spacing, i.e. (π, π) means $(\pi/a, \pi/a)$.
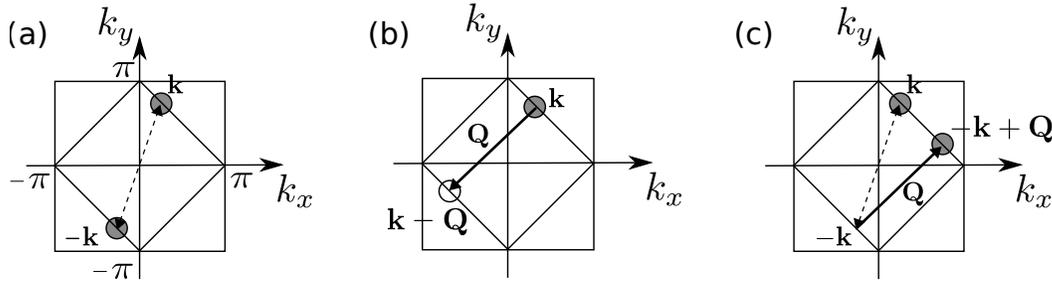
Fig. 10.1: First Brillouin zone with scattering processes on the Fermi surface of the half-filled square lattice. (a) Particle-particle momentum correlations of Cooper pairs, i.e. particle-particle scattering of pairs with COM momentum zero close to the Fermi surface. (b) Particle-hole scattering with nesting vector $\mathbf{Q} = (\pi, \pi)$ in a CDW state. (c) Particle-particle momentum correlations of η-pairs, which have COM momentum $\mathbf{Q}$.

Finite temperature

In order to evaluate the noise correlations at finite temperature, one needs to include the excitations of Bogoliubov quasiparticles above the BCS ground state [285]. They form a non-interacting Fermi gas so that their statistics is described by the Fermi-Dirac distribution $f(E_\mathbf{k}) = 1/(e^{\beta E_\mathbf{k}} + 1)$. The chemical potential for the quasiparticles is pinned to zero since their total number is not a conserved quantity. Due to the gap in the excitation spectrum $E_\mathbf{k}$ the distribution $f(E_\mathbf{k})$ approaches zero in the limit $\beta \to \infty$ for *all* momenta $\mathbf{k}$, which is different from the usual Fermi step function for electron occupations and means that quasiparticle excitations are gapped out. Expressing the original fermionic operators through the quasiparticle operators $\alpha_\mathbf{k}$ and $\beta_\mathbf{k}$ via the Bogoliubov-Valatin transformation [299, 300]

$$
\begin{aligned}
c^\dagger_{\mathbf{k},\uparrow} &= u_\mathbf{k}\alpha^\dagger_\mathbf{k} - v_\mathbf{k}\beta_\mathbf{k} \\
c_{-\mathbf{k},\downarrow} &= v_\mathbf{k}\alpha^\dagger_\mathbf{k} + u_\mathbf{k}\beta_\mathbf{k},
\end{aligned}
\tag{10.9}
$$

we can write the momentum-momentum correlation function as

$$
\begin{aligned}
\langle n_{\mathbf{k},\uparrow} n_{\mathbf{k}',\downarrow} \rangle &= \langle c^\dagger_{\mathbf{k},\uparrow} c_{\mathbf{k},\uparrow} c^\dagger_{\mathbf{k}',\downarrow} c_{\mathbf{k}',\downarrow} \rangle \\
&= \Big\langle \left(u_\mathbf{k}\alpha^\dagger_\mathbf{k} - v_\mathbf{k}\beta_\mathbf{k} \right) \left(u^\star_\mathbf{k}\alpha_\mathbf{k} - v^\star_\mathbf{k}\beta^\dagger_\mathbf{k} \right) \\
&\qquad \left(v^\star_{-\mathbf{k}'}\alpha_{-\mathbf{k}'} + u^\star_{-\mathbf{k}'}\beta^\dagger_{-\mathbf{k}'} \right) \left(v_{-\mathbf{k}'}\alpha^\dagger_{-\mathbf{k}'} + u_{-\mathbf{k}'}\beta_{-\mathbf{k}'} \right) \Big\rangle
\end{aligned}
\tag{10.10}
$$

and the momentum distribution as

$$
\langle n_{\mathbf{k},\sigma} \rangle = u^2_\mathbf{k} f(E_\mathbf{k}) + v^2_\mathbf{k}(1 - f(E_\mathbf{k})).
\tag{10.11}
$$

In Eq. (10.11) we have already identified the distribution function of thermally excited quasiparticles $\langle \alpha^\dagger_\mathbf{k}\alpha_\mathbf{k} \rangle = \langle \beta^\dagger_\mathbf{k}\beta_\mathbf{k} \rangle = f(E_\mathbf{k})$ and used the fact that off-diagonal terms in quasiparticle operators do not contribute to averages. Noting that the α- and

β-quasiparticles are statistically independent, $\langle \alpha_{\mathbf{k}}^\dagger \alpha_{\mathbf{k}} \beta_{\mathbf{k}'}^\dagger \beta_{\mathbf{k}'} \rangle = \langle \alpha_{\mathbf{k}}^\dagger \alpha_{\mathbf{k}} \rangle \langle \beta_{\mathbf{k}'}^\dagger \beta_{\mathbf{k}'} \rangle$, applying Wick's theorem, e.g.

$$
\begin{aligned}
\langle \alpha_{\mathbf{k}}^\dagger \alpha_{\mathbf{k}} \alpha_{-\mathbf{k}'}^\dagger \alpha_{-\mathbf{k}'} \rangle &= \langle \alpha_{\mathbf{k}}^\dagger \alpha_{\mathbf{k}} \rangle \langle \alpha_{-\mathbf{k}'}^\dagger \alpha_{-\mathbf{k}'} \rangle + \langle \alpha_{\mathbf{k}}^\dagger \alpha_{-\mathbf{k}'} \rangle \langle \alpha_{\mathbf{k}} \alpha_{-\mathbf{k}'}^\dagger \rangle \\
&= f(E_{\mathbf{k}}) f(E_{\mathbf{k}'}) + \delta_{\mathbf{k},-\mathbf{k}'} f(E_{\mathbf{k}})(1 - f(E_{\mathbf{k}})) \\
&= \langle \beta_{\mathbf{k}}^\dagger \beta_{\mathbf{k}} \beta_{-\mathbf{k}'}^\dagger \beta_{-\mathbf{k}'} \rangle,
\end{aligned}
\tag{10.12}
$$

and subtracting the momentum distributions from Eq. (10.10), which cancels most terms, we arrive at expressions for the noise correlations at finite temperature in the BCS approximation:

$$
\mathcal{C}_{\uparrow\downarrow}^{\mathrm{BCS}}(\mathbf{k}, \mathbf{k}') = \delta_{\mathbf{k},-\mathbf{k}'} \frac{|\Delta_{\mathbf{k}}|^2}{4 E_{\mathbf{k}}^2} \left[1 - 4 f(E_{\mathbf{k}})(1 - f(E_{\mathbf{k}})) \right],
\tag{10.13}
$$

$$
\mathcal{C}_{\uparrow\uparrow}^{\mathrm{BCS}}(\mathbf{k}, \mathbf{k}') = \delta_{\mathbf{k},\mathbf{k}'} \frac{|\Delta_{\mathbf{k}}|^2}{4 E_{\mathbf{k}}^2} \left[1 - 4 f(E_{\mathbf{k}})(1 - f(E_{\mathbf{k}})) \right] + \delta_{\mathbf{k},\mathbf{k}'} f(E_{\mathbf{k}})(1 - f(E_{\mathbf{k}})).
\tag{10.14}
$$

As expected, the correlation signal of BCS pairing in Eq. (10.13) is reduced by thermally excited quasiparticles. Note that $2 f(E_{\mathbf{k}})(1 - f(E_{\mathbf{k}}))$ is the probability for single-particle occupation of the pair state $(\mathbf{k} \uparrow, -\mathbf{k} \downarrow)$, namely that either $\mathbf{k} \uparrow$ is occupied and $-\mathbf{k} \downarrow$ is empty or the reverse. In the normal state, $\mathcal{C}_{\uparrow\downarrow}^{\mathrm{BCS}}$ vanishes together with the gap, while $\mathcal{C}_{\uparrow\uparrow}^{\mathrm{BCS}}$ turns into the binomial variance $f(\epsilon_{\mathbf{k}} - \mu)(1 - f(\epsilon_{\mathbf{k}} - \mu))$ for a free particle state with energy $\epsilon_{\mathbf{k}}$ to be occupied or not.

Exactly at the Fermi surface (of the non-interacting system) $E_{\mathbf{k}} \to \Delta_{\mathbf{k}}$ and the prefactors in Eqs. (10.13) and (10.14) cancel such that the gap parameter drops out. We let from now on denote by $\bar{\mathbf{k}}$ a vector on the Fermi surface. Then it holds that $\mathcal{C}_{\uparrow\uparrow}^{\mathrm{BCS}}(\bar{\mathbf{k}}, \bar{\mathbf{k}}) = \frac{1}{4}$ at any temperature. Incidentally, the same is true for the Hubbard model at half filling, where due to particle-hole symmetry $\langle n_{\mathbf{Q}-\mathbf{k},\sigma} \rangle = 1 - \langle n_{\mathbf{k},\sigma} \rangle$ for the nesting vector $\mathbf{Q} = (\pi, \pi)$, as was discussed in Sect. 8.2.1. On the non-interacting Fermi surface where the condition $\bar{\mathbf{k}} = \mathrm{mod}\left(\mathbf{Q} - \bar{\mathbf{k}}, \mathbf{G} \right)$ with a reciprocal lattice vector $\mathbf{G}$ is met, i.e. at $\bar{k} = (0, \pm\pi)$ or $\bar{k} = (\pm\pi, 0)$, this implies $\langle n_{\bar{\mathbf{k}}} \rangle = \frac{1}{2}$ and

$$
\mathcal{C}_{\uparrow\uparrow}(\bar{\mathbf{k}}, \bar{\mathbf{k}}) = \langle n_{\bar{\mathbf{k}}} \rangle (1 - \langle n_{\bar{\mathbf{k}}} \rangle) = \frac{1}{4}
\tag{10.15}
$$

at any interaction strength and temperature. We used this as a check for verifying the Monte Carlo simulations presented in Sect. 10.4. For momenta exactly on the Fermi surface, the noise correlations between different spin species read

$$
\begin{aligned}
\mathcal{C}_{\uparrow\downarrow}^{\mathrm{BCS}}(\bar{\mathbf{k}}, -\bar{\mathbf{k}}) &= \frac{1}{4} \left[1 - 4 f(\Delta_{\mathbf{k}})(1 - f(\Delta_{\mathbf{k}})) \right] \\
&= \frac{1}{4} \left[1 - \cosh^{-2}\left(\frac{\beta \Delta_{\mathbf{k}}}{2} \right) \right] = \frac{1}{4} \tanh^2\left(\frac{\beta \Delta_{\mathbf{k}}}{2} \right).
\end{aligned}
\tag{10.16}
$$
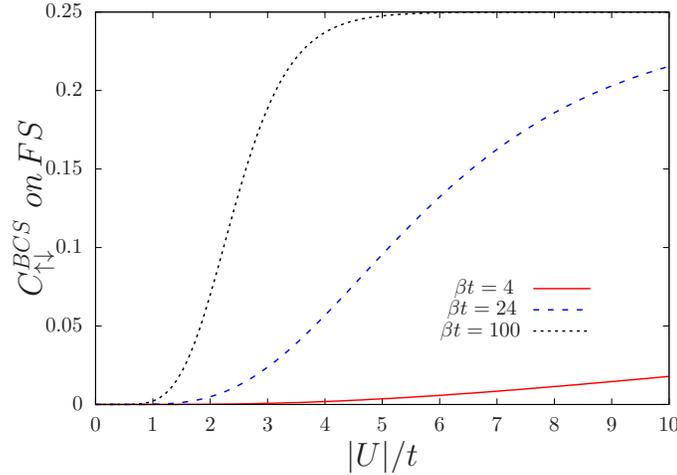
Fig. 10.2: Upper bounds to the noise correlation signal $C_{\uparrow\downarrow}^{BCS}(\bar{\mathbf{k}}, -\bar{\mathbf{k}})$ exactly at the Fermi surface (FS) as a function of attractive Hubbard interaction for the 2d square lattice. The curves are an upper bound to the "exact" result in BCS theory since the gap parameter in Eq. (10.16) was approximated by its mean-field value at zero temperature Eq. (10.17).

Inserting into (10.16) the mean-field (MF) s-wave solution of the gap equation for the Hubbard model on the square lattice [120]

$$\Delta_{\mathrm{MF}} \sim t\, e^{-2\pi\sqrt{t/U}} \quad \text{(T=0)}, \tag{10.17}$$

which is an upper bound on the gap at finite temperature, one realizes that the noise correlation signal for different spin species $\mathcal{C}_{\uparrow\downarrow}^{\mathrm{BCS}}(\bar{\mathbf{k}}, -\bar{\mathbf{k}})$ is strongly suppressed for small Hubbard attraction $|U|$ (see Fig. 10.2) due to the ease with which Bogoliubov quasiparticles can be excited across a gap that is exponentially small in the attractive interaction strength. As shown in Fig. 10.2, for intermediate values of $|U|/t$ with $\beta t = 24$ the signal $\mathcal{C}_{\uparrow\downarrow}^{\mathrm{BCS}}(\bar{\mathbf{k}}, -\bar{\mathbf{k}})$ still remains well below the maximum possible value of $\frac{1}{4}$ by a factor of 2 to 4. At the lowest inverse temperature of $\beta t \approx 4$ that was reached [20] to date in a cold atoms experiment, noise correlations between different spin species are so small as to be essentially unobservable in the BCS limit of small $|U|/t$. This conclusion follows already from the mean-field analysis at finite temperature and applies both to the lattice and the continuum model. Given that mean-field theory overestimates the gap parameter, one may expect that the noise correlations will be even smaller once quantum fluctuations are fully taken into account, which is the subject of Sect. 10.4.

Non-zero center of mass (COM) momenta

It was pointed out in Ref. [264] that the mean-field approximation underlying Eq. (10.5) results in an inconsistency which can only be resolved by taking quantum fluctuations,

namely correlations between Cooper pairs, into account. In the language of Feynman diagrams, vertex corrections in the superfluid state need to be evaluated [264, 285] to recover the particle number conservation, which is violated by the standard BCS ansatz of Eq. (10.4). This diagrammatic calculation leads, for a continuum model in the BCS limit and at zero temperature, to the dependence [264]

$$
\mathcal{C}_{\uparrow\downarrow}(\mathbf{k}, \mathbf{k}') = \frac{\Delta^2}{4E_{\mathbf{k}}^2} \left[\delta_{\mathbf{k}, -\mathbf{k}'} + \frac{1}{\langle N_p \rangle} \langle n_p \rangle(\mathbf{q}) \right] + \tilde{\mathcal{C}}_{\mathrm{bg}}(\mathbf{k}, \mathbf{k}'),
\tag{10.18}
$$

where $\langle n_p \rangle(\mathbf{q} = \mathbf{k} + \mathbf{k}')$ $(\mathbf{q} \neq 0)$ is the momentum distribution function of Cooper pairs with non-zero center of mass momentum, $\langle N_p \rangle = (\langle N_\uparrow \rangle + \langle N_\downarrow \rangle)/2$ is the average number of pairs and $\tilde{\mathcal{C}}_{\mathrm{bg}}$ is a background contribution [264]. The noise away from the central peak at $\delta_{\mathbf{k}, -\mathbf{k}'}$ scales like $1/\langle N_p \rangle$ and has an angular dependence $\langle n \rangle(\mathbf{q}) \sim 1/|\mathbf{q}|$. This dependence on $\mathbf{q}$ is a generic feature of structure factors in bosonic and spin systems and can be deduced from a generalization of the Heisenberg uncertainty principle [301]. Although Eq.(10.18) is derived in Ref. [264] for a continuum model, we expect that the main features of non-zero momentum pairs and a smooth background contribution carry over to the Hubbard model.

Sect. 10.4 presents numerically exact DQMC calculations of noise correlations for the Hubbard model at half filling for low and experimentally relevant high temperatures. When the interactions are tuned, this system represents an example of the BCS-to-BEC crossover, however, with the peculiarity that at half filling the ground state of the attractive Hubbard model is degenerate, admitting long-range charge density wave (CDW) order in addition to s-wave superconductivity (SC), which is present at any filling. Both the diagonal (CDW) and off-diagonal (SC) correlations give a signature in the noise correlations.

Several theoretical works have focused on noise correlations in the ground state of Hubbard-like models. A variational Monte Carlo study investigating the smearing effects in the noise correlations due to a harmonic trapping potential and the detectability of density wave order (which coexists with superfluidity in a supersolid state) was presented in [302]. How more unconventional forms of pairing, which arise in spin imbalanced systems and can lead for instance to fermion pairs with non-zero center of mass momentum (Fulde-Ferrell-Larkin-Ovchinnikov phase), leave their fingerprint in the noise correlations, was studied in [303] for a one-dimensional attractive Hubbard model with DMRG as well as in [304] for one- and two-dimensional systems in a mean-field approximation.

10.4   Numerical results from QMC

The momentum-momentum correlation function $\langle n_{\mathbf{k},\sigma} n_{\mathbf{k}',\sigma'} \rangle$ is the Fourier transform of a four-operator correlation function

$$\langle n_{\mathbf{k}\sigma} n_{\mathbf{k}'\sigma'} \rangle = \frac{1}{N^2} \sum_{\mathbf{ijlm}}^{N} e^{i\mathbf{k}(\mathbf{i}-\mathbf{j})} e^{i\mathbf{k}'(\mathbf{l}-\mathbf{m})} \langle c_{\mathbf{i}\sigma}^{\dagger} c_{\mathbf{j}\sigma} c_{\mathbf{l}\sigma'}^{\dagger} c_{\mathbf{m}\sigma'} \rangle \tag{10.19}$$

where $\mathbf{i}, \mathbf{j}, \mathbf{l}, \mathbf{m}$ and $\mathbf{k}, \mathbf{k}'$ are vectors representing the sites in real and momentum space and N is the total number of sites. Eq. (10.19) involves four sums over all lattice sites which is computationally expensive if evaluated naively. However, as shown below, in one Hubbard-Stratonovich configuration computing two sums turns out to be sufficient. We first consider the case where both spin states are equal, $\sigma = \sigma'$. For each configuration of the Hubbard-Stratonovich auxiliary field, $\{\mathbf{s}\}$, Wick's theorem can be applied to write the four-operator correlation function in terms of products of single-particle Green's functions:

$$\langle c_{i\sigma}^{\dagger} c_{j\sigma} c_{l\sigma}^{\dagger} c_{m\sigma} \rangle_{\{\mathbf{s}\}} = \langle c_{i\sigma}^{\dagger} c_{j\sigma} \rangle_{\{\mathbf{s}\}} \langle c_{l\sigma}^{\dagger} c_{m\sigma} \rangle_{\{\mathbf{s}\}} + \langle c_{i\sigma}^{\dagger} c_{m\sigma} \rangle_{\{\mathbf{s}\}} \langle c_{j\sigma} c_{l\sigma}^{\dagger} \rangle_{\{\mathbf{s}\}} \tag{10.20}$$

Pulling the phase factors in (10.19) into the averages in (10.20), the Fourier transformation can be carried out, which leads to

$$\langle n_{\mathbf{k}\sigma} n_{\mathbf{k}'\sigma} \rangle_{\{\mathbf{s}\}} = \langle n_{\mathbf{k}\sigma} \rangle_{\{\mathbf{s}\}} \langle n_{\mathbf{k}'\sigma} \rangle_{\{\mathbf{s}\}} + \delta_{\mathbf{k},\mathbf{k}'} \langle n_{\mathbf{k}\sigma} \rangle_{\{\mathbf{s}\}} - \langle c_{\mathbf{k}\sigma}^{\dagger} c_{\mathbf{k}'\sigma} \rangle_{\{\mathbf{s}\}} \langle c_{\mathbf{k}'\sigma}^{\dagger} c_{\mathbf{k}\sigma} \rangle_{\{\mathbf{s}\}}. \tag{10.21}$$

Thus, for one Hubbard-Stratonovich configuration the momentum-momentum correlation function for $\sigma = \sigma'$ is given in terms of the momentum distribution function, $\langle n_{\mathbf{k}\sigma} \rangle_{\{\mathbf{s}\}}$, and the expectation value of a scattering term in momentum space, $\langle c_{\mathbf{k}\sigma}^{\dagger} c_{\mathbf{k}'\sigma} \rangle_{\{\mathbf{s}\}}$, which constitutes the true two-body term. This formula is more economical from a computational point of view as computing each terms involves only two sums over all sites whereas the original expressions (10.19) and (10.20) required four sums over all sites. Since the weight of a Hubbard-Stratonovich configuration factorizes for different spin states, it is obvious that

$$\langle n_{\mathbf{k}\sigma} n_{\mathbf{k}'\sigma'} \rangle_{\{\mathbf{s}\}} = \langle n_{\mathbf{k}\sigma} \rangle_{\{\mathbf{s}\}} \langle n_{\mathbf{k}'\sigma'} \rangle_{\{\mathbf{s}\}} \tag{10.22}$$

for $\sigma \neq \sigma'$.

For the calculation of noise correlations it turned out to be practical to store the fermionic Green's functions for every 10th Monte-Carlo step on hard disk so that any desired equal-time quantity can be computed afterwards. Since we are only interested in equal-time correlations, we save the Green's function $\langle c_i(\tau_l) c_j^{\dagger}(\tau_l) \rangle_{\{\mathbf{s}\}}$ for the Hubbard-Stratonovich configuration $\{\mathbf{s}\}$ at a randomly chosen imaginary time slice τ_l. In parameter regimes with a sign problem, the sign of the determinant of the Green's function needs to be also recomputed (unless it is stored together with the Green's function). The memory requirements are huge, but manageable; for the

simulations presented in this an the following chapter in total 30 TB of hard disk memory were needed. Averages are computed from 96 independent Markov chains with 500 to 1000 measurement steps per Markov chain taken at intervals of 10 Monte Carlo steps each.

10.4.1   Attractive Hubbard model at half filling

The noise correlation data in this and the following sections is for half filling, where the attractive and repulsive Hubbard model are identical, and although the simulations at high temperature (Fig. 10.6 and Fig. 10.10) were performed for the repulsive model and those at low temperature for the attractive one (Fig. 10.6 and Fig. 10.9), we choose the language of the attractive model throughout for the sake of a consistent presentation. The spin-down particle-hole transformation $c_{\mathbf{i},\downarrow} = c_{i_x i_y,\downarrow} \leftrightarrow (-1)^{i_x+i_y} c^\dagger_{i_x i_y,\downarrow}$, that maps the attractive to the repulsive Hubbard model at half filling, reads in momentum space [234]

$$
\begin{aligned}
c_{\mathbf{k},\downarrow} &\leftrightarrow c^\dagger_{-(\mathbf{k}+\mathbf{Q}),\downarrow} \\
c_{\mathbf{k},\uparrow} &\leftrightarrow c_{\mathbf{k},\uparrow},
\end{aligned}
\tag{10.23}
$$

where $\mathbf{Q} = (\pi, \pi)$ is the nesting vector of the square lattice. Consequently, momentum-momentum correlations are transformed according to

$$
\hat{n}_{\mathbf{k},\uparrow} \hat{n}_{\mathbf{k}',\downarrow} \leftrightarrow \hat{n}_{\mathbf{k},\uparrow}(1 - \hat{n}_{-(\mathbf{k}'+\mathbf{Q}),\downarrow}),
\tag{10.24}
$$

and a peak in the momentum-momentum correlations at $\mathbf{k} = -\mathbf{k}'$ for $U < 0$ corresponds to a dip at $\mathbf{k} = \mathbf{k}' \pm \mathbf{Q}$ for $U > 0$, where either sign can be used since the difference $2\mathbf{Q}$ between the two options is equal to a reciprocal lattice vector.

s-wave pairing correlations

Fig. 10.3 (a-c) shows the momentum distribution for a single spin species $\langle n_{\mathbf{k}} \rangle$ next to the noise correlations $\mathcal{C}_{\uparrow\downarrow}(\mathbf{k}, \mathbf{k}' = -\mathbf{k})$ [Fig. 10.3(d-f)] for three interactions $U/t = -1, -4, -6$ at half filling and $\beta t = 8$. For increasing interactions, $\langle n_{\mathbf{k},\sigma} \rangle$ is smeared out around the non-interacting Fermi surface, which reflects the fact that momentum is not a good quantum number anymore due to the non-commutativity of the kinetic and interaction term in the Hubbard Hamiltonian Eq. (8.6). The noise correlations in Fig. 10.3 (d-f) visualize that particle-particle scattering, which is the essence of the Cooper pairing mechanism, occurs in a small region around the Fermi surface. One should keep in mind that at half filling the Hubbard model possesses a three-component order parameter (see Sect. 8.2) so that the transition temperature to a long-range superconducting state is suppressed to zero by the Mermin-Wagner theorem [238].

In the absence of spontaneous symmetry breaking, which cannot occur on the finite systems that are used both in QMC simulations and cold atom experiments,

$$\langle n_{\mathbf{k},\sigma}\rangle \qquad\qquad \mathcal{C}_{\uparrow\downarrow}(\mathbf{k},-\mathbf{k})$$
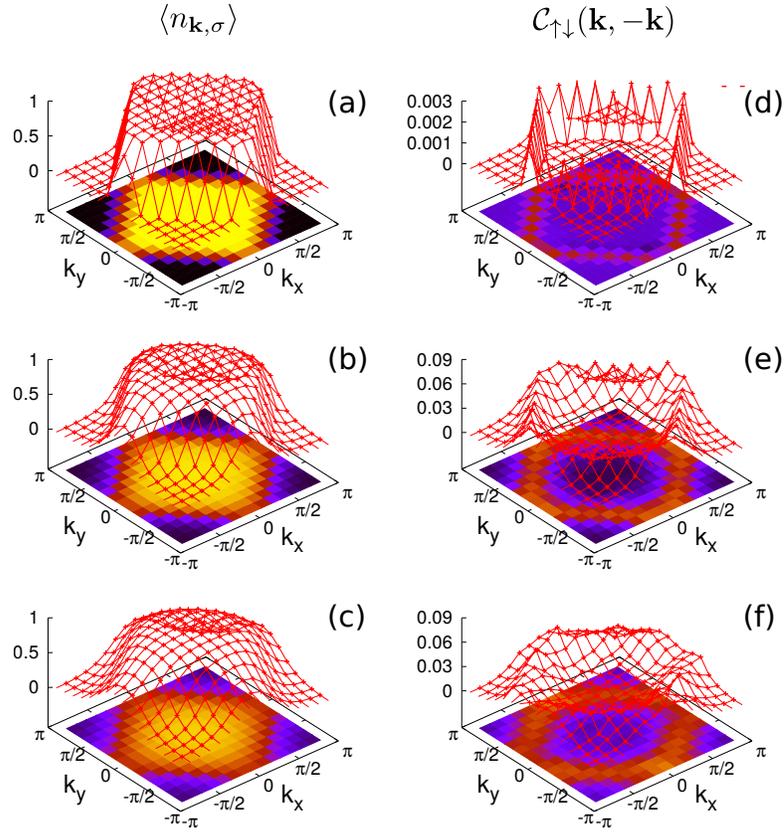
Fig. 10.3: Momentum distribution function $\langle n_{\mathbf{k},\sigma}\rangle$ (a)-(c) and corresponding noise correlations $\mathcal{C}_{\uparrow\downarrow}(\mathbf{k},\mathbf{k}'=-\mathbf{k})$ as a function of $\mathbf{k}=(k_x,k_y)$ (d)-(f). The plots correspond from top to bottom to $U/t=-1,-4,-6$ at half filling with linear system size $L=16$ and inverse temperature $\beta t=8$.
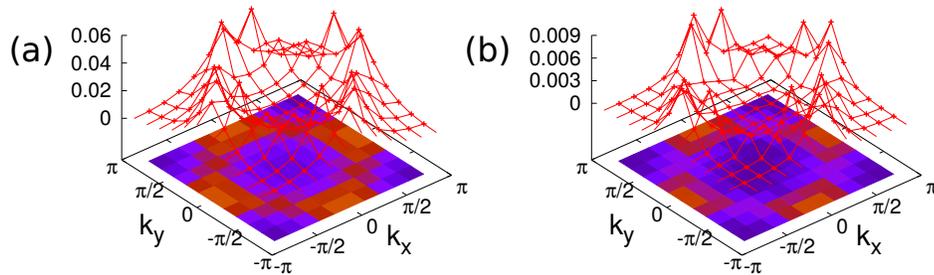
Fig. 10.4: (a) shows $\mathcal{C}_{\uparrow\uparrow}(\mathbf{k},\mathbf{k}'=\mathbf{k})$ in comparison with $\mathcal{C}_{\uparrow\downarrow}(\mathbf{k},\mathbf{k}'=-\mathbf{k})$ (b) for $\beta t=24$, $L=12$ and $U/t=-2$ with filling $\langle n\rangle=0.79$ ($\mu/t=-1.36$).

superconducting order must be detected through correlations of the order parameter, rather than the order parameter itself, and how they behave as functions of system size. Since we have not performed a finite-size scaling analysis, none of the data presented in the following can be interpreted as indicating forms of long-range order. Rather it merely illustrates the various scattering mechanisms that are at work in momentum space and which can possibly give rise to various types of long-range order. This point is inherently missed by the mean-field treatment of Sect. 10.3 which assumes a long-range ordered state. The noise correlations at high temperatures are the result of preformed pairing without long-range superconducting order.

The juxtaposition of $\mathcal{C}_{\uparrow\uparrow}(\mathbf{k}, \mathbf{k}' = \mathbf{k})$ and $\mathcal{C}_{\uparrow\downarrow}(\mathbf{k}, \mathbf{k}' = -\mathbf{k})$ in Fig. 10.4(a-b) for $U/t = -2$ and $\langle n \rangle = 0.79$ at $\beta t = 24$ shows that the former is roughly an order of magnitude larger. This can be understood from the form of the mean-field Eqs. (10.13) and (10.14), with thermally excited quasiparticles reducing $\mathcal{C}_{\uparrow\downarrow}^{\text{BCS}}(\mathbf{k}, -\mathbf{k})$ while the thermal contribution to $\mathcal{C}_{\uparrow\uparrow}^{\text{BCS}}(\mathbf{k}, \mathbf{k})$ cancels exactly at the Fermi surface. The gap being exponentially small for small Hubbard interaction (see Eq.(10.17)), thermal excitation of quasiparticles are important for $U/t = -2$ even at a large inverse temperature of $\beta t = 24$.

Figs. 10.5(a,b) show the noise correlations $\mathcal{C}_{\uparrow\downarrow}(\mathbf{k}, -\mathbf{k})$ as a function of momentum $\mathbf{k}$ for two different attractive interactions at half filling and for relatively low temperatures. The signal is mainly concentrated on the Fermi surface where pairs of particles with opposite spin undergo scattering processes of the type $(\mathbf{k} \uparrow, -\mathbf{k} \downarrow) \leftrightarrow (\mathbf{k} \downarrow, -\mathbf{k} \uparrow)$, which are at the heart of the Cooper pairing mechanism [251, 252]. The peaks at the high-symmetry points $X_1 = (\pm\pi, 0)$ and $X_2 = (0, \pm\pi)$ are considerably larger than at other momenta on the Fermi surface. This is connected to the fact that these momenta allow additional scattering processes, namely Umklapp scattering $(\mathbf{k} \uparrow, -\mathbf{k} \downarrow) \equiv (X_1 \uparrow, X_1 \downarrow) \leftrightarrow (X_2 \uparrow, X_2 \downarrow)$, which allows a pair of particles to scatter from one side of the Fermi surface to the other with momentum conservation provided by a reciprocal lattice vector.[3]

Fig. 10.5(c,d) presents diagonal cuts of the noise correlations $\mathcal{C}_{\uparrow\downarrow}(\mathbf{k}, -\mathbf{k})$ through the first Brillouin zone. The temperature is $\beta t = 24$ for $U/t = -1$ to $U/t = -5$ and $\beta t = 16$ for $U/t = -7, -7.2, -9$. The height of the peaks on the Fermi surface as a function of $|U|/t$ follows an initial exponential increase for small $|U|/t$ and decreases again as soon as $|U|/t$ reaches the bandwidth. This is reminiscent of the behaviour of the pairing correlations. Interestingly, there is also a peak at $\mathbf{k} = 0$ and $\mathbf{k} = (\pm\pi, \pm\pi)$, which also increases initially as a function of $|U|/t$ and diminishes again for larger $|U|/t$. The value of $|U|/t$ where the peaks at $\mathbf{k} = 0$ and $\mathbf{k} = (\pm\pi, \pm\pi)$ reach their maxima seems to be larger than the value where the peaks on the Fermi surface are maximal. In Fig. 10.6 diagonal cuts of $\mathcal{C}_{\uparrow\downarrow}(\mathbf{k}, -\mathbf{k})$ through the first Brillouin zone are shown for high temperature, $\beta t = 4$. Here, there are also peaks at $\mathbf{k} = 0$ and $\mathbf{k} = (\pm\pi, \pm\pi)$,

---

[3] For the given Fermi surface at half filling there are many more possible Umklapp scattering processes. However, the process discussed in the main text is the only one where the pair has zero COM. Only these pairs are detected by the noise correlation signal $\mathcal{C}_{\uparrow\downarrow}(\mathbf{k}, -\mathbf{k})$.
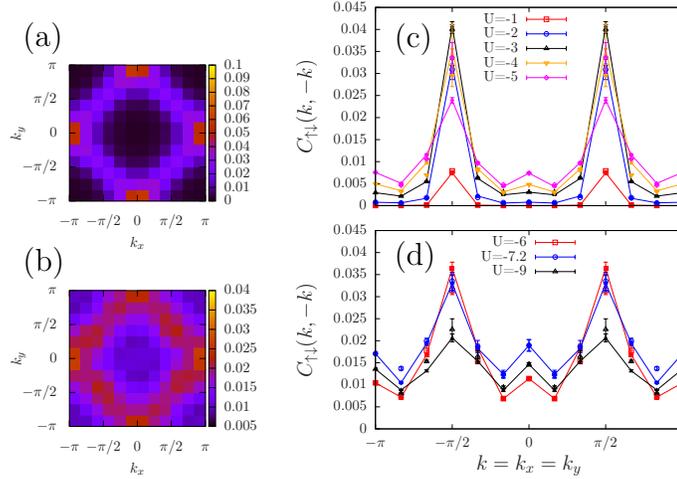
Fig. 10.5: Noise correlations $\mathcal{C}_{\uparrow\downarrow}(\mathbf{k}, -\mathbf{k})$ for $U/t = -3$, $\beta t = 24$ (a) and $U/t = -9$, $\beta t = 16$ (b) at half filling. The right column (c,d) shows diagonal cuts through the first Brillouin zone from $(-\pi, -\pi)$ to (π, π) (open symbols) and from $(-\pi, \pi)$ to $(\pi, -\pi)$ (closed symbols), respectively, for different attractive interactions at $\beta t = 24$ (c) and $\beta t = 16$ (d).

which increase steadily as a function of $|U|/t$, unlike the peaks on the Fermi surface, which decrease for $|U|/t > 6$.

The presence of the peaks at $\mathbf{k} = 0$ and $\mathbf{k} = (\pm\pi, \pm\pi))$ should in some way be connected to the enlarged symmetry of the Hubbard model at half filling (see Sect. 8.2), where CDW and SC correlations are of equal strength and the order parameter is a three-component vector which can fluctuate between SC components (in the xy-plane) and the CDW component (along the z-direction). This is a result of the global pseudospin rotational symmetry of the model [305]. The existence of three collective gapless modes was inferred [305], whereas in a superfluid spontaneously breaking $U(1)$ symmetry there is only one of those so-called Goldstone modes [306]. Subsequently, it was argued [307] that the additional collective modes are artifacts of the high symmetry of the Hubbard model and that symmetry-violating interactions and processes in more realistic models would make them unobservable in condensed matter systems. In constrast, ultracold atoms in optical lattices provide an almost perfect realization of the Hubbard model.

One may speculate that the peaks at $\mathbf{k} = 0$ and $\mathbf{k} = (\pm\pi, \pm\pi))$ are related to the existence of these collective modes that are due to the $SU(2)$ pseudospin symmetry of the Hubbard model at half filling. To verify this hypothesis simulations away from half filling would be necessary, where CDW correlations are short-ranged and SC correlations become dominant so that the symmetry of the order parameter is reduced from $SU(2)$ to $U(1)$. If the hypothesis is correct, the peaks at $\mathbf{k} = 0$ and $\mathbf{k} = (\pm\pi, \pm\pi)$ should vanish away from half filling.
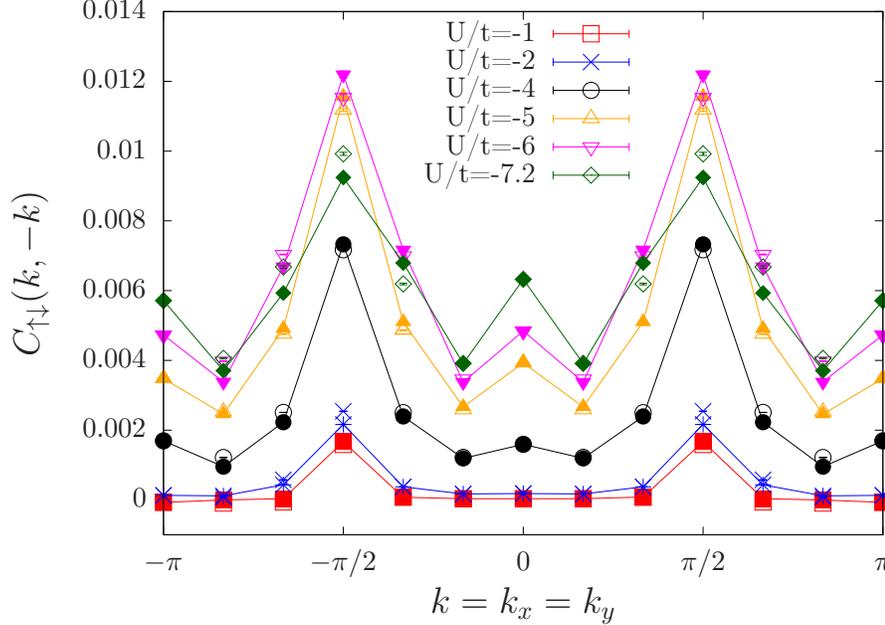
Fig. 10.6: Noise correlations along diagonal cuts through the first Brillouin zone; $L = 12$ and $\beta t = 4$, half filling. Open symbols denote a cut from $(-\pi, -\pi)$ to (π, π) and closed symbols from $(-\pi, \pi)$ to $(\pi, -\pi)$.

Charge density wave (CDW) correlations

In addition to pairing correlations, discussed so far, there are also CDW correlations present at half filling, which are revealed through anticorrelations in the noise correlations for the same spin species. $\mathcal{C}_{\uparrow\uparrow}(\mathbf{k}, \mathbf{k}' = \mathbf{k} \pm \mathbf{Q})$, plotted as a function of $\mathbf{k}$, shows negative dips when $\mathbf{k}$ is close to the non-interacting Fermi surface (Fig. 10.7 (a)), as a result of particle-hole scattering between opposite sides of the Fermi surface that are connected by the nesting vector $\mathbf{Q} = (\pi, \pi)$. These correlations are captured by the mean field CDW state Eq. (10.8). Stated differently, $\mathcal{C}_{\uparrow\uparrow}(\mathbf{k}, -\mathbf{k})$ exhibits isolated negative peaks for $\mathbf{k} = (\pm\pi/2, \pm\pi/2)$ due to CDW correlations, see Fig.10.7 (b). The depth of the negative peak as a function of $|U|$ follows the general trend that was already discussed for pairing correlations: After an exponential increase for small $|U|$ a maximum is reached when $|U|$ approaches some $|U|_{\max}$ that is comparable to the bandwidth. For larger $|U|$ the correlations decrease again. At $\beta t = 24$, we find a maximum value of $|\mathcal{C}_{\uparrow\uparrow}(\mathbf{k}, \mathbf{k} + \mathbf{Q})|_{\mathbf{k}\in\text{FS}}| \approx 0.1$ at $|U|_{\max}/t \approx 5$, which is smaller than the non-interacting bandwidth $W/t = 8$. The large positive peaks in $C_{\uparrow\uparrow}(\mathbf{k}, -\mathbf{k})$ at $\mathbf{k} = (0, \pm\pi)$ and $\mathbf{k} = (\pm\pi, 0)$ are exactly equal to $\frac{1}{4}$ in accordance with Eq. (10.15).

Furthermore, $\mathcal{C}_{\uparrow\uparrow}(\mathbf{k}, -\mathbf{k})$ shows small positive correlations with peaks at $\mathbf{k} = \mathbf{0}$ and $\mathbf{k} = (\pm\pi, \pm\pi)$, which are of the same height within error bars and which are presumably
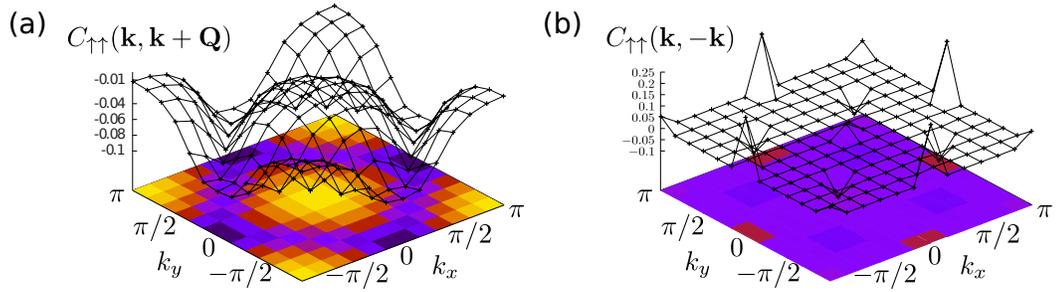
Fig. 10.7: Noise correlations between equal spin species $\mathcal{C}_{\uparrow\uparrow}(\mathbf{k}, \mathbf{k} + \mathbf{Q})$ in (a) and $\mathcal{C}_{\uparrow\uparrow}(\mathbf{k}, -\mathbf{k})$ in (b) for $U/t = -5, \beta t = 24$ at half filling; $\mathbf{Q} = (\pi, \pi)$. The anticorrelations at the Fermi surface in (a) and the negative peaks in (b) are signatures of CDW correlations.

of similar origin[4] as the peaks at the same $\mathbf{k}$-values in $\mathcal{C}_{\uparrow\downarrow}(\mathbf{k}, -\mathbf{k})$ (see Fig. 10.6).

In cold atom experiments, a peak at $\mathbf{k} = \mathbf{0}$ might not be observable as it is masked by the autocorrelation peak [10, 48], which is several orders of magnitude larger than the actual noise correlations and arises from the fact that every atom is perfectly correlated with itself. The peaks at $\mathbf{k} = (\pm\pi, \pm\pi)$ are probably masked by the dominating Bragg peaks of the square lattice [10, 48]. However, it may be possible to suppress the peaks at reciprocal lattice vectors by ramping down the optical lattice adiabatically during the time-of-flight expansion such that quasi-momenta are mapped onto true momenta [10].

Searching for η-pairing correlations

An interesting aspect about η-pairs is that, being exact excited eigenstates [230], they are contained in thermal states of the Hubbard model and, having COM momentum $\mathbf{Q} \equiv \vec{\pi} = (\pi, \pi)$ their momentum correlations should be quite distinct from Cooper pairs with zero COM momentum.

The appropriate momentum correlator for detecting η-pairs is $\mathcal{C}_{\uparrow\downarrow}(\mathbf{k}, \mathbf{k}' = -\mathbf{k} + \mathbf{Q})$. Two particles with COM momentum $\mathbf{k}' + \mathbf{k} = \mathbf{Q}$ and individual momenta $\mathbf{k}$ and $\mathbf{k}'$ located on the Fermi surface are shown in Fig. 10.8. Fig. 10.8(b) indicates that the signal is concentrated on the Fermi surface. Therefore, in Figs. 10.8(c-d) we show cuts of $\mathcal{C}_{\uparrow\downarrow}(\mathbf{k}, -\mathbf{k} + \mathbf{Q})$ along one edge of the square Fermi surface marked in green in Figs. 10.8(c-d). Both for low temperature, $\beta t = 24$ [Fig. 10.8(c)] and high temperature, $\beta t = 4$ [Fig. 10.8(d)] positive correlations are peaked at $\mathbf{k} = \Sigma = (\pi/2, \pi/2)$ and negative correlations appear at $\mathbf{k} = X = (0, \pi)$ for all but the smallest values of $|U|/t$. The insets in Fig. 10.8(a) and (b) show the dependence of the peak height at the Σ- and X-points on the attractive interaction strength.

---

[4] Note that if there were spontaneous breaking of the translational symmetry with ordering vector $\mathbf{Q}$, which, however, never happens in simulations on finite systems, the Brillouin zone would be halved with new reciprocal lattice vectors that are integral multiples of $\frac{2\pi}{2a} = \frac{\pi}{a}$. In this new magnetic Brillouin zone $\mathbf{k} = \mathbf{0}$ and $\mathbf{k} = (\pm\pi, \pm\pi)$ are the same states.
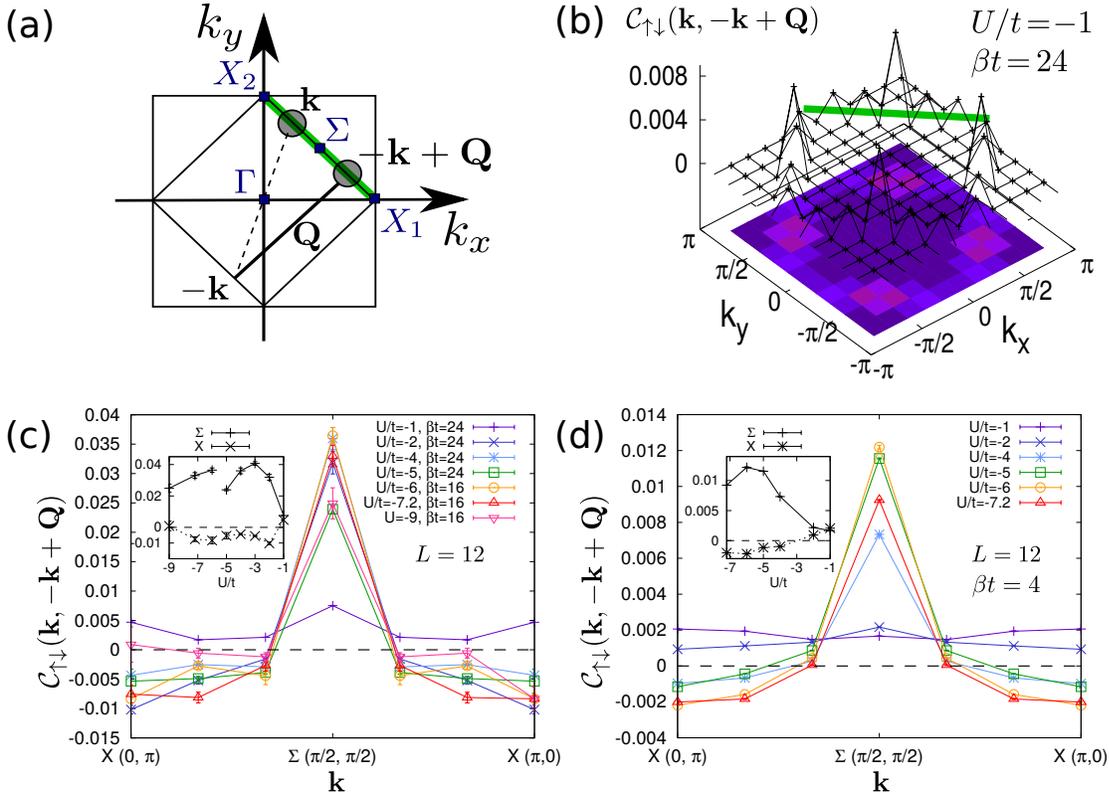
Fig. 10.8: Is there evidence for η-pairing in the noise correlations $\mathcal{C}_{\uparrow\downarrow}(\mathbf{k}, -\mathbf{k} + \mathbf{Q})$? (a) First Brillouin zone of the square lattice extending over $-\pi \leq k_x \leq \pi$ and $-\pi \leq k_y \leq \pi$. Special momentum points of high symmetry are marked by blue symbols. The grey circles show a pair with the special property that both partners are located on the Fermi surface and that the pair has COM momentum $\mathbf{Q} = (\pi, \pi)$. (b) $\mathcal{C}_{\uparrow\downarrow}(\mathbf{k}, -\mathbf{k} + \mathbf{Q})$ as a function of $\mathbf{k}$ for $\beta t = 24$, $U/t = -1$, $L = 12$. (c) and (d) show cuts through the first Brillouin zone along the direction $X_1 - \Sigma - X_2$, which is indicated by the green line in (a) and (b).

Comparison with Fig. 10.6 shows that the pronounced peak in $\mathcal{C}_{\uparrow\downarrow}(\mathbf{k}, -\mathbf{k} + \mathbf{Q})$ at $\mathbf{k} = \Sigma$ is of precisely the same height as the peak in $\mathcal{C}_{\uparrow\downarrow}(\mathbf{k}, -\mathbf{k})$ at the same $\mathbf{k}$-value. Thus it seems likely that this peak is simply the result of Cooper pairing and the special high symmetry of the half-filled Hubbard model on the square lattice. Indeed, as mentioned already above, if there were spontaneous symmetry, halving the Brillouin zone and promoting the nesting vector $\mathbf{Q}$ to a reciprocal lattice vector, the momentum pairs $(\mathbf{k}, -\mathbf{k} + \mathbf{Q}) \simeq (\mathbf{k}, -\mathbf{k})$ would be equivalent up to a reciprocal lattice vector. In conclusion, Fig. 10.8 presents no conclusive evidence for η-pairing.

It should be noted that a ground state with long-range η-pairing correlations has been demonstrated in the strong-coupling limit of an attractive Hubbard mode with one particle less than half filling [233]. This is the analogue of the Nagaoka ferromagnetic phase in the repulsive Hubbard model at $U/t = \infty$ [308].

10.4.2   Integrated noise correlation signal

In order to reveal the angular dependence of the correlation function $\mathcal{C}_{\uparrow\downarrow}(\mathbf{k}, \mathbf{k}')$, we consider the integrated noise correlation signal

$$I_{\uparrow\downarrow}(\mathbf{q}) = \sum_{\mathbf{k}} \left(\langle n_{\mathbf{k},\uparrow} n_{-\mathbf{k}+\mathbf{q},\downarrow} \rangle - \langle n_{\mathbf{k},\uparrow} \rangle \langle n_{-\mathbf{k}+\mathbf{q},\downarrow} \rangle \right). \tag{10.25}$$

$\mathbf{q}$ is the center-off-mass (COM) momentum of a pair of $\uparrow$- and $\downarrow$-species. In a BCS state, which contains only pairs with zero COM, $I_{\uparrow\downarrow}(\mathbf{q})$ is described by a δ-function at $\mathbf{q} = 0$. The BCS state is not an exact eigenstate of the Hubbard Hamiltonian Eq. (C.1), and one expects residual interactions between Cooper pairs, which lead to scattering into pair states with non-zero COM momentum.

Results for the integrated noise correlations $I_{\uparrow\downarrow}(\mathbf{q})$ in the half-filled model at low temperatures ($\beta t = 16, 24$) are presented in Fig. 10.9 along cuts through the first Brillouin zone of the square lattice. Cuts where $\mathbf{q}$ runs along the diagonals, e.g. from $(-\pi, -\pi)$ to (π, π), are contrasted with cuts parallel to the momentum coordinate axes. Due to symmetry, ideally, the values of $I_{\uparrow\downarrow}(\mathbf{q})$ should coincide for the two diagonal cuts where either $q_x = q_y$ or $q_x = -q_y$, and similarly for the two cuts where either $q_x = 0$ or $q_y = 0$. Deviations are within error bars and increase for larger $|U|/t$. The error bars are obtained from a simple error propagation applied to Eq. (10.25).

Fig. 10.9(a) (and also Fig. 10.10(a) at high temperature) suggests that for small $|U|$ pairs have their non-zero COM momentum $\mathbf{q}$ preferentially in the direction $q_x = \pm q_y$, which is favoured over $q_x = 0$ or $q_y = 0$. This anisotropy can be easily understood from the diamond-shaped Fermi surface (insets Fig. 10.9(a)), where opposite-spin partners in pairs which have COM momentum along the diagonal of the Brillouin zone are connected by the nesting vector $\mathbf{Q} = (\pi, \pi)$, although the precise mechanism, being related to pair-pair scattering in the weak-coupling limit, is not immediately clear.

As a function of $|U|$, the peak height $I_{\uparrow\downarrow}(\mathbf{q} = 0)$ follows the general trend of a rapid increase for small $|U|$ and a decrease as soon as $|U|$ exceeds the bandwidth and thus tracks qualitatively the U-dependence of s-wave superconducting pairing correlations in the phase diagram of the attractive Hubbard model (see Sect. 8.3). As the particle density is tuned away from half filling (not shown), the peak height $I_{\uparrow\downarrow}(\mathbf{q} = 0)$ increases rapidly and thus again follows the behaviour of the s-wave pairing correlations as depicted in Fig. 8.2(b).

A significant population of non-zero COM pairs is visible for $U = -9$ (Fig. 10.9(f)), where $I(\mathbf{q})$ is broadened around $\mathbf{q} = 0$, and there seem to be more pairs with non-zero COM along the coordinate axes than along the diagonal of the Brillouin zone, in contrast to the case of $U = -1$ (Fig. 10.9(a)).

In Fig. 10.10 we show the integrated noise correlations for high temperature $\beta t = 4$. Here, population of non-zero COM pair states is visible for all values of U. The peak height $I_{\uparrow\downarrow}(\mathbf{q} = 0)$ is by approximately a factor of two smaller than at low temperatures $\beta = 16, 24$ (Fig. 10.9) and it also increases with increasing $|U|$ up to a maximum value
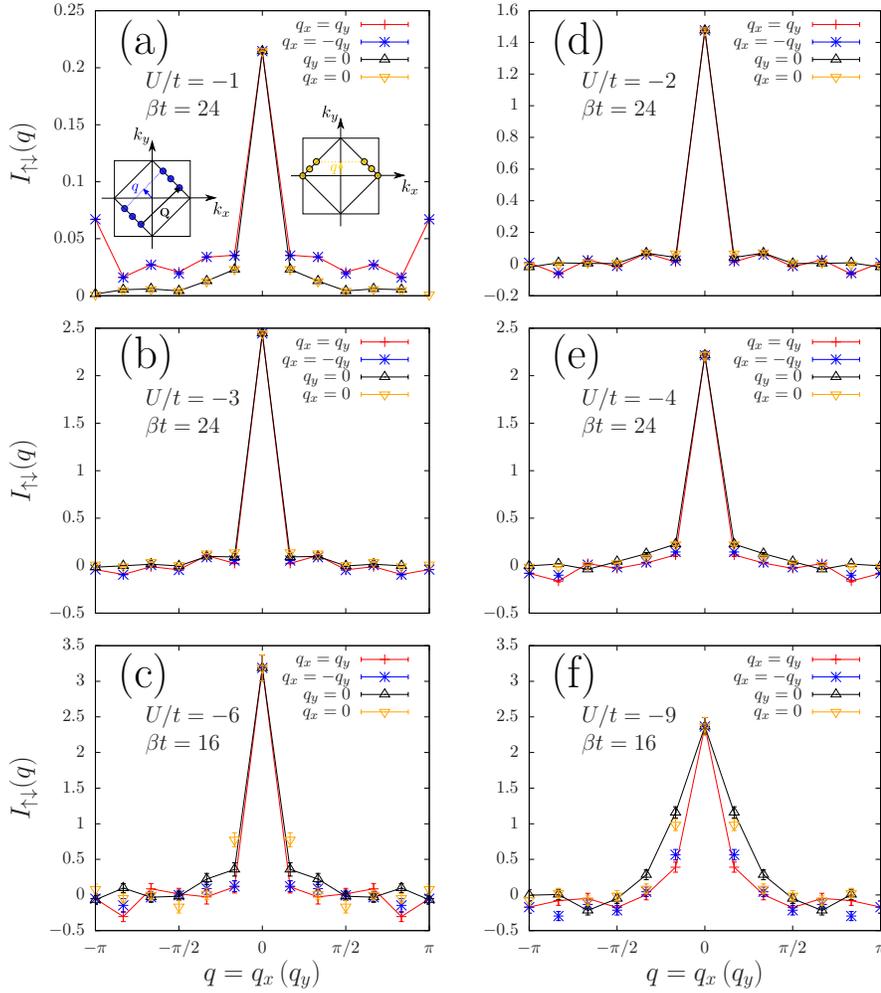
Fig. 10.9: Integrated noise correlations $I_{\uparrow\downarrow}(\mathbf{q})$ as a function of COM momentum $\mathbf{q}$ for the attractive Hubbard model at half filling and low temperatures $\beta t = 24$ (for $U/t = -1, -2, -3, -4$) and $\beta t = 16$ (for $U/t = -6, -9$); linear system size $L = 12$. The small insets in (a) show pairs with non-zero COM momentum $\mathbf{q}$ either along the diagonal of the Brillouin zone (left inset, blue) or parallel to the momentum axes (right inset, orange).

of $|U|$ that is proportional to the bandwidth. For $|U| \geq 4$, negative values of $I_{\uparrow\downarrow}(\mathbf{q})$ appear around the corners of the Brillouin zone. Having seen that superconducting noise correlations are present both close to the superconducting ground state (at $\beta t = 24$) and in the normal state, we ask the question whether a divergence of the s-wave pairing structure factor with system size, which signals *true* long-range order and has been used for locating the phase boundary in numerical simulations [25], might be reflected in a similar divergence of some quantity that can be derived entirely from
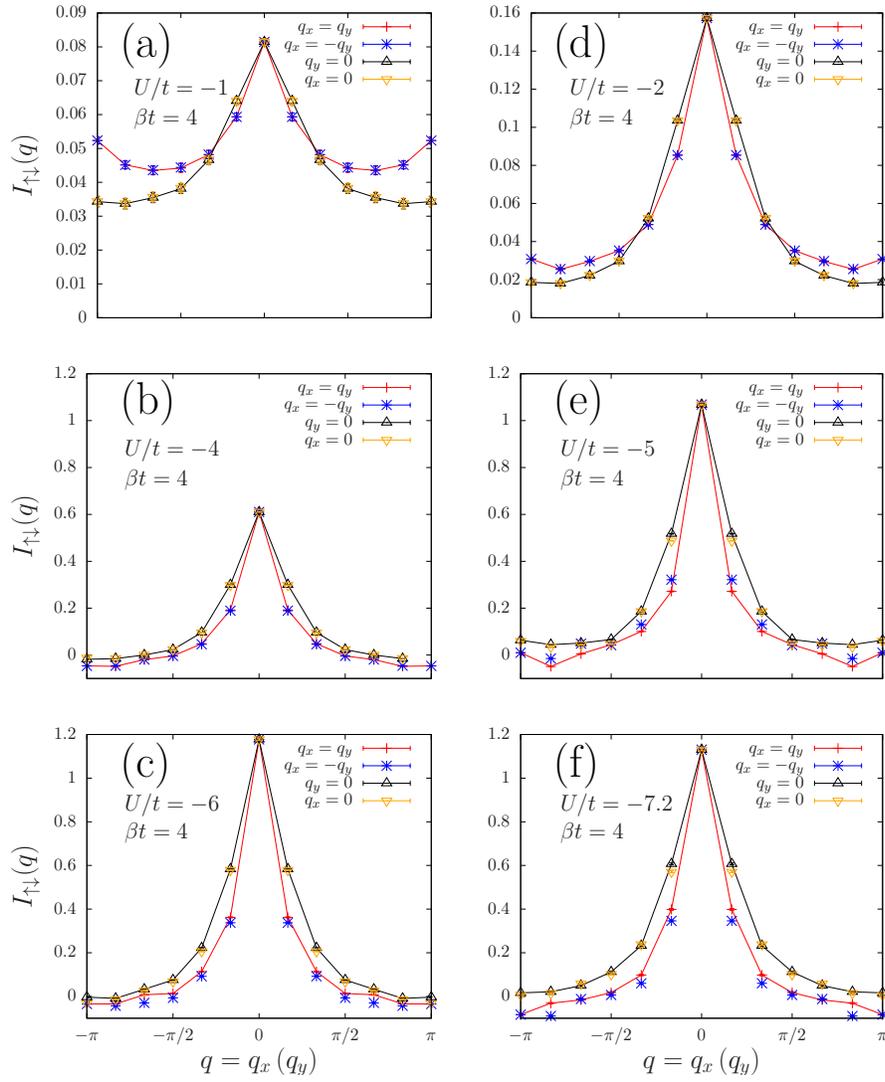
Fig. 10.10: Integrated noise correlation signal $I_{\uparrow\downarrow}(\mathbf{q})$ at high temperature, $\beta t = 4$; system size $L = 12$.

noise correlation measurements . The zero-momentum s-wave pairing structure factor

$$
\begin{aligned}
P_s &= \frac{1}{2N} \sum_{i,j} \langle c_{i\uparrow}^\dagger c_{i\downarrow}^\dagger c_{j\downarrow} c_{j\uparrow} + c_{i\downarrow} c_{i\uparrow} c_{j\uparrow}^\dagger c_{j\downarrow}^\dagger \rangle \\
&= \frac{1}{N} \left\{ \sum_{i=j} (\langle n_{i\uparrow} n_{i\downarrow} \rangle - \frac{1}{2} \langle n_{i\uparrow} + n_{i\downarrow} \rangle + \frac{1}{2}) + \sum_{i \neq j} \langle c_{i\uparrow}^\dagger c_{j\uparrow} c_{i\downarrow}^\dagger c_{j\downarrow} \rangle \right\}
\end{aligned}
\tag{10.26}
$$

is contained in the integrated noise correlation signal $I_{\uparrow\downarrow}(\mathbf{q}=\mathbf{0})$ according to

$$
\begin{aligned}
I_{\uparrow\downarrow}(\mathbf{q}=\mathbf{0}) &= \sum_{\mathbf{k}} \langle n_{\mathbf{k},\uparrow} n_{-\mathbf{k},\downarrow} \rangle - \sum_{\mathbf{k}} \langle n_{\mathbf{k},\uparrow} \rangle \langle n_{-\mathbf{k},\downarrow} \rangle \\
&= P_s + \frac{1}{N} \left[\frac{1}{2} \sum_{\mathbf{i}} (\langle n_{\mathbf{i},\uparrow} + n_{\mathbf{i},\downarrow} \rangle - 1) \right] \\
&\quad + \frac{1}{N} \sum_{\substack{\mathbf{i},\mathbf{l} \\ \mathbf{l} \neq \mathbf{0}}} \langle n_{\mathbf{i},\uparrow} n_{\mathbf{i}+\mathbf{l},\downarrow} \rangle + \frac{1}{N} \sum_{\substack{\mathbf{i},\mathbf{j},\mathbf{l} \\ \mathbf{i} \neq \mathbf{j}, \mathbf{l} \neq \mathbf{0}}} \langle c_{\mathbf{i},\uparrow}^\dagger c_{\mathbf{j},\uparrow} c_{\mathbf{i}+\mathbf{l},\downarrow}^\dagger c_{\mathbf{j}+\mathbf{l},\downarrow} \rangle \\
&\quad - \sum_{\mathbf{k}} \langle n_{\mathbf{k},\uparrow} \rangle \langle n_{-\mathbf{k},\downarrow} \rangle,
\end{aligned}
\tag{10.27}
$$

where the terms in the second line of Eq. (10.27) describe both spin density wave (SDW) and extended s-wave pairing correlations. It can be shown [309] that for the specific case of the Hubbard model at half filling extended s-wave pairing correlations vanish identically while away from half filling s-wave and extended s-wave pairing correlations are proportionally related. Furthermore, due to the pseudo-spin rotational symmetry of the Hubbard model at half filling [49] CDW correlations $\langle n_{\mathbf{i}} n_{\mathbf{j}} \rangle = \langle (n_{\mathbf{i},\uparrow} + n_{\mathbf{i},\downarrow})(n_{\mathbf{j},\uparrow} + n_{\mathbf{j},\downarrow}) \rangle$ are equal in magnitude to pairing correlations, and they constitute a lower bound away from half filling, which was recently employed in a cold atom experiment to infer the presence of superconducting correlations from CDW correlations measured in a quantum gas microscope [22]. Correlations of the form $\langle n_{\mathbf{i},\sigma} n_{\mathbf{j},\sigma} \rangle$ are contained in $I_{\sigma\sigma}(\mathbf{q}=\mathbf{0})$. In conclusion, the correlations in Eq. (10.27) are either directly obtainable from time-of-flight measurements or related by symmetry, which opens the way for experimental finite-size scaling of $I_{\uparrow\downarrow}(\mathbf{q}=\mathbf{0})$ based on the expected scaling with linear system size, $P_s(L) \sim L^{2-\eta(T_{KT})} f(\xi/L)$ with $\eta(T_{KT}) = \frac{1}{4}$ and $f(\xi/L)$ a scaling function, at the Kosterlitz-Thouless transition of the 2D attractive Hubbard model away from half filling [24, 25, 310].

Chapter 11

Quantum state tomography (QST) with determinantal QMC

Loosely speaking the determinantal quantum Monte Carlo method consists in computing a large sum over free fermions systems in varying external potentials: It suffices to compute any quantity (in any single-particle basis) for free fermions and average over Monte Carlo samples. This is a huge conceptual simplification compared to path integral methods. The generality of the free fermion decomposition [119] allows to carry the measurement part of the BSS algorithm to its extreme by calculating the full quantum state on a small subsystem A, that is all elements of the reduced density matrix $\rho_A = \text{Tr}_{B=\bar{A}}(\rho)$, which is given by the partial trace of the global density matrix $\rho = e^{-\beta\hat{H}}/Z$ over the complement system B. This amounts to performing exact diagonalization inside the measurement part of the Monte Carlo procedure.

The following sections present proof of principle calculations for a square plaquette. There are numerous ramifications that motivate computing the equilibrium probabilities of individual microstates, i.e. the diagonal elements of ρ_A. By superimposing a specific experimental measurement protocol, the effect of parity projection [16], i.e. the inability to dinstinguish doublons and holes in the imaging process, on the experimentally observed particle configurations can be assessed (see Sect. 9.4.3), which is important at intermediate Hubbard interaction, where holes and doublons appear frequently.

Remarkably, measuring experimentally the second moment of the density matrix, its purity $\text{Tr}(\rho_A^2)$, is possible without exponential effort [311, 312]. In view of recent proposals to use machine learning with neural networks to reconstruct a full quantum state from a limited number of experimental measurements [313], access to all elements of ρ_A is of potential interest. Alternative numerical approaches relying on the replica representation of Rényi entropies $\text{Tr}[\rho_A^n]$ [314] require complicated modifications in the topology of the simulation cell, whereas the brute force numerical scheme described in this chapter does not affect the core of the DQMC algorithm and all diagonal and off-diagonal elements of the reduced density matrix, as well as its eigenvalues, the *entanglement spectrum*, can be obtained. However, computational and memory

resources that grow exponentially with the subsystem size are required, which limits the subsystem size to maximally $N_s = 9$ sites.[1]

From a methodological point of view there are connections with various types of numerical cluster approaches. Eqs. (11.2) and (11.3) below give the exact state on a cluster that is self-consistently embedded in a *correlated* bath and can be used to compare with computationally less expensive methods that solve the cluster system exactly, but treat the bath degrees of freedom only approximately.

Finally, a strong motivation for studying the detailed structure of a local quantum state comes from the phenomenology of the high-temperature phase of the repulsive Hubbard model (or more generally of high-T_c superconductors) where for temperatures $\beta \leq 4-5$ where DQMC simulations are still possible due to a mild sign problem [142] a pseudogap develops in the single-particle spectral function [315]. The pseudogap in the *attractive* Hubbard model is well understood in terms of local bound pairs of fermions without long-range phase coherence, the gap being associated with the binding energy of the pair. A natural question is whether similar preformed objects are responsible for the pseudogap observed in the *repulsive* Hubbard model (or more generally in the normal state of high-T_c superconductors), which would lead to Anderson's picture [316] of interpreting spin singlets as "preformed Cooper pairs" that become superconducting when the AFM Mott insulator of the parent compound is doped.

11.1   Born's rule for many-body states

In a state of a non-interacting Fermi system, Wick's theorem applied to a product of n pairings of fermionic operators results in the determinant formula

$$\left\langle \left(c_{i_1} c_{j_1}^\dagger\right) \left(c_{i_2} c_{j_2}^\dagger\right) \cdots \left(c_{i_n} c_{j_n}^\dagger\right) \right\rangle_0 = \det\left(G_{i_\alpha j_\beta}^{(0)}\right), \quad \text{with } \alpha, \beta = 1, \ldots, n, \qquad (11.1)$$

where $G_{i_\alpha j_\beta}^{(0)}(\tau = 0) = \langle c_{i_\alpha}(\tau = 0) c_{j_\beta}^\dagger(0)\rangle_0$ is the equal-time Green's function of the non-interacting Fermi system. This formula, which is proven in Appendix D, is the basis for extracting the elements of the reduced density matrix from an equilibrium state, which in the DQMC framework is encoded in a sum over free fermion systems parametrized by auxiliary field configurations $\{\mathbf{s}\}$. The diagonal and off-diagonal elements of the reduced density matrix in the Fock basis can be written as

$$\langle\alpha|\rho|\alpha\rangle = \sum_{\{\mathbf{s}\}} \text{Tr}\left(\rho_{\{\mathbf{s}\}} \, \hat{\Pi}_\alpha\right) \qquad (11.2)$$

$$\langle\beta|\rho|\alpha\rangle = \sum_{\{\mathbf{s}\}} \text{Tr}\left(\rho_{\{\mathbf{s}\}} \, \hat{\hat{\Xi}}_{\alpha\to\beta}\right), \quad \alpha \neq \beta \qquad (11.3)$$

---

[1]The computational complexity of DQMC for simulating the total system of N sites is $\sim \beta N^3$ and can be completely decoupled from the costly "exact diagonalization" inside each HS sample if the single-particle Green's functions are saved on disk for every HS configuration (or after a number of Monte Carlo steps proportional to the autocorrelation time). This requires several hundred GB of hard disk memory per parameter set (β, U).

Here, $\hat{\Pi}_\alpha = |\alpha\rangle\langle\alpha|$ are projectors onto individual Fock states

$$|\alpha\rangle = |\alpha_\uparrow\rangle \otimes |\alpha_\downarrow\rangle = |n_{1,\uparrow}, n_{1,\downarrow}; n_{2,\uparrow}, n_{2,\downarrow}; \ldots; n_{N_s,\uparrow}, n_{N_s,\downarrow}\rangle \tag{11.4}$$

on the substem A with N_s sites and $\hat{\Xi}_{\alpha\to\beta} = |\beta\rangle\langle\alpha|$ is a transition operator[2] between two Fock states $|\alpha\rangle$ and $|\beta\rangle$. $\rho_{\{\mathbf{s}\}}$ is the global density matrix of the free fermion system with auxiliary field configuration $\{\mathbf{s}\}$, which is sampled via Monte Carlo.

Since for one auxiliary field configuration $\{\mathbf{s}\}$ the reduced density matrix factorizes between spin species,

$$(\langle\beta_\uparrow| \otimes \langle\beta_\downarrow|)\, \rho^\uparrow_{A,\{\mathbf{s}\}} \otimes \rho^\downarrow_{A,\{\mathbf{s}\}}\, (|\alpha_\uparrow\rangle \otimes |\alpha_\downarrow\rangle) = \langle\alpha_\uparrow|\rho^\uparrow_{A,\{\mathbf{s}\}}|\beta_\uparrow\rangle\langle\alpha_\downarrow|\rho^\downarrow_{A,\{\mathbf{s}\}}|\beta_\downarrow\rangle, \tag{11.5}$$

at most $2 \times 2^{N_s} \times 2^{N_s}$ matrix elements need to be computed to express all $4^{N_s} \times 4^{N_s}$ elements of $\rho_{A,\{\mathbf{s}\}}$. (In this crude estimate we have disregarded the block diagonal structure of $\rho^\sigma_{A,\{\mathbf{s}\}}$ with respect to particle number N^σ_A which reduces the size of the largest particle number block for one spin species to $\binom{N_s}{\lfloor N_s/2\rfloor} \cdot \binom{N_s}{\lfloor N_s/2\rfloor}$ with $\lfloor x\rfloor$ denoting the largest integer that is smaller than x.) Therefore, the limiting factor is the memory requirement for storing all elements of $\rho_{A,\{\mathbf{s}\}}$ for Monte Carlo averaging, rather than the computation of individual elements. ρ_A has block diagonal structure (Sect. 11.2.1), but, unlike typical lattice Hamiltonians, it is not sparse in the occupation basis.

In the following, we discuss the computation for a single spin component, thereby dropping all spin indices in the notation. We use hats to distinguish the number operator $\hat{n}_i = c^\dagger_i c_i$ from the occupation number n_i and write

$$\hat{\Pi}_\alpha = \prod_{i \in N_s} [\hat{n}_i n_i + (1 - \hat{n}_i)(1 - n_i)] = \prod_{i \text{ occupied}} \hat{n}_i \prod_{j \text{ unoccupied}} (1 - \hat{n}_j). \tag{11.6}$$

The transition operator $\hat{\Xi}_{\alpha\to\beta}$ can be written as

$$\hat{\Xi}_{\alpha\to\beta} = \hat{T}_{\alpha\to\beta}\, \hat{\Pi}_\alpha, \tag{11.7}$$

where $\hat{\Pi}_\alpha$ projects onto the Fock state $|\alpha\rangle$, which is then converted into $|\beta\rangle$ by a combination of appropriately chosen creation and annihilation operators

$$\hat{T}_{\alpha\to\beta} = (-1)^p \left(\prod_{\substack{c=N^+ \\ i_1 < i_2 < \cdots < i_{N^+}}}^{1} c^\dagger_{i_c} \right) \left(\prod_{\substack{a=N^- \\ j_1 < j_2 < \cdots < j_{N^-}}}^{1} c_{j_a} \right). \tag{11.8}$$

---

[2] An operator $\hat{X}^{\beta\leftarrow\alpha}_{\mathbf{j}} = |\beta\rangle_{\mathbf{j}}\langle\alpha|_{\mathbf{j}}$ connecting the states $|\alpha\rangle$ and $|\beta\rangle$ of a local many-body basis, in the simplest case for a single site $\mathbf{j}$, is commonly known in the literature as Hubbard X-operator [317]. This notation was introduced by Hubbard [318] to deal with the situation where the effect of adding or removing an electron depends strongly on the local environment.

The sequences of site indices $\mathcal{I}^+ = \{i_1, i_2, \ldots, i_{N^+}\}$ and $\mathcal{I}^- = \{j_1, j_2, \ldots, j_{N^-}\}$, ordered according to the chosen fermion ordering, denote the lattice sites where the N^+ creation and N^- annihilation operators must act to convert $|\alpha\rangle$ into $|\beta\rangle$. Since ρ_A is block diagonal with respect to the total particle number $N_{A,\sigma} = \sum_{i \in A} n_{i,\sigma}$ for each spin species σ (see Sect. 11.2.1), there must be as many creation as annihilation operators and $N^+ = N^-$. The fermionic phase

$$(-1)^p = \prod_{i_c=1}^{N^+} e^{i\pi \sum_{i_c < l < N_s} n_l^{(\gamma)}} \prod_{j_a=1}^{N^-} e^{i\pi \sum_{j_a < k < N_s} n_k^{(\alpha)}} \tag{11.9}$$

with $\mathbf{n}^{(\alpha)}$ the vector of occupation numbers for state $|\alpha\rangle$ and $\mathbf{n}^{(\gamma)}$ for state $|\gamma\rangle \equiv \prod_{a=N^-}^{1} c_{j_a} |\alpha\rangle$ ensures that $\hat{T}_{\alpha \to \beta} |\alpha\rangle = |\beta\rangle$. Given that $N^+ = N^-$, one can bring the operator product in Eq. (11.8) into the paired form as it appears on the left-hand side of Eq. (11.1) by commuting fermionic operators. From this an additional phase factor arises:

$$(-1)^{p'} = (-1)^{\sum_{i=1}^{N^+} i} = (-1)^{\frac{N^+}{2}(N^+ + 1)}. \tag{11.10}$$

With regard to a practical implementation for the evaluation of the expectation values in the right-hand side of Eqs. (11.2) and (11.3) for one particular auxiliary field configuration $\{\mathbf{s}\}$, a few remarks are in order: The fact that an occupied site is represented by a projector of the form $\hat{n}_i = (1 - c_i c_i^\dagger)$ (for unoccupied sites $1 - \hat{n}_i = c_i c_i^\dagger$) means that the expectation value of the total projector onto a Fock state Eq. (11.6), when multiplied out, is a sum of terms which can be written as a binary tree for the occupied sites where each leaf is of the form of Eq. (11.1). The branches of the binary tree need to be summed over to obtain the projector Eq. (11.6). In combination with $\hat{T}_{\alpha \to \beta}$, the projector $\hat{\Pi}_\alpha$ needs only be realized on sites that are unaffected by the hopping operators in $\hat{T}_{\alpha \to \beta}$ since the hopping operators already guarantee that occupation number states $\alpha' \neq \alpha$ are eliminated by the action of $\hat{T}_{\alpha \to \beta}$.

The algorithm for computing $\langle \beta | \rho_A | \alpha \rangle_{\{\mathbf{s}\}}$ between the occupation number states $|\alpha\rangle$ and $|\beta\rangle$ for a single Hubbard-Stratonovich configuration $\{\mathbf{s}\}$ is detailed in the following pseudocode listing. The main task consists in collecting the correct row and column indices for the submatrices that enter the determinant formula Eq. (11.1). The factors in line 19 are those from Eqs. (11.9) and (11.10). The final result for an interacting system is obtained by summing over all Hubbard-Stratonovich configurations $\{\mathbf{s}\}$. The Monte Carlo timeseries of the diagonal element of ρ_A corresponding to one of the two Néel states on a plaquette is displayed in Fig. 11.1. There are rare outliers that exceed to maximum probability of 1. The histogram of probabilities on the right is slightly bimodal but smooth; the mean value is around $P_{\text{Néel}} \approx 0.12$. For a projective measurement one would expect a binary distribution of probabilities with only the probabilities 0 or 1 appearing.

Result: Matrix element $\langle\beta|\rho_A|\alpha\rangle_{\{\mathbf{s}\}}$ between the occupation number states $|\alpha\rangle$ and $|\beta\rangle$.

Input:

- Occupation states $|\alpha\rangle = |\alpha_\uparrow\rangle \otimes |\alpha_\downarrow\rangle$ and $|\beta\rangle = |\beta_\uparrow\rangle \otimes |\beta_\downarrow\rangle$ bitcoded as integers $[\alpha_\uparrow], [\alpha_\downarrow], [\beta_\uparrow], [\beta_\downarrow]$

- Single-particle Green's function $G^{(0)}(1:N_{\text{sites},A}, 1:N_{\text{sites},A}; \sigma = \uparrow, \downarrow)$ for Hubbard-Stratonovich configuration $\{\mathbf{s}\}$, restricted to subsystem A.

1: **for** $\sigma = \uparrow, \downarrow$ **do**
2:     $[t_1] = \text{XOR}([\alpha_\sigma], [\beta_\sigma]);$ $[t_2] = \text{NOT}([t_1])$
3:     $[t_-] = \text{AND}([t_1], [\alpha_\sigma]);$ $\mathcal{I}_- = \text{bitonesToSitelist}([t_-])$
4:     $[t_+] = \text{NOT}(\text{AND}([t_1], [\beta_\sigma]));$ $\mathcal{I}_+ = \text{bitonesToSitelist}([t_+])$
5:     $[t_3] = \text{AND}([\alpha_\sigma], [t_2]);$ $\mathcal{I}_{\text{occ, unaffected}} = \text{bitonesToSitelist}([t_3])$
6:     $N_{\text{occ}} = |\mathcal{I}_{\text{occ, unaffected}}|$
7:     $r_\sigma = 0$
8:     **for** $b = 0 : N_{\text{occ}}$ **do**   ▷ Loop over "branches" for occupied sites
9:         $\mathcal{I}_{\text{occ, unaffected}}^{\text{branch}} = \{i_k \in \mathcal{I}_{\text{occ, unaffected}} \mid k\text{-th bit in } [b] \text{ is set.}\}$
10:         $N_{\text{BitonesBranch}} = |\mathcal{I}_{\text{occ, unaffected}}^{\text{branch}}|$
11:         $\mathcal{I}_{\text{proj}} = \mathcal{I}_{\text{occ, unaffected}}^{\text{branch}} \cup \mathcal{I}_{\text{unocc, unaffected}}$
12:         $\mathcal{R} = \mathcal{I}_{\text{proj}} \cup \mathcal{I}_-$ ▷ List of lattice sites for row indices
13:         $\mathcal{C} = \mathcal{I}_{\text{proj}} \cup \mathcal{I}_+$ ▷ List of lattice sites for column indices
14:         $k = |\mathcal{C}|(= |\mathcal{R}|)$
15:         **for** $i = 1 : k$ **do**
16:             **for** $j = 1 : k$ **do**
17:                 $G_k^{(0)}(i, j) = G^{(0)}(\mathcal{R}(i), \mathcal{C}(j); \sigma)$
18:         $r_\sigma = r_\sigma + (-1)^{N_{\text{BitonesBranch}}} \det\left(G_k^{(0)}\right)$
19: $\langle\beta|\rho_A|\alpha\rangle_{\{\mathbf{s}\}} = (-1)^{p_\uparrow}(-1)^{p'_\uparrow}(-1)^{p_\downarrow}(-1)^{p'_\downarrow} r_\uparrow \cdot r_\downarrow$

Notation: $[x]$ means that the integer x is to be replaced by its binary bit string, where each bit indicates the occupation of a lattice site. $|\mathcal{I}|$ denotes the number of elements in the list $\mathcal{I}$ and bitonesTopSitelist$([x])$ is a routine that returns a list of lattice sites corresponding to the positions in the bitstring $[x]$ where the bit is set.
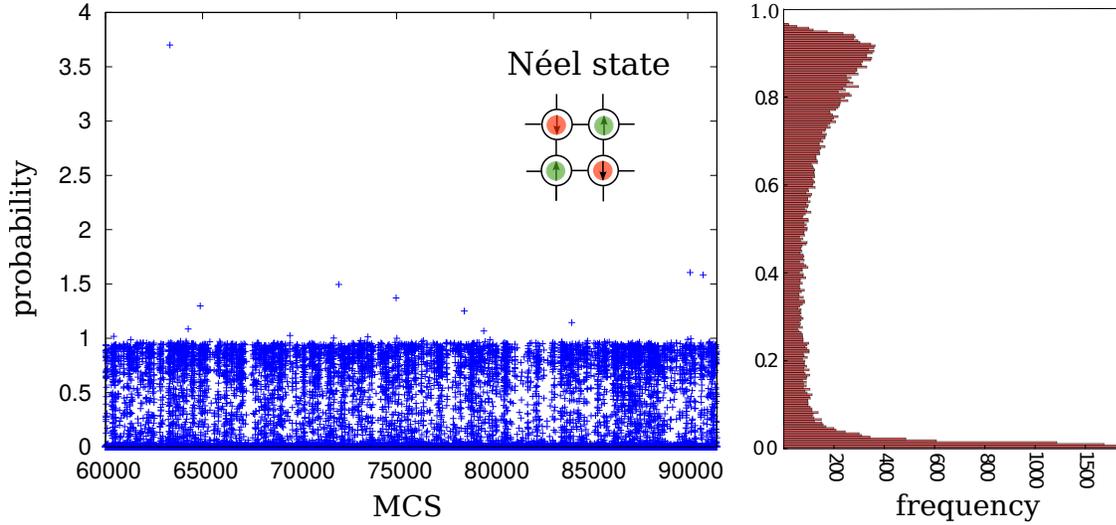
Fig. 11.1: Monte Carlo timeseries of the probability P for one of the two plaquette Néel states. Note the violation of $P \leq 1$ for rare outliers. $U/t = 7.2, \beta t = 4$, system size $L \times L$ with $L = 12$.

11.2 Symmetries of the reduced density matrix

The form of the global density matrix

$$\rho = \frac{1}{Z} e^{-\beta(H - \mu N)} \quad \text{with} \quad Z = \text{Tr}\left(e^{-\beta H}\right)$$

implies that a symmetry operation represented by a unitary operator U which obeys the commutation relation $[H - \mu N, U] = 0$, is trivially also a symmetry of the global density matrix:

$$U^\dagger \rho U = \rho. \tag{11.11}$$

In the following it is discussed how symmetries of the Hamiltonian affect the block diagonal structure of the reduced density matrix ρ_A of a subsystem A. Details on the exact diagonalization of the Hubbard model by means of symmetries are discussed in Refs. [229, 319]; a analytical diagonalization exploiting all symmetries was carried out in Ref. [320] for a single plaquette of the Hubbard model and in Ref. [321] for a plaquette of the $t - J$ model.

11.2.1 Particle number conservation

The eigenstates of the reduced density matrix retain their good quantum numbers when the corresponding operator of the total system is a direct sum of the operators of

Mulliken symbol	dim.	basis function	symmetry
A_1	1	$(x^2 + y^2) \cdot z^2$	s
A_2	1	$(x^2 + y^2) \cdot z$	s
B_1	1	$x^2 - y^2$	$d_{x^2-y^2}$
B_2	1	xy	d_{xy}
E	2	x, y	p_x, p_y

Table 11.1: Irreducible representations of the symmetry group D_4.

its subsystems [322]. This is the case for the particle number $\hat{N}_\sigma = \hat{N}_{A,\sigma} + \hat{N}_{B,\sigma}$ (or the z component of the total spin $\hat{M} = \hat{N}_\uparrow - \hat{N}_\downarrow$) and consequently ρ_A is block diagonal with respect to the quantum numbers $N_{A,\sigma} = \sum_{\mathbf{i} \in A} n_{\mathbf{i},\sigma}$. For brevity, we denote particle number sectors on the subsystem A in the following by $(N_\uparrow, N_\downarrow)$, where $N_\sigma \equiv N_{A,\sigma}$.

11.2.2 Lattice symmetry: point group D_4

We focus in the following on the point group symmetry of the square lattice, the non-Abelian dihedral group D_4 with $h = 8$ group elements

$$D_4 = \{\mathcal{E}, C_{2z}, C_{4z}, C_{4z}^{-1}, C_{2x}, C_{2y}, C_{2xy}, C_{2x\bar{y}}\} \tag{11.12}$$

comprising the identity $\mathcal{E}$ and (assuming that the square is lying in the $x - y$ plane) rotations by π around the x, y and z axes, C_{2x}, C_{2y} and C_{2z}, rotations by π around the diagonal lines $x = y$ and $x = -y$, C_{2xy} and $C_{2x\bar{y}}$, and clockwise and counterclockwise rotations by $\pi/2$ around the z axis, C_{4z} and C_{4z}^{-1}.

The group D_4 has five irreducible representations, four one-dimensional representations with the Mulliken symbols A_1, A_2, B_1, and B_2, and one two-dimensional representation E. They are listed in Tab. 11.1 together with their symmetries. (see [323] for the character table and the irreducible representation matrices of E).

We denote by $\mathcal{L}_{A(B)}$ the geometric object consisting of the lattice sites in subsystem A (or in its complement B). Consider the subgroup $\tilde{\mathcal{G}}$ of lattice symmetry operations that can be written as

$$R = R^{(A)} R^{(B)} \quad \text{with} \quad R^{(A)} \mathcal{L}_A = \mathcal{L}_A \text{ and } R^{(B)} \mathcal{L}_B = \mathcal{L}_B, \tag{11.13}$$

where $R^{(A)}$ ($R^{(B)}$) acts only on sites in A (B). By

$$P_R = P_R^{(A)} \otimes P_R^{(B)} \tag{11.14}$$

we denote the corresponding operator that acts onto wave functions in second quantization rather than lattice sites (cf. Eq. (11.17) below). Then the general invariance of the global ρ under all elements R of the point group $\mathcal{G}$

$$P_R^\dagger \rho P_R = \rho \tag{11.15}$$

implies for the subgroup $\tilde{\mathcal{G}}$ of elements R' which can be written in the specific form Eq. (11.13) that

$$
\begin{aligned}
\text{Tr}_B \left(P_{R'}^{(A)\dagger} \otimes P_{R'}^{(B)\dagger} \rho \, P_{R'}^{(A)} \otimes P_{R'}^{(B)} \right) &= \text{Tr}_B \left(\rho \right) \equiv \rho_A \\
\Rightarrow P_{R'}^{(A)\dagger} \text{Tr}_B \left(P_{R'}^{(B)\dagger} \rho \, P_{R'}^{(B)} \right) P_{R'}^{(A)} &= \rho_A \\
\Rightarrow P_{R'}^{(A)\dagger} \rho_A P_{R'}^{(A)} &= \rho_A.
\end{aligned}
\tag{11.16}
$$

In the last step the basis independence of the trace operation and the definition of the reduced density matrix was used. Thus, ρ_A is invariant under all joint lattice symmetries R' of $\mathcal{L}_A$ and $\mathcal{L}_B$ that map each subset of lattice sites separately back onto itself according to Eq. (11.13). If either $\mathcal{L}_A$ or $\mathcal{L}_B$ has reduced symmetry (e.g. a square plaquette embedded in a rectangular system or a rectangular plaquette inside a square system), then only the largest common symmetry subgroup $\tilde{\mathcal{G}}$ of the point group $\mathcal{G}$ is inherited by ρ_A. An illustrative example is shown in the inset of Fig. 11.3 where the plaquette $\mathcal{L}_A$ possesses the full symmetry of the square, but due to its location at the corner of a system with open boundary conditions the complement lattice $\mathcal{L}_B$ is only invariant under $C_{2x\bar{y}}$, which is reflected in the symmetries of the diagonal elements of ρ_A (see main panel of Fig. 11.3).

11.2.3   Group theoretic techniques: projection operator method

The relation between transformation operators acting in the many-body Hilbert space and the symmetry operations acting on coordinates is provided by Wigner's convention [323, Chapt. 3]

$$
\hat{P}_R f(Rx) = f(x) \Leftrightarrow \hat{P}_R f(x) = f(R^{-1}x),
\tag{11.17}
$$

where $\hat{P}_R$ is the operator acting onto wave functions in second quantization while the symmetry operator R acts onto indices of creation and annihilation operators.

The fermion ordering in the definition of the states is chosen such that site indices of creation operators increase from right to left and creation operators for $\uparrow$-particles are to the left of operators for $\downarrow$-particles, e.g. $| \uparrow_4 \downarrow_3 \uparrow_2 \downarrow_1 \rangle \equiv c_{4\uparrow}^\dagger c_{2\uparrow}^\dagger c_{3\downarrow}^\dagger c_{1\downarrow}^\dagger |\text{vac}\rangle$. As an illustration of Eq. (11.17) and of the action of the symmetry operators $\hat{P}_R$ on the many-body Hilbert space, consider the example

$$
\begin{aligned}
\hat{C}_{4z} |0\,0\,\uparrow_2\uparrow_1\rangle = \hat{C}_{4z} c_{2,\uparrow}^\dagger c_{1,\uparrow}^\dagger |\text{vac}\rangle &= c_{C_{4z}^{-1}(2),\uparrow}^\dagger c_{C_{4z}^{-1}(1),\uparrow}^\dagger |\text{vac}\rangle = c_{1,\uparrow}^\dagger c_{3,\uparrow}^\dagger |\text{vac}\rangle \\
&= -|0\,\uparrow_3\,0\,\uparrow_1\rangle,
\end{aligned}
\tag{11.18}
$$

which shows how the matrix elements of $\hat{P}_R$ can be constructed. In the particle number block $(N_\uparrow, N_\downarrow)$, the operators $\hat{P}_R$ are permutation matrices of size $\dim(N_\uparrow, N_\downarrow) \times$

$\dim(N_\uparrow, N_\downarrow)$, where $\dim(N_\uparrow, N_\downarrow) = \begin{pmatrix} N_s \\ N_\uparrow \end{pmatrix} \cdot \begin{pmatrix} N_s \\ N_\downarrow \end{pmatrix}$, with an additional sign structure coming from the fermionic exchanges. Since the spatial symmetry operations do not affect the spin states, it is convenient to write $\hat{P}_R$ as the tensor product $\hat{P}_R = \hat{P}_{R,\uparrow} \otimes \hat{P}_{R,\downarrow}$ with $\hat{P}_{R,\sigma}$ acting only on creation operators of spin σ. Having obtained a matrix representation of the symmetry operators $\hat{P}_R$ on the particle number sector $(N_\uparrow, N_\downarrow)$, we can decompose this subspace of Hilbert space further into the irreducible invariant subspaces of D_4 via the projection operator technique [323] (see also [321] for a detailed discussion). In the decomposition of a reducible representation the n-th irreducible representation occurs a_n times, given by [323]

$$a_n = \frac{1}{h} \sum_R \chi^{(n)}(R)^\star \chi(R), \tag{11.19}$$

where $\chi^{(n)}(R)$ is the character of the group element R in the n-th irreducible representation and $\chi(R) \equiv \mathrm{Tr}\,(P_R) = \sum_i [P_R]_{ii}$ is the character of R in the reducible matrix representation. Applying the formula (11.19) to each particle number sector $(N_\uparrow, N_\downarrow)$ of a square plaquette we obtain the group structure presented in Tab. 11.2.

$N_\uparrow, N_\downarrow$	Dimension $= \begin{pmatrix} N_s \\ N_\uparrow \end{pmatrix} \cdot \begin{pmatrix} N_s \\ N_\downarrow \end{pmatrix}$	Irreducible representations
$0,0$	1	A_1
$1,0$	4	$A_1 \oplus B_2 \oplus E$
$2,0$	6	$A_2 \oplus B_2 \oplus 2E$
$1,1$	16	$3A_1 \oplus A_2 \oplus B_1 \oplus 3B_2 \oplus 4E$
$3,0$	4	$A_2 \oplus B_1 \oplus E$
$2,1$	24	$3A_1 \oplus 3A_2 \oplus 3B_1 \oplus 3B_2 \oplus 6E$
$4,0$	1	B_1
$3,1$	16	$A_1 \oplus 3A_2 \oplus 3B_1 \oplus B_2 \oplus 4E$
$2,2$	36	$6A_1 \oplus 4A_2 \oplus 6B_1 \oplus 4B_2 \oplus 8E$

Table 11.2: Group structure of the Hilbert space for a single square plaquette of the Hubbard model. Shown is the reduction of the subspaces of fixed particle number $(N_\uparrow, N_\downarrow)$ into irreducible invariant subspaces of the symmetry group D_4. The table is symmetric under exchange of $N_\uparrow$ and $N_\downarrow$. Particle number sectors $(N_\uparrow, N_\downarrow)$ above half filling have the same group structure as their particle-hole symmetric counterparts $(N_s - N_\uparrow, N_s - N_\downarrow)$ with $N_s = 4$.

We wish to decompose the particle number sector $(N_\uparrow, N_\downarrow)$ into blocks of states such that the application of a lattice symmetry operation to a state mixes only states within the same block.

Let $|\phi_{i\lambda}^{(n)}\rangle$ denote a normalized basis state that transforms according to the λ-th copy of the i-th row in the n-th irreducible representation. Then each occupation

number state $|\alpha\rangle$ can be expanded as

$$|\alpha\rangle = \sum_{n=1}^{c} \sum_{i=1}^{l_n} \sum_{\lambda=1}^{a_n} b_{i\lambda}^{(n)} |\phi_{i\lambda}^{(n)}\rangle, \tag{11.20}$$

where c is the number of irreducible representations, which is equal to the number of conjugacy classes [323] (here, for D_4, c=5), l_n is the dimension of the n-th irreducible representation, and λ labels the a_n different copies of the n-th irreducible representation.

The symmetry transfer operator is defined as [323]

$$\mathcal{P}_{ij}^{(n)} = \frac{l_n}{h} \sum_{R} \Gamma^{(n)}(R)_{ij}^{\star} P_R, \tag{11.21}$$

where $\Gamma^{(n)}(R)$ is the matrix representation of the group element R in the n-th irreducible representation and the sum runs over all group elements. $\mathcal{P}_{ii}^{(n)}$ acts as a projector onto the i-th row of the n-th irreducible representation, while $\mathcal{P}_{ij}^{(n)}$ transfers the i-th row into the j-th row according to[3]

$$\mathcal{P}_{ij}^{(n)} |\phi_{k\lambda}^{(m)}\rangle = \begin{cases} |\phi_{j\lambda}^{(n)}\rangle & \text{if } i = k \text{ and } n = m \\ 0 & \text{else} \end{cases}, \qquad \mathcal{P}_{ii}^{(n)} |\phi_{i\lambda}^{(n)}\rangle = |\phi_{i\lambda}^{(n)}\rangle. \tag{11.23}$$

Note that if there are several copies λ of the same irreducible representation n, then the projection operator $\mathcal{P}_{ii}^{(n)}$ applied to a basis state $|\alpha\rangle$ will return a basis state for only a single copy $\lambda(\alpha)$:

$$\mathcal{P}_{ii}^{(n)} |\alpha\rangle \sim |\phi_{i\lambda(\alpha)}^{(n)}\rangle. \tag{11.24}$$

By letting $\mathcal{P}_{ii}^{(n)}$ act onto each state $|\alpha\rangle$ of the particle number sector $(N_\uparrow, N_\downarrow)$ and collecting all non-zero states that are linearly independent, all copies of the n-th irreducible representation are generated. In this projection method, it may happen that the same basis state (up to a global phase) is generated multiple times.

Once all basis vectors $|\phi_{i\lambda}^{(n)}\rangle$ have been constructed, the reduced density matrix can be transformed from the occupation to the representation basis via

$$\rho_A^{(\text{representation})} = S^\dagger \rho_A^{(\text{occupation})} S \tag{11.25}$$

---

[3] This is a consequence of the "great orthogonality theorem" [323] for irreducible representation matrices:

$$\sum_{R} \Gamma^{(n)}(R)_{ij}^{\star} \Gamma^{(m)}(R)_{kl} = \frac{h}{l_n} \delta_{nm} \delta_{ik} \delta_{jl}. \tag{11.22}$$

The matrices $\Gamma^{(n)}(R)$ denote all inequivalent, irreducible, unitary representations of the group and the summation R runs over all group elements.

with the transformation matrix $S_{\alpha,(n,i,\lambda)} = \langle \alpha | \phi_{i\lambda}^{(n)} \rangle$. As can be seen from Fig. 11.2, when written in the irreducible representation basis, the reduced density matrix ρ_A does not have non-vanishing matrix elements between states of different symmetry and acquires a blockdiagonal form. More importantly, we are in a position to attach symmetry labels to the eigenvalues of ρ_A.

11.2.4   Spin inversion symmetry

For a finer symmetry labelling it is useful to implement the spin inversion symmetry $\mathcal{S} = \{\mathcal{E}, \sigma_h\}$ where $\sigma_h = \prod_{i \in A} \sigma_i^x$ flips all spins on subsystem A. All symmetry operations of the lattice symmetry group D_4 commute with the spin inversion operation since they act onto different degrees of freedom (site indices of creation operators on the one hand and spin indices on the other hand). Therefore, we can form the direct-product group $D_{4h} = D_4 \times \mathcal{S}$ with 16 group elements, the original 8 from D_4, each multiplied by the identity or by spin inversion, and organize the states into the irreducible invariant subspaces of D_{4h}. In order to apply the projection operator method for generating the irreducible basis states, one needs to know the irreducible representation matrices of D_{4h} (see Eq.(11.21)). It can be shown [323] that the direct product of two irreducible representations forms an irreducible representation of the direct product group.

If the Hilbert space is first decomposed into subspaces of fixed particle number $H = \prod_{\oplus N_\uparrow, N_\downarrow = 0}^{N_s} H_{(N_\uparrow, N_\downarrow)}$, then spin inversion symmetry $\mathcal{S}$ can only be used for further block diagonalization inside subspaces with equal spin populations since it is obviously not possible to construct eigenstates of σ_h that lie only in $H_{(N_\uparrow, N_\downarrow)}$ whenever $N_\uparrow \neq N_\downarrow$. Including spin inversion leads to the finer group structure of the subspaces with $N_\uparrow = N_\downarrow = 1$ and $N_\uparrow = N_\downarrow = 2$ shown in Tab. 11.3 where the additional label g (u) indicates whether the basis function is even (odd) under spin inversion.

$N_\uparrow, N_\downarrow$	Irreducible representations
$1,1$	$3A_{1,g} \oplus B_{1,g} \oplus 2B_{2,g} \oplus 2E_g \oplus A_{2,u} \oplus B_{2,u} \oplus 2E_u$
$2,2$	$5A_{1,g} \oplus A_{2,g} \oplus 4B_{1,g} \oplus 3B_{2,g} \oplus 4E_g \oplus A_{1,u} \oplus 3A_{2,u} \oplus 2B_{1,u} \oplus B_{2,u} \oplus 4E_u$

Table 11.3: Group structure of the spin-balanced subspaces of the single-plaquette Hubbard model. The decomposition of the subspaces is done with respect to the irreducible invariant subspaces of D_{4h}. The subscript g (u) denotes a wave function that is even (odd) under flipping all spins on the plaquette.

11.3   Error bars

Due to statistical fluctuations ρ_A cannot be perfectly Hermitian, however, the deviations from Hermiticity, $\Delta_H = \rho_A - \rho_A^\dagger$, are smaller than the error bars of the corresponding

off-diagonal elements, and ρ_A is found to be normalized, $\mathrm{Tr}(\rho_A) = 1 \pm \varepsilon$, with an inaccuracy ranging from $\varepsilon \lesssim 10^{-5}$ $(0 \leq U \leq 4)$ to $\varepsilon \approx (1-3) \times 10^{-2}$ (large U, $4 \leq U \leq 10$) for $\beta t = 4$. For low temperatures the inaccuracy is slightly larger $(\epsilon \approx 3 \times 10^{-2})$ for all values of U (see insets in Fig. 11.6). Furthermore, ρ_A is positive semi-definite within statistical uncertainty, as required for a valid density matrix.

11.4 QST for a plaquette in the Hubbard model

A simple argument [324] for an isolated plaquette shows that local antiferromagnetic correlations favour d-wave pairing correlations, namely the operator that connects the antiferromagnetic 4-particle ground state $|4\rangle$ to the two-hole ground state $|2\rangle$ must have $d_{x^2-y^2}$ symmetry. The matrix element

$$\langle 2|\Delta_d|4\rangle \neq 0 \tag{11.26}$$

is large when the pairing operator $\Delta_d = (c_{3,\uparrow}c_{2,\downarrow} - c_{3,\uparrow}c_{4,\downarrow} + \cdots)$ has the sign structure for d-wave symmetry. On the other hand $\langle 2|\Delta_s|4\rangle = 0$ for an s-wave pairing operator. The following sections investigate the quantum state on a plaquette of the Hubbard model embedded in a bath of 12×12 sites which are treated numerically exactly.

11.4.1 Diagonal elements of $\rho_{A=\square}$

Fig. 11.3 shows the probabilities $P(s)$ of all plaquette configurations s on a plaquette which is located at the corner of a system with open boundary conditions. The integer $s \in \{0, 1, \ldots, 255\}$ encodes the Fock configuration on a plaquette through its binary representation $[b(s)] = [n_4^\uparrow n_3^\uparrow n_2^\uparrow n_1^\uparrow n_4^\downarrow n_3^\downarrow n_2^\downarrow n_1^\downarrow]$ where n_i^σ is the occupation number for spin σ at one of the four sites (shown in the upper right inset) and the notation $[\ ]$ converts integer codes into bit representations (see Appendix E for a complete list of all plaquette configurations and their integer codes).

The most probable states, the states with integer code [105] and [150], are the two Néel states; they are followed by the 12 other spin-only states which together would span the Hilbert space in a Heisenberg-like description. From the upper left panel of Fig. 11.3 one can see that for $U = 7.2$, $T/t = 0.35$ and half filling, on a plaquette there are $\sim 24\%$ Néel states, $\sim 40\%$ spin-only states (excluding the two Néel states), the remaining $\sim 36\%$ are states with charge fluctuations.

The arrangement with the plaquette at the corner, shown in the upper right inset in Fig. 11.3, does not possess the full symmetry of the square, the only symmetry operations which can be written in the form Eq. (11.13) being $\{E, C_{2x\bar{y}}\}$. This is reflected in asymmetries of the probabilities for plaquette configurations with a single hole (see main panel of Fig. 11.3 with plaquette configurations drawn next to representative data points): In the presence of a boundary the hole prefers to have many neighbours rather than sit at the boundary which would limit the number of possible hopping
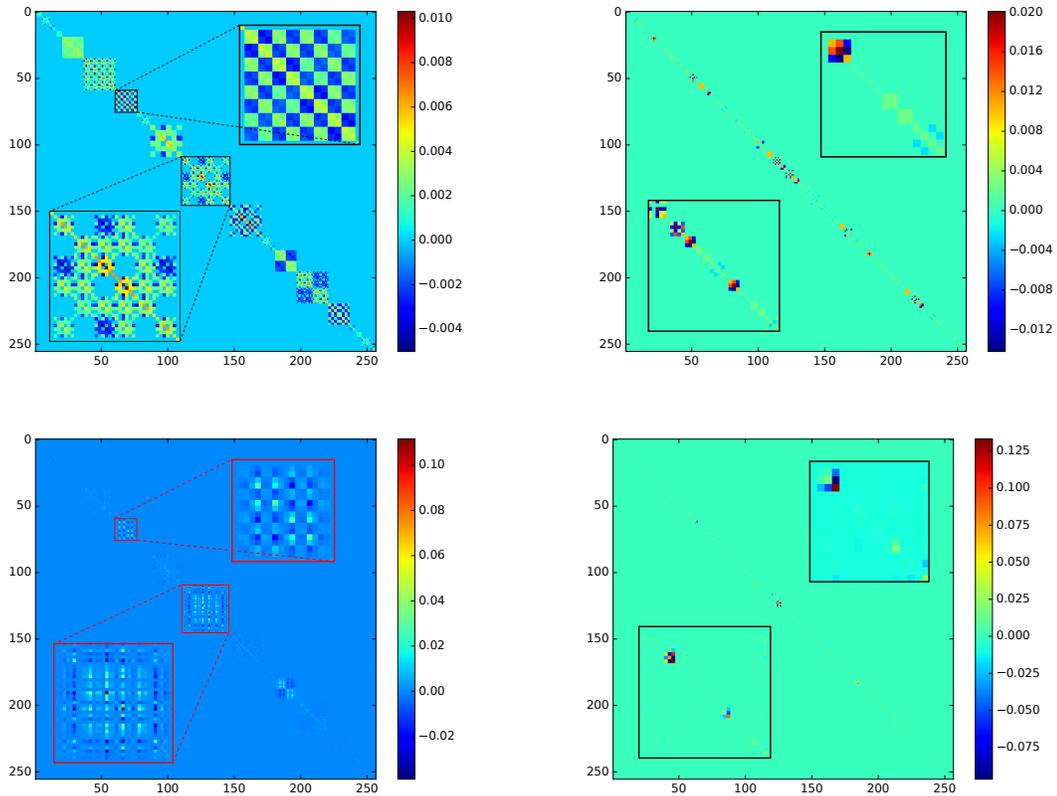
Fig. 11.2: Transformation of the reduced density matrix $\rho_{A=\square}$ from the occupation basis (left column) to the representation basis (right column) of the symmetry group D_{4h}. First row $U = 0, \beta t = 4$; second row $U = 6t, \mu = 3t, \beta t = 4$. The total system size is $L \times L$ with $L = 12$. The insets show the enlarged particle number blocks $(N_\uparrow = 2, N_\downarrow = 2)$ and $(N_\uparrow = 1, N_\downarrow = 3)$ in the lower left and upper right corner, respectively. Note that the block $(2, 2)$ in the inset is decomposed with respect to the irreducible representations of D_{4h} while in the main panel only the symmetry group D_4 is used.
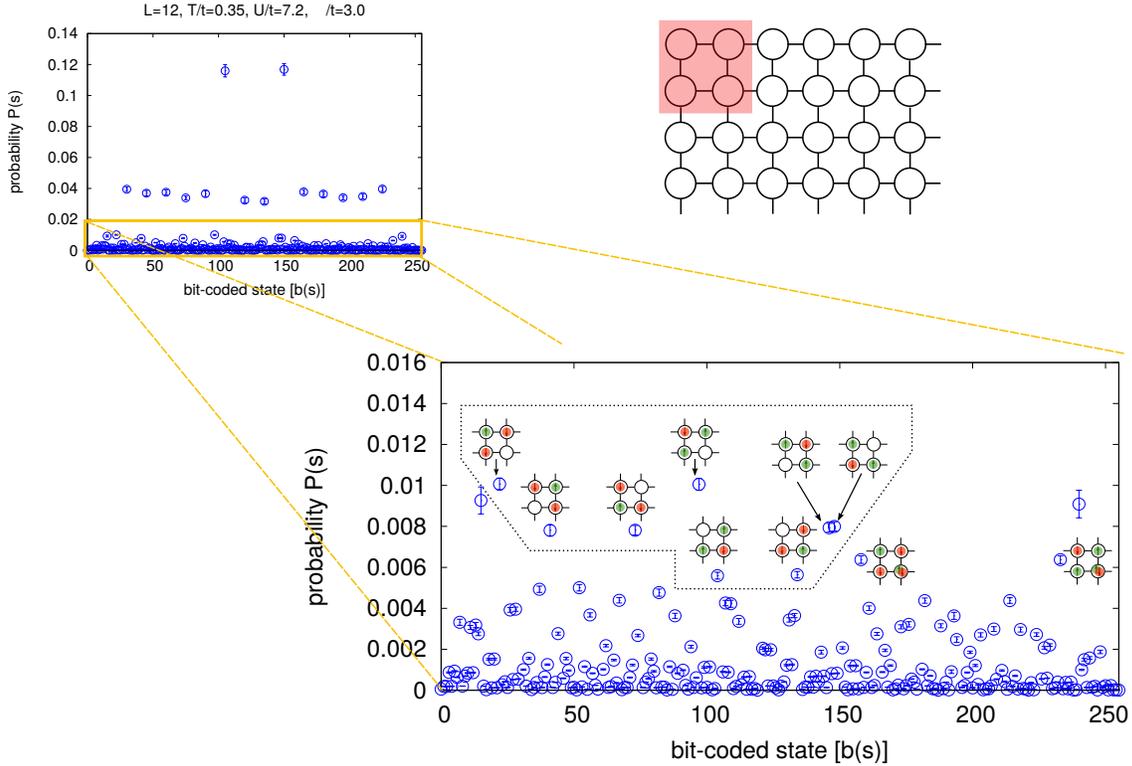
Fig. 11.3: Probabilities $P(s)$ of particle number configurations s in Fock space on a plaquette that is located at the corner of a large 12×12 system with open boundary conditions. The binary representation of the integer s encodes the Fock space configuration. **Upper left panel:** The most probably states are the two Néel states, followed by the remaining 12 spin-only states. **Main panel:** Plaquette states with charge fluctuations. The asymmetric location of the plaquette leads to a disruption of symmetries that would be present in a translationally invariant system, which is clearly visible in the probabilities. Symmetry-related states have the same probability. $T/t = 0.35, U/t = 7.2, \mu/t = 3.0$.

processes. Therefore, among the configurations shown, the one with the hole located precisely at the corner has the lowest probability. Note that configurations that are related by the symmetry operation $\{E, C_{2x\bar{y}}\}$ do occur with the same probability.

Fig. 11.4 shows the probabilities of selected plaquette occupation number states in the repulsive Hubbard model at half filling for low temperature $\beta t = 16$ or 24 (a) and high temperature $\beta t = 4$ (b). Here, periodic boundary conditions are used so that the full symmetry of the square is preserved. Occupation number states that are related by symmetries are grouped into classes of states, which are labelled by the bitcode $[b(s)]$ of the member with the smallest bitcode within the class. A list of all 34 classes of symmetry-related states with the bitcodes of their representatives can be found in Appendix E.

At low temperature [Fig. 11.4(a)] two datasets for different temperatures, $\beta t = 24$ for $U/t \leq 5$ and $\beta t = 16$ for $U/t \geq 6$, have been combined, which is indicated by
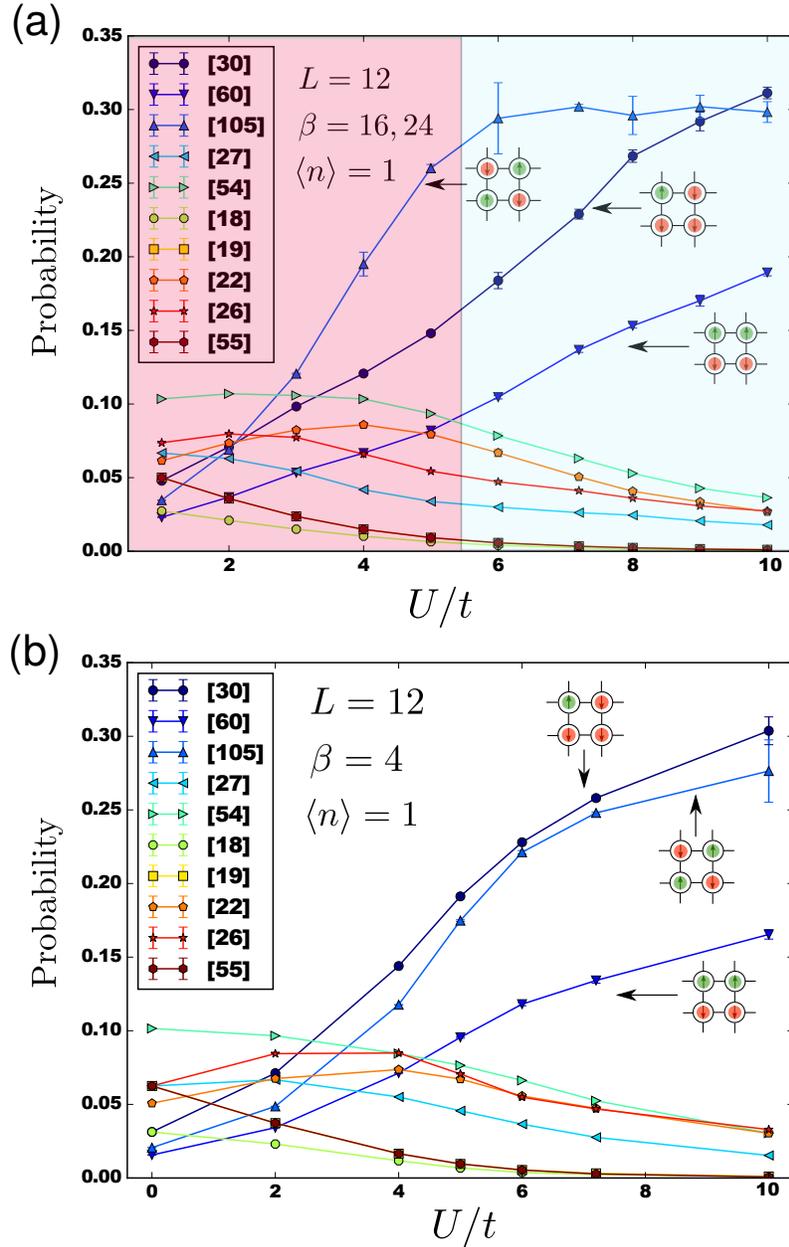
Fig. 11.4: Probabilities of selected plaquette configurations as a function of interaction (at half filling). The numbers in angular brackets [ ] denote the bitcoded representative of a class of symmetry related plaquette configurations (see Appendix E). The probability shown for a particular representative is the sum of probabilities of all configurations in the corresponding class.

different colours of the background shading. For $U/t \geq 3$, the most probable states are the two Néel states. The second most important class of states [30] comprises those

states with three particles of one spin and one particle of the opposite spin. Taking into account spin-inversion symmetry there 8 such states and their probabilities have been summed up in Fig. 11.4. This explains why this class of states appears with higher probability in Fig. 11.4 than the class of states [60], consisting of only 4 states, namely the spin configurations that are FM aligned in one direction and AFM aligned in the other one. The multiplicities of different classes of states, which are essential for interpreting Fig. 11.4, are also given in Appendix E.

To illustrate that detailed information can be gleaned from Fig. 11.4 we consider next the classes [27] and [54], which both have a multiplicity of 16 states. The class of states [27], comprising plaquette configurations with a neighbouring doublon-hole pair and the singly-occupied sites in a FM configuration, has smaller probability than states [54] representing a neighbouring doublon-hole pair with the singly-occupied sites arranged in an AFM configuration. Note also that the classes of states [19] and [55] have exactly the same probability due to particle-hole symmetry at half filling.

The plaquette probabilities at high temperature $\beta t = 4$ [Fig. 11.4(b)] are qualitatively very similar to those at low temperature, indicating that local correlations of the low-temperature phase are already well developed at $\beta t = 4$.

In Fig. 11.5(a) the doping dependence of the plaquette probabilities is presented for experimentally relevant inverse temperature $\beta t = 4$ and for repulsive interaction $U/t = 2, 4$, and 7.2. Error bars in Fig. 11.5(a) are deduced from the spread of datapoints within one class of states which should have the same probability due to symmetry. The selected plaquette configurations have at least one doubly occupied site so that for large Hubbard repulsion they represent the intermediate virtual states through which pairwise and ring exchange interactions in an effective spin Hamiltonian are mediated [247–249]. A typical pathway of hopping processes leading in fourth order perturbation theory to ring exchange interactions is illustrated in Fig. 11.5(b).

The overall trend is that the amplitude of states with charge fluctuations is reduced with increasing Hubbard repulsion. The amplitude of states with neighbouring doublon-hole pairs decreases as t/U, in accordance with second order perturbation theory. Plaquette configurations with a doublon-hole pair on diagonally opposite corners ([53]), occurring as intermediate states in ring-exchange pathways [Fig. 11.5(b)], have a very small probability at all fillings, which is for large U/t approximately an order of magnitude smaller than that of states with neighbouring doublon-hole pairs ([27],[54]), as to be expected on the basis of fourth order perturbation theory.

Based on Fig. 11.5(a), very detailed observations regarding correlation effects can be made. For example, a signal for local correlation lies in the differences of probability between similar configurations such as [23] and [53] or [19] and [25], which would be equally likely, if the singly and doubly occupied sites were placed on the lattice randomly, with say probability p_d for a doubly occupied site and p_s for a singly occupied one. It is important to note that [19] has multiplicity 16, whereas [25] has multiplicity 8 (see Appendix E). Thus, the observation that the classes [19] and [25] have almost the same probabilities in Fig. 11.5(a) indicates that the probability
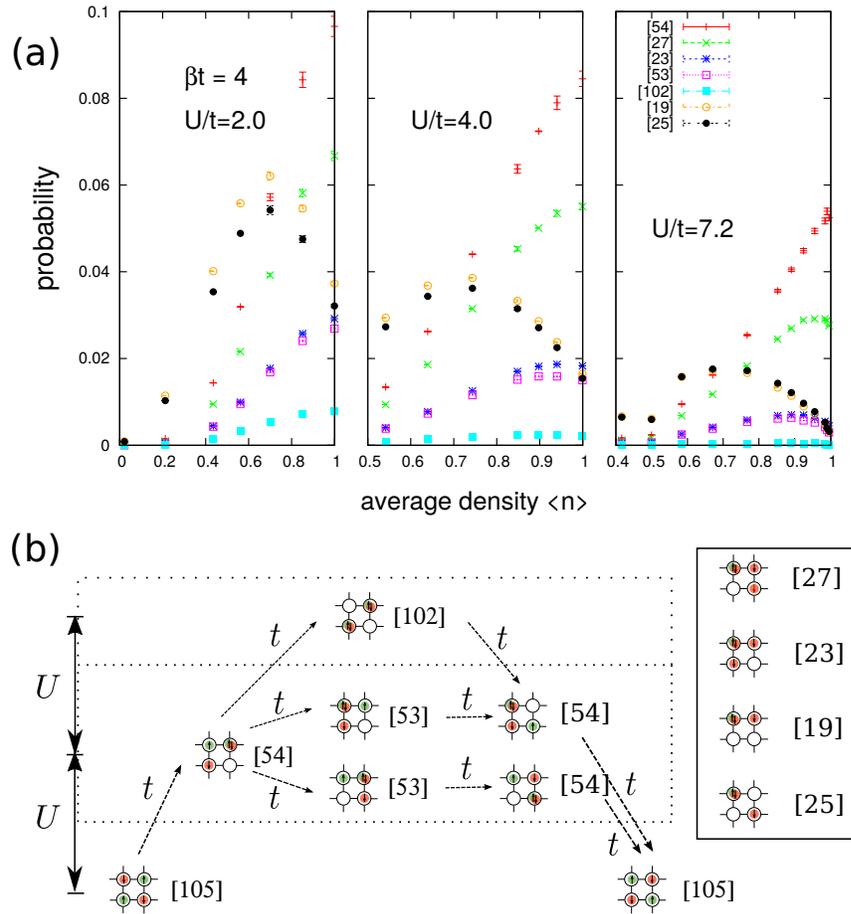
Fig. 11.5: (a) Doping dependence of the probability of selected plaquette configurations with at least one doubly occupied site; $\beta t = 4$, $U/t = 2, 4, 7.2$. The total system size is $L \times L$ with $L = 12$. The aggregated probabilities are the sum over all states that are related by lattice or spin inversion symmetry (see Appendix E). Note the non-monotonic behaviour at quarter filling $\langle n \rangle = 0.5$ in subfigure (a) for $U/t = 7.2$. (b) Typical pathways of ring exchange processes in fourth order perturbation theory, where some of the plaquette configurations in (a) appear as intermediate states. Away from half filling also third order spin exchange processes with intermediate states such as [19] or [25] are present.

per individual configuration of states [25] is kinetically enhanced compared to states from [19], since the former allow for more hopping processes on the plaquette. Note also in Fig. 11.5(a) at $U/t = 7.2$ the discontinuous jump at quarter filling $\langle n \rangle \approx 0.5$.

11.4.2   Off-diagonal elements of $\rho_{A=\square}$

With the knowledge of all off-diagonal elements of the reduced density matrix, we can compute the entanglement spectrum and resolve it according to symmetry sectors.
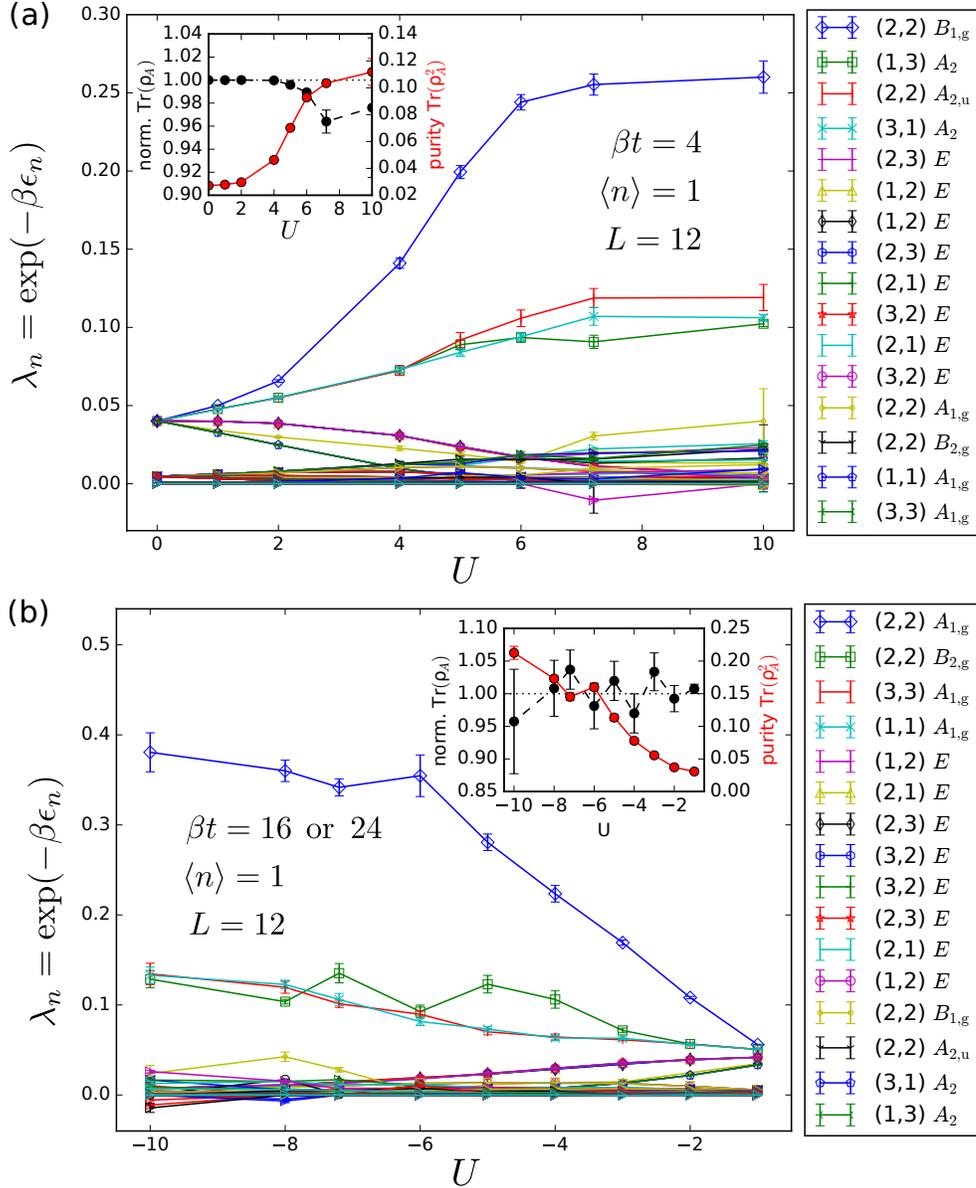
Fig. 11.6: Eigenvalues $\{\lambda_n\}_{n=1}^{4^{N_s}=256}$ of the reduced density matrix $\rho_{A=\square}$ on a plaquette at half filling and inverse temperature (a) $\beta t = 4$ and (b) $\beta t = 24$ (for $|U|/t \leq 5$) or $\beta t = 16$ (for $|U|/t \geq 6$). Eigenvalues are labelled according to irreducible representations of the symmetry group D_4 of the square as well as spin inversion symmetry. The plaquette is embedded in an $L \times L$ system with $L = 12$ and periodic boundary conditions. The inset shows the normalization $\mathrm{Tr}\,(\rho_{A=\square})$ and purity $\mathrm{Tr}\,(\rho_{A=\square}^2)$ of the reduced density matrix.

Fig. 11.6 shows the eigenvalue spectrum of the plaquette reduced density matrix $\rho_{A=\square}$ at half filling as a function of Hubbard interaction for high (a) and low (b) temperature. The 16 most important eigenstates of $\rho_{A=\square}$ are labelled by their symmetry sectors $(N_{A,\uparrow}, N_{A,\downarrow})M$ where $(N_{A,\uparrow}, N_{A,\downarrow})$ is the particle number sector and M is the Mulliken symbol describing the symmetry of the state under the operations of the symmetry group D_{4h} which combines the symmetries of the square and spin inversion symmetry. The data for high temperature in Fig. 11.6(a) is presented for the repulsive Hubbard model, while for the low temperature data in Fig. 11.6(b) we have chosen the language of the attractive Hubbard model. At half filling, both models are exactly equivalent; the eigenstates of $\rho_{A=\square}$ for the repulsive Hubbard model are related to those of the attractive model by the spin-down particle hole transformation Eq. (8.21). We point out that equivalent states in both models behave differently under symmetry operations of the point group, which is reflected in their Mulliken symbols. There is a one-to-one correspondence between the Mulliken symbols of equivalent states in the repulsive and attractive model, for example states with symmetry $(2,2)A_{2,u}$ in the language of the positive-U model correspond to states with symmetry $(2,2)B_{2,g}$ in the negative-U model, etc. We stress that in the presentation of Fig. 11.6(a) and (b) same colours do not necessarily imply that the states are equivalent in the two models[4].

Error bars have been obtained with the bootstrap method, in which the matrix diagonalization is repeated $\sim 10^3$ times, each time adding Gaussian noise with a standard deviation of the size of the deviation from Hermiticity $|\langle \beta|\Delta_H|\alpha\rangle|$ to each matrix element $\langle \beta|\rho_A|\alpha\rangle$. The well-resolved symmetry-related degeneracies seen in Figs. 11.6 (a) and (b) indicate that this error analysis is sound[5].

The insets in Fig. 11.6(a) and (b) show the normalization $\mathrm{Tr}\,(\rho_{A=\square})$ and the purity $\mathrm{Tr}\,(\rho^2_{A=\square})$ of the plaquette reduced density matrix. The purity increases with interaction strength, signalling that the state becomes closer to the $T = 0$ limiting case of a product state of non-entangled plaquettes. For non-interacting fermions ($U = 0$) the plaquette is most mixed with its environment; then there is a pronounced upturn in $\mathrm{Tr}\,(\rho^2_{A=\square})$ around $U = 5$, which levels off for $U \to 10$. The purity at $\beta t = 4$ (Fig. 11.6(a)) is by a factor of two smaller than at $\beta t = 24$ (Fig. 11.6(b)), as to be expected due to thermal entropy. $\rho_{A=\square}$ is normalized within error bars, which, however, increase for larger U and lower temperature.

Focusing first on results for high temperature Fig. 11.6(a), we observe that at $U = 0$ the 16 most important eigenstates are all degenerate and clearly separated from the remaining eigenstates with lower weight. As the interactions are switched on, the multiplet splits into two singlet-triplet type sequences, namely the four states $|s^{(1)}\rangle \in (2,2)B_{1,g}$ and $\{|t_0^{(1)}\rangle \in (2,2)A_{2,u}, |t_-^{(1)}\rangle \in (1,3)A_2, |t_+^{(1)}\rangle \in (3,1)A_2\}$, and the four states $|s^{(2)}\rangle \in (2,2)A_{1,g}$ and $\{|t_0^{(2)}\rangle \in (2,2)B_{2,g}, |t_-^{(2)}\rangle \in (1,1)A_{1,g}, |t_+^{(2)}\rangle \in (3,3)A_{1,g}\}$, and into

---

[4] The colours are based on the sequence of energy levels at $|U|/t = 4$.

[5] Due to the normalization all elements of ρ_A have correlations among them so that adding Gaussian noise idependently to all elements cannot be entirely correct.

a degenerate octet of eigenstates with p-wave symmetry (labelled by the irreducible representation label E).

The states with p-wave symmetry are both spin and pseudospin doublets, which together with the fact that their irreducible representation E is two-dimensional explains their eightfold degeneracy [320]. The degeneracy will be lifted either by applying an external magnetic field or by shifting the chemical potential away from the half filling point $\mu = \frac{U}{2}$. It is remarkable how well the degeneracy of the octet is preserved in the Monte Carlo data of Fig. 11.6(a) and (b).

In comparison with the grand canonical eigensystem of an isolated 4-site Hubbard model, which is worked out analytically in Ref. [320], the succession of energy levels appears changed in Fig. 11.6(a) and (b) in that the "entanglement energy" of the octet is lower (i.e. it has a heigher weight in the thermal state) than that of the low-weight singlet-triplet-structure $\{|s^{(2)}\rangle, |t^{(2)}_{\pm,0}\rangle\}$ for $|U| < 6$. This shows that the method presented here can resolve fine differences between the energy spectrum of an isolated plaquette [320] and of a plaquette embedded in a much larger system. Note that it is not simply the difference in temperature between the ground state spectrum of Ref. [320] and our "entanglement energy" spectrum, which could explain this discrepancy, since it occurs also at $\beta = 24$ in Fig. 11.6(b) and since temperature cannot change the relative order of the statistical weights.

For $U > 4$, the degeneracy of the high-weight triplet $|t^{(1)}_{\pm,0}\rangle$ is lifted, and concomitantly the purity of the reduced density matrix increases (see inset Fig. 11.6 (a)). The fact that the octet of eigenstates remains perfectly degenerate in the interval $4 \leq U \leq 6$ supports the picture that the lifting of the degeneracy in $|t^{(1)}_{\pm,0}\rangle$ is not merely an artifact of larger error bars. The low-weight singlet state $|s^{(2)}\rangle \in (2,2)A_{1,g}$ shows non-monotonic behaviour as a function of U and its weight appears to increase again for $U > 6$. However, the error bars are too large to draw any conclusions.

In Fig. 11.6(b) entanglement spectra for two low temperatures, $\beta t = 24$ (for $|U|/t \leq 5$) and $\beta t = 16$ (for $|U|/t \geq 6$), are combined. Due to issues of ergodicity at large Hubbard interactions (see Sect. 4.3.2) it was not possible to reach lower temperatures for $|U|/t \geq 6$. The eigenvalue spectra $\{\lambda_n\}$ have a qualitatively similar dependence on U both for high and low temperature. In both cases, multiplets of degenerate states that exist in the sector with charge fluctuations for small U mix for large $|U|/t$ and give rise to a broad structureless "band" of small eigenvalues, from which a low-lying singlet state seems to separate off. However, large error bars prevent a conclusive statement.

It must be stessed again that equivalent states in the repulsive and attractive Hubbard model, i.e. states related by the spin-down particle-hole transformation Eq. (8.21), are labelled by different Mulliken term symbols. When discussing now to the low-temperature spectrum of $\rho_{A=\square}$ displayed in Fig. 11.6(b), we refer to the Mulliken symbols shown next to Fig. 11.6(b). For the positive-U Hubbard model, the singlet-triplet type structures are comprised of the four states $|s^{(1)}\rangle \in (2,2)A_{1,g}$ and

$\{|t_0^{(1)}\rangle \in (2,2)B_{2,g}, |t_+^{(1)}\rangle \in (3,3)A_{1,g}, |t_-^{(1)}\rangle \in (1,1)A_{1,g}\}$ and the four states $|s^{(2)}\rangle \in (2,2)B_{1,g}$ and $\{|t_0^{(2)}\rangle \in (2,2)A_{2,u}, |t_+^{(2)}\rangle \in (3,1)A_2, |t_-^{(2)}\rangle \in (1,3)A_2\}$. In between the two singlet-triplet structures there is again an octet of degenerate states. A remarkable difference to the high-temperature spectrum is that the degeneracy of the high-weight triplet is lifted at smaller $|U|/t$, namely at $|U|/t = 2$ for $\beta t = 24$ compared to $U/t = 4$ for $\beta t = 4$. The weight of $|t_0^{(1)}\rangle$ increases rapidly, the subsequent decrease at $|U|/t = 6$ must be attributed to the change in temperature from $\beta t = 24$ to $\beta t = 16$ when changing from the dataset with $\beta t = 24$ for $|U|/t \leq 5$ to the dataset with $\beta t = 16$ for $|U|/t \geq 6$.

Next, we turn to the doping dependence of the plaquette entanglement spectrum, which is displayed in Fig. 11.7 for the repulsive Hubbard model at $U/t = 6$ and high temperature $\beta t = 4$. As discussed in Sect. 4.6, the DQMC algorithm suffers from a sign problem in the repulsive Hubbard model when particle-hole symmetry is broken by tuning the chemical potential away from the half-filling point $\mu = \frac{U}{2}$. Nevertheless, at relatively high temperature around $\beta t = 4$ simulations are still possible due to a mild sign problem [142] that can be offset by acquiring more statistics in longer Monte Carlo runs. Fig. 11.7 shows the eigenvalue spectrum $\{\lambda_n\}_{n=1}^{4^{N_s}}$ of the plaquette ($N_s = 4$) reduced density matrix $\rho_{A=\square}$ with coloured stripes indicating blocks of fixed particle number $(N_\uparrow, N_\downarrow)$.

Symmetries of the most important eigenstates

At half filling, the leading eigenstate of the plaquette reduced density matrix has $d_{x^2-y^2}$-wave (B_{1g}) symmetry, whereas around quarter filling, $\langle n \rangle \approx 0.5$, it has s-wave (A_{1g}) symmetry (see first and fourth row of Fig. 11.7). The invariant subspace labelled by $(2,2)B_{1g}$ consists of four states and $(2,2)A_{2u}$ consists of three states (see Tab. 11.3), but it turns out that a single state from each symmetry multiplet has by far the largest coefficient, namely:

$$(2,2)B_{1,g} \ni |\psi_1\rangle \sim \frac{1}{\sqrt{2}}(|\downarrow\uparrow\uparrow\downarrow\rangle + |\uparrow\downarrow\downarrow\uparrow\rangle) + \dots \tag{11.27a}$$

$$(2,2)A_{2,u} \ni |\psi_2\rangle \sim \frac{1}{\sqrt{2}}(|\downarrow\uparrow\uparrow\downarrow\rangle - |\uparrow\downarrow\downarrow\uparrow\rangle) + \mathcal{O}(t/U). \tag{11.27b}$$

Dots in Eq. (11.27a) indicate states from the same symmetry multiplet without double occupancy but with much smaller weight. Thus, the leading eigenvectors of $\rho_{A=\square}$ in the particle number sector $(2,2)$ at half filling are the symmetric and antisymmetric combinations of the two Néel states, as to be expected. Note that for $U \gtrsim 6$ an additional p-wave doublet (E_u^x, E_u^y) appears in the particle number sector $(2,2)$ (see first row of Fig. 11.7). The leading eigenvectors in the particle number sector $(1,1)$ at quarter filling are

$$(1,1)A_{1,g} \ni |\psi_3\rangle \sim \frac{1}{2}(|\uparrow \, h \, h \, \downarrow\rangle + |h \, \uparrow\downarrow \, h\rangle + |h \, \downarrow\uparrow \, h\rangle + |\downarrow \, h \, h \, \uparrow\rangle) + \dots, \tag{11.28}$$

Fig. 11.7: Eigenvalue spectrum $\{\lambda_n\}_{n=1}^{4^{N_s}}$ of the reduced density matrix $\rho_{A=\square}$ for a plaquette ($N_s = 4$), organized into particle number sectors, which are indicated by coloured segments. $U/t = 6$, $\beta t = 4$, and total linear system size $L = 12$; rows from top to bottom correspond to decreasing filling $\langle n \rangle$. For clarity, only eigenvalues larger than 0.01 are labelled by the irreducible subspace to which the corresponding eigenvector belongs. Error bars (not shown) are of the order of $1 - 5\%$.

i.e. two holes in diagonally opposite corners, which maximizes their kinetic energy, and a set of states with smaller weight with two neighbouring holes, which have p-wave symmetry (labelled by $E_{u(g)}^{x(y)}$ in the fourth row in Fig. 11.7). The character of the leading eigenstates in the particle number sectors $(2,2)$ and $(1,1)$ as described by Eqs. (11.27a) and (11.28) hardly changes with doping. The leading eigenstate from the symmetry sector $(1,3)A_2$

$$(1,3)A_2 \ni |\psi_4\rangle \sim \frac{1}{2}\left(|\uparrow\downarrow\downarrow\downarrow\rangle + |\downarrow\uparrow\downarrow\downarrow\rangle - |\downarrow\downarrow\uparrow\downarrow\rangle - |\downarrow\downarrow\downarrow\uparrow\rangle\right) + \mathcal{O}(t/U) \quad (11.29)$$

and its spin-reversed counterpart from the symmetry sector $(3,1)A_2$ are degenerate with the leading eigenstate from $(2,2)A_{2,u}$ (Eq. (11.27b)) up to $U/t \lesssim 4$ (at $\beta t = 4$). Finally, we list the state

$$(2,2)A_{1,g} \ni |\psi_5\rangle \sim \frac{1}{2}\left(|\uparrow\uparrow\downarrow\downarrow\rangle + |\uparrow\downarrow\uparrow\downarrow\rangle + |\downarrow\uparrow\downarrow\uparrow\rangle + |\downarrow\downarrow\uparrow\uparrow\rangle\right) + \mathcal{O}(t/U), \quad (11.30)$$

with spins that are ferromagnetically aligned along one coordinate axis and antiferromagnetically in the other direction and which separates off from the "band" of low-lying states for large $|U|$ (see Fig. 11.6(a)).

11.5   Conclusion

In this chapter we have provided proof of principle calculations that it is possible in an equilibrium DQMC simulation to obtain the full reduced density matrix of a small subsystem embedded in a much larger system that can be interpreted as the exact correlated bath. The sequence of "entanglement energy" levels of the embedded plaquette was shown to differ from the sequence of levels for an isolated plaquette [320].

The possiblity of computing the full quantum state of a subsystem is a unique feature of the DQMC framework, which is based on the free fermion decomposition [119]. Due to the factorization of the Monte Carlo weight into a spin-$\uparrow$ and spin-$\downarrow$ part, the computational cost for obtaining all elements of ρ_A scales like $2 \times (2^{N_s} \times 2^{N_s})$, rather than $4^{N_s} \times 4^{N_s}$, in one Monte Carlo sample. However, the storage requirement for all elements is $4^{N_s} \times 4^{N_s}$, which is forbidding for e.g. $N_s = 9$. If individual (particle number and point group) symmetry sectors are targeted by performing the transformation Eq. (11.25) in every Monte Carlo step rather than computing all elements of ρ_A in the occupation number basis, the number of non-vanishing matrix elements of ρ_A that need to be kept for Monte Carlo averaging can be reduced to $a_n \times a_n$, where a_n is the number of copies of the n-th irreducible representation that appear in the decomposition of a given particle number sector (see Eq. (11.19)). The additional cost of the basis transformation Eq. (11.25) in every Monte Carlo step can be compensated by a finer granularity of the parallelization.

This would give access to 3×3 subsystems that can already capture the effect of next nearest neighbour hopping t', which needs to be included to describe qualitatively

the electronic band structure of cuprates. At least for temperatures, where DQMC simulations are still possible in spite of the sign problem [142], one may thus hope to gain some insight into the role of local correlations in the high-temperature phase of a prototypical model for high-T_c superconductors, whose pseudogap regime and anomalous normal state commonly referred to as "strange" metal phase is still poorly understood [5].

A model for which the presented approach is particularly useful is the plaquette Hubbard model studied in [325] and [326], which interpolates between isolated plaquettes and a uniform square lattice taking the interplaquette hopping as a tunable parameter.

Appendix A

Hubbard-Stratonovich transformation

The generic Hubbard-Stratonovich (HS) transformation [115, 116] is based on the Gaussian integral identity

$$e^{\hat{A}^2/2} = \frac{1}{\sqrt{2\pi}} \int_{-\infty}^{\infty} d\phi \, e^{-\phi^2/2 - \phi\hat{A}}. \tag{A.1}$$

If $\hat{A}$ is a single-particle operator, the above identity has transformed the two-body operator $\exp(\hat{A}^2/2)$ into the integral of a single-particle operator coupled to a bosonic field ϕ. Considering the Hubbard interaction

$$H_U = U n_\uparrow n_\downarrow, \tag{A.2}$$

there are several ways to rewrite the interaction $n_\uparrow n_\downarrow$ as the square of an operator. Each of the fermionic identities

$$n_\uparrow n_\downarrow = \frac{1}{2}\left(n_\uparrow + n_\downarrow - 1\right)^2 + \frac{1}{2}(n_\uparrow + n_\downarrow - 1) \tag{A.3a}$$

$$n_\uparrow n_\downarrow = -\frac{1}{2}\left(n_\uparrow - n_\downarrow\right)^2 + \frac{1}{2}(n_\uparrow + n_\downarrow) \tag{A.3b}$$

$$n_\uparrow n_\downarrow = \frac{1}{4}(n_\uparrow + n_\downarrow)^2 - \frac{1}{4}(n_\uparrow - n_\downarrow)^2 \tag{A.3c}$$

leads to a different HS decoupling of the interaction term. Inserting Eq. (A.3a) for the case of attractive ($U < 0$) interactions and Eq. (A.3b) for repulsive ($U > 0$ interactions into the Gaussian integral identity, we obtain

$$e^{-\Delta\tau n_\uparrow n_\downarrow} = \begin{cases} e^{-\frac{\Delta\tau}{2}U(n_\uparrow + n_\downarrow - 1)} \int_{-\infty}^{\infty} d\phi \, e^{-\frac{1}{2}\phi^2 + \sqrt{-\Delta\tau U}(n_\uparrow + n_\downarrow - 1)\phi} & \text{for } U < 0, \\ e^{-\frac{\Delta\tau}{2}U(n_\uparrow - n_\downarrow)} \int_{-\infty}^{\infty} d\phi \, e^{-\frac{1}{2}\phi^2 + \sqrt{\Delta\tau U}(n_\uparrow - n_\downarrow)\phi} & \text{for } U > 0. \end{cases} \tag{A.4}$$

The different choices for $U > 0$ and $U < 0$ ensure that the coupling constant $\sqrt{\Delta\tau|U|}$ between the fermionic operators and the field ϕ is a real number. The decoupling

Eq. (A.3c) would introduce two squared operators necessitating a double integral over two independent bosonic fields after HS transformation.

Since the fermionic number operator $\hat{n}_\sigma$ has eigenvalues 0 or 1, the integral in Eq. (A.4) can take on only two possible values [117]

$$\int_{-\infty}^{\infty} d\phi\, e^{-\frac{1}{2}\phi^2} = \sqrt{2\pi}, \tag{A.5}$$

$$\int_{-\infty}^{\infty} d\phi\, e^{-\frac{1}{2}\phi^2 \pm \sqrt{\Delta\tau|U|}\phi} = \sqrt{2\pi} e^{\frac{1}{2}\Delta\tau|U|}. \tag{A.6}$$

Then one can replace the integral over a continuous bosonic field ϕ by a sum over the two possible values of a discrete (Ising) variable $s = \pm 1$, e.g. for the case $U > 0$:

$$\int_{-\infty}^{\infty} e^{-\frac{1}{2}\phi^2 + \sqrt{\Delta\tau U}(n_\uparrow - n_\downarrow)\phi} = \frac{1}{2}\sqrt{2\pi} \sum_{s=\pm 1} e^{\alpha s(n_\uparrow - n_\downarrow)}. \tag{A.7}$$

Because of

$$\sum_{s=\pm 1} e^{\alpha s(n_\uparrow - n_\downarrow)} = \begin{cases} 2 & n_\sigma = n_{-\sigma} \\ 2\cosh\alpha & n_\sigma \neq n_{-\sigma} \end{cases} \tag{A.8}$$

one obtains the two possible values of the integral if one chooses

$$\cosh\alpha = e^{\frac{1}{2}\Delta\tau U}. \tag{A.9}$$

With this we arrive at the discrete Hubbard-Stratonovich transformation due to Hirsch [117]:

$$e^{-\Delta\tau U n_\uparrow n_\downarrow} = \frac{1}{2} \begin{cases} e^{-\frac{\Delta\tau}{2} U(n_\uparrow + n_\downarrow)} \sum_{s=\pm 1} e^{\alpha s(n_\uparrow - n_\downarrow)} & \text{for } U > 0 \qquad \text{(A.10a)} \\ e^{-\frac{\Delta\tau}{2} U(n_\uparrow + n_\downarrow - 1)} \sum_{s=\pm 1} e^{\alpha s(n_\uparrow + n_\downarrow - 1)} & \text{for } U < 0, \qquad \text{(A.10b)} \end{cases}$$

where in both cases

$$\cosh\alpha = e^{\frac{1}{2}\Delta\tau|U|}. \tag{A.11}$$

For $U > 0$ the auxiliary field couples to the local magnetization $m_z = n_\uparrow - n_\downarrow$, for $U < 0$ it couples to the local charge $n = n_\uparrow + n_\downarrow$. In the former case, the resulting single-particle Hamiltonian breaks the $SU(2)$ spin-rotational symmetry of the original fermionic system, which is only restored after Monte Carlo sampling over many auxiliary field configurations. The HS transformation in which the auxiliary field couples to the charge has the advantage that it preserves the $SU(2)$-spin symmetry of the original fermionic model for every single HS configuration since both spin species appear

symmetrically (with the same sign). One could use this transformation also for $U > 0$, however then it comes at the expense of a complex parameter α which requires complex data types in a computer implementation [53].

There is a multitude of ways of performing the HS transformation. Being a mathematical identity, we could also imagine applying different forms of HS transformations to individual sets of sites.

Appendix B

The Trotter-Suzuki mapping for quantum Ising models

In the following it will be shown for the particular case of a transverse-field Ising model how the partition function of a D-dimensional quantum system can be mapped onto that of an effective (D+1)-dimensional classical system. This mapping is the basis for path integral QMC simulations of the transverse field Ising model. Our exposition follows Ref. [154].

The quantum Hamiltonian describing the transverse field Ising model consists of two non-commuting parts:

$$\hat{H} = \hat{H}_0 + \hat{V} = -\Gamma \sum_{i=1}^{N} \hat{S}_i^x - \sum_{ij=1}^{N} J_{ij} \hat{S}_i^z \hat{S}_j^z, \tag{B.1}$$

where $\hat{S}_i^\alpha$ denote the usual Pauli operators. With the help of the generalized Trotter formula [327]

$$\exp[\hat{O}_1 + \hat{O}_2] = \lim_{M \to \infty} \left(\exp(\hat{O}_1/M) \exp(\hat{O}_2/M) \right)^M \tag{B.2}$$

a sum of non-commuting operators $\hat{O}_1, \hat{O}_2$ can be split into products. Applying this to the exponential in the partition sum of the quantum Hamiltonian

$$Z = \mathrm{Tr} e^{-\beta(\hat{H}_0 + \hat{V})} \tag{B.3}$$

gives

$$\exp[-\beta(\hat{H}_0 + \hat{V})] = \lim_{M \to \infty} \left(\exp\left[\frac{-\beta \hat{H}_0}{M}\right] \exp\left[\frac{-\beta \hat{V}}{M}\right] \right)^M. \tag{B.4}$$

Next, we insert between the operators resolutions of identities

$$\mathbb{1}_k = \sum_{S_{1,k},\ldots,S_{N,k}} |S_{1,k},\ldots,S_{N,k}\rangle\langle S_{1,k},\ldots,S_{N,k}| \tag{B.5}$$

where $|S_{i,k}\rangle$ are eigenstates of the $\hat{S}_i^z$ operator. This leads to

$$Z = \lim_{M\to\infty} {\sum_{\left\{\{S_{i,k}\}_{i=1}^N\right\}_{k=1}^M}}' \prod_{k=1}^M \langle S_{1,k} S_{2,k}, \ldots, S_{N,k}|$$
$$\times \left[\exp\left(\frac{-\beta\hat{H}_0}{M}\right)\exp\left(\frac{-\beta\hat{V}}{M}\right)\right] |S_{1,k+1} S_{2,k+1}, \ldots, S_{N,k+1}\rangle. \tag{B.6}$$

The sum $\sum'$ is over all inserted eigenstates with the constraint that $S_{i,1} = S_{i,M+1}$ for all $i = 1, \ldots, N$, which is a consequence of the trace operation. With the inserted eigenstates it becomes apparent that one has introduced an additional dimension to the system, which is called the "Trotter dimension" and is labelled by the index k. To make the calculation explicit another M sets of identities are inserted between the transverse field terms and the Ising terms which leads to

$$\prod_{k=1}^M \prod_{k'=1}^M \langle S_{1,k}, S_{2,k}, \ldots, S_{N,k}| \exp\left(\frac{\beta\Gamma}{M}\sum_{i=1}^N \hat{S}_i^x\right) |S_{1,k'} S_{2,k'}, \ldots, S_{N,k'}\rangle$$

$$\langle S_{1,k'}, S_{2,k'}, \ldots, S_{N,k'}| \exp\left(\frac{\beta}{M}\sum_{ij} J_{ij}\hat{S}_i^z\hat{S}_j^z\right) |S_{1,k+1} S_{2,k+1}, \ldots, S_{N,k+1}\rangle \tag{B.7}$$

$$= C^{NM/2} \exp\left(\frac{1}{2}\ln\coth\left(\frac{\beta\Gamma}{M}\right)\sum_{i=1}^N\sum_{k=1}^M S_{i,k}S_{i,k+1}\right) \exp\left(\sum_{i,j=1}^N\sum_{k=1}^M \frac{\beta J_{ij}}{M}S_{i,k}S_{j,k}\right)$$

with $C = \frac{1}{2}\sinh\left(\frac{2\beta\Gamma}{M}\right)$. In deriving this result we have used that the Ising interactions are diagonal in the $\hat{S}_i^z$ eigenbasis so that the operators can be replaced by their eigenvalues. Then, the additionally introduced primed states disappear again due to the orthogonality of different eigenstates. For rewriting the matrix elements of the off-diagonal transverse field part $\sum_i \hat{S}_i^x$ in terms of the S^z eigenvalues for $|S_{i,k}\rangle$ and $|S_{i,k+1}\rangle$ the following identity was used

$$\langle S_{i,k}|e^{a\hat{S}^x}|S_{i,k+1}\rangle = \left[\frac{1}{2}\sinh(2a)\right]^{1/2}\exp\left(\frac{S_{i,k}S_{i,k+1}}{2}\ln\coth(a)\right). \tag{B.8}$$

This relation can be verified by inserting the eigenvalues of the $\hat{S}^z$ operator explicitly and comparing with the identity

$$e^{a\hat{S}^x} = \cosh(a)\mathbb{1} + \sinh(a)\hat{S}^x, \tag{B.9}$$

which follows from $(\hat{S}^x)^2 = \mathbb{1}$. Since the eigenvalues $S_{i,k}$ appearing in (B.7) are classical Ising variables that can take on the values ± 1, the Trotter-Suzuki mapping has enabled us to recast the partition sum of the D-dimensional quantum Ising model into a partition sum of an effective classical Ising model in D+1 dimensions. This partition function in the M-th order Trotter approximant reads

$$Z_M = C^{NM/2} \operatorname{Tr}_{\{S_{i,k}\}} \exp\left(-\beta H_{\text{class.}}(\{S_{i,k}\})\right) \tag{B.10}$$

where the classical effective Hamiltonian

$$H_{\text{class.}}(\{S_{i,k}\}) = \sum_{i,j=1}^{N} \sum_{k=1}^{M} \left[-K_{ij} S_{i,k} S_{j,k} - \delta_{ij} K_M S_{i,k} S_{i,k+1} \right] \tag{B.11}$$

is that of an anisotropic (D+1)-dimensional Ising model with rescaled spatial couplings $K_{ij} = \frac{J_{ij}}{M}$ and *ferromagnetic* couplings $K_M = \frac{1}{2\beta} \ln \coth \left(\frac{\beta \Gamma}{M} \right)$ in the additional Trotter dimension. The strict equivalence between the quantum and the classical model holds only in the limit $M \to \infty$.

This derivation makes explicit the relation between arbitrary transverse field Ising models and their counterparts of *ferromagnetically stacked* classical Ising models.

Appendix C

Full counting statistics for a BCS mean-field state

The Hamiltonian of the single-band Fermi-Hubbard model in momentum space reads

$$\mathcal{H}_{U<0} = \sum_{\mathbf{k},\sigma}(\varepsilon_{\mathbf{k}} - \mu)\hat{c}^\dagger_{\mathbf{k},\sigma}\hat{c}_{\mathbf{k},\sigma} - \frac{|U|}{N_{\text{sites}}}\sum_{\mathbf{k},\mathbf{k}',\mathbf{q}} \hat{c}^\dagger_{\mathbf{k}+\mathbf{q}/2,\uparrow}\hat{c}^\dagger_{-\mathbf{k}+\mathbf{q}/2,\downarrow}\hat{c}_{\mathbf{k}'+\mathbf{q}/2,\uparrow}\hat{c}_{-\mathbf{k}'+\mathbf{q}/2,\downarrow}, \quad \text{(C.1)}$$

with the single-particle band structure $\varepsilon_{\mathbf{k}} = -2t(\cos(k_x a) + \cos(k_y a))$ for the square lattice. The standard BCS mean-field analysis starts with the BCS *reduced* Hamiltonian which neglects the sum over $\mathbf{q}$ in (C.1) and considers only scattering between pairs of zero center-of-mass momentum ($\mathbf{q} = 0$). Under the assumption of a non-zero s-wave pairing order parameter $\Delta = \sum_{\mathbf{k}'}\langle\hat{c}_{\mathbf{k},\uparrow}\hat{c}_{-\mathbf{k},\downarrow}\rangle$ a mean-field decoupling is performed. The resulting quadratic Hamiltonian is then solved with a Bogoliubov transformation [285] with coefficients

$$v_{\mathbf{k}}^2 = 1 - u_{\mathbf{k}}^2 = \frac{1}{2}\left(1 - \frac{\varepsilon_{\mathbf{k}}^{(\text{HF})} - \mu(n,U)}{E_{\mathbf{k}}}\right), \quad \text{(C.2)}$$

which are parametrized by the chemical potential μ and Δ, the gap parameter. $E_{\mathbf{k}}^2 = (\varepsilon_{\mathbf{k}}^{(\text{HF})} - \mu(n,U))^2 + \Delta^2(n,U)$ are the excitation energies of the fermionic Bogoliubov quasiparticles. In order to take into account density-density interactions at the mean-field level, it is necessary to include the Hartree-Fock potential in the single-particle energies: $\varepsilon_{\mathbf{k}}^{(\text{HF})} = \varepsilon_{\mathbf{k}} - |U|\frac{n}{2}$ where $n = (N_\uparrow + N_\downarrow)/N_{\text{sites}}$ is the filling. The mean-field ground state takes the standard form in terms of the BCS coefficients (C.2)

$$|\text{BCS}\rangle = \prod_{\mathbf{k}}\left(u_{\mathbf{k}}(\mu,\Delta) + v_{\mathbf{k}}(\mu,\Delta)\hat{c}^\dagger_{\mathbf{k},\uparrow}\hat{c}^\dagger_{-\mathbf{k},\downarrow}\right)|\text{vac}\rangle, \quad \text{(C.3)}$$

where $\mu(n,U)$ and $\Delta(n,U)$ are self-consistent solutions [273] of the gap equation

$$\frac{1}{|U|} = \frac{1}{N_{\text{sites}}}\sum_{\mathbf{k}\in\text{1st BZ}}\frac{1}{2\sqrt{(\varepsilon_{\vec{k}} - \mu - |U|\frac{n}{2})^2 + \Delta^2}}, \quad \text{(C.4)}$$

and the number equation

$$n = 1 - \frac{1}{N_{\text{sites}}} \sum_{\mathbf{k} \in \text{1st BZ}} \frac{\varepsilon_{\vec{k}} - \mu - |U|\frac{n}{2}}{\sqrt{(\varepsilon_{\vec{k}} - \mu - |U|\frac{n}{2})^2 + \Delta^2}}. \tag{C.5}$$

For general filling n and Hubbard interaction U these self-consistent equations need to be solved numerically to obtain μ and Δ. At half filling ($n = 1$) the number equation has the solution $\mu = -|U|/2$ for any choice of Δ provided that the single-particle dispersion relation $\varepsilon_{\mathbf{k}}$ is particle-hole symmetric around $\varepsilon_{|\mathbf{k}|=k_F} = 0$ such that the integral in (C.5) vanishes. Thus, the inclusion of the Hartree shift in the single-particle energies has preserved, at the mean-field level, the particle-hole symmetry which the Hubbard model posseses for half filling. In the atomic limit $t/U = 0$ the solutions are $\mu = -|U|/2$ and $\Delta = |U|\sqrt{n(2-n)}/2$.

The BCS state is the ground state of a quadratic (mean-field) Hamiltonian and therefore Wick's theorem can be used to factorize any correlation function into sums of products of single-particle Green's functions. Following closely the method of Ref. [261], the generating function for the total particle number is written as

$$\chi^{(N)}(\phi) = \langle e^{i\phi \hat{N}_A} \rangle = \langle \prod_{i \in A} \prod_{\sigma=\uparrow,\downarrow} e^{i\phi(1-\hat{n}_{i,\sigma})} \rangle = \langle \prod_{i \in A} \prod_{\sigma=\uparrow,\downarrow} E_{i\sigma} F_{i\sigma}(\phi) \rangle, \tag{C.6}$$

where $E_{i\sigma} = \hat{c}_{i\sigma} + \hat{c}_{i\sigma}^\dagger$ and $F_{i\sigma} = \hat{c}_{i\sigma} + e^{i\phi}\hat{c}_{i\sigma}^\dagger$. In the second equation of (C.6) the particle-hole symmetry of the Hubbard Hamiltonian was used to replace the total particle number by the total hole number, which simplifies the analysis [261] as the identity $e^{i\lambda(1-\hat{c}_i^\dagger \hat{c}_i)} = E_i F_i(\phi)$ can then be used. The multipoint correlation function (C.6) is contracted according to Wick's theorem, and, taking into account the fermionic anticommutation relations, the non-zero full contractions [261] constitute a determinant:

$$\chi^{(N)}(\phi) = \det_{\substack{i,j=1,N_s \\ \sigma,\sigma'=\uparrow,\downarrow}} (\langle E_{i\sigma} F_{j\sigma'}(\phi) \rangle) \tag{C.7}$$

$$= \prod_{k=1}^{2N_s} (\mu_k + (1 - \mu_k)e^{i\phi}). \tag{C.8}$$

In the last step we have introduced the eigenvalues μ_k of the matrix of normal and anomalous Green's functions:

$$M = \begin{pmatrix} \langle \hat{c}_{i\uparrow}^\dagger \hat{c}_{j\uparrow} \rangle_{i,j \in A} & \langle \hat{c}_{i\uparrow} \hat{c}_{j\downarrow} \rangle_{i,j \in A} \\ \langle \hat{c}_{i\downarrow} \hat{c}_{j\uparrow} \rangle_{i,j \in A} & \langle \hat{c}_{i\downarrow}^\dagger \hat{c}_{j\downarrow} \rangle_{i,j \in A} \end{pmatrix}. \tag{C.9}$$

The Green's functions, which are restricted to subsystem A, are computed for the BCS state (C.3). As described in detail in [261], complex conjugate pairs of eigenvalues of M can interfere in Eq. (C.8) leading to a suppression of odd versus even values in the particle number distribution $P(N_A)$. Complex eigenvalues can appear as soon as non-zero values of the anomalous Green's functions $\langle \hat{c}_{i\uparrow} \hat{c}_{j\downarrow} \rangle_{i,j \in A} = -\langle \hat{c}_{j\downarrow} \hat{c}_{i\uparrow} \rangle_{i,j \in A} \neq 0$ destroy the hermiticity of M, which makes evident that BCS pairing is at the origin of the even-odd effect in the distibution $P(N_A)$.

Appendix D

Wick's theorem and determinant formula

In this appendix we prove a determinant formula for high-order correlation functions in non-interacting fermion systems. It expresses Wick's theorem in the compact form

$$\left\langle \left(c_{i_1} c_{j_1}^\dagger\right) \left(c_{i_2} c_{j_2}^\dagger\right) \cdots \left(c_{i_n} c_{j_n}^\dagger\right) \right\rangle_0 = \det\left(G_{i_\alpha, j_\beta}^{(0)}\right), \tag{D.1}$$

where

$$G_{ij}^{(0)}(\tau) = \langle c_{i_\alpha}(\tau) c_{j_\beta}^\dagger(0) \rangle_0 \tag{D.2}$$

is the single-particle Green's function of the free fermion system, and $\alpha, \beta = 1, \ldots, n$.

The proof goes by induction. The case $n = 1$ is true by virtue of the definition (D.2). The induction step from n to $n + 1$ uses the generalized *Wick's theorem* [118, § 24], which states that in a thermal or ground state of a free fermion system the expectation value of the product of $m + 1$ operators $A, B_1, \ldots, B_m$ which each are linear in fermionic creation and annihilation operators can be decomposed into the sum of m expectation values of the same products with all possible contractions [118, § 24] of one of the operators, for example A, with all the others:

$$\langle T_\tau \left(B_1 \cdots B_m A\right)\rangle_0 = \sum_{1 \leq i \leq m} \left\langle T_\tau \left(B_1 \cdots \overset{\frown}{B_i \cdots B_m A}\right)\right\rangle_0. \tag{D.3}$$

T_τ denotes the time-ordering operator, which can be omitted for equal time correlators.

Writing all non-vanishing contractions for a product of $n + 1$ pairs of fermionic

operators as in Eq. (D.1) results in

$$
\begin{aligned}
\left\langle \left(c_{i_1}c_{j_1}^\dagger\right)\cdots\left(c_{i_{n+1}}c_{j_{n+1}}^\dagger\right)\right\rangle_0 =& -G^{(0)}_{i_1,j_{n+1}}\left\langle\left(c_{i_{n+1}}c_{j_1}^\dagger\right)\left(c_{i_2}c_{j_2}^\dagger\right)\cdots\left(c_{i_n}c_{j_n}^\dagger\right)\right\rangle_0 \\
& -\sum_{k=2}^{n-1} G^{(0)}_{i_k,j_{n+1}}\left\langle\left(c_{i_1}c_{j_1}^\dagger\right)\left(c_{i_2}c_{j_2}^\dagger\right)\cdots\left(c_{i_{n+1}}c_{j_k}^\dagger\right)\left(c_{i_{k+1}}c_{j_{k+1}}^\dagger\right)\cdots\left(c_{i_n}c_{j_n}^\dagger\right)\right\rangle_0 \\
& -G^{(0)}_{i_n,j_{n+1}}\left\langle\left(c_{i_1}c_{j_1}^\dagger\right)\cdots\left(c_{i_{n-1}}c_{j_{n-1}}^\dagger\right)\left(c_{i_{n+1}}c_{j_{n+1}}^\dagger\right)\right\rangle_0 \\
& +G^{(0)}_{i_{n+1},j_{n+1}}\left\langle\left(c_{i_1}c_{j_1}^\dagger\right)\cdots\left(c_{i_n}c_{j_n}^\dagger\right)\right\rangle_0 .
\end{aligned}
\tag{D.4}
$$

The minus-sign, e.g. in the second line of Eq. (D.4), comes from the permutation of $c_{i_{n+1}}$ with $c_{j_k}^\dagger$. Using the induction hypothesis Eq. (D.1), valid for n pairs of fermionic operators, the remaining correlators in Eq. (D.4) can be expressed as determinants

$$
\begin{aligned}
\left\langle\left(c_{i_1}c_{j_1}^\dagger\right)\cdots\left(c_{i_{n+1}}c_{j_{n+1}}^\dagger\right)\right\rangle_0 =& -G^{(0)}_{i_1,j_{n+1}}\cdot\det\begin{pmatrix} G^{(0)}_{i_{n+1},j_1} & G^{(0)}_{i_{n+1},j_2} & \cdots & G^{(0)}_{i_{n+1},j_n} \\ G^{(0)}_{i_2,j_1} & G^{(0)}_{i_2,j_2} & \cdots & G^{(0)}_{i_2,j_n} \\ \vdots & \vdots & \ddots & \vdots \\ G^{(0)}_{i_n,j_1} & G^{(0)}_{i_n,j_2} & \cdots & G^{(0)}_{i_n,j_n} \end{pmatrix} \\
& -G^{(0)}_{i_2,j_{n+1}}\cdot\det\begin{pmatrix} G^{(0)}_{i_1,j_1} & G^{(0)}_{i_1,j_2} & \cdots & G^{(0)}_{i_1,j_n} \\ G^{(0)}_{i_{n+1},j_1} & G^{(0)}_{i_{n+1},j_2} & \cdots & G^{(0)}_{i_{n+1},j_n} \\ \vdots & \vdots & \ddots & \vdots \\ G^{(0)}_{i_n,j_1} & G^{(0)}_{i_n,j_2} & \cdots & G^{(0)}_{i_n,j_n} \end{pmatrix} - \cdots \\
& -G^{(0)}_{i_n,j_{n+1}}\cdot\det\begin{pmatrix} G^{(0)}_{i_1,j_1} & G^{(0)}_{i_1,j_2} & \cdots & G^{(0)}_{i_1,j_n} \\ \vdots & \vdots & \ddots & \vdots \\ G^{(0)}_{i_{n-1},j_1} & G^{(0)}_{i_{n-1},j_2} & \cdots & G^{(0)}_{i_{n-1},j_n} \\ G^{(0)}_{i_{n+1},j_1} & G^{(0)}_{i_{n+1},j_2} & \cdots & G^{(0)}_{i_{n+1},j_n} \end{pmatrix} \\
& +G^{(0)}_{i_{n+1},j_{n+1}}\cdot\det\begin{pmatrix} G^{(0)}_{i_1,j_1} & G^{(0)}_{i_1,j_2} & \cdots & G^{(0)}_{i_1,j_n} \\ G^{(0)}_{i_2,j_1} & G^{(0)}_{i_2,j_2} & \cdots & G^{(0)}_{i_2,j_n} \\ \vdots & \vdots & \ddots & \vdots \\ G^{(0)}_{i_n,j_1} & G^{(0)}_{i_n,j_2} & \cdots & G^{(0)}_{i_n,j_n} \end{pmatrix} .
\end{aligned}
\tag{D.5}
$$

By rearranging rows in (D.5), it can be concluded that (D.5) is the expansion of the $(n+1)\times(n+1)$ determinant

$$
\det\begin{pmatrix} G^{(0)}_{i_1,j_1} & G^{(0)}_{i_1,j_2} & \cdots & G^{(0)}_{i_1,j_{n+1}} \\ G^{(0)}_{i_2,j_1} & G^{(0)}_{i_2,j_2} & \cdots & G^{(0)}_{i_2,j_{n+1}} \\ \vdots & \vdots & \ddots & \vdots \\ G^{(0)}_{i_{n+1},j_1} & G^{(0)}_{i_{n+1},j_2} & \cdots & G^{(0)}_{i_{n+1},j_{n+1}} \end{pmatrix}
\tag{D.6}
$$

along the last column according to Laplace's formula. This completes the inductive proof. Except for the last determinant in Eq. (D.5), row exchanges are necessary to obtain the correct submatrix structure. In the determinant accompanying the single-particle Green's function $G^{(0)}_{i_k,j_{n+1}}$ in Eq. (D.5) we need to perform $(n-k)$ row permutations which results in a factor $(-1)^{n-k}$ such that the total sign is $(-1)^{n-k+1}$, which is identical to the alternating factor $(-1)^{n+1+k}$ coming from Laplace's formula.

state label [x] multiplicity

[0] 1	[26] 16	[105] 2
[1] 8	[27] 16	[107] 8
[3] 8	[30] 8	[111] 4
[6] 4	[31] 8	[119] 4
[7] 8	[51] 4	[123] 8
[15] 2	[53] 8	[126] 4
[17] 4	[54] 16	[127] 8
[18] 8	[55] 16	[255] 1
[19] 16	[60] 4	
[22] 8	[61] 16	
[23] 8	[63] 8	
[24] 4	[102] 2	
[25] 8	[103] 8	

numbering of plaquette sites

$$n^\uparrow_4 n^\uparrow_3 n^\uparrow_2 n^\uparrow_1 n^\downarrow_4 n^\downarrow_3 n^\downarrow_2 n^\downarrow_1$$
occupation numbers

$$[\mathsf{x}] = [\, b_8 b_7 b_6 b_5 \; b_4 b_3 b_2 b_1 \,]$$
binary string

Fig. E.1: Representative configurations for the classes of symmetry-related plaquette configurations.

Appendix E

List of symmetry-related classes of states for a single plaquette

As illustrated in Fig. E.1, each of the 256 plaquette states can be labelled by an integer x between 0 and 255 with the convention that its binary representation $[x]$ corresponds to the occupation numbers on the plaquette; the four least significant bits denote occupation numbers for spin-$\downarrow$.

The leftmost column of Fig. E.1 shows microscpic configurations of spin-$\uparrow$ and spin-$\downarrow$ particles on the plaquette. States that are related by a symmetry operation of the point group D_4 of the square or by spin-inversion are grouped into classes of symmetry-related states. The 34 classes are listed with a representative spin configuration for each class, its bitcoded label and the number of symmetry-related states in the class ("multiplicity"). We choose as a representative from each class the state with the smallest bitcoded label.

Special sets of states are the two Néel states (labelled by [105]), the 16 states in the spin-only subspace (with representatives [15],[30],[60] and [105]), the states with neighbouring doublon-hole pairs in a spin-only background ([27], [54]) and the states with diagonally-opposite doublon-hole pairs in a spin-only background ([23],[53]).

Bibliography

[1] E. Lifshitz and L. Pitajewski. *Statistical Physics: Part 2.* 3rd. Pergamon, London, 1977 (cit. on p. 1).

[2] P. Fazekas. *Lecture notes on electron correlation and magnetism.* eng. Series in modern condensed matter physics. Singapore: World Scientific, 1999, 1 Online, 777 Seiten) (cit. on pp. 1, 168, 171, 177, 179, 181, 218).

[3] A. Avella and F. Mancini. *Strongly correlated systems: numerical methods.* **176**. Springer Science & Business Media, 2013 (cit. on p. 1).

[4] J. Eisert, M. Cramer, and M. B. Plenio. "Colloquium: Area laws for the entanglement entropy". Rev. Mod. Phys. **82** (1 2010), 277 (cit. on p. 1).

[5] B. Keimer, S. A. Kivelson, M. R. Norman, S. Uchida, and c. Zaanen J. "From quantum matter to high-temperature superconductivity in copper oxides". Nature **518** (2015), 179 (cit. on pp. 2–4, 175, 212, 258).

[6] P. Anderson. "Resonating valence bonds: A new kind of insulator?" Materials Research Bulletin **8** (1973), 153 (cit. on p. 2).

[7] L. Savary and L. Balents. "Quantum spin liquids: a review". Reports on Progress in Physics **80** (2017), 016502 (cit. on p. 2).

[8] R. Feynman. Int. J. Theor. Phys. **21** (1982), 467 (cit. on p. 2).

[9] S. LLoyd. Science **273** (1996), 1073 (cit. on p. 2).

[10] I. Bloch, J. Dalibard, and W. Zwerger. "Many-body physics with ultracold gases". Rev. Mod. Phys. **80** (3 2008), 885 (cit. on pp. 2, 3, 169, 170, 216, 217, 229).

[11] R. Blatt and C. F. Roos. "Quantum simulations with trapped ions". Nature Physics **8** (2012), 277 (cit. on pp. 2, 4, 136).

[12] K. Winkler, G. Thalhammer, F. Lang, R. Grimm, J. Hecker Denschlag, A. J. Daley, A. Kantian, H. P. Büchler, and P. Zoller. "Repulsively bound atom pairs in an optical lattice". **441** (2006), 853. eprint: cond-mat/0605196 (cit. on pp. 2, 182, 184, 185).

[13] W. S. Bakr, J. I. Gillen, A. Peng, S. Fölling, and M. Greiner. "A quantum gas microscope for detecting single atoms in a Hubbard-regime optical lattice". Nature **462** (2009), 74. arXiv: 0908.0174 [cond-mat.quant-gas] (cit. on pp. 2, 190, 206).

[14] J. F. Sherson, C. Weitenberg, M. Endres, M. Cheneau, I. Bloch, and S. Kuhr. "Single-atom-resolved fluorescence imaging of an atomic Mott insulator". **467** (2010), 68. arXiv: 1006.3799 [cond-mat.quant-gas] (cit. on pp. 2, 190).

[15] E. Haller, J. Hudson, A. Kelly, D. A. Cotta, B. Peaudecerf, G. D. Bruce, and S. Kuhr. "Single-atom imaging of fermions in a quantum-gas microscope". Nature Physics **11** (2015), 738. arXiv: 1503.02005 [cond-mat.quant-gas] (cit. on pp. 2, 190).

[16] M. F. Parsons, A. Mazurenko, C. S. Chiu, G. Ji, D. Greif, and M. Greiner. "Site-resolved measurement of the spin-correlation function in the Fermi-Hubbard model". Science **353** (2016), 1253 (cit. on pp. 2, 190, 204, 206, 235).

[17] L. W. Cheuk, M. A. Nichols, K. R. Lawrence, M. Okan, H. Zhang, E. Khatami, N. Trivedi, T. Paiva, M. Rigol, and M. W. Zwierlein. "Observation of spatial charge and spin correlations in the 2D Fermi-Hubbard model". Science **353** (2016), 1260 (cit. on pp. 2, 3, 190, 208, 212).

[18] J. H. Drewes, E. Cocchi, L. A. Miller, C. F. Chan, D. Pertot, F. Brennecke, and M. Köhl. "Thermodynamics versus Local Density Fluctuations in the Metal–Mott-Insulator Crossover". Phys. Rev. Lett. **117** (13 2016), 135301 (cit. on pp. 2, 190).

[19] T. A. Hilker, G. Salomon, F. Grusdt, A. Omran, M. Boll, E. Demler, I. Bloch, and C. Gross. "Revealing Hidden Antiferromagnetic Correlations in Doped Hubbard Chains via String Correlators". ArXiv e-prints (2017). arXiv: 1702.00642 (cit. on pp. 2, 190).

[20] A. Mazurenko, C. S. Chiu, G. Ji, M. F. Parsons, M. Kanász-Nagy, R. Schmidt, F. Grusdt, E. Demler, D. Greif, and M. Greiner. "Experimental realization of a long-range antiferromagnet in the Hubbard model with ultracold atoms". Nature **545** (2017), 462 (cit. on pp. 2, 3, 6, 169, 183, 190, 204–212, 214, 221).

[21] P. T. Brown, D. Mitra, E. Guardado-Sanchez, P. Schauß, S. S. Kondov, E. Khatami, T. Paiva, N. Trivedi, D. A. Huse, and W. S. Bakr. "Spin-imbalance in a 2D Fermi-Hubbard system". Science **357** (2017), 1385. eprint: http://science.sciencemag.org/content/357/6358/1385.full.pdf (cit. on pp. 2, 3, 174).

[22] D. Mitra, P. T. Brown, E. Guardado-Sanchez, S. S. Kondov, T. Devakul, D. A. Huse, P. Schauss, and W. S. Bakr. "Quantum gas microscopy of an attractive Fermi-Hubbard system". ArXiv e-prints (2017). arXiv: 1705.02039 (cit. on pp. 2, 3, 169, 174, 190, 212, 234).

[23]   F. Šimkovic, Y. Deng, N. V. Prokof'ev, B. V. Svistunov, I. S. Tupitsyn, and E. Kozik. "Magnetic correlations in the two-dimensional repulsive Fermi-Hubbard model". **96**, 081117 (2017), 081117. arXiv: `1706.07556 [cond-mat.str-el]` (cit. on p. 3).

[24]   R. T. Scalettar, E. Y. Loh, J. E. Gubernatis, A. Moreo, S. R. White, D. J. Scalapino, R. L. Sugar, and E. Dagotto. "Phase diagram of the two-dimensional negative-U Hubbard model". Phys. Rev. Lett. **62** (12 1989), 1407 (cit. on pp. 3, 168, 176–179, 218, 234).

[25]   T. Paiva, R. R. dos Santos, R. T. Scalettar, and P. J. H. Denteneer. "Critical temperature for the two-dimensional attractive Hubbard model". Phys. Rev. B **69** (18 2004), 184501 (cit. on pp. 3, 176, 178, 198, 232, 234).

[26]   T. Paiva, R. Scalettar, M. Randeria, and N. Trivedi. "Fermions in 2D Optical Lattices: Temperature and Entropy Scales for Observing Antiferromagnetism and Superfluidity". Phys. Rev. Lett. **104** (6 2010), 066406 (cit. on pp. 3, 176, 198).

[27]   S. Humeniuk and H. P. Büchler. "Full Counting Statistics for Interacting Fermions with Determinantal Quantum Monte Carlo Simulations". Physical Review Letters **119**, 236401 (2017), 236401. arXiv: `1706.08951 [cond-mat.str-el]` (cit. on pp. 3, 6).

[28]   C. Lacroix, P. Mendels, and F. Mila, eds. *Introduction to Frustrated Magnetism.* Springer, 2010 (cit. on pp. 3, 4).

[29]   H. Diep, ed. *Frustrated Spin Systems.* World Scientific Publishing, 2004 (cit. on pp. 3, 4).

[30]   S. V. Isakov and R. Moessner. "Interplay of quantum and thermal fluctuations in a frustrated magnet". Phys. Rev. B **68** (10 2003), 104409 (cit. on pp. 4, 104, 108, 109, 123, 125, 129, 133).

[31]   R. Moessner, S. L. Sondhi, and P. Chandra. "Two-Dimensional Periodic Frustrated Ising Models in a Transverse Field". Phys. Rev. Lett. **84** (19 2000), 4457 (cit. on pp. 4, 105).

[32]   R. Moessner and S. L. Sondhi. "Ising models of quantum frustration". Phys. Rev. B **63** (22 2001), 224401 (cit. on pp. 4, 105, 124).

[33]   S. Wenzel, T. Coletta, S. E. Korshunov, and F. Mila. "Evidence for Columnar Order in the Fully Frustrated Transverse Field Ising Model on the Square Lattice". Phys. Rev. Lett. **109** (18 2012), 187202 (cit. on p. 4).

[34]   M. Powalski, K. Coester, R. Moessner, and K. P. Schmidt. "Disorder by disorder and flat bands in the kagome transverse field Ising model". Phys. Rev. B **87** (5 2013), 054404 (cit. on p. 4).

[35] L.-P. Henry and T. Roscilde. "Order-by-Disorder and Quantum Coulomb Phase in Quantum Square Ice". Phys. Rev. Lett. **113** (2 2014), 027204 (cit. on p. 4).

[36] F. Mintert and C. Wunderlich. "Ion-Trap Quantum Logic Using Long-Wavelength Radiation". Phys. Rev. Lett. **87** (25 2001), 257904 (cit. on pp. 4, 153).

[37] D. Porras and J. I. Cirac. "Effective Quantum Spin Systems with Trapped Ions". Phys. Rev. Lett. **92** (20 2004), 207901 (cit. on pp. 4, 101, 153).

[38] H. Labuhn, D. Barredo, S. Ravets, S. de Léséleuc, T. Macrì, T. Lahaye, and A. Browaeys. "Tunable two-dimensional arrays of single Rydberg atoms for realizing quantum Ising models". Nature **534** (2016), 667. arXiv: `1509.04543 [cond-mat.quant-gas]` (cit. on p. 4).

[39] V. Lienhard, S. de Léséleuc, D. Barredo, T. Lahaye, A. Browaeys, M. Schuler, L.-P. Henry, and A. M. Läuchli. "Observing the space- and time-dependent growth of correlations in dynamically tuned synthetic Ising antiferromagnets". ArXiv e-prints (2017). arXiv: `1711.01185 [quant-ph]` (cit. on p. 4).

[40] K. Kim, M.-S. Chang, R. Islam, S. Korenblit, L.-M. Duan, and C. Monroe. "Entanglement and Tunable Spin-Spin Couplings between Trapped Ions Using Multiple Transverse Modes". Phys. Rev. Lett. **103** (12 2009), 120502 (cit. on pp. 4, 136).

[41] J. W. Britton, B. C. Sawyer, A. C. Keith, C.-C. J. Wang, J. K. Freericks, H. Uys, M. J. Biercuk, and J. J. Bollinger. "Engineered two-dimensional Ising interactions in a trapped-ion quantum simulator with hundreds of spins". Nature, Volume 484, Issue 7395, pp. 489-492 (2012) **484** (2012), 489 (cit. on pp. 4, 5, 101, 102, 133).

[42] R. Islam, C. Senko, W. C. Campbell, S. Korenblit, J. Smith, A. Lee, E. E. Edwards, C.-C. J. Wang, J. K. Freericks, and C. Monroe. "Emergence and Frustration of Magnetism with Variable-Range Interactions in a Quantum Simulator". Science **340** (2013), 583. eprint: `http://science.sciencemag.org/content/340/6132/583.full.pdf` (cit. on pp. 4, 136).

[43] A. W. Sandvik. "Computational Studies of Quantum Spin Systems". AIP Conf. Proc. **1297** (2010), 135 (cit. on pp. 5, 9, 17, 25, 33, 42, 57, 95, 118, 123, 158).

[44] R. Blankenbecler, D. Scalapino, and R. Sugar. "Monte Carlo calculations of coupled boson-fermion systems. I". Phys. Rev. D **24** (8 1981), 2278 (cit. on pp. 5, 9, 15, 67, 77).

[45] F. Michel and H. G. Evertz. "Lattice Dynamics of the Heisenberg chain coupled to finite frequency bond phonons" (2007) (cit. on pp. 5, 19, 58, 60, 62).

[46] F. Michel. PhD thesis. University of Graz, 2007 (cit. on pp. 5, 60, 62).

[47] S. Humeniuk. "Quantum Monte Carlo study of long-range transverse-field Ising models on the triangular lattice". Phys. Rev. B **93** (10 2016), 104412 (cit. on p. 5).

[48] S. Fölling. "Quantum Noise Correlation Experiments with Ultracold Atoms". *Quantum Gas Experiments: Exploring Many-Body States.* Ed. by P. Törmä and K. Sengstock. World Scientific Publishing Co, 2015, 145 (cit. on pp. 6, 212, 215, 216, 229).

[49] C. N. Yang and S. Zhang. "SO4 symmetry in a Hubbard model". Modern Physics Letters B **04** (1990), 759. eprint: http://www.worldscientific.com/doi/pdf/10.1142/S0217984990000933 (cit. on pp. 6, 173, 234).

[50] J. W. Negele and H. Orland. *Quantum many-particle systems.* Perseus Books, 1998 (cit. on pp. 10, 18).

[51] F James. "Monte Carlo theory and practice". Reports on Progress in Physics **43** (1980), 1145 (cit. on p. 10).

[52] J. Doob. *Stochastic Processes.* Wiley and Sons, New York, 1953 (cit. on p. 11).

[53] F. Assaad. "Quantum Monte Carlo methods on lattices: The determinantal approach". *Quantum Simulations of Complex Many-Body Systems: From Theory to Algorithms.* Ed. by J. Grotendorst, D. Marx, and A. Muramatsu. **10**. NIC Series. John von Neumann Institute for Computing, Jülich, 2002, 99 (cit. on pp. 11, 85, 87, 261).

[54] M. P. Nightingale and H. W. J. Blöte. "Dynamic Exponent of the Two-Dimensional Ising Model and Monte Carlo Computation of the Subdominant Eigenvalue of the Stochastic Matrix". Phys. Rev. Lett. **76** (24 1996), 4548 (cit. on pp. 11, 14).

[55] H. Suwa and S. Todo. "Markov Chain Monte Carlo Method without Detailed Balance". Phys. Rev. Lett. **105** (12 2010), 120603 (cit. on p. 12).

[56] N. Metropolis, A. W. Rosenbluth, M. N. Rosenbluth, A. H. Teller, and E. Teller. "Equation of State Calculations by Fast Computing Machines". J. Chem. Phys. **21** (1953), 1087 (cit. on p. 13).

[57] W. K. Hastings. "Monte Carlo sampling methods using Markov chains and their applications". Biometrika **57** (1970), 97. eprint: /oup/backfile/content_public/journal/biomet/57/1/57.1.97/4/57-1-97.pdf (cit. on p. 13).

[58] L. Pollet, S. M. A. Rombouts, K. Van Houcke, and K. Heyde. "Optimal Monte Carlo updating". Phys. Rev. E **70** (5 2004), 056705 (cit. on p. 13).

[59] D. Landau and K. Binder. *A Guide to Monte Carlo Simulations in Statistical Physics.* 2nd. Cambridge University Press, 2005 (cit. on pp. 14, 95).

[60] R. H. Swendsen and J.-S. Wang. "Nonuniversal critical dynamics in Monte Carlo simulations". Phys. Rev. Lett. **58** (2 1987), 86 (cit. on pp. 14, 35, 40, 43).

[61]   U. Wolff. "Collective Monte Carlo Updating for Spin Systems". Phys. Rev. Lett. **62** (4 1989), 361 (cit. on pp. 14, 39, 40, 46, 48).

[62]   S. Sachdev. *Quantum Phase Transitions*. 2nd. Cambridge University Press, Cambridge, 2014 (cit. on pp. 14, 95, 97, 116, 120, 140, 151, 155, 162).

[63]   V. Ambegaokar and M. Troyer. "Estimating errors reliably in Monte Carlo simulations of the Ehrenfest model". American Journal of Physics **78** (2010), 150. arXiv: 0906.0943 [physics.comp-ph] (cit. on p. 15).

[64]   U. Schollwöck. "The density-matrix renormalization group in the age of matrix product states". Annals of Physics **326** (2011), 96. arXiv: 1008.3477 [cond-mat.str-el] (cit. on p. 15).

[65]   J. Eisert, M. Cramer, and M. B. Plenio. "Colloquium: Area laws for the entanglement entropy". Rev. Mod. Phys. **82** (1 2010), 277 (cit. on p. 15).

[66]   F. Verstraete and J. I. Cirac. "Renormalization algorithms for Quantum-Many Body Systems in two and higher dimensions". eprint arXiv:cond-mat/0407066 (2004). eprint: cond-mat/0407066 (cit. on p. 15).

[67]   P. Corboz, T. M. Rice, and M. Troyer. "Competing States in the *t*-*J* Model: Uniform *d*-Wave State versus Stripe State". Phys. Rev. Lett. **113** (4 2014), 046402 (cit. on p. 15).

[68]   J. Gubernatis, N. Kawashima, and P. Werner. *Quantum Monte Carlo methods: Algorithms for lattice models*. Cambridge University Press, Cambridge, 2016 (cit. on p. 15).

[69]   J. E. Hirsch, R. L. Sugar, D. J. Scalapino, and R. Blankenbecler. "Monte Carlo simulations of one-dimensional fermion systems". Phys. Rev. B **26** (9 1982), 5033 (cit. on pp. 15, 17).

[70]   M. Suzuki, S. Miyashita, and A. Kuroda. "Monte Carlo Simulation of Quantum Spin Systems. I". Progress of Theoretical Physics **58** (1977), 1377. eprint: /oup/backfile/content_public/journal/ptp/58/5/10.1143/ptp.58.1377/2/58-5-1377.pdf (cit. on p. 15).

[71]   N. Kawashima and J. E. Gubernatis. "Generalization of the Fortuin-Kasteleyn transformation and its application to quantum spin simulations". Journal of Statistical Physics **80** (1995), 169. eprint: cond-mat/9502065 (cit. on p. 15).

[72]   B. B. Beard and U.-J. Wiese. "Simulations of Discrete Quantum Systems in Continuous Euclidean Time". Phys. Rev. Lett. **77** (25 1996), 5130 (cit. on p. 15).

[73]   N. V. Prokof'ev, B. V. Svistunov, and I. S. Tupitsyn. "Exact, complete, and universal continuous-time worldline Monte Carlo approach to the statistics of discrete quantum systems". Journal of Experimental and Theoretical Physics **87** (1998), 310 (cit. on pp. 15, 61).

[74] H. G. Evertz, G. Lana, and M. Marcu. "Cluster algorithm for vertex models". Phys. Rev. Lett. **70** (7 1993), 875 (cit. on pp. 15, 40, 75).

[75] H. G. Evertz. "The loop algorithm". Advances in Physics **52** (2003), 1. eprint: `cond-mat/9707221` (cit. on p. 15).

[76] S. Sorella. "Green Function Monte Carlo with Stochastic Reconfiguration". Phys. Rev. Lett. **80** (20 1998), 4558 (cit. on p. 16).

[77] For reviews consult, e.g., R. R. dos Santos, Introduction to Quantum Monte Carlo Simulations for Fermionic Systems. Braz. J. Phys. **33**, 36 (2003); F. F. Assaad and H. G. Evertz, Worldline and Determinantal Quantum Monte Carlo Methods for Spins, Phonons and Electrons. Lecture Notes in Physics **739**, 277 (2008). (cit. on pp. 16, 67, 68, 72, 74, 77, 84, 86, 87, 191, 192).

[78] S. Zhang, J. Carlson, and J. E. Gubernatis. "Constrained path Monte Carlo method for fermion ground states". Phys. Rev. B **55** (12 1997), 7464 (cit. on p. 16).

[79] D. M. Ceperley and B. J. Alder. "Ground State of the Electron Gas by a Stochastic Method". Phys. Rev. Lett. **45** (7 1980), 566 (cit. on p. 16).

[80] G. H. Booth, A. J. W. Thom, and A. Alavi. "Fermion Monte Carlo without fixed nodes: A game of life, death, and annihilation in Slater determinant space". The Journal of Chemical Physics **131** (2009), 054106. eprint: `http://aip.scitation.org/doi/pdf/10.1063/1.3193710` (cit. on p. 16).

[81] K. van Houcke, F. Werner, E. Kozik, N. Prokof'ev, B. Svistunov, M. J. H. Ku, A. T. Sommer, L. W. Cheuk, A. Schirotzek, and M. W. Zwierlein. "Feynman diagrams versus Fermi-gas Feynman emulator". Nature Physics **8** (2012), 366. arXiv: `1110.3747 [cond-mat.quant-gas]` (cit. on p. 16).

[82] M. B. Hastings, I. González, A. B. Kallin, and R. G. Melko. "Measuring Renyi Entanglement Entropy in Quantum Monte Carlo Simulations". Phys. Rev. Lett. **104** (15 2010), 157201 (cit. on p. 16).

[83] S. V. Isakov, M. Hastings, and R. Melko. "Topological entanglement entropy of a Bose–Hubbard spin liquid". Nature Physics **7** (2011), 772–775 (cit. on p. 16).

[84] S. Humeniuk and T. Roscilde. "Quantum Monte Carlo calculation of entanglement Rényi entropies for generic quantum systems". Phys. Rev. B **86**, 235116 (2012), 235116. arXiv: `1203.5752 [cond-mat.str-el]` (cit. on p. 16).

[85] F. F. Assaad, T. C. Lang, and F. Parisen Toldin. "Entanglement spectra of interacting fermions in quantum Monte Carlo simulations". Phys. Rev. B **89** (12 2014), 125121 (cit. on p. 16).

[86] J. Liu, Y. Qi, Z. Y. Meng, and L. Fu. "Self-learning Monte Carlo method". Phys. Rev. B **95** (4 2017), 041101 (cit. on pp. 16, 81).

[87]   P. Broecker, J. Carrasquilla, R. G. Melko, and S. Trebst. "Machine learning quantum phases of matter beyond the fermion sign problem". Scientific Reports **7**, 8823 (2017), 8823. arXiv: `1608.07848 [cond-mat.str-el]` (cit. on p. 16).

[88]   A. W. Sandvik. "A generalization of Handscomb's quantum Monte Carlo scheme-application to the 1D Hubbard model". Journal of Physics A: Mathematical and General **25** (1992), 3667 (cit. on pp. 17, 19, 20, 58, 59, 193).

[89]   O. F. Syljuåsen and A. W. Sandvik. "Quantum Monte Carlo with directed loops". Phys. Rev. E **66** (4 2002), 046701 (cit. on pp. 17, 23, 25, 27–31, 42, 51, 66, 75).

[90]   A. W. Sandvik and J. Kurkijärvi. "Quantum Monte Carlo simulation method for spin systems". Phys. Rev. B **43** (7 1991), 5950 (cit. on pp. 17, 19).

[91]   A. W. Sandvik, R. R. P. Singh, and D. K. Campbell. "Quantum Monte Carlo in the interaction representation: Application to a spin-Peierls model". Phys. Rev. B **56** (22 1997), 14510 (cit. on pp. 17, 19, 58, 60, 61).

[92]   A. W. Sandvik. "Stochastic series expansion method with operator-loop update". Phys. Rev. B **59** (22 1999), R14157 (cit. on pp. 17, 28, 193).

[93]   D. C. Handscomb. "The Monte Carlo method in quantum statistical mechanics". Mathematical Proceedings of the Cambridge Philosophical Society **58** (1962), 594–598 (cit. on p. 19).

[94]   D. C. Handscomb. "A Monte Carlo method applied to the Heisenberg ferromagnet". Mathematical Proceedings of the Cambridge Philosophical Society **60** (1964), 115–122 (cit. on p. 19).

[95]   A. W. Sandvik. "Stochastic series expansion method for quantum Ising models with arbitrary interactions". Phys. Rev. E **68** (5 2003), 056701 (cit. on pp. 23, 34–37, 39, 40, 43, 44, 48, 49, 66, 114, 115, 117, 135, 137).

[96]   E. Luijten and H. W. J. Blöte. "Monte Carlo method for spin models with long-range interactions". Int. J. Mod. Phys. C **6** (1995), 359 (cit. on pp. 35, 36).

[97]   K. Fukui and S. Todo. "Order-N cluster Monte Carlo method for spin systems with long-range interactions". Journal of Computational Physics **228** (2009), 2629 (cit. on pp. 35, 36, 39, 43, 135–137, 139, 148, 153).

[98]   N. Laflorencie, I. Affleck, and M. Berciu. "Critical phenomena and quantum phase transition in long range Heisenberg antiferromagnetic chains". Journal of Statistical Mechanics: Theory and Experiment **2005** (2005), P12001 (cit. on p. 35).

[99]   C. Koop and S. Wessel. "Quantum phase transitions in effective spin-ladder models for graphene zigzag nanoribbons". Phys. Rev. B **96** (16 2017), 165114 (cit. on p. 35).

[100] A. Walker. "An efficient method for generating discrete random variables with general distributions". ACM Trans. Math. Softw. **3** (1977), 253 (cit. on p. 39).

[101] D. Knuth. *The Art of Computer Programming, Seminumerical Algorithms.* thirds. **2**. 119. Addison Wesley, Reading, 1997 (cit. on p. 39).

[102] R. H. Swendsen, J.-S. Wang, and A. M. Ferrenberg. "New Monte Carlo Methods for Improved Efficiency of Computer Simulations in Statistical Mechanics". *The Monte Carlo Method in Condensed Matter Physics.* Ed. by K. Binder. Springer, Berlin, 1991 (cit. on p. 41).

[103] H.-J. Xu, B. Bergersen, and Z. Rácz. "Long-range interactions generated by random Lévy flights: Spin-flip and spin-exchange kinetic Ising model in two dimensions". Phys. Rev. E **47** (3 1993), 1520 (cit. on p. 46).

[104] G. H. Wannier. "Antiferromagnetism. The Triangular Ising Net". Phys. Rev. **79** (2 1950), 357 (cit. on pp. 51, 103, 104, 124).

[105] S. Biswas, G. Rakala, and K. Damle. "Quantum cluster algorithm for frustrated Ising models in a transverse field". Phys. Rev. B **93** (23 2016), 235103 (cit. on pp. 51–54, 66, 129).

[106] A. Dorneich and M. Troyer. "Accessing the dynamics of large many-particle systems using the stochastic series expansion". Phys. Rev. E **64** (6 2001), 066701 (cit. on pp. 58, 59).

[107] A. A. Abrikosov, L. Gorkov, and I. Dzyaloshinski. *Methods of Quantum FIeld Theory in Statistical Physics.* Dover Publications, New York, 1963 (cit. on p. 60).

[108] G. Rickayzen. *Green's Functions and Condensed Matter.* Academic Press, London, 1980 (cit. on p. 62).

[109] L. Pollet and N. Prokof'ev. "Higgs Mode in a Two-Dimensional Superfluid". Phys. Rev. Lett. **109** (1 2012), 010401 (cit. on p. 65).

[110] B. Berg. *Markov Chain Monte Carlo Simulations and their Statistical Analysis.* World Scientific, Singapore, 2004 (cit. on p. 65).

[111] E. Loh Jr. and J. Gubernatis. "Stable numerical simulations of models of interacting electrons in condensed-matter physics." *Electronic Phase Transitions.* Ed. by W. Hanke and Y. Kopaev. **32**. Modern Problems in Condensed Matter Sciences. North-Holland, Amsterdam, 1992. Chap. 4, 177 (cit. on pp. 67, 82, 84–87).

[112] R. R. dos Santos. "Introduction to Quantum Monte Carlo simulations for fermionic systems". Braz. J. Phys. **33** (2003), 36 (cit. on pp. 67–69, 72, 73, 77, 87).

[113] M. Suzuki. "Generalized Trotter's formula and systematic approximants of exponential operators and inner derivations with applications to many-body problems". Communications in Mathematical Physics **51** (1976), 183 (cit. on p. 68).

[114] R. M. Fye. "New results on Trotter-like approximations". Phys. Rev. B **33** (9 1986), 6271 (cit. on p. 68).

[115] J. Hubbard. "Calculation of Partition Functions". Phys. Rev. Lett. **3** (2 1959), 77 (cit. on pp. 68, 259).

[116] R. L. Stratonovich. Doklady Akad. Nauk S.S.S.R. **115** (1957), 1097 (cit. on pp. 68, 259).

[117] J. E. Hirsch. "Discrete Hubbard-Stratonovich transformation for fermion lattice models". Phys. Rev. B **28** (7 1983), 4059 (cit. on pp. 68, 168, 260).

[118] A. Fetter and J. Walecka. *Quantum Theory of Many-Particle Systems*. McGraw-Hill, New York, 1971 (cit. on pp. 72, 269).

[119] T. Grover. "Entanglement of Interacting Fermions in Quantum Monte Carlo Calculations". Phys. Rev. Lett. **111** (13 2013), 130402 (cit. on pp. 72, 191, 192, 195, 235, 257).

[120] J. E. Hirsch. "Two-dimensional Hubbard model: Numerical simulation study". Phys. Rev. B **31** (7 1985), 4403 (cit. on pp. 73, 90, 177, 178, 221).

[121] G. H. Golub and C. F. Van Loan. *Matrix Computations*. 3rd. The Johns Hopkins University Press, Baltimore, 1996 (cit. on pp. 77, 84).

[122] G. Alvarez et al. "New algorithm to enable 400+ TFlop/s sustained performance in simulations of disorder effects in high-Tc superconductors". *2008 SC - International Conference for High Performance Computing, Networking, Storage and Analysis*. 2008, 1 (cit. on p. 78).

[123] P. K. V. V. Nukala, T. A. Maier, M. S. Summers, G. Alvarez, and T. C. Schulthess. "Fast update algorithm for the quantum Monte Carlo simulation of the Hubbard model". Phys. Rev. B **80** (19 2009), 195111 (cit. on p. 78).

[124] R. T. Scalettar, R. M. Noack, and R. R. P. Singh. "Ergodicity at large couplings with the determinant Monte Carlo algorithm". Phys. Rev. B **44** (19 1991), 10502 (cit. on pp. 79–81).

[125] W. Xu, W. McGehee, W. Morong, and B. DeMarco. "Bad Metal in a Fermi Lattice Gas". ArXiv e-prints (2016). arXiv: `1606.06669 [cond-mat.quant-gas]` (cit. on p. 81).

[126] S. R. White, D. J. Scalapino, R. L. Sugar, E. Y. Loh, J. E. Gubernatis, and R. T. Scalettar. "Numerical study of the two-dimensional Hubbard model". Phys. Rev. B **40** (1 1989), 506 (cit. on p. 82).

[127] L. Blum, F. Cucker, M. Shub, and S. Smale. *Complexity and Real Computation.* 1998th ed. Springer, 2012 (cit. on p. 84).

[128] A. Tomas, C. C. Chang, R Scalettar, and Z. Bai. "Advancing Large Scale Many-Body QMC Simulations on GPU Accelerated Multicore Systems". *2012 IEEE 26th International Parallel and Distributed Processing Symposium, Shanghai, 2012.* 2012 (cit. on p. 84).

[129] E. Y. Loh, J. E. Gubernatis, R. T. Scalettar, S. R. White, D. J. Scalapino, and R. L. Sugar. "Sign problem in the numerical simulation of many-electron systems". Phys. Rev. B **41** (13 1990), 9301 (cit. on p. 87).

[130] S. Chandrasekharan and U.-J. Wiese. "Meron-Cluster Solution of Fermion Sign Problems". Phys. Rev. Lett. **83** (16 1999), 3116 (cit. on pp. 88, 89, 93).

[131] M. Troyer and U.-J. Wiese. "Computational Complexity and Fundamental Limitations to Fermionic Quantum Monte Carlo Simulations". Phys. Rev. Lett. **94** (17 2005), 170201 (cit. on pp. 88, 89, 93).

[132] C. Wu and S.-C. Zhang. "Sufficient condition for absence of the sign problem in the fermionic quantum Monte Carlo algorithm". Phys. Rev. B **71** (15 2005), 155115 (cit. on pp. 91, 92).

[133] A. Messiah. *Quantum Mechanics.* North-Holland, Amsterdam, 1969 (cit. on pp. 91, 92).

[134] Z.-X. Li, Y.-F. Jiang, and H. Yao. "Solving the fermion sign problem in quantum Monte Carlo simulations by Majorana representation". Phys. Rev. B **91** (24 2015), 241117 (cit. on p. 93).

[135] L. Wang, Y.-H. Liu, M. Iazzi, M. Troyer, and G. Harcos. "Split Orthogonal Group: A Guiding Principle for Sign-Problem-Free Fermionic Simulations". Phys. Rev. Lett. **115** (25 2015), 250601 (cit. on p. 93).

[136] Z. C. Wei, C. Wu, Y. Li, S. Zhang, and T. Xiang. "Majorana Positivity and the Fermion Sign Problem of Quantum Monte Carlo Simulations". Phys. Rev. Lett. **116** (25 2016), 250601 (cit. on p. 93).

[137] Z.-X. Li, Y.-F. Jiang, and H. Yao. "Majorana-Time-Reversal Symmetries: A Fundamental Principle for Sign-Problem-Free Quantum Monte Carlo Simulations". Phys. Rev. Lett. **117** (26 2016), 267002 (cit. on p. 93).

[138] S. Chandrasekharan. "Fermion bag approach to fermion sign problems". The European Physical Journal A **49** (2013), 90 (cit. on p. 93).

[139] E. F. Huffman and S. Chandrasekharan. "Solution to sign problems in half-filled spin-polarized electronic systems". Phys. Rev. B **89** (11 2014), 111101 (cit. on p. 93).

[140] F Barahona. "On the computational complexity of Ising spin glass models". Journal of Physics A: Mathematical and General **15** (1982), 3241 (cit. on p. 93).

[141]   F. Alet, K. Damle, and S. Pujari. "Sign-Problem-Free Monte Carlo Simulation of Certain Frustrated Quantum Magnets". Phys. Rev. Lett. **117** (19 2016), 197203 (cit. on p. 93).

[142]   V. I. Iglovikov, E. Khatami, and R. T. Scalettar. "Geometry dependence of the sign problem in quantum Monte Carlo simulations". Phys. Rev. B **92** (4 2015), 045110 (cit. on pp. 93, 236, 255, 258).

[143]   J. E. Hirsch. "Connection between world-line and determinantal functional-integral formulations of the Hubbard model". Phys. Rev. B **34** (5 1986), 3216 (cit. on p. 94).

[144]   P. Broecker and S. Trebst. "Numerical stabilization of entanglement computation in auxiliary-field quantum Monte Carlo simulations of interacting many-fermion systems". Phys. Rev. E **94** (6 2016), 063306 (cit. on p. 94).

[145]   J. Cardy. *Scaling and Renormalization in Statistical Physics.* Cambridge Lecture Notes in Physics 5. Cambridge University Press, 1996 (cit. on pp. 95, 120, 141, 159).

[146]   M. E. Fisher and M. N. Barber. "Scaling Theory for Finite-Size Effects in the Critical Region". Phys. Rev. Lett. **28** (23 1972), 1516 (cit. on pp. 96, 121, 153, 159).

[147]   K. Binder and D. Heermann. *Monte Carlo Simulation in Statistical Physics.* 80 Springer Series in Solid-State Sciences. Springer-Verlag, Berlin, 1992 (cit. on pp. 97, 99).

[148]   K. Binder. "Finite size scaling analysis of ising model block distribution functions". Zeitschrift für Physik B Condensed Matter **43** (1981), 119 (cit. on pp. 98, 99).

[149]   K. Binder. "Critical Properties from Monte Carlo Coarse Graining and Renormalization". Phys. Rev. Lett. **47** (9 1981), 693 (cit. on pp. 98, 99).

[150]   K. Binder. "Finite size scaling analysis of ising model block distribution functions". English. Zeitschrift für Physik B Condensed Matter **43** (1981), 119 (cit. on pp. 99, 117, 123).

[151]   J. Stephenson. "IsingModel Spin Correlations on the Triangular Lattice. III. Isotropic Antiferromagnetic Lattice". Journal of Mathematical Physics **11** (1970), 413 (cit. on p. 103).

[152]   S Alexander and P Pincus. "Phase transitions of some fully frustrated models". Journal of Physics A: Mathematical and General **13** (1980), 263 (cit. on pp. 104, 106).

[153]   D. Blankschtein, M. Ma, and A. N. Berker. "Fully and partially frustrated simple-cubic Ising models: Landau-Ginzburg-Wilson theory". Phys. Rev. B **30** (3 1984), 1362 (cit. on pp. 104, 106, 109, 129).

[154] S. Suzuki, J.-i. Inoue, and B. K. Chakrabarti. *Quantum Ising Phases and Transitions in Transverse Ising Models.* Springer Berlin Heidelberg, 2013 (cit. on pp. 104, 263).

[155] S.-Z. Lin, Y. Kamiya, G.-W. Chern, and C. D. Batista. "Stiffness from Disorder in Triangular-Lattice Ising Thin Films". Phys. Rev. Lett. **112** (15 2014), 155702 (cit. on pp. 104, 110).

[156] B Nienhuis, H. J. Hilhorst, and H. W. J. Blote. "Triangular SOS models and cubic-crystal shapes". Journal of Physics A: Mathematical and General **17** (1984), 3559 (cit. on p. 105).

[157] M. El-Batanouny and F. Wooten. *Symmetry and Condensed Matter Physics: A Computational Approach.* Cambridge University Press, 2008 (cit. on p. 106).

[158] D. J. Amit. *Field Theory, the Renormalization Group and Critical Phenomena.* 2 Revised. World Scientific Publishing Co Pte Ltd, 2008 (cit. on pp. 107, 108).

[159] A. Muramatsu. *Spontaneous Symmetry Breaking and Field-Theory I.* Lecture Notes, University of Stuttgart, 2013 (cit. on pp. 107, 108, 150).

[160] L. Wang. "Exploring cluster Monte Carlo updates with Boltzmann machines". Phys. Rev. E **96** (5 2017), 051301 (cit. on pp. 108, 129).

[161] R. R. Netz and A. N. Berker. "Monte Carlo mean-field theory and frustrated systems in two and three dimensions". Phys. Rev. Lett. **66** (3 1991), 377 (cit. on p. 109).

[162] S. N. Coppersmith. "Low-temperature phase of a stacked triangular Ising antiferromagnet". Phys. Rev. B **32** (3 1985), 1584 (cit. on pp. 109, 124).

[163] O. Heinonen and R. G. Petschek. "Critical behavior of a frustrated Ising system". Phys. Rev. B **40** (13 1989), 9052 (cit. on pp. 109, 124).

[164] J.-J. Kim, Y. Yamada, and O. Nagai. "Reanalysis of a stacked triangular Ising antiferromagnet by use of Monte Carlo simulations". Phys. Rev. B **41** (7 1990) (cit. on pp. 109, 124).

[165] M. Žukovič, L. Mižišin, and A. Bobák. "Low-Temperature Properties of Ising Antiferromagnet on a Stacked Triangular Lattice". Acta Physica Polonica, A **126** (2014), 40 (cit. on pp. 109, 124).

[166] J. M. Kosterlitz and D. J. Thouless. "Ordering, metastability and phase transitions in two-dimensional systems". Journal of Physics C: Solid State Physics **6** (1973), 1181 (cit. on pp. 109, 178).

[167] J. Borwein, M. L. Glasser, R. C. McPhedran, J. G. Wan, and I. J. Zucker. *Lattice Sums Then and Now.* Cambridge University Press, 2013 (cit. on p. 112).

[168] P. Ribeiro, J. Vidal, and R. Mosseri. "Exact spectrum of the Lipkin-Meshkov-Glick model in the thermodynamic limit and finite-size corrections". Phys. Rev. E **78** (2 2008), 021106 (cit. on pp. 114, 131).

[169] A. Dutta and J. K. Bhattacharjee. "Phase transitions in the quantum Ising and
       rotor models with a long-range interaction". Phys. Rev. B **64** (18 2001), 184106
       (cit. on pp. 116, 118, 120, 121, 129, 139, 140, 144, 151, 153, 155, 158).

[170] S. K. Baek, J. Um, S. D. Yi, and B. J. Kim. "Quantum Monte Carlo study of
       the transverse-field quantum Ising model on infinite-dimensional structures".
       Phys. Rev. B **84** (17 2011), 174419 (cit. on p. 121).

[171] W. A. C. Erkelens, L. P. Regnault, J. Rossat-Mignod, J. E. Moore, R. A.
       Butera, and L. J. de Jongh. "Observation of Crossover to 4-Dimensional Critical
       Behaviour". EPL (Europhysics Letters) **1** (1986), 37 (cit. on p. 121).

[172] S. N. Saadatmand, S. D. Bartlett, and I. P. McCulloch. "Phase diagram of
       the quantum Ising model with long-range interactions on an infinite-cylinder
       triangular lattice". Phys. Rev. B **97** (15 2018), 155116 (cit. on pp. 125, 133).

[173] K. Binder and D. W. Heermann. *Monte Carlo Simulation in Statistical Physics:
       An Introduction.* 5th ed. Graduate Texts in Physics 0. Springer-Verlag Berlin
       Heidelberg, 2010 (cit. on p. 129).

[174] P. M. Chaikin and T. C. Lubensky. *Principles of condensed matter physics.*
       Cambridge University Press, Cambridge, UK, 2000 (cit. on pp. 129, 140, 145,
       156, 157).

[175] E. Marinari and G. Parisi. "Simulated Tempering: A New Monte Carlo Scheme".
       EPL (Europhysics Letters) **19** (1992), 451 (cit. on p. 133).

[176] J. G. Bohnet, B. C. Sawyer, J. W. Britton, M. L. Wall, A. M. Rey, M. Foss-Feig,
       and J. J. Bollinger. "Quantum spin dynamics and entanglement generation
       with hundreds of trapped ions". Science **352** (2016), 1297. arXiv: `1512.03756`
       `[quant-ph]` (cit. on pp. 133, 190).

[177] J. M. Kosterlitz. "The critical properties of the two-dimensional xy model".
       Journal of Physics C: Solid State Physics **7** (1974), 1046 (cit. on pp. 135, 142–144,
       148).

[178] J. Bhattacharjee, S. Chakravarty, J. L. Richardson, and D. J. Scalapino. "Some
       properties of a one-dimensional Ising chain with an inverse-square interaction".
       Phys. Rev. B **24** (7 1981), 3862 (cit. on pp. 135, 139, 140, 142, 145, 151).

[179] E. Luijten and H. Meßingfeld. "Criticality in One Dimension with Inverse
       Square-Law Potentials". Phys. Rev. Lett. **86** (23 2001), 5305 (cit. on pp. 135,
       137, 151).

[180] J. M. Kosterlitz. *Topological Defects and Phase Transitions.* Nobel Lecture. 2016
       (cit. on p. 135).

[181] P. W. Anderson, G. Yuval, and D. R. Hamann. "Exact Results in the Kondo Problem. II. Scaling Theory, Qualitatively Correct Solution, and Some New Results on One-Dimensional Classical Statistical Models". Phys. Rev. B **1** (11 1970), 4464 (cit. on pp. 135, 140–142).

[182] G.-D. Lin, S.-L. Zhu, R. Islam, K. Kim, M.-S. Chang, S. Korenblit, C. Monroe, and L.-M. Duan. "Large-scale quantum computation in an anharmonic linear ion trap". EPL (Europhysics Letters) **86** (2009), 60004 (cit. on p. 136).

[183] J. Zhang, G. Pagano, P. W. Hess, A. Kyprianidis, P. Becker, H. Kaplan, A. V. Gorshkov, Z.-X. Gong, and C. Monroe. "Observation of a many-body dynamical phase transition with a 53-qubit quantum simulator". Nature **551** (2017), 601 (cit. on p. 136).

[184] M. Knap, A. Kantian, T. Giamarchi, I. Bloch, M. D. Lukin, and E. Demler. "Probing Real-Space and Time-Resolved Correlation Functions with Many-Body Ramsey Interferometry". Phys. Rev. Lett. **111** (14 2013), 147205 (cit. on pp. 136, 154).

[185] G.-D. Lin, C. Monroe, and L.-M. Duan. "Sharp Phase Transitions in a Small Frustrated Network of Trapped Ion Spins". Phys. Rev. Lett. **106** (23 2011), 230402 (cit. on p. 136).

[186] K. Huang. *Statistical Mechanics.* 3rd. John Wiley & Sons, New York, 1966 (cit. on p. 138).

[187] D. Ruelle. "Statistical mechanics of a one-dimensional lattice gas". Comm. Math. Phys. **9** (1968), 267 (cit. on p. 138).

[188] F. Dyson. "Existence of a phase-transition in a one-dimensional Ising ferromagnet". English. Communications in Mathematical Physics **12** (1969), 91 (cit. on p. 139).

[189] D. J. Thouless. "Long-Range Order in One-Dimensional Ising Systems". Phys. Rev. **187** (2 1969), 732 (cit. on p. 139).

[190] D. R. Nelson and J. M. Kosterlitz. "Universal Jump in the Superfluid Density of Two-Dimensional Superfluids". Phys. Rev. Lett. **39** (19 1977), 1201 (cit. on p. 140).

[191] J. M. Kosterlitz. "Phase Transitions in Long-Range Ferromagnetic Chains". Phys. Rev. Lett. **37** (23 1976), 1577 (cit. on pp. 140–142).

[192] J. L. Cardy. "One-dimensional models with 1/r 2 interactions". Journal of Physics A: Mathematical and General **14** (1981), 1407 (cit. on p. 140).

[193] D. Nelson. "Defect-mediated phase transitions". *Phase Transitions and Critical Phenomena.* Ed. by C. Domb and J. Lebowitz. Academic Press, 1983 (cit. on p. 141).

[194] P. W. Anderson and G Yuval. "Some numerical results on the Kondo problem and the inverse square one-dimensional Ising model". Journal of Physics C: Solid State Physics **4** (1971), 607 (cit. on p. 142).

[195] G. Ortiz and H. Nishimori. *Elements of Phase Transitions and Critical Phenomena.* Oxford University Press, 2011 (cit. on p. 144).

[196] H. Weber and P. Minnhagen. "Monte Carlo determination of the critical temperature for the two-dimensional XY model". Phys. Rev. B **37** (10 1988), 5986 (cit. on p. 148).

[197] K. Harada and N. Kawashima. "Universal jump in the helicity modulus of the two-dimensional quantum XY model". Phys. Rev. B **55** (18 1997), R11949 (cit. on p. 148).

[198] K. Harada and N. Kawashima. "Kosterlitz-Thouless Transition of Quantum XY Model in Two Dimensions". Journal of the Physical Society of Japan **67** (1998), 2768. eprint: https://doi.org/10.1143/JPSJ.67.2768 (cit. on p. 148).

[199] R. B. Griffiths. "Correlations in Ising Ferromagnets. I". Journal of Mathematical Physics **8** (1967), 478. eprint: http://dx.doi.org/10.1063/1.1705219 (cit. on p. 151).

[200] R. Islam et al. "Onset of a quantum phase transition with a trapped ion quantum simulator". Nature Communications **2** (2011) (cit. on p. 153).

[201] S. Fey and K. P. Schmidt. "Critical behavior of quantum magnets with long-range interactions in the thermodynamic limit". Phys. Rev. B **94** (7 2016), 075156 (cit. on p. 154).

[202] M. F. Maghrebi, Z.-X. Gong, M. Foss-Feig, and A. V. Gorshkov. "Causality and quantum criticality in long-range lattice models". Phys. Rev. B **93** (12 2016), 125128 (cit. on pp. 155, 157–159).

[203] I. Frérot, P. Naldesi, and T. Roscilde. "Entanglement and fluctuations in the XXZ model with power-law interactions". Phys. Rev. B **95** (24 2017), 245111 (cit. on p. 156).

[204] J. Sak. "Recursion Relations and Fixed Points for Ferromagnets with Long-Range Interactions". Phys. Rev. B **8** (1 1973), 281 (cit. on pp. 157, 159).

[205] E. Luijten and H. W. J. Blöte. "Boundary between Long-Range and Short-Range Critical Behavior in Systems with Algebraic Interactions". Phys. Rev. Lett. **89** (2 2002), 025703 (cit. on p. 159).

[206] M. Picco. "Critical behavior of the Ising model with long range interactions". ArXiv e-prints (2012). arXiv: 1207.1018 [cond-mat.stat-mech] (cit. on p. 159).

[207]   T. Blanchard, M. Picco, and M. A. Rajabpour. "Influence of long-range interac-
        tions on the critical behavior of the Ising model". EPL (Europhysics Letters)
        101 (2013), 56003 (cit. on p. 159).

[208]   T. Horita, H. Suwa, and S. Todo. "Upper and lower critical decay exponents
        of Ising ferromagnets with long-range interaction". Phys. Rev. E **95** (1 2017),
        012143 (cit. on p. 162).

[209]   M. C. Angelini, G. Parisi, and F. Ricci-Tersenghi. "Relations between short-
        range and long-range Ising models". Phys. Rev. E **89** (6 2014), 062120 (cit. on
        p. 162).

[210]   C. Behan, L. Rastelli, S. Rychkov, and B. Zan. "Long-Range Critical Exponents
        near the Short-Range Crossover". Phys. Rev. Lett. **118** (24 2017), 241601 (cit.
        on p. 162).

[211]   P. Werner, K. Völker, M. Troyer, and S. Chakravarty. "Phase Diagram and
        Critical Exponents of a Dissipative Ising Spin Chain in a Transverse Magnetic
        Field". Phys. Rev. Lett. **94** (4 2005), 047201 (cit. on p. 165).

[212]   M. C. Gutzwiller. "Effect of Correlation on the Ferromagnetism of Transition
        Metals". Phys. Rev. Lett. **10** (5 1963), 159 (cit. on p. 167).

[213]   J. Hubbard. "Electron correlations in narrow energy bands". Proceedings of the
        Royal Society of London A: Mathematical, Physical and Engineering Sciences
        276 (1963), 238. eprint: http://rspa.royalsocietypublishing.org/
        content/276/1365/238.full.pdf (cit. on p. 167).

[214]   J. Kanamori. "Electron Correlation and Ferromagnetism of Transition Met-
        als". Progress of Theoretical Physics **30** (1963), 275. eprint: /oup/backfile/
        content_public/journal/ptp/30/3/10.1143/ptp.30.275/2/30-3-
        275.pdf (cit. on p. 167).

[215]   J. Hubbard. "Electron correlations in narrow energy bands. II. The degenerate
        band case". Proceedings of the Royal Society of London A: Mathematical,
        Physical and Engineering Sciences **277** (1964), 237. eprint: http://rspa.
        royalsocietypublishing.org/content/277/1369/237.full.pdf (cit.
        on p. 167).

[216]   F. Gebhard. *The Mott Metal-Insulator Transition.* Springer Tracts in Modern
        Physics 137. Springer-Verlag, Berlin, 2000 (cit. on pp. 167, 171).

[217]   M. Imada, A. Fujimori, and Y. Tokura. "Metal-insulator transitions". Rev. Mod.
        Phys. **70** (4 1998), 1039 (cit. on p. 167).

[218]   J. G. Bednorz and K. A. Müller. "Possible highTc superconductivity in the
        BaLaCuO system". Zeitschrift für Physik B Condensed Matter **64** (1986), 189
        (cit. on p. 167).

[219] Y. Kamihara, H. Hiramatsu, M. Hirano, R. Kawamura, H. Yanagi, T. Kamiya, and H. Hosono. "Iron-Based Layered Superconductor: LaOFeP". Journal of the American Chemical Society **128** (2006). PMID: 16881620, 10012. eprint: https://doi.org/10.1021/ja063355c (cit. on p. 167).

[220] D. J. Scalapino. "A common thread: The pairing interaction for unconventional superconductors". Rev. Mod. Phys. **84** (4 2012), 1383 (cit. on p. 167).

[221] J. Bardeen, L. N. Cooper, and J. R. Schrieffer. "Theory of Superconductivity". Phys. Rev. **108** (5 1957), 1175 (cit. on pp. 168, 176, 178).

[222] T. Esslinger. "Fermi-Hubbard Physics with Atoms in an Optical Lattice". Annual Review of Condensed Matter Physics **1** (2010), 129. eprint: https://doi.org/10.1146/annurev-conmatphys-070909-104059 (cit. on p. 169).

[223] D. Jaksch, C. Bruder, J. I. Cirac, C. W. Gardiner, and P. Zoller. "Cold Bosonic Atoms in Optical Lattices". Phys. Rev. Lett. **81** (15 1998), 3108 (cit. on p. 169).

[224] H. P. Büchler. "Microscopic Derivation of Hubbard Parameters for Cold Atomic Gases". Phys. Rev. Lett. **104** (9 2010), 090402 (cit. on p. 170).

[225] A. Avella, F. Mancini, and T. Saikawa. "The 2-site Hubbard and t-J models". The European Physical Journal B - Condensed Matter and Complex Systems **36** (2003), 445 (cit. on p. 170).

[226] S. Murmann, A. Bergschneider, V. M. Klinkhamer, G. Zürn, T. Lompe, and S. Jochim. "Two Fermions in a Double Well: Exploring a Fundamental Building Block of the Hubbard Model". Phys. Rev. Lett. **114** (8 2015), 080402 (cit. on p. 171).

[227] E. Cocchi, L. A. Miller, J. H. Drewes, C. F. Chan, D. Pertot, F. Brennecke, and M. Köhl. "Measuring entropy and mutual information in the two-dimensional Hubbard model". ArXiv e-prints (2016). arXiv: 1612.04627 [cond-mat.quant-gas] (cit. on pp. 171, 206).

[228] F. H. L. Essler, H. Frahm, F. Göhmann, A. Klümper, and V. E. Korepin. *The One-Dimensional Hubbard Model*. Cambridge University Press, Cambridge, 2005 (cit. on p. 171).

[229] G. Fano, F. Ortolani, and A. Parola. "Electron correlations in the two-dimensional Hubbard model: A group-theoretical and numerical study". Phys. Rev. B **46** (2 1992), 1048 (cit. on pp. 172, 240).

[230] C. N. Yang. "η pairing and off-diagonal long-range order in a Hubbard model". Phys. Rev. Lett. **63** (19 1989), 2144 (cit. on pp. 173, 229).

[231] H. Shiba. "Magnetic Susceptibility at Zero Temperature for the One-Dimensional Hubbard Model". Phys. Rev. B **6** (3 1972), 930 (cit. on p. 173).

[232] R. Micnas, J. Ranninger, and S. Robaszkiewicz. "Superconductivity in narrow-band systems with local nonretarded attractive interactions". Rev. Mod. Phys. **62** (1 1990), 113 (cit. on pp. 173, 178, 198, 200).

[233] R. R. P. Singh and R. T. Scalettar. "Exact demonstration of η pairing in the ground state of an attractive-U Hubbard model". Phys. Rev. Lett. **66** (24 1991), 3203 (cit. on pp. 174, 230).

[234] A. F. Ho, M. A. Cazalilla, and T. Giamarchi. "Quantum simulation of the Hubbard model: The attractive route". Phys. Rev. A **79** (3 2009), 033620 (cit. on pp. 174, 218, 224).

[235] P. A. Lee, N. Nagaosa, and X.-G. Wen. "Doping a Mott insulator: Physics of high-temperature superconductivity". Rev. Mod. Phys. **78** (1 2006), 17 (cit. on p. 175).

[236] G. Deutscher. *New Superconductors: From Granular to High T_c*. World Scientific Publishing, Singapore, 2006 (cit. on p. 176).

[237] T. A. Maier, M. Jarrell, A. Macridin, and C. Slezak. "Kinetic Energy Driven Pairing in Cuprate Superconductors". Phys. Rev. Lett. **92** (2 2004), 027005 (cit. on p. 176).

[238] N. D. Mermin and H. Wagner. "Absence of Ferromagnetism or Antiferromagnetism in One- or Two-Dimensional Isotropic Heisenberg Models". Phys. Rev. Lett. **17** (22 1966), 1133 (cit. on pp. 176, 224).

[239] D. Y. Xing, M. Liu, and C. D. Gong. "Van Hove singularity and isotope effect in high-T_c copper oxides". Phys. Rev. B **44** (22 1991), 12525 (cit. on p. 177).

[240] A. J. Leggett. *Modern Trends in the Theory of Condensed Matter*. Ed. by A. Pedalski and J. Przystawa. Springer, Berlin, 1980 (cit. on p. 178).

[241] P. Nozières and S. Schmitt-Rink. "Bose condensation in an attractive fermion gas: From weak to strong coupling superconductivity". Journal of Low Temperature Physics **59** (1985), 195 (cit. on pp. 178, 199, 200).

[242] G. V. Chester. "Difference between Normal and Superconducting States of a Metal". Phys. Rev. **103** (6 1956), 1693 (cit. on p. 178).

[243] B. Kyung, A. Georges, and A.-M. S. Tremblay. "Potential-energy-driven (BCS) to kinetic-energy-driven (BEC) pairing in the two-dimensional attractive Hubbard model: Cellular dynamical mean-field theory". Phys. Rev. B **74** (2 2006), 024501 (cit. on p. 178).

[244] E. Manousakis. "The spin-1/2 Heisenberg antiferromagnet on a square lattice and its application to the cuprous oxides". Rev. Mod. Phys. **63** (1 1991), 1 (cit. on p. 179).

[245] A. Koetsier, F. van Liere, and H. T. C. Stoof. "Imbalanced antiferromagnet in an optical lattice". Phys. Rev. A **81** (2 2010), 023628 (cit. on p. 179).

[246]   A. B. Harris and R. V. Lange. "Single-Particle Excitations in Narrow Energy Bands". Phys. Rev. **157** (2 1967), 295 (cit. on pp. 179, 181).

[247]   J.-Y. P. Delannoy, M. J. P. Gingras, P. C. W. Holdsworth, and A.-M. S. Tremblay. "Néel order, ring exchange, and charge fluctuations in the half-filled Hubbard model". Phys. Rev. B **72** (11 2005), 115114 (cit. on pp. 181, 182, 206, 210, 250).

[248]   M Takahashi. "Half-filled Hubbard model at low temperature". Journal of Physics C: Solid State Physics **10** (1977), 1289 (cit. on pp. 182, 206, 250).

[249]   A. H. MacDonald, S. M. Girvin, and D. Yoshioka. "$\frac{t}{U}$ expansion for the Hubbard model". Phys. Rev. B **37** (16 1988), 9753 (cit. on pp. 182, 206, 250).

[250]   L. Landau and E. Lifshitz. *Quantum Mechanics.* 3rd. Pergamon, London, 1977 (cit. on p. 183).

[251]   L. N. Cooper. "Bound Electron Pairs in a Degenerate Fermi Gas". Phys. Rev. **104** (4 1956), 1189 (cit. on pp. 183, 226).

[252]   L. N. Cooper. *Microscopic Quantum Interference Effects in the Theory of Superconductivity.* Nobel Lecture. 1972 (cit. on pp. 183, 226).

[253]   M. Randeria, J.-M. Duan, and L.-Y. Shieh. "Superconductivity in a two-dimensional Fermi gas: Evolution from Cooper pairing to Bose condensation". Phys. Rev. B **41** (1 1990), 327 (cit. on pp. 184, 203).

[254]   R. Piil and K. Mølmer. "Tunneling couplings in discrete lattices, single-particle band structure, and eigenstates of interacting atom pairs". Phys. Rev. A **76** (2 2007), 023607 (cit. on p. 185).

[255]   D. Petrosyan, B. Schmidt, J. R. Anglin, and M. Fleischhauer. "Quantum liquid of repulsively bound pairs of particles in a lattice". Phys. Rev. A **76** (3 2007), 033606 (cit. on pp. 186, 187).

[256]   L. S. Levitov, H. Lee, and G. B. Lesovik. "Electron counting statistics and coherent states of electric current". Journal of Mathematical Physics **37** (1996), 4845 (cit. on p. 190).

[257]   *Quantum Noise in Mesoscopic Physics*, edited by Yu. V. Nazarov (Kluwer, Dordrecht 2003) (cit. on p. 190).

[258]   R. de-Picciotto, M. Reznikov, M. Heiblum, V. Umansky, G. Bunin, and D. Mahalu. "Direct observation of a fractional charge". Physica B Condensed Matter **249** (1998), 395 (cit. on p. 190).

[259]   L. Saminadayar, D. C. Glattli, Y. Jin, and B. Etienne. "Observation of the $e/3$ Fractionally Charged Laughlin Quasiparticle". Phys. Rev. Lett. **79** (13 1997), 2526 (cit. on p. 190).

[260]   A. Öttl, S. Ritter, M. Köhl, and T. Esslinger. "Correlations and Counting Statistics of an Atom Laser". Phys. Rev. Lett. **95** (9 2005), 090404 (cit. on p. 190).

[261]   R. W. Cherng and E. Demler. "Quantum noise analysis of spin systems realized with cold atoms". New Journal of Physics **9** (2007), 7 (cit. on pp. 190, 268).

[262]   W. Belzig, C. Schroll, and C. Bruder. "Density correlations in ultracold atomic Fermi gases". Phys. Rev. A **75** (6 2007), 063611 (cit. on pp. 190, 200).

[263]   S. Braungardt, A. Sen(De), U. Sen, R. J. Glauber, and M. Lewenstein. "Fermion and spin counting in strongly correlated systems". Phys. Rev. A **78** (6 2008), 063613 (cit. on p. 190).

[264]   A. Lamacraft. "Particle correlations in a Fermi superfluid". Phys. Rev. A **73** (1 2006), 011602 (cit. on pp. 190, 221, 222).

[265]   S. Braungardt, M. Rodríguez, A. Sen(De), U. Sen, R. J. Glauber, and M. Lewenstein. "Counting of fermions and spins in strongly correlated systems in and out of thermal equilibrium". Phys. Rev. A **83** (1 2011), 013601 (cit. on p. 190).

[266]   M. Gring, M. Kuhnert, T. Langen, T. Kitagawa, B. Rauer, M. Schreitl, I. Mazets, D. A. Smith, E. Demler, and J. Schmiedmayer. "Relaxation and Prethermalization in an Isolated Quantum System". Science **337** (2012), 1318 (cit. on p. 190).

[267]   S.-A. Cheong and C. L. Henley. "Many-body density matrices for free fermions". Phys. Rev. B **69** (7 2004), 075111 (cit. on pp. 191, 192).

[268]   I. Peschel. "Calculation of reduced density matrices from correlation functions". Journal of Physics A: Mathematical and General **36** (2003), L205 (cit. on pp. 191–193).

[269]   M.-C. Chung and I. Peschel. "Density-matrix spectra of solvable fermionic systems". Phys. Rev. B **64** (6 2001), 064412 (cit. on pp. 192, 193).

[270]   F. Parisen Toldin and F. F. Assaad. "Entanglement Hamiltonian of interacting fermionic models". ArXiv e-prints (2018). arXiv: `1804.03163 [cond-mat.str-el]` (cit. on p. 195).

[271]   A. H. Al-Mohy and N. J. Higham. "Improved inverse scaling and squaring algorithms for the matrix logarithm". SIAM J. Sci. Comput. **34** (2012), C152 (cit. on p. 196).

[272]   D. M. Eagles. "Possible Pairing without Superconductivity at Low Carrier Concentrations in Bulk and Thin-Film Superconducting Semiconductors". Phys. Rev. **186** (2 1969), 456 (cit. on pp. 199, 200).

[273]   A. J. Leggett, in *Modern Trends in the Theory of Condensed Matter*, edited by A. Pedalski and J. Przystawa (Springer, Berlin, 1980). (cit. on pp. 199, 200, 267).

[274] L. Belkhir and M. Randeria. "Collective excitations and the crossover from Cooper pairs to composite bosons in the attractive Hubbard model". Phys. Rev. B **45** (9 1992), 5087 (cit. on p. 200).

[275] L. D. Landau and E. M. Lifshitz. *Quantum Mechanics*. 3rd. Sec. 133. Pergamon, Oxford, 1987 (cit. on p. 203).

[276] P. M. Preiss, R. Ma, M. E. Tai, J. Simon, and M. Greiner. "Quantum gas microscopy with spin, atom-number, and multilayer readout". Phys. Rev. A **91** (4 2015), 041602 (cit. on p. 206).

[277] I. Lovas, B. Dóra, E. Demler, and G. Zaránd. "Full counting statistics of time-of-flight images". Phys. Rev. A **95** (2017), 053621 (cit. on p. 212).

[278] M Moreno-Cardoner, J. F. Sherson, and G. D. Chiara. "Non-Gaussian distribution of collective operators in quantum spin chains". New Journal of Physics **18** (2016), 103015 (cit. on p. 212).

[279] Z. Y. Meng, T. C. Lang, S. Wessel, F. F. Assaad, and A. Muramatsu. "Quantum spin liquid emerging in two-dimensional correlated Dirac fermions". Nature **464** (2010), 847 (cit. on p. 212).

[280] S. Sorella, Y. Otsuka, and S. Yunoki. "Absence of a Spin Liquid Phase in the Hubbard Model on the Honeycomb Lattice". Scientific Reports **2** (2012), 992 (cit. on p. 212).

[281] Nozières. *Theory of Interacting Fermi Systems*. Benjamin, New York, 1964 (cit. on p. 215).

[282] S. Huotari et al. "Momentum Distribution and Renormalization Factor in Sodium and the Electron Gas". Phys. Rev. Lett. **105** (8 2010), 086403 (cit. on p. 215).

[283] B. Hetényi. "Drude and Superfluid Weights in Extended Systems: The Role of Discontinuities and -Peaks in the One- and Two-Body Momentum Densities". Journal of the Physical Society of Japan **81** (2012), 023701. eprint: `http://dx.doi.org/10.1143/JPSJ.81.023701` (cit. on pp. 215, 216).

[284] C. A. Regal, M. Greiner, S. Giorgini, M. Holland, and D. S. Jin. "Momentum Distribution of a Fermi Gas of Atoms in the BCS-BEC Crossover". Phys. Rev. Lett. **95** (25 2005), 250404 (cit. on p. 215).

[285] J. R. Schrieffer. *Theory of Superconductivity*. Frontiers in Physics, Reading, MA. 1964 (cit. on pp. 215, 217, 219, 222, 267).

[286] D. J. Scalapino, S. R. White, and S. Zhang. "Insulator, metal, or superconductor: The criteria". Phys. Rev. B **47** (13 1993), 7995 (cit. on p. 216).

[287] M. Greiner, O. Mandel, T. Esslinger, T. W. Hänsch, and I. Bloch. "Quantum phase transition from a superfluid to a Mott insulator in a gas of ultracold atoms". Nature **415** (2002), 39 (cit. on p. 216).

[288] S. Fölling, F. Gerbier, A. Widera, O. Mandel, T. Gericke, and I. Bloch. "Spatial quantum noise interferometry in expanding ultracold atom clouds". Nature **434** (2005), 481. eprint: `cond-mat/0503587` (cit. on p. 216).

[289] I. B. Spielman, W. D. Phillips, and J. V. Porto. "Mott-Insulator Transition in a Two-Dimensional Atomic Bose Gas". Phys. Rev. Lett. **98** (8 2007), 080404 (cit. on p. 216).

[290] T. Rom, T. Best, D. van Oosten, U. Schneider, S. Fölling, B. Paredes, and I. Bloch. "Free fermion antibunching in a degenerate atomic Fermi gas released from an optical lattice". Nature **444** (2006), 733. eprint: `cond-mat/0611561` (cit. on p. 216).

[291] M. Greiner, C. A. Regal, J. T. Stewart, and D. S. Jin. "Probing Pair-Correlated Fermionic Atoms through Correlations in Atom Shot Noise". Phys. Rev. Lett. **94** (11 2005), 110401 (cit. on pp. 216, 217).

[292] V. Guarrera, N. Fabbri, L. Fallani, C. Fort, K. M. R. van der Stam, and M. Inguscio. "Noise Correlation Spectroscopy of the Broken Order of a Mott Insulating Phase". Phys. Rev. Lett. **100** (25 2008), 250403 (cit. on p. 216).

[293] J. Simon, W. S. Bakr, R. Ma, M. E. Tai, P. M. Preiss, and M. Greiner. "Quantum simulation of antiferromagnetic spin chains in an optical lattice". Nature **472** (2011), 307. arXiv: `1103.1372 [cond-mat.quant-gas]` (cit. on p. 216).

[294] M. Messer, R. Desbuquois, T. Uehlinger, G. Jotzu, S. Huber, D. Greif, and T. Esslinger. "Exploring Competing Density Order in the Ionic Hubbard Model with Ultracold Fermions". Phys. Rev. Lett. **115** (11 2015), 115303 (cit. on p. 216).

[295] E. Altman, E. Demler, and M. D. Lukin. "Probing many-body states of ultracold atoms via noise correlations". Phys. Rev. A **70** (1 2004), 013603 (cit. on pp. 216–218).

[296] L. Mathey, E. Altman, and A. Vishwanath. "Noise Correlations in One-Dimensional Systems of Ultracold Fermions". Phys. Rev. Lett. **100** (24 2008), 240401 (cit. on p. 218).

[297] C. Nayak. "Density-wave states of nonzero angular momentum". Phys. Rev. B **62** (8 2000), 4880 (cit. on p. 218).

[298] L. Mathey, A. Vishwanath, and E. Altman. "Noise correlations in low-dimensional systems of ultracold atoms". Phys. Rev. A **79** (1 2009), 013609 (cit. on p. 218).

[299] N. Bogoliubov. Nuovo Cimento **7** (1958), 794 (cit. on p. 219).

[300] J. Valatin. Nuovo Cimento **7** (1958), 843 (cit. on p. 219).

[301] L. Pitaevskii and S. Stringari. "Uncertainty principle, quantum fluctuations, and broken symmetries". Journal of Low Temperature Physics **85** (1991), 377 (cit. on p. 222).

[302] Y. Fujihara, A. Koga, and N. Kawakami. "Superfluid properties of ultracold fermionic atoms in two-dimensional optical lattices". Phys. Rev. A **81** (6 2010), 063627 (cit. on p. 222).

[303] A. Lüscher, R. M. Noack, and A. M. Läuchli. "Fulde-Ferrell-Larkin-Ovchinnikov state in the one-dimensional attractive Hubbard model and its fingerprint in spatial noise correlations". Phys. Rev. A **78** (1 2008), 013637 (cit. on p. 222).

[304] T. Paananen, T. K. Koponen, P. Törmä, and J.-P. Martikainen. "Noise correlations of the ultracold Fermi gas in an optical lattice". Phys. Rev. A **77** (5 2008), 053602 (cit. on p. 222).

[305] S. Zhang. "Pseudospin symmetry and new collective modes of the Hubbard model". Phys. Rev. Lett. **65** (1 1990), 120 (cit. on p. 227).

[306] S. Hoinka, P. Dyke, M. G. Lingham, J. J. Kinnunen, G. M. Bruun, and C. J. Vale. "Goldstone mode and pair-breaking excitations in atomic Fermi superfluids". Nature Physics **13** (2017), 943. arXiv: 1707.00406 [cond-mat.quant-gas] (cit. on p. 227).

[307] I. Fomin, P. Schmitteckert, and P. Wölfle. "Comment on "Pseudospin symmetry and new collective modes of the Hubbard model"". Phys. Rev. Lett. **69** (1 1992), 214 (cit. on p. 227).

[308] Y. Nagaoka. "Ferromagnetism in a Narrow, Almost Half-Filled s Band". Phys. Rev. **147** (1 1966), 392 (cit. on p. 230).

[309] S. Zhang. "Constraints on s-wave pairing in the Hubbard model". Phys. Rev. B **42** (1 1990), 1012 (cit. on p. 234).

[310] A. Moreo, D. Scalapino, and E. Dagotto. "Phase separation in the Hubbard model". Phys. Rev. B **43** (13 1991), 11442 (cit. on p. 234).

[311] H. Pichler, L. Bonnes, A. J. Daley, A. M. Läuchli, and P. Zoller. "Thermal versus entanglement entropy: a measurement protocol for fermionic atoms with a quantum gas microscope". New Journal of Physics **15** (2013), 063003 (cit. on p. 235).

[312] R. Islam, R. Ma, P. M. Preiss, M. E. Tai, A. Lukin, M. Rispoli, and M. Greiner. "Measuring entanglement entropy in a quantum many-body system". Nature **528** (2015), 77 (cit. on p. 235).

[313] G. Torlai, G. Mazzola, J. Carrasquilla, M. Troyer, R. Melko, and G. Carleo. "Neural-network quantum state tomography". Nature Physics (2018), 10.1038/s41567 (cit. on p. 235).

[314] C.-M. Chung, L. Bonnes, P. Chen, and A. M. Läuchli. "Entanglement spectroscopy using quantum Monte Carlo". Phys. Rev. B **89** (19 2014), 195147 (cit. on p. 235).

[315] R. Preuss, W. Hanke, and W. von der Linden. "Quasiparticle Dispersion of the 2D Hubbard Model: From an Insulator to a Metal". Phys. Rev. Lett. **75** (7 1995), 1344 (cit. on p. 236).

[316] P. W. Anderson, P. A. Lee, M Randeria, T. M. Rice, N Trivedi, and F. C. Zhang. "The physics behind high-temperature superconducting cuprates: the 'plain vanilla' version of RVB". Journal of Physics: Condensed Matter **16** (2004), R755 (cit. on p. 236).

[317] S. G. Ovchinnikov and V. V. Val'kov. *Hubbard Operators in the Theory of Strongly Correlated Electrons.* Imperial College Press, London, 2004 (cit. on p. 237).

[318] J. Hubbard. "Electron correlations in narrow energy bands - IV. The atomic representation". Proceedings of the Royal Society of London A: Mathematical, Physical and Engineering Sciences **285** (1965), 542. eprint: `http://rspa.royalsocietypublishing.org/content/285/1403/542.full.pdf` (cit. on p. 237).

[319] C. Noce and M. Cuoco. "Exact-diagonalization method for correlated-electron models". Phys. Rev. B **54** (18 1996), 13047 (cit. on p. 240).

[320] R. Schumann. "Thermodynamics of a 4-site Hubbard model by analytical diagonalization". Annalen der Physik **11** (2002), 49 (cit. on pp. 240, 254, 257).

[321] K. A. Kuns, A. M. Rey, and A. V. Gorshkov. "d". Phys. Rev. A **84** (6 2011), 063639 (cit. on pp. 240, 243).

[322] L. Chen and S. Moukouri. "Numerical renormalization-group study of the one-dimensional t-J model". Phys. Rev. B **53** (4 1996), 1866 (cit. on p. 241).

[323] M. Tinkham. *Group Theory and Quantum Mechanics.* McGraw-Hill, New York, 1964 (cit. on pp. 241–245).

[324] D. J. Scalapino and S. A. Trugman. "Local antiferromagnetic correlations and dx2-y2 pairing". Philosophical Magazine Part B **74** (1996), 607. eprint: `http://dx.doi.org/10.1080/01418639608240361` (cit. on p. 246).

[325] A. M. Rey, R. Sensarma, S. Fölling, M. Greiner, E. Demler, and M. D. Lukin. "Controlled preparation and detection of d-wave superfluidity in two-dimensional optical superlattices". EPL (Europhysics Letters) **87** (2009), 60001 (cit. on p. 258).

[326] T. Ying, R. Mondaini, X. D. Sun, T. Paiva, R. M. Fye, and R. T. Scalettar. "Determinant quantum Monte Carlo study of d-wave pairing in the plaquette Hubbard hamiltonian". Physical Review Letters **90**, 075121 (2014), 075121. arXiv: `1401.7226 [cond-mat.str-el]` (cit. on p. 258).

[327] H. Trotter. "On the product of semi-groups of operators". Proc. Am. Math. Soc. **10** (1959), 545–551 (cit. on p. 263).

Acknowledgments

I started my PhD in Stuttgart under the supervision of Prof. Dr. Alejandro Muramatsu whose unfortunate death came much too early. I learned a lot in many, also non-scientific aspects and I am grateful to him for that. I wish to thank Stefan Wessel for constant support after the death of Alejandro Muramatsu, an open ear, and for inviting me several times to the RWTH Aachen for discussions. I really appreciate that. Next I want to thank Hans Peter Büchler for taking over the official supervision from December 2015 onwards and thus giving me the opportunity to finish my PhD in Stuttgart. I am also thankful to Maria Daghofer for accepting to review my thesis.

During my PhD I have received help and inspiration from many different sides. I wish to thank Daniel Huerga for being an excellent colleague in difficult times, for many scientific discussions and also for careful proofreading of large parts of my thesis. I am equally grateful to Feiming Hu, who, with his priorities of "good sleep, hope, and a smile on your face" appeared unexpectedly to support our small team in a critical moment. His expertise was very important. It is also a pleasure to thank George Jackeli and Salvatore Manmana for interesting discussions and Zi Yang Meng for inviting me to visit his group in Beijing. I also thank Tommaso Roscilde for helpful discussions.

For an always friendly atmosphere and the nice conversations during lunchtime I want to thank all the members and fellow PhD students of the theory groups who I met here in Stuttgart: Alexander Moreno, Yuan Miao, Sebastian Weber, Przemyslaw Bienias, Krzysztof Jachymski, Thorsten Treffon, David Peter, Nicolai Lang, Jan Kumlin, Adam Bühler, Aditjya Venkata, Tobias Ilg, Kevin Kleinbeck, Luca Jibuti, Kai Guther, and Mirco Marahrens. A special thanks deserve David Peter and Nicolai Lang for keeping the IT infrastructure in excellent shape, from which I have profited. For the organizational part I thank Ildiko Polyak and Oliver Nagel, especially for taking charge of the "Reisekostenabrechnung".

Finally, I want to thank my family and friends for supporting me throughout these years and my brother for proofreading parts of this thesis.

Erklärung zur Dissertation

Hiermit erkläre ich, dass ich die von mir vorgelegte Dissertation mit dem Titel

"Quantum Monte Carlo Studies of Strongly Correlated Systems for Quantum Simulators"

selbständig verfasst, die benutzen Quellen und Hilfsmittel vollständig angegeben und Passagen der Arbeit - einschließlich Abbildungen -, die anderen Werken im Wortlaut oder sinngemäß entnommen sind, als solche in jedem Einzelfall kenntlich gemacht habe; dass ich diese Dissertation noch in keinem anderen Promotionsverfahren eingereicht habe und dass sie bis auf die angegebenen Teilpublikationen noch nicht veröffentlicht worden ist.

Stuttgart, 9. Mai 2018   Stephan Humeniuk

Publikationen

1. S. Humeniuk, *Quantum Monte Carlo Study of Long-range Transverse-Field Ising Models on the Triangular Lattice*, Phys. Rev. B **93**, 104412 (2016).

2. S. Humeniuk and H. P. Büchler, *Full Counting Statistics for Interacting Fermions with Determinantal Quantum Monte Carlo Simulations*, Phys. Rev. Lett. **119**, 236401 (2017).